

APPLICATION OF MICROSTRUCTURAL
ENGINEERING TO THE CONTROLLED COOLING
OF STEEL WIRE ROD

By

PETER CAMERON CAMPBELL

Dip.Eng., Saint Mary's University, 1981
B.Eng., Technical University of Nova Scotia, 1983
M.A.Sc., Technical University of Nova Scotia, 1984

A THESIS SUBMITTED IN PARTIAL FULFILLMENT

OF

THE REQUIREMENTS FOR THE DEGREE OF

DOCTOR OF PHILOSOPHY

in

THE FACULTY OF GRADUATE STUDIES

DEPARTMENT OF METALS AND

MATERIALS ENGINEERING

We accept this thesis as conforming
to the required standard

THE UNIVERSITY OF BRITISH COLUMBIA

January 1989

© Peter Cameron Campbell, 1989

In presenting this thesis in partial fulfilment of the requirements for an advanced degree at the University of British Columbia, I agree that the Library shall make it freely available for reference and study. I further agree that permission for extensive copying of this thesis for scholarly purposes may be granted by the head of my department or by his or her representatives. It is understood that copying or publication of this thesis for financial gain shall not be allowed without my written permission.

Department of METALS AND MATERIALS ENG.

The University of British Columbia
1956 Main Mall
Vancouver, Canada
V6T 1Y3

Date MARCH 9 / 1989

Abstract

The concept of microstructural engineering has been applied to Stelmor cooling of steel wire rod. The Stelmor process is situated immediately following the rod mill and utilizes forced air to cool steel rod from the rolling temperature, through austenite transformation, down to a temperature suitable for handling. A mathematical model has been developed for the prediction of the mechanical properties of the steel rod as a function of cooling parameters in the process and steel composition. The model is based on one-dimensional heat conduction within the rod and is limited to plain-carbon eutectoid and hypoeutectoid steels. Phase transformation kinetics in the model, for both the austenite-ferrite and austenite-pearlite reactions, have been characterized through the use of the Avrami equation. A combination of experimental and literature data have been employed for the development of equations to quantitatively predict the microstructure formed in the steel rod after transformation. A modified Gladman equation was adopted for the strength predictions.

Validation of the model has been achieved with controlled cooling experiments conducted in the laboratory. The experiments were designed to simulate the Stelmor process, involving a range of steel grades, rod diameters and air velocities. Thermal histories in steel rod samples during forced air cooling were acquired by mounting a thermocouple at the centreline of each rod. After cooling, the rod samples were subjected to microstructural examination and mechanical testing. Results from this investigation were utilized to develop relationships among steel composition, thermal history and ferrite fraction, ferrite grain diameter and pearlite interlamellar spacing. The laboratory data was also utilized to modify the strength predictions of the Gladman equation.

In order to obtain information on cooling conditions in an industrial setting, a series of experiments has been conducted on an operating Stelmor line at the No. 2 Rod Mill of Stelco Hilton Works. The technique followed in the plant trials was similar to that employed in the laboratory and the thermal histories of the test rods allowed the mathematical model to

be "tuned" to operating conditions. Mechanical properties for several industrial steel grades were also measured during the plant trials, and have been applied to test the predictive capability of the model.

Comparisons of the model-predicted thermal histories, microstructures and mechanical properties with those measured in both the laboratory and plant tests have been made. The results of the thermal history comparison for both laboratory and plant conditions showed good agreement between the model-predicted and measured centreline temperatures of control-cooled steel rod. Predicted temperatures during the austenite-ferrite and austenite-pearlite phase transformations were within the expected error associated with prediction of transformation kinetics. Good agreement was obtained between model-predicted and measured ferrite fraction, ferrite grain diameter and interlamellar pearlite spacing. Yield strengths and ultimate tensile strengths predicted by the model for the laboratory and plant tests displayed excellent agreement with measured strengths.

In order to obtain a test of the predictive capability of the model under Stelmor line conditions, an independent set of ultimate tensile strengths for Stelmor-cooled steel grades was obtained. These samples were taken directly from grades being processed on the line. A comparison between model-predicted and measured UTS for these grades yielded excellent agreement in the 1020-1040 and eutectoid composition range, with a fair prediction obtained for 1055-1065 grades.

Table of Contents

Abstract	ii
List of Tables	viii
List of Figures	x
List of Symbols	xxi
Acknowledgement	xxvi
Chapter 1 - INTRODUCTION	1
1.1 Wire Rod	1
1.2 The Stelmor Process	2
1.3 Microstructural Engineering	5
Chapter 2 - LITERATURE REVIEW	7
2.1 Isothermal Phase Transformations	7
2.1.1 Introduction	7
2.1.2 Theory	7
2.1.3 The Proeutectoid Ferrite Reaction	16
2.1.4 The Pearlite Reaction	19
2.2 Continuous Cooling Phase Transformations	23
2.2.1 Theory	23
2.2.2 Applications	29
2.2.2.1 Kirkaldy and Co-authors	29
2.2.2.2 Umemoto and Co-authors	35
2.2.2.3 Hawbolt, Brimacombe and Co-authors	39
2.2.2.4 Other Work	46
2.3 Structure/Property Relationships	50
2.3.1 Theory	50
2.3.2 Empirical Formulas	52
2.4 Scope and Objectives	56
Chapter 3 - MATHEMATICAL MODEL	59
3.1 Heat Flow Considerations	59
3.1.1 Model Formulation	59
3.1.2 Boundary Conditions	66
3.2 Phase Transformations	68
3.3 Microstructure-Properties	69

Chapter 4 - LABORATORY EXPERIMENTS	72
4.1 Rod Cooling Tests	72
4.1.1 Objectives and Introduction	72
4.1.2 Stelmor Simulator	72
4.1.3 Tube Furnace	74
4.1.4 Rod Sample Preparation	75
4.1.5 Experimental Procedure	77
4.1.6 Microstructural Evaluation	79
4.1.7 Mechanical Testing	81
4.1.8 Prior Austenite Grain Size Measurement	82
4.2 Transformation Kinetics	82
4.2.1 Equipment	83
4.2.2 Sample Preparation	84
4.2.3 Procedure	85
4.2.3.1 Isothermal Tests	85
4.2.3.2 Continuous-cooling Tests	86
4.2.4 Prior Austenite Grain Size Measurement	87
Chapter 5 - PLANT TRIALS EXPERIMENTS	89
5.1 Objectives and Introduction	89
5.2 Sample Preparation	89
5.3 Air Velocity Measurements	91
5.4 Thermal Response Measurement	92
5.5 Microstructural Evaluation	94
5.6 Mechanical Testing	96
5.7 Segregation Checks	97
Chapter 6 - LABORATORY RESULTS	99
6.1 Results of Rod Cooling Tests	99
6.1.1 Thermal History and Heat-Transfer Coefficients	99
6.1.2 Microstructures	108
6.1.2.1 Ferrite Fraction	109
6.1.2.2 Ferrite Grain Diameter	115
6.1.2.3 Pearlite Spacing	117
6.1.3 Mechanical Properties	119

6.2 Phase Transformation Kinetics Results	123
6.2.1 Isothermal Tests	123
6.2.1.1 Eutectoid Grades	123
6.2.1.2 Hypoeutectoid Grades	129
6.2.2 Continuous-Cooling Tests	139
6.3 Prior Austenite Grain Size Results	144
6.4 Regression Equations	144
6.4.1 Isothermal Tests	144
6.4.2 Continuous-Cooling Tests	149
Chapter 7 - RESULTS OF PLANT TRIALS	153
7.1 Air Velocities	153
7.2 Thermal History and Heat-Transfer Coefficients	154
7.2.1 Experimental Results	154
7.2.2 Regression Equations	168
7.3 Microstructure	170
7.3.1 Ferrite Fraction	170
7.3.1.1 Experimental Results	170
7.3.1.2 Regression Equations	176
7.3.2 Ferrite Grain Diameter	180
7.3.2.1 Experimental Results	180
7.3.2.2 Regression Equations	183
7.3.3 Pearlite Spacing	188
7.3.3.1 Experimental Results	188
7.3.3.2 Regression Equations	190
7.4 Mechanical Properties	194
7.4.1 Experimental Results	194
7.4.2 Regression Equations	198
7.4.2.1 Steels With > 50% Ferrite	201
7.4.2.2 Steels With < 50% Ferrite	204
7.5 Segregation	207
Chapter 8 - MODEL VALIDATION AND PREDICTIONS	209
8.1 Model Validation	209
8.2 Sensitivity Analysis	210
8.2.1 Heat Transfer Effects	210
8.2.2 Steel Composition Effects	227

8.2.3 Phase Transformation Kinetics Effects	235
8.2.4 Microstructural Effects	248
8.3 Model Predictions	251
8.3.1 Laboratory Tests	251
8.3.1.1 Thermal Histories	251
8.3.1.2 Microstructures	258
8.3.1.3 Mechanical Properties	261
8.3.2 Plant Trials	263
8.3.2.1 Thermal Histories	263
8.3.2.2 Microstructures	284
8.3.2.3 Mechanical Properties	287
8.3.3 Rods From Normal Plant Production	290
Chapter 9 - Summary and Conclusions	293
9.1 Summary	293
9.2 Conclusions	294
9.3 Future Work	295
References	297
Appendix 1	303
Appendix 2	309
Appendix 3	312
Appendix 4	319

List of Tables

<u>Table</u>	<u>Page</u>
3.1	Constants for use with Eq. (3.8). 67
4.1	Chemical analysis of rod samples used in laboratory experiments. 77
4.2	Summary of laboratory experiment grades, diameters and air velocities. 79
4.3	Summary of temperature ranges utilized in isothermal transformation kinetics tests. 86
4.4	Summary of cooling rates utilized for continuous cooling tests. 87
5.1	Chemical analysis of rods in plant trials. 90
5.2	Summary of grades, diameters and number of tests completed in plant trials. 94
5.3	Grades and diameters of material cut from production coils and tested mechanically. 96
6.1	Values of kinetic parameter n_p , determined for Steel B (1070) as a func- tion of isothermal transformation temperature. 127
6.2	Composition of two 1080 grades for comparison of transformation kinetics with Steel B (1070), in Fig. 6.18. 129
6.3	Values of kinetic parameter n_F and n_p , determined for Steel C (1038) as a function of isothermal transformation temperature. 134
6.4	Composition of 1040 grade used for comparison of transformation kinetics with Steel C in Figs. 6.22 (a) and (b). 134
6.5	Values for n_F and n_p , determined for Steel E (1020) as a function of isothermal transformation temperature. 139
6.6	Composition of 1025 grade used for comparison of transformation kinetics with Steel E in Figs. 6.24 (a) and (b). 139
6.7	Prior austenite grain sizes measured in laboratory and industrial steel rods. 144
6.8	Average n_F for Steels C and E, plus values for four grades from the literature. 145
7.1	Measured undercoolings and pearlite spacings in 1080 Steel A. 193
8.1	Mean values of parameters investigated in the sensitivity analysis of the mathematical model. 213

8.2	Variation in rod microstructure and strength as a function of parameters tested in the sensitivity analysis for 1080 steel.	216
8.3	Variation in rod microstructure and strength as a function of parameters tested in the sensitivity analysis for 1040 steel.	217
8.4	Variation in rod microstructure and strength as a function of parameters tested in the sensitivity analysis for 1017 steel.	218
8.5	Variation in rod strength as a function of changes in pearlite spacing for the 1080 steel.	249
8.6	Variation in rod strength as a function of changes in steel microstructure for the 1040 steel.	250
8.7	Variation in rod strength as a function of changes in steel microstructure for the 1017 steel.	251
8.8	Summary of Stelmor-line cooled, industrial rod grades and diameters employed for comparison with model UTS predictions.	290
A2.1	Results of mechanical tests on laboratory Steel C (1038).	309
A2.2	Results of mechanical tests on laboratory Steel B (1070).	310
A2.3	Results of mechanical tests on laboratory Steel D (1037).	310
A2.4	Results of mechanical tests on laboratory Steel E (1020).	311
A3.1	Results of mechanical tests on plant trials Steel C (1038).	312
A3.2	Results of mechanical tests on plant trials Steel E (1020).	313
A3.3	Results of mechanical tests on plant trials Steel F (1080).	314
A3.4	Results of mechanical tests on plant trials Steel G (1037).	315
A3.5	Results of mechanical tests on plant trials Steel H (1035).	316
A3.6	Results of mechanical tests on plant trials Steel I (1017).	317
A3.7	Results of mechanical tests on plant trials Steel J (1022).	318

List of Figures

<u>Figure</u>	<u>Page</u>
1.1 Schematic diagram of a Stelmor line [4]. A - Delivery pipe and water box, B - Laying head, C - Conveyor, D - Plenum chambers, E - Coil forming chamber.	4
2.1 Example of fraction transformed versus time for a first-order reaction.	9
2.2 Example of sigmoidal transformation kinetics; Avrami equation with $n=3$	13
2.3 Fe-C phase diagram depicting equilibrium concentrations for the formation of proeutectoid ferrite from austenite at temperature T_1	17
2.4 Diffusion field in austenite in front of growing proeutectoid ferrite. Concentrations refer to Fig. 2.3.	19
2.5 Formation of pearlite by repeated nucleation and edgewise and sidewise growth [17].	22
2.6 Graphical representation of the additivity rule. Path A-B-C is the course of transformation for temperature T_1 , and A-D-E is the path for temperature T_2 . The dashed line depicts the instantaneous change in temperature from T_1 to T_2 after fraction X_1 has transformed.	24
2.7 Graphical representation of the method employed by Kirkaldy [30] for calculation of the CCT-Start curve from the TTT-Start curve for the pearlite transformation.	32
2.8 Predicted and measured TTT diagrams from Kirkaldy and Venugopalan [36].	34
2.9 Predicted and measured CCT diagram from Kirkaldy and Venugopalan [36].	35
2.10 Predicted and measured fraction of martensite in a Jominy end-quench bar as a function of distance from the quenched end, from Umemoto <i>et al.</i> [27].	36
2.11 Thermal histories for steel rods predicted and measured by Agarwal and Brimacombe [23]. Also included in the figure are plots of predicted pearlite fraction transformed versus time.	40
2.12 Measured values for n and b calculated from (a) $t=0$ at T_{A_1} and (b) $t=0$ at t_{AV-TTT} , from Hawbolt <i>et al.</i> [24].	42
2.13 Measured and predicted fraction of pearlite transformed versus time for four cooling rates from Hawbolt <i>et al.</i> [24]; (a) 7.5°C/s, (b) 20.0°C/s.	43
2.14 Measured values for n and b used in the Avrami equation, for 1025, 1040 and 1060 steel [25,42]; (a) n_F , (b) n_P , (c) lnb_F and (d) lnb_P	44

2.15	Method for determining pearlite start temperature during cooling of hypoeutectoid steel from Suehiro <i>et al.</i> [48]. The A and B lines represent the change in carbon concentration in the retained austenite for two different cooling rates.	49
2.16	Effect of solid-solution elements on the strength of ferrite [52].	51
2.17	Predicted and measured values of the lower yield stress, plotted as a function of the product of ferrite fraction and square root of ferrite diameter, by Kouwenhoven [54].	53
2.18	Predicted (a) yield and (b) ultimate strengths, calculated from the Gladman equations [55], plotted as a function of the measured values.	55
3.1	Thermal conductivity as a function of temperature; (a) austenite with various carbon contents, (b) ferrite and pearlite [59].	61
3.2	Specific heat as a function of temperature: (a) austenite with various carbon contents, (b) pearlite [59].	62
3.3	Specific heat as a function of temperature for ferrite [59-62].	63
3.4	Latent heat of transformation calculated for the two austenite decomposition reactions as a function of temperature; (a) austenite-pearlite and (b) austenite-ferrite.	65
3.5	Mean and minimum measured pearlite spacings as a function of undercooling below T_{A1} from the literature [70-75].	71
4.1	Schematic diagram of the air delivery system for the Stelmor cooling simulation experiments.	73
4.2	Velocity profiles for three blower pressures. Note the constant velocity across the width of the duct.	74
4.3	Schematic diagram of method employed to mount thermocouples at centreline position in rods for Stelmor simulation tests.	76
4.4	Diagram showing test rod in position under constant velocity duct for typical cooling test. Thermocouple leads are connected to a chart recorder and data logger.	78
4.5	Schematic diagram of dilatometer apparatus utilized for phase transformations experiments.	84
5.1	Schematic diagram of one zone of the Stelmor line demonstrating the direction of air flow through the bed.	91
5.2	Layout of section from Stelmor line showing locations for air velocity measurements.	92
5.3	Schematic diagram depicting the variation in rod packing at the centre and edge of the Stelmor line.	93

6.1	Typical thermal history measured in 11-mm diameter rod (Steel D 1037), cooled with an air velocity of 22 m/s under laboratory conditions.	99
6.2	Thermal history measured at rod centreline in laboratory cooling tests on Stelmor simulator; (a) Steel B (1070), (b) Steel C (1038), (c) Steel D (1037) and (d) Steel E (1020).	100
6.3	Heat-transfer coefficients calculated from the measured thermal histories at the rod centreline in laboratory tests, with both a finite-difference and lumped-parameter technique; (a) rod B4 - 15 mm diameter, 9 m/s air velocity, (b) rod B9 - 8 mm diameter, 22 m/s air velocity.	104
6.4	Measured heat-transfer coefficients plotted against $(\text{air velocity})^{0.466}/(\text{rod diameter})^{0.534}$ according to Eq. (6.4). The line shown is the prediction based on combined radiative and convective cooling (Eqs. (3.8) and (3.9)). Heat-transfer coefficients measured at (a) 800°C, (b) 725°C, (c) 525°C.	106
6.5	Heat-transfer coefficients plotted against $(\text{air velocity})^{0.466}/(\text{rod diameter})^{0.534}$ according to Eq. (6.4). Values have been calculated from rod cooling rates due to Hanada <i>et al.</i> [83].	108
6.6	Measured ferrite fraction versus cooling rate at 750°C; (a) Steel B (1070), (b) Steel C (1037) and (c) Steel E (1020).	110
6.7	Typical photomicrographs taken on the image analyzer (a) Steel B (1070), (b) Steel C (1038) and (c) Steel E (1020)	112
6.8	Measured ferrite grain diameter versus cooling rate at 750°C; (a) Steel B (1070), (b) Steel C (1038) and (c) Steel E (1020).	115
6.9	Measured and predicted pearlite spacing plotted against the undercooling below T_{A1} for Steel B (1070).	117
6.10	Typical SEM micrograph of Steel B (1070), displaying pearlite colonies.	118
6.11	Measured strengths of laboratory Steel B (1070) plotted against the average cooling rate at 750°C, (a) yield strengths, (b) ultimate strengths.	120
6.12	Measured strengths of laboratory Steels C (1038) and D (1037) plotted against the average cooling rate at 750°C, (a) yield strengths, (b) ultimate strengths.	121
6.13	Measured strengths of laboratory Steel E (1020) plotted against the average cooling rate at 750°C, (a) yield strengths, (b) ultimate strengths.	122
6.14	Typical dilatometer response and thermal history for phase transformation kinetics experiments. Dilatometer output has been scaled to match sample temperature. Data is for 1070 Steel B with an isothermal temperature of 663°C.	124

6.15	Diagrams displaying technique for converting dilatometer response to fraction transformed. (a) Dilatometer response showing values of D_{MIN} , D_{MAX} and D_T , (b) Data after conversion to fraction transformed versus time.	125
6.16	Linearization of the Avrami equation demonstrating the procedure applied for determining the constants n and b	126
6.17	Fraction transformed-versus-time for Steel B (1070) under isothermal conditions. The isothermal temperature is included adjacent to each curve.	127
6.18	Natural logarithm of b_p plotted against undercooling below T_{A1} for Steel B and two grades from the literature [24,66].	128
6.19	Dilatometer response-versus-time for two isothermal tests on 1038 Steel C contrasting the shape and magnitude of the curve for an austenite-ferrite only and an austenite-ferrite-pearlite transformation.	130
6.20	Figure depicting the method followed for separating the isothermal dilatometer-versus-time curve into two transformation events.	132
6.21	Fraction transformed-versus-time for Steel C (1038) under isothermal conditions. The isothermal temperature is included adjacent to each curve. (a) 723 to 693°C and (b) 683 to 643°C.	133
6.22	Natural logarithm of kinetic parameter b plotted against undercooling for Steel C (1038). Also included are data due to Hawbolt <i>et al.</i> [42]. (a) $\ln b_p$ against undercooling below T_{A3} and (b) $\ln b_p$ against undercooling below T_{A1}	135
6.23	Fraction transformed-versus-time for Steel E (1020) under isothermal conditions. The isothermal temperature is included adjacent to each curve. (a) 767 to 722°C and (b) 711 to 650°C.	137
6.24	Natural logarithm of kinetic parameter b plotted against undercooling for Steel E (1020). Also included are data due to Hawbolt <i>et al.</i> [25]. (a) $\ln b_p$ against undercooling below T_{A3} and (b) $\ln b_p$ against undercooling below T_{A1}	138
6.25	(a) Measured sample thermal history and (b) measured dilatometer response plotted as a function of time for 1038 Steel C (CCT Test #4). ..	141
6.26	Measured sample dilation minus dilation due to temperature change, plotted against total time. Transformation start time is indicated by the time at which the curve deviates from a constant value.	142
6.27	Measured CCT ferrite start times for Steels C (1038) and E (1020), plotted with start times for hypoeutectoid grades from the literature [25,42].	143

6.28	Measured CCT start temperatures for Steel B (1070), plotted against the time below T_{A_1} . Also included are start times for other eutectoid grades [24,66].	143
6.29	Measured values of n_p for both laboratory and literature steels, plotted as a function of the carbon content. Also included in the figure is the prediction of n based on Eq. (6.8).	146
6.30	Natural logarithm of b_F plotted as a function of undercooling below T_{A_3} for both laboratory and literature steels. The lines represent the predicted average $\ln b_F$ based on Eq. (6.9).	147
6.31	Natural logarithm of b_p (hypoeutectoid grades) plotted as a function of undercooling below T_{A_1} for both laboratory and literature steels. The lines represent the predicted $\ln b$ for Steels C and E based on Eq. (6.10).	148
6.32	Natural logarithm of b_p (eutectoid grades) plotted as a function of undercooling below T_{A_1} for both laboratory and literature steels. The line represents the predicted $\ln b$ based on Eq. (6.11).	149
6.33	Measured and predicted CCT start times for Steels C (1038) and E (1020), plotted against time below T_{A_3} . The lines plotted in the figure are based on Eq. (6.12).	150
6.34	Measured and predicted CCT start temperatures for pearlite in Steels C (1038) and E (1020), plotted against the time below T_{A_1} . The lines plotted in the figure are based on Eq. (6.13).	151
6.35	Measured and predicted CCT start temperatures for Steel B (1070), plotted against the time below T_{A_1} . The lines plotted are based on Eq. (6.14).	152
7.1	Average air velocities measured on Stelmor Lines 2 and 3. Grey area indicates \pm one standard deviation for the measurements.	154
7.2	Thermal history measured at rod centreline in plant cooling tests, for 15-mm diameter rods; (a) 1038 Steel C and (b) 1020 Steel E.	155
7.3	Thermal history measured at rod centreline in plant cooling tests, for 9.1-mm diameter rods; (a) 1080 Steel F, (b) 1037 Steel G and (c) 1017 Steel I.	156
7.4	Thermal history measured at rod centreline in plant cooling tests, for 7.5-mm diameter rods; (a) 1080 Steel F, (b) 1035 Steel H and (c) 1022 Steel J.	157
7.5	Thermal history measured at rod centreline for plant trials cooled without production coils on the Stelmor bed.	160

7.6	Measured heat-transfer coefficients for plant full air tests, plotted against (air velocity) ^{0.466} /(rod diameter) ^{0.534} according to Eq. (6.4). The line included is the predicted value based on convection only. Heat-transfer coefficients measured at (a) 800°C, (b) 750°C, (c) 700°C, (d) 550°C and (e) 450°C.	162
7.7	Measured heat-transfer coefficients for plant zero air tests, plotted against (air velocity) ^{0.466} /(rod diameter) ^{0.534} according to Eq. (6.4). The line included is the predicted value based on convection only. Heat-transfer coefficients measured at (a) 800°C, (b) 750°C, (c) 700°C and (d) 550°C.	164
7.8	Measured heat-transfer coefficients for plant trials without production coils on the Stelmor line, plotted against (air velocity) ^{0.466} /(rod diameter) ^{0.534} according to Eq. (6.4). The line included is the predicted value based on convection and radiation. Heat-transfer coefficients measured at (a) 800°C, (b) 700°C and (c) 450°C.	166
7.9	Calculated values for radiative heat-transfer coefficients from the plant trials, plotted against temperature. Also included is the predicted value from Eq. (3.9).	169
7.10	Radiation Correction Factor "RCF" for centre and edge of bed plotted against temperature. Lines are calculated from the regression equation for both parameters (Eqs. (7.2a) and (7.2b)).	169
7.11	Measured ferrite fractions for plant trial steels plotted against the average cooling rate at 750°C, (a) Steel F (1080), (b) Steels C (1038), G (1037) and H (1035), and (c) Steels E (1020), I (1017) and J (1022).	171
7.12	Typical photomicrographs taken on the image analyzer; (a) Steel F (1080), (b) Steel G (1037) and (c) Steel J (1022).	173
7.13	Ferrite fraction obtained in all laboratory and plant-trial steels plotted as a function of cooling rate measured at 750°C. (a) near-eutectoid grades, (b) 1035-1038 grades and (c) 1017-1022 grades.	177
7.14	Predicted versus measured ferrite fraction for near-eutectoid steels. Predicted values are calculated based on Eq. (7.4).	179
7.15	Predicted versus measured ferrite fraction for hypoeutectoid steels. Predicted values are calculated using Eq. (7.5).	180
7.16	Measured ferrite grain diameters for plant trial steels plotted against the average cooling rate at 750°C; (a) Steel F (1080), (b) Steels C (1038), G (1037) and H (1035), and (c) Steels E (1020), I (1017) and J (1022).	181
7.17	Ferrite grain diameter in all laboratory and plant-trial steels plotted as a function of cooling rate measured at 750°C; (a) near-eutectoid grades, (b) 1035-1038 grades and (c) 1017-1022 grades.	184
7.18	Ferrite grain diameter versus cooling rate for steel grades from the literature; (a) 0.18 %C, 1.3 %Mn steel from Choquet <i>et al.</i> [85] and (b) 0.15 %C, 0.4 %Mn steel from Tamura [38].	186

7.19	Predicted versus measured ferrite grain diameters for near-eutectoid steels. Predicted values are calculated using Eq. (7.6).	187
7.20	Predicted versus measured ferrite grain diameters for hypoeutectoid steels. Predicted values are calculated using Eq. (7.7).	188
7.21	Measured and predicted pearlite spacings for plant trial steels plotted against the average undercooling below T_{A1} . The line is based on a best-fit from Pellisier <i>et al.</i> 's data and the shaded area indicates \pm one standard deviation from the best-fit line. (a) Steel F (1080) and (b) Steel H (1035).	189
7.22	Typical micrograph from SEM of steel microstructure displaying pearlite colonies in (a) Steel F (1080) and (b) Steel H (1035).	191
7.23	Reciprocal pearlite spacing plotted against the undercooling below T_{A1} for experimental and literature steels. The best-fit line is based on Eq. (7.8).	193
7.24	Measured strengths of plant trial Steel F (1080) plotted against the average cooling rate at 750°C; (a) yield strength and (b) ultimate strength.	195
7.25	Measured strengths of plant trial Steels C (1038), G (1037) and H (1035) steels plotted against the average cooling rate at 750°C; (a) yield strength and (b) ultimate strength.	196
7.26	Measured strengths of plant trial Steels E (1020), I (1017) and J (1022), plotted against the average cooling rate at 750°C; (a) yield strength and (b) ultimate strength.	197
7.27	Predicted-versus-measured strength for laboratory and plant trial rods, as determined from the Gladman equations (Eqs. (2.58) and (2.59)); (a) yield strength and (b) ultimate tensile strength.	199
7.28	Predicted-versus-measured yield strength for steels containing greater than 50% ferrite. Predicted values are based on Eq. (7.9).	202
7.29	Predicted-versus-measured ultimate tensile strength for steels containing greater than 50% ferrite. Predicted values are based on Eq. (7.10).	203
7.30	Predicted-versus-measured yield strength for steels containing less than 50% ferrite. Predicted values are based on Eq. (7.11).	206
7.31	Predicted-versus-measured ultimate tensile strength for steels containing less than 50% ferrite. Predicted values are based on Eq. (7.12).	207
8.1	Analytical and model-predicted solution for thermal response at the surface and centreline of a steel rod during cooling. (a) 15-mm diameter rod with $h=150\text{W/m}^2\text{C}$ and (b) 5.5-mm diameter rod with $h=250\text{W/m}^2\text{C}$	211

8.2	Model-predicted thermal histories for the 1080, 1040 and 1017 steel grades employed in the sensitivity analysis.	212
8.3	Effect of variation in rod diameter on the model-predicted thermal history of 10-mm diameter steel rod. (a) 1080 steel, (b) 1040 steel and (c) 1017 steel.	214
8.4	Effect of variation in cooling air velocity on the model-predicted thermal history of 10-mm diameter steel rod. (a) 1080 steel, (b) 1040 steel and (c) 1017 steel.	219
8.5	Effect of variation in heat-transfer coefficient on the model-predicted thermal history of 10-mm diameter steel rod. (a) 1080 steel, (b) 1040 steel and (c) 1017 steel.	221
8.6	Effect of variation in ambient air temperature on the model-predicted thermal history of 10-mm diameter steel rod. (a) 1080 steel, (b) 1040 steel and (c) 1017 steel.	223
8.7	Effect of variation in latent heat of phase transformation on the model-predicted thermal history of 10-mm diameter steel rod. (a) 1080 steel, (b) 1040 steel and (c) 1017 steel.	225
8.8	Effect of variation in carbon content on the model-predicted thermal history of 10-mm diameter steel rod. (a) 1080 steel, (b) 1040 steel and (c) 1017 steel.	228
8.9	Effect of variation in manganese content on the model-predicted thermal history of 10-mm diameter steel rod. (a) 1080 steel, (b) 1040 steel and (c) 1017 steel.	231
8.10	Effect of variation in silicon content on the model-predicted thermal history of 10-mm diameter steel rod. (a) 1080 steel, (b) 1040 steel and (c) 1017 steel.	233
8.11	Effect of variation in CCT-start time for ferrite on the model-predicted thermal history of 10-mm diameter steel rod. (a) 1040 steel and (b) 1017 steel.	236
8.12	Effect of variation in CCT-start time for pearlite on the model-predicted thermal history of 10-mm diameter steel rod. (a) 1080 steel, (b) 1040 steel and (c) 1017 steel.	237
8.13	Effect of variation in n_F on the model-predicted thermal history of 10-mm diameter steel rod. (a) 1040 steel and (b) 1017 steel.	240
8.14	Effect of variation in n_p on the model-predicted thermal history of 10-mm diameter steel rod. (a) 1080 steel, (b) 1040 steel and (c) 1017 steel.	241
8.15	Effect of variation in b_F on the model-predicted thermal history of 10-mm diameter steel rod. (a) 1040 steel and (b) 1017 steel.	243
8.16	Effect of variation in b_p on the model-predicted thermal history of 10-mm diameter steel rod. (a) 1080 steel, (b) 1040 steel and (c) 1017 steel.	244

8.17	Effect of variation in prior austenite grain size on the model-predicted thermal history of 10-mm diameter steel rod. (a) 1080 steel, (b) 1040 steel and (c) 1017 steel.	247
8.18	Measured and model-predicted thermal response at the centreline of a steel rod for Steel B (1070). (a) Test B3, 15-mm diameter, 11 m/s air velocity, (b) Test B7, 11-mm diameter, 10 m/s air velocity and (c) Test B9, 8-mm diameter, 22 m/s air velocity.	252
8.19	Measured and model-predicted thermal response at the centreline of a steel rod for Steel C (1038). (a) Test C3, 11-mm diameter, 10 m/s air velocity, (b) Test C7, 8-mm diameter, 6 m/s air velocity and (c) Test C5, 8-mm diameter, 22 m/s air velocity.	254
8.20	Measured and model-predicted thermal response at the centreline of a steel rod for Steel E (1020). (a) Test E4, 11-mm diameter, 6 m/s air velocity, (b) Test E7, 8-mm diameter, 6 m/s air velocity (c) Test E5, 8-mm diameter, 22 m/s air velocity.	256
8.21	Model-predicted-versus-measured ferrite fractions for Steels B (1070), C (1038) and E (1020), from the laboratory experiments. The shaded area in the figure indicates \pm one standard deviation of the predicted value.	258
8.22	Model-predicted-versus-measured ferrite grain diameters for Steels B (1070), C (1038) and E (1020), from the laboratory experiments. The shaded area in the figure indicates \pm one standard deviation of the predicted value.	259
8.23	Model-predicted-versus-measured mean interlamellar pearlite spacings for Steels B (1070), C (1038) and E (1020), from the laboratory experiments. The shaded area represents approximately the \pm one standard deviation in the predicted value.	260
8.24	Model-predicted strengths plotted as a function of measured strengths from the laboratory tests; (a) yield strength and (b) ultimate tensile strength.	262
8.25	Measured and model-predicted thermal history for Steel C (1038), 15-mm diameter rods cooled in plant tests. (a) Test C55, centre - "air on", (b) Test C57, edge - "air on", (c) Test C61, centre - "air off" and (d) Test 62, edge - "air off".	264
8.26	Measured and model-predicted thermal history for Steel E (1020), 15-mm diameter rods cooled in plant tests. (a) Test E55, centre - "air on", (b) Test E56, edge - "air on" and (c) Test E51, centre - "air off".	267
8.27	Measured and model-predicted thermal history for Steel F (1080), 9.1-mm diameter rods cooled in plant tests. (a) Test F56, centre - "air on" and (b) Test F60, edge "air on".	269
8.28	Measured and model-predicted thermal history for Steel G (1037), 9.1-mm diameter rods cooled in plant tests. (a) Test G56, centre - "air on", (b) Test G60, edge - "air on" and (c) Test G57, centre - "air off".	270

8.29	Measured and model-predicted thermal history for Steel I (1017), 9.1-mm diameter rods cooled in plant tests. (a) Test I56, centre - "air on", (b) Test I53, edge - "air on", (c) Test I60, centre - "air off" zone 1, "air on" remaining zones and (d) Test I52, edge - "air off" zone 1, "air on" remaining zones.	273
8.30	Measured and model-predicted thermal history for Steel F (1080), 7.5-mm diameter rods cooled in plant tests. (a) Test F71, centre - "air on", (b) Test F77, edge - "air on", (c) Test F73, centre - "air off" and (d) Test F72, edge - "air off".	276
8.31	Measured and model-predicted thermal history for Steel H (1035), 7.5-mm diameter rods cooled in plant tests. (a) Test H55, centre - "air on", (b) Test H57, centre - "air on" zone 1, "air off" zones 2 and 3, "air on" zone 4 and (c) Test H60, centre - "air off" zone 1, "air on" zones 2 to 4.	279
8.32	Measured and model-predicted thermal history for Steel J (1022), 7.5-mm diameter rods cooled in plant tests. (a) Test J59, centre - "air on", (b) Test J60, edge - "air on", (c) Test J51, centre - "air on" zone 1, "air off" zones 2 and 3, "air on" zone 4 and (d) Test J58, centre - "air off" zone 1, "air on" zones 2 to 4.	282
8.33	Model-predicted-versus-measured ferrite fractions for Steels C (1038), E (1020), F (1070), G (1037), H (1035), I (1017) and J (1022) from the plant trials. The shaded area in the figure indicates \pm one standard deviation of the predicted value.	285
8.34	Model-predicted-versus-measured ferrite grain diameters for Steels C (1038), E (1020), F (1070), G (1037), H (1035), I (1017) and J (1022) from the plant trials. The shaded area in the figure indicates \pm one standard deviation of the predicted value.	286
8.35	Model-predicted-versus-measured pearlite spacing for Steels C (1038), E (1020), F (1070), G (1037), H (1035), I (1017) and J (1022) from the plant trials. The shaded area in the figure indicates \pm one standard deviation of the predicted value.	287
8.36	Model-predicted strengths plotted as a function of measured strengths from the plant trials; (a) yield strength and (b) ultimate tensile strength.	289
8.37	Model-predicted-versus-measured ultimate tensile strength of industrial Stelmor-cooled rod. The shaded area in the figure indicates \pm one standard deviation of the predicted value.	291
A1.1	Diagram depicting the central node used for development of the finite difference equations.	304
A1.2	Diagram depicting the general internal node used for development of the finite difference equations.	305

A1.3	Diagram depicting the surface node used for development of the finite difference equations.	307
A4.1	Manganese concentrations measured by EPMA, as a function of position in the rod. The dashed line represents the results of the spectrographic analysis.	319

List of Symbols

b	Kinetic parameter in Avrami Equation (2.17)
b_F	Kinetic parameter for ferrite in Avrami Equation (2.17)
b_P	Kinetic parameter for pearlite in Avrami Equation (2.17)
b_v	Burgers vector
Bi	Biot number
C	Empirical constant used in Equation (3.7)
C_i	Concentration of species i , moles/m ³
C_p	Specific heat, Ws/kg°C
CR	Average rod cooling rate, °C/s
CVD	Constant velocity duct
d	Grain diameter, m
d_γ	Prior austenite grain diameter, m
d_α	Ferrite grain diameter, m
D	Rod diameter, m
D_B	Grain boundary diffusion coefficient, m ² /s
D_C	Diffusion coefficient of carbon, m ² /s
D_{DIL}	Dilatometer response, mV
D_{MAX}	Maximum dilatometer reading after transformation, mV
D_{MIN}	Minimum dilatometer reading prior to transformation, mV
$D_{THERMAL}$	Dilatometer response due to a temperature change, mV
D_T	Dilatometer change due to phase transformation, mV
D_V	Grain volume diffusion coefficient, m ² /s
f_α	Volume fraction of ferrite
$f_{\alpha Eq}$	Equilibrium ferrite fraction
f_P	Volume fraction of pearlite

Fo	Fourier number
G	Growth rate, m/s
Gr	Grashof number
ΔG_C	Critical free energy for nucleation, ergs
G_S	Grain boundary surface energy, ergs/m ²
G_V	Grain boundary volume energy, ergs/m ³
h	Heat-transfer coefficient, W/m ² ·°C
h_c	Heat-transfer coefficient due to convection, W/m ² ·°C
h_{ov}	Overall heat-transfer coefficient, W/m ² ·°C
h_r	Heat-transfer coefficient due to radiation, W/m ² ·°C
ΔH_i	Enthalpy of the austenite-ferrite or austenite-pearlite phase transformation, J/kg
I	Nucleation rate, number of nuclei/m ³ ·s
I_C, I_E, I_S	Nucleation rate at the grain corner, edge and surface, respectively, number of nuclei/m ³ ·s
INT	Symbol used to represent integral in Equation (2.39)
J_0, J_1	Bessel functions of the first kind, orders zero and one
k	Thermal conductivity, W/m·°C
K	Rate constant
K_b	Constant used in Equation (2.55)
K_E	Constant used in Equation (2.44)
K_Y	Constant used in Equation (2.56)
L	Line tension of a dislocation, m
\bar{L}	Characteristic length, m
m	Kinetic parameter in modified Avrami Equation (2.43)
n	Kinetic parameter in Avrami Equation (2.17)
n_F	Kinetic parameter for ferrite in Avrami Equation (2.17)
n_P	Kinetic parameter for pearlite in Avrami Equation (2.17)

N	Number of nucleation sites per unit volume
N_f	Dislocation density, number/m ³
N_0	Original number of nucleation sites per unit volume
Nu	Nusselt number
p	Empirical constant used in Equation (3.7)
Pr	Prandtl number
q	Heat flow rate, W, and kinetic parameter dependent on the mode of diffusion in Equation (2.39)
q_{TR}	Heat released during phase transformation, W
Q	Activation energy, cal/mole
r	Radius, m
r_s	Original rod radius, m
r_i	Radius at node i , m
R	Gas constant, cal/°C·mole
RCF_C	Radiation correction factor for centre of the Stelmor line
RCF_E	Radiation correction factor for edge of the Stelmor line
Re	Reynolds number
$\%RA$	%Reduction in area
S	Half-thickness, m
S, S_E, S_N	Variables used to represent the logarithms of time in Equation (2.50)
S_A	Apparent interlamellar pearlite spacing, m
S_p	Mean interlamellar pearlite spacing, m
t	Time, s
Δt	Time step, s
t_{AV-TTT}	Empirically determined TTT start time, s
t_C	Time relative to position of TTT curve in Equation (2.44), s
t_{CCT-F}	Empirically determined CCT start time for ferrite transformation, s

t_{CCT-P}	Empirically determined CCT start time for pearlite transformation, s
t_S, t_F	Transformation start and finish time in Equation (2.51), s
t_0	Time required for 50% transformation at the TTT nose temperature in Equation (2.45), s
$t_{0.2}$	Time to reach 0.2 fraction transformed, s
$t_{0.5}$	Time to reach 0.5 fraction transformed, s
$t_{0.9}$	Time to reach 0.9 fraction transformed, s
T	Temperature, °C
ΔT	Temperature change, °C
T_A	Ambient temperature, °C
T_E	Equilibrium temperature, °C
T_0	Initial temperature, °C
T_N	Nose temperature of C-curve, °C
T_S	Surface temperature, °C
T_{A3}	Austenite-ferrite equilibrium transformation temperature, °C
T_{A1}	Austenite-pearlite equilibrium transformation temperature, °C
T_{Acm}	Austenite-carbide equilibrium transformation temperature, °C
U, U_E, U_N	Variables used to represent inverse temperature in Equation (2.50), °C ⁻¹
UTS	Ultimate tensile strength, MPa
v_τ	Volume of particle formed at time τ , m ³
v	Air velocity, m/s
v_∞	Bulk air velocity, m/s
V	Volume, m ³
V_e	Extended volume, m ³
w	Cooling rate, °C/s

w_U, w_L	Upper and lower critical cooling rates in Equations (2.46) and (2.47)
x	Empirical constant used in Equation (3.7) and symbol denoting undercooling below equilibrium temperature, °C
X	Fraction transformed and distance, m
YS	Yield strength, MPa
τ	Incubation time, s
ν	Nucleation frequency, number of nuclei/s
α	Symbol denoting ferrite
β	Symbol denoting any beta phase
γ	Symbol denoting austenite
γ_n	Root of transcendental equation times rod radius, Equation (8.1)
$\Delta\phi$	Incremental angle used in nodal equations
λ	Particle spacing, m
λ_n	Characteristic root of Bessel function
σ_S	Yield strength of the matrix, MPa
σ_f	Flow stress, MPa
σ_i	Friction stress, MPa
σ_{LY}	Lower yield stress, MPa
ρ	Density, kg/m ³
σ	Stefan-Boltzman constant, $5.67 \cdot 10^{-8}$ W/m ² ·°C
ε	Emissivity
θ	Virtual time, s
μ	Kinematic viscosity, N·m ²
ψ_B	Grain boundary velocity, m/s

Acknowledgement

I would like to express my sincere thanks to Professors E.B. Hawbolt and J.K. Brimacombe for their patience and guidance throughout the course of the work. The assistance of Mr. Binh Chau during the transformation kinetics study and other parts of the work was invaluable and also warrants a note of thanks. Much of the equipment required for the experimental aspect of the thesis could not have been built without the advice and help of Mr. Bob Butters and Mr. Pat Wenman. Discussions and consultation on the workings of Manuscript™ with Professor A. Poursartip are very much appreciated.

I would like to thank Stelco Inc. for their financial assistance and cooperation throughout the plant trials. In particular, Mr. Jim Lait, Mr. Dave Overby, Mr. Simon Roberts and Mr. Peter Dalgleish were instrumental in preparation and implementation of the plant trials, and I thank them for their help. The information supplied by Ms. Mary Wells, on the various aspects of the Stelmor process is also appreciated.

The encouragement from and informal discussions with several fellow grad students in the department cannot go without acknowledgement; in particular Barry "Dash" Wiskel, Steve "Stevie Ray Slag" Cockcroft, Dave "Dr. Digital" Tripp, Andrew "The Shaker" Shook, Nigel Tuffrey, Rajeev Kamat, and R.B. Mahapatra.

I'd like to express my gratitude for the support, financial and otherwise, shown by my parents and family. They have been a source of wisdom and strength throughout my university studies.

Finally, the confidence and encouragement provided by Kathy Nolan has made this possible.

Chapter 1 - INTRODUCTION

1.1 Wire Rod

Steel wire rod is perhaps one of the most versatile products of a modern steelmaking facility. Ranging from 5.5 to 13.5 mm in diameter, wire rod is manufactured for a multitude of applications, including nails, bolts, tire cord, welding rod, wire rope, bicycle spokes, wire netting and other forms that are commonly found in automobiles, industrial equipment and electrical appliances. Subsequent processing for wire rod includes rolling, drawing, extruding and cold heading.

Steel wire rod can be grouped into two main categories; plain-carbon and alloy steel grades. Plain-carbon wire rods can be divided further, into the five subsections included below [1].

- (1) **Standard Quality** - Rods may contain up to 0.23 %C maximum and are used for a wide variety of products.
- (2) **Cold Finished Bar Quality** - Rods are rolled from steel grades intended for producing straightened and cut bars with good machining properties.
- (3) **Medium High Carbon and High Carbon Quality** - Rods with greater than 0.23 %C and intended for higher strength applications such as tire bead and mechanical springs.
- (4) **Welding Quality** - Rods are produced from special grades with close control of steel composition.
- (5) **Cold Heading Quality** - Rods are intended for the production of wire which will be rolled, extruded or headed. Thus, removal of seams in the billet prior to rolling is critical.

Production of steel wire rod begins in the rod mill, with square billets (usually ~100 mm square of varying length). The first step is to heat the billets up to a temperature suitable for rolling (~1260°C). Rolling of the billet to the final dimensions can take place in as many as 23 stands, with speeds for small diameter rods exiting the final finishing stand, reaching

55 m/s. A water box is situated after the finishing mill to bring the rod to an intermediate temperature prior to continuous cooling. In the water box (or boxes), high pressure water is forced against the surface of the rod to remove scale and provide rapid cooling. Owing to the high speed of the material, typical residence times in the water box are fractions of a second. The water box also controls the temperature at which the rod is supplied to the rod cooling apparatus. In the past, rods were coiled into bundles and allowed to cool unassisted, as the material was subjected to a lead patenting process in which desired properties could be imparted to the rod, prior to wire drawing etc.. The lead patenting process consists of heating of steel rod into the austenitic range, then placing it into a molten lead bath, usually at 500 to 600°C. In effect, the process provides an initial rapid cooling rate, leading to an isothermal treatment at which the austenite decomposition reactions take place. By controlling the temperature of the lead bath, the cooling rate and isothermal transformation temperature of the steel can be controlled. More recently, for both economic and health related reasons, heat treatment of the wire rod directly after rolling has become standard in the industry. Various media have been employed to assist in the extraction of heat from the rods, in order to provide steel microstructures and mechanical properties, resembling those of lead patenting. Commercially, the most successful of these processes has been the Stelmor process, developed as a joint effort by Stelco Inc., a steel rod producer, and Morgan Engineering, a rod mill manufacturer.

1.2 The Stelmor Process

Since its development, nearly 25 years ago, the Stelmor process has become the most popular patenting process in the world. In a recent review article [2], the success of the Stelmor process was indicated by the fact that there are 69 mills with 153 Stelmor lines operating in 26 countries. World capacity for production of wire rod through this technique, has been rated at 21 million t/y [3].

The main objective of patenting of steel wire rod is to produce material with a microstructure that is appropriate for the subsequent processing steps. Microstructural control is achieved through variation in steel thermal history. In the lead patenting process, this is adjusted by varying the lead bath temperature. Some of the more recent processes have employed water and molten salt baths for imparting desired cooling characteristics. The Stelmor process however, utilizes forced air as a cooling medium. A schematic diagram of a typical Stelmor line is provided in Fig 1.1 [4]. As can be seen, the water boxes (A) are located immediately prior to the laying head of the line. At the laying head (B), the straight rod is formed into a continuous coil, and dropped onto the moving bed (C). Movement of the coils was originally accomplished by a chain conveyor; newer Stelmor lines possess roller conveyors. Fans force air up through the plenum chambers (D), where louvers are situated to redirect the air to desired locations. Typically, Stelmor lines possess from 4 to 6 zones, each with its own plenum chamber allowing independent control of air flow. To achieve very low cooling rates, modern Stelmor lines can be outfitted with insulating covers or with covers possessing radiant tubes.

The temperature of steel rod arriving at the Stelmor line laying head is controlled by water pressure in the water boxes. Typically, laying-head temperatures are between 800 and 900°C. This temperature is adjusted depending on the degree of scale desired. In general, a heavy scale is provided by a higher temperature and is intended for products with a long outdoor storage period or where a mechanical descaling operation is employed. A higher laying head temperature may also supply steel with a larger austenite grain size, which can produce larger ferrite grains and greater pearlite fractions [1]. A lower laying head temperature results in a light scale with a smaller yield loss, and is suitable for chemical descaling.

Once the rod has passed from the laying head onto the moving bed, cooling is provided by the forced air, supplied through the plenum chambers. Heat in the rods is also lost by radiation. The cooling rate can be controlled by the velocity of air and the speed of

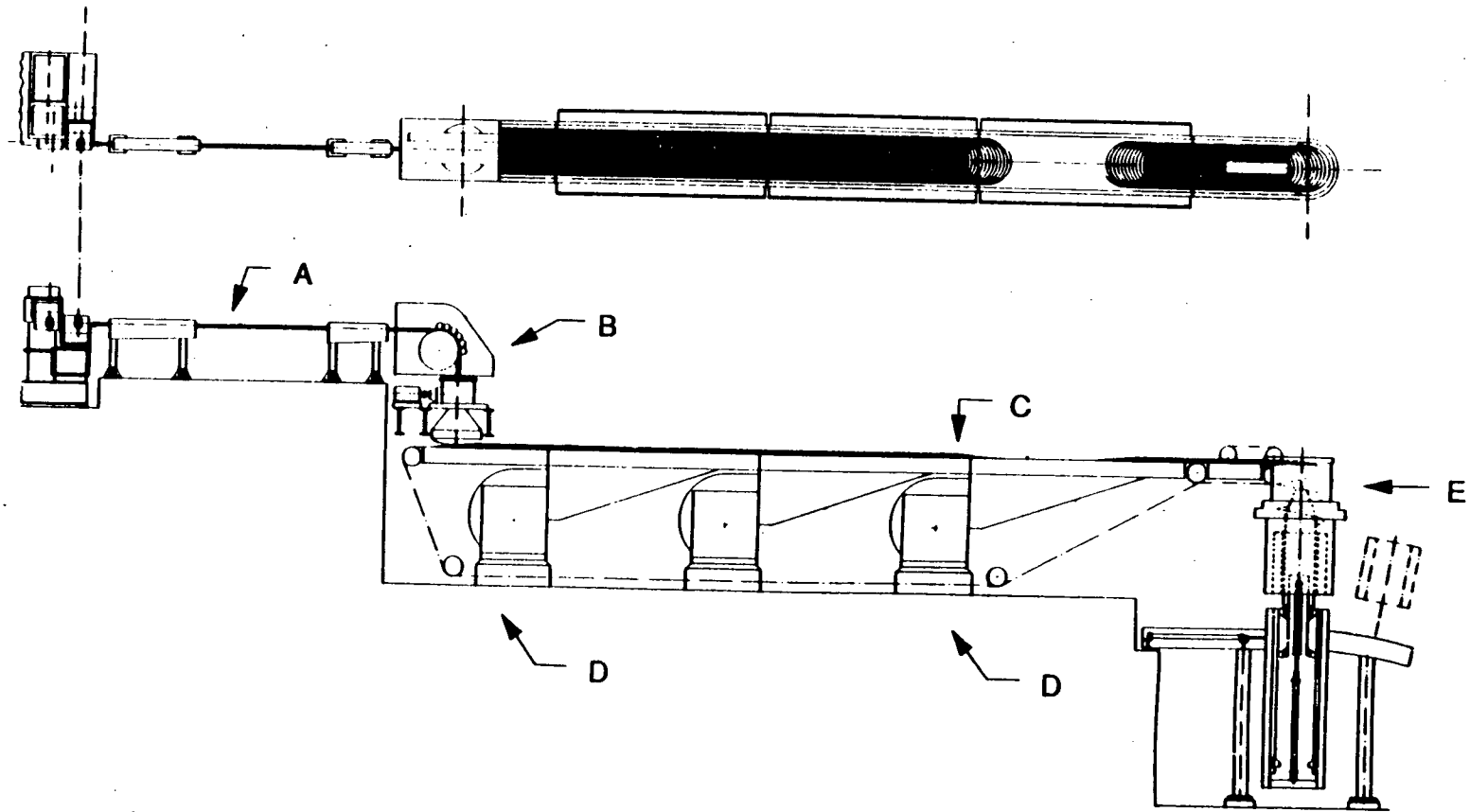


Fig. 1.1 - Schematic diagram of a Stelmor line [4]. A - Delivery pipe and water box, B - Laying head, C - Conveyor, D - Plenum chambers, E - Coil forming chamber.

the line; the latter affects the degree of packing of the rods on the bed. A higher line speed results in a larger spacing between loops, a slower speed in a smaller spacing. A larger spacing results in greater radiation to the surroundings and less reradiation to other rods, and also provides for more effective convective heat loss. Line speeds available in the Stelmor process may vary from 0.05 to 1.3 m/s, but typically a speed of 0.5 m/s is used [2]. Cooling rates attainable with the process range from 0.08 °C/s for the slow-cool Stelmor equipped with radiant tubes, to a maximum of 15 °C/s for standard Stelmor cooling. The cooling rate also can be affected by the air velocities from zone to zone along the length of the bed, as each can be controlled independently. Thus, it is possible to cool rapidly with high air velocity in the first zone, then decrease the cooling rate employing a lower air velocity in the second zone. The actual practice is dependent on the product and properties desired.

One of the major reasons for the success of the Stelmor process has been its ability to handle a variety of steel grades, intended for a multitude of applications. For example, high carbon products that will undergo a subsequent wire drawing operation such as cord for radial tire, must possess a microstructure of fine pearlite. To achieve this, a high initial cooling rate is required to bring the rod down to a low austenite-pearlite transformation temperature. The Stelmor line can provide these conditions by running at a high speed with maximum air velocity. Conversely, for low carbon grades intended for automatic welding rod, the rod ideally will possess a maximum amount of coarse ferrite to provide maximum drawability. This can be attained by slow cooling through the austenite-ferrite transformation temperatures, which requires Stelmor settings of very slow line speed and no cooling air.

1.3 Microstructural Engineering

The relationship between microstructure and mechanical properties in metals has been a topic of extensive research. Unfortunately, most of this work has resulted in a qualitative assessment of the link between structure and properties. The emerging field of microstructural engineering is concerned with the quantitative prediction of the properties of a metal product as a function of its composition and thermal history. At the root of microstructural

engineering is the mathematical model, based on the fundamental laws of conservation of heat, mass, energy and momentum. Depending on the process being considered, the conservation of any or all of these entities may be applied. Although mathematical modelling is an integral component of the the microstructural engineering approach, it can easily be seen that without laboratory, pilot plant or in-plant experimental data to link the model to the operating process, it is only an academic exercise.

In the present case, the concept of microstructural engineering has been applied to the controlled cooling of steel wire rod during Stelmor line processing. The project is one segment of a large research programme initiated in the Centre for Metallurgical Process Engineering at U.B.C., which has as its goal the prediction of the mechanical properties of steel as a function of process variables (external cooling, product shape/dimensions, production rate) and the inherent characteristics of the steel (composition and austenite grain size). The approach relies heavily on laboratory and industrial data, to link the fundamentals of heat transfer and physical metallurgy phenomena, with process design and operation.

The following thesis presents the work performed on development of a mathematical model for the prediction of strength in Stelmor-cooled steel rod. The major objectives for the research were to provide an accurate method for estimation of the microstructure formed in continuously cooled steel and relate the microstructure to the mechanical properties of the material. In order to predict microstructure, the thermal history of the steel plus the transformation kinetics for the austenite decomposition reactions must be known. Owing to the lack of data concerning structure\property relationships, phase transformation kinetics and heat transfer during Stelmor cooling of steel rod, a series of plant and laboratory trials was conducted.

Chapter 2 - LITERATURE REVIEW

2.1 Isothermal Phase Transformations

2.1.1 Introduction

A thorough understanding of the transformations that take place in pure metals and metal alloy systems is necessary for control of properties in these materials. The microstructure in metals plays an important role in determining the mechanical properties of the material. Several basic questions come to mind when one considers phase transformations. What is the mechanism for the change from one phase to another? What conditions are required before this event will take place? What are the kinetics of the reaction and how are they affected by variables such as temperature, time or impurities? It can easily be seen that answers are needed to each of these questions to provide an adequate description of the evolution of the microstructure of a metal. It is the purpose of this section to deal with the transformations that take place in metals at constant temperature with particular attention to the decomposition of austenite in plain carbon steels.

2.1.2 Theory

Phase transformations in metal alloys can loosely be divided into two categories: (1) nucleation and growth reactions and (2) martensitic reactions. Nucleation and growth processes possess an interface with the parent phase, where movement is normally controlled by the diffusion of carbon [5,6]. Martensitic transformations are not diffusion controlled but are characterized by a highly mobile interface and cooperative movement of atoms. Another major difference between nucleation and growth processes and the martensitic process is the dependence on time. Martensitic transformations are virtually independent of time i.e. at a given temperature a certain fraction of the austenite will transform rapidly and then the reaction will cease. Nucleation and growth processes however, will continue until a minimum free energy for the assembly is reached, during isothermal phase changes. The rate of transformation is highly dependent on temperature for nucleation and growth events. With

increased undercooling below the equilibrium temperature, the rate of transformation rapidly increases. The fraction of martensite is known to be dependent on temperature but the velocity at which it forms is not. The range of steel grades and cooling rates to be studied in this work will in all cases produce a ferrite/pearlite microstructure; thus, as a result, nucleation and growth events only will be treated in this survey of the literature.

Considering the reaction kinetics first for a homogeneous reaction, the probability for transformation in any given location will be the same throughout the untransformed phase. Thus the rate of transformation will be proportional to the untransformed volume. This is equivalent to a first-order rate process. Setting the original volume equal to V and calling the volume of material transformed from say α to β , V^β , the rate of change can be given as:

$$\frac{dV^\beta}{dt} = K(V - V^\beta) \quad (2.1)$$

Rearranging and integrating, the fraction transformed can be given by:

$$\frac{V^\beta}{V} = X = 1 - \exp(-Kt) \quad (2.2)$$

where X represents the fraction transformed and K is known as the rate constant. A plot of fraction transformed versus time for a first-order process is given in Fig. 2.1.

Nucleation and growth processes are somewhat more complex. Considering that nuclei require a certain incubation time before they become stable and able to support growth, this time can be denoted as τ . The nucleation rate for the event per unit volume is given by I . Also for reactions in which there is no change in composition between the product and the parent phase, the movement of the interface between the two phases can be considered to be a linear function of time. Thus for any isothermal process, the growth rate in any direction is assumed to be constant and equal to G . Therefore, the number of nuclei formed between time τ and $\tau + dt$ is $IV^\alpha dt$, where V^α represents the volume fraction of untransformed α . Likewise, assuming spherical particles, any nuclei formed at time τ have a volume v_r after time t given by:

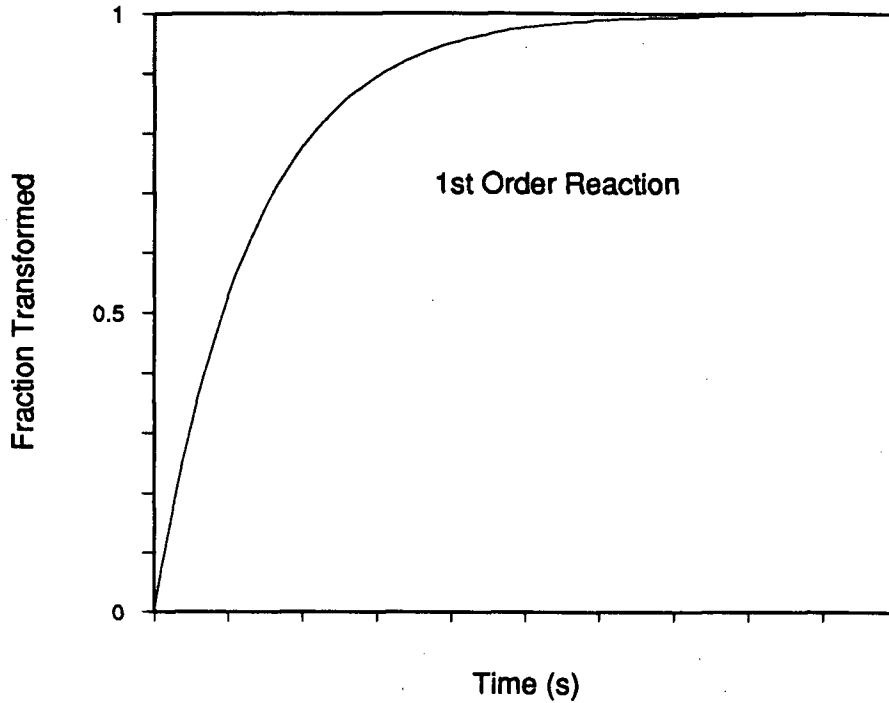


Fig. 2.1 - Example of fraction transformed-versus-time for a first-order reaction.

$$v_{\tau} = \frac{4}{3} \pi G^3 (t - \tau)^3 \quad (2.3)$$

where growth occurs equally in all directions. Combining the two expressions for nucleation and growth into a formula for the change in volume for nuclei formed at some time $t \geq \tau$

$$dV^{\beta} = v_{\tau} IV^{\alpha} dt \quad (2.4)$$

Substituting for v_{τ} and considering the initial stages of the transformation where $V^{\alpha} \sim V$,

$$V^{\beta} = \frac{4}{3} \pi V \int_{\tau}^t IG^3 (t - \tau)^3 dt \quad (2.5)$$

Finally, assuming that I is constant with respect to time, the equation can be integrated to yield:

$$X = \frac{V^{\beta}}{V} = \frac{\pi}{3} IG^3 (t - \tau)^4 \quad (2.6)$$

However, this treatment is valid only for the early stages of transformation where $V^\alpha \sim V$ and no impingement occurs. As can easily be imagined, growing particles of β must at some point impinge on one another. In metals, the two growing regions develop a common interface after which growth ceases; however, growth can continue in other directions. Thus, in order to fully describe the transformation, we must consider this impingement in our analysis. The first attempt at dealing with this problem was made by Johnson and Mehl [7] and Avrami [8,9,10].

In their treatment, Johnson and Mehl made several assumptions, some of which have been applied in developing the previous equations. These are:

- (1) transformation takes place by nucleation and growth,
- (2) nucleation rate I and the growth rate G are both constant with time,
- (3) nucleation occurs randomly throughout the matrix, and
- (4) the reaction produces true spheres except when impingement occurs.

To handle impingement the authors employed what Avrami later called "extended" volume. The extended volume, V_e^β , represents the total volume of β that would form if nucleation and growth were able to take place in material already transformed, as well as the untransformed region. Unlike Eq. (2.4) the extended volume can be written as:

$$dV_e^\beta = v_\tau I (V^\alpha + V^\beta) dt \quad (2.7)$$

and

$$V_e^\beta = \frac{4}{3} \pi V \int_\tau^t I G^3 (t - \tau)^3 dt \quad (2.8)$$

The major differences between the real and extended volumes of transformed α are that nucleation in the latter case is considered to take place in transformed regions and that impingement of grains does not halt growth. The advantage of using the extended volume is that it provides an expression for the volume of transformed material without the geometrical considerations needed to incorporate impingement of growing grains. Thus for a valid solution to be obtained, a relationship between V_e^β and V^β is required. Consider that after some

time t , a fraction equal to $(1 - V^\beta/V)$ remains untransformed. Then during the next time step dt , the true volume will increase by an amount dV^β and the extended volume by dV_e^β . Of the new extended volume formed, a certain fraction will lie in previously untransformed regions. On average it can be seen that a fraction equal to $(1 - V^\beta/V)$, will contribute to dV^β while the remainder of dV_e^β will lie in previously transformed material. This is true only if dV_e^β is considered to be formed by totally random nucleation. Thus the two volumes can be related by:

$$dV^\beta = \left(1 - \frac{V^\beta}{V}\right) dV_e^\beta \quad (2.9)$$

and, through integration,

$$V_e^\beta = -V \ln\left(1 - \frac{V^\beta}{V}\right) \quad (2.10)$$

Substituting into Eq. (2.8)

$$\ln(1 - X) = -\frac{4\pi}{3} G^3 \int_\tau^t I(t - \tau)^3 dt \quad (2.11)$$

Integration of Eq. (2.11) can only be performed by making assumptions about the variation of I with time. If I is constant with respect to time,

$$X = 1 - \exp\left(-\frac{\pi}{3} G^3 I (t - \tau)^4\right) \quad (2.12)$$

This expression is known as the Johnson-Mehl equation. It should be noted that in the limit as $t \rightarrow 0$, i.e. for initial stages of the transformation, the expansion of the right-hand side of Eq. (2.12) becomes Eq. (2.6). This is in agreement with the assumptions made in deriving Eq. (2.6).

In general it probably is not reasonable to assume that the nucleation rate will remain constant during phase transformations in solid metals. A more reasonable approach to the description of the nucleation event is given by Avrami [8-10]. He proposed that nucleation would take place only at certain preferred sites in the parent phase. Suppose for example,

there are N_0 sites available in the α phase. After some time t , there will be N sites remaining and during a small time step dt , an amount $dN = -N\nu dt$ will disappear where ν represents the frequency with which individual sites become stable nuclei. Integrating provides the number of sites remaining at any time,

$$N = N_0 \exp(-\nu t) \quad (2.13)$$

and the nucleation rate can thus be expressed as:

$$I = -\frac{dN}{dt} = N_0 \nu \exp(-\nu t) \quad (2.14)$$

Substitution into Eq. (2.11) and integration by parts yields:

$$X = 1 - \exp\left[\left(\frac{8\pi N_0 G^3}{\nu^3}\right)\left\{\exp(-\nu t) - 1 + \nu t - \frac{\nu^2 t^2}{2} + \frac{\nu^3 t^3}{6}\right\}\right] \quad (2.15)$$

In the limit there are two forms of this equation corresponding to very large and very small values of νt . If we assume very small values for νt then from Eq. (2.14) it can be seen that the nucleation rate I remains a constant. For this case, Eq. (2.15) reduces to Eq. (2.12). If on the other hand, νt is very large, then all nucleation sites are quickly consumed at an early stage of the reaction and Eq. (2.15) reduces to

$$X = 1 - \exp\left(-\frac{4\pi}{3} N_0 G^3 t^3\right) \quad (2.16)$$

A more general form for the isothermal transformation equation has been provided by Avrami [8-10] as follows,

$$X = 1 - \exp(-bt^n) \quad (2.17)$$

and is known as the Avrami equation. Comparison of the Johnson-Mehl and Avrami equations reveals that for cases where the nucleation rate varies from some decreasing function of time to a constant, the value of n should increase from 3 to 4. The value of b represents the relative magnitude of the nucleation and growth rates. The n value in the Avrami equation will also depend greatly on the shape of the growing particle. For example if the growth is

two-dimensional i.e. a disc shaped particle, then $3 \leq n \leq 2$. Likewise for one-dimensional growth $2 \leq n \leq 1$. A summary of n values for a variety of nucleation and growth conditions has been given by Christian [5].

An example of applying the Avrami equation to provide a plot of X versus t is shown in Fig. 2.2. A value of 3 was used for n , and the shape of the curve is characteristically sigmoidal. As can be seen, the reaction begins sluggishly corresponding to the early stages of nucleation but the reaction rate increases with time until at later stages impingement occurs, resulting in a continuously decreasing rate until the reaction is complete.

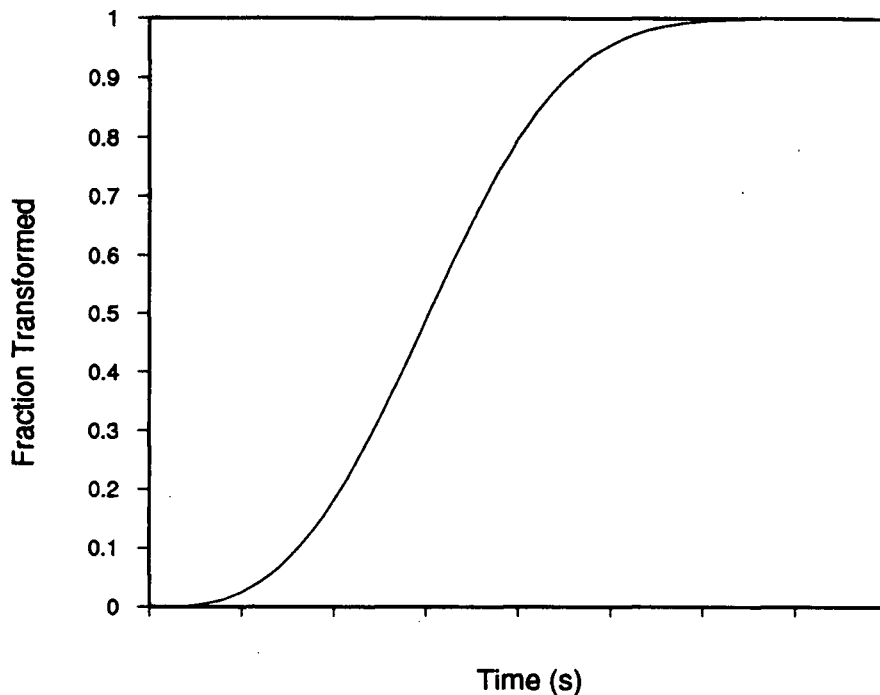


Fig. 2.2 - Example of sigmoidal transformation kinetics; Avrami equation with $n=3$.

A somewhat different approach, with particular interest to description of the decomposition of austenite in steels was proposed by Zener [11]. As was the case for the previous authors, Zener recognized that transformation takes place by a nucleation and growth process. His treatment of nucleation was based on classical nucleation theory and involved the thermodynamic description of the formation of a stable phase at a given temperature.

Classical nucleation theory predicts that the formation of a stable spherical nuclei will not take place until a critical radius is reached. In other words, for particles or germ nuclei smaller than the critical size, a small increase in the radius will result in a net increase in the free energy. This is due to the competing energies associated with the decrease in volume energy and increase in surface energy and their relationship to the radius. Zener showed that the probability for formation of a nuclei of the critical size is a function of the free energy barrier provided by this difference in volume and surface energies. Considering a spherical particle and homogeneous nucleation, the critical energy can be written as,

$$\Delta G_c = \frac{16}{3} \pi \frac{G_s^3}{G_v^2} \quad (2.18)$$

where G_s is the energy of the interface per unit area and G_v is the free energy change per unit volume. Relating these two energies to temperature, Zener showed why the undercooling plays such an important role in the kinetics of nucleation. He also showed the effect of grain boundaries on nucleation rates, comparing the interfacial energy required for a spherical nuclei completely surrounded by austenite and a hemispherical nuclei bounded on its planar side by a grain boundary and its curved side by austenite. Using typical values for free energies at an undercooling of 100°C he showed that the nucleation of pearlite in steel is approximately $10^{650,000}$ more likely at the grain boundary.

Another important contribution made by Zener was his description of the kinetics of phase-boundary propagation. In this treatment, he related the velocity of the boundary to the diffusion of atoms both across the boundary and in the parent phase. Equating atom fluxes in both of these locations the velocity was given as,

$$\psi_B = -\frac{D}{(C_2 - C_1)_B} \left(\frac{\delta C_2}{\delta X} \right)_B \quad (2.19)$$

where D is the diffusivity, C_2 and C_1 are the concentration of solute atoms on either side of the boundary, and $(\delta C_2 / \delta X)_B$ is the gradient of solute in the parent phase. Using this expression for velocity with some simplifying assumptions about the gradient, Zener was able to

make some important observations about the effect of radius and temperature on the kinetics of phase boundary propagation. In particular, by assuming that the ΔC for carbon diffusion is directly related to undercooling below the equilibrium temperature and the diffusivity varies as,

$$D \sim e^{-Q/RT} \quad (2.20)$$

and that the diffusion distance is inversely proportional to undercooling, he was able to relate the velocity of the boundary to the temperature, giving:

$$\psi_B \sim (\Delta T)^2 e^{-Q/RT} \quad (2.21)$$

where Q is the activation energy for diffusion of carbon in austenite and ΔT represents the undercooling. The form of this equation suggests that the velocity will be a minimum at low undercoolings when ΔT is small and at large undercoolings when the temperature is low and the diffusion term is small, reaching a maximum at some intermediate undercooling. This is in agreement with the shape of the experimental Time-Temperature-Transformation (TTT) curves for steels. The characteristic C-shape of these curves indicates slow kinetics at low and high temperatures with maximum transformation rates occurring at intermediate temperatures. Zener thus provided the framework for the description of growth kinetics in isothermal transformations based on a knowledge of the equilibrium phase diagram and the diffusivity of the solute atom in question.

Although Zener's work offered insight into the source for grain boundary nucleation in steels, it was a particularly simple treatment of a much more complicated system. Hobstetter [6] provided a review of nucleation theory, summarizing a number of advances for describing nucleation under various conditions. In particular he presented literature on the effect of a two component system, degree of coherency between nuclei and parent phase, state of the grain boundary and presence of dislocations. Useful qualitative results are offered, but an accurate method for predicting nucleation rates in a multicomponent system remains unresolved.

2.1.3 The Proeutectoid Ferrite Reaction

The formation of ferrite from austenite in hypoeutectoid steels is known to occur by a nucleation and growth process. Excellent reviews on the development and morphology of proeutectoid ferrite grains and their origin in steel are given by Aaronson [12] and Reynolds *et al.* [13]. Aaronson rationalized the morphology of ferrite in terms of growth mechanisms. In particular, comparisons between experimental data and theories concerning rates of nucleation and growth for various ferrite morphologies were made. Speich *et al.* [14] also provided experimental and theoretical considerations on nucleation and growth of proeutectoid ferrite with particular concern for ferrite transformed from deformed austenite. Owing to the various morphologies resulting from the proeutectoid reaction (see Ref. [12]-Dubé morphological classification system), it is not possible to apply one transformation mechanism for description of all resulting shapes. In view of the range of steel compositions and cooling rates being considered in the present study, only grain boundary allotriomorphs will be discussed.

Studies of proeutectoid ferrite nucleation [13] reveal that high-angle grain boundaries are more effective as nucleation sites than are low-angle boundaries. The reasons for this are not fully understood. Using the models proposed by Cahn [15], Speich *et al.* [14] have shown from an energy consideration only, the prime site for nucleation of ferrite should be austenite grain corners followed by grain edges then grain boundaries. The authors emphasize however that this is true only for incoherent interfaces between the parent and product phases. A semicoherent interphase boundary results from an orientation relationship existing between the parent and product grains. The surface energy is thereby reduced and may explain the apparent dominance of nucleation at austenite grain boundaries as opposed to grain corners or edges. Coherency or semicoherency during nucleation requires that the ferrite adopt the special Kurdjumov-Sachs orientation relationship with respect to the austenite [14]. However, during growth, it seems that many of the proposed models make use of incoherent interfaces. In general it is accepted that the growth of grain boundary

allotriomorphs can be separated into thickening and lengthening kinetics. Making use of an incoherent interface and assuming long range diffusion of carbon as being the rate controlling step, ferrite thickening kinetics can be described with a simple one-dimensional diffusion model to yield a parabolic growth rate:

$$S = Kt^{1/2} \quad (2.22)$$

where S is the half-thickness, K is the parabolic rate constant, including a diffusivity term and t is time. According to Speich *et al.* [14], experimental data for S in steels agrees with calculations when appropriate values are used for K .

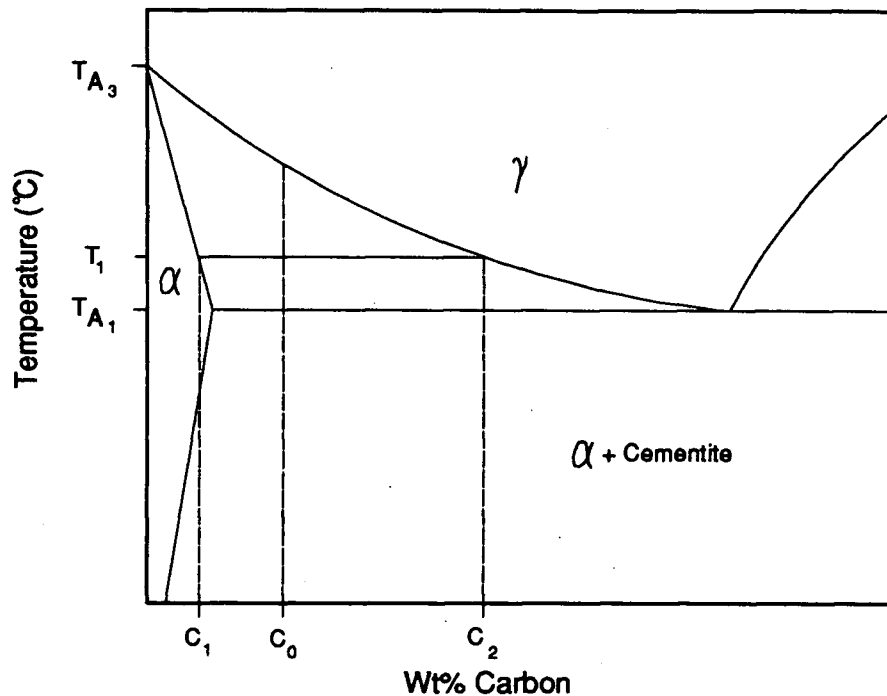


Fig. 2.3 - Fe-C phase diagram depicting equilibrium concentrations for the formation of proeutectoid ferrite from austenite at temperature T_1 .

Lengthening of the precipitate during growth has also been considered assuming diffusion control. Hillert [16] has proposed an equation for description of the lengthening rate of grain boundary allotriomorphs; Speich *et al.* [14] report reasonable agreement with experimental data.

Owing to the fact that thickening of grain boundary allotriomorphs is a much slower process than lengthening, it is very common to have austenite grain boundaries completely covered with ferrite grains before an appreciable amount of growth has occurred. In these cases, usually associated with larger undercoolings and higher nucleation rates, impingement occurs early. If adjacent grains possess a similar orientation, coalescence can take place among the impinged grains due to the driving force of minimized interfacial energy, forming a single ferrite grain or a reduced number of grains[14].

Referring to the Fe-C phase diagram, Fig. 2.3, in order to initiate growth of ferrite in a supersaturated matrix of austenite, a nuclei of composition C_1 must first form. As outlined previously, this will take place almost certainly at an austenite grain boundary. The growth of this grain of ferrite into the austenite of original composition C_0 can only take place if carbon diffuses away from the ferrite/austenite interface. A diffusion field will thus be established where the rate of advance of the interface is controlled by the removal of carbon. The diffusion field can be represented as shown in Fig. 2.4 where C_2 is the equilibrium concentration of carbon in the austenite.

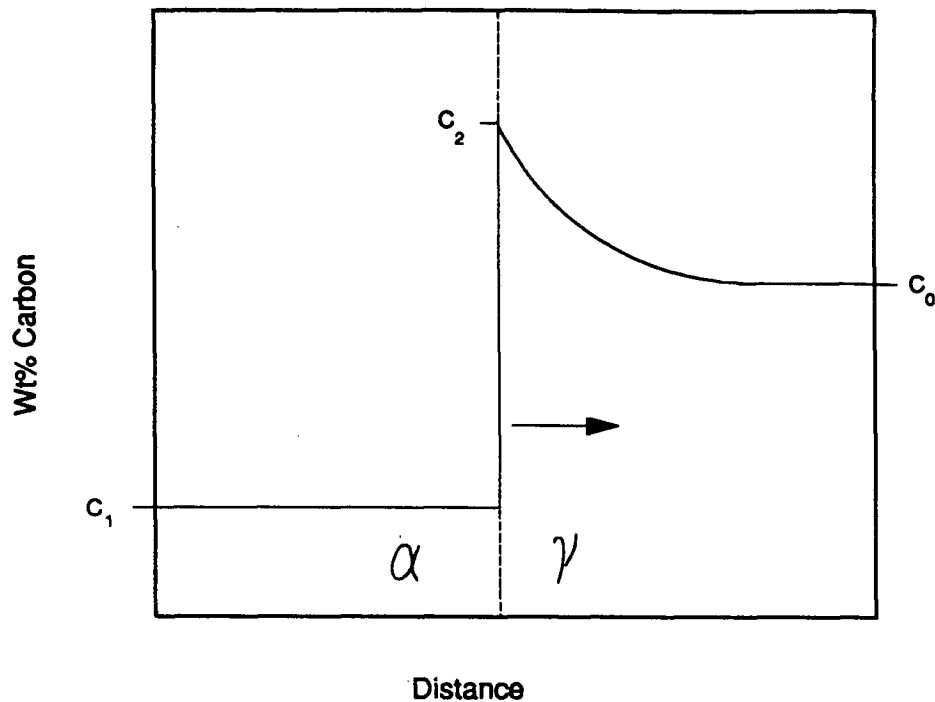


Fig. 2.4 - Diffusion field in austenite in front of growing proeutectoid ferrite. Concentrations refer to Fig. 2.3.

2.1.4 The Pearlite Reaction

Pearlite is the product of eutectoid transformation in steels and perhaps one of the most recognizable microstructures. The characteristic lamellar structure also exists in non-ferrous alloys. The name pearlite stems from the fact that properly polished and etched steel exhibits a "pearly constituent" when viewed under a light microscope. A clue to the cooperative growth mechanism in the formation of pearlite, is provided by the alternating layers of the carbon-rich cementite phase and the lesser carbon ferrite phase.

Mechanisms for the nucleation and growth of pearlite have been the topic of research for many years and are included in an excellent review article provided by Hillert [17]. Among the areas of interest was the active nucleus to provide initiation of the pearlite reaction. According to Hillert, early wisdom proposed that the active nucleus for pearlite should be cementite since ferrite was found to nucleate bainite. Also it was suggested that the

cementite nucleus should exhibit a Widmanstätten relationship with the retained austenite. Proeutectoid ferrite was found to bear no relationship to pearlitic ferrite, according to Hillert, and it was proposed that it thus could not have acted as an active nucleus for growth. However, subsequent metallographic work by Modin, as reported by Hillert, revealed that an orientation relationship does in fact exist between proeutectoid ferrite and pearlitic ferrite in hypoeutectoid steels. According to Hillert, work conducted by Hultgren and Öhlin have supported Modin's findings. In most cases, proeutectoid ferrite was found to be of the same crystallographic orientation as pearlitic ferrite. Furthermore, a similar result was revealed for hypereutectoid steels in that proeutectoid cementite and pearlitic cementite possessed the same orientation. Thus it would seem that both ferrite and cementite can act as an active nucleus in pearlite formation from austenite.

Regarding orientation relationships with the parent austenite grains, Hillert [17] generalized Smith's findings together with those of other authors to state that: "The ferrite and cementite constituents of pearlite can have any orientation relationships to the matrix austenite except for those which allow the formation of interfaces which are partially coherent with the matrix austenite." Orientation relationships between the ferrite and cementite in pearlite were also discussed by Hillert. In keeping with the statement above, he found that orientation relationships between the ferrite and cementite should not affect growth as long as orientations that would allow coherency with the austenite are avoided. Further work on ferrite-cementite orientations, summarized by Ridley [18], showed that a relationship does in fact exist. The two most important of these, as reported by Ridley, are the Pitsch-Petch and the Bagaryatski relationships.

<u>Pitsch-Petch</u>	<u>Bagaryatski</u>
$[100]_c$ 2-3° from $[13\bar{1}]_\alpha$	$[100]_c$ $[0\bar{1}1]_\alpha$
$[010]_c$ 2-3° from $[113]_\alpha$	$[010]_c$ $[1\bar{1}\bar{1}]_\alpha$
$(001)_c$ $(5\bar{2}1)_\alpha$	$(001)_\alpha$ $(211)_\alpha$

The subscripts c and α refer to pearlitic cementite and ferrite, respectively.

According to Ridley [18], both relationships have been encountered in the same specimen. Ridley also recognized that in order to maintain a highly mobile interface between the pearlite and the austenite matrix, it is necessary to avoid orientation relationships between these phases. Pitsch as reported by Ridley did extensive work on the relationship between growing pearlite and the matrix austenite. He found that pearlite nucleated at a clean austenite grain boundary exhibited the Pitsch-Petch relationship and that the pearlitic ferrite bore the Kurdjumov-Sachs relationship to the austenite grain on which nucleation had occurred. Both pearlitic constituents showed no relationship to the austenite in which growth was occurring. For pearlite nucleated at proeutectoid cementite interfaces, the Bagaryatski relationship has been found by Pitsch. In this case the pearlitic cementite showed a common orientation with the proeutectoid cementite. Neither the ferrite nor cementite exhibited a relationship with the austenite in which growth was taking place.

Perhaps the most significant contribution by Hillert [17], was the theory proposed for the initial stages of nucleation and growth. Up until that time, it was generally accepted that the growth of pearlite takes place by edgewise growth and sidewise nucleation. In other words, a curved growth front is maintained as the lamellae nucleated early in the reaction grow ahead of adjacent, newly formed plates. As the carbon is depleted for example, in the region around a cementite nuclei, a nuclei of ferrite would be able to form and grow. This is represented in Fig. 2.5. This theory was found to be untrue by Hillert. By repeated polishing and etching of a steel sample containing proeutectoid cementite and pearlite, a series of photographs at 1 μm intervals was produced. By transferring the photographs to motion picture film, a chronological history of the pearlite colony was produced. It was thus found that all of the cementite in the pearlite originated from a single stem of cementite which had grown from the proeutectoid cementite. The formation of pearlite was shown to consist of two woven crystals; one ferrite and one cementite. The theory of repeated nucleation and edgewise growth therefore does not hold for pearlite.

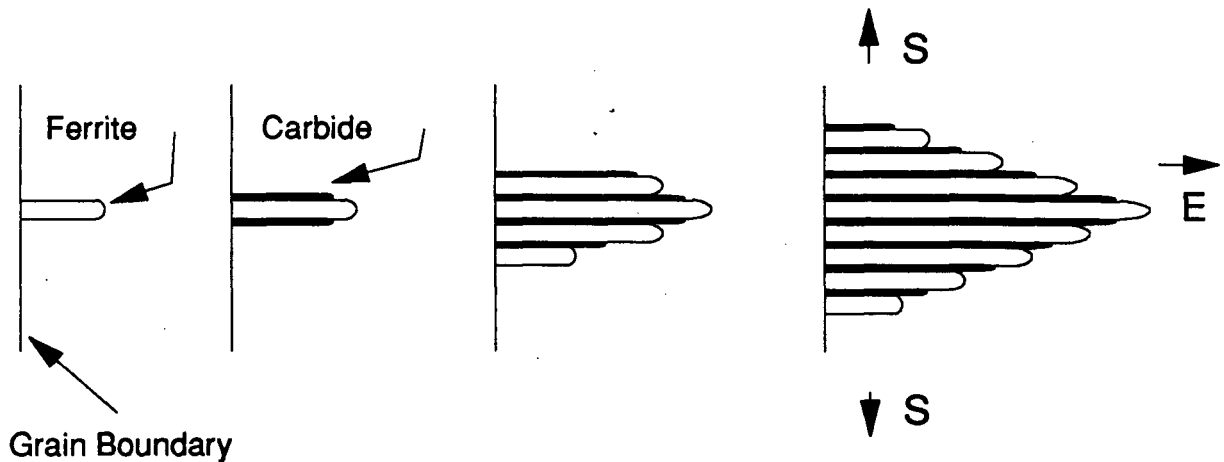


Fig. 2.5 - Formation of pearlite by repeated nucleation and edgewise and sidewise growth [17].

The degree of cooperation between the two pearlitic phases during nucleation and growth can have an effect on the subsequent structure. Hillert [17] has proposed that nucleation is not a well defined event but rather is a gradual process where cooperation is established after some time. The resulting pearlite colony grows at the highly mobile incoherent growth front, formed between the pearlitic ferrite and cementite and the parent austenite. Ridley [18] has proposed that a low degree of cooperation can result in a degenerate pearlite structure.

In the preceding sections the highlights of isothermal decomposition of austenite to ferrite and pearlite have been presented. Although not intended to provide a rigorous assessment of available literature on the topic, it is hoped that an overview of the more important nucleation and growth mechanisms has conveyed the background necessary for understanding the development of non-isothermal kinetics.

2.2 Continuous Cooling Phase Transformations

2.2.1 Theory

During non-isothermal transformations in metals, the independent variation of grain nucleation and growth makes description of transformation kinetics much more complicated than for the isothermal event. A simplifying assumption can be applied, in order to provide description of the non-isothermal transformation in terms of isothermal kinetics. This assumption, known as the additivity principle, considers the transformation rate to be controlled only by the temperature of the assembly and the fraction transformed. This assumption implies that the assembly has no memory or that transformation occurs at each temperature, independent of the previous thermal history. Expressed in equation form:

$$\frac{dX}{dt} = f(X, T) \quad (2.23)$$

where dX/dt is the transformation rate, X is the fraction transformed and T is the reaction temperature.

This principle also can be depicted readily with a graph of fraction transformed vs. time as given in Fig. 2.6. Consider two isothermal transformations, one at temperature T_1 , the other at T_2 . The principle of additivity requires that if an amount of transformation X_1 were allowed to take place at T_1 , over a period of time t_1 , upon an instantaneous change in temperature from T_1 to T_2 , the reaction would continue at the new temperature as if all of the transformation had taken place at that temperature. In other words, as depicted by the graph in Fig. 2.6, the reaction would initially follow \overline{AB} , be brought instantaneously to the new temperature T_2 along the dashed line \overline{BD} , then proceed along the line \overline{DE} , corresponding to temperature T_2 . Thus the additivity principle implies that the transformation occurring in a material has no memory of its thermal history. The only factors affecting the course of transformation are the present temperature and the fraction transformed in the material.

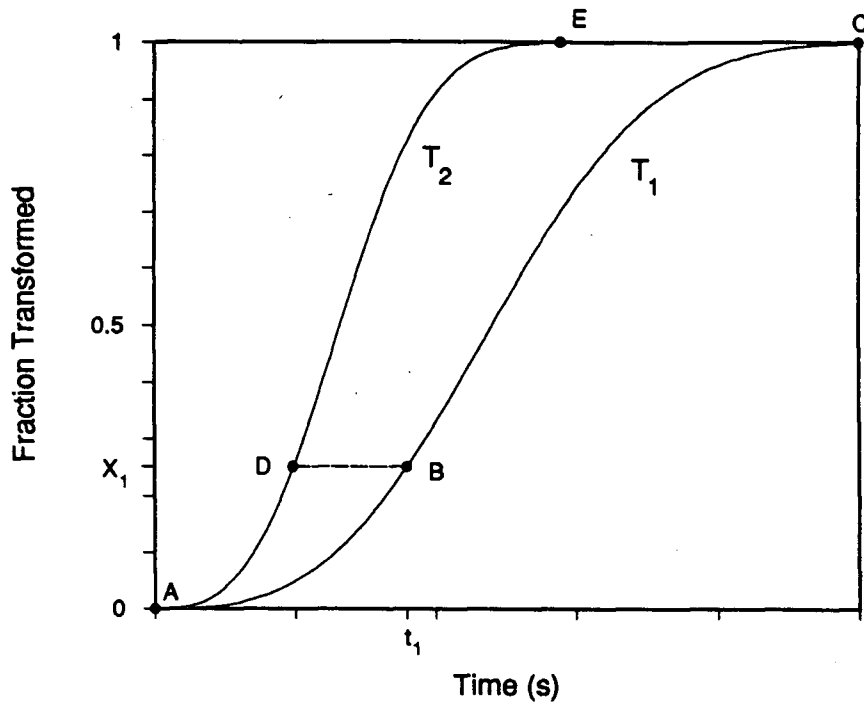


Fig. 2.6 - Graphical representation of the additivity rule. Path A-B-C is the course of transformation for temperature T_1 , and A-D-E is the path for temperature T_2 . The dashed line depicts the instantaneous change in temperature from T_1 to T_2 after fraction X_1 has transformed.

The additivity principle can also be applied through an equation originally given by Scheil [19]. In attempting to describe incubation times for transformation as a function of temperature during cooling of steel, he suggested that the cooling curve could be approximated as a series of isothermal steps of short time duration. Assuming that the isothermal time needed for incubation is $\tau(T)$ and the time step is equal to dt , at each temperature a fraction of incubation time equal to $dt/\tau(T)$ will be consumed. Thus for consumption of incubation over a range of temperatures during continuous cooling, the incremental fractions consumed at each isothermal temperature can be summed. When this summation becomes unity, incubation should be complete i.e.

$$\int_0^1 \frac{dt}{\tau(T)} = 1 \quad (2.24)$$

It can easily be seen that the Scheil equation can be applied to any event in which the isothermal time taken to achieve a certain degree of reaction is known, whether it be the incubation or the transformation period. Similarly, for a reaction in which the cooling rate is constant and equal to w , Eq. (2.24) can be expressed as

$$\int_{T_S}^{T_F} \frac{dT}{\tau(T)} = w \quad (2.25)$$

where T_S and T_F are the start and finish temperatures of transformation, respectively.

Although additivity can be seen as a useful tool for the prediction of continuous-cooling phase transformations from isothermal kinetics, various researchers have proposed restrictions for its use. In developing his equation for phase transformation kinetics under isothermal conditions, Avrami [8-10] promoted the concept of additivity and suggested a range over which its application should be valid. Known as the "isokinetic" range, it restricted the applicability of additivity to temperatures and conditions over which the ratio of the nucleation rate I , to the growth rate G , remains a constant. Proposing that the characteristic kinetics of the reaction remain unchanged when this ratio remains constant, Avrami suggested that additivity should thus apply.

Another restriction to the application of additivity during non-isothermal phase transformations was proposed by Cahn [20,21]. Recognizing that Avrami's suggestion of constant nucleation-to-growth ratio was a special case and that additivity could be expected outside this range, Cahn postulated the theory of nucleation site saturation. This theory proposes that all nucleation sites are consumed at an early stage in the transformation event and that the reaction thus will be controlled by the growth rate. Because the growth rate should be directly related to transformation temperature, the rule of additivity should then hold. Two criteria were proposed by Cahn to suggest when the assumption of site saturation should be valid. The first is based on a tetrakaidehedra model for grain shape and is expressed by the following equations:

$$I_C (\text{corner}) > 2.5 \frac{G}{d_p^4} \quad (2.26)$$

$$I_E (\text{edge}) > 1000 \frac{G}{d_p^4} \quad (2.27)$$

$$I_S (\text{surface}) > 6000 \frac{G}{d_p^4} \quad (2.28)$$

where I_C is the nucleation rate at the grain corners, I_E is the nucleation rate at the grain edges, I_S is the nucleation rate at the grain surfaces, G is the growth rate and d_p is the diameter of the parent grain.

The second criterion for early site saturation proposed by Cahn assumes that only one nuclei will be formed for each parent grain in the matrix. The criterion then is given as:

$$\frac{G t_{0.5}}{d_p} \leq 0.5 \quad (2.29)$$

where $t_{0.5}$ represents the time taken to achieve 50% of the transformation.

Considering the fundamental aspects of the additivity principle Christian [5] postulated that a transformation will be additive if the reaction rate can be expressed as two independent functions, one in terms of fraction transformed and the other in terms of temperature,

$$\frac{dX}{dt} = \frac{f_1(T)}{f_2(X)} \quad (2.30)$$

where $f_1(T)$ represents a function of temperature only and $f_2(X)$ represents a function of fraction transformed only.

The Avrami equation (Eq. (2.17)) obeys Christian's theory for the applicability of additivity under certain conditions, as will be shown. First, by rearrangement and solving for time,

$$t = \left[\frac{\ln(1-X)}{-b} \right]^{1/n} \quad (2.31)$$

Now differentiating Eq. (2.17) with respect to t ,

$$\frac{dX}{dT} = -nb t^{n-1} \exp(-b t^n) \quad (2.32)$$

Substituting Eq. (2.31) for t into Eq. (2.32) and rearranging,

$$\frac{dX}{dT} = \frac{n(-b)^{1/n}}{\left(\frac{1}{1-X}\right) \left[\frac{1}{\ln(1-X)}\right]^{n-1}} \quad (2.33)$$

By inspection of Eq. (2.33), it can be seen that Christian's theory for an additive transformation is upheld if the value of n is constant and b is a function of temperature only, over the temperature range for the reaction. Thus given these conditions, the Avrami equation is suitable for the description of phase transformation kinetics during a non-isothermal process.

Conditions for the application of additivity during the cooling of plain carbon eutectoid steels have been critically assessed by Kuban [22]. He has shown that the conditions proposed by Avrami and Cahn did not hold experimentally for all nucleation and growth conditions during the formation of pearlite from austenite, despite the fact that the reaction was shown to be additive. Consequently Kuban proposed another condition for additivity with respect to the pearlite transformation based on "effective site saturation". From the Johnson-Mehl equation (Eq. (2.12)) and the values he calculated for nucleation and growth rates from experimental data, an equation was proposed for application of effective site saturation as follows:

$$t_{0.2} \geq 0.38 t_{0.9} \quad (2.34)$$

where $t_{0.2}$ is the time required to reach 20% transformed and $t_{0.9}$ is the time to reach 90% transformed. Similar to Cahn's criteria for site saturation, effective site saturation suggests that the early stage of the transformation makes a greater contribution to the reaction than the later stages. This criterion then was applied to underpin the use of additivity during the transformation of pearlite to austenite in a eutectoid steel. Earlier, Agarwal and Brimacombe [23] and Hawbolt *et al.* [24] had employed the additivity principle with the Avrami equation to successfully describe eutectoid transformation in steels under continuous-cooling conditions.

The validity in applying the additivity principle to the proeutectoid ferrite transformation is unclear due to the rate controlling mechanism in the reaction. The long range diffusion of carbon away from the advancing ferrite interface results in parabolic growth rates, as pointed out previously. Also, it would be expected that the rate of change of temperature during continuous cooling would have an effect on the diffusion field ahead of the growing ferrite, implying that the instantaneous growth rate would be a function of the thermal history. In spite of these complications, Hawbolt *et al.* [25] have successfully applied additivity and the Avrami equation to the continuous cooling transformation of a 1025 plain-carbon steel. Additivity during ferrite growth also has been tested by Kamat *et al.* [26]. Subjecting a 1010 steel to a step quench thermal history, as well as complete transformation from austenite to ferrite at two isothermal temperatures, the transformation kinetics were shown to behave as represented in Fig. 2.6. A similar technique has been employed by Umemoto *et al.* [27] to reveal additive behaviour in the transformation of pearlite. Research on the readjustment of the diffusion field and boundary compositions at the ferrite/austenite interface during growth of ferrite is presently being modelled mathematically by Kamat [28]. The work is intended to examine the rate at which carbon can adjust at the interface as the ferrite reaction proceeds during continuous cooling. This study should help to explain why the proeutectoid reaction is experimentally an additive event.

Although additivity has been found to be applicable to both the ferrite and pearlite transformations in steels, calculation of incubation time using the Scheil equation (Eq. (2.24)) has had mixed results. Agarwal and Brimacombe [23] used tabulated TTT diagrams and the Scheil equation for prediction of start times during continuous cooling in eutectoid steels. In all cases they found that the start time predicted for the onset of reaction was greater than the experimental start times. In a subsequent paper, Hawbolt *et al.* [24] reported a detailed study into the consumption of incubation and its applicability to additivity, also for a eutectoid carbon steel. Integration of the Scheil equation over a range of cooling rates yielded values of 0.2 to 0.24 at the experimental start time rather than the value of unity

according to Eq. (2.24). Hawbolt *et al.* [25] similarly examined the use of additivity for incubation during transformation to proeutectoid ferrite in a 1025 steel. As for pearlite, the integration of the Scheil equation over a range of temperatures resulted in values much less than 1. However, this is in disagreement with Kirkaldy and Sharma [29] who have shown that the use of additivity for conversion of TTT to CCT (Continuous-Cooling Transformation) start times should be valid in the case of low alloy steels. It would thus seem that the application of additivity to incubation times for the decomposition of austenite in plain carbon steels is still somewhat in question.

2.2.2 Applications

2.2.2.1 Kirkaldy and Co-authors

The application of isothermal transformation kinetics to non-isothermal reactions in steel has become a common method for predicting the microstructural evolution during thermal treatment of steels. Recognizing the importance in prediction of microstructures formed during the traditional Jominy end-quench test, Kirkaldy [30] developed a method for characterizing phase transformations based on thermodynamic and kinetic considerations. This method, developed for low alloy eutectoid steels, can be summarized as:

- (1) Calculate the cooling curves in a Jominy bar as a function of depth assuming infinite quench conditions,
- (2) Shift each cooling curve so that time zero corresponds to the eutectoid temperature for the alloy in question,
- (3) Calculate the isothermal incubation time as a function of undercooling,
- (4) Transform the TTT incubation times to continuous cooling,
- (5) Calculate the growth velocity of pearlite and integrate from the CCT start time to obtain fraction transformed,
- (6) By difference, calculate fraction of retained austenite,
- (7) From retained austenite, calculate fraction of martensite and the hardness of the Jominy bar as a function of depth.

The thermal history for a given depth in the Jominy bar was calculated neglecting the latent heat of transformation, during the austenite/pearlite reaction and employing the time-dependent Fourier equation for heat conduction. Making use of Zener's [11] expression for pearlite growth velocity Eq. (2.21), Kirkaldy applied an equation of the form

$$\psi_p = K D_c(T) (\Delta T)^2 \quad (2.35)$$

where ψ_p is the growth velocity of pearlite, K is a thermodynamic rate constant and $D_c(T)$ is the effective temperature-dependent diffusivity of carbon in austenite. Applying literature values for carbon diffusivities and average pearlite growth velocities, the thermodynamic constant K was calculated. In order to make the approach suitable for meaningful predictions in commercial alloys, the effect of small amounts of alloy additions were included in the calculations of diffusivity and undercooling. Both parameters were expressed as the summation of individual alloy influences on the ternary system, ignoring synergistic effects. Differences between the austenite stabilizers (e.g. Mn, Ni, Cu) and ferrite stabilizers (e.g. Cr, Mo, Si) and their respective behaviour with regards to partitioning were also included. Kirkaldy recognized that the austenite stabilizers do not tend to partition over the temperature range associated with the pearlite transformation, however they do affect the undercooling through a change in the eutectoid temperature for the alloy. Ferrite stabilizers on the other hand, tend to partition between the ferrite and cementite. According to Kirkaldy, due to the small values of volume diffusion coefficients for these elements, partitioning rates and thus rates of growth of pearlite will be controlled by grain boundary diffusion.

The incubation times for the onset of the pearlite reaction in Kirkaldy's work [30], were based on equations due to Russell [31]. The equation for a volume diffusion process is given by:

$$\tau = \frac{\alpha l}{D_v (\Delta T)^2} \quad (2.36)$$

and correspondingly for boundary diffusion,

$$\tau = \frac{\beta T}{D_B(\Delta T)^3} \quad (2.37)$$

where D_V and D_B represent the diffusion coefficients for volume and grain boundary diffusion of carbon, respectively. Adopting a procedure similar to the calculations employed for growth velocities, the effects of both austenite and ferrite stabilizers have been included in determining the values of diffusivity and undercooling.

Conversion of isothermal incubation time to continuous-cooling, was made by an expression due to Grange and Keifer [32]. This method proposed that a steel with a constant cooling rate, as shown in Fig. 2.7, will intersect the TTT-Start curve at temperature T_B and time t_B . Also, as shown in the figure, it is assumed that the line intersects the CCT curve for the same steel at a different temperature T_C and time t_C . Grange and Keifer proposed that the amount of transformation that takes place between temperature T_B and T_C on continuous cooling, could be approximated by the amount of transformation that takes place isothermally at temperature $T_D=(T_B+T_C)/2$. Hence, the transformation start time during continuous cooling can be given by:

$$t_D = t_C - t_B \quad (2.38)$$

Using a trial and error approach, the CCT-Start curve can be calculated utilizing Eq. (2.38) and the TTT-Start curve. Comparison of Eq. (2.38) with the Scheil equation reveals that Kirkaldy's relationship places more emphasis on the lower transformation temperatures, i.e. temperatures closer to the actual start temperature. This essentially ignores the incubation time consumed during small undercoolings at temperatures close to the eutectoid. It also suggests that incubation time is not consumed linearly.

Based on an assumed austenite grain geometry and the nucleation of one pearlite nodule per shared austenite grain boundary surface, Kirkaldy developed integration equations for the pearlite growth velocities. One equation was intended for early growth periods when impingement had not occurred and the other for growth after impingement. A calculation of

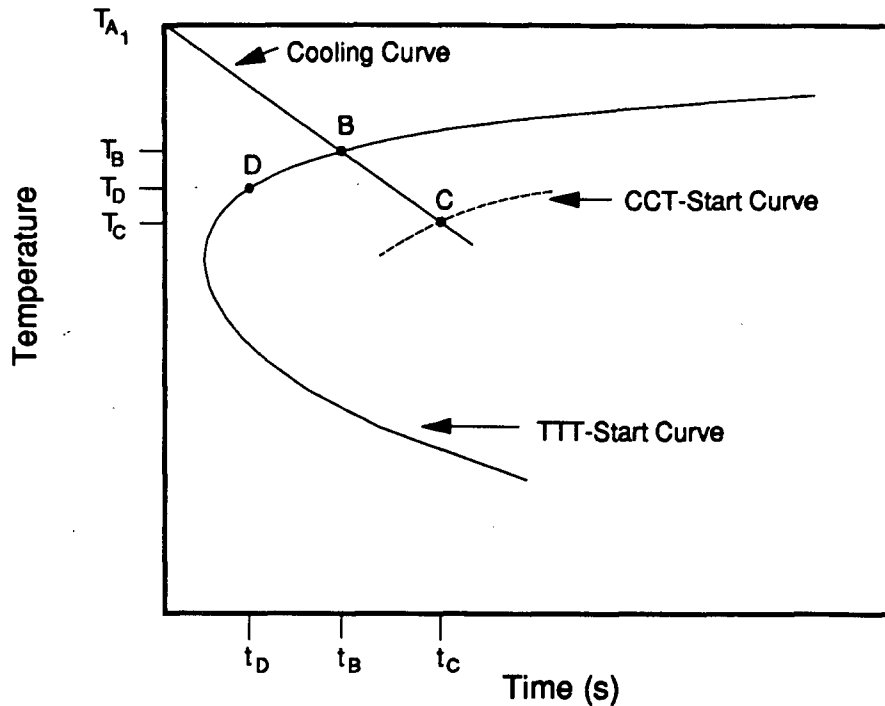


Fig. 2.7 - Graphical representation of the method employed by Kirkaldy [30] for calculation of the CCT-Start curve from the TTT-Start curve for the pearlite transformation.

the fraction of martensite in a 4068 steel Jominy bar was made and compared with experimental results. The lack of precise agreement between the calculated and experimental values was attributed to the crude treatments given to the nucleation and growth of the pearlite.

In a continuation of the work on prediction of hardenability in steels, Kirkaldy *et al.* [33] employed a similar approach to hypoeutectoid low alloy steels. Recognizing the weakness in the prediction of incubation times for isothermal transformations, a semi-empirical method was followed. This was applied to both the ferrite and pearlite transformations. Included in the expression were terms for the effect of prior austenite grain size and undercooling. Conversion of TTT incubation times to CCT curves was accomplished through the use of "Avrami's additivity rule" but the details of this calculation were not included. The

model was used to predict hardness as a function of distance through a Jominy bar and comparison with 80 tabulated curves for low alloy hypoeutectoid steels yielded good agreement.

Greater attention to the thermodynamics of phase transformations was given in a further contribution by Kirkaldy *et al.* [34]. This work concentrated on the prediction of the phase boundaries in commercial steels and the influence of alloying elements on their positions. Adopting a technique for incorporating the influence of ternary elements on free energies and activities in the Fe-C system [35], the phase boundaries for the ferrite and austenite regions for Fe-C-X alloys were evaluated. Good agreement was found with the literature, concerning the effect of various alloying additions on the positions of the phase boundaries.

Kirkaldy and Venugopalan [36] extended the work on description of TTT and CCT diagrams based on thermodynamic concerns. Zener type (Eq. 2.21) expressions were adopted for calculation of the time needed to obtain a certain fraction transformed, i.e.

$$\tau(X, T) = \frac{1}{F(d_\gamma) D \Delta T^q} \int_0^X \frac{dX}{X^{2(1-X)^3} (1-X)^{2X/3}} \quad (2.39)$$

where $F(d_\gamma)$ is the prior austenite grain size term and q is dependent on the mode of diffusion control (grain boundary or volume). By employing a series expansion for the dependence of the diffusion coefficient D on concentrations of alloying elements, the time to reach a certain fraction for both the ferrite and pearlite reactions was given as:

$$\tau_F = \frac{59.6(\%Mn) + 1.45(\%Ni) + 67.7(\%Cr) + 24.4(\%Mo)}{2^{(d_\gamma - 1)^2} \Delta T^3 \exp\left(\frac{-23,500}{RT}\right)} \quad INT \quad (2.40)$$

$$\tau_P = \frac{1.79 + 5.42(\%Cr + \%Mo + 4\%Mo\%Ni)}{2^{(d_\gamma - 1)^2} \Delta T^3 D} \quad INT \quad (2.41)$$

where D is evaluated as,

$$\frac{1}{D} = \frac{1}{\exp\left(\frac{-27,500}{RT}\right)} + \frac{0.01\%Cr + 0.52\%Mo}{\exp\left(\frac{-37,000}{RT}\right)} \quad (2.42)$$

The *INT* in Eqs. (2.40) and (2.41) represents the integral from Eq. (2.39) and can be solved for any value of *X*. Comparison of the results of these equations with published TTT curves from U.S. Steel data showed good to excellent agreement. An example of a predicted and measured TTT curve is shown in Fig. 2.8.

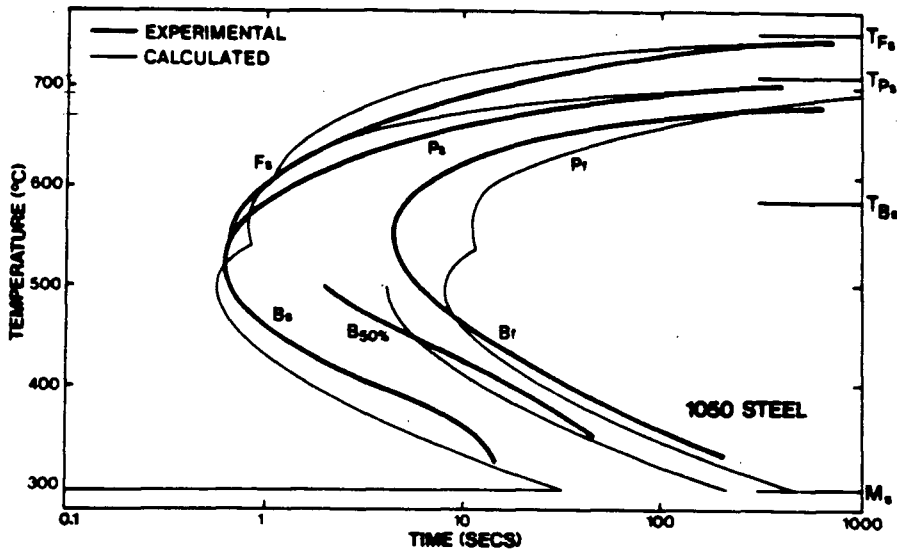


Fig. 2.8 - Predicted and measured TTT diagram for a 1050 steel from Kirkaldy and Venugopalan [36].

Although denoted as the Avrami equation by Kirkaldy and Venugopalan [36], the Scheil equation was employed to convert TTT to CCT start times. From the correlations of Eqs. (2.40) and (2.41), predictions were made for CCT start times. A comparison between available CCT curves for a range of steels yielded good agreement. An example of the predictive capability is shown in Fig. 2.9. This method is seen as a major contribution to prediction of phase transformation kinetics during both isothermal and non-isothermal processes. However, once again the final purpose of the study was to predict Jominy end-quench hardenabilities.

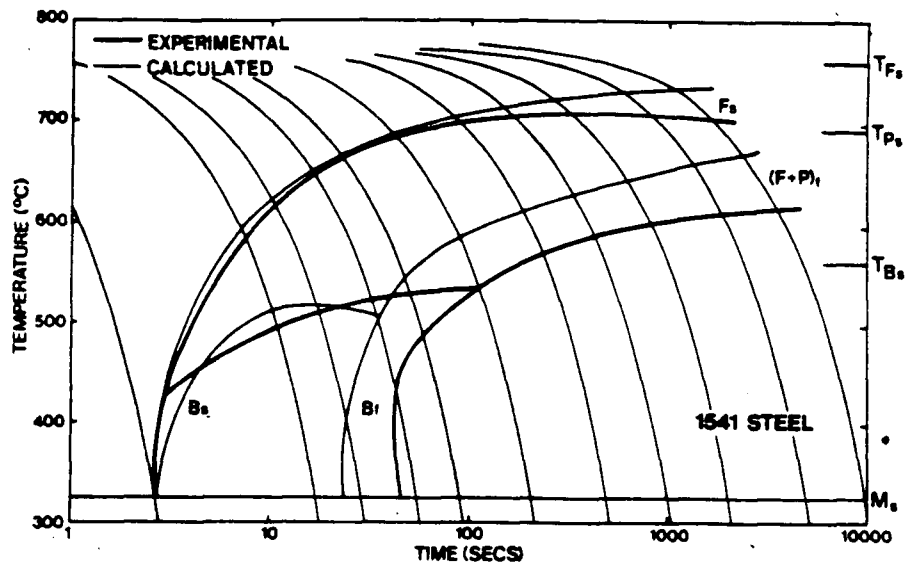


Fig. 2.9 - Predicted and measured CCT diagram for a 1541 steel from Kirkaldy and Venugopalan [36].

2.2.2.2 Umemoto and Co-authors

The effect of discontinuous cooling on the transformation of pearlite in steels was addressed by Shimizu and Tamura [37]. Employing the Scheil equation to calculate incubation consumption times, the start of transformation was predicted utilizing TTT start curves. The summation procedure was continued through a change in cooling rate (increase or decrease) and predicted start times were compared to measured CCT start curves. Experiments were also performed on a hypereutectoid steel to examine the effect of discontinuous cooling on the transformation of pearlite. The results of the work showed that the manner of consumption of incubation i.e. by continuous or discontinuous cooling, had no effect on the transformation behaviour of pearlite provided the transformation start temperatures were the same. This result suggests that additivity holds for the incubation period of the pearlite transformation.

Umemoto *et al.* [27] applied the prediction of phase transformations in steels to calculate Jominy bar hardenabilities. Only one grade of steel, plain-carbon eutectoid, was consid-

ered in the work. The Scheil equation was used to describe incubation for the pearlite reaction and a variation on the form of the Avrami equation incorporating the prior austenite grain size was proposed for the transformation. This equation was given as:

$$X = 1 - \exp\left(-b \frac{t^n}{d_\gamma^m}\right) \quad (2.43)$$

where d_γ is the prior austenite grain diameter and m is a constant dependent upon the nucleation site for the transformation event. Values for n and m have been suggested by Tamura for various transformations, based on geometric considerations. Combining expressions for thermal history and Jominy bar position with Eq. (2.43), a formula was developed to relate austenite grain size and section size to the fraction of pearlite transformed [27]. By assuming that the retained austenite after completion of the pearlite transformation results in martensite, a prediction of martensite fraction was made as a function of depth in the Jominy bar. The results of the predictions are compared with measured values in Fig. 2.10. As can be seen, the agreement is good.

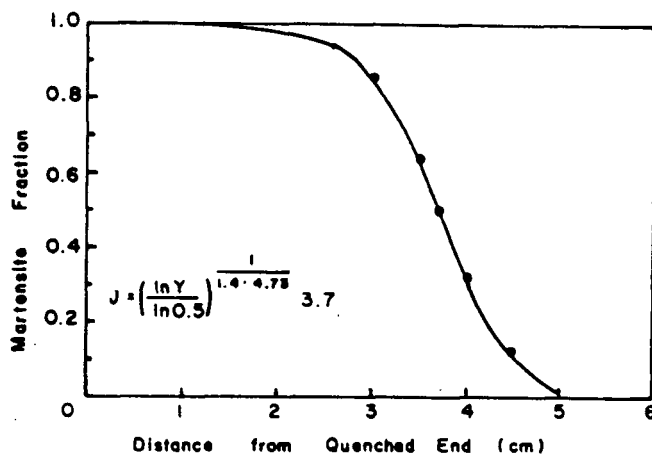


Fig. 2.10 - Predicted and measured fraction of martensite in a Jominy end-quench bar as a function of distance from the quenched end, from Umemoto *et al.* [27].

In a later paper on the prediction of hardenabilities in eutectoid steels, Umemoto *et al.* [39] modified the approach for prediction of isothermal transformation kinetics. Recognizing the relation between the value of b in the Avrami equation and the shape of the TTT C-curve, a parabolic expression was proposed such that:

$$b = \exp[-K_E(T - T_N)^2 - t_C] \quad (2.44)$$

where K_E indicates the extension of the parabola, T_N is the nose temperature and t_C is the relative position of the C-curve in the time scale. These constants are evaluated from the TTT diagram for the material in question. Instead of employing the Scheil equation to predict incubation time only, it was applied to the complete reaction starting at the eutectoid temperature. Thus by combining Eqs. (2.43) and (2.44) with the Scheil equation, the following relation was given for fraction transformed:

$$X = 1 - \exp\left[-\left\{\int_T^{T_0} \exp\left(-\frac{K_E}{n}\right)(T - T_N)^2 dT\right\}^n \frac{\ln 2}{w^n t_0^n}\right] \quad (2.45)$$

where w is the constant cooling rate and t_0 is the time required for 50% transformation at the nose temperature. By simplifying this integral and rearranging to solve for cooling rate, expressions for the upper critical cooling rate and lower critical cooling rate were derived. The upper critical cooling rate w_U was defined as the rate required to produce 1% pearlite, and the lower critical cooling rate w_L as the rate required to produce 1% martensite, in a given steel. These were given as:

$$w_U = \frac{1}{t_0} \left(\frac{\ln 0.5}{\ln 0.99}\right)^{1/n} \sqrt{\frac{n\pi}{K_1}} \approx \frac{69^{1/n}}{t_0} \sqrt{\frac{n\pi}{K_E}} \quad (2.46)$$

$$w_L = \frac{1}{t_0} \left(\frac{\ln 0.5}{\ln 0.01}\right)^{1/n} \sqrt{\frac{n\pi}{K_1}} \approx \frac{0.15^{1/n}}{t_0} \sqrt{\frac{n\pi}{K_E}} \quad (2.47)$$

or combining the two equations,

$$w_L = \left(\frac{\ln 0.99}{\ln 0.01}\right)^{1/n} w_U = (2.2 \times 10^{-3})^{1/n} w_U \quad (2.48)$$

Comparison of the critical cooling rates calculated for a commercial grade 1095 steel with values reported in the literature provided good agreement according to the authors. However only one grade of steel and one microstructural component was considered. The method also was applied for the prediction of Jominy distances, or depths at which 50% martensite had been achieved, for a range of steel compositions with good results.

The method employed by Umemoto *et al.* [27,39] for predicting phase transformation kinetics in Jominy bars, was applied directly to data on the transformation kinetics of pearlite [40]. Using a cylindrical steel sample outfitted with a longitudinal dilatometer, the progress of the austenite/pearlite transformation during isothermal and continuous cooling was monitored. The TTT curve obtained in the experiments was analyzed to evaluate the constants in Eq. (2.44), for calculation of parameter b in the Avrami equation. The value of n was taken to be 4 as suggested by the Johnson-Mehl equation. Comparison between the measured course of the isothermal reaction with that predicted by the Avrami equation yielded reasonable agreement. For prediction of continuous cooling transformations, Eq. (2.45) was applied and once again agreement between the predicted and measured fractions transformed as a function of time gave reasonable results. However, there are a few problems with the experimental procedure. Firstly, the samples used for dilatometry were extremely large (3-mm diameter x 10-mm length) relative to the assumption of negligible gradients during cooling or isothermal holding, especially in light of the fact that a longitudinal dilatometer is used. Also in their generation of data for isothermal transformations, no mention was made of the heat generated by formation of pearlite from austenite. At the temperatures reported, (601-632°C), the reaction kinetics are sufficiently fast to cause significant reheating of the sample. This was not addressed in their calculations. Finally, the method used to generate continuous cooling data is somewhat in question as the samples were rapidly cooled from the austenitizing temperature to 650°C, which is well below the A_1 temperature for the steel being studied. After reaching this temperature, various linear cooling rates were employed to

generate continuous cooling data. Obviously this method does not employ continuous cooling throughout the incubation and growth periods for pearlite. The continuous cooling rates were also very small (0.15-0.95°C/s) and within a narrow range.

Umemoto *et al.* [41] have also studied isothermal and continuous cooling transformation behaviour in hypoeutectoid steels. Instead of describing the isothermal kinetics by means of the Avrami equation, a modified Johnson-Mehl form was adopted. This was given as:

$$X = 1 - \left[1 + \frac{1}{d_f^m} \frac{K(T)}{2} (t - \tau)^n \right]^{-2} \quad (2.49)$$

where τ represents the incubation time for the ferrite reaction and $K(T)$ represents an empirically determined rate constant. Good agreement between experimental ferrite fraction transformed and values predicted from Eq. (2.49) was obtained for two hypoeutectoid steels (1020,1043). The authors also noted poor agreement between predicted ferrite transformed by the Johnson-Mehl equation and the measured values. The experimental data was generated using the same equipment as described in ref. [40]. The equation developed for isothermal transformation was applied to continuous cooling using additivity and compared with experimental results from the dilatometer. Agreement between measured and predicted fractions of ferrite formed as a function of time was quite good. However, as was the case previously, a limited range of low cooling rates was applied to the steel.

2.2.2.3 Hawbolt, Brimacombe and Co-authors

Among the first techniques to appear in the literature which set out to describe phase transformations in a continuously cooled steel in terms of isothermal transformation kinetics, heat of transformation and heat flow considerations, was by Agarwal and Brimacombe [23]. The model was intended to provide prediction of microstructural evolution of pearlite during continuous cooling of steel wire rod. The Scheil equation was employed for conversion of TTT to CCT start times and the Avrami equation was utilized to calculate transformation kinetics. An iterative finite-difference technique for solution of the coupled heat transfer and transformation equations was applied. The values of n and b , for use in the Avrami equation,

were determined from published TTT diagrams for eutectoid steels. The same TTT curves were adopted for the prediction of CCT start times. Comparison of predicted cooling curves with those determined experimentally, as shown in Fig. 2.11, reveal that the shape and relative amount of recalescence displayed by the predicted curves agree well with experiment. Indicated in the figure is the heat-transfer coefficient assumed at the surface of the rod, h , and the rod diameter, d_o . Consistently however, the predicted time for transformation start lags behind the experimental value. It was recognized that such an approach could provide accurate predictions for thermal histories and microstructural evolution in steel rods, provided a better technique for determination of CCT start times could be found.

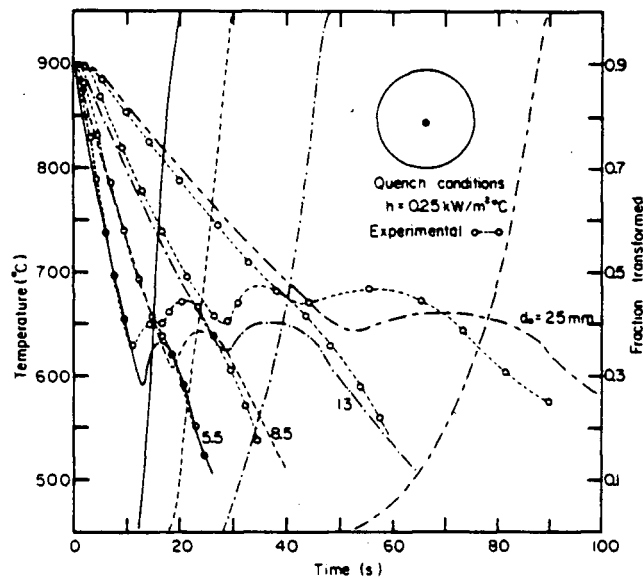


Fig. 2.11 - Thermal histories for steel rods predicted and measured by Agarwal and Brimacombe [23]. Also included in the figure are plots of predicted pearlite fraction transformed versus time.

The use of a dilatometer to measure the kinetics of austenite decomposition reactions has been refined by Hawbolt *et al.* [24]. Unlike other researchers [40], a diametral rather than a longitudinal dilatometer was used. The purpose of the work was to determine values for the kinetic constants n and b in the Avrami equation. To simplify their work, the steel under study was a plain-carbon 1080 with the transformation product limited to pearlite. The

start time of the pearlite transformation was calculated from an experimentally determined CCT curve. This was accomplished by continuously cooling samples and analyzing the response of the dilatometer to indicate the time and temperature of the onset of the pearlite reaction. The technique employed an evaluation of the n and b parameters through linearization of the Avrami equation and a best fit procedure. Whereas previous researchers [23,33,36-39] had used $t=0$ at T_{A_1} for the evaluation of the Avrami equation constants, Hawbolt *et al.* calculated the constants based on an empirically determined TTT start time, t_{AV-TTT} . The n value from the latter calculation was found to be essentially constant over the range of temperatures studied. The authors recognized the significance of constant n in that it indicates a common site of nucleation and growth geometry for the temperature range examined. In addition, a constant n satisfies additivity requirements for the use of the Avrami equation during continuous cooling. The values of b were found to be dependent on transformation temperature as expected. Figure 2.12 shows the values of n and b determined by both methods.

The fact that n was found to be constant and b was a function solely of temperature provided support for the assumption that the transformation of austenite to pearlite can be considered as an additive reaction. The validity of applying additivity to the incubation period of the transformation was also tested, as was mentioned before. Results of applying the Scheil equation to the incubation period, the transformation period and the combined incubation and growth period indicated that transformation is an additive process; however incubation is not. The use of the Scheil equation for estimation of the incubation time in continuous-cooling transformations would lead to severe over predictions in the CCT start time. Thus an experimentally determined CCT start time was employed.

Predictions of continuous-cooling transformation curves were made using the calculated n and b values and experimental CCT start times. An example of the results, compared with experimentally determined thermal histories, are shown in Fig. 2.13. As can be seen, the method provides excellent agreement.

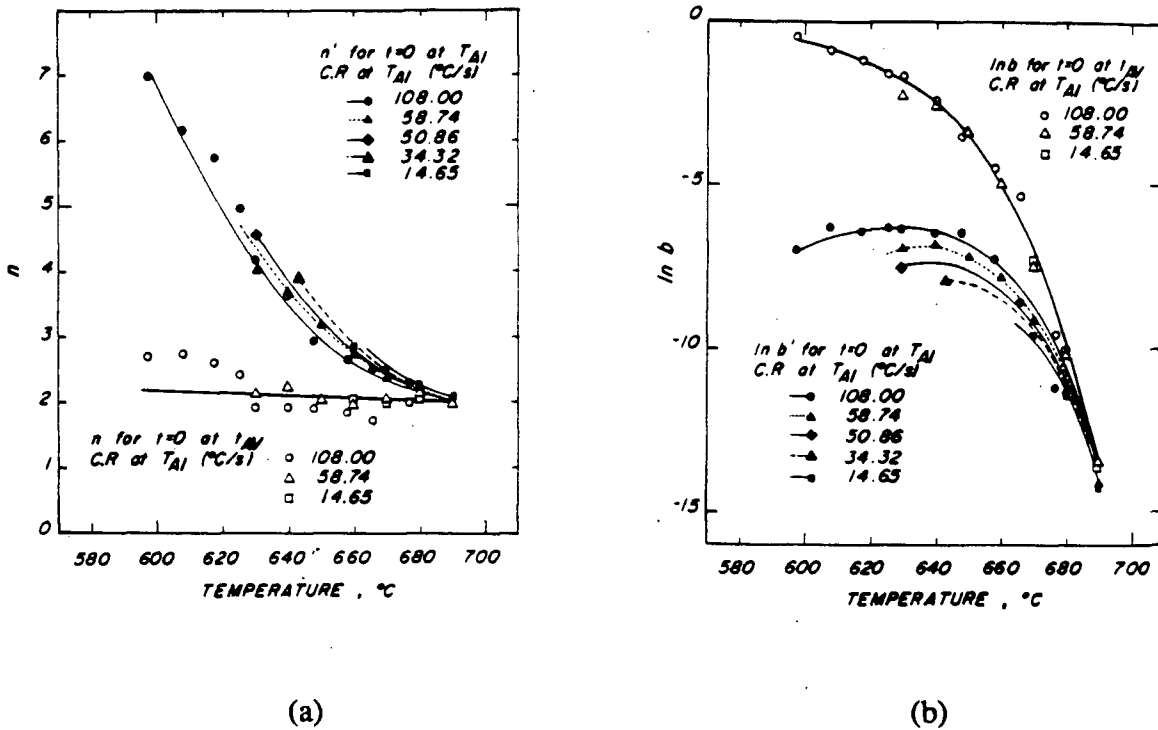
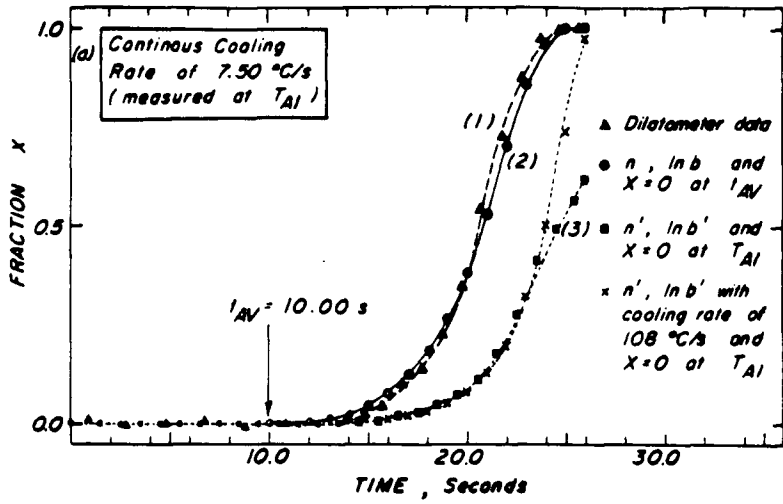
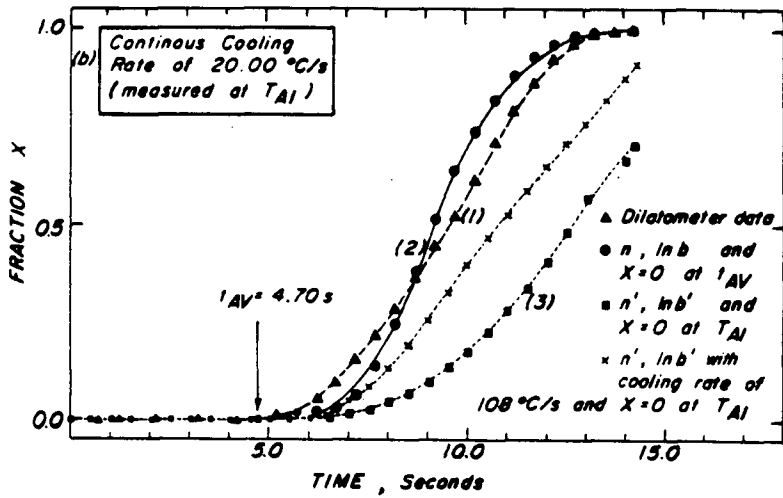


Fig. 2.12 - Measured values for n and b calculated from (a) $t=0$ at T_{A1} and (b) $t=0$ at t_{AV-TTT} , from Hawbolt *et al.* [24].

Investigations into the transformation behaviour of the austenite/pearlite and austenite/ferrite have been performed by Hawbolt *et al.* [25] for a 1025 plain-carbon steel. Once again a diametral dilatometer was employed to characterize the kinetics of the transformation. The n and b values were found by linearization of the Avrami equation, and experimental CCT start times were determined. Other hypoeutectoid grades (1040,1060) have also been evaluated using an identical technique [42]. The n and b values determined for these three steel grades are shown in Fig. 2.14. Results of the work on the 1025 steel were again used to evaluate the application of the Scheil equation to both the incubation and transformation stages of the ferrite and pearlite reactions. The transformation period of the reaction was found to obey additivity for both phases formed; however this was not the case for



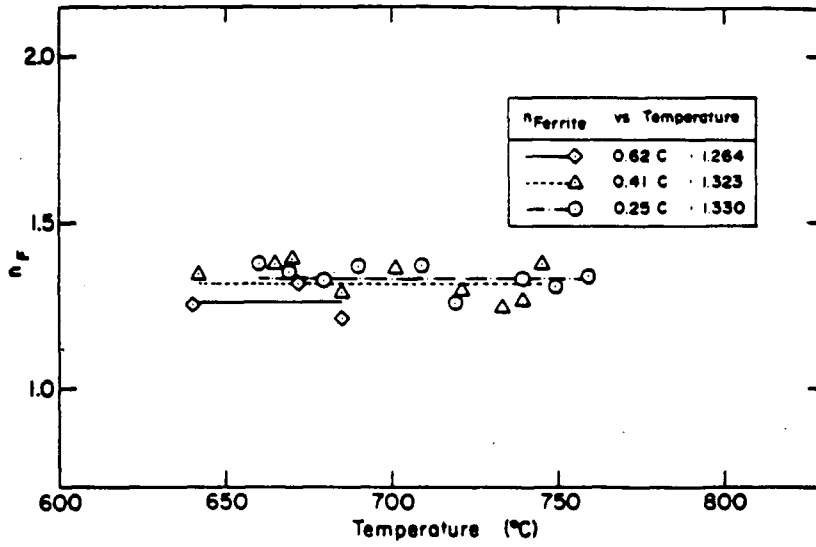
(a)



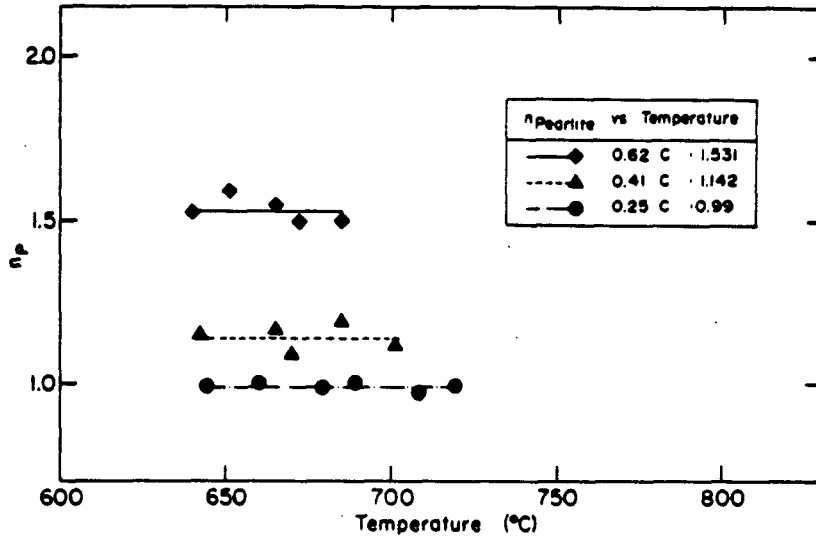
(b)

Fig. 2.13 - Measured and predicted fraction of pearlite transformed versus time for four cooling rates from Hawbolt *et al.*[24]; (a) 7.5°C/s, (b) 20.0°C/s.

incubation. From this work, it would seem that empirical determination of CCT start times from a series of continuous-cooling experiments, is necessary for the prediction of accurate thermal histories and microstructures in steels.

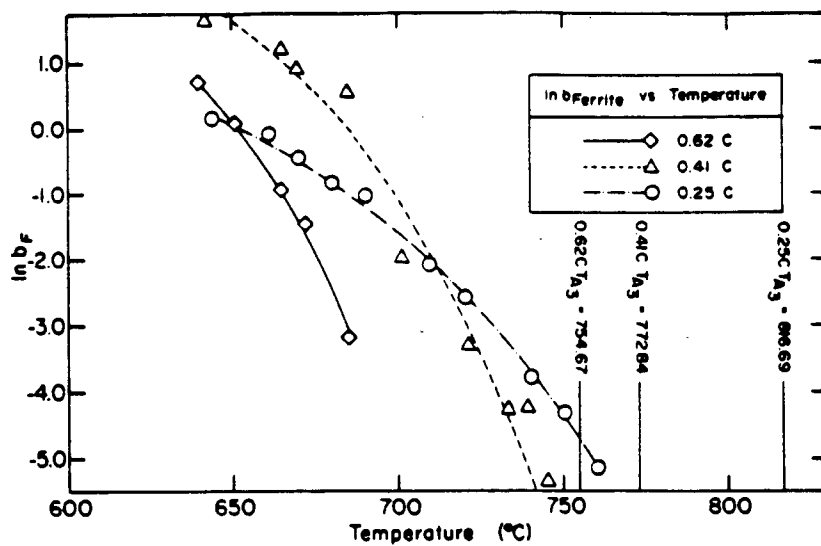


(a)

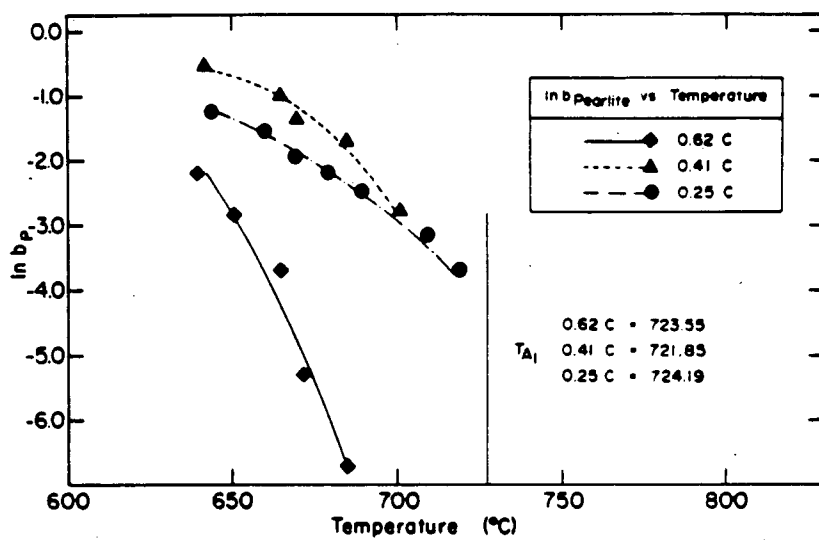


(b)

Fig. 2.14 - Measured values for n and b used in the Avrami equation, for 1025, 1040 and 1060 steel [25,42]; (a) n_F , (b) n_P , (c) $\ln b_F$ and (d) $\ln b_P$.



(c)



(d)

Fig. 2.14 - Measured values for n and b used in the Avrami equation, for 1025, 1040 and 1060 steel [25,42]; (a) n_F , (b) n_P , (c) $\ln b_F$ and (d) $\ln b_P$.

2.2.2.4 Other Work

A totally empirical approach has been provided for the prediction of microstructures and mechanical properties in steels by Blondeau *et al.* [43]. Based on published CCT diagrams for commercial-grade steels, a mathematical model was developed that calculates the microstructure formed after a continuous-cooling operation. Simplifying assumptions regarding heat flow for typical industrial processes were made to construct thermal histories for the steel. Some of the processes included in the study were the heat affected zone in welds, Jominy bars and cooling after rolling of rod or strip. Nomograms for different sample shapes were constructed to determine characteristic cooling curves rapidly. To predict material microstructures, the appropriate CCT diagram was described in terms of 10 critical cooling rates which separated and defined the time-temperature boundaries of the martensite, bainite, ferrite and pearlite regions of the CCT diagram. Nomograms were constructed for calculation of these critical rates as well. Based on knowledge of the cooling curve for a test sample and the composition-dependent critical cooling velocities, an interpolation was made to calculate the resulting microstructure. Empirical formulae also were developed to relate the calculated microstructure to the hardness and mechanical properties of the material based on the relative fractions of ferrite, pearlite, bainite and martensite. Comparisons between calculated and measured mechanical properties revealed moderate agreement. An inherent problem in models of this type is the dependence on empirical data over such a wide range of compositions, temperatures and microstructures as well as validity of the necessary simplifying assumptions.

A semi-empirical method was employed by Sakomoto *et al.* [44] for simulation of phase transformations in low-alloy steels with application to hot-rolled strip. TTT curves for 65 low-alloy steels from the U.S. Steel compendium of isothermal transformation data were used to develop empirical equations for isothermal start times. The authors considered a TTT diagram to consist of 5 separate C-curves; namely ferrite start, pearlite start and finish, and bainite start and finish. Four parameters were used to fit each of these curves including the

equilibrium transformation temperature, T_E , the nose temperature of the C-curve, T_N , the natural log of the time for the C-curve to intersect the equilibrium transformation temperature, t_E , and the natural log of the time to transformation start at the nose, t_N . A multiple regression technique was utilized to generate an expression for each of the C-curves in terms of the four variables as follows

$$\frac{S - S_E}{S_N - S_E} = \frac{1}{\exp(-1/2)} \left(\frac{U - U_E}{U_N - U_E} \right)^{1/2} \exp \left[-\frac{1}{2} \left(\frac{U - U_E}{U_N - U_E} \right) \right]^2 \quad (2.50)$$

where $U = 1000/T$, $U_E = 1000/T_E$, $U_N = 1000/T_N$, $S = \ln t$, $S_E = \ln t_E$, $S_N = \ln t_N$, and T and t are the desired temperature and time for isothermal transformation start. The ability of this technique to predict TTT start times was given for a low alloy 0.33%C steel with reasonable agreement.

Conversion of TTT to CCT curves by Sakomoto *et al.* [44] was performed using the Scheil equation. The calculation of fraction transformed for the isothermal transformations of ferrite, pearlite and bainite was made by the equation:

$$X = \left[\frac{\ln t - \ln t_S}{\ln t_F - \ln t_S} \right]^2 \quad (2.51)$$

where t_S and t_F are the start and finish times for the respective reactions and t is the transformation time. As can be seen, this is the square of an additive expression. No explanation for using this technique was offered. Eq. (2.45) was used to calculate the fraction transformed during continuous cooling by summing the isothermal contributions over the appropriate temperature range. Comparison of a predicted and measured CCT diagram was given but only for one grade of steel. The results were also used to calculate the microstructure produced during cooling on the run-out table of a hot strip mill.

Prediction of non-isothermal heat-treatment processes has been the topic of interest for a group of Hungarian authors [45,46,47]. The additivity principle has been applied to the transformation event with the kinetic parameters of the Avrami equation being determined from dilatometry. Application has been made to the case hardening of carburized steel bars.

Details of the model developed to solve for temperature in the bar were not provided. Results were given in terms of temperature, microstructure and hardness through the cross-section of the bar but comparison with experimental bar microstructures and hardnesses were not made.

Suehiro *et al.* [48] and Yada [49] have predicted microstructural evolution during the cooling of low-carbon steel strip. Their model was centered around prediction of phase transformations from deformed austenite, however the description of kinetics was based on the same theories as for undeformed austenite. Attributing the small incubation times to the low amounts of carbon in the steels considered, the ferrite reaction was assumed to begin when the temperature had fallen below T_{A_3} . Two different equations were employed to describe the phase transformation kinetics: firstly for nucleation and growth reactions, the growth rate was given as:

$$\frac{dX}{dt} = \frac{K_1}{d_\gamma} (IG^3)^{1/4} \left(\ln \frac{1}{1-X} \right)^{3/4} (1-X) \quad (2.52)$$

and secondly for the case of site saturation during nucleation

$$\frac{dX}{dt} = \frac{K_2 G}{d_\gamma} (1-X) \quad (2.53)$$

where d_γ is the austenite grain size and K_1 and K_2 are constants. The growth rate of ferrite was determined from a Zener expression, Eq. (2.21), which had been modified by Hillert [16] (known as the Zener-Hillert equation), and the pearlite growth rate from a volume-diffusion control model. Recognizing the change in the mean carbon concentration in the austenite during transformation to ferrite, a method was proposed for adjusting the growth rate of ferrite as the reaction continued. This involved the use of boundary conditions from the phase diagram to evaluate the amount of carbon rejected by the ferrite during each time step. By monitoring the mean composition of the retained austenite, a method also was formulated for the prediction of pearlite start. As displayed in Fig. 2.15, it was assumed that

pearlite started and ferrite ended when the mean carbon concentration in the austenite intersected the extrapolated A_{cm} line below T_{A1} . The authors suggested the use of Eq. (2.52) for the initial stages of ferrite growth with a switch to Eq. (2.53) for the later stages. The pearlite growth was calculated from Eq. (2.53). The constants K_1 and K_2 were evaluated empirically from a single grade of steel. The model was used to calculate relative amounts of microstructural constituents, hardness and strength in low-carbon steels.

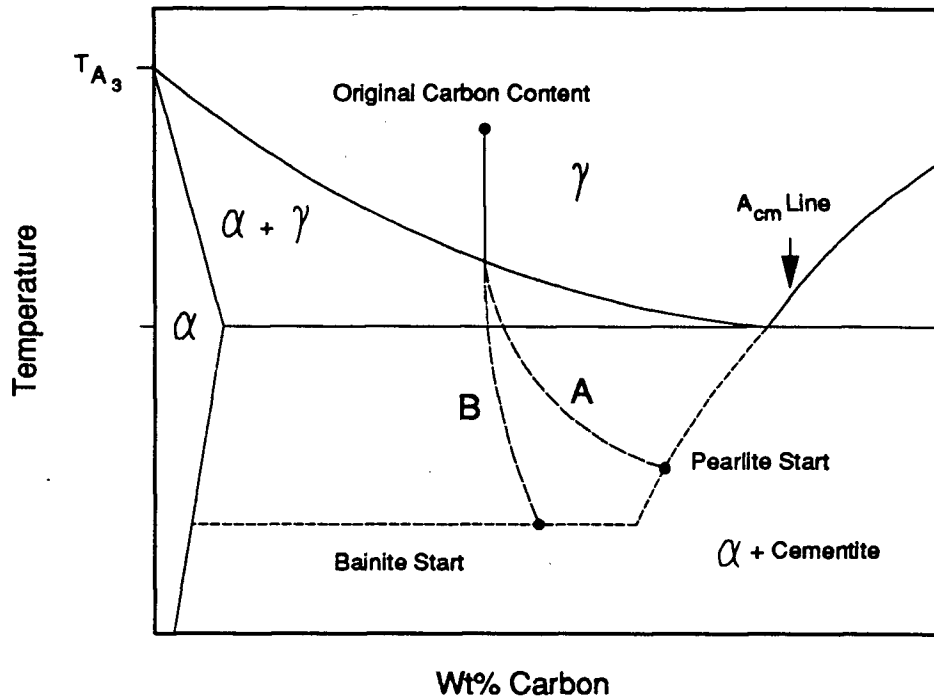


Fig. 2.15 - Method for determining pearlite start temperature during cooling of hypoeutectoid steel from Suehiro *et al.* [48]. The A and B lines represent the change in carbon concentration in the retained austenite for two different cooling rates.

From the foregoing discussion it would seem that the application of additivity to the non-isothermal transformation of austenite to ferrite/pearlite in low-carbon steels is justified, whereas the use of additivity for describing incubation remains unsubstantiated. However, predictions of microstructure and thermal histories in steels of various shapes and sizes have been made with promising results.

2.3 Structure /Property Relationships

2.3.1 Theory

The relationship between microstructure and the corresponding mechanical properties in steels, has long been an area of concern for metallurgists. The achievement of an understanding is complicated by the fact that there are many mechanisms contributing to the properties of steel. Theoretical advances into the relationship between structure and properties in metals [50] and composite materials [51] have been summarized, but a complete description is intractable due to the complexity of the problem [51]. In a review article on strengthening mechanisms in steels, Marder [52] has suggested four separate mechanisms:

- (1) solid-solution strengthening,
- (2) dispersion hardening,
- (3) dislocation strengthening and
- (4) hardening by high-angle grain boundaries.

Solid-solution strengthening can be exhibited by both substitutional and interstitial elements. The amount of strengthening is related to the distortion caused by the atom in the lattice. As a result, interstitial elements which cause greater lattice distortions, contribute more to strengthening. This can be on the order of 10-100 times greater than that caused by substitutional elements. An example of the effects of various alloying elements on the strength of ferrite is shown in Fig. 2.16 [52].

Dispersion hardening in steels is usually a result of second-phase carbides or nitrides which can vary in both size and shape. The theory of dispersion strengthening was first proposed by Orowan [53], and assumes that there are an array of undeformable spherical particles in a matrix. Orowan showed that the yield stress was inversely proportional to the spacing of the particles such that:

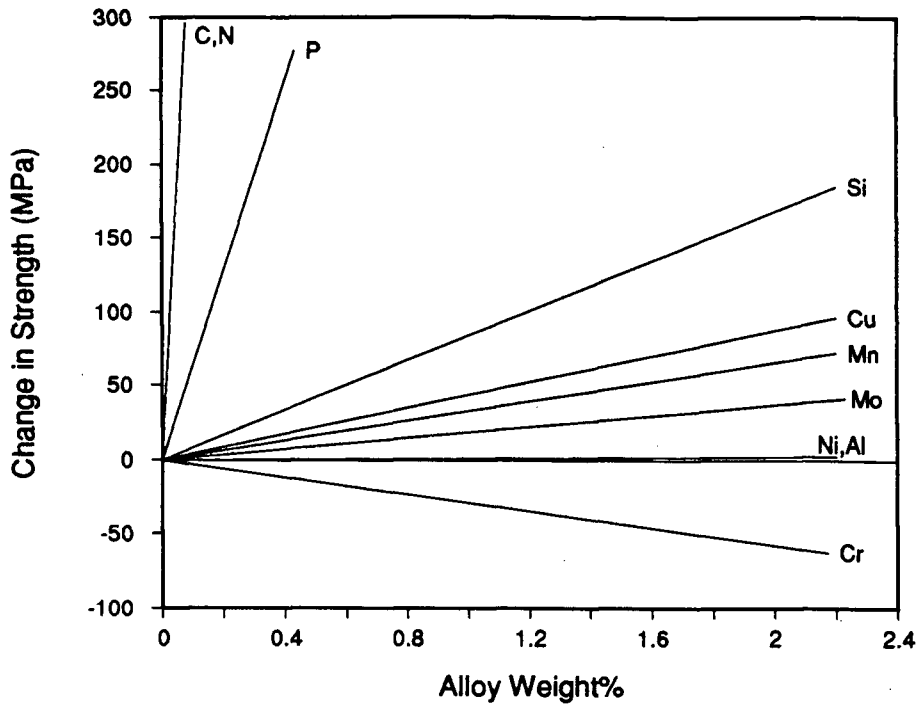


Fig. 2.16 - Effect of solid-solution elements on the strength of ferrite [52].

$$YS = \sigma_s + \frac{2L}{b\lambda} \quad (2.54)$$

where σ_s is the yield strength of the matrix, L is the line tension of a dislocation, b , is the Burgers vector and λ is the particle spacing. Modifications of Eq. (2.54) have included the effect of the shape and size of the second-phase particles.

Dislocation strengthening is caused by interactions between dislocations in the metal lattice. Dislocations are created in a number of ways including cold working, quenching strains, low-temperature transformations etc., and can lead to significant changes in the strength of a matrix. The flow stress has been shown to be related to the density of dislocations by the following relationship:

$$\sigma_f = \sigma_s + K_b N_f^{1/2} \quad (2.55)$$

where σ_f equals the flow stress, σ_0 is the matrix flow stress, K_1 is a constant incorporating the Burgers vector and the shear modulus and N_f is the dislocation density.

The effect of grain boundaries on the strength of metals has been attributed to the suggestion that grain boundaries act as barriers for the movement of dislocations. An empirical relation proposed for relating strength to grain size can be represented by [52]:

$$YS = \sigma_i + K_Y d^{-1/2} \quad (2.56)$$

where σ_i is the friction stress needed to move dislocations, K_Y is a constant and d is the grain diameter. Equation (2.56), known as the Hall-Petch equation, has been shown to apply to a variety of metal alloy systems.

2.3.2 Empirical Formulas

Accurate prediction of strengths in steels must take into account the effects of the strengthening mechanisms listed above. Owing to the nature of the present study, the discussion will be limited to ferrite/pearlite, plain-carbon and low-alloy steels. Almost exclusively, relationships developed between strength and microstructure in steels have been empirical. Some of the more important studies pertaining to the prediction of strength in steels are listed below.

Among the first comprehensive treatments of the tensile properties of ferrite/pearlite steels with the aim of developing useful structure/property relationships was provided by Kouwenhoven [54]. The objective of his work was to relate the Lüders strain at the lower yield point in steels to the composition and microstructure. The study involved nearly 70 different grades of steel made in the laboratory. The carbon content was varied from 0.04 to 0.82%, manganese from 0.22 to 1.90% and silicon from 0.03 to 2.98%. After a suitable heat treatment of the material, mechanical testing to determine tensile strength was performed. Each sample was also characterized in terms of the ferrite/pearlite fraction and the ferrite grain size. Owing to the fact that most of the steels consisted of 90% ferrite or more, the

morphology of the pearlite was not considered as important and thus not measured. Using a multiple linear regression technique and separating the solid-solution strengthening effects according to microstructure, the following equation was derived:

$$\sigma_{LY} = 52.9f_{\alpha} + (372.4 + 92.1\%Mn)f_p + 70.6\%Si + 25.5f_{\alpha}d_{\alpha}^{-1/2} \quad (2.57)$$

where σ_{LY} is the lower yield strength, f_{α} is the ferrite fraction, f_p is the pearlite fraction, and d_{α} is the ferrite grain diameter, in mm. The units of stress are MPa. Results of the predictive capability of Eq. (2.57) are shown in Fig. 2.17. Agreement between predicted and measured strengths is seen to be quite good.

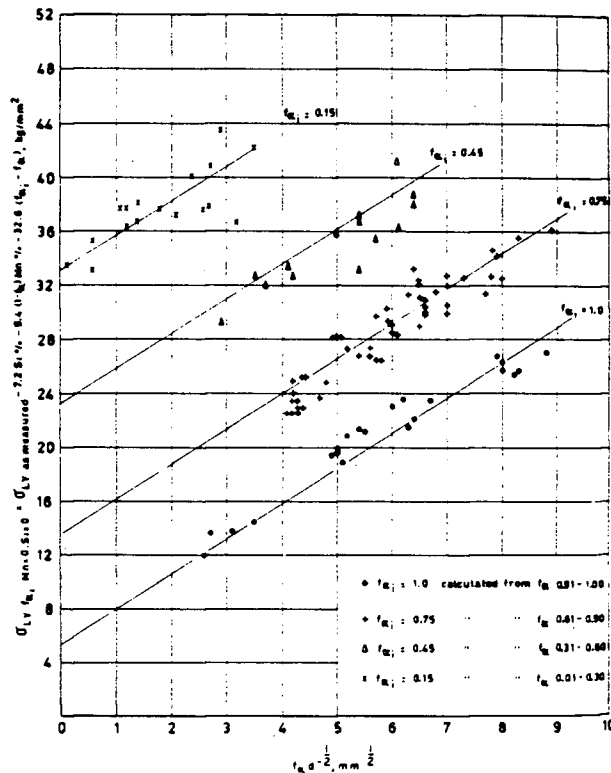


Fig. 2.17 - Predicted and measured values of the lower yield stress, plotted as a function of the product of ferrite fraction and square root of ferrite diameter, by Kouwenhoven [54].

Recognizing the lack of attention given to pearlite morphology and steels with greater pearlite contents in the study by Kouwenhoven, Gladman *et al.* [55] set out to clarify the

structure/property relationships in higher carbon steels. Over 40 grades of steel were studied with three carbon levels, 0.4, 0.6 and 0.8%, two manganese levels 0.85 and 1.4%, two silicon levels 0.3 and 0.9%, and two nitrogen levels 0.007 and 0.017%. Some steels also contained grain refining additions. Variation in morphology of the ferrite/pearlite was achieved through austenitizing treatments and cooling practices. The microstructure was characterized by ferrite/pearlite fraction, ferrite grain diameter, pearlite spacing and pearlite colony size. Although the compositions of the grades were specified based on a factorial design, the interdependence of the microstructural features with each other and composition, made this technique inappropriate for structure/property relationship determination. Instead a multiple linear regression technique was applied. Following a statistical procedure to determine the most significant contributors to strength, equations for strength were given as:

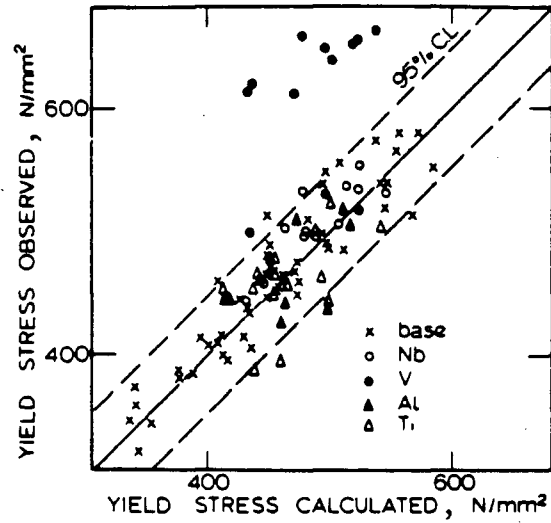
$$YS = f_{\alpha}^{1/3} [35.4 + 58.5\%Mn + 17.4d_{\alpha}^{-1/2}] + (1 - f_{\alpha}^{1/3}) [178.6 + 3.85S_p^{-1/2}] + 63.1\%Si + 425.0(\%N)^{1/2} \quad (2.58)$$

$$UTS = f_{\alpha}^{1/3} [246.4 + 1142.7(\%N)^{1/2} + 18.17d_{\alpha}^{-1/2}] + (1 - f_{\alpha}^{1/3}) [719.2 + 3.54S_p^{-1/2}] + 97.0\%Si \quad (2.59)$$

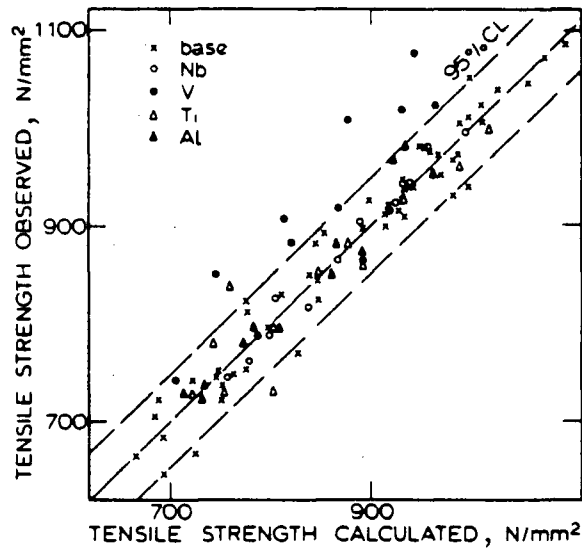
where S_p represents the interlamellar spacing of pearlite. The units used for the study were mm for spacing and ferrite diameter, and strengths were in MPa. These equations are commonly known as the Gladman equations.

Results of the observed and calculated yield and ultimate strengths from Gladman *et al.*'s work are shown in Fig. 2.18. Reasonable predictions of strength have been made by the equation, however, there is a substantial amount of scatter.

Although the Gladman equations were developed for medium to high carbon steels, Speich and Rice [56] have successfully applied them to lower carbon steels. The purpose of the work was to investigate the effects of controlled cooling on the properties of three low-carbon steels; 1008, 1022 and 1030. Of particular interest was the effect of slow cooling on the properties of the steels. Material used in the tests was obtained from a commercial rod



(a)



(b)

Fig. 2.18 - Predicted (a) yield and (b) ultimate strengths, calculated from the Gladman equations [55], plotted as a function of the measured values.

mill. Cooling rates between 0.05°C/s and 13.8°C/s were imparted to rod samples after appropriate austenitizing. Two temperatures were used to provide two prior austenite grain sizes. The material was then mechanically tested, and the microstructure evaluated in terms of

ferrite/pearlite fraction, ferrite diameter and pearlite spacing. Despite the fact that the Gladman equations were formulated based on higher carbon grades, it was found that reasonable estimates for both yield and ultimate strengths were provided.

Thus it would seem that the Gladman equations are a useful tool for the prediction of mechanical properties in ferrite/pearlite plain carbon steels. Owing to the paucity of data concerning structure-versus-properties in these materials, it is quite possible that a greater amount of effort will be needed to provide more accurate, semi-empirical relationships. Such was the case in the present study.

2.4 Scope and Objectives

The objectives of the present work can be stated as follows:

- (1) Development of a mathematical model for the prediction of thermal history in Stelmor-cooled steel rod, as a function of rod diameter, Stelmor line cooling conditions and steel composition.
- (2) Incorporation of the transformation kinetics for the austenite-ferrite and austenite-pearlite reactions in the model, based on the Avrami equation, and development of a technique for quantitative prediction of the microstructure evolved in continuously-cooled plain-carbon steels.
- (3) Through the use of mechanical properties and microstructural data, development of empirical structure-property relationships, and incorporation in the model for the prediction of strengths in Stelmor-cooled steel rod as a function of steel composition and process variables.

The first of these objectives is concerned with the prediction of heat transfer within the cooling rod and from its surface. This requires a numerical method for solution, owing to the fact that the thermophysical properties of steel, the transformation kinetics of austenite and the boundary conditions are dependent on temperature. Laboratory-scale rod cooling tests will be utilized to test correlations for the prediction of heat-transfer coefficients at the

surface of cylindrical bodies. A similar set of experiments is required on an operating Stelmor line to characterize heat-transfer conditions in the plant. The plant data will allow the model to be effectively "tuned" to plant conditions.

The second objective requires investigation of the kinetics of the austenite-ferrite and austenite-pearlite phase transformations. The Avrami equation will be utilized to characterize the reaction kinetics, but appropriate values for the empirical parameters n and b in the equation must be determined. The method to be employed for the investigation of phase transformation kinetics will be based on that outlined previously by Hawbolt *et al.* [24,25], and will comprise both isothermal and continuous cooling tests. Information obtained from these experiments will allow the prediction of transformation kinetics in plain-carbon steels, based on the additivity principle and empirical equations for the CCT start time. Owing to the paucity of data in the literature concerning quantitative prediction of the microstructure evolved in plain-carbon steels during continuous cooling, experiments will also be conducted with the purpose of determining ferrite fraction, ferrite grain diameter and pearlite spacing in continuously-cooled steel rod, as a function of steel composition and thermal history. Equations based on accepted theory from the literature and empirical data will be employed to predict the microstructure formed in the rod.

The final aim of the model is to relate the microstructure that is formed during cooling and composition of the steel, to the mechanical properties of the steel rod. Once again, a paucity of data concerning quantitative relationships for a wide range of plain-carbon steels has required additional experiments concerning structure-property relationships. Continuously-cooled steel rod, for which the microstructural features have been quantified, will be tested in tension to determine mechanical properties. Existing data and structure-property relationships from the literature can be augmented with the experimental data to improve the correlations and extend the range of applicability.

Validation of the model will be made utilizing thermal history, microstructure and mechanical properties data gathered from both the laboratory and plant trials. A final check can also be made by comparing model strength predictions with an independent group of steel grades processed on the Stelmor line.

Industrially, the ability to predict microstructure and mechanical properties, is seen as a powerful tool. Not only can the model be run to predict strength in rods of certain composition and cooling conditions, but it can also be employed to calculate appropriate cooling rates to provide the steel rod with a desired strength or microstructure. It would also be suitable as a research tool, in that it could be used to predict how certain grades of steel would behave during Stelmor cooling, without having to perform expensive trial-and-error experiments in the plant.

Chapter 3 - MATHEMATICAL MODEL

3.1 Heat Flow Considerations

From the previous discussion on the effect of time and temperature on transformation kinetics of the austenite decomposition reactions, it is obvious that the prediction of microstructural evolution during the cooling of steel rods is not possible without an accurate knowledge of temperature in the material. This can only be achieved realistically through the appropriate application of the laws of heat transfer.

For the cooling of steel rod, heat is transferred by a combination of conduction inside the steel, and radiation and convection from the rod surface to the surroundings.

3.1.1 Model Formulation

Radial heat conduction within the steel rod is governed by Fourier's Law which in cylindrical coordinates is (from Kreith and Black [57]):

$$\frac{\partial}{\partial r} \left(k \frac{\partial T}{\partial r} \right) + \frac{k}{r} \frac{\partial T}{\partial r} + q_{TR} = \rho C_p \frac{\partial T}{\partial t} \quad (3.1)$$

where r is the radius of the cylinder, T is the temperature, q_{TR} is the rate of heat evolution (in this case due to the austenite decomposition reaction), ρ is the density of the material, C_p is the specific heat, and t is time. In order to apply Eq. (3.1) to the present case several simplifying assumptions were made:

- (i) The rod is considered to be infinitely long and axial gradients are assumed to be small; thus heat flow in the axial direction is negligible.
- (ii) The initial temperature of the steel rod is assumed to be uniform.
- (iii) The rods are radially symmetric.
- (iv) Temperature is independent of angular displacement.
- (v) The rod cross-section is assumed to be uniform over its length.

Considering boundary conditions for solution of Eq. (3.1), at the centreline of the rod the heat flux is assumed to be zero (adiabatic conditions associated with a symmetrical temperature distribution),

$$t > 0, r = 0 \quad -k \frac{\partial T}{\partial r} = 0 \quad (3.2)$$

and at the surface of the rod the rate of heat transfer can be characterized by an effective heat-transfer coefficient, dependent on conditions of radiation and convection

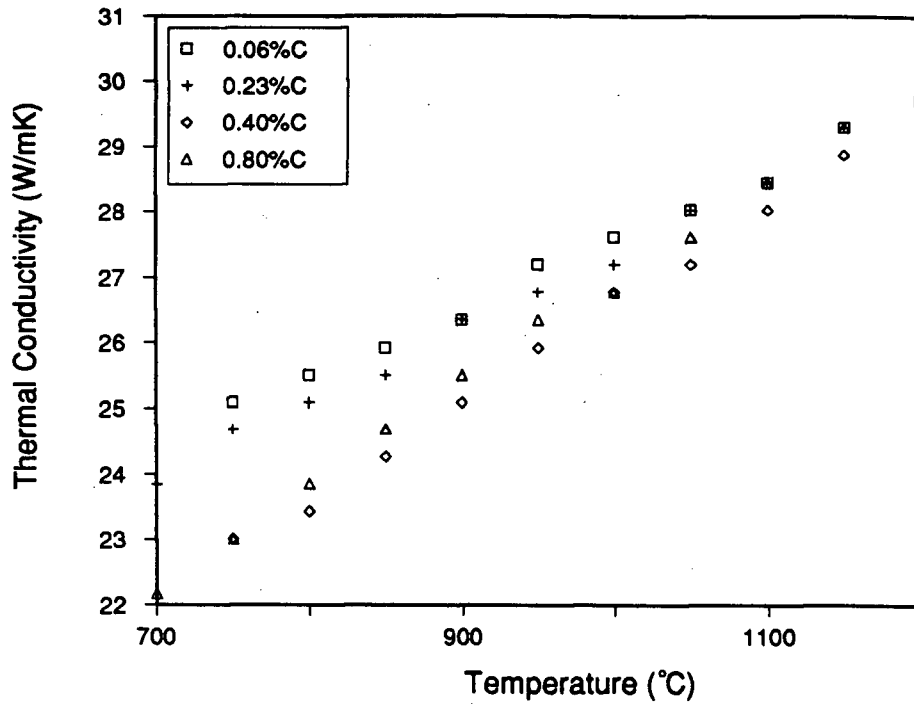
$$t > 0, r = r_s \quad -k \frac{\partial T}{\partial r} = h_{ov}(T_s - T_a) \quad (3.3)$$

where r_s is the radius of the rod, h_{ov} is the effective heat transfer coefficient, T_s is the surface temperature and T_a is the ambient temperature of the surroundings. For the initial condition, the rod is assumed to be isothermal

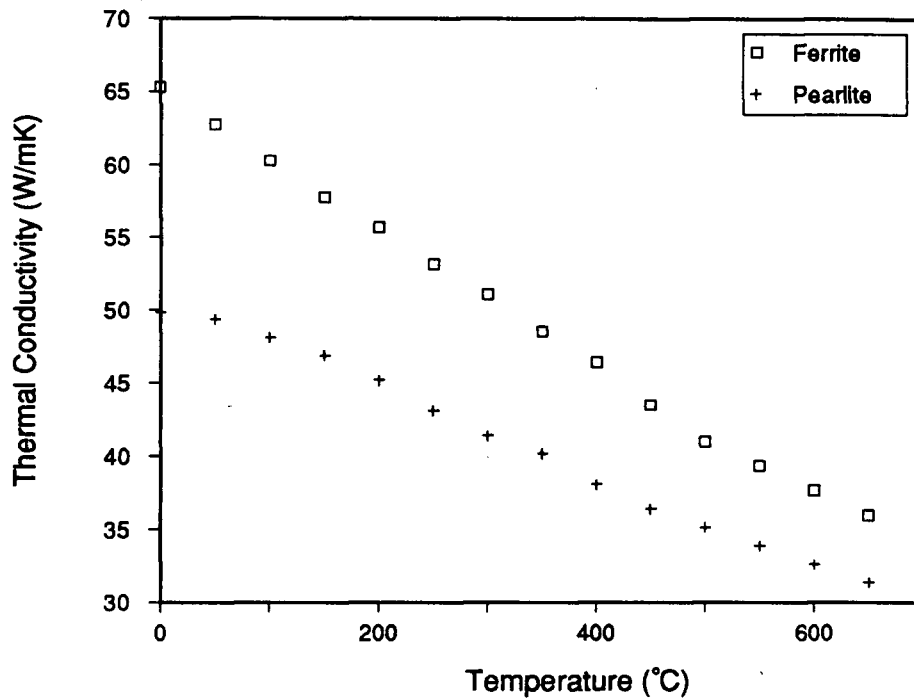
$$t = 0, 0 \leq r \leq r_s \quad T = T_0 \quad (3.4)$$

where T_0 represents the rod temperature, normally at the laying head.

Solution of Eq. (3.1) is not possible analytically due to the variation of k , ρ , C_p and q_{TR} as a function of temperature. Hence time and temperature have been discretized into small intervals and the one-dimensional implicit finite-difference technique has been applied. By performing a heat balance on the volume element surrounding each node, a system of algebraic equations is obtained. A derivation of the equations based on this technique, in cylindrical coordinates, is provided in Appendix 1. Three types of nodes, - surface nodes, internal nodes and centreline nodes - can be identified for the geometry being considered. The equations for all nodes can be expressed in the form of a tridiagonal matrix which was solved using Thomas' algorithm [58].



(a)



(b)

Fig. 3.1 - Thermal conductivity as a function of temperature; (a) austenite with various carbon contents, (b) ferrite and pearlite [59].

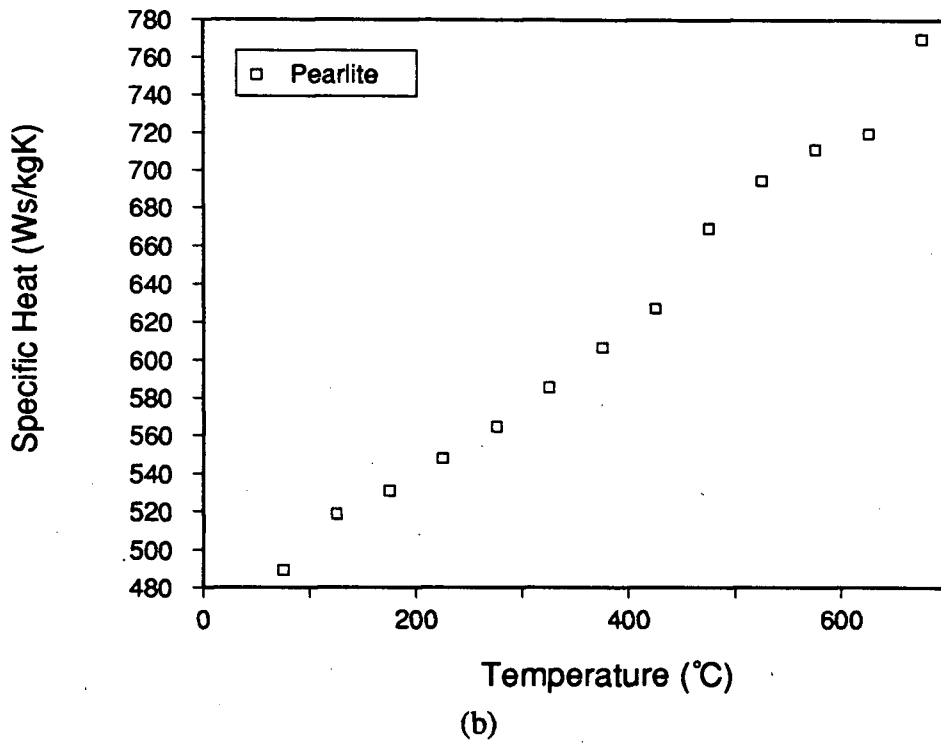
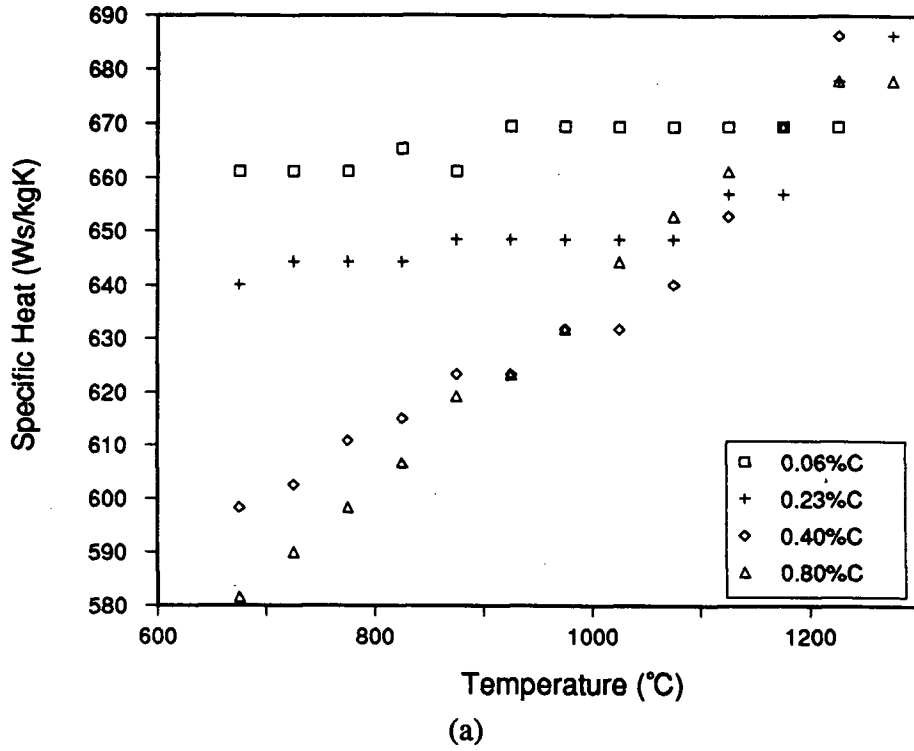


Fig. 3.2 - Specific heat as a function of temperature: (a) austenite with various carbon contents, (b) pearlite [59].

Variation of steel thermal conductivity over, a range of temperatures, was obtained from the literature [59]. Employing a curve-fitting technique, a polynomial was fitted to approximate k as a function of temperature, phase present and carbon concentration (Fig. 3.1). A similar technique was applied in determining the specific heats for both the austenite and pearlite, as shown in Fig. 3.2. However, the variation in specific heat of ferrite over the temperature range of interest, proved to be quite different. Included in Fig. 3.3 are specific heat values for pure iron, tabulated from the literature [59-62]. As can be seen, an anomaly exists in the data, at approximately 770 °C. This discontinuity is related to the change in ferromagnetic properties of Fe at the Curie point, according to Smallman [63], and is not associated with the austenite-ferrite phase transformation. The line plotted through the points in Fig. 3.3 is from Barin *et al.* [61]; they considered five distinct temperature ranges for the regression in order to obtain a good fit. Calculation of the thermal conductivity and specific heat for the phases in the steel is accomplished through the use of an appropriate polynomial equation. For ferrite, the five equations from Barin *et al.*, have been employed.

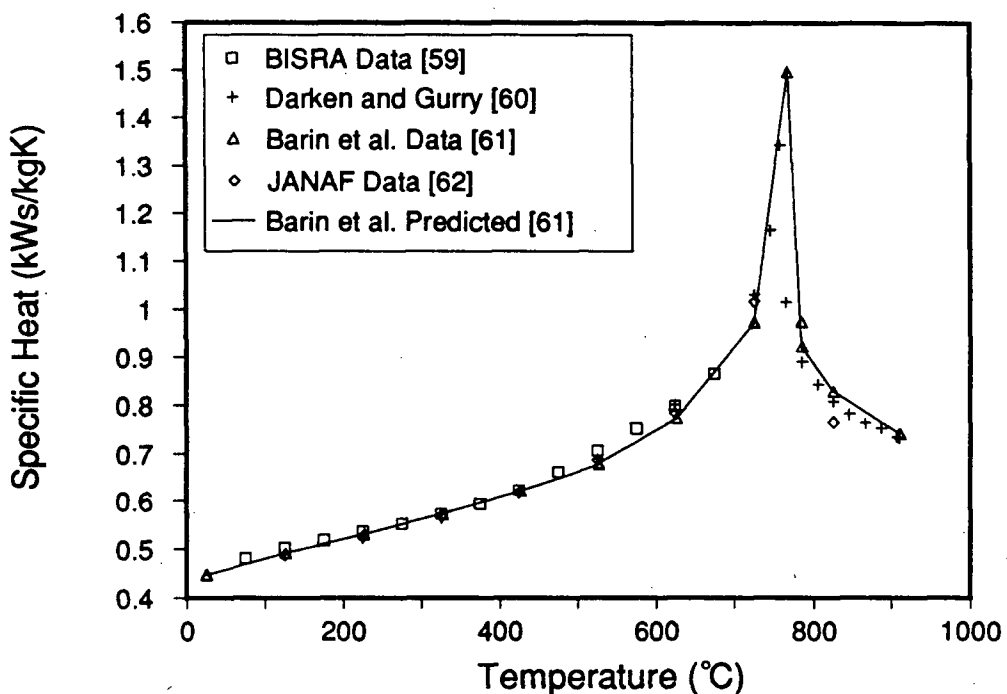


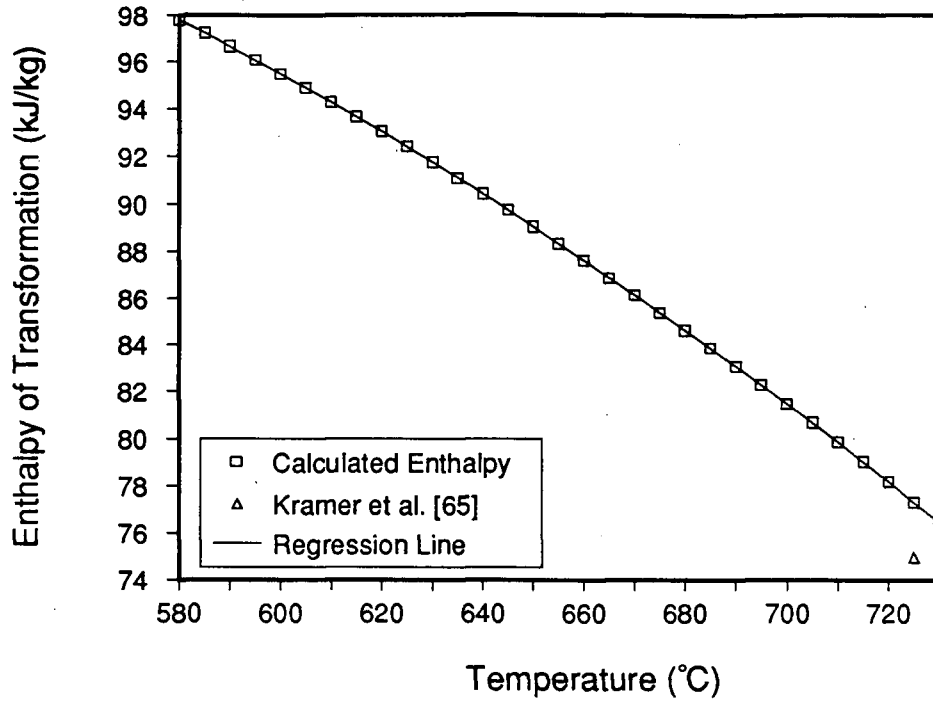
Fig. 3.3 - Specific heat as a function of temperature for ferrite [59-62].

Another variable considered as a function of temperature in the model, is the latent heat of transformation for both the austenite-ferrite and austenite-pearlite reactions. Owing to the variation of specific heats for ferrite, pearlite and austenite as a function of temperature discussed in the preceding paragraph, it would be expected that the transformation heat will vary considerably over the temperature range of interest. The heat of transformation for the pearlite reaction has been measured as -77.0 kJ/kg at 1000 K [64]. This value is in agreement with the data of Kramer *et al.*, who investigated the effect of pearlite spacing on the enthalpy of transformation. Thus, knowing the ΔH_1 for transformation at temperature T_1 , the heat of transformation at temperature T_i , is given by:

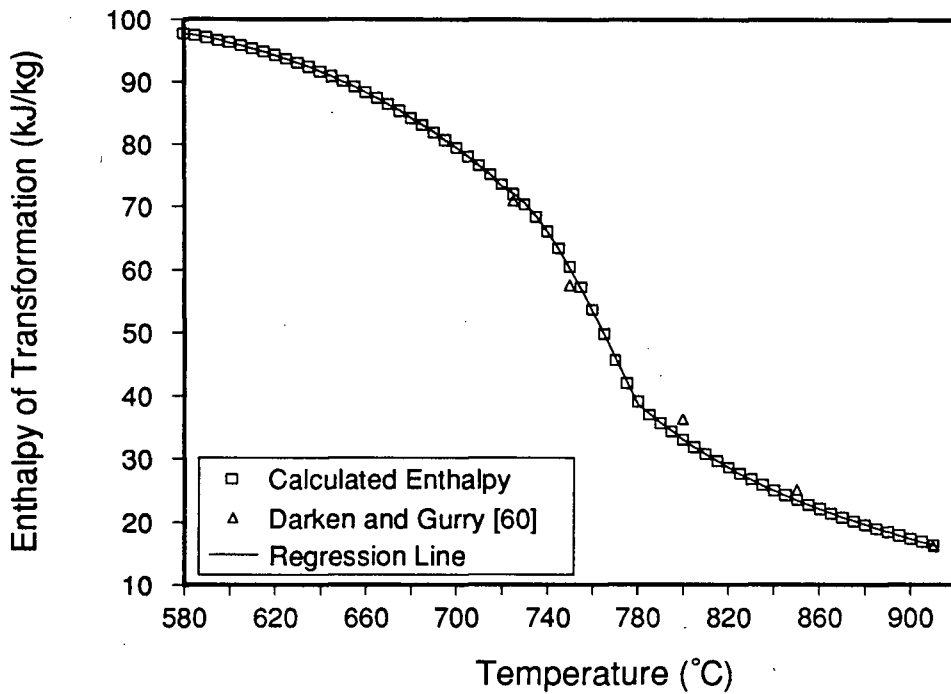
$$\Delta H_i = \Delta H_1 + \int_{T_1}^{T_i} (C_{p,J} - C_{p,A}) dT \quad (3.5)$$

where ΔC_p is the difference in specific heat between the reactants and products. Employing the polynomial equations developed for the dependence of specific heat of the various phases as a function of temperature, Eq. (3.5) has been solved over a temperature range applicable to the formation of pearlite. The results of the integration are presented in Fig. 3.4 (a). As can be seen the calculated values agree well with experiment. This data has been employed to fit a third-order polynomial equation for calculation of latent heats in the model.

The latent heat of transformation for the austenite-ferrite reaction has also been calculated from integration of Eq. (3.5). The results are shown in Fig. 3.4 (a), where ΔH is plotted as a function of temperature. Referring to Fig. 3.3, the change in slope of the C_p curve at the ferromagnetic transition is evident in the plot for transformation enthalpy as a function of temperature. As temperature for the reaction decreases from 770 to 730°C , the heat released doubles from about 35 to 70 kJ/kg. The regression line plotted in Fig. 3.4 (b) is actually three separate curves, each solved for a temperature range. The equations for these curves will be employed in the model for the calculation of the heat of transformation for ferrite.



(a)



(b)

Fig. 3.4 - Latent heat of transformation calculated for the two austenite decomposition reactions as a function of temperature; (a) austenite-pearlite and (b) austenite-ferrite.

The rate of release of the latent heat is dependent on the transformation rate. For a small increment of time Δt the fraction transformed can be denoted by ΔX , and the heat generated per unit volume is thus given by:

$$q_{TR} = \rho \Delta H_i \frac{\Delta X}{\Delta t} \quad (3.6)$$

By inserting the appropriate latent heats and incremental fractions for the pearlite and ferrite reactions, the quantity of heat released over each time step can be calculated. The rate of the phase transformation will be covered in a following section.

The advantage of the implicit finite-difference method is that it has unconditional stability which is not affected by node size or time step. Normally the rod was discretized into 11 nodes resulting in a node size of 0.5 mm for a 10 mm diameter, as an example. Likewise, the time steps were chosen usually to be 0.1 s. For comparison, the model was run with 21 and 6 nodes. Under identical conditions, the 21 node and 11 node temperature predictions were essentially the same, however, accuracy was seen to diminish for the 6 node case.

3.1.2 Boundary Conditions

The boundary conditions to which the solution of Eq. (3.1) is subject, must take into account the two modes of heat transfer at the surface of the rod, i.e., radiation and convection. Considering first convection, correlations are available for the cross-flow of a fluid over the surface of a cylinder [57],:

$$\overline{Nu}_D = C Re^p Pr^{1/3} \quad (3.7)$$

where \overline{Nu}_D is the mean Nusselt number, Re is the Reynolds number, Pr is the Prandtl number and C and p are empirically determined constants which depend on the magnitude of the Reynolds number.

Thus the heat-transfer coefficient at the rod surface can be calculated from the following expression:

$$\bar{h}_c = \frac{k}{D} C \left(\frac{\rho v D}{\mu} \right)^p \left(\frac{C_p \mu}{k} \right)^{1/3} \quad (3.8)$$

The material properties in Eq. (3.8) are evaluated at the mean-film temperature at each time step in the calculations. The values for C and p have been determined over ranges of Reynolds numbers as shown in Table 3.1 [57].

Table 3.1 - Constants for use with Eq. (3.8).

Re	C	p
0.4-4	0.989	0.330
4-40	0.911	0.385
40-4000	0.683	0.466
4000-40,000	0.193	0.618
40,000-400,000	0.0266	0.805

The heat-transfer coefficient for radiation can be written as follows:

$$h_r = \sigma \epsilon \frac{(T_s^4 - T_A^4)}{(T_s - T_A)} \quad (3.9)$$

where σ is the Stefan-Boltzman constant, ϵ is the emissivity and T_s and T_A are the rod surface temperature and the ambient air temperature, respectively.

The convective and radiative heat-transfer coefficients can be combined to yield an overall heat transfer coefficient:

$$h_{ov} = h_c + h_r \quad (3.10)$$

This expression for h_{ov} is applied to Eq. (3.3) for solution of the boundary conditions at the rod surface. The value for the emissivity of the steel surface has been assumed equal to 0.8 [57].

3.2 Phase Transformations

As has been outlined, several methods exist for the prediction of microstructural evolution in steels. The method chosen for this work is the use of empirically determined CCT start times to indicate the onset of the transformations and the Avrami equation to solve for the fraction transforming at each time step.

Incubation time in the model is calculated empirically based on the undercooling below the equilibrium transformation temperature. As cooling progresses, the temperature is monitored to determine if it has gone below the T_{A1} or T_{A3} for the appropriate transformation. Once the equilibrium temperature has been reached, the time below this temperature is compared with the start time predicted by the empirical CCT start equation. When the delta time below T_{A1} or T_{A3} exceeds the predicted start time, calculations begin for the fraction of a phase formed at each time step.

The calculation of fraction transformed for each node during a time step is based on the Avrami equation and the additivity principle. Considering any node i that has just exceeded the transformation start time, the fraction transformed over a small Δt can be expressed as:

$$X_{i,j} = 1 - \exp[-b(T_{i,j})\Delta t^n] \quad (3.11)$$

where $X_{i,j}$ is the fraction transformed at node i over the initial time step j ; $b(T_{i,j})$ is the value for b as a function of temperature; Δt is the time step or time spent at that temperature; and n is the geometric constant from the Avrami equation. Now, considering the next time step and the i th node, the fraction transformed is given by:

$$X_{i,j+1} = 1 - \exp[-b(T_{i,j+1})\theta_{i,j+1}^n] \quad (3.12)$$

where $\theta_{i,j+1}$ is known as the virtual time which in this case represents the time taken to form fraction $X_{i,j}$ at temperature $T_{i,j+1}$ plus the time step, Δt . The time taken to form fraction $X_{i,j}$ at temperature $T_{i,j+1}$ is equal to:

$$t_{i,j+1} = \left[\frac{\ln \frac{1}{1-X_{i,j}}}{b(T_{i,j+1})} \right]^{-\frac{1}{n}} \quad (3.13)$$

and thus the virtual time for the $j+1$ th time step becomes:

$$\theta_{i,j+1} = t_{i,j+1} + \Delta t \quad (3.14)$$

The incremental fraction transformed over the $j+1$ th time step in the i th node is then:

$$\Delta X_{i,j+1} = X_{i,j+1} - X_{i,j} \quad (3.15)$$

The release of latent heat over the time step can be estimated from Eq. (3.6) and (3.15), and must be included iteratively in the heat flow calculations. Experience has shown that three to four iterations are required for a temperature difference of less than 10^{-4} °C over successive calculations [66].

Calculations for fraction transformed are continued until the equilibrium fraction for the particular phase has been reached. The equilibrium fraction can be determined empirically from fraction transformed-versus-cooling rate data or it can be obtained from the phase diagram following a technique given by Suehiro *et al.* [48] (Fig. 2.14), using the extension of the A_{cm} line below the T_{A_1} for calculation of the pearlite start temperature or ferrite finish. The phase diagram for the steel, as a function of composition, has been outlined previously [34,35] and is utilized to calculate equilibrium fractions and phase boundary compositions at each temperature. For temperatures above T_{A_1} , the predicted phase boundaries have been employed to calculate the equilibrium fraction of ferrite for each time step. Extrapolation of the phase boundaries for temperatures below T_{A_1} allowed the prediction of the equilibrium ferrite and pearlite fractions, in the mathematical model.

3.3 Microstructure-Properties

The prediction of microstructure and mechanical properties in the model is based on essentially empirical considerations. As was seen in the Gladman equations (Eqs. (2.58) and (2.59)), the strength of ferrite/pearlite is dependent on the ferrite fraction, solid solution

strengthening effects in ferrite and pearlite, the ferrite grain diameter and the pearlite spacing. As the amount of carbon is varied in a plain carbon steel, the relative importance of these parameters is changed.

As indicated in Section 2.2.2, the fraction of ferrite in the steel can be predicted from both empirical as well as thermodynamic considerations. The ferrite grain diameter is based on an empirical relationship to cooling rate and steel composition. Recent work in the literature has suggested that the ferrite diameter is related linearly to the square root of the reciprocal cooling rate [67,68]; thus multiple regression techniques have been applied to relate ferrite diameter to thermal history and steel composition. Owing to the narrow range of prior austenite grain sizes encountered during Stelmor cooling, the prediction of ferrite grain sizes has been made assuming a constant austenite grain size.

Prediction of pearlite spacing in both eutectoid and hypoeutectoid grades was based on the degree of undercooling below the A_1 temperature. Theory suggests that the reciprocal pearlite spacing should be a linear function of undercooling below T_{A_1} [69]. Figure 3.5 shows some of the literature data on pearlite spacing, which reinforces the reciprocal spacing-versus-undercooling relationship [70-75]. Because most of this work has been based on high purity Fe-C systems, verification of the linearity must be undertaken for commercial grade steels. The average undercooling for the formation of pearlite can be calculated based on the predicted steel thermal history, employing a weighting to each temperature relative to the fraction of pearlite formed. The pearlite spacing then is calculated from the average undercooling.

Conversion of the microstructural predictions and composition to yield and ultimate tensile strength in this study was carried out using an equation of the form proposed by Gladman *et al.* [55] or Kouwenhoven [54] (Eqs. (2.57-2.59)). Owing to the paucity of data in this area, it is necessary to combine results from several studies to provide a more accurate relationship between strength and microstructure.

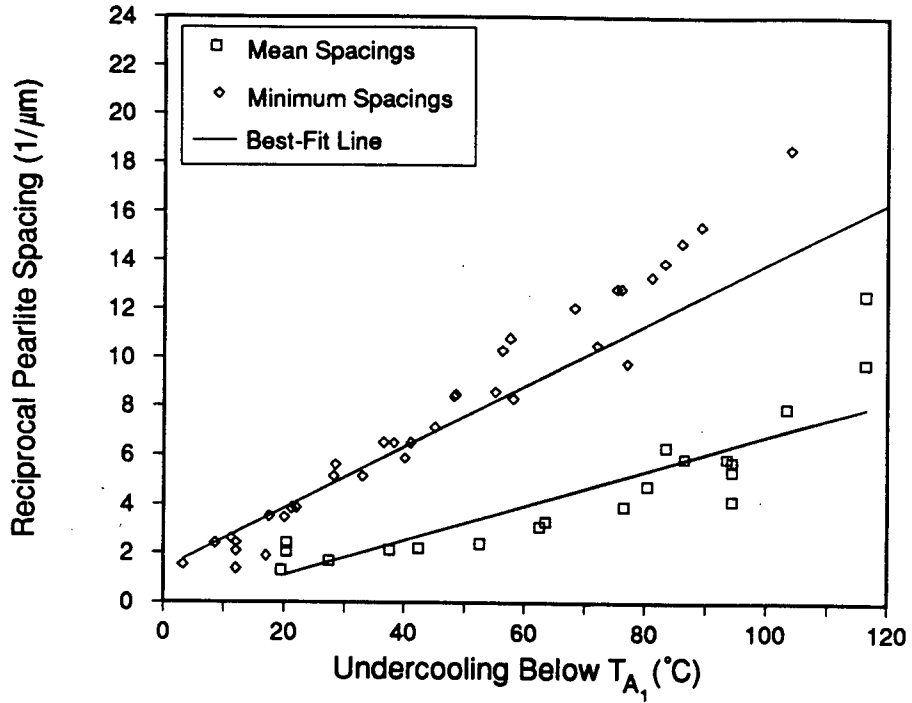


Fig. 3.5 - Mean and minimum measured pearlite spacings as a function of undercooling below T_{A_1} from the literature [70-75].

Chapter 4 - LABORATORY EXPERIMENTS

4.1 Rod Cooling Tests

4.1.1 Objectives and Introduction

Laboratory experiments were formulated with the intention of maximizing the variety and quantity of data, while minimizing the number of individual tests. As has been outlined, information is needed concerning three aspects of Stelmor cooling: (1) thermal history and heat transfer, (2) phase transformations and microstructural evolution and (3) microstructure-mechanical property relationships. The thermal response information is necessary to validate techniques utilized for determination of heat-transfer coefficients and to verify the capability of the mathematical model to predict temperature. The phase transformation data is required to compare predicted transformation kinetics with those measured in the tests as well as to link thermal history of the steel to the microstructure formed for various steel compositions. Mechanical property/microstructure data are needed to augment existing data so that accurate predictions of properties can be made in the model.

The experimental apparatus employed in the experiments, comprised a resistance-heated tube furnace to heat rod samples to a desired temperature, and a specially designed air cooling system to cool the rods at a controlled rate. Each rod sample was instrumented with an axially mounted thermocouple, attached to a data logger and strip chart recorder. After each test, the rods were sectioned for examination of the microstructure; and tensile samples were prepared to measure tensile properties. By varying rod diameter, rod composition and air velocity, Stelmor line behaviour could be simulated.

4.1.2 Stelmor Simulator

The aim in the design and construction of the air cooling system was to blow air at a constant velocity over a of 20-cm long by 2.5 cm wide area. Pressurized by a 10-h.p., Rootes-type air compressor with a rated capacity of nearly 100 l/s, air was discharged through a "constant velocity duct" (CVD). A schematic diagram of the system is shown in

Fig. 4.1. As can be seen, the air was supplied to the duct via a 5-cm I.D. pipe. An orifice plate is situated approximately 15 pipe-diameters upstream of a right-angle joint in the pipe, to minimize its effect on air velocity at the discharge. The flow rate of the air was controlled by the valve shown in the Fig. 4.1 or by the compressor bleed valve. Just below the valve, a length of 5-cm square ducting has been inserted before entry into the CVD. The outlet begins as a 5-cm square at the top and expands to 20 cm in one transverse direction while reducing to 2.5 cm in the other direction. Five vanes were mounted inside the upper zone of the CVD to facilitate uniform airflow through the discharge. To increase back pressure in the system and even out the velocity distribution at the bottom of the blower, a 60-mesh screen was inserted 5 cm upstream of the blower outlet. Utilizing a pitot tube, air velocities were measured over a grid at the outlet of the blower at a height corresponding to the test rod position. A total of 57 locations were included in the grid, and the blower outlet was modified until a satisfactory constant velocity zone was achieved.

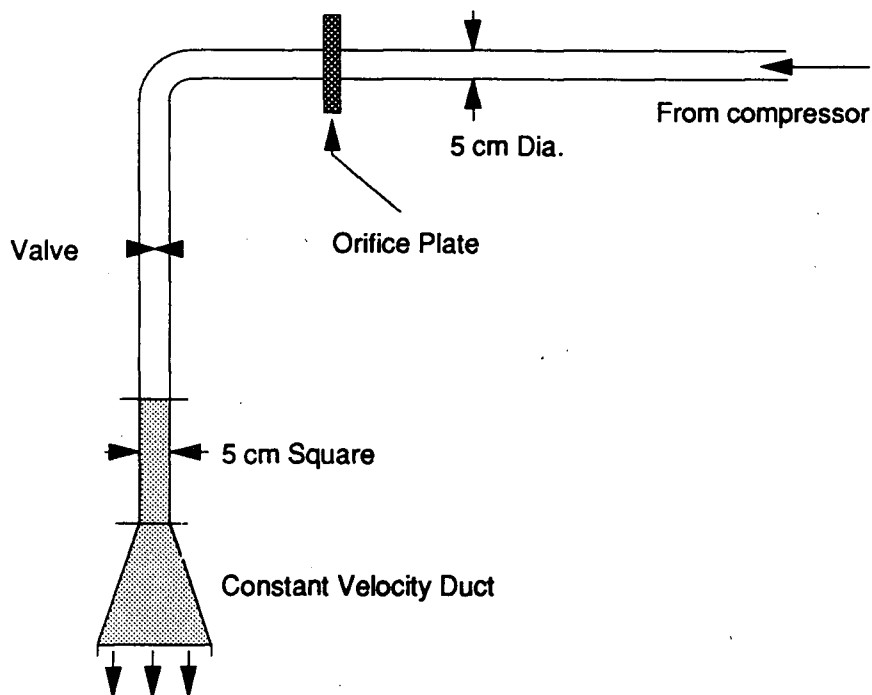


Fig. 4.1 - Schematic diagram of the air delivery system for the Stelmor cooling simulation experiments.

Results of some of the velocity profile measurements made on the system are shown in Fig. 4.2, and reveal a relatively constant velocity over the cooling duct. From average velocities obtained for each profile and corresponding orifice plate pressure drops, a relationship between these two parameters was obtained which precluded the need for velocity measurements prior to each rod cooling test. The average maximum air velocity attainable from the system was found to be 22 m/s, which compares favorably with air velocities on an industrial Stelmor line. The apparatus was seen as an effective and simple way of supplying air of constant velocity for the continuous cooling of steel rods.

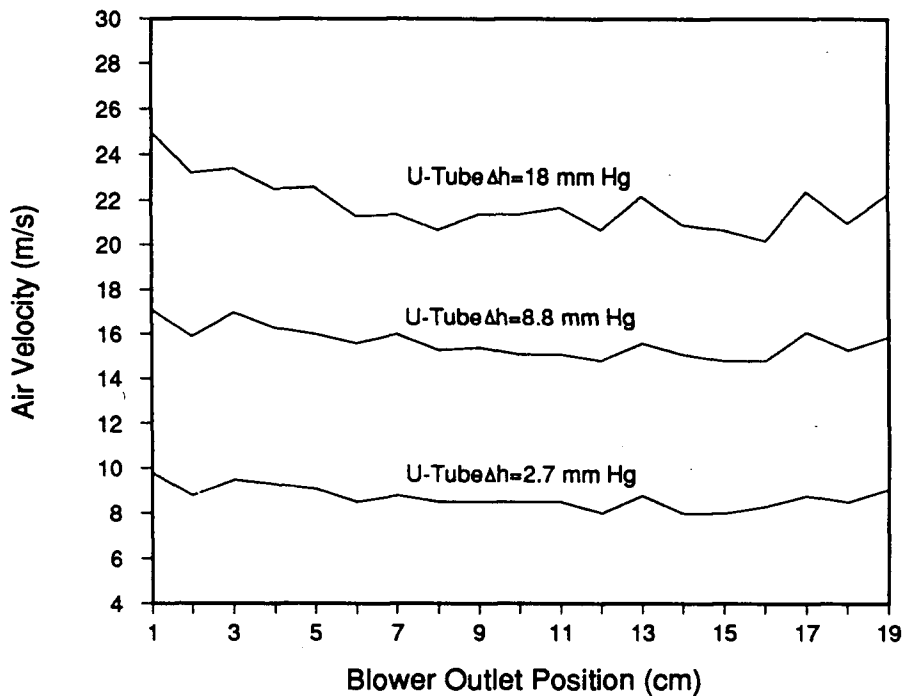


Fig. 4.2 - Velocity profiles for three blower pressures. Note the constant velocity across the width of the duct.

4.1.3 Tube Furnace

In order to attain a uniform temperature along the length of the test rods prior to cooling, it was found that a tube furnace with a particularly flat temperature profile was required. A wound resistance type furnace, with a diameter suitable for easy removal of hot test rods was selected. The furnace was constructed from a 6.3-cm O.D. quartz tube 68.6 cm

in length with a 5-cm I.D., wound with 2.4-mm chromel strip, 0.406-mm thick. Sixteen turns per 10-cm length, over the length of the tube, provided a total resistance of 25.6 Ω . With a power supply of 220 volts, the maximum temperature of the furnace was aimed at 900°C. Insulation was provided by wrapping two layers of 6.4-mm thick fibrefrax sheet over the tube and the whole assembly was placed inside an outer insulating shell of thermobestos, which was encased in an aluminum sheet.

After a proper bake-in, the temperature uniformity down the length of the furnace was tested. To protect the quartz tube from damage during testing, an alumina tube (4.45-mm O.D.) was inserted into the furnace and was in position for the profile tests. To minimize scale formation during rod heat-up, the furnace was flushed with nitrogen gas at about 3 l/min. Radiant heat losses were reduced by stuffing fibrefrax wool in the ends of the furnace tube. A chromel-alumel thermocouple was inserted into the furnace at 1 cm intervals to determine the temperature profile. Thermocouple measurements indicated that the temperature over the central 20 cm section of the furnace was within $\pm 5^\circ\text{C}$ of the mean. This was considered adequate for isothermal austenitizing of the test rods.

4.1.4 Rod Sample Preparation

Material employed for most of the rod-cooling experiments was obtained in coil form from the Stelco No. 2 Rod Mill, although some was machined from bar stock. Each test rod was cut from the appropriate coil and mechanically straightened so that it would fit into the cooling apparatus. The temperature in each sample was monitored by mounting a 0.25 mm diameter chromel-alumel thermocouple at the centreline of the rod as shown in Fig. 4.3. The extrinsic thermocouple, sheathed in 1.6 mm diameter mullite, was introduced through a 1.65 mm diameter hole drilled to the rod centreline. A low-carbon steel set screw, threaded through an orthogonal hole, anchored the thermocouple junction at the centreline position.

Several plain-carbon steel compositions and rod diameters were employed in the laboratory tests. Although rod mills produce material as small as 5.5 mm in diameter, test rods were limited to 8 mm due to the difficulty of mounting the centreline thermocouples. The

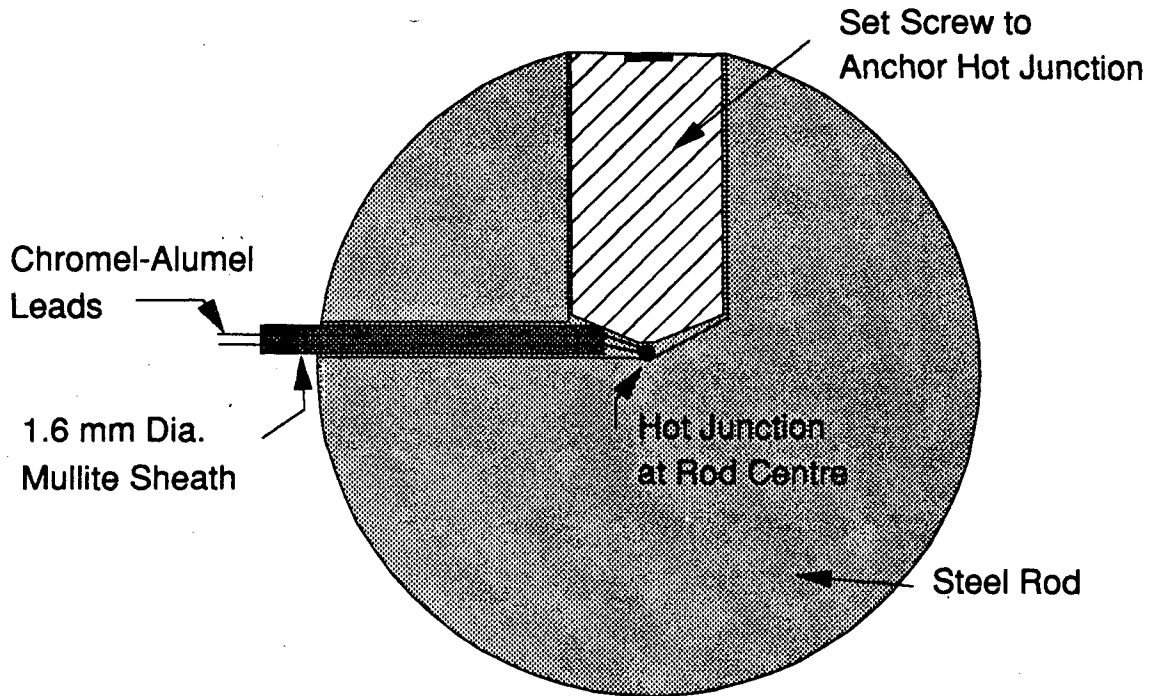


Fig. 4.3 - Schematic diagram of method employed to mount thermocouples at centreline position in rods for Stelmor simulation tests.

largest diameter studied in the tests was 15 mm. It was decided that the steel compositions for the tests should fall into one of three general categories: (1) eutectoid or near 1080 composition which would produce a predominantly pearlitic microstructure, (2) a 1035-1040 grade with approximately 50/50 ferrite-pearlite produced and (3) a 1015-1020 grade which would produce a predominantly ferritic microstructure. From the commercial rod coils supplied, suitable material falling into these ranges were chosen. Table 4.1 presents the chemical analysis for the five grades investigated in the laboratory tests. As can be seen, Steels A and B are near eutectoid grades; one 1080 and the other 1070, Steels C and D are 1038 and 1037, respectively, and Steel E is a 1020.

Steel A was supplied as 12.6 mm diameter, straight bar but was machined down to test rods of 10 mm and 8 mm diameter. Steel B had an original diameter of 20.6 mm, and after straightening was machined to 8, 11 and 15 mm diameter. Steels C and E were 15 mm original diameter and were machined to 8 and 11 mm samples. Steel D was received straight

Table 4.1 - Chemical analysis of rod samples used in laboratory experiments.

Grade code	C	Mn	P	S	Si	Cu	Ni	Cr	Mo	V	Cb	ASA	N
A	0.789	0.74	0.021	0.033	0.237	0.005	0.002	0.052	0.002	0.002	0.002	0.036	0.005
B	0.69	0.76	0.014	0.019	0.22	0.008	0.005	0.028	0.002	0.002	0.002	0.015	0.006
C	0.393	0.82	0.016	0.021	0.28	0.007	0.007	0.027	0.002	0.002	0.002	0.034	0.006
D	0.377	0.79	0.007	0.024	0.238	0.009	0.005	0.034	0.002	0.002	0.002	0.033	0.006
E	0.201	0.50	0.005	0.009	0.017	0.007	0.003	0.020	0.002	0.002	0.002	0.038	0.006

at 12.6 mm diameter but was machined down to 8 and 11 mm sizes. Steels A and D were employed primarily for the running in of the equipment; thus most of the data obtained is for Steels B, C and E.

To facilitate easy movement of the test rods to and from the furnace, an insulated handle was threaded into one end of each sample. The handle also provided a base to connect the thermocouple leads with extension wires. The chromel-alumel wire was insulated with a heat resistant fibreglass coating and fixed along the outer surface of the rod. To minimize interference with air flow, the thermocouple wire was positioned away from the rod surface, near the central portion of the rod.

4.1.5 Experimental Procedure

Prior to each test, the tube furnace was heated to the appropriate austenitizing temperature and allowed to soak while the nitrogen flush was maintained. The austenitizing temperature for the tests was 850°C; however for the lower carbon steels the austenitizing temperature was nearer 875°C. The temperature in each rod during heating was monitored by a two-channel strip chart recorder (Kipp & Zonen model# BD 41) and by a data logger (John Fluke Mfg. Inc. model# 2280). Upon reaching the aim temperature, the rod was allowed to soak for five minutes. The compressor then was started and the air temperature exiting the blower outlet was measured with a thermometer. By referring to the pressure drop across the orifice plate and correlations for discharge air velocity, the cooling air velocity could be

determined. To adjust air velocity from test to test, the flow rate of air from the compressor was controlled by the valve shown in Fig. 4.1, or by bleeding air from a line parallel to the one shown.

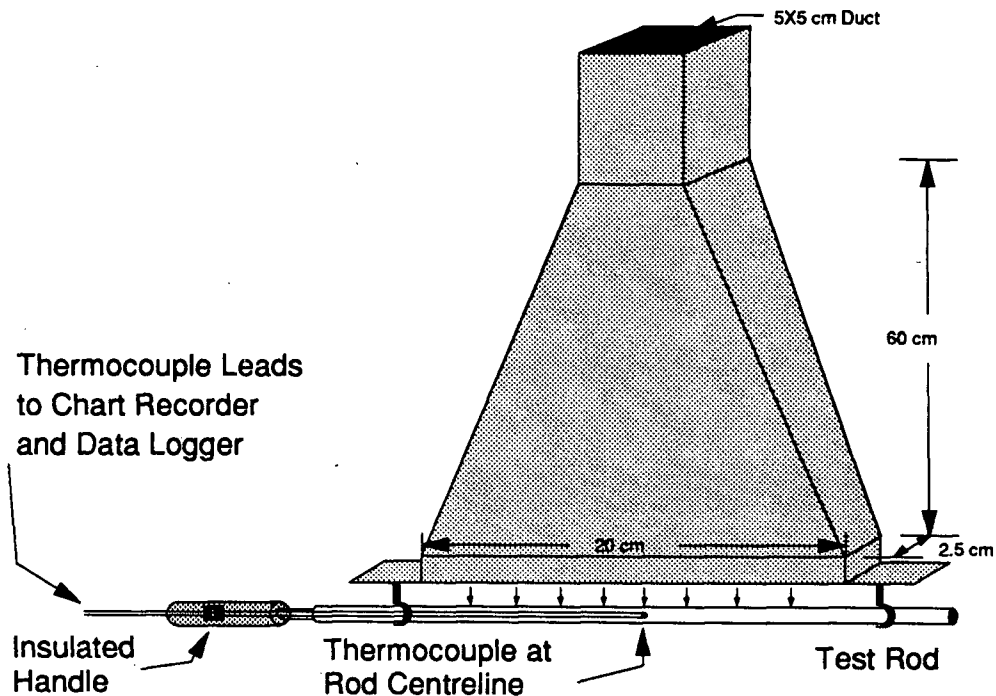


Fig. 4.4 - Diagram showing test rod in position under constant velocity duct for typical cooling test. Thermocouple leads are connected to a chart recorder and data logger.

After the appropriate hold time at temperature, each rod was quickly withdrawn from the furnace and placed below the blower outlet in the support shown in Fig. 4.4. Thermal response of the centreline thermocouple in the rod was monitored by both the chart recorder and the data logger (scan rate utilized for the tests was the maximum available on the data logger, 1 Hz). Once the rod had passed below approximately 400°C, the blower was switched off and the rod was removed from the cooling apparatus. Three to four tests were made for each steel grade and rod diameter, cooled at a different air velocity. A summary of the variables measured in the laboratory experiments is shown in Table 4.2. The procedure

was repeated for all of the rods to yield greater than 30 separate experiments, including preliminary trials. The thermal history data was transferred to a PC for analysis of heat-transfer coefficients.

Table 4.2 - Summary of laboratory experiment grades, diameters and air velocities.

Rod Grade	Rod Diameter (mm)	Air Velocity (m/s)
A (1080)	10	20, 18, 16, 14, 21, 20, 9, 11, 19, 22
B (1070)	15	22, 16, 11, 9
B	11	22, 10, 6
B	8	22, 15, 6
C (1038)	11	22, 15, 10, 6
C	8	22, 13, 6
D (1037)	11	22, 16, 12
E (1020)	11	22, 15, 13, 6
E	8	22, 12, 6

4.1.6 Microstructural Evaluation

Samples cut approximately 6 mm from the thermocouple location in each rod sample were employed for microstructural evaluation. After setting the samples in cold-mount, and grinding and polishing to a 1 μ m finish, an etch procedure dependent on the feature sought, was employed to reveal the underlying grain structure. According to the Gladman equations discussed in Chapter 2, the strength should be directly affected by three microstructural features: (1) ferrite/pearlite fraction, (2) ferrite grain diameter and (3) pearlite interlamellar spacing. Thus the aim of the metallographic work was to quantify each of these features in terms of the steel composition and the thermal history of the sample.

A Wild-Leitz Image Analysis system was employed to quantify the ferrite fraction and ferrite grain diameter. Nonetheless, a significant amount of time was required to develop etch techniques for revealing rod microstructure. The most common etchant for plain carbon steels, 2-4% nitric acid in alcohol, or nital, can cause confusion between pearlitic ferrite and proeutectoid ferrite, due to the fact that pearlite colonies with shallow angles to the plane of polish, can etch white to grey under the light microscope. This varying degree of greyness in some of the pearlite colonies was considered unsatisfactory for the accurate measurement of

ferrite fraction. The nital etch however, did show a significant contrast at ferrite-ferrite grain boundaries which made it attractive for use in measuring ferrite grain diameters. The other common etchant for steels is 4-5% picric acid in alcohol, or picral. A picral etch provides excellent contrast between ferrite and pearlite under the light microscope with no possibility for confusion between phases; however the ferrite-ferrite grain boundaries are not attacked. Thus, a combination of the two etchant solutions was proposed as an alternative for revealing both grain boundaries and phase fractions. For higher carbon steels where small amounts of ferrite were present, it was not necessary to use nital in the etchant solution since there were no ferrite-ferrite grain boundaries present.

From the tests, it was determined that a solution of 15 ml 2% nital combined with 85ml 5% picral yielded the best etching results with regards to both ferrite fraction and ferrite diameter for the 1038 and 1020 grades of steel (Steel C and E). However a 5% picral etch was utilized for the 1070 grade (Steel B). Application of the etchant to the sample surface was through the use of a cotton swab, soaked with etch solution. The swab was gently rotated against the sample to provide uniform etching. A time of between 10 and 15 seconds was found to be optimal for contact of the swab to the rod sample.

Image analysis of the rod microstructures was carried out at a magnification of 350-700X. The image analyzer system was equipped with an automatic focusing and automatic light control capability and could be controlled both manually or by pre-programmed software. Initial analysis was concerned with microstructural variation across the diameter of the rod and with surface-center differences. It was later found that a consistent etch was difficult to obtain near the rod edges; hence the work was confined to measurements at the sample centre only. In any event, because the temperature was measured at the centreline of the test rods, this was the logical position for the microstructural evaluation. The stage of the microscope was programmed so that a total of 49 separate locations on a 7x7 grid were measured. The image from the microscope first was digitized by the computer, based on preset threshold levels for light intensities; then measurements on the resulting bitplane were

made. Essentially the total number of computer screen pixels that were turned on versus the number that were off, were employed to determine area fraction for an image. Grain diameters were calculated based on the average number of pixels across each microstructural feature. Automatic statistical analysis was applied to each group of 49 measurements to obtain the mean value and a degree of variability.

Measurement of pearlite spacings was accomplished only for the 1070 grade. The technique followed photographing pearlite colonies at a suitable magnification with a SEM (scanning electron microscope, ETEC Autoscan). Then the pearlite spacing was measured by the random intercept method [76,77] according to which concentric circles were drawn on an acetate sheet with the radius of the circles not exceeding the dimensions of the pearlite micrograph. Three circles with 83, 50 and 40 mm diameters were adopted for the analysis. The circumference of each circle was calculated from the circle diameter and the pearlite spacing was estimated by counting the total number of intersections the circles made with pearlite lamellae. Taking the total line length and dividing by the number of intercepts yielded the apparent spacing. The apparent pearlite spacing, S_A , can then be related to the mean true spacing, S_p , through a surface area consideration given by Underwood [76] which results in

$$S_p = \frac{S_A}{2} \quad (4.1)$$

In order to examine a significantly large number of pearlite colonies, sixteen photographs were taken for each rod sample. Once again, the areas for spacing measurement were confined to the centre of the rod cross-section. Magnification for all the photographs was between 5,000 and 10,000 times. The SEM magnification was routinely calibrated with a NBS standard grating.

4.1.7 Mechanical Testing

After the controlled cooling measurements were completed in the laboratory experiments, the rods were sectioned through the thermocouple junction to determine its location.

The resulting two halves of each rod provided material suitable for mechanical testing. Tensile specimens were prepared according to ASTM Standard A370 [78], which for the 8 mm diameter rods, required a 4.0 mm diameter with a 16 mm nominal gauge length. Owing to the small diameter and length of the tensile specimen, it was possible to produce two samples from each of the two 10-cm halves of the rod, to yield 4 tensiles per test rod. For the 11 mm rods, 6.25-mm diameter samples with a gauge length of 25 mm were prepared, and for the 15 mm rods, 8.75-mm diameter specimens with a 35-mm gauge length were machined. Testing was carried out on a standard Instron Tensile machine equipped with a 90 kN load cell. Strain in the samples was measured by a clip-on extensometer; a cross-head speed of 0.508 mm/min was utilized for generation of load-elongation curves on all tensile specimens.

After completion of tensile testing, yield and tensile loads were determined from the charts. A 0.2% strain offset technique was adopted for the calculation of the yield point from the load-elongation curves. Failed samples were also saved and reduction-in-area measurements were performed to determine relative ductility.

4.1.8 Prior Austenite Grain Size Measurement

In order to determine the austenite grain size in steels utilized for the laboratory experiments, rods for each grade of steel and each diameter were subjected to the same thermal treatment described for the cooling tests in Section 4.1.5.; however after the hold time at peak temperature, they were quenched in water. This provided a grain structure of predominantly martensite, which when etched with the proper procedures, reveals the prior austenite grain boundaries. Micrographs were taken of the grain boundary structure, and the number of grains per unit area were counted to determine the average grain size, according to ASTM Standard E112 [79].

4.2 Transformation Kinetics

Measurement of austenite-ferrite and austenite-pearlite phase transformation kinetics have been made on three of the grades used in the laboratory rod-cooling experiments. The

purpose of the present tests was to determine the Avrami equation kinetic constants, n and b , and to obtain CCT start times and temperatures, for a range of steel compositions. The following sections outline the equipment and describe the procedure employed to obtain the kinetic data.

4.2.1 Equipment

The apparatus for the dilatometer studies has been described previously [24]. A schematic diagram of the equipment is shown in Fig. 4.5. The design of the equipment is intended to maximize the accuracy of temperature control and measurement of phase transformation kinetics. As can be seen from the figure, temperature is monitored by a 0.25-mm diameter, intrinsic, chromel-alumel thermocouple welded onto the surface of the tubular sample. Dimensional changes in the sample are monitored via a dilatometer placed across the diameter of the sample in the same plane as the thermocouple. The dilatometer is a modified water-cooled, quartz-tipped extensometer. Diametral rather than longitudinal dimension changes were chosen to minimize the error associated with temperature gradients over the length of a sample.

For each run, samples were mounted in the apparatus as shown in Fig. 4.5. Heat was supplied resistively through a 60 Hz device capable of delivering 500 amp, via the water-cooled end supports. Current to the sample was adjusted to provide the desired temperature utilizing a Si-controlled phase shifter which was connected to the sample thermocouple. Thermal history control was obtained by adjusting controller set point to match desired times and temperatures. To minimize decarburization at the sample surface, a quartz tube was placed around the tubular sample as shown in the figure, with an argon flow provided across the tube surface and down its centre. Tests were limited to two per sample, also to limit effects of decarburization.

Data for each test consisted of temperature and dilatometer response as a function of time. A PC was equipped with an A/D board in order to provide rapid sampling of the tests. To limit noise and provide protection for the board, an isolation amplifier was placed

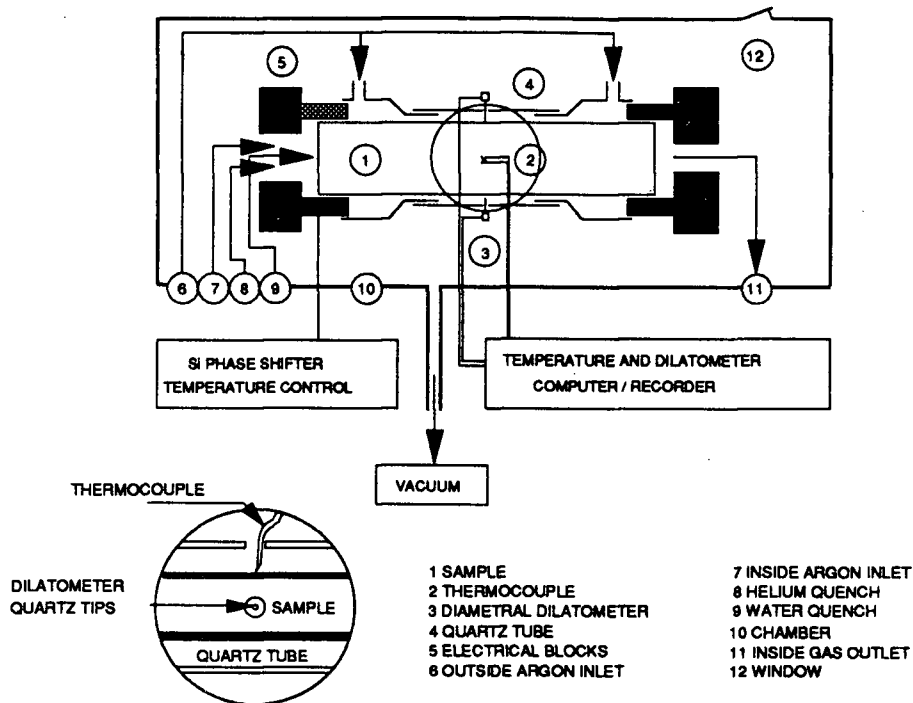


Fig. 4.5 - Schematic diagram of dilatometer apparatus utilized for phase transformations experiments.

between the equipment and the PC. This allowed independent amplification of the signals to obtain maximum resolution from the A/D board. Sampling rates were adjusted according to the type of test being run and the total test time, but in general the frequency was between 50 to 200 Hz.

4.2.2 Sample Preparation

Sample preparation for the tests consisted of straightening of commercial rod coil samples through hot tension, prior to machining. An Instron tensile machine was modified with an induction coil to provide hot tension capabilities. Peak temperature during straightening was approximately 800°C, and a strain of 10% was imparted to all samples. After straightening, samples were fully annealed. In order to limit temperature gradients through the wall of the tubular samples, a thin wall thickness was chosen. It was found that a thickness of 0.8 mm was suitable for a tube diameter of 8 mm and a length of 100 mm.

Owing to the thin wall, a special procedure for machining of the tubes with small cuts and a support mandrel, was required. Thickness variation around the tube in the vicinity of the thermocouple and dilatometer was limited to 0.1 mm.

Tests were performed on three steel grades from the laboratory experiments. These included the 1070 Steel B, the 1038 Steel C and the 1020 Steel E. A complete chemical analysis for these grades has been provided previously in Table 4.1.

4.2.3 Procedure

Two types of experiments were performed for the work under consideration: isothermal tests and continuous-cooling tests. The isothermal tests were designed to provide transformation kinetics for determination of the Avrami equation constants, and the continuous-cooling tests for the construction of CCT start curves for the steel in question. Peak temperatures employed for both sets of tests were identical to the austenitizing temperatures used for the laboratory rod-cooling experiments: 850°C for the 1070 and 1038 grades and 875°C for the 1020 grade.

4.2.3.1 Isothermal Tests

Due to the nature of the heat source, time to temperature in the samples was rapid with the central area of the tubes becoming much hotter than the ends. After a 5 minute hold time at temperature, the set point was quickly changed to the desired isothermal temperature, and a burst of helium gas providing rapid cooling of the sample. Upon reaching the isothermal temperature, the controller supplied a current suitable for the desired isothermal temperature to be maintained. Dilatometer response and sample temperature were monitored continuously throughout the test via both a PC and a strip chart recorder for quick reference. Actual temperatures employed for the tests were dependent on the grade of steel and transformation reaction being studied. Table 4.3 summarizes the temperature ranges and the total number of tests employed for the three grades of steel.

Table 4.3 - Summary of temperature ranges utilized in isothermal transformation kinetics tests.

Steel Grade	Temperature Range (°C)	Total
B	640-670	4
C	650-730	8
E	660-775	10

As is indicated in the temperature ranges listed in Table 4.3, both austenite-ferrite and austenite-pearlite transformation reactions have been included in the study. Data from each test consisted of dilatometer response and a corresponding temperature. The time interval between points was calculated from the sampling frequency for each test. For a constant temperature, dilation of a sample should only be due to volume changes associated with the austenite decomposition reactions. Thus conversion of dilatometer data to fraction transformed is straightforward when it is assumed that volume change in the sample is proportional to fraction transformed. A detailed explanation of the technique for this conversion is given in Chapter 6.

4.2.3.2 Continuous-cooling Tests

The heat-up and hold time utilized for isothermal tests was repeated for continuous-cooling tests. The same three grades, Steels B, C and E were employed, as for the isothermal tests. Cooling was imparted to the tubular samples using two methods. For higher cooling rates, helium was forced down the tube centre and over its' outside surface to provide natural cooling. The controller was turned off for these tests, cooling rate being controlled by the relative velocity of the helium. Slower cooling rates required the adjustment of controller set point. This was accomplished by connecting the set point dial to a constant speed motor via a rubber belt. By varying the relative diameters of the controller dial and the motor drive, various rates of change of set point and thus various cooling rates could be obtained. Linear cooling rates were applied to the tubular samples in this way. A summary of the cooling rates employed for the CCT tests is given in Table 4.4, along with the total number of tests

performed on each grade. As can be seen a wide variety of cooling rates are available with the equipment. Data from these tests consisted once again of dilatometer response with corresponding sample temperature. Both were recorded by the PC and CCT start times and temperatures were readily determined from the change in dilation in the sample at transformation initiation. The technique will be explained in greater depth in Chapter 6.

Table 4.4 - Summary of cooling rates utilized for continuous cooling tests.

Steel Grade	Cooling Rate Range ($^{\circ}\text{C/s}$)	Total
B	0.5-40	7
C	0.5-20	6
E	0.2-50	7

4.2.4 Prior Austenite Grain Size Measurement

As was mentioned in the previous section, the thermal history imparted to the tubular samples prior to the TTT and CCT kinetics tests, was intended to simulate the thermal history of the laboratory rod cooling experiments. The purpose for this was to match as best as possible, the initial grain structure in both sets of tests. The dependence of transformation kinetics on the prior austenite grain size in steels has been proposed by Umemoto *et al.* [27], as outlined in Chapter 2 (Eq. (2.43)). Although the present experiments have been designed to provide the same austenite grain size in the both dilatometer and rod cooling test samples, it is expected that differences in sample sizes and thermal history prior to cooling, may give rise to slight variations in grain diameter. As a result, a simulation of the thermal histories for heat-up prior to TTT or CCT tests was conducted, to determine the prior austenite grain size in dilatometer samples. These test were accomplished on the Gleeble 1500 (Duffers Scientific) Thermomechanical Simulator. Similar to the dilatometer equipment previously described, the Gleeble unit is capable of resistively heating tubular steel samples, with a 0.8-mm wall thickness and 8-mm diameter. However, unlike the previous dilatometer, the tubular samples are approximately 25 mm in length. Sample temperature was monitored by a 0.25-mm diameter, chromel-alumel thermocouple spot welded to the surface of the tube. A

computer-controlled feedback system allowed pre-programming of sample thermal history to simulate the TTT and CCT heat-up periods. Quenching of the samples, after the appropriate thermal treatment, was provided by a water spray, axially through the inside of the tube. As was the case for the solid rod samples, the tubular samples were sectioned and etched to reveal the prior austenite grain boundaries in the martensitic microstructure.

Chapter 5 - PLANT TRIALS EXPERIMENTS

5.1 Objectives and Introduction

The objectives of the plant trials were essentially the same as for the laboratory experiments in that rod samples were cooled under known conditions, the centreline temperature was recorded, microstructural features were measured and mechanical testing was performed. The major difference between the two sets of tests was that the plant trials were intended to provide valuable information regarding heat-transfer conditions on an operating Stelmor line. From this information, the heat-transfer coefficients could be quantified as a function of variables such as rod diameter, air velocity, line speed or bed position.

As was the case for the rods tested in the lab, microstructural information and mechanical properties data also could be obtained from the plant trials. Moreover, the trials provided an opportunity to measure actual air velocities on the Stelmor deck for comparison with velocities and temperature measurements obtained in the laboratory.

5.2 Sample Preparation

Following a technique identical to that adopted for the laboratory tests, rod samples were cut from commercial coils and straightened. Thermocouples were mounted at the rod centreline as outlined previously. To prevent test rods from dropping through the loops stacked on the Stelmor bed, 45-cm long samples were prepared as compared with 30-cm lengths for the laboratory tests. A 0.25-mm diameter chromel-alumel thermocouple was utilized; however unlike the laboratory tests, the fibreglass insulator was wrapped with a layer of stainless steel braiding to increase strength and abrasion resistance, as the rods moved down line. The test rods were used as received, i.e., no machining of the diameter was done. Material for the tests was chosen from a range of commercial grades supplied by Stelco Inc.. As was the case for the laboratory tests, three groups of compositions were sought (1) a near eutectoid 1070 to 1080, (2) a medium carbon 1035 to 1040 and (3) a lower

carbon 1015 to 1020. A list of rod grades studied in the plant trials is provided in Table 5.1. Two of the grades, C and E were identical to those under investigation in the laboratory experiments and thus were assigned the same letter code.

Table 5.1 - Chemical analysis of rod samples used in plant trials.

Grade code	C	Mn	P	S	Si	Cu	Ni	Cr	Mo	V	Cb	ASA	N
C	0.393	0.82	0.016	0.021	0.28	0.007	0.007	0.027	0.002	0.002	0.002	0.034	0.006
E	0.201	0.50	0.005	0.009	0.017	0.007	0.003	0.020	0.002	0.002	0.002	0.038	0.006
F	0.772	0.87	0.011	0.017	0.163	0.007	0.004	0.024	0.002	0.002	0.002	0.041	0.005
G	0.369	0.77	0.006	0.015	0.19	0.006	0.003	0.024	0.002	0.002	0.002	0.002	0.006
H	0.335	0.72	0.010	0.015	0.244	0.008	0.004	0.026	0.002	0.002	0.002	0.023	0.006
I	0.183	0.38	0.002	0.014	0.004	0.006	0.004	0.014	0.002	0.002	0.002	0.002	0.004
J	0.200	0.95	0.004	0.007	0.174	0.007	0.004	0.023	0.002	0.002	0.002	0.033	0.005

From the table it can be seen that the rod compositions fall within the ranges intended. Rod diameters in the tests were in three sizes: 7.5, 9.1 and 15 mm. The lower limit on the diameter was set by the difficulty of drilling small rods for insertion of thermocouples. In total, over ninety rods were instrumented for testing in the plant trials. Before testing, each thermocouple junction and set screw were examined and checked for good connection.

The Stelmor lines at Stelco's #2 Rod Mill can be divided into four separate zones. Each zone possesses individual air control with the setting either full on or full off. From examination of the bed, it became apparent that each zone could be further divided into nine sections. Each interchangeable section is bolted into place and can be removed easily for repair or replacement. A sketch of one such zone is shown in Fig. 5.2. As can be seen, a higher density of openings for air flow exist at the edge of the bed as compared to the centre. Numbers indicate the locations of velocity measurements. In total, sixteen separate sections on two separate lines were investigated yielding nearly 450 individual air velocities.

5.3 Air Velocity Measurements

To quantify air velocities encountered on a Stelmor line, a series of pitot tube measurements were conducted while the rod mill was down. The down period allowed careful placement of a pitot tube on the bed, perpendicular to the air flow. As was shown previously and depicted in Fig. 5.1, the air is forced through the bed at a rather shallow angle and not vertically as might be expected. The pitot tube was placed perpendicular to the flow of air and velocities were calculated from the difference in pressure measured with an inclined manometer (Dwyer Instruments Inc.) between openings in the tube perpendicular to and parallel to the air flow.

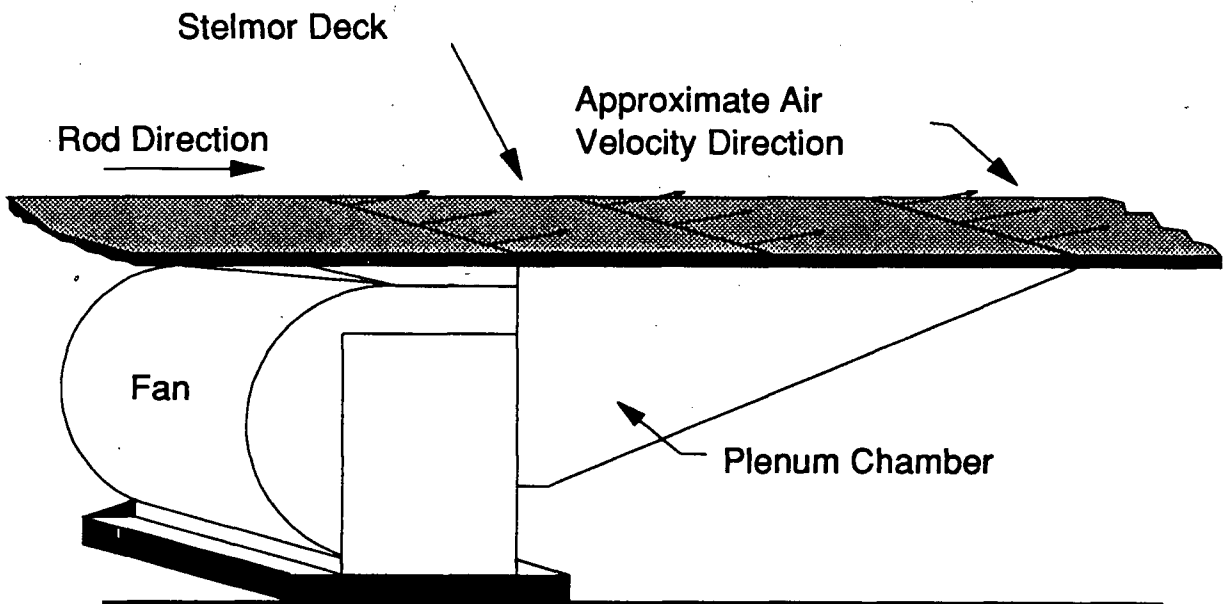


Fig. 5.1 - Schematic diagram of one zone of the Stelmor line demonstrating the direction of air flow through the bed.

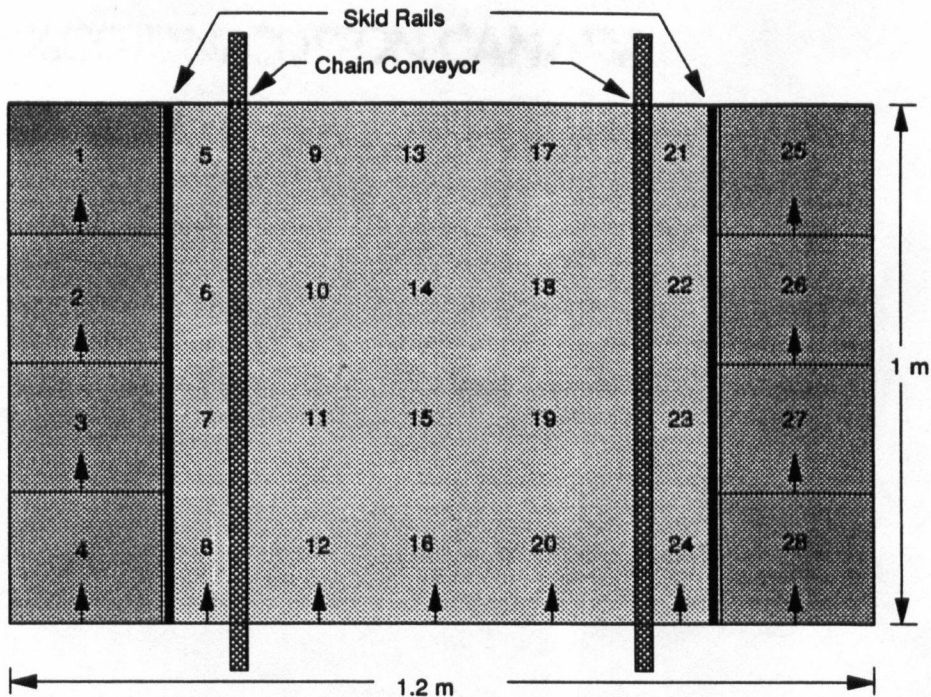


Fig. 5.2 - Layout of section from Stelmor line showing locations for air velocity measurements.

5.4 Thermal Response Measurement

The procedure for measurement of the thermal response of steel rods on the Stelmor line was similar to that developed for the laboratory tests. A tube furnace was placed adjacent to the operating line to preheat the instrumented rods. The furnace was identical to that described in Section 4.1.3, except that a stainless steel tube (5.6 cm I.D.) was inserted as a liner instead of alumina. Instrumented rods were placed in the furnace and heated to the desired temperature (850°C for 1040 and higher carbon or 875°C for 1020), once again with a constant nitrogen flow of 1 - 6 l/min to prevent scale formation. Upon reaching the test temperature, samples were soaked for an additional 5 minutes, although scheduling in the mill made this difficult to achieve. The rod temperature during heat-up and soak was monitored by a two channel chart recorder (Kipp & Zonen model# BD 41).

After completion of the soak time, the thermocouple leads were disconnected from the chart recorder and hooked to a small hand-held data logger (Metrosonics Co. model#

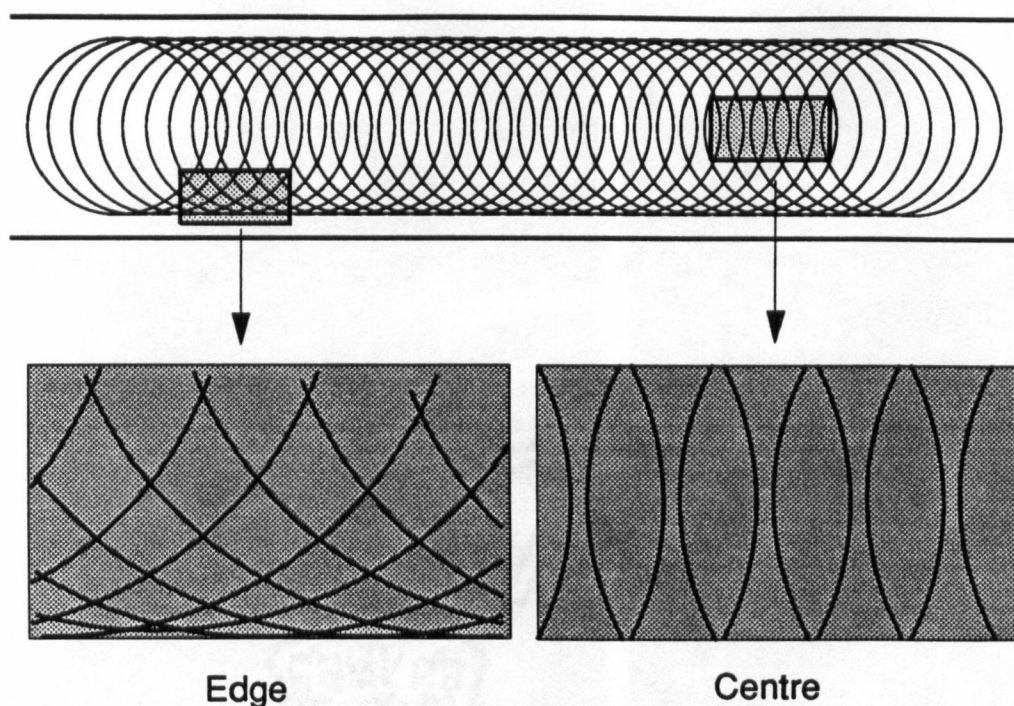


Fig. 5.3 - Schematic diagram depicting the variation in rod packing at the centre and edge of the Stelmor line.

DL-702) to record thermal response during cooling on the Stelmor line. Each rod was quickly withdrawn from the furnace and woven into the desired location in the Stelmor line loops by physically lifting the hot production rods vertically off the bed, laying the test rod in place, then restoring the coil to its natural position. Figure 5.3 indicates the difference in rod density at the edge of the bed as compared to the centre. An attempt was made to match the test rod compositions and diameters with those being processed on the line but in some instances this was not possible. Once the rod was in position and travelling down the bed with the loops, the data logger was manually carried along the length of the bed at the end of which the rod was removed before the reform tub. Each test rod was allowed to cool to room temperature and was saved. The sampling frequency for the data logger was 4 Hz, with the minimum, maximum and mean temperature being stored for each one second period. Owing to memory limitations in the device, stored data was periodically dumped into a PC situated in the Stelmor line office.

The various line settings were recorded for each test. Depending on the grade and diameter being rolled in the mill, line velocity, laying head temperature and blower settings could be adjusted by the operator. With assistance provided by trimmers at the end of the line, several loops were cut from a handful of production coils. These loops, marked so that their orientation on the bed could be determined, were saved for mechanical testing. Due to excellent cooperation from the personnel working on and around the No. 2 Rod Mill, nearly 70 tests were completed over a five day period. A summary of grades, diameters and the number of tests completed is provided in Table 5.2.

Table 5.2 - Summary of grades, diameters and number of tests completed in plant trials.

Rod Grade	Rod Diameter (mm)	Centre Bed Tests	Edge Bed Tests
C	15	7	4
E	15	7	1
F	9.1	4	3
F	7.5	5	4
G	9.1	4	3
H	7.5	6	2
I	9.1	6	2
J	7.5	5	5

In addition to the conditions listed above, the thermal response of rods cooled without production loops on the bed was measured. This involved the normal rod heat-up procedure, after which the rod was manually held above the Stelmor deck and the temperature was recorded. These experiments were intended to determine the effect of the presence of the loops on radiation and convection heat-transfer.

5.5 Microstructural Evaluation

Evaluation of the microstructures produced in the plant experiments was undertaken following the same techniques as for the laboratory tests. The three main parameters to be quantified were: (1) ferrite/pearlite fraction, (2) ferrite grain diameter and (3) pearlite interlamellar spacing.

The same computer-controlled image analysis system was employed to determine ferrite fractions and ferrite grain diameters. However the etch procedure was altered slightly to improve the ferrite fraction determination. Results from laboratory rods suggested that the ferrite fractions being measured on the system were too low with respect to steel composition and cooling rate. Thus based on a point counting procedure to quantify the ferrite fractions manually in some of the material, it was decided that a two-step procedure should be employed for estimating the ferrite fraction and grain diameter. Firstly, the samples were etched with 15% nital/85% picral to reveal the ferrite/ferrite grain boundaries and thus provide a measure of the mean grain diameter. Good contrast at the grain boundaries, however, resulted in under estimations of the ferrite fraction, and thus the procedure was repeated with a 100% picral etch. This etching practice was also adopted for the laboratory test material to ensure the results were consistent.

Application of the etchant to the plant steel was the same as for the laboratory procedure. A cotton ball soaked in the appropriate etchant was applied to the surface with a gentle circular motion for a predetermined amount of time (between 10 and 15 seconds). The sample was then washed in water and dried in alcohol. Care was taken to ensure that each rod received an identical polish and etch treatment within reasonable limits.

Pearlite spacing measurements also were carried out on two grades of steel - F (1080) and H (1035) - from the plant trials. The procedure followed for determination of the spacing was essentially the same as for the laboratory steels; however a different SEM (Hitachi model# S-570) was utilized, which expedited the photo taking segment of the work. Owing to the better photographic capability of this machine, most photos were taken at a magnification of 5,000X. Once again sixteen photographs per sample were obtained at or near the centreline of the sample. For the H steel, however, 30-36 photos were taken to obtain the same number of pearlite colonies due to the presence of about 60% proeutectoid ferrite. These measurements were made to determine if the pearlite spacing-versus-undercooling relationship, depicted in Fig. 3.3, was affected by the presence of the proeutectoid ferrite

phase. Determination of the spacing was made utilizing an acetate sheet on which concentric circles had been drawn. The sheet was applied to the micrographs of pearlite colonies and a count of the number of intersections that pearlite lamellae made with the circumferences of the circles indicated the average or apparent spacing. For steel H (1035) the values had to be corrected for the fraction of ferrite present in the steel. This was done by a point counting technique [77] to determine the ferrite fraction, then adjusting the length of the circumference in proportion to the fraction. In general 2500 to 3500 individual lamellae were intersected in the characterization of each test sample.

5.6 Mechanical Testing

Rod loops cut from production material were mechanically tested at the rod mill facilities. The standard procedure for measuring rod tensile strength was followed which consisted of cutting a length of rod approximately 45 cm long from the loop and without straightening or machining, placing it directly into the tensile test machine. Special grips were utilized to hold the rods and failure did not occur in the grips. The original rod diameter was measured and after failure the reduction in area was calculated. Owing to the technique adopted, only the ultimate strength of the material was determined. A summary of the grades and diameters of the production test rods is given in Table 5.3.

Table 5.3 - Grades and diameters of material cut from production coils and tested mechanically.

Rod Grade	Rod Diameter (mm)	C	Mn	Si
1065 (2)	7.1	0.63	0.78	0.23
1022	7.5	0.21	0.98	0.017
1022	7.5	0.22	0.91	0.29
1070	7.5	0.70	0.77	0.23
Torque Rod	9.1	0.58	0.95	0.25
1536	9.1	0.35	1.17	0.16
1060	9.1	0.61	0.75	0.24
1015	9.1	0.16	0.54	0.02
1038	12.7	0.38	0.77	0.27
Spring	12.7	0.66	0.96	0.25

Test rods were sectioned at the thermocouple position and the two central portions of the remaining pieces cut for tensile testing. From the three diameters of rods obtained in the plant trials, tensile samples were machined to three different sizes: 3.8 mm diameter (from the 7.5 mm dia. rod), 4.6 mm diameter (from the 9.1 mm dia. rod), and 8.84 mm diameter (from the 15 mm dia. rod). Gauge lengths for these tensile samples were 16, 20 and 35 mm, respectively.

Unlike the laboratory tensile tests, the strain was measured by monitoring the cross-head position and converting it to strain units rather than utilizing the clip-on extensometer. A cross-head speed of 0.508 mm/min was employed for all tests. The stress-strain curve produced from these tests provided the 0.2% offset yield strength and the ultimate strength for each test rod. Failed samples were saved and the reduction in area for each was measured.

5.7 Segregation Checks

It is well known that segregation in steel wire rod, can seriously affect its drawability. Various elements have been considered as prime culprits for centreline segregation in wire rod, resulting in the formation of martensite and a drastic reduction in drawability. The most important of these concerning plain-carbon steel are carbon, sulphur, manganese and phosphorous [80-82]. The literature also recognizes that continuously cast steels are more prone to segregation than are ingot cast steels. All laboratory and plant steels were ingot cast. In order to determine the integrity of the rod material employed in the plant trials, as well as those used in the laboratory experiments, inspection of the rods for segregation has been performed. It would also be expected that segregation in the dilatometer steel samples could markedly affect the transformation kinetics determined for the various grades studied.

According to Van Vuuren [81], centreline segregation of phosphorous in steel rod, was important when the ladle analysis indicated greater than 0.020 wt% phosphorous. Tables 4.1 and 5.1 display that most steels employed for the two sets of trials possessed phosphorous levels significantly smaller than this amount. Sulphur distributions in the rods were evaluated

by the standard sulphur-print method [80]. Rod samples were cross-sectioned and the surface was ground and polished. Bromide photographic paper was soaked in a 4% H_2SO_4 solution for 3 minutes, then carefully placed on the polished surface of the rod. After 5 minutes the paper was withdrawn, then fixed, washed and dried. Thus a permanent record of the sulphur distribution in the rod samples was obtained. Examination of the rods for carbon segregation was due to the method suggested by Stacey [80]. It consisted of etching a polished rod cross-section with 2% nital and determining the degree of concentration of carbides along the centreline. The final segregation check was for the distribution of manganese in the rods. Microsegregation of Mn in continuously cast steels and its relationship to centreline formation of martensite in wire rod has been discussed previously [82]. As manganese is known to significantly affect the hardenability of steels, an electron probe micro-analyzer was utilized to determine Mn concentrations in the various steel grades. The machine employed was a Cameca SX-50, in the University of British Columbia's Geology Department. A sample from each grade of steel listed in Tables 4.1 and 5.1 was examined, with settings of 20 kV, 30 μA and a count time of 50 seconds. The background count was taken for 25 seconds and the spot size was 1.5 by 1.5 μm . Twenty locations across the diameter of each rod were examined.

Chapter 6 - LABORATORY RESULTS

6.1 Results of Rod Cooling Tests

6.1.1 Thermal History and Heat-Transfer Coefficients

Results from the laboratory rod-cooling tests consisted of digitized temperature-versus-time data measured at a sampling rate of 1 Hz. The data was transferred into a PC for analysis and plotting. An example of a typical thermal history at the rod centreline measured during the tests, for Steel D (1037), is shown in Fig. 6.1. The curve exhibits the expected recalescence due to the heat released during the austenite decomposition reactions.

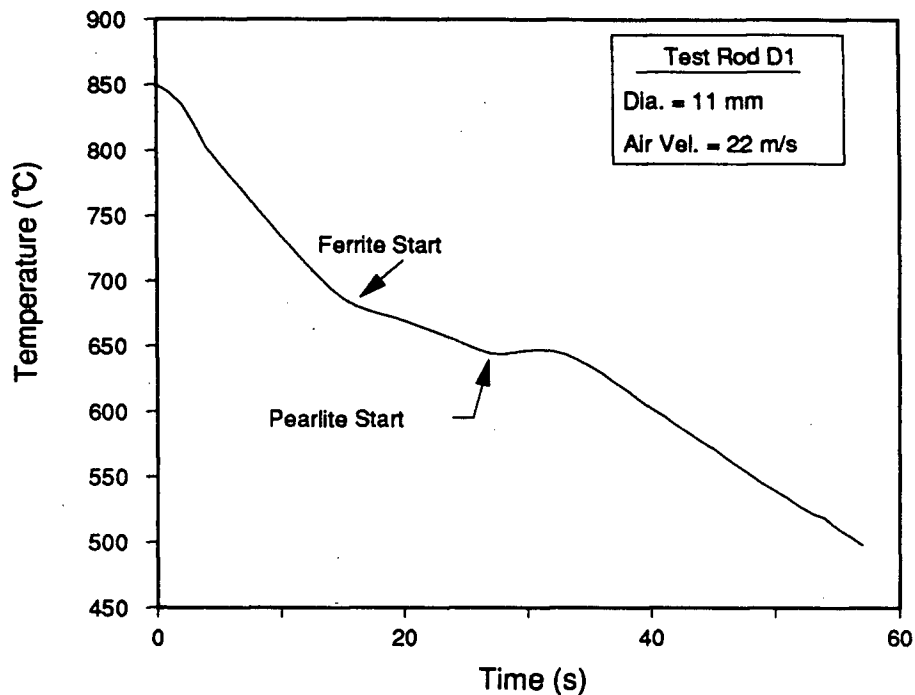
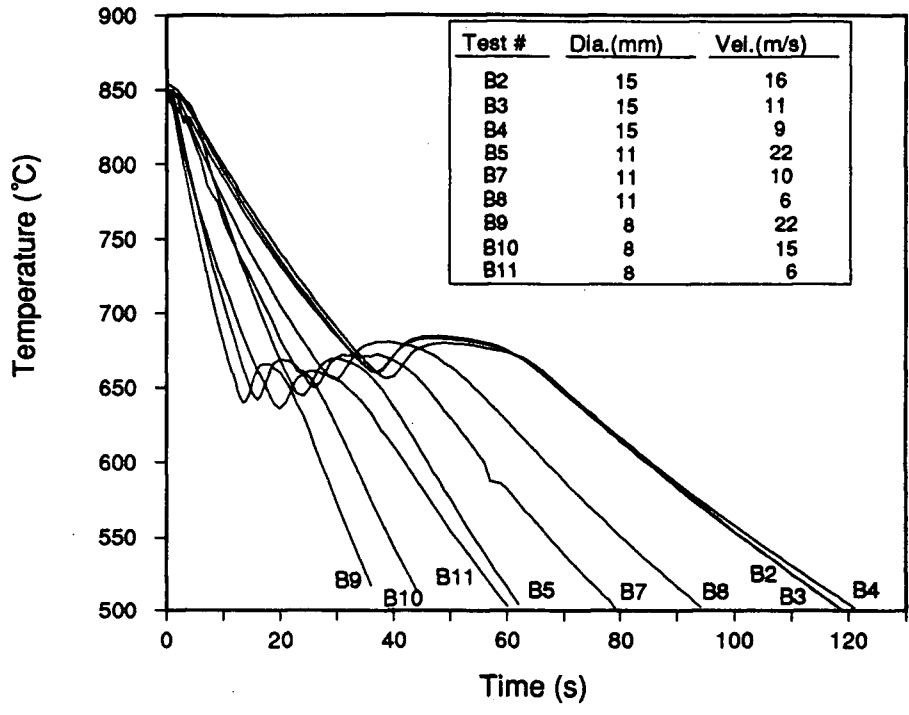
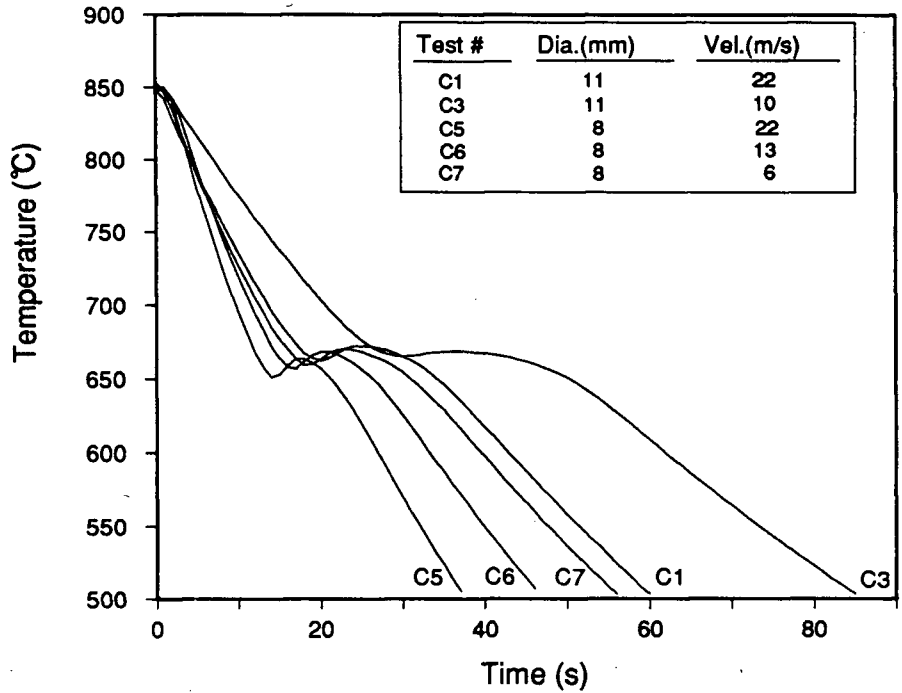


Fig. 6.1 - Typical thermal history measured in 11-mm diameter rod (Steel D 1037), cooled with an air velocity of 22 m/s under laboratory conditions.

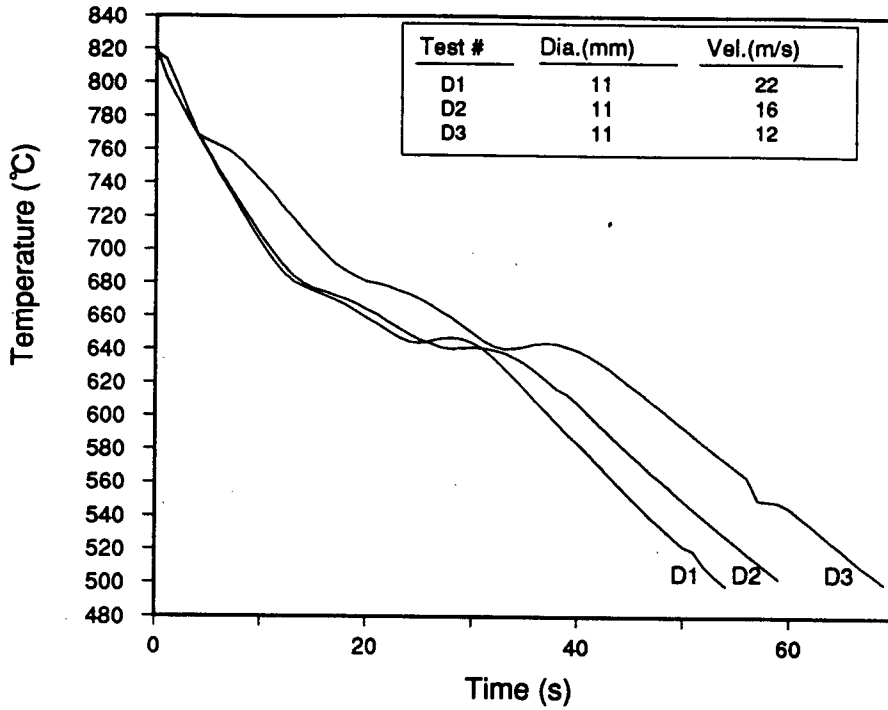


(a)

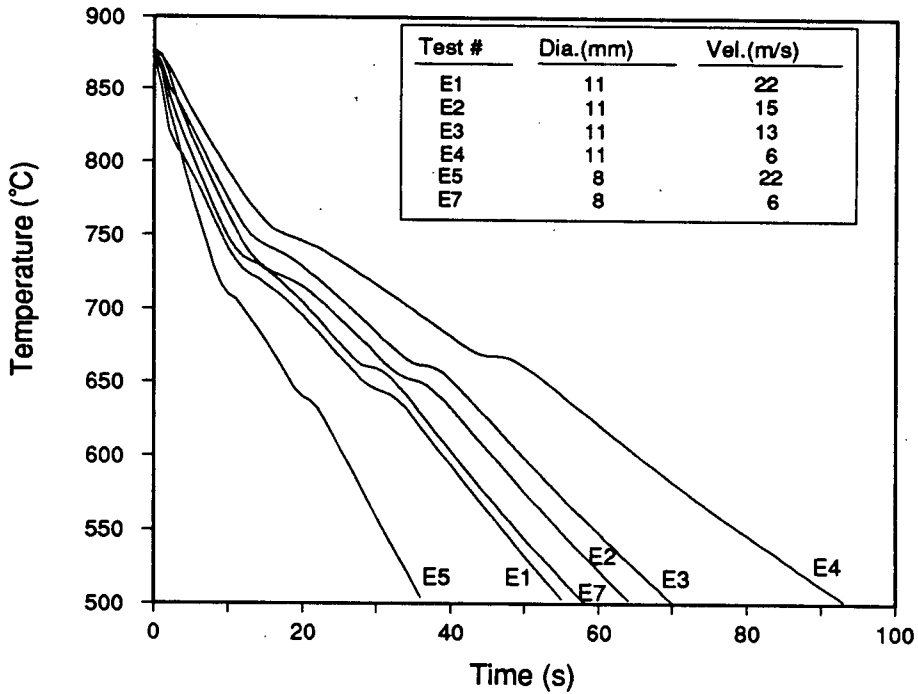


(b)

Fig. 6.2 - Thermal history measured at rod centreline in laboratory cooling tests on Stelmor simulator; (a) Steel B (1070), (b) Steel C (1038), (c) Steel D (1037) and (d) Steel E (1020).



(c)



(d)

Fig. 6.2 - Thermal history measured at rod centreline in laboratory cooling tests on Stelmor simulator; (a) Steel B (1070), (b) Steel C (1038), (c) Steel D (1037) and (d) Steel E (1020).

All of the thermal histories measured at the rod centreline during the laboratory tests, are presented in Figs. 6.2 (a) to (d), which also display the rod diameters and air velocities employed. Thus, the effect of variations in composition on the kinetics of the austenite decomposition reactions can be seen clearly. The cooling curve for Steel B (1070) exhibits recalescence corresponding to the austenite-pearlite reaction and as the carbon content decreases, the magnitude of the recalescence due to pearlite formation decreases and the influence of the austenite-ferrite transformation on cooling rate is seen to increase.

The laboratory thermal history data was analyzed to obtain heat-transfer coefficients for each time interval during individual tests. Two techniques were adopted for this purpose: one assumed an isothermal rod (negligible internal resistance), while the other was based on a finite-difference technique to back calculate an effective heat-transfer coefficient from the measured centreline temperature. Assuming negligible internal resistance, the heat-transfer coefficient can be calculated for each time interval from the following equation:

$$h_{ov} = -\ln\left(\frac{T_A - T}{T_A - T_0}\right) \frac{\rho C_p r \Delta t}{2} \quad (6.1)$$

where T_0 and T are the initial and final rod temperatures over a time period Δt , T_A is the ambient air temperature and r is the radius of the rod. The specific heat of the steel C_p is calculated based on the composition and phases present at an intermediate temperature, for the time step under consideration. Application of Eq. (6.1) is valid when the Biot modulus for the system is much less than 1 [57]. The Biot modulus is given by:

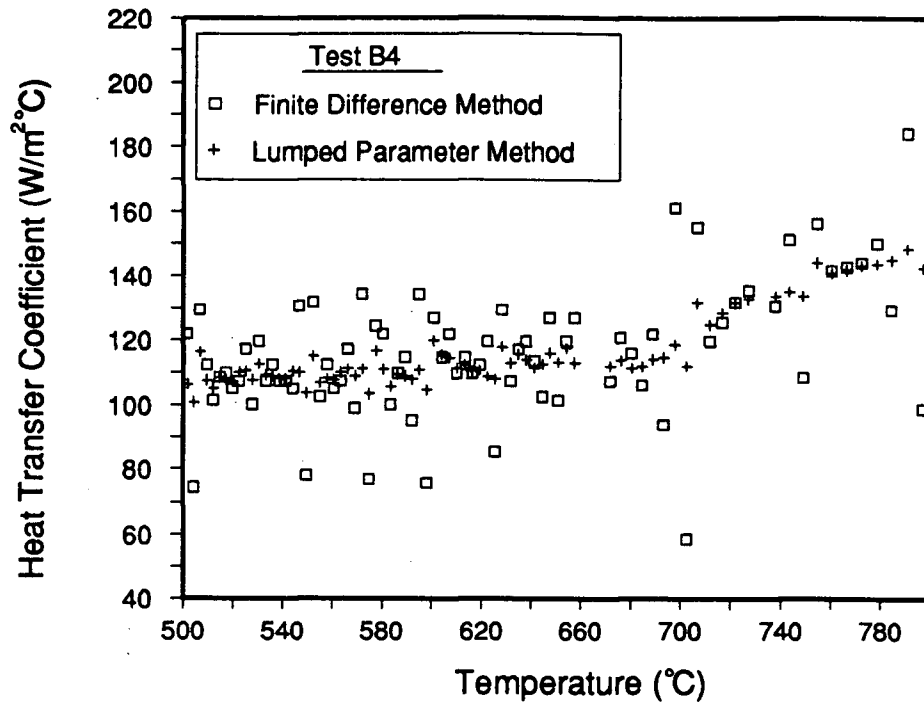
$$Bi = \frac{h\bar{L}}{k} \quad (6.2)$$

where h is the heat transfer coefficient, \bar{L} is a characteristic length for the system or the ratio of volume to surface area, and k is the thermal conductivity of the material. In general if $Bi \ll 1.0$, there will be an error of less than 5% in applying Eq. (6.1). For a typical rod-cooling test, the rod diameter was ~ 10 mm, the heat transfer coefficient was ~ 200 W/m²°C, and thermal conductivity ~ 25 W/m°C. The Biot number for such a test is then 0.08.

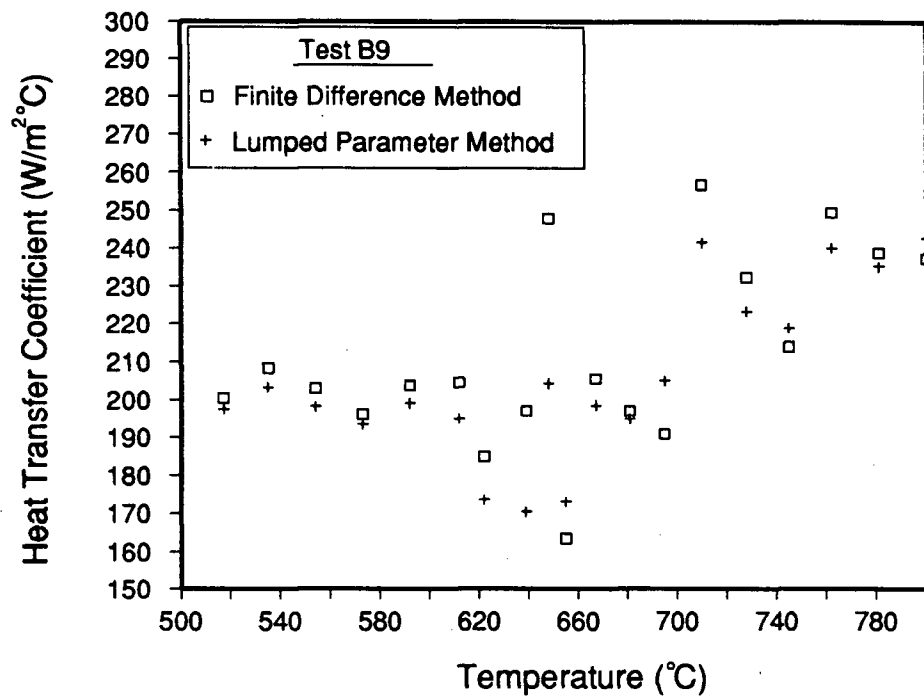
The second method employed to calculate the heat-transfer coefficient at the surface of the rod involved the application of the finite-difference technique. An iterative scheme was employed whereby the heat-transfer coefficient was initially guessed, then the temperature within the rod was calculated and compared with the measured value from the laboratory tests. Once the predicted temperature achieved a reasonable match with the measured value in successive iterations (within 0.01°C), the heat-transfer coefficient was stored and calculations were continued to the next time step. Since this method does not assume an isothermal rod, the results do not depend on the magnitude of the Biot modulus.

Results of both methods are shown in Fig. 6.3 (a) and (b) where the calculated value of the heat-transfer coefficient is plotted as a function of the rod centreline temperature for two of the cooling tests. Both sets of results are for Steel B, with B4 being a 15-mm diameter rod cooled by air at 9 m/s and B9 an 8-mm diameter rod cooled by 22 m/s air. Inspection of these figures shows that the heat-transfer coefficients calculated by both methods are in good agreement, except for some minor differences. Whereas the values calculated by the lumped-parameter analysis show a fairly constant downward trend of heat-transfer coefficient with decreasing temperature, the finite-difference technique results exhibit much more scatter. This is due to the fact that the lumped-parameter analysis assumes there is no gradient through the rod and thus is less sensitive to small fluctuations in temperature during cooling. The degree of scatter can be seen to be greater for the larger diameter rod, where the gradient through the sample is larger. Agreement between the two methods lends support for their use in determining overall heat-transfer coefficients from the laboratory data.

From plots such as those shown in Fig. 6.3, average values for heat-transfer coefficients over narrow temperature ranges (10°C) were obtained for each test. These values were then compared with the predictions from equations for heat-transfer coefficients given in Chapter 3, i.e. Eqs. (3.8) and (3.9). Referring to Eq. (3.8) it can be seen that the convective heat-transfer coefficient is a function of both the rod diameter and the air velocity impinging on the rod surface. By inspection this relationship can be simplified to be:



(a)



(b)

Fig. 6.3 - Heat-transfer coefficients calculated from the measured thermal histories at the rod centreline in laboratory tests, with both a finite-difference and lumped-parameter technique; (a) rod B4 - 15 mm diameter, 9 m/s air velocity, (b) rod B9 - 8 mm diameter, 22 m/s air velocity.

$$h_c \propto \frac{v_\infty^p}{D^{1-p}} \quad (6.3)$$

where v_∞ is the fluid velocity and D is the diameter of the cylinder. As was previously mentioned, the value for the constant p is dependent on the magnitude of the Reynolds number. Assuming a rod temperature of 800°C, with a rod diameter of 10 mm, an air velocity of 15 m/s and density and viscosity of air calculated based on a mean film temperature of 683K, the Reynolds number is approximately equal to 2430. At lower rod temperatures, e.g. 450°C, assuming a 10-mm diameter and 15 m/s air velocity, the Reynolds number is approximately equal to 3800. Lower air velocities and smaller rod diameters will result in correspondingly lower values for the Reynolds number. In general, referring to Table 3.1, the corresponding value for p is 0.466. Rewriting, Eq. (6.3) then becomes,

$$h_c \propto \frac{v_\infty^{0.466}}{D^{0.534}} \quad (6.4)$$

Applying Eq. (6.4) to the data gathered for the laboratory tests, plots of heat-transfer coefficient against the right hand side of the equation, $v_\infty^{0.466}/D^{0.534}$, should reveal a linear relationship within a narrow temperature range. Figs. 6.4 (a), (b) and (c) depict the measured values of heat-transfer coefficient at three separate temperatures versus the velocity/diameter term as calculated from Eq. (6.4). Considering the scatter exhibited by the measured heat-transfer coefficients in Fig. 6.3 ($\sim \pm 10\%$), the data plotted in Fig. 6.4 shows reasonable linearity over the ranges of velocity and diameter investigated. The line plotted in each figure is the value of the heat-transfer coefficient predicted for combined convective and radiative heat transfer as calculated from Eqs. (3.8) and (3.9). For these predictions the appropriate surface temperature was used to evaluate both h , and the mean film temperature for calculation of the thermophysical properties of the air. Good agreement between the predicted and measured heat-transfer coefficients is evident in all three figures.

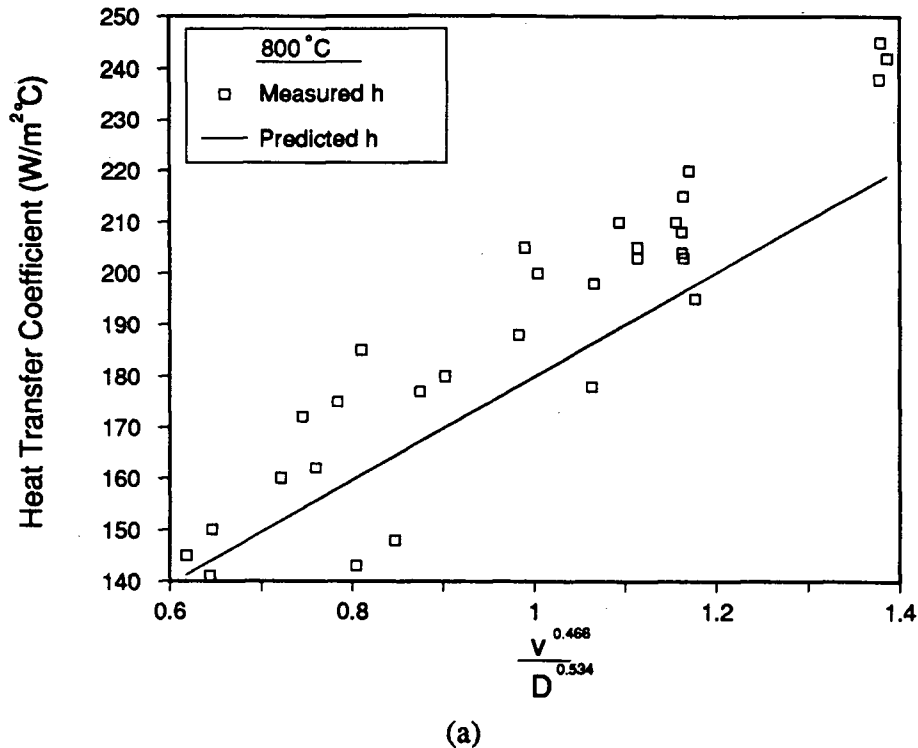
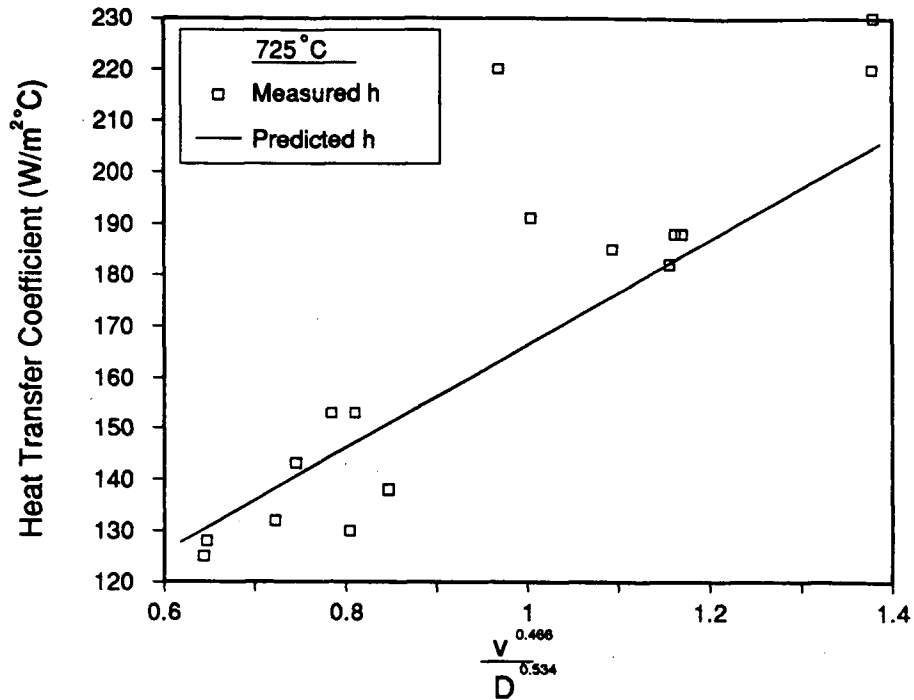
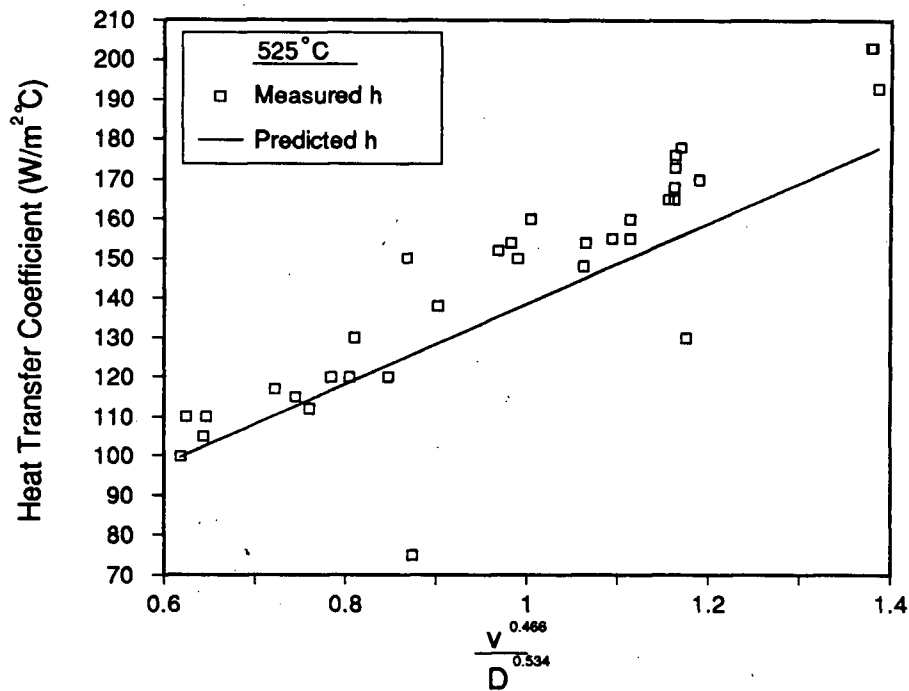


Fig. 6.4 - Measured heat-transfer coefficients plotted against $(\text{air velocity})^{0.466}/(\text{rod diameter})^{0.534}$ according to Eq. (6.4). The line shown is the prediction based on combined radiative and convective cooling (Eqs. (3.8) and (3.9)). Heat-transfer coefficients measured at (a) 800°C, (b) 725°C, (c) 525°C.

Heat-transfer coefficients, calculated from rod cooling rates as a function of air velocity, also have been obtained from a study by Hanada *et al.* [83]. The procedure followed in their experiments was similar to that outlined in Chapter 4 for the laboratory rod cooling tests. Two rod diameters were employed: 5.5 and 11mm. Each rod contained a hole drilled to the centreline into which a thermocouple was mounted. Dimensions for the width and depth of the hole were not given; similarly no information was given whether or not the hole was plugged after insertion of the thermocouple. Each test consisted of heating of the test rod to 900°C, then after a suitable time at temperature, placing the rod in a known air velocity, and measuring the temperature response during cooling. Results were given in terms of the average cooling rate for each test, measured between 740 and 480°C. Following the same procedure for converting thermal history to heat-transfer coefficients, as outlined in Section 6.1.1, plots of predicted and calculated heat-transfer coefficients as a function of the



(b)



(c)

Fig. 6.4 - Measured heat-transfer coefficients plotted against $(\text{air velocity})^{0.466}/(\text{rod diameter})^{0.534}$ according to Eq. (6.4). The line shown is the prediction based on combined radiative and convective cooling (Eqs. (3.8) and (3.9)). Heat-transfer coefficients measured at (a) 800°C , (b) 725°C , (c) 525°C .

ratio of velocity to diameter (Eq. (6.4)) can be made as shown in Fig. 6.5. The predicted line is based on Eqs. (3.8) and (3.9) as was the case for the laboratory results. Once again good agreement between measured and predicted heat-transfer coefficients is observed. Thus, accurate prediction of heat-transfer coefficients as a function of rod diameter, cooling air velocity and ambient and rod surface temperature, can be made using Eqs. (3.8) and (3.9), for well-defined laboratory conditions.

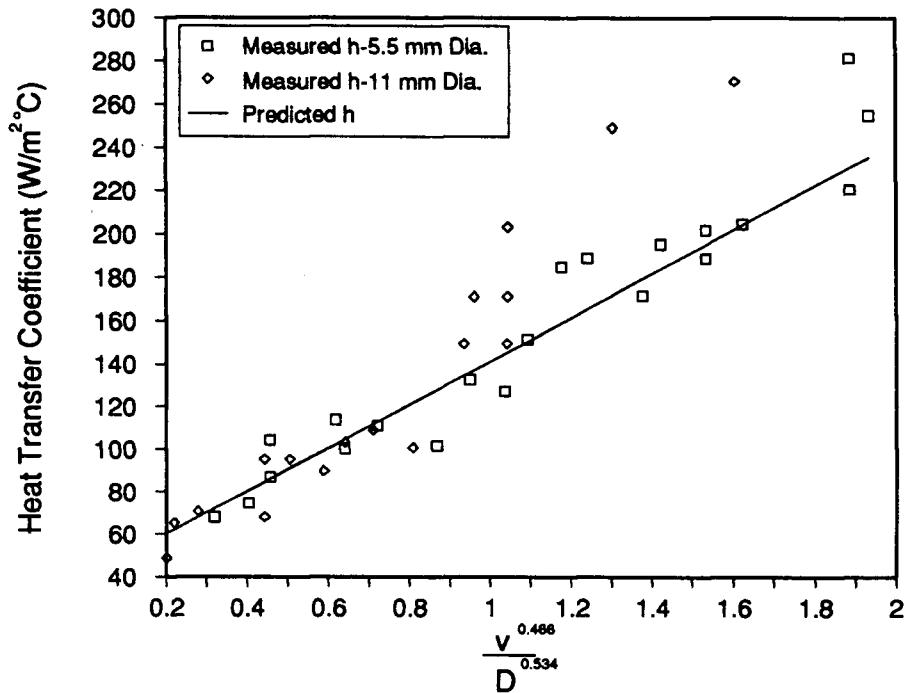


Fig. 6.5 - Heat-transfer coefficients plotted against $(\text{air velocity})^{0.466}/(\text{rod diameter})^{0.534}$ according to Eq. (6.4). Values have been calculated from rod cooling rates due to Hanada *et al.* [83].

6.1.2 Microstructures

The microstructure of each rod was characterized by measuring: (1) ferrite fraction, (2) ferrite grain diameter and (3) pearlite spacing. Owing to variations observed in the degree of etch across the diameter of the rod samples and the inherent difficulties of comparing values taken under differing etch conditions, microstructural features were measured only at the centreline position of each rod.

Owing to the paucity of literature on the prediction of microstructure in plain-carbon steels after continuous cooling, results from both the laboratory investigation and the plant trials were analyzed to develop empirical relationships. In this Section, only the results of the microstructural analysis of the laboratory investigation will be presented. Chapter 7 presents formulation of empirical equations for ferrite fraction, ferrite grain diameter and pearlite spacing, making use of both laboratory and plant trials results.

6.1.2.1 Ferrite Fraction

The fraction of ferrite formed from austenite during cooling of a plain-carbon steel, is related both to the steel composition and to the cooling rate. Results of the ferrite fraction measured at the centreline of the rod samples are plotted against average cooling rate, measured at 750°C, in Figs. 6.6 (a), (b) and (c). Each point on the graph represents the average of forty-nine separate areas measured by the image analyzer, described previously. As can be seen from the figures, the ferrite fraction increases as the carbon content of the steel decreases. This is in agreement with the equilibrium phase diagram for Fe-C. Inspection of each figure also shows the relationship between cooling rate and ferrite fraction. As the cooling rate increases, the fraction of ferrite decreases, although the effect is not as drastic as for changes in carbon content of the steel. The decrease in ferrite fraction with increase in cooling rate is a function of the relative nucleation and growth rates of ferrite over a range of temperatures. As cooling rate increases, the time required for incubation of ferrite nuclei at relatively high temperatures is not attained. Thus the reaction is forced to occur at lower temperatures. As transformation temperature is forced below T_{A1} , extrapolation of the γ/α and $\gamma/\text{Fe}_3\text{C}$ boundaries [25,84] indicate decreasing fractions of ferrite depending on the degree of undercooling. Thus as cooling rate increases, the temperature at which ferrite forms decreases and correspondingly, a reduced fraction of ferrite is formed.

Figures 6.7 (a), (b) and (c) show typical microstructures for the three steel grades studied, as revealed by the image analyzer. A visual comparison between these photos shows the increase in the volume of ferrite at the expense of pearlite, with decreasing carbon content.

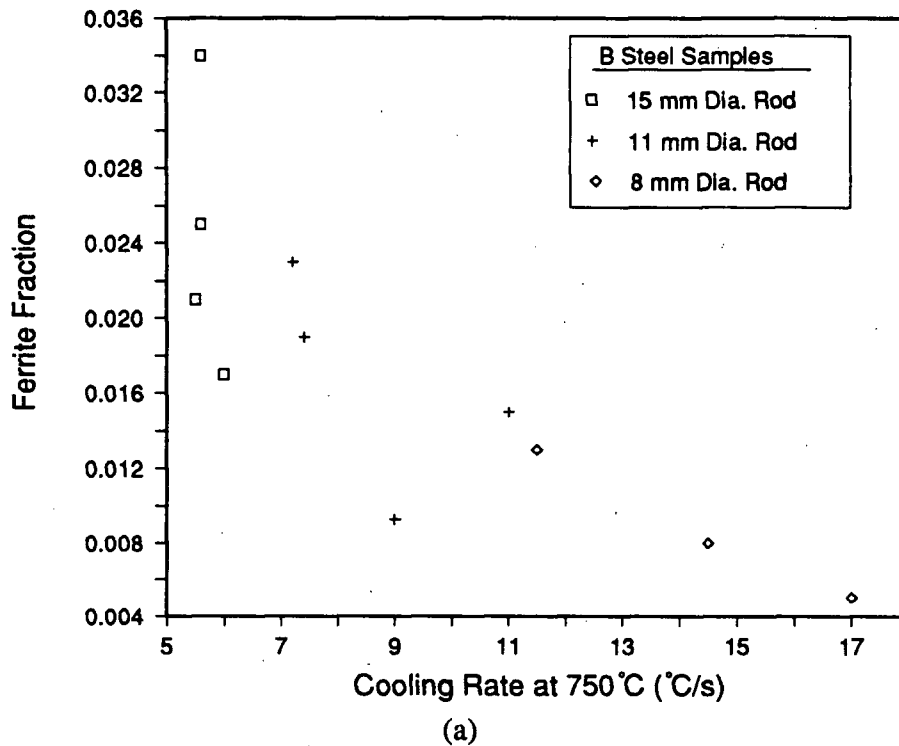


Fig. 6.6 - Measured ferrite fraction versus cooling rate at 750°C; (a) Steel B (1070), (b) Steel C (1037) and (c) Steel E (1020).

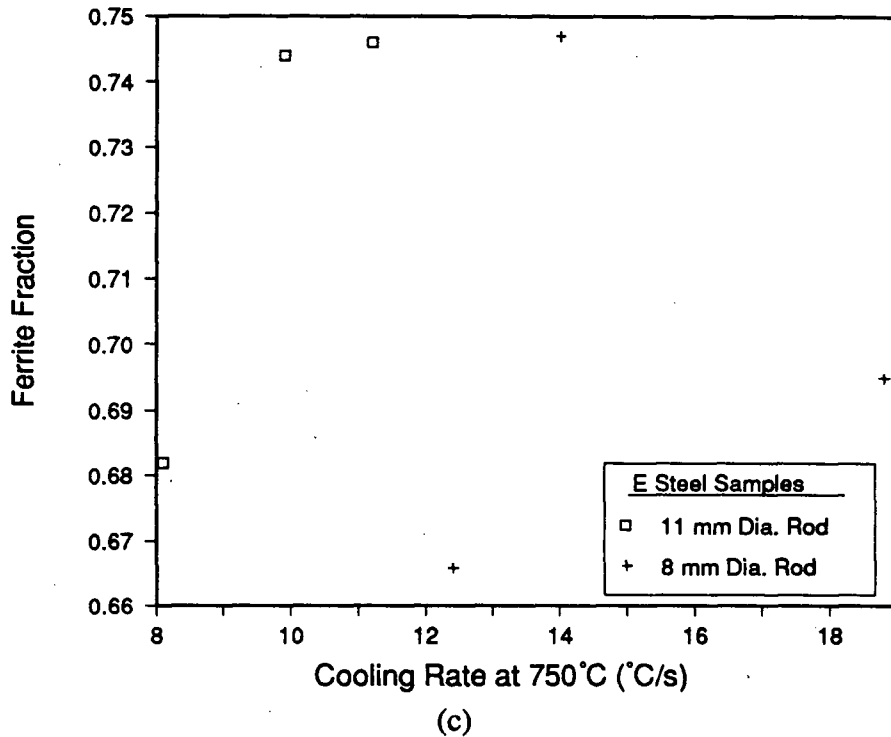
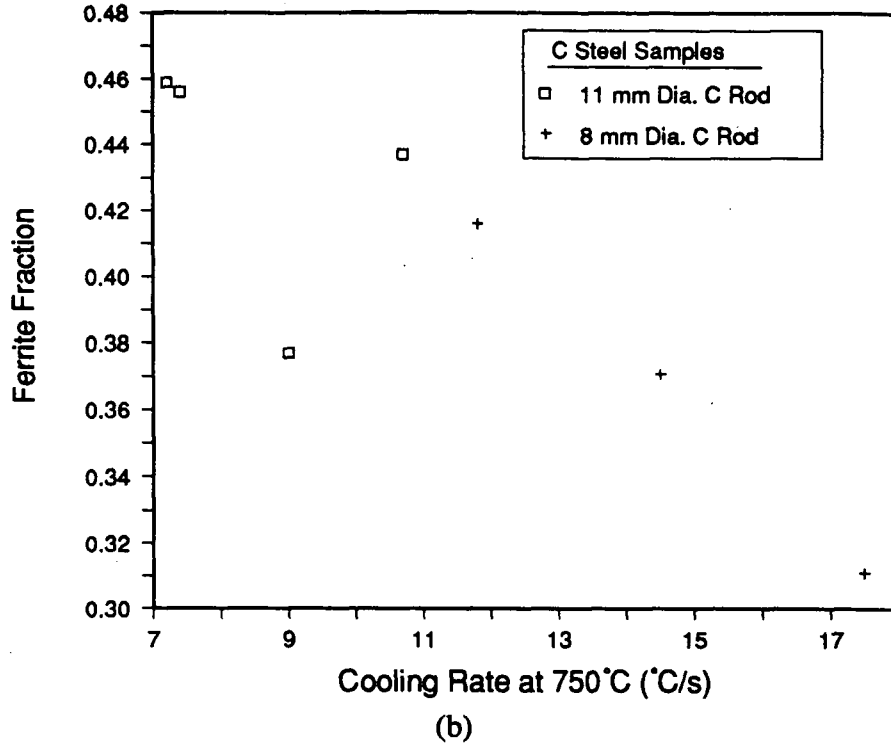
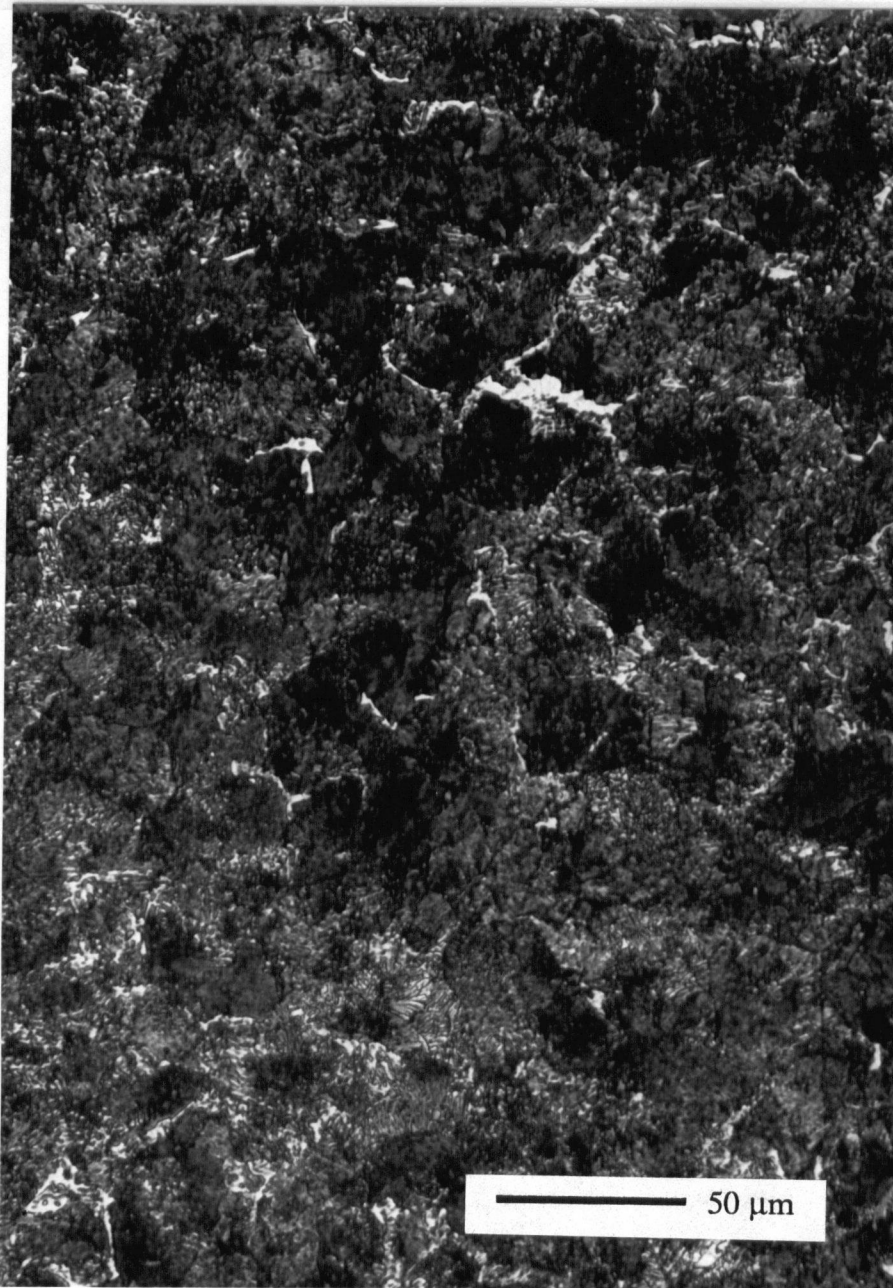
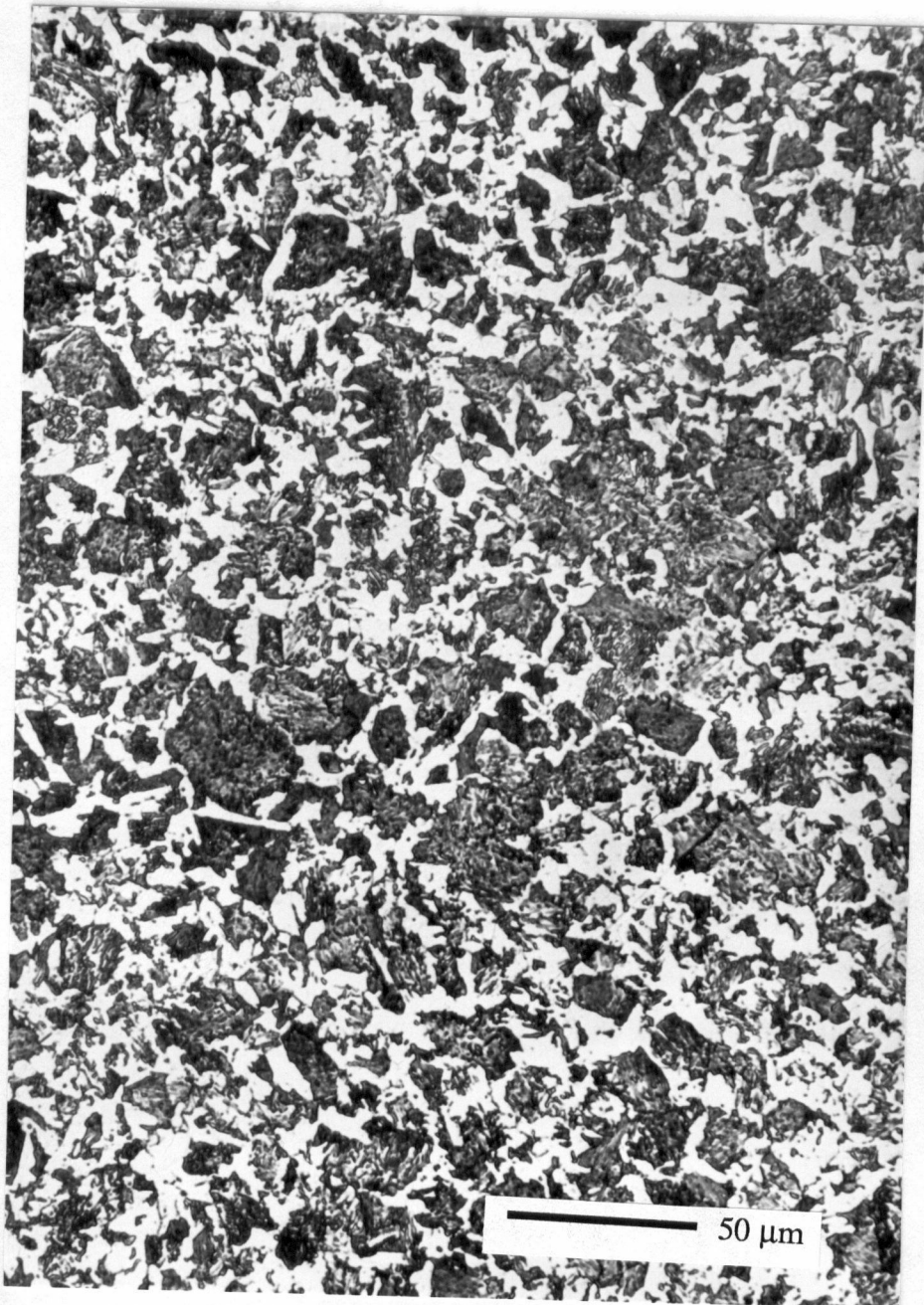


Fig. 6.6 - Measured ferrite fraction versus cooling rate at 750°C; (a) Steel B (1070), (b) Steel C (1038) and (c) Steel E (1020).



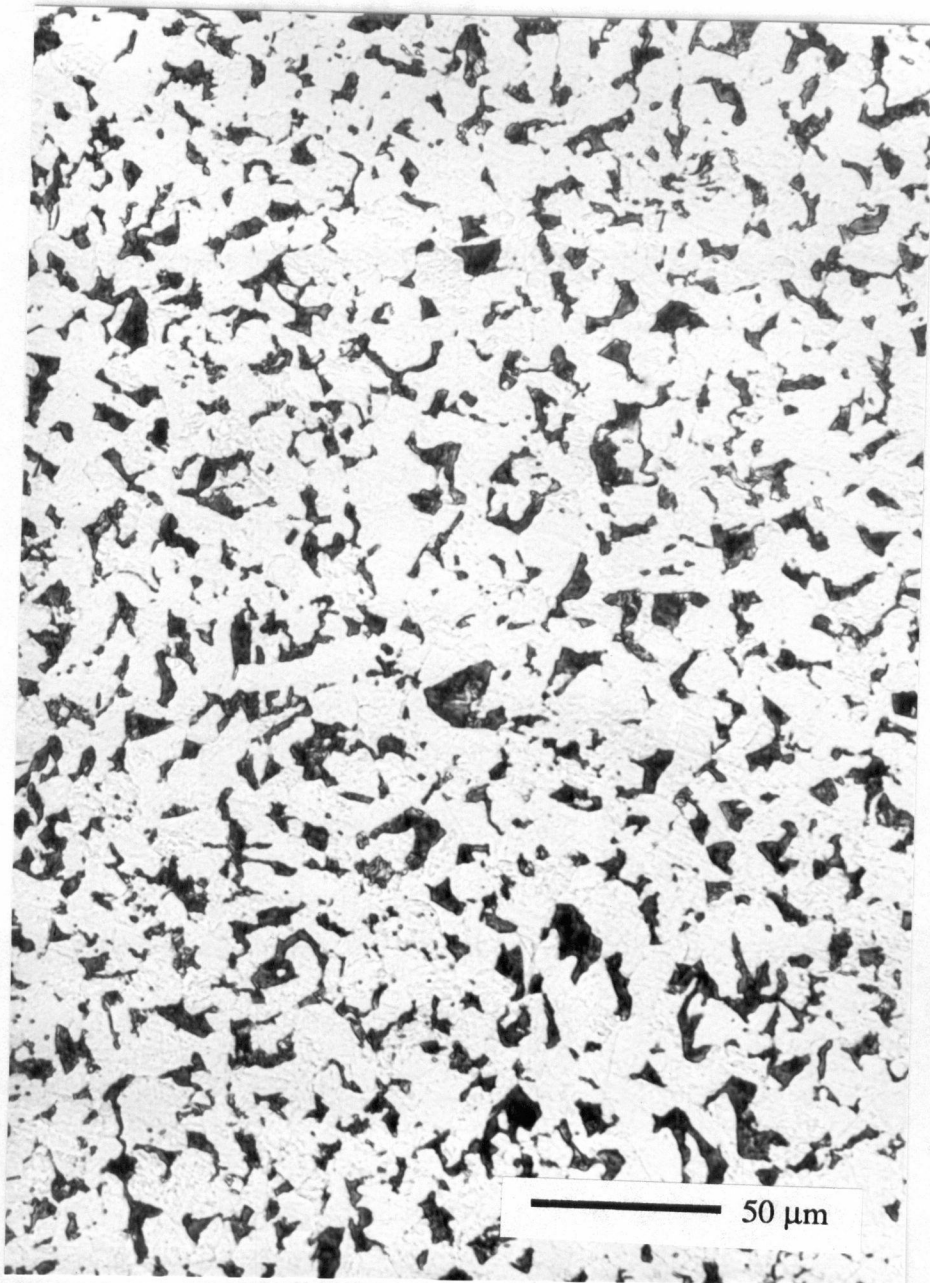
(a)

Fig. 6.7 - Typical photomicrographs taken on the image analyzer (a) Steel B (1070), (b) Steel C (1038) and (c) Steel E (1020) .



(b)

Fig. 6.7 - Typical photomicrographs taken on the image analyzer (a) Steel B (1070), (b) Steel C (1038) and (c) Steel E (1020) .



(c)

Fig. 6.7 - Typical photomicrographs taken on the image analyzer (a) Steel B (1070), (b) Steel C (1038) and (c) Steel E (1020) .

6.1.2.2 Ferrite Grain Diameter

The average ferrite grain diameter, measured in three grades of laboratory test rods, is summarized in Figs. 6.8 (a), (b) and (c). Once again the values represent the average of forty-nine areas measured by the image analyzer. As was the case for ferrite fraction, diameter is plotted against the average cooling rate measured at 750°C. Similar to the measured ferrite fractions, ferrite grain diameter also shows an inverse relationship with cooling rate which can be explained through the change in nucleation rate of ferrite as a function of temperature. As cooling rate increases and transformation temperature decreases, the rate of formation of stable ferrite nuclei increases, resulting in more ferrite grains per unit volume. Combined with the decreased ferrite fraction at lower temperatures, this leads to a smaller average ferrite grain diameter.

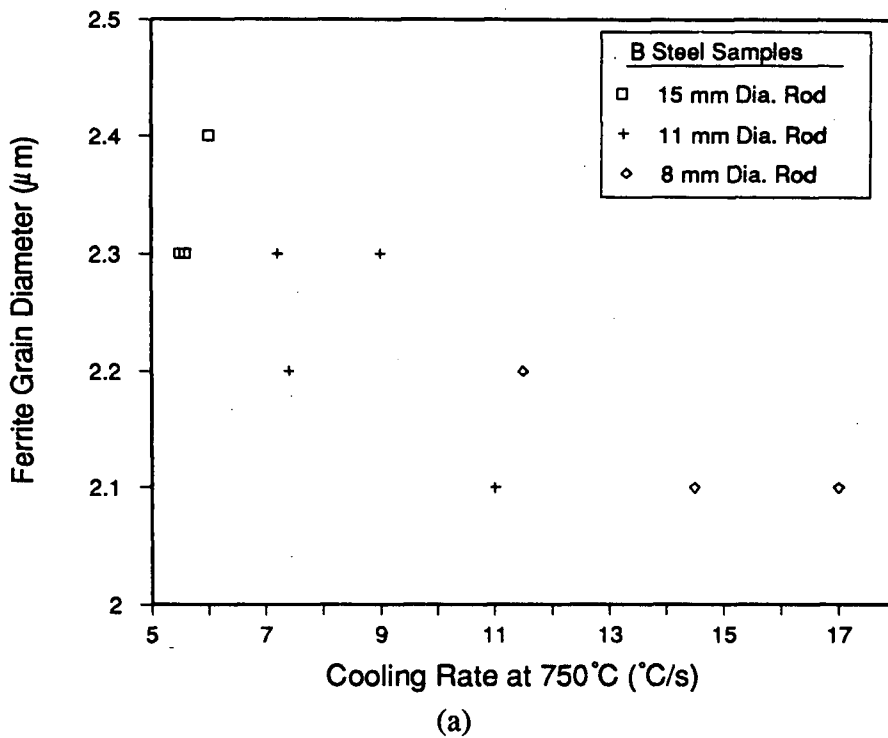


Fig. 6.8 - Measured ferrite grain diameter versus cooling rate at 750°C; (a) Steel B (1070), (b) Steel (1038) C and (c) Steel E (1020).

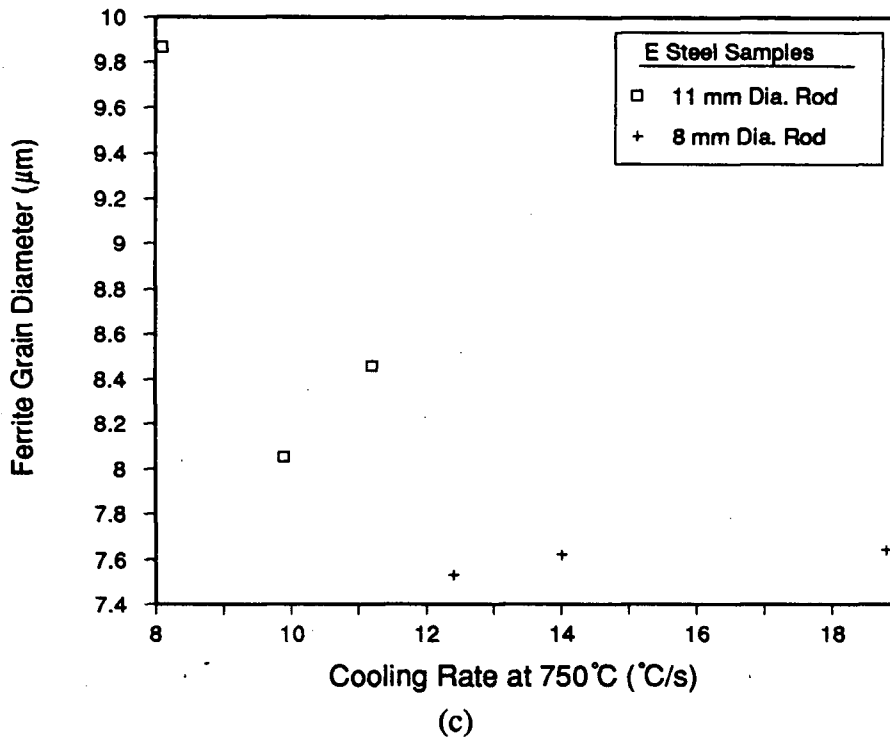
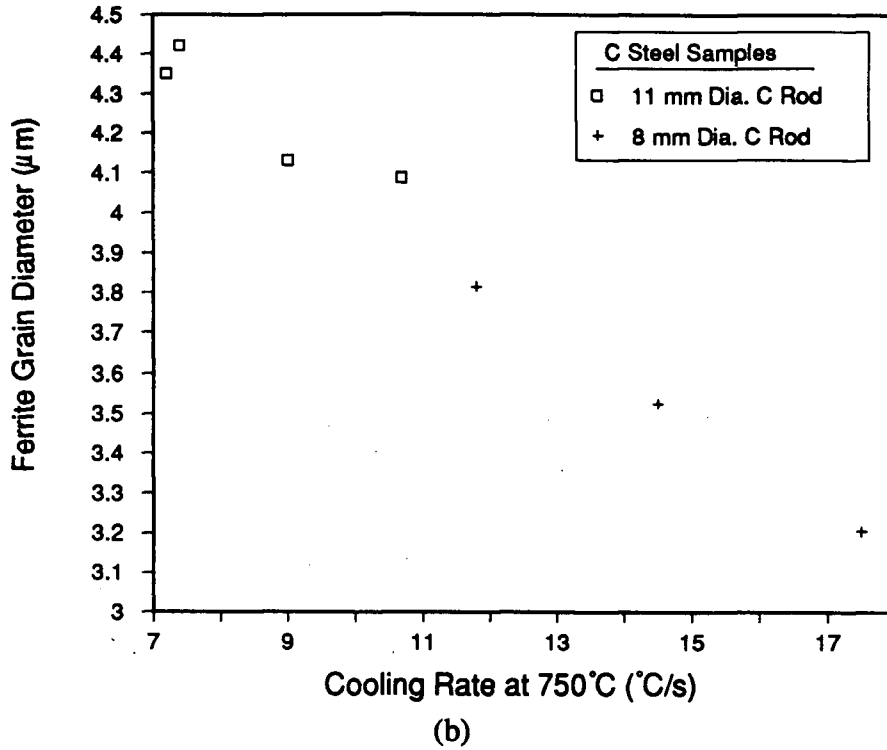


Fig. 6.8 - Measured ferrite grain diameter versus cooling rate at 750°C; (a) Steel B (1070), (b) Steel C (1038) and (c) Steel E (1020).

6.1.2.3 Pearlite Spacing

Pearlite spacings have been determined for Steel B (1070). Results from the work are shown in Fig. 6.9, where the reciprocal mean pearlite spacing is plotted against the undercooling below T_{A_1} , together with a best-fit line derived from the spacing data given by Pellisier *et al.* [74]. The error bar plotted with each point represents one standard deviation from the mean measured value. The solid line in the figure is the best-fit line and the dashed lines represent \pm one standard deviation of the y prediction from the linear regression equation used. Although the relative error in determining pearlite spacing is seen to be large, the trend towards finer pearlite spacings with increased undercoolings is in agreement with the findings of Pellisier *et al.*.

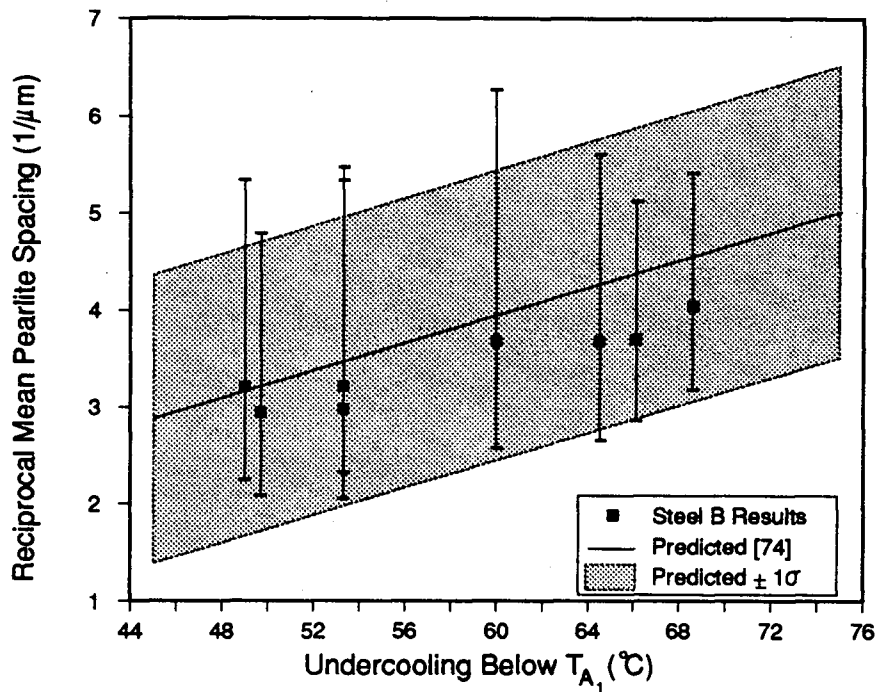


Fig. 6.9 - Measured and predicted pearlite spacing plotted against the undercooling below T_{A_1} for Steel B (1070).



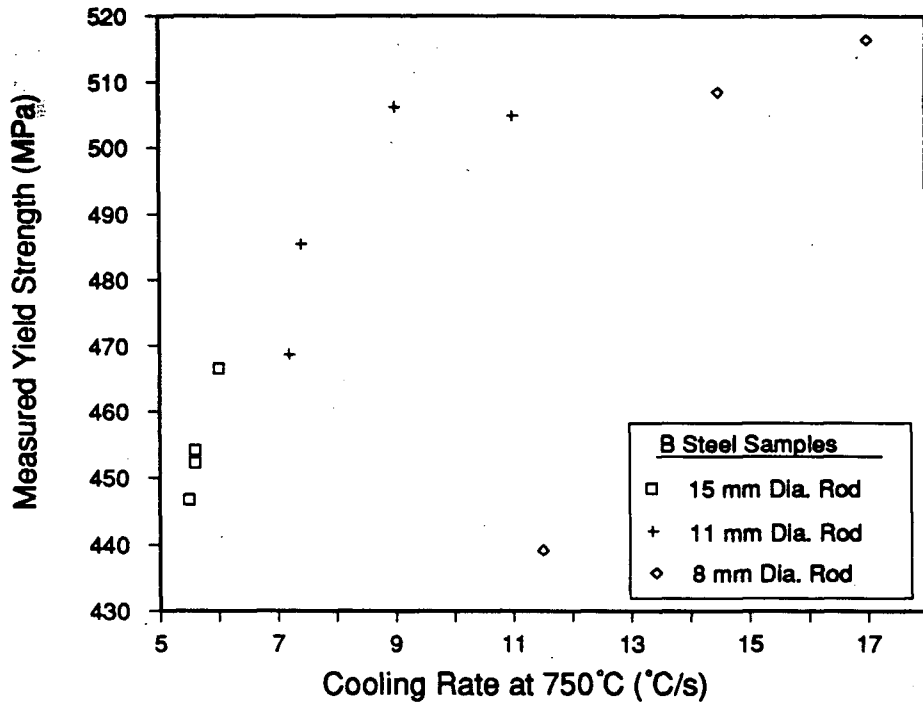
Fig. 6.10 - Typical SEM micrograph of Steel B (1070), displaying pearlite colonies.

A typical SEM photomicrograph of Steel B is shown in Fig. 6.10. As can be seen the pearlite fraction is close to 100%. Results for ferrite fraction in this grade also revealed very little ferrite, as reported in Section 6.1.2.1. The figure represents a typical photomicrograph from which pearlite spacing was determined. At least six different pearlite colonies can be recognized; thus with a minimum of sixteen photographs per sample taken, nearly one hundred colonies were encountered for each rod sample.

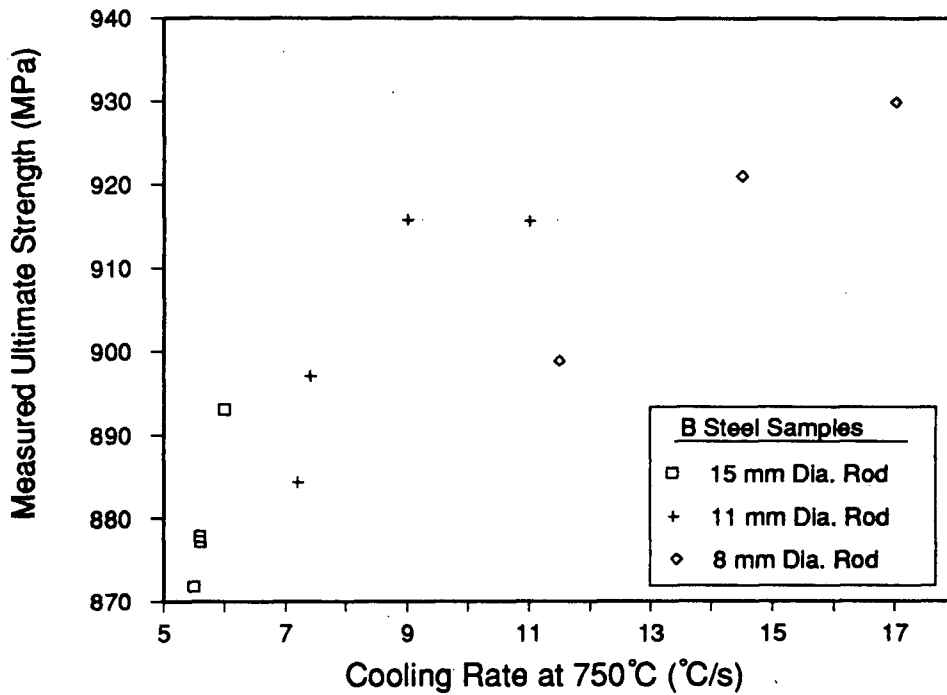
6.1.3 Mechanical Properties

Results from mechanical testing of the laboratory steels were analyzed to determine the yield strength, ultimate tensile strength and the % reduction in area for each rod test sample. A 0.2% strain offset was applied to the load-elongation charts to determine yield load. The ultimate load attained during each test was taken as the peak load from the load-elongation curve. The diameter of the reduced section of each sample was measured prior to tensile testing, and after the test, the diameter at the point of fracture was measured to enable calculation of stresses and %R.A.. As was mentioned, due to the rod lengths and diameters of some of the tensile specimens used, either two or four samples could be obtained from each cooling test sample. The results of the tests are summarized in Figs. 6.11 to 6.13, where both average yield and ultimate strength for each sample are plotted as a function of the measured rod cooling rate at 750°C. As can be seen in the plots, strength increases with increase in cooling rate for most rods tested. A complete listing of the mechanical test results is given in Appendix 2 and the variation in strength within each rod sample is seen to be quite small. This would indicate that the rods were homogeneous in composition and uniformly cooled during the Stelmor simulation tests.

Results obtained from the laboratory tests were combined with those from the plant trials to develop relationships needed for the prediction of mechanical properties. These are reported in Chapter 7.

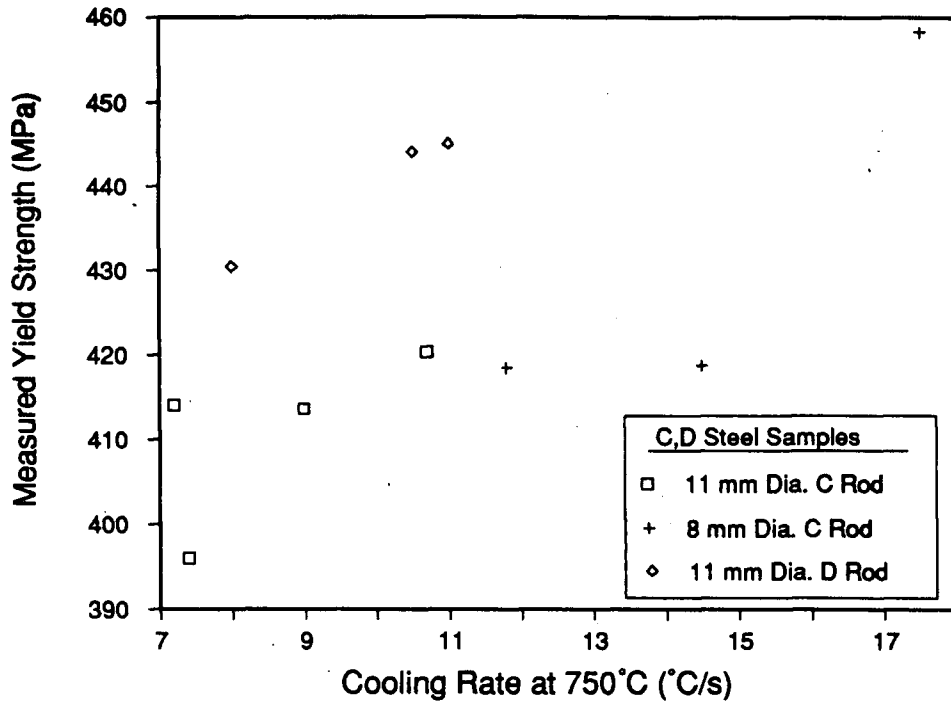


(a)

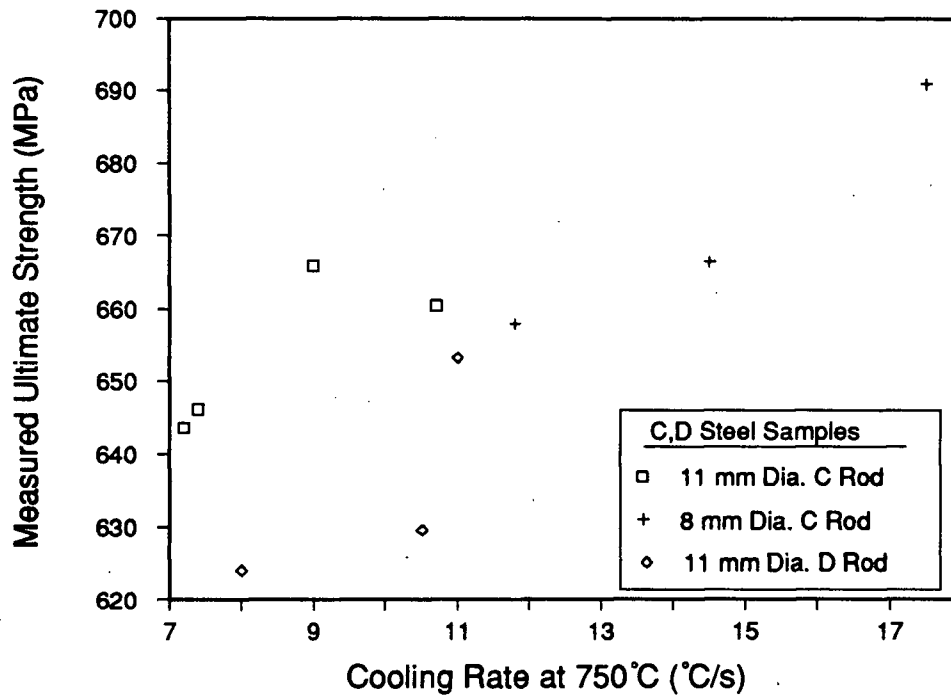


(b)

Fig. 6.11 - Measured strengths of laboratory Steel B (1070) plotted against the average cooling rate at 750°C, (a) yield strengths, (b) ultimate strengths.

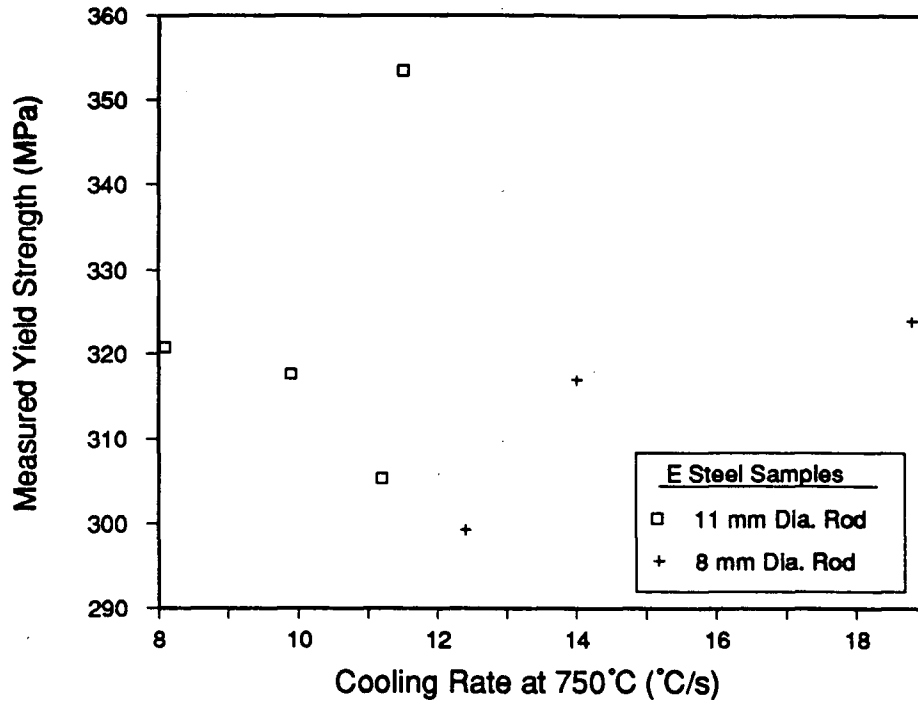


(a)

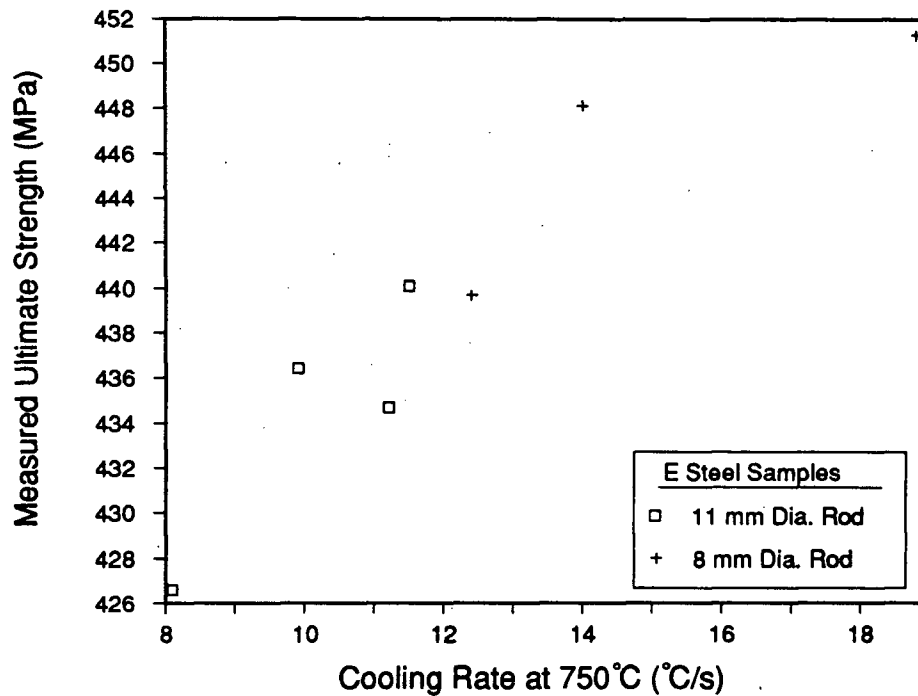


(b)

Fig. 6.12 - Measured strengths of laboratory Steels C (1038) and D (1037) plotted against the average cooling rate at 750°C, (a) yield strengths, (b) ultimate strengths.



(a)



(b)

Fig. 6.13 - Measured strengths of laboratory Steel E (1020) plotted against the average cooling rate at 750°C, (a) yield strengths, (b) ultimate strengths.

6.2 Phase Transformation Kinetics Results

Results from the dilatometer study, consisted of both isothermal and continuous cooling transformation kinetics. The isothermal kinetics were characterized applying the Avrami equation and calculating the constants n and b . The continuous cooling data were used to indicate CCT start times for the three grades of steels.

6.2.1 Isothermal Tests

6.2.1.1 Eutectoid Grades

The results from the isothermal dilatometer tests comprised temperature and sample dilation as a function of time. Typical thermal history and dilatometer response from an isothermal test, is provided in Fig. 6.14. For convenience the dilatometer signal, typically on the order of fractions of millivolts, has been scaled to the level of the sample temperature. The signal from both the thermocouple and the dilatometer exhibit a certain amount of noise despite attempts at filtering. As can be seen, the rod was cooled rapidly from a temperature of 750°C to the isothermal test temperature of approximately 670°C. Owing to the decrease in sample temperature, the dilatometer responds correspondingly. Once the isothermal temperature is achieved, the dilatometer reflects an expected incubation time, before start of the austenite-pearlite transformation. Subsequently the characteristic sigmoidal curve for the transformation is witnessed in the dilatometer response. The sampling rate used for the test shown was 25 Hz per channel.

After digitally smoothing the dilatometer signal by averaging from three to five data points, the data was converted to fraction transformed. Fig. 6.15 (a) shows the smoothed signal with the three parameters required for conversion of dilatometer response to fraction transformed. The results shown in Fig. 6.14 are for Steel B which is a 1070 grade and does contain a small fraction of proeutectoid ferrite. However, owing to the amount of ferrite present at the isothermal test temperatures (~1-3%), analysis of the dilatometer-fraction transformed data has been made assuming a 100% pearlitic microstructure. Assuming that D_{MIN}

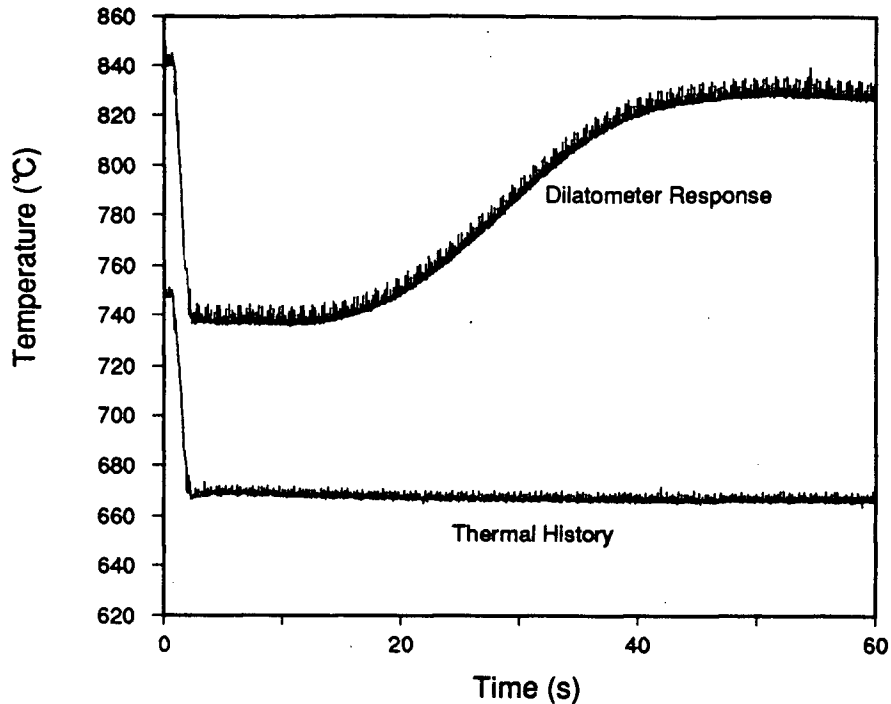


Fig. 6.14 - Typical dilatometer response and thermal history for phase transformation kinetics experiments. Dilatometer output has been scaled to match sample temperature. Data is for 1070 Steel B with an isothermal temperature of 663°C.

and D_{MAX} represent the diameter of a fully austenitic sample and a fully pearlitic sample respectively at the isothermal test temperature, as indicated in Fig. 6.15 (a), and that D_T can be given by:

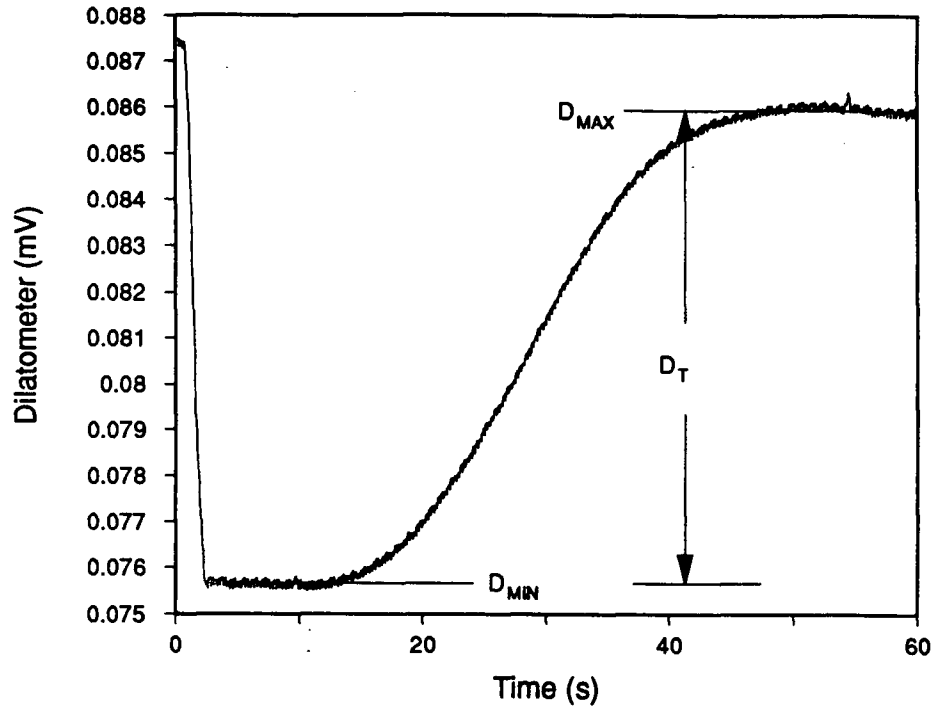
$$D_T = D_{MAX} - D_{MIN} \quad (6.5)$$

then the fraction of austenite transformed to pearlite is:

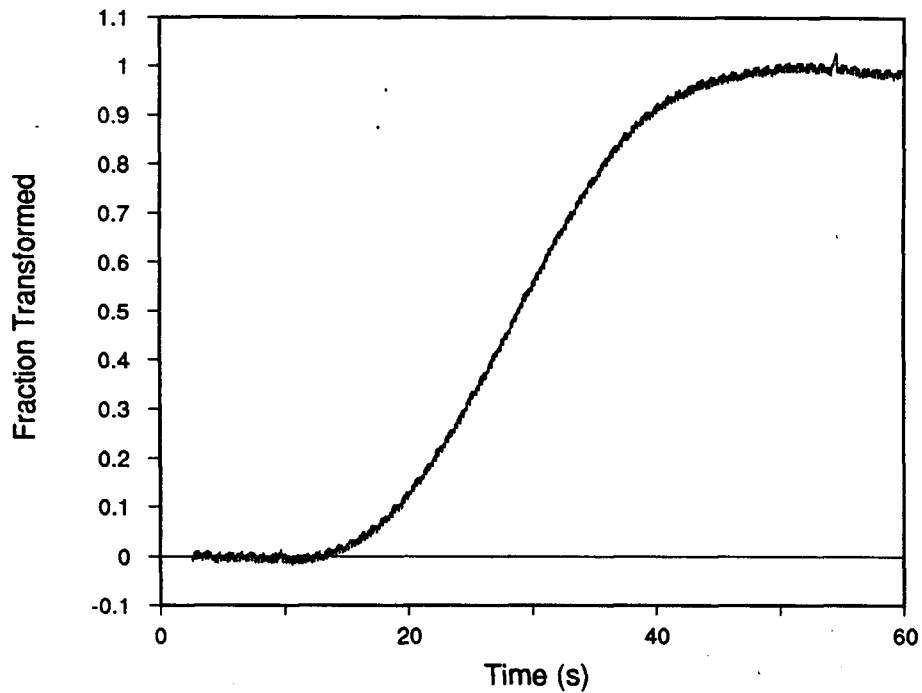
$$X = \frac{D - D_{MIN}}{D_T} \quad (6.6)$$

where D represents the diameter between D_{MIN} and D_{MAX} , and X is the fraction transformed. Results of the conversion of the dilatometer data shown in Fig. 6.15 (a), to a plot of fraction transformed as a function of time, is given in Fig. 6.15 (b).

The final step in the calculation of n and b from the data involves the linearization of the Avrami equation. Thus, by taking natural logarithms of both sides of Eq. (2.17),



(a)



(b)

Fig. 6.15 - Diagrams displaying technique for converting dilatometer response to fraction transformed. (a) Dilatometer response showing values of D_{MIN} , D_{MAX} and D_T , (b) Data after conversion to fraction transformed versus time.

$$\ln \left[\ln \left[\frac{1}{(1-X)} \right] \right] = n(\ln t) + \ln b \quad (6.7)$$

From the data shown in Fig. 6.15 (b) for fraction versus time, a plot of $\ln(\ln(1/(1-X)))$ against $\ln t$ is provided in Fig. 6.16. Through application of a linear regression technique, the start time of the reaction can be determined from the best fit. The slope of the best fit line also provides the value of n and the y-intercept the value for $\ln b$. For reference, the plot also includes indications of linear fraction transformed.

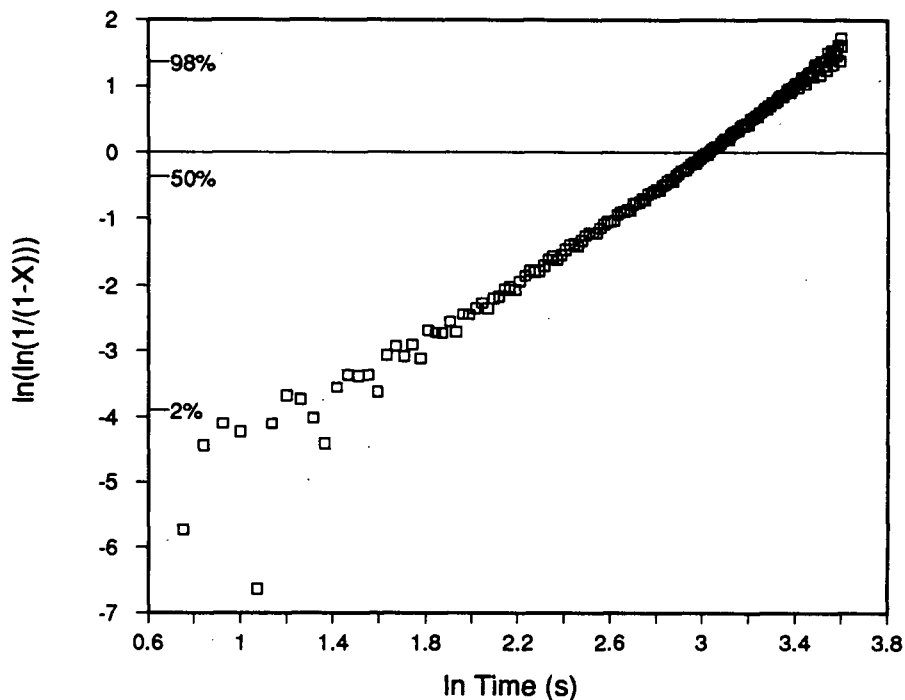


Fig. 6.16 - Linearization of the Avrami equation demonstrating the procedure applied for determining the constants n and b .

Results of the conversion of dilatometer response to fraction transformed for Steel B are provided in Fig. 6.17. The figure includes results for four isothermal test temperatures. As the test temperature decreases, transformation kinetics for the austenite-to-pearlite transformation can be seen to increase. As mentioned previously, owing to the small amounts of ferrite formed in this steel, the transformation is considered as austenite to pearlite only. Employing the linearization technique depicted in Fig. 6.16, the values for n (slope of the

best-fit line) at each temperature were first determined. An average n , based on all four temperatures, then was calculated to represent the range of temperatures. This average n was reapplied to the data for calculation of the corresponding b at each isothermal temperature. Table 6.1 contains the values for n at each temperature and the average n for the four.

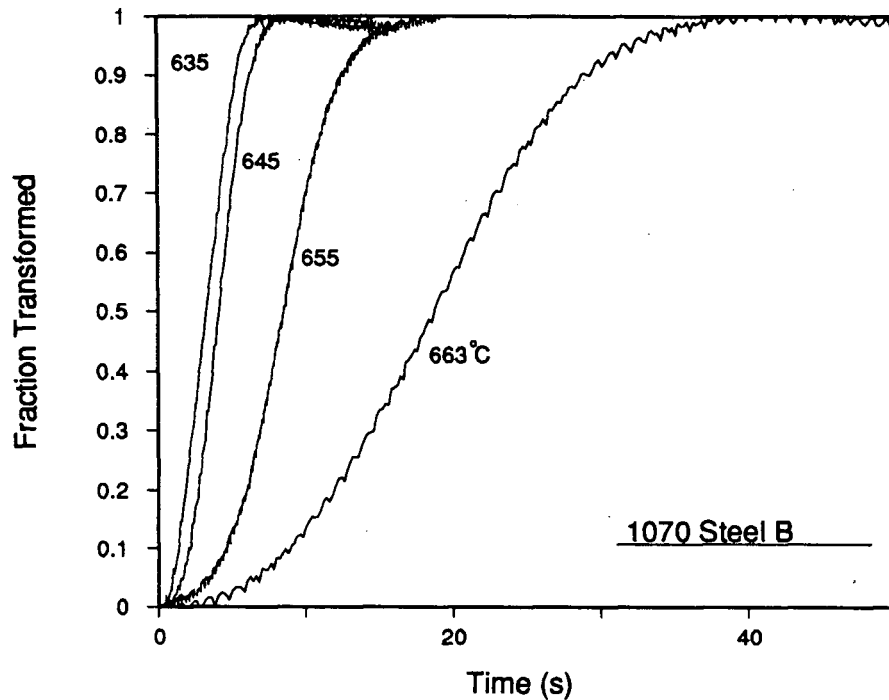


Fig. 6.17 - Fraction transformed-versus-time for Steel B (1070) under isothermal conditions. The isothermal temperature is included adjacent to each curve.

Table 6.1 - Values of kinetic parameter n_p , determined for Steel B (1070) as a function of isothermal transformation temperature.

Temperature (°C)	n_p
663	2.52
655	2.49
645	2.24
635	1.94
AVG	2.3

Values for $\ln b$ are plotted in Fig 6.18 as a function of the undercooling below T_{A1} . Also shown in the figure are the results for two grades of 1080 steel reported by Hawbolt *et al.*

[24] and Iyer [66]. The compositions for these grades are listed in Table 6.2. As can be seen in Fig. 6.18, $\ln b$ values for the three grades are in reasonable agreement; however Iyer's data appears to be somewhat lower than the other two, and this may be due to the method followed in assessing his data. Instead of choosing a constant value for average n , Iyer used the best-fit n for each temperature and the corresponding b . The values he reported for n , varied from 1.6 to 3.2. The higher values, reported for medium undercooling, result in a lower value for b . Thus if an average n were used, a higher b would be attained in the medium undercooling ranges. The data analyzed by both Hawbolt *et al.* and Iyer, has been obtained through hand digitizing of strip chart recorder curves, and for each isothermal transformation includes only 20 or so points. Within the limits of error of this method, agreement between the values for b_p among the three grades is seen to be reasonable.

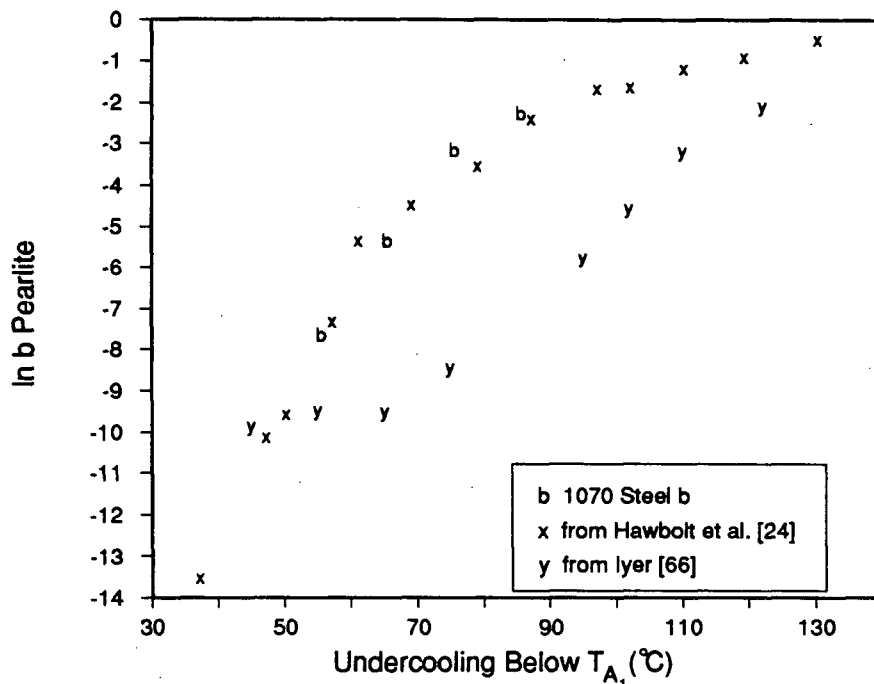


Fig. 6.18 - Natural logarithm of b_p plotted against undercooling below T_{A_1} for Steel B and two grades from the literature [24,66].

Table 6.2 - Composition of two 1080 grades for comparison of transformation kinetics with Steel B (1070), in Fig. 6.18.

Reference	%C	%Mn	%Si
Steel B (1070)	0.69	0.74	0.24
Hawbolt <i>et al.</i> [24]	0.795	0.91	0.49
Iyer [66]	0.82	0.82	0.26

6.2.1.2 Hypoeutectoid Grades

Owing to the transformation of austenite to both ferrite and pearlite in hypoeutectoid steels, dilatometer data has been treated slightly differently than that reported for the eutectoid grades. For isothermal tests completed above the A_1 temperature, results were treated similarly to the eutectoid grades, since only one transformation product is formed. However, as the test temperature was lowered, a method for separating the two austenite decomposition reactions had to be developed. Unfortunately, for the grades studied, the end of the austenite-ferrite and start of the austenite-pearlite reactions were not obvious from the dilatometer response-versus-time plots. This required that the fractions of ferrite and pearlite formed in the tests had to be determined from an indirect method. The technique followed, was based on the calculation of the equilibrium fractions of ferrite and pearlite from the predicted phase diagram for each grade. Owing to the utilization of one sample for at least two tests, metallographic checks of the predicted ferrite-pearlite fractions were only made for a portion of the isothermal tests. Good agreement between the predicted and measured ferrite fractions was obtained. As a further indication of the fractions of the two phases, comparison of the relative magnitudes of D_T for tests above or near T_{A_1} with tests below T_{A_1} were also conducted. Recognizing that at T_{A_1} , a hypoeutectoid steel will form the maximum fraction of ferrite, the D_T for an isothermal test should increase steadily with decreasing temperature until the A_1 temperature is achieved. At temperatures below T_{A_1} , where pearlite formation is possible, there should be a discontinuous increase in the magnitude of D_T . The magnitudes of D_T can then be compared to indicate the relative fractions of ferrite and pearlite formed during each isothermal test. An example of the difference in D_T for two isothermal tests on 1038 Steel C

is shown in Fig. 6.19. Comparing the dilatometer curves from the two tests, the response can be seen to be quite different. The higher temperature test (713°C), which is for the ferrite transformation only, reveals a continuously decreasing reaction rate, with the D_T equal to 0.009 mV. For the lower temperature test (663°C) the magnitude of the dilatometer response can be seen to be much larger and the shape of the curve is different. As the reaction proceeds for this test, it seems that the reaction rate increases, although the scale employed in the figure makes this somewhat difficult to detect. In addition, comparing the relative magnitudes of the dilatometer responses, at 663°C D_T equals 0.017 mV while at 713°C it is about 0.009 mV. The relative magnitudes of D_T and the difference in shape between the two curves point to the formation of pearlite in the lower temperature test. The next step is to separate the portion of the curve due to ferrite from the portion due to pearlite so that the kinetics of the two reactions can be assessed independently.

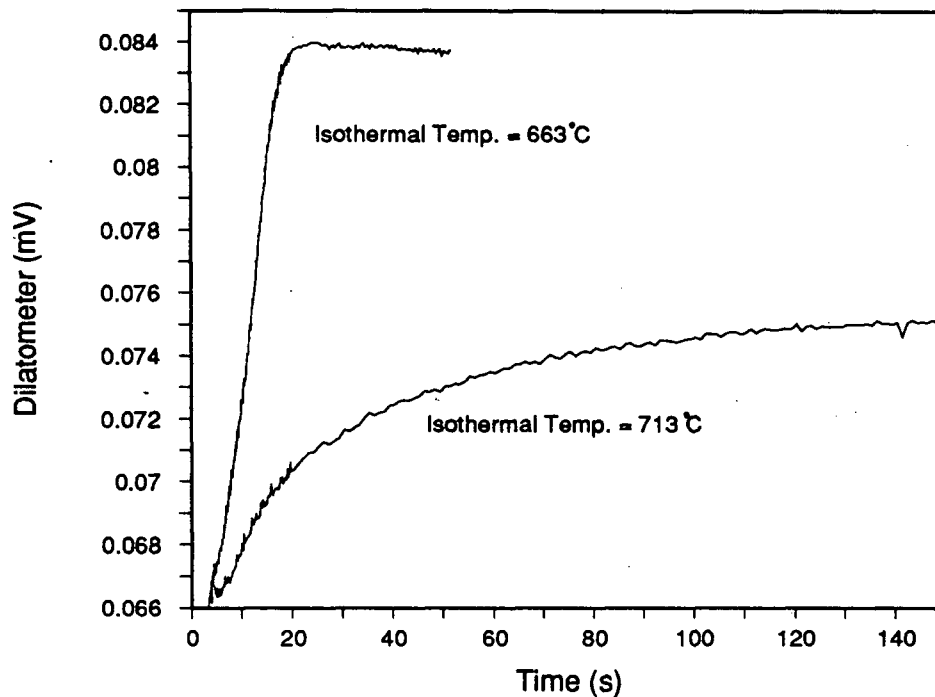


Fig. 6.19 - Dilatometer response-versus-time for two isothermal tests on 1038 Steel C contrasting the shape and magnitude of the curve for an austenite-ferrite only and an austenite-ferrite-pearlite transformation.

An estimate of the relative amounts of ferrite and pearlite formed in a hypoeutectoid steel can be made from the relative magnitude of D_7 and from the phase diagram. Comparing the two tests in Fig. 6.19, and assuming the expansion due to transformation from austenite to ferrite is essentially the same as for austenite to pearlite, the ferrite fraction formed is approximately 0.009/0.017 or 53%. Referring to the composition for Steel C in Table 4.2, the wt% of carbon is equal to 0.393. Applying the phase diagram for this grade, as given from the method due to Kirkaldy *et al.* [34,35], and adopting the lever rule, the fraction of ferrite formed should be approximately 50% at equilibrium. Referring to Fig. 6.20, the dilatometer response for the isothermal test similar to that shown for Steel C at 663°C, is redrawn together with a line indicating a fraction of 0.5. Recognizing that there is not a rapid transition between the two transformations, a period over which simultaneous formation of both phases must take place. After comparison of the shape of the curve with those for which ferrite had been the only transformation product, it was determined that an overlap region corresponding to the last 10% of the ferrite transformation and the first 10% of the pearlite transformation may be present. This is for steels with approximately 0.40% carbon and should differ with variation in the original carbon content of the steel. The reason for the significant overlap is thought to be due to the variation in carbon content ahead of the growing ferrite, as a function of time. Nucleation and growth of pearlite cannot take place until the carbon concentration exceeds some critical value, depending on the temperature and alloying elements present. It would be expected that certain regions of the steel attain this critical carbon concentration prior to others and nucleate pearlite. Thus, simultaneously, it is recognized that both proeutectoid ferrite and pearlite may be transforming. The overlap period is depicted in Fig. 6.20. By separating the original curve into two parts corresponding to each transformation event and normalizing to the appropriate fraction, the kinetic parameters n and b can be determined by the same method as was employed for the eutectoid grades. However, the calculations are performed excluding the region over which

simultaneous transformation is believed to take place. In addition, the relative fraction of ferrite and pearlite is calculated from the phase boundary extrapolation for each test temperature.

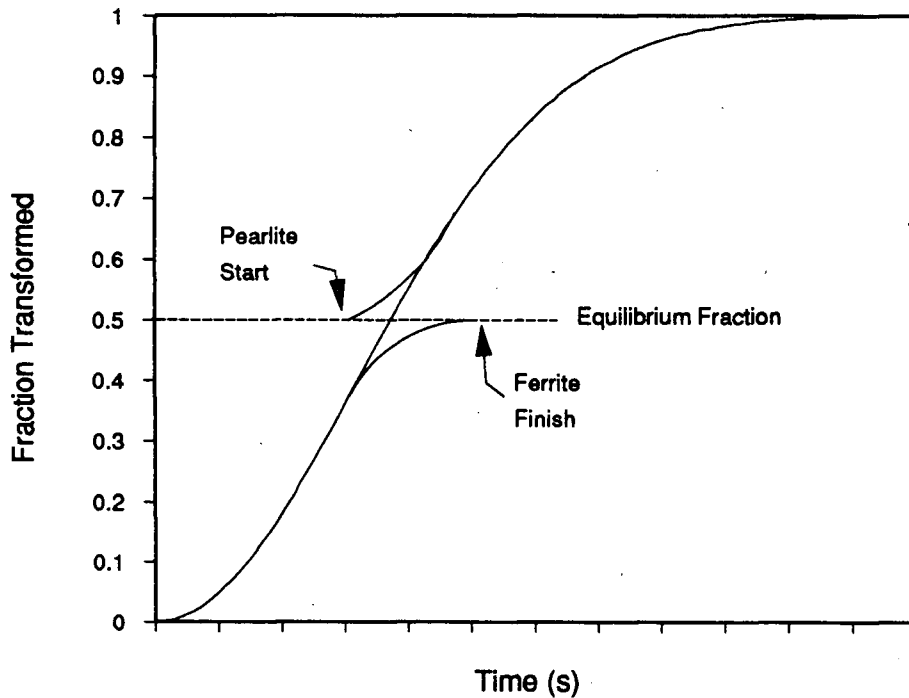
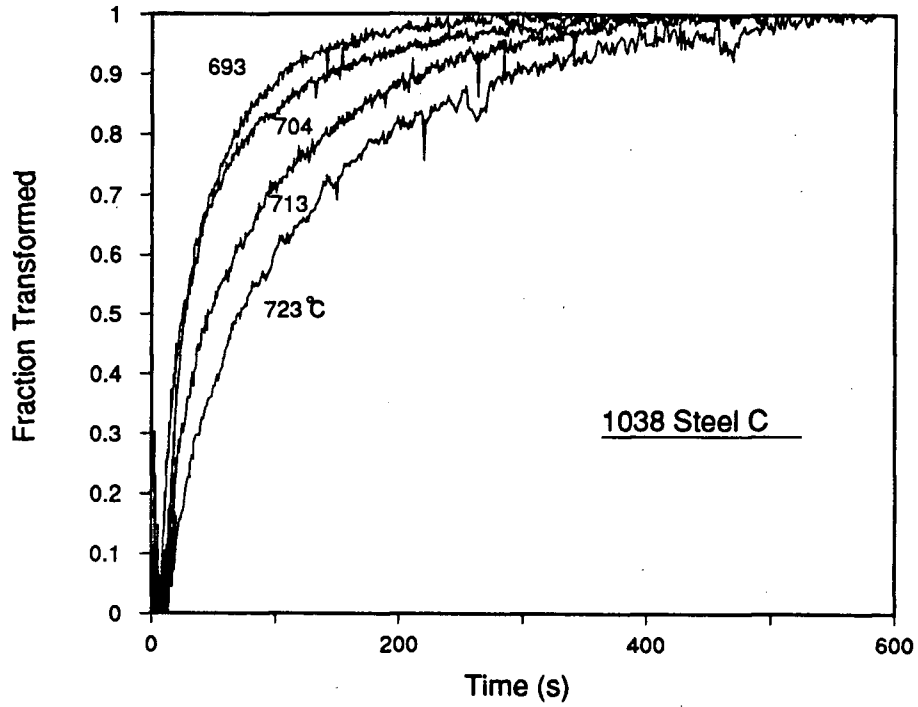


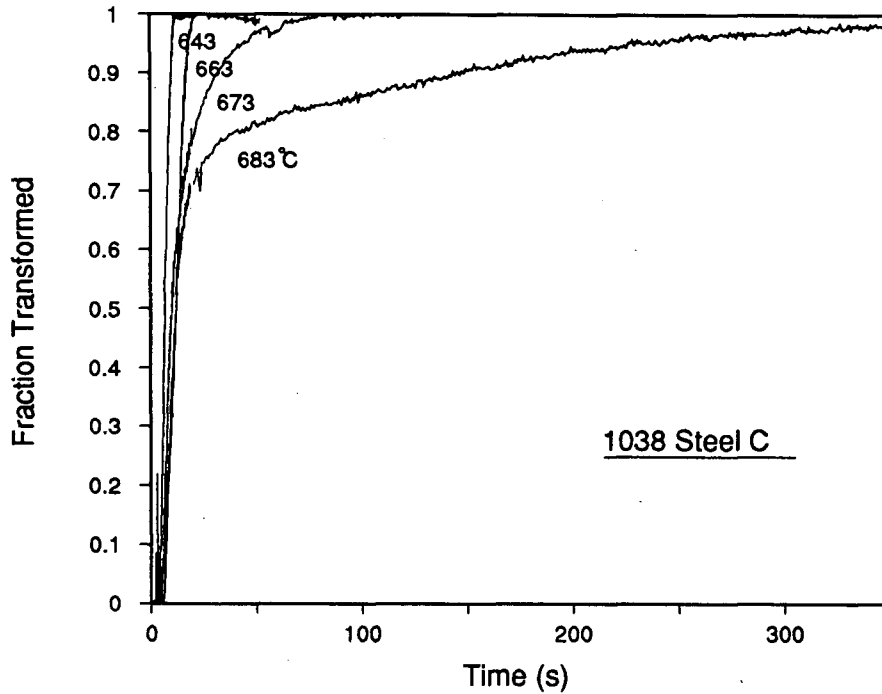
Fig. 6.20 - Figure depicting the method followed for separating the isothermal dilatometer-versus-time curve into two transformation events.

Results of dilatometer tests on Steel C (1038) are shown in Fig. 6.21 (a) and (b). In the figures, the original dilatometer response has been normalized for comparison and there has been no attempt to separate the ferrite and the pearlite portions of the plots. As can be seen, a lower transformation temperature results in increased transformation kinetics. Also the shape of the curves seems to change as the temperature falls below 690°C.

Dilatometer data for Steel C has been analyzed to determine the values of n and b for both the austenite-ferrite and austenite-pearlite transformations. Table 6.3 shows the average values for n_F and n_P are 0.88 and 1.3, respectively. The average n values for each transformation were used to calculate the corresponding value for b at each isothermal temperature. Fig. 6.22 (a) contains the results of $\ln b$ determined for the ferrite transformation and Fig.



(a)



(b)

Fig. 6.21 - Fraction transformed-versus-time for Steel C (1038) under isothermal conditions. The isothermal temperature is included adjacent to each curve. (a) 723 - 693°C and (b) 683 - 643°C.

6.22 (b) for the pearlite transformation. In both figures the undercooling below the equilibrium temperature is plotted on the abscissa; (T_{A_3} for ferrite and T_{A_1} for pearlite). Also plotted in both figures are the values of b for a comparable 1040 grade as measured by Hawbolt *et al.* [42]. The method adopted for calculation of b values from Hawbolt *et al.*, was not based on a constant n value. As was mentioned for the eutectoid steels, it is difficult comparing the b values for the different steels, with each steel possessing a different method for the parameter's calculation. The composition of the 1040 grade is given in Table 6.4. The average n values for this grade were found to be 1.14 ± 0.06 for pearlite and 1.32 ± 0.1 for ferrite.

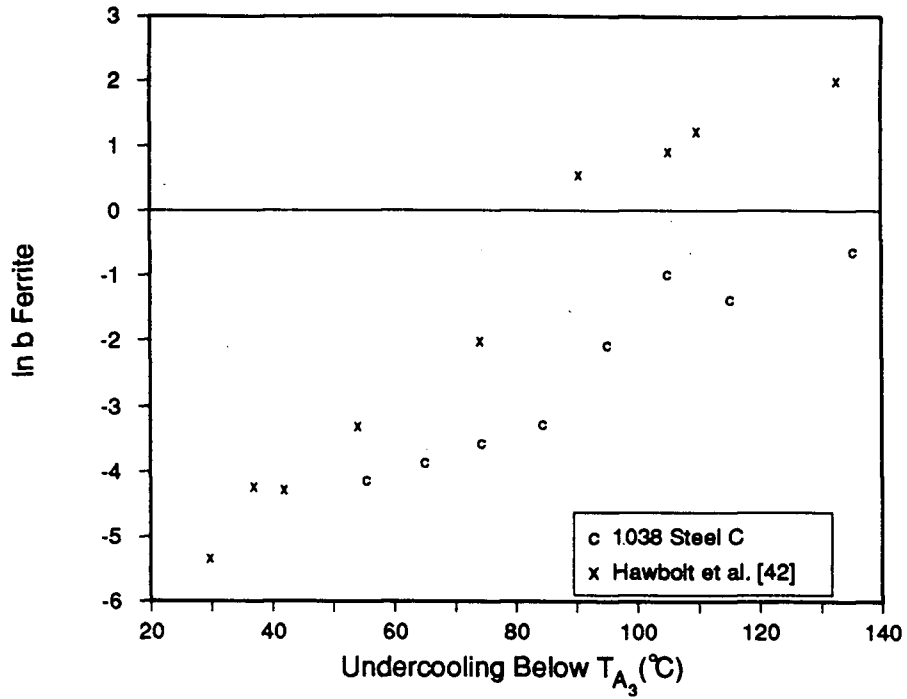
Table 6.3 - Values of kinetic parameter n_F and n_P , determined for Steel C (1038) as a function of isothermal transformation temperature.

Temperature ($^{\circ}\text{C}$)	n_F	n_P
723	0.82	-
713	0.79	-
704	0.72	-
693	0.78	-
683	0.88	-
673	0.92	1.10
663	1.36	1.43
643	0.80	1.37
AVG	0.88	1.3

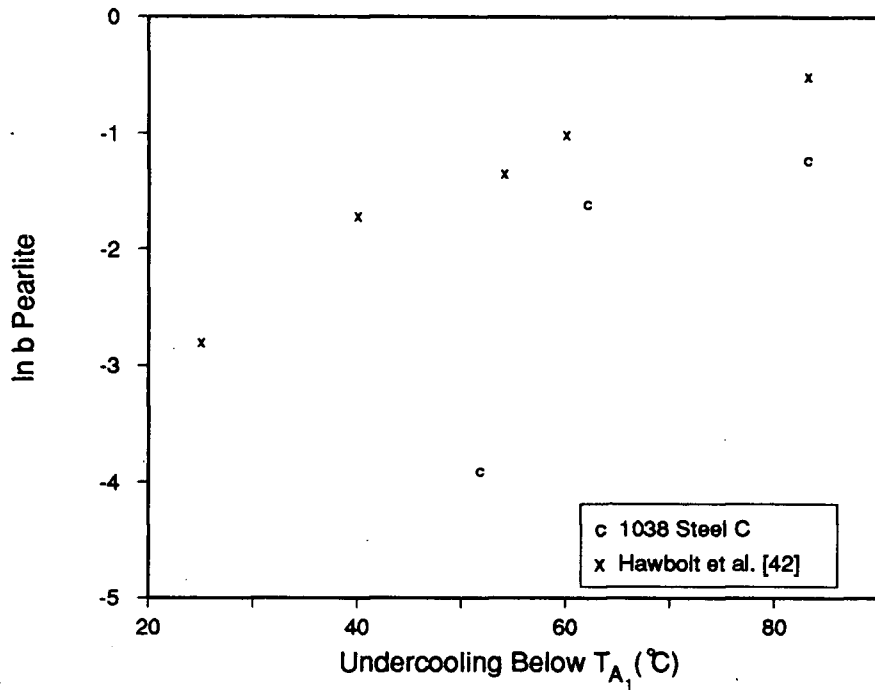
Table 6.4 - Composition of 1040 grade used for comparison of transformation kinetics with Steel C in Figs. 6.22 (a) and (b).

Reference	%C	%Mn	%Si
Steel C (1038)	0.393	0.82	0.28
Hawbolt <i>et al.</i> [42]	0.41	0.76	0.24

A similar procedure has been employed for assessment of the Steel E (1020). For temperatures above T_{A_1} , the dilatometer curves were converted to fraction transformed versus time and normalized to 100% ferrite. The n and b values were calculated by linearization of the Avrami equation as was the case for the 1070 and 1040 grades. For steels transformed at temperatures well below the A_1 , the curves had to be separated into a ferrite portion and a



(a)

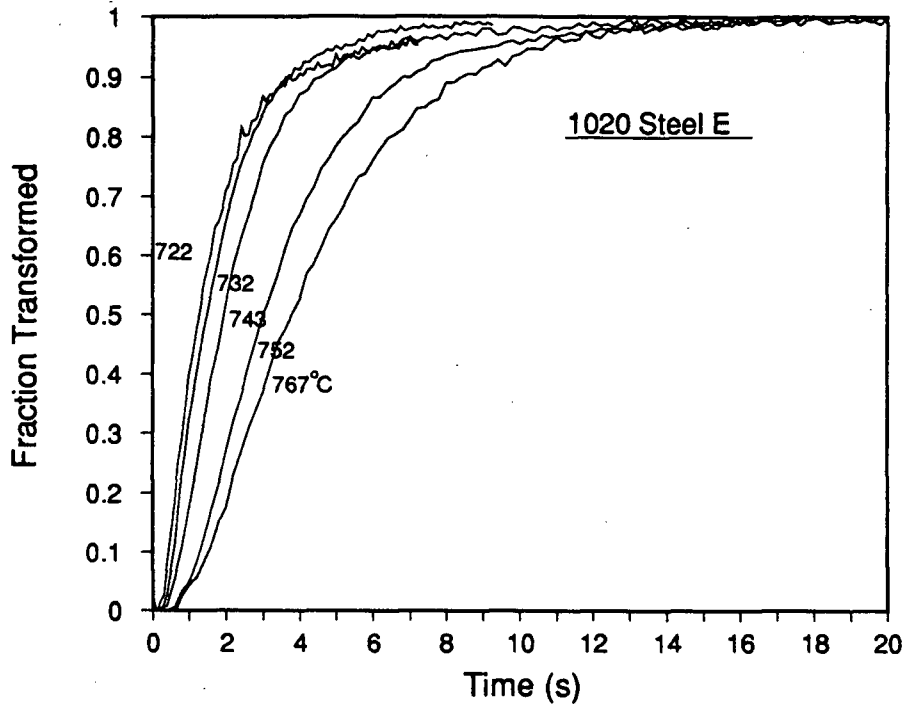


(b)

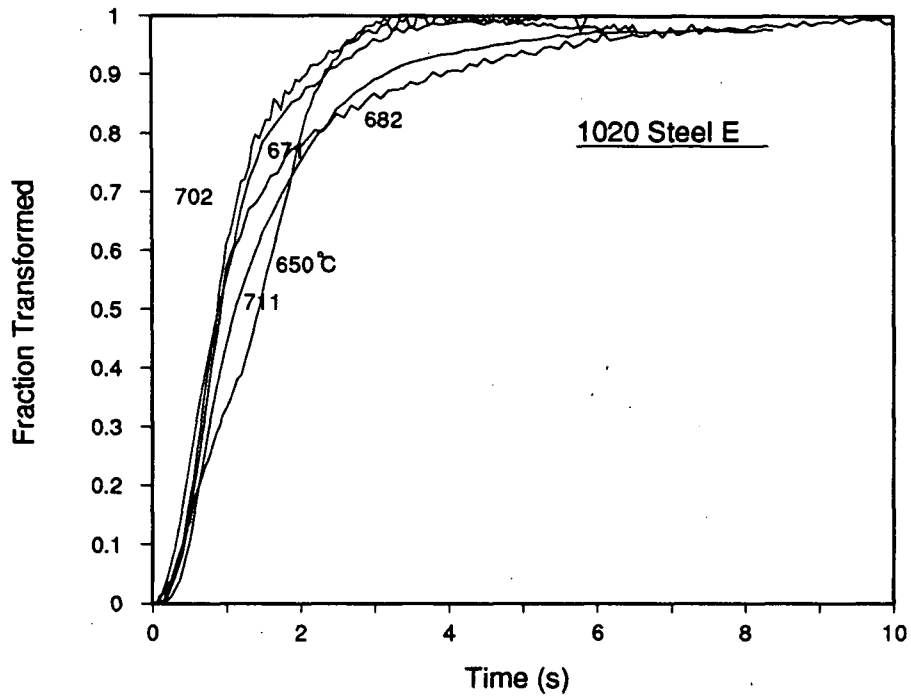
Fig. 6.22 - Natural logarithm of kinetic parameter b plotted against undercooling for Steel C (1038). Also included are data due to Hawbolt *et al.* [42]: (a) $\ln b_F$ against undercooling below T_{A_3} and (b) $\ln b_P$ against undercooling below T_{A_1} .

pearlite portion. The method outlined for evaluating the 1040 grades has been applied, with the appropriate fractions calculated from the equilibrium fraction as determined from the phase diagram. Metallographic checks on the relative fractions of ferrite and pearlite formed in Steel E revealed the formation of a Widmanstätten structure for the proeutectoid ferrite. The relative fractions agreed with those calculated from extrapolations of the A_{cm} line. The presence of Widmanstätten ferrite is not surprising considering the isothermal temperatures employed for the tests.

Plots of fraction transformed versus time, for ten isothermal dilatometer tests on Steel E are given in Figs. 6.23 (a) and (b). As can be seen, results are reasonable for the higher temperature transformations; however, with decreasing temperature the fraction transformed-versus-time curves overlap and display unexpected behaviour. The cause for this is not known but it could be due to the formation of Widmanstätten ferrite in the low temperature tests or by variation in wall thickness of the tubular samples. The values for n_F and n_P calculated from the isothermal tests are given in Table 6.5, where the variation in n is seen to be quite small. The average n for all isothermal tests, is given in the table for both the ferrite and pearlite transformations. Figures 6.24 (a) and (b) contain the results for $\ln b$ as a function of the undercooling below T_{A_1} and T_{A_3} . Plotted in the figures also are the results for a 1025 steel reported by Hawbolt *et al.* [25]. The composition for the steel is given in Table 6.6 and an average n of 1.33 ± 0.1 and 0.99 ± 0.03 for ferrite and pearlite respectively, were reported. Comparing b for both steels it seems that the kinetics are faster for the 1020 grade, for the same degree of undercooling, however care must be exercised when comparing b values for steels with different values for n .

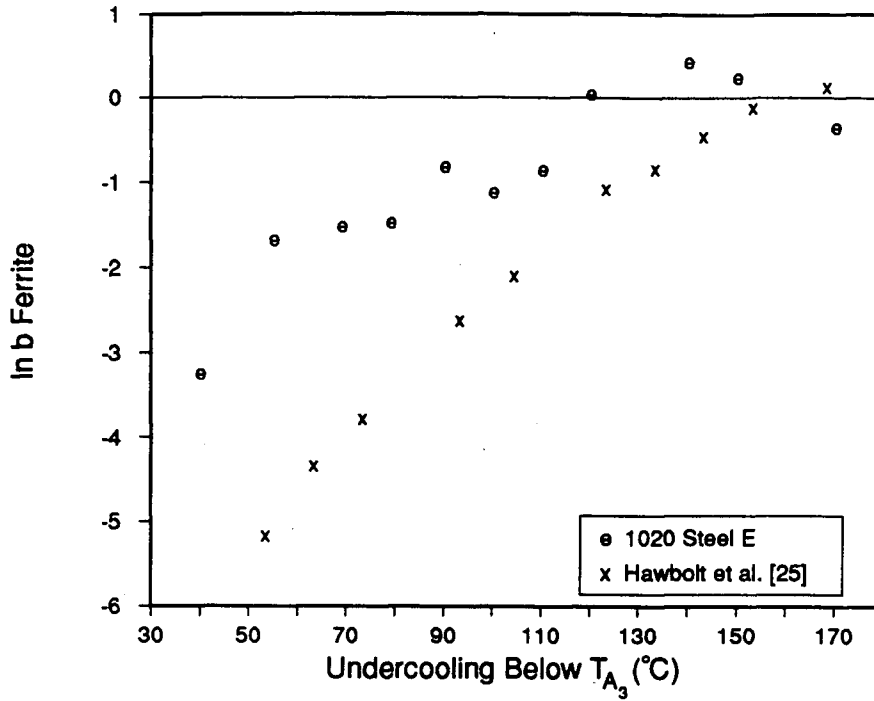


(a)

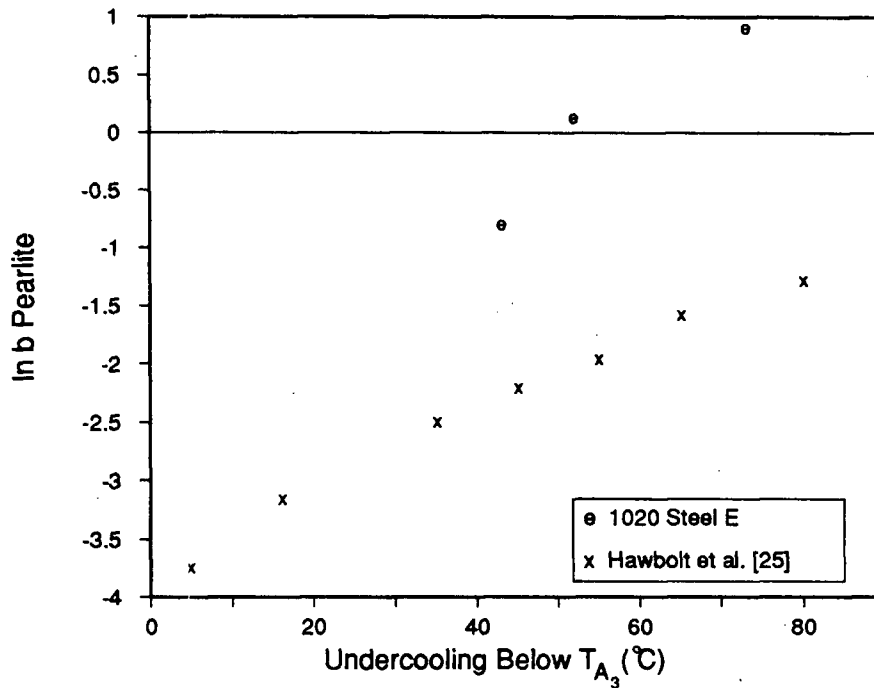


(b)

Fig. 6.23 - Fraction transformed-versus-time for Steel E (1020) under isothermal conditions. The isothermal temperature is included adjacent to each curve. (a) 767 - 722°C and (b) 711 - 650°C.



(a)



(b)

Fig. 6.24 - Natural logarithm of kinetic parameter b plotted against undercooling for Steel E (1020). Also included are the data due to Hawbolt *et al.* [25]. (a) $\ln b_F$ against undercooling below T_{A_3} and (b) $\ln b_P$ against undercooling below T_{A_1} .

Table 6.5 - Values for n_F and n_P , determined for Steel E (1020) as a function of isothermal transformation temperature.

Temperature (°C)	n_F	n_P
767	1.19	-
752	1.18	-
743	1.17	-
732	1.16	-
722	1.15	-
711	1.14	-
702	1.19	-
682	1.15	0.97
671	1.20	0.96
652	1.20	0.96
AVG	1.17	0.96

Table 6.6 - Composition of 1025 grade used for comparison of transformation kinetics with Steel E in Figs. 6.24 (a) and (b).

Reference	%C	%Mn	%Si
Steel E (1020)	0.201	0.50	0.017
Hawbolt <i>et al.</i> [25]	0.25	0.46	0.21

6.2.2 Continuous Cooling Tests

Continuous-cooling transformation tests were performed to determine CCT start times for the laboratory test steels. The procedure employed for sample preparation and equipment set-up, was identical to that followed for the isothermal tests. Samples were heated to a suitable austenitizing temperature, with both dilatometer response and temperature being monitored by the PC. After 5 minutes at temperature, the sample was forced to cool at a predetermined rate, until well below the temperature for completion of the austenite decomposition reactions. Results from the tests consisted of dilatometer and sample temperature responses. A typical thermal history and dilatometer response for Steel C (1038) is shown in Fig. 6.25, which indicates that a linear cooling rate has been achieved for this particular test. Also given in the figure is the A_3 temperature for the steel which is 778°C.

The dilatometer response, plotted in Fig. 6.25 (b), also displays a linear drop with temperature prior to transformation start. However, as the austenite begins to transform to ferrite a corresponding expansion occurs, as is reflected in the shape of the dilatometer curve.

A number of continuous cooling tests similar to that depicted in Fig. 6.25, have been performed on Steels B, C and E (1070, 1038 and 1020, respectively). In order to determine the exact start time and temperature for the tests, the following technique was employed.

- (1) Determine the expansion coefficient of austenite as a function of temperature from the initial part of the dilatometer curve.
- (2) Use the calculated expansion coefficient to predict the change in dilation as a function of sample temperature.
- (3) Choose an isothermal temperature close to the start temperature of the transformation, and subtract the sample dilation due to temperature from the actual dilatometer response.
- (4) Plot this difference as a function of test time and determine the time at which D_{DIL} minus $D_{THERMAL}$, or ΔD , deviates from a constant value.

An example of ΔD plotted against time for Steel C is shown in Fig. 6.26. As can be seen, for the first part of the test, the value remains essentially constant. But as transformation begins, an abrupt change in ΔD takes place. This corresponds to the transformation start time. By subtracting the time at which temperature passed below T_{A_3} , the continuous cooling start time and temperature below T_{A_3} can be calculated. This technique can be applied readily to both pearlite and ferrite start times.

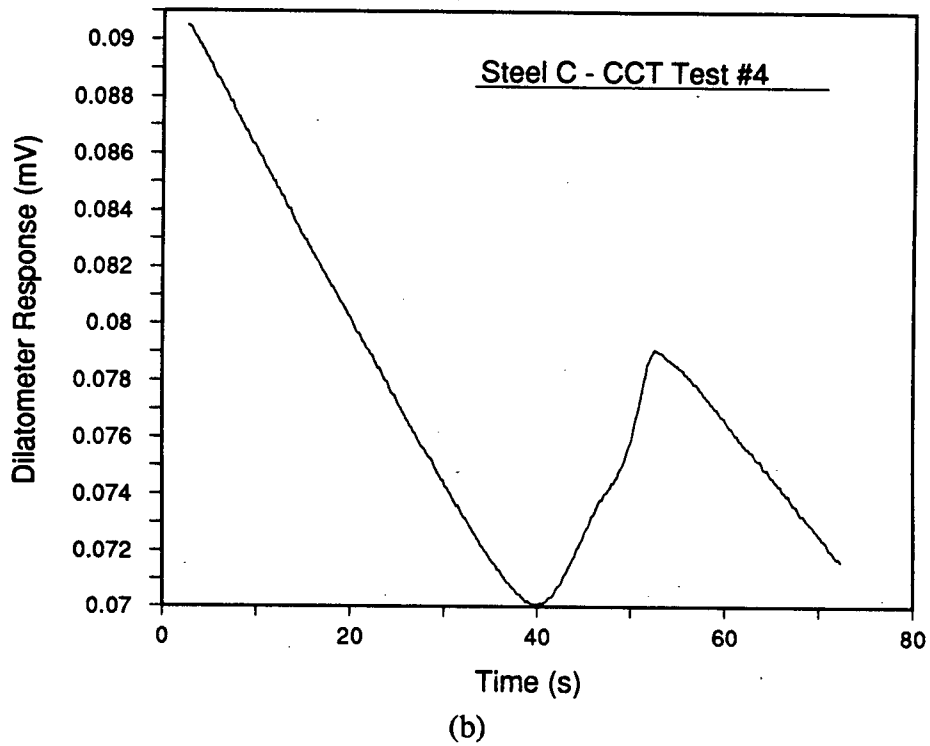
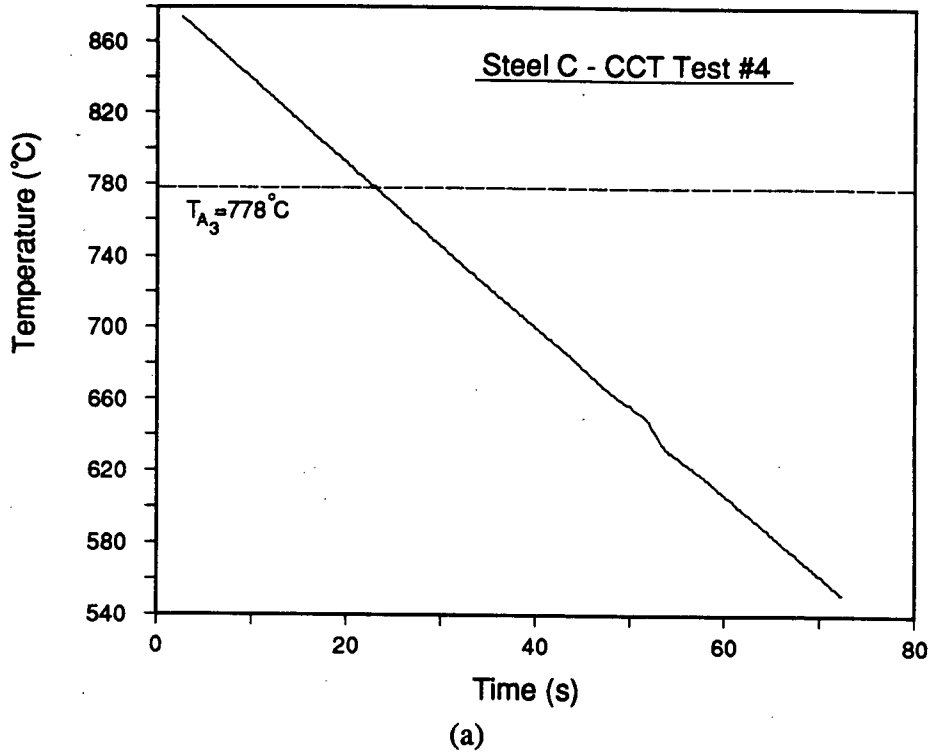


Fig. 6.25 - (a) Measured sample thermal history and (b) measured dilatometer response plotted as a function of time for 1038 Steel C (CCT Test #4).

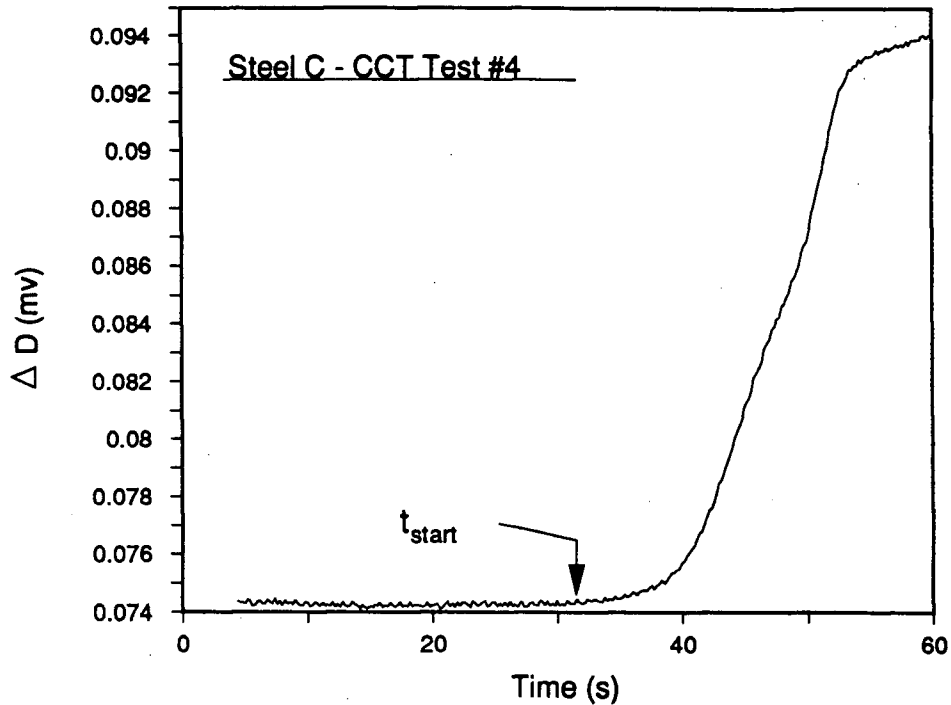


Fig. 6.26 - Measured sample dilation minus dilation due to temperature change, plotted against total time. Transformation start time is indicated by the time at which the curve deviates from a constant value.

Results of CCT ferrite start times for Steels C (1038) and E (1020) are presented in Fig. 6.27, as a function of time below T_{A_3} . Also included in the figure are results for other hypoeutectoid grades (ref.[25,42]). The same technique has been applied for determination of the CCT start times for pearlite in hypoeutectoid grades. CCT start times for a range of plain-carbon steels of approximately eutectoid composition have been determined following the technique outlined in the previous paragraphs. Included in Fig. 6.28 are measured CCT start times for other eutectoid steel grades [24,66].

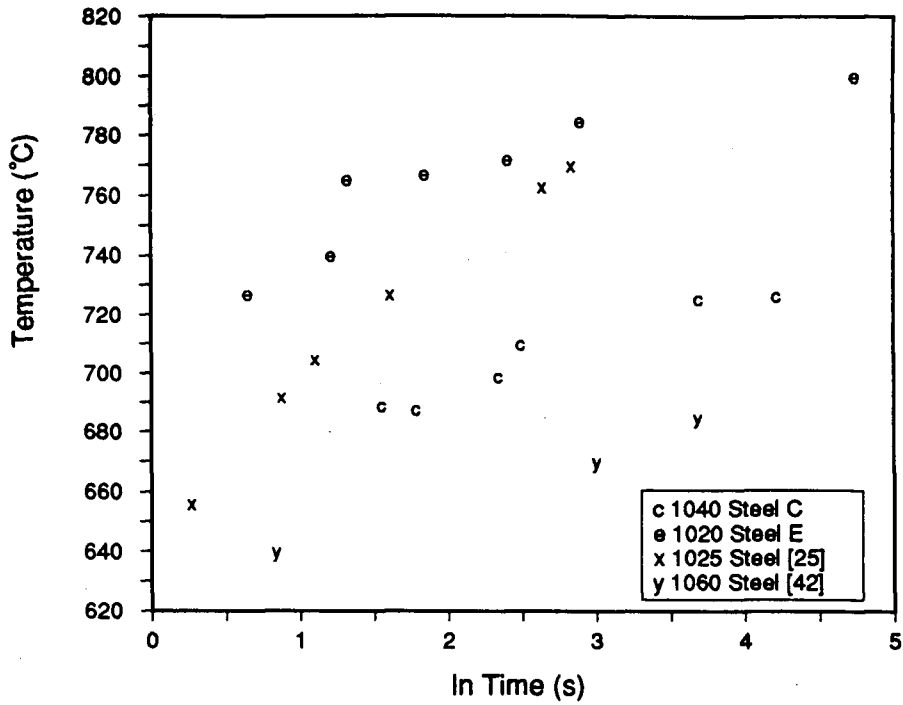


Fig. 6.27 - Measured CCT ferrite start times for Steels C (1038) and E (1020), plotted with start times for hypoeutectoid grades from the literature [25,42].

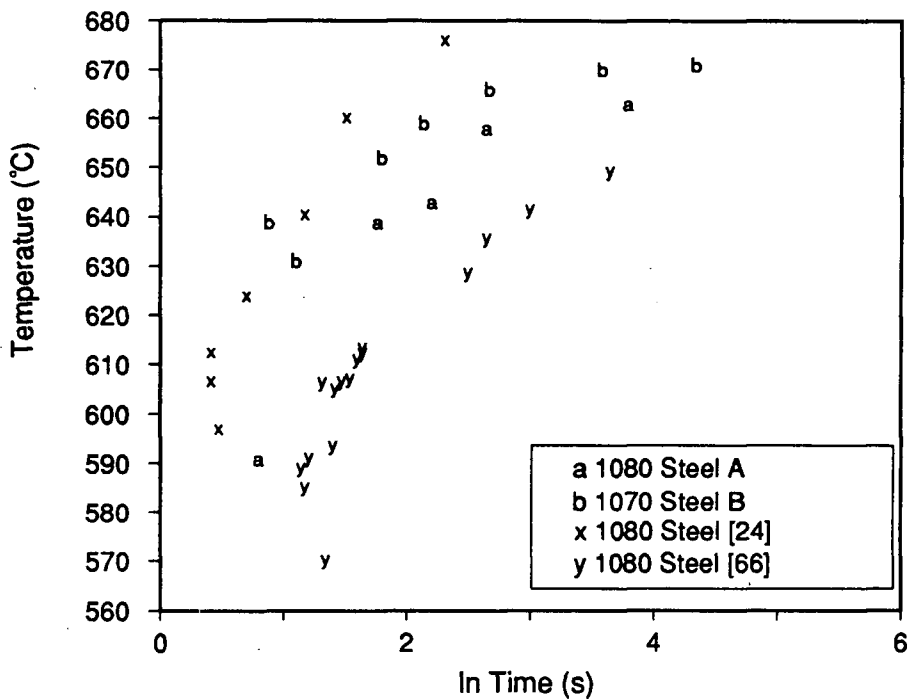


Fig. 6.28 - Measured CCT start temperatures for Steel B (1070), plotted against the time below T_{A1} . Also included are start times for other eutectoid grades [24,66].

6.3 Prior Austenite Grain Size Results

Prior austenite grain sizes have been determined in rods employed for the laboratory cooling tests and tubular samples from the dilatometer tests as outlined in Chapter 4, as well as rods extracted from the Stelmor line at the laying head. Results of the grain size measurements for these steel samples are included in Table 6.7. Unfortunately, distinct prior austenite grain boundaries could not be resolved in the low carbon E Steel (1020), partly due to the presence of proeutectoid ferrite, and thus grain size measurement could not be made. The asterisk (*) in the table corresponding to the tubular 1070 sample indicates that an accurate measurement of the grain size was not made; however, a direct comparison of the apparent grain sizes in the tubular and rod samples for this grade showed approximately the same average size. The table shows excellent agreement between the prior austenite grain sizes in the Steel C tubular and rod samples. Also, the laboratory grades are in good agreement with the Stelmor line grade, although the grain size is slightly larger in the Stelmor sample. This is not surprising when it is considered that the industrial grade has been quenched from a peak temperature of approximately 1000°C, while the laboratory grades had a peak temperature of 850°C. The uncertainty associated with these measurements is ± 0.5 ASTM #.

Table 6.7 - Prior austenite grain sizes measured in industrial grade and laboratory trials steel rods.

Grade	Sample	ASTM #	Ave. Grain Diameter (μm)
Stelmor (1060)	Rod	7.5	27
Steel B (1070)	Rod	8.5	19
Steel B (1070)	Tubular	*	*
Steel C (1038)	Rod	9	16
Steel C (1038)	Tubular	9.1	15.8

6.4 Regression Equations

6.4.1 Isothermal Tests

Utilizing results from the steel grades included in the present study, combined with data from the literature, equations for n and b as a function of steel composition and temperature have been developed. Considering first the ferrite transformation in hypoeutectoid

steels, two grades have been included in this study and kinetic data is available for four grades from the literature [25,26,42]. The n values for each of these steels, are included in Table 6.8, together with the average for all six grades which has been calculated as 1.16. This value will thus be taken as n_F in the model.

Table 6.8 - Average n_F for Steels C and E, plus values for four grades from the literature.

Steel	n_F
C-1038	0.88
E-1020	1.17
1060 [42]	1.26
1040 [42]	1.32
1025 [25]	1.33
1010 [26]	1.00
AVG	1.16

Unlike the random variation in n witnessed for the ferrite reaction, the n values encountered for pearlite in hypoeutectoid steels showed a trend with respect to carbon concentration. A plot of n_p as a function of carbon content of the steel is shown in Fig. 6.29 for five grades of hypoeutectoid steel plus Steel B (1070) and a 1080 eutectoid grade. The figure shows that as the carbon content of the steel is increased, the average n increases. Also included in the figure is the predicted value of n based on a multiple linear regression of the following form:

$$n_p = 3.01(\%C)^2 - 1.06(\%C) + 0.50(\%Mn) + 0.792 \quad (6.8)$$

where $\%C$ and $\%Mn$ represent the weight per cents of carbon and manganese in the steel, respectively. Agreement between the measured and predicted values of n_p is seen to be reasonable; thus Eq. (6.8) was used in the model for calculation of n as a function of steel composition for both eutectoid and hypoeutectoid grades.

Prediction of b from the data proved to be much more difficult than for n . Considering first the ferrite reaction, Fig. 6.30 presents the measured values for $\ln b$ from the present study, plotted against the undercooling below T_{A_3} . The $\ln b$ values for Steels C and E have

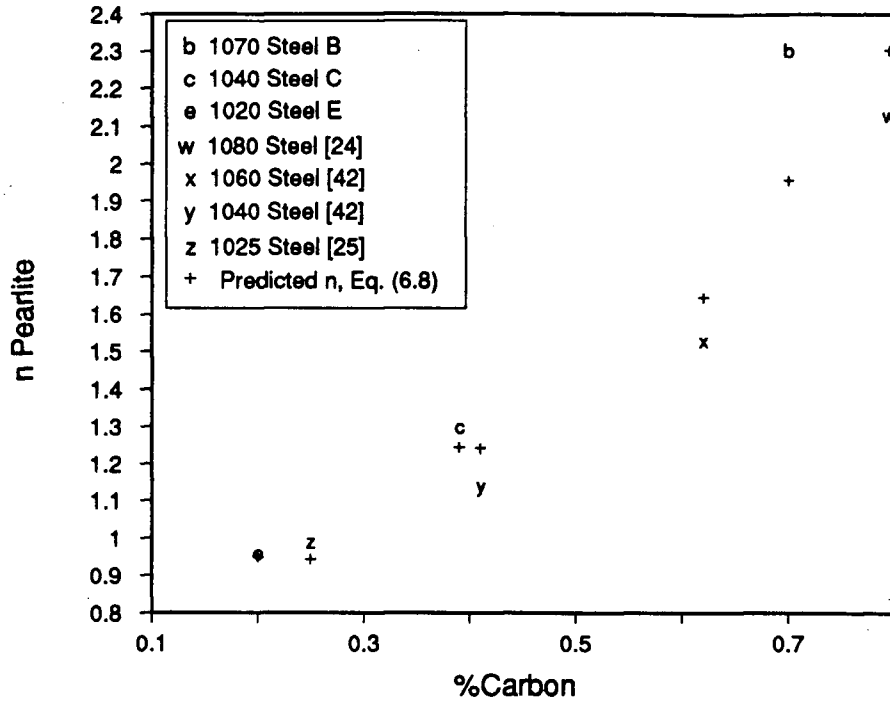


Fig. 6.29 - Measured values of n_p for both laboratory and literature steels, plotted as a function of the carbon content. Also included in the figure is the prediction of n based on Eq. (6.8).

been calculated based on the average n_F i.e., 1.16. Owing to the fact that the published values for b_F are based on n_F varying as a function of temperature [25,42], and showed poor agreement with the present data (Figs. 6.22 (a) and 6.24 (a)), they have not been included in the graph. For both grades depicted in Fig. 6.30, as temperature decreases or undercooling increases, the value of $\ln b_F$ increases. Also evident is the fact that $\ln b_F$ is greater for the steel with the lower carbon content. Taking a simplistic view of the ferrite transformation, at a similar undercooling below T_{A_3} for the 1020 and 1038 grades, the driving force for formation of ferrite from austenite can be considered approximately equal. Thus the transformation kinetics will depend to a large extent on the rate at which carbon can diffuse in the austenite, ahead of the growing ferrite. Recognizing that the diffusion coefficient for carbon in austenite increases with temperature, identical undercoolings for the two steels indicate a higher

transformation temperature for the lower carbon grade and thus faster reaction kinetics. This is in agreement with the kinetics measured for Steels C and E. Utilizing both grades, an expression for $\ln b_F$ as a function of undercooling and %C was found:

$$\ln b_F = -0.0145x + 3.98 \ln x - 5.39(\%C) - 16.5 \quad (6.9)$$

where x represents the undercooling below T_{A_3} . Equation (6.9) is included in Fig. 6.30 for Steels C and E. Although only two grades of steel have been utilized in the regression for Eq. (6.9) and the effect of %Mn on kinetics could not be determined, the equation should provide for the calculation of b_F as a function of temperature and %C within a reasonable range of error.

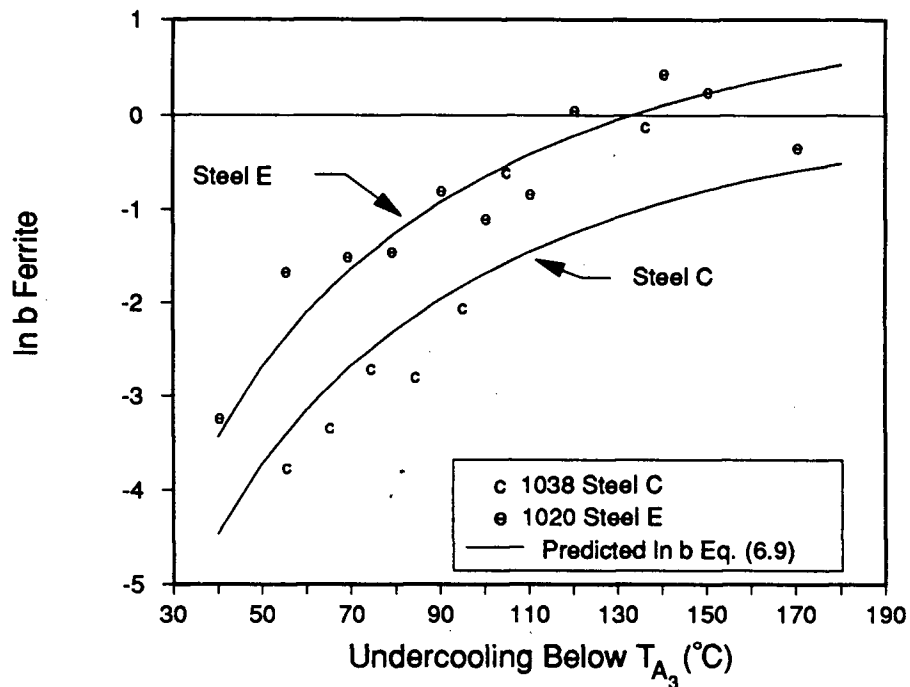


Fig. 6.30 - Natural logarithm of b_F plotted as a function of undercooling below T_{A_3} for laboratory Steels C (1038) and E (1020). The lines represent the predicted $\ln b$ based on Eq. (6.9).

A similar treatment has been applied to the pearlite transformation in the hypoeutectoid grades. Included in Fig. 6.31 are results for Steels C and E from the dilatometer study.

Values from the literature were not included for the reasons outlined previously concerning $\ln b_p$. Once again a multiple linear regression technique has been applied to the data to determine an expression for $\ln b_p$ in terms of steel composition and undercooling and yielded:

$$\ln b_p = 0.0419x + 0.357x^{0.5} - 10.2y - 1.90 \quad (6.10)$$

where x is the undercooling below T_{A_1} and y represents $\%C + \%Mn/6$. Although a limited number of data points have been utilized for the regression, Eq. (6.10) can be employed to indicate the variation in b as a function of temperature and steel composition. Predictions of $\ln b_p$ for both Steel C and E are included in Fig. 6.31.

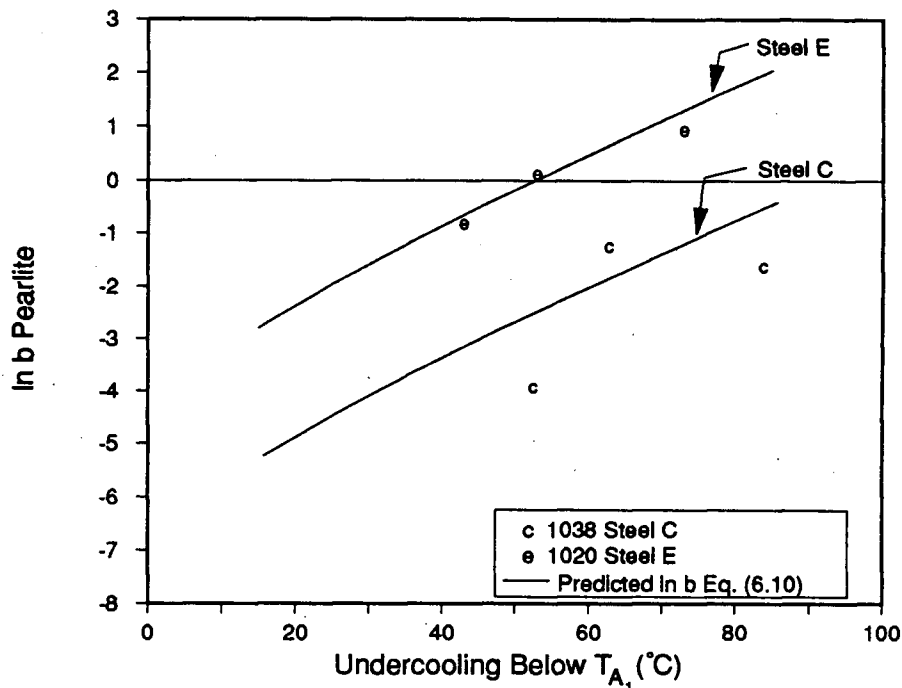


Fig. 6.31 - Natural logarithm of b_p (hypoeutectoid grades) plotted as a function of undercooling below T_{A_1} for laboratory Steels C (1038) and E (1020). The lines represent the predicted $\ln b$ based on Eq. (6.10).

Finally, the variation in b_p as a function of temperature for the pearlite reaction in eutectoid steel has been considered. Employing the data for Steel B plus that obtained from Hawbolt *et al.* [24], an expression for b in terms of the temperature only is,

$$\ln b_p = -41.5x^{0.0723} e^{-0.0364x} \quad (6.11)$$

where x is the undercooling below T_{A_1} . The predictive capability of Eq. (6.11) is shown in Fig. 6.32, where $\ln b$ is plotted against the undercooling below T_{A_1} . As can be seen, an excellent agreement between the predicted and measured results for Steel B has been achieved. Equation (6.11) thus was incorporated in the model for prediction of b_p in eutectoid steels.

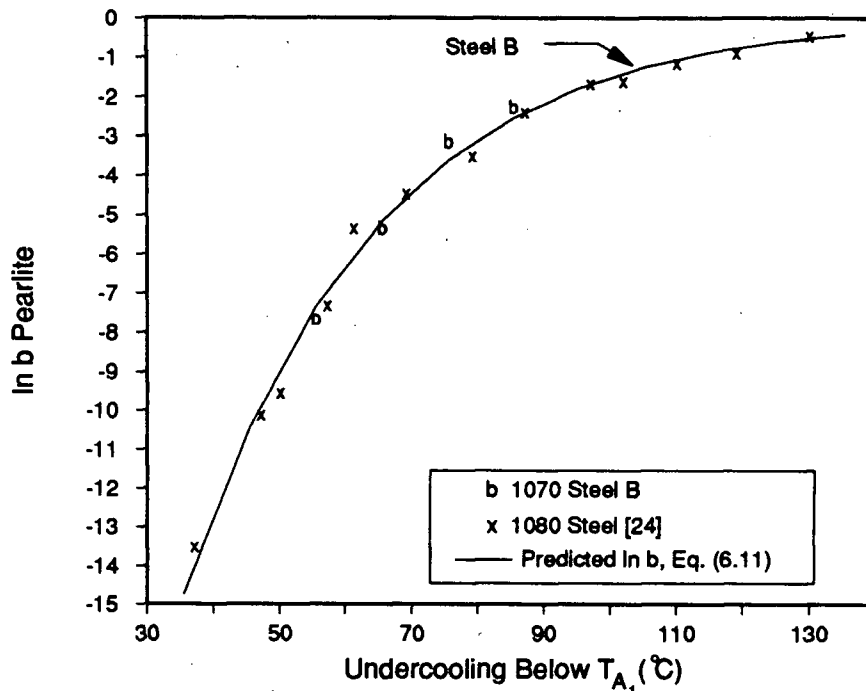


Fig. 6.32 - Natural logarithm of b_p (eutectoid grades) plotted as a function of undercooling below T_{A_1} for both laboratory and literature steels. The line represents the predicted $\ln b$ based on Eq. (6.11).

6.4.2 Continuous Cooling Tests

Formulation of regression equations for the prediction of CCT start times, as a function of steel composition and temperature, have been made for Steels B, C and E (1070, 1038 and 1020, respectively). Prediction of CCT start times for hypoeutectoid steels is based on data from Steels C and E, combined with results from the literature; the equation developed is:

$$\ln t_{CCT-F} = 0.0232x - 3.93 \ln x + 4.82y + 15.1 \quad (6.12)$$

where x is the undercooling below T_{A_3} and y represents $\%C + \%Mn/6$. From Eq. (6.12) and the appropriate values for constants and steel compositions, the CCT start times for steels C and E have been calculated. The results are shown in Fig. 6.33 and as can be seen the agreement between the measured and predicted values is quite good.

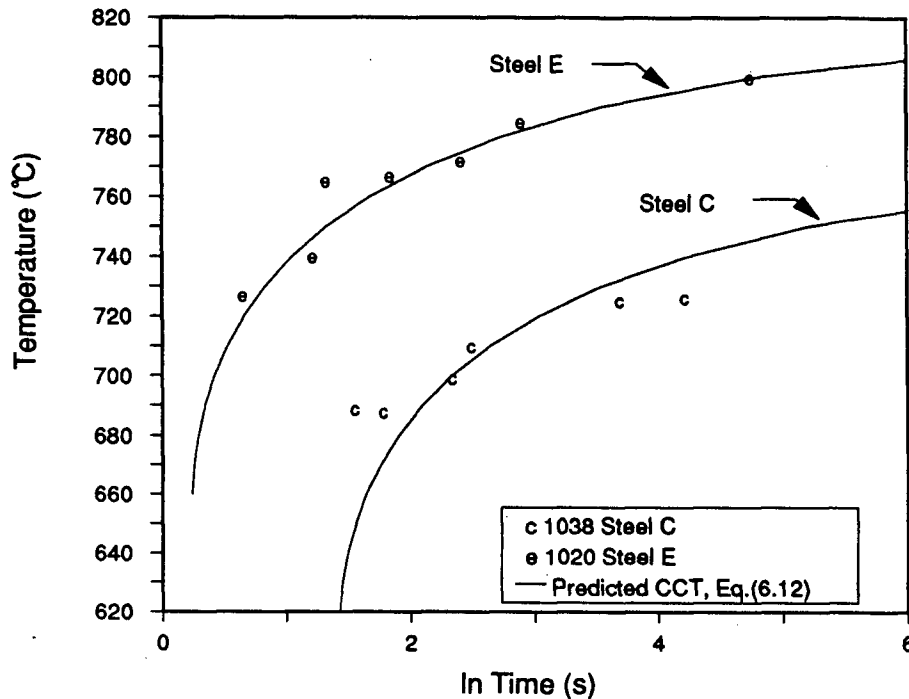


Fig. 6.33 - Measured and predicted CCT start times for Steels C (1038) and E (1020), plotted against time below T_{A_3} . The lines plotted in the figure are based on Eq. (6.12).

Prediction of the start time for the pearlite reaction in hypoeutectoid steels as a function of undercooling below T_{A_1} , has been made utilizing a technique similar to that for ferrite start times. From the continuous cooling dilatometer tests, the time and temperature for start of the pearlite transformation has been estimated employing the dilatometer-versus-time response. Results of the measured start times are plotted in Fig. 6.34. The data has been utilized to develop the following equation for prediction of CCT start times for pearlite in hypoeutectoid steels:

$$\ln t_{CCT-P} = -0.142x + 3.29 \ln x - 2.68 \quad (6.13)$$

where x is the undercooling below T_{A_1} . As can be seen in the figure, a significant degree of scatter is evident in the data.

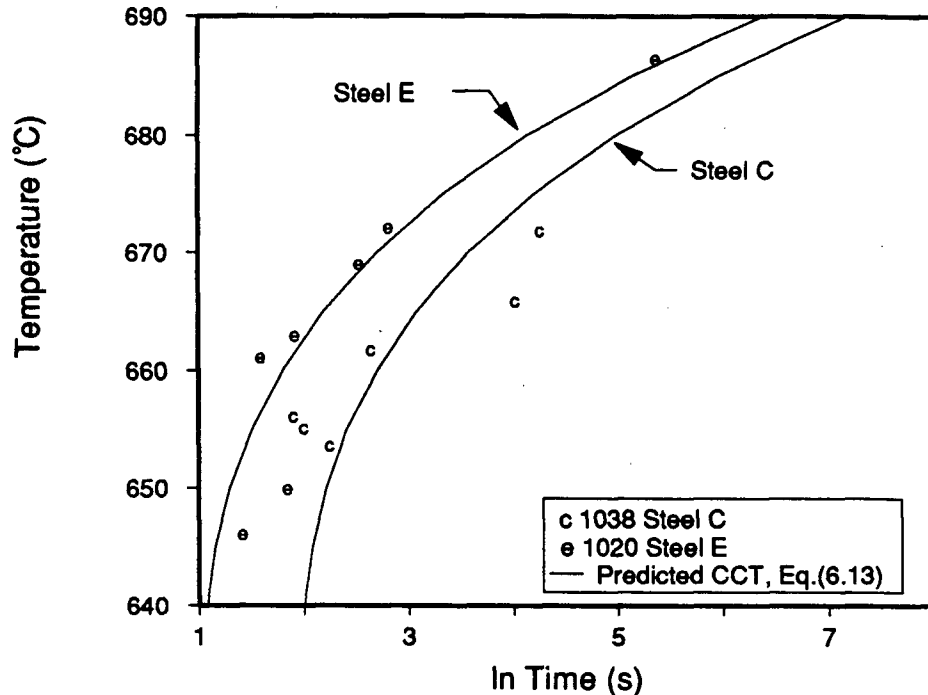


Fig. 6.34 - Measured and predicted CCT start temperatures for pearlite in Steels C (1038) and E (1020), plotted against the time below T_{A_1} . The lines plotted in the figure are based on Eq. (6.13).

A multiple linear regression technique has been employed to provide a relationship between CCT start time, steel composition and undercooling below T_{A_1} , for the pearlite reaction in eutectoid steels. Data employed for the regression included Steels A (1080) and B (1070) plus two eutectoid grades from the literature. The resulting equation is:

$$\ln t_{CCT-P} = 29.7 + 0.0582x - 8.62 \ln x + 6.27y \quad (6.14)$$

where x is the undercooling below T_{A_1} , and y is $\%C + \%Mn/6$. The predictive capability of Eq. (6.14) is displayed in Fig. 6.35. As was the case for the hypoeutectoid grades, very good

agreement between measured and predicted CCT start times has been achieved. CCT start times for both the ferrite and pearlite transformations will be based on Eqs. (6.12) to (6.14), in the model.

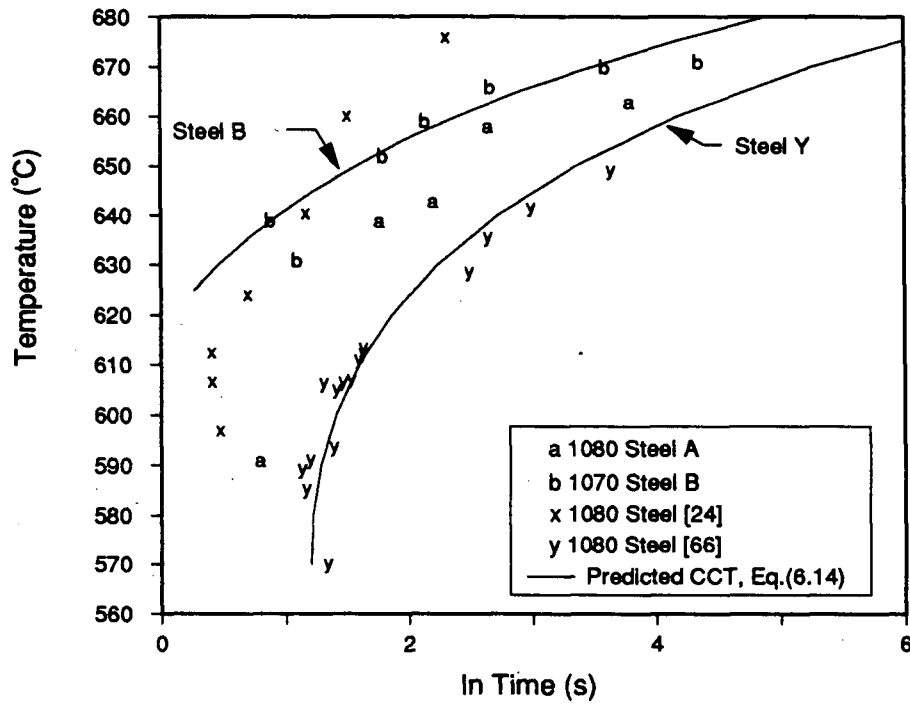


Fig. 6.35 - Measured and predicted CCT start temperatures for Steel B (1070), plotted against the time below T_{A1} . The lines plotted are based on Eq. (6.14).

Chapter 7 - RESULTS OF PLANT TRIALS

The following sections contain results from the plant trials conducted at the Stelco No. 2 Rod Mill. Data has been obtained for a range of cooling air velocities present on the Stelmor line. The thermal history of test rods placed directly on the bed and allowed to cool with production rods, has been measured. In addition, the thermal history has been recorded for test rods cooled on the Stelmor line, without production coils in place. Mechanical properties and rod microstructures have been evaluated for the test rods. The results of this work have been combined with results from the laboratory tests to develop empirical equations for the prediction of steel microstructure and strength.

7.1 Air Velocities

Air velocities measured on the Stelmor line, have been utilized to construct a velocity profile as a function of position across the width of the deck. This was accomplished by taking pitot tube measurements and determining the mean of all values obtained at each of the seven locations, shown previously in Fig. 5.2. Average velocities for Stelmor lines 2 and 3 are presented in Fig. 7.1. Comparison of the air velocities on the two lines reveals excellent agreement, where the shaded area in the figure represents \pm one standard deviation of the measured values. The average velocities measured at the edge of the bed seem to be much greater than those measured at the central region, to accommodate the higher packing density of rods at the edge of the bed as compared to the centre (Fig. 5.3). The higher velocities are required to achieve uniform cooling conditions across the bed. The measured air velocities can be utilized to predict convective heat-transfer coefficients on the Stelmor line (Eq. (3.8)), as a function of rod position on the bed. It would also be expected that effective air velocities for the bed, with production coils in place on the deck, would be somewhat lower due to interference by adjacent rods.

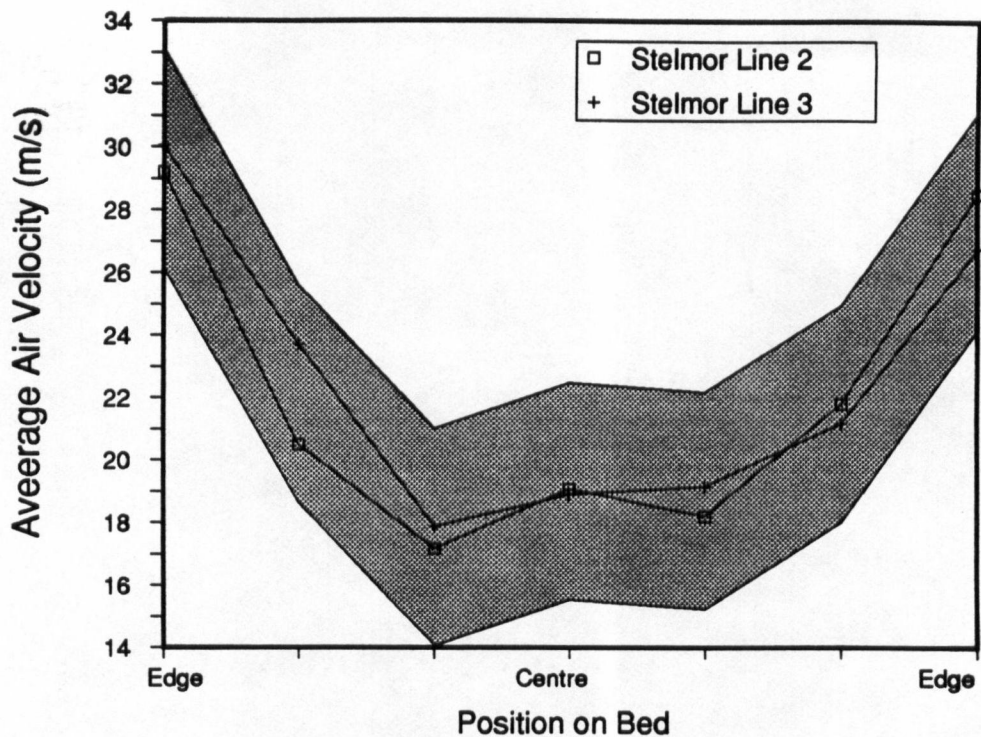
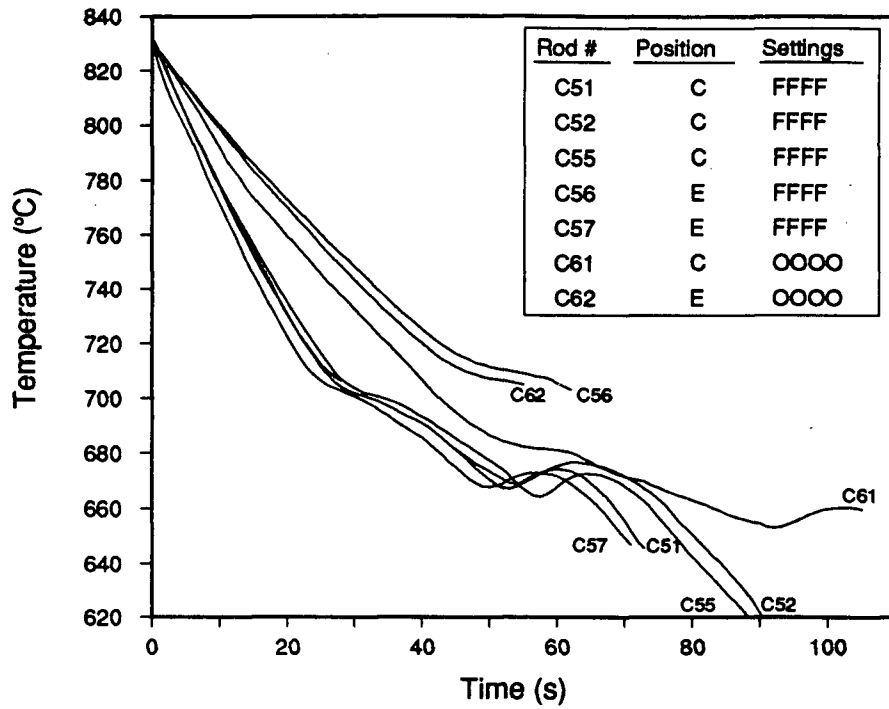


Fig. 7.1 - Average air velocities measured on Stelmor Lines 2 and 3. Grey area indicates \pm one standard deviation for the measurements.

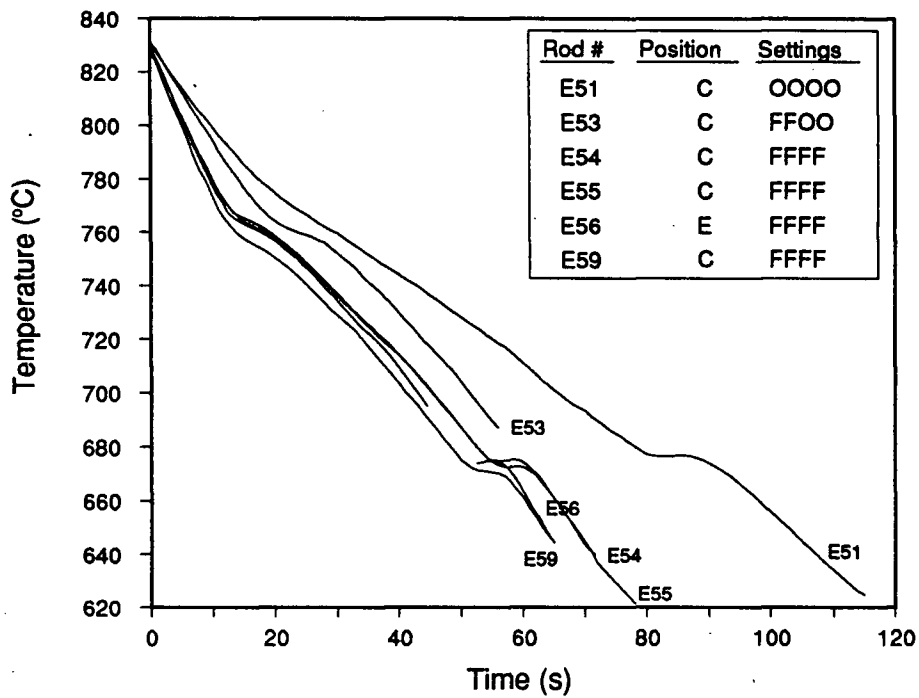
7.2 Thermal History and Heat-transfer Coefficients

7.2.1 Experimental Results

Typical thermal history data measured during the plant trials are shown in Figs. 7.2 to 7.4, for the 15 mm, 9.1 mm and 7.5 mm diameter rods, respectively. Comparison of these results with Fig. 6.2 shows that thermal histories for the industrial rods are similar to results obtained from the laboratory tests. In some of the tests, however, erratic thermal response during cooling, likely due to vibration and movement of test rods on the Stelmor line, resulted in poor thermocouple contact. A small portion of the plant tests (~10%), provided thermal histories which proved to be meaningless, however for most, at least some segment of the response yielded reasonable results.

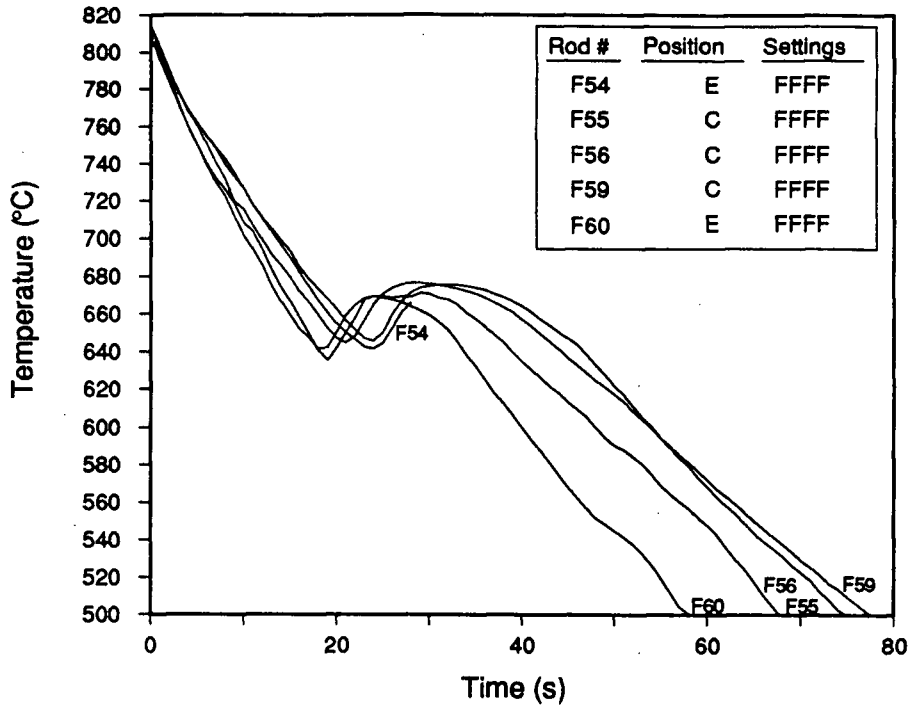


(a)

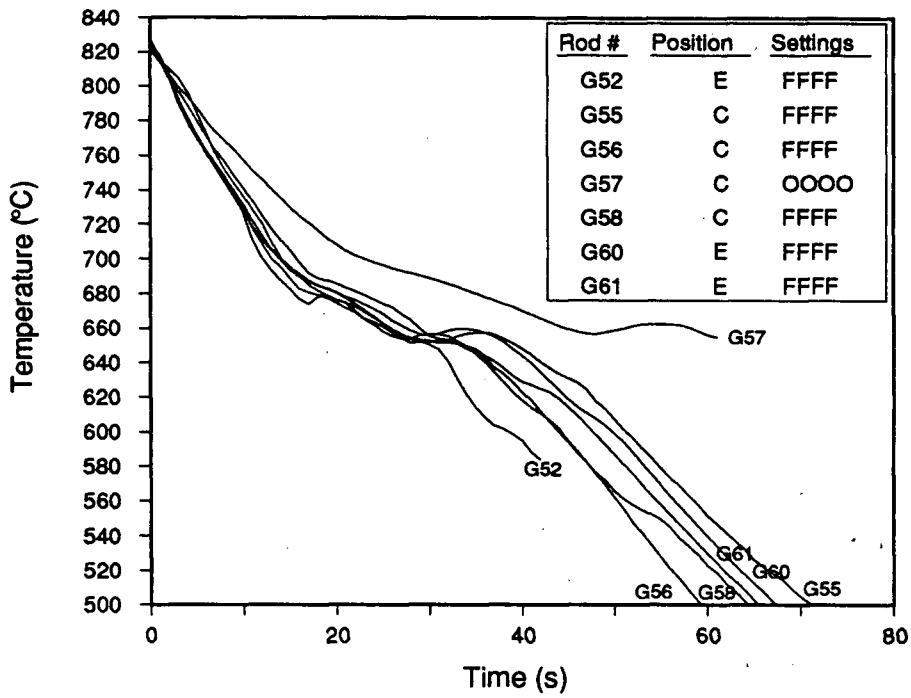


(b)

Fig. 7.2 - Thermal history measured at rod centreline in plant cooling tests, for 15-mm diameter rods; (a) 1038 Steel C and (b) 1020 Steel E.



(a)



(b)

Fig. 7.3 - Thermal history measured at rod centreline in plant cooling tests, for 9.1-mm diameter rods; (a) 1080 Steel F, (b) 1037 Steel G and (c) 1017 Steel I.

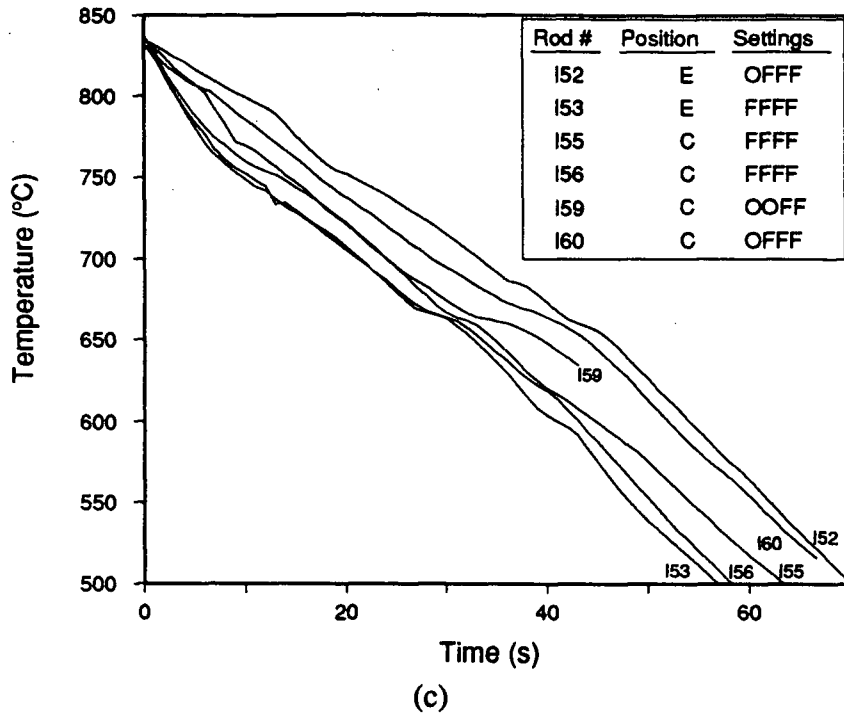


Fig. 7.3 - Thermal history measured at rod centreline in plant cooling tests, for 9.1-mm diameter rods; (a) 1080 Steel F, (b) 1037 Steel G and (c) 1017 Steel I.

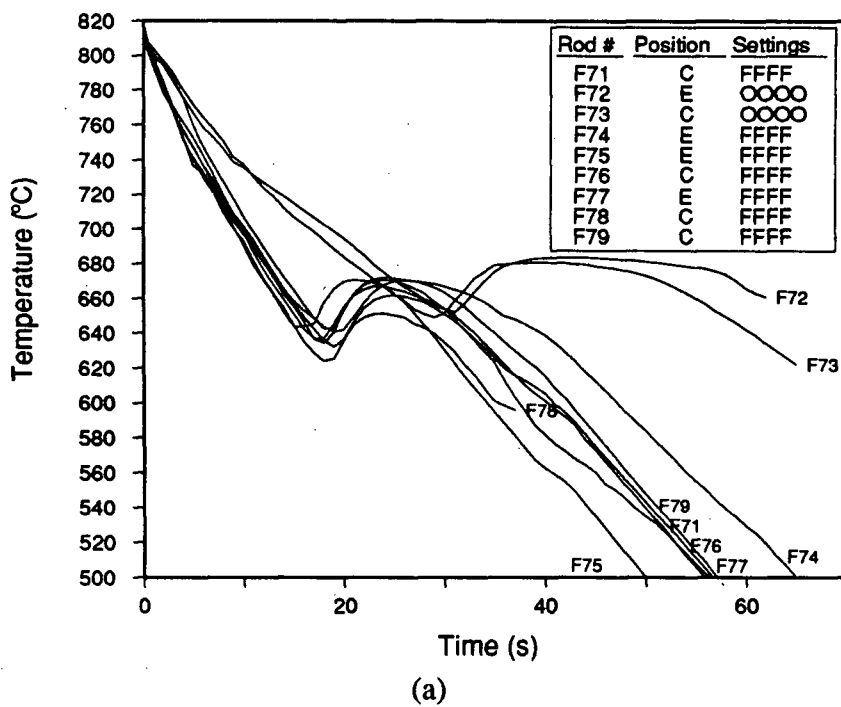


Fig. 7.4 - Thermal history measured at rod centreline in plant cooling tests, for 7.5-mm diameter rods; (a) 1080 Steel F, (b) 1035 Steel H and (c) 1022 Steel J.

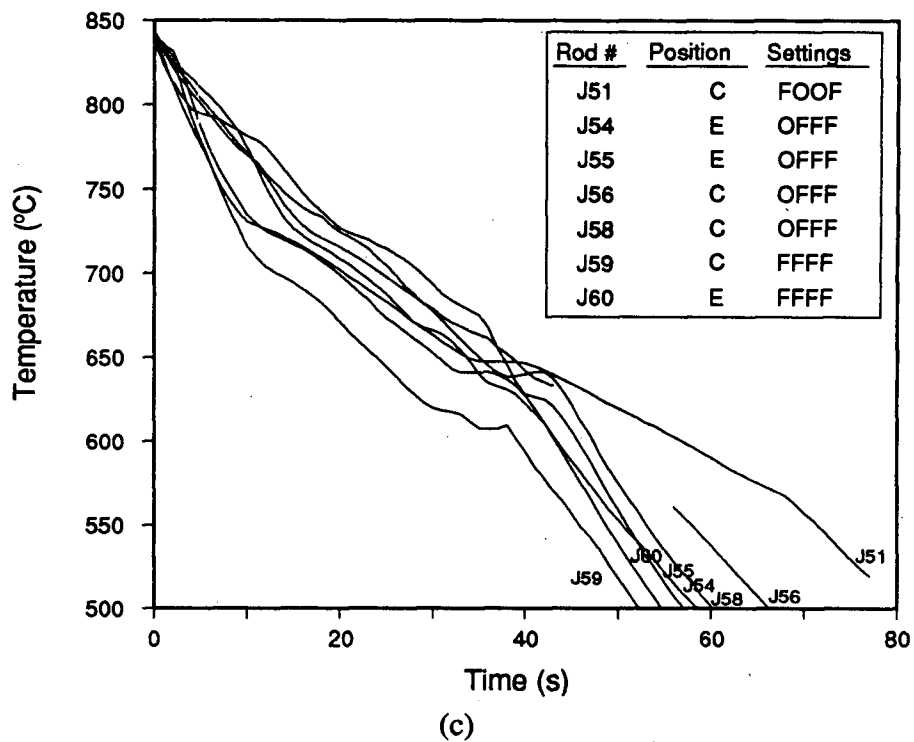
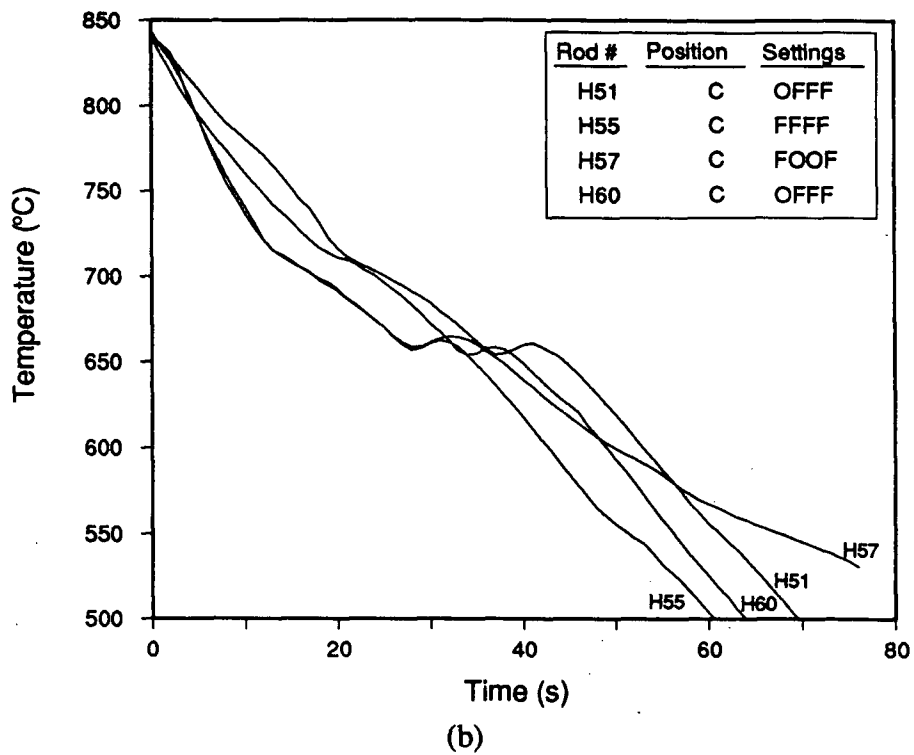


Fig. 7.4 - Thermal history measured at rod centreline in plant cooling tests, for 7.5-mm diameter rods; (a) 1080 Steel F, (b) 1035 Steel H and (c) 1022 Steel J.

Referring to Figs. 7.2 to 7.4, the Rod # column indicates the rod grade as given in Table 5.1, and rod test number. The Position column refers to the location of the test rod on the bed; C being the centre of the bed and E the edge of the bed. Air settings employed are included in the Settings column, with O and F representing zero or full air velocity, respectively. The four letters represent settings at each of the four zones of the Stelmor line. Comparison of thermal history obtained for full air with that for zero air, shows a substantial difference in the average rod cooling rate. However, for rods placed at the edge of the bed, as compared to those placed at the centre, differences in average rod cooling rate are much more difficult to detect. A comparison between the cooling conditions at these two positions is better made in terms of the associated heat-transfer coefficients. Characteristic cooling curves for each of the three general rod grades, are apparent in Figs. 7.2 to 7.4. The eutectoid grade, Steel F, shows an austenite-pearlite transformation recalescence only whereas the hypoeutectoid grades exhibit both an austenite-ferrite and austenite-pearlite recalescence.

Thermal histories recorded for rods cooled without production coils on the bed, are given in Fig. 7.5. The rod diameters are provided in the plot, as well as the rod grade code and number. Rod diameter can be seen to influence the average cooling rate, as the 15-mm diameter rods display a much lower rate than the 9.1- or 7.5-mm diameter rods. However, the difference in average cooling rate between the 9.1- and 7.5-mm diameter rods, is not as obvious.

Conversion of thermal history to heat-transfer coefficients has been accomplished for the plant trials, adopting the same two methods outlined for the laboratory tests. Utilizing plots of heat-transfer coefficient versus rod temperature, similar to Fig. 6.4 for the laboratory tests, the average measured heat-transfer coefficient, at several temperatures, was determined. For comparison, measured heat-transfer coefficients are plotted with predicted values in Figs. 7.6 (a) to (e) and 7.7 (a) to (d), which represent full air and zero air tests, respectively. Once again the x-axis is the ratio of air velocity to the rod diameter, each raised to the appropriate power as indicated by Eq. (6.4). The line plotted in the figures represents the predicted value

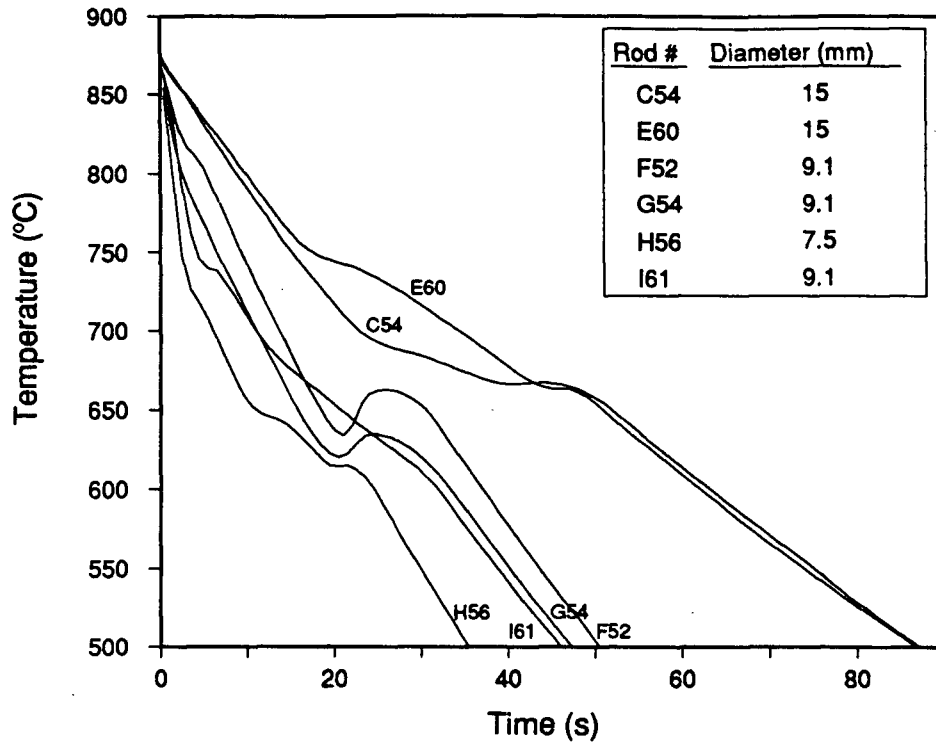


Fig. 7.5 - Thermal history measured at rod centreline for plant trials cooled without production coils on the Stelmor bed.

for the convective heat-transfer coefficient, only. For the full air tests, the convective coefficient was determined from Eq. (3.8). However, for the zero air tests, it was found that the effect of natural convection could not be ignored. Thus, convective heat-transfer coefficients for zero air velocity tests were calculated from a combination of Eq. (3.8) for forced convection (with air velocity assumed equal to Stelmor line velocity), and the following equation for natural convection [57],

$$Nu = 0.53(GrPr)^{0.25} \quad (7.1)$$

Over the range of line speeds typical for the Stelmor line, the heat-transfer coefficients due to forced convection and natural convection have been calculated from Eqs. (3.8) and (7.1), as ~ 25 and ~ 5 $W/m^2 \cdot ^\circ C$, respectively. These values were found to be essentially constant over the range of line speeds, rod diameters and temperatures encountered during Stelmor cooling. Thus, for zero air conditions, the convective heat-transfer coefficient in the model

was assumed to be equal to $30 \text{ W/m}^2\cdot\text{°C}$. Initially, no attempt was made to predict the radiative heat-transfer coefficient. This was due to the fact that radiation heat transfer from plant test rods is much more complicated than radiation heat transfer in the laboratory, where rods essentially radiate to the surrounding room, which can be considered a blackbody at uniform ambient temperature. In the plant, such conditions do not hold since rods radiate to one another as well as to the surroundings. This makes the prediction of h_r much more difficult, involving geometric considerations, view factors, etc.. In order to quantify the relative value of the radiative heat-transfer coefficients, for each cooling condition, Figs. 7.6 and 7.7 can be employed to estimate the difference between the overall measured heat-transfer coefficient and the predicted value from convection alone. Based on the good agreement between predicted and measured heat-transfer coefficients for the laboratory tests, Eq. (3.8) provides an accurate value for h_c as a function of air velocity and rod diameter. Furthermore, good agreement between measured and predicted heat-transfer coefficients from plant trials in which there were no production coils on the bed, were obtained as shown in Fig. 7.8. The predicted heat-transfer coefficient plotted in the figure has been calculated from Eq. (3.8) and (3.9), assuming an average air velocity of 25 m/s. These results also lend support for prediction of the convective portion of the heat-transfer coefficient by Eq. (3.8). Thus, the difference between the measured overall heat-transfer coefficient and the heat-transfer coefficient predicted for convection, displayed in Figs. 7.6 and 7.7, can be taken as the heat-transfer coefficient due to radiation. The relative value of h_r as a function of temperature, can then be constructed from data for h_{ov} and predicted h_c over a range of temperatures.

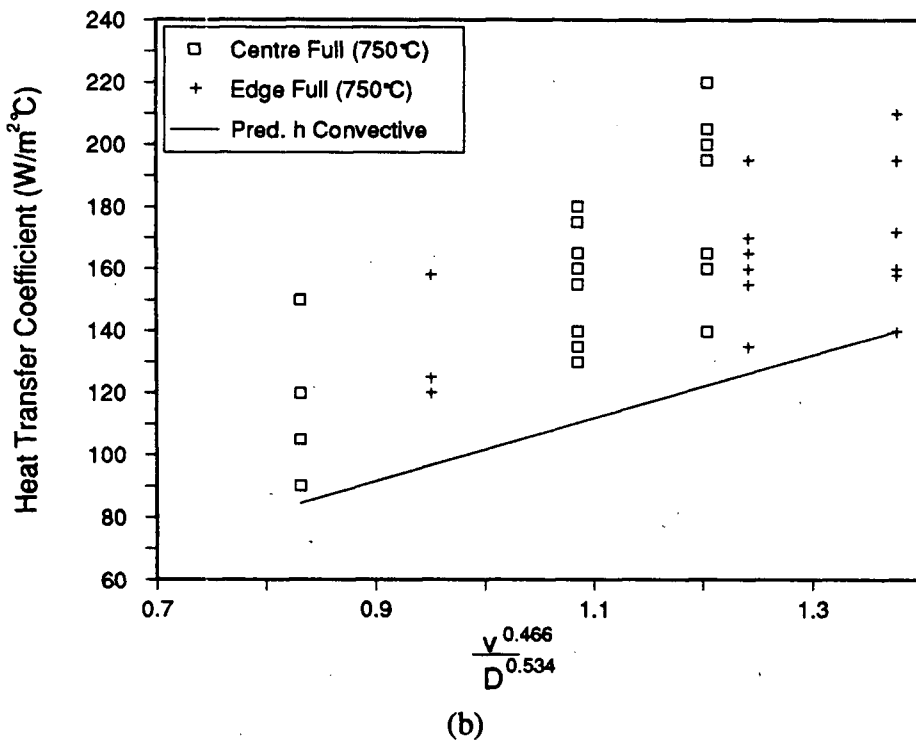
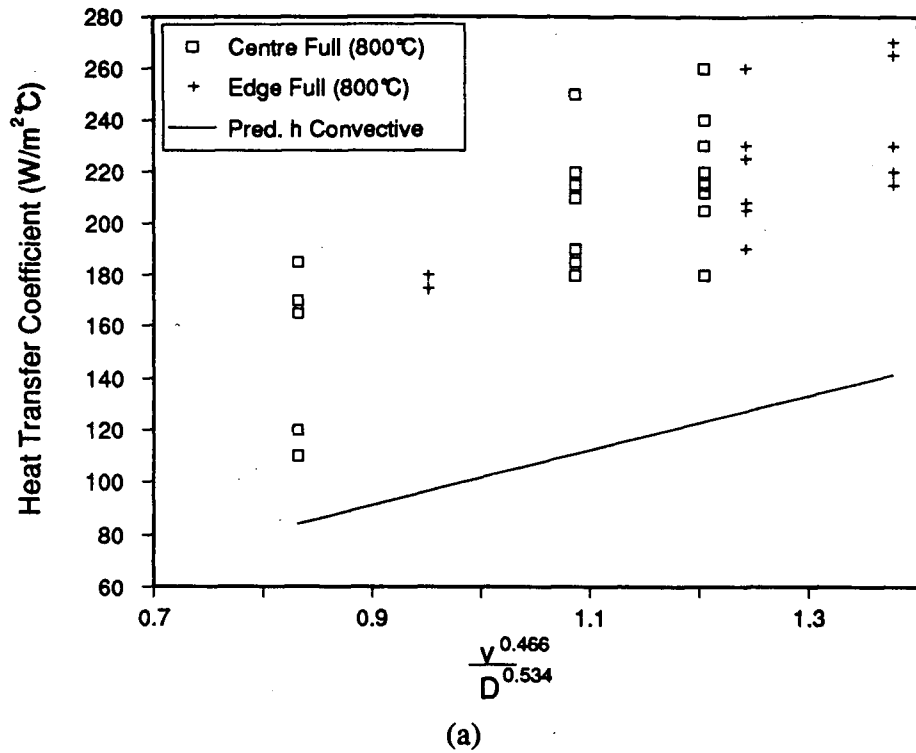


Fig. 7.6 - Measured heat-transfer coefficients for plant full air tests, plotted against (air velocity)^{0.466}/(rod diameter)^{0.534} according to Eq. (6.4). The line included is the predicted value based on convection only. Heat-transfer coefficients measured at (a) 800°C, (b) 750°C, (c) 700°C, (d) 550°C and (e) 450°C.

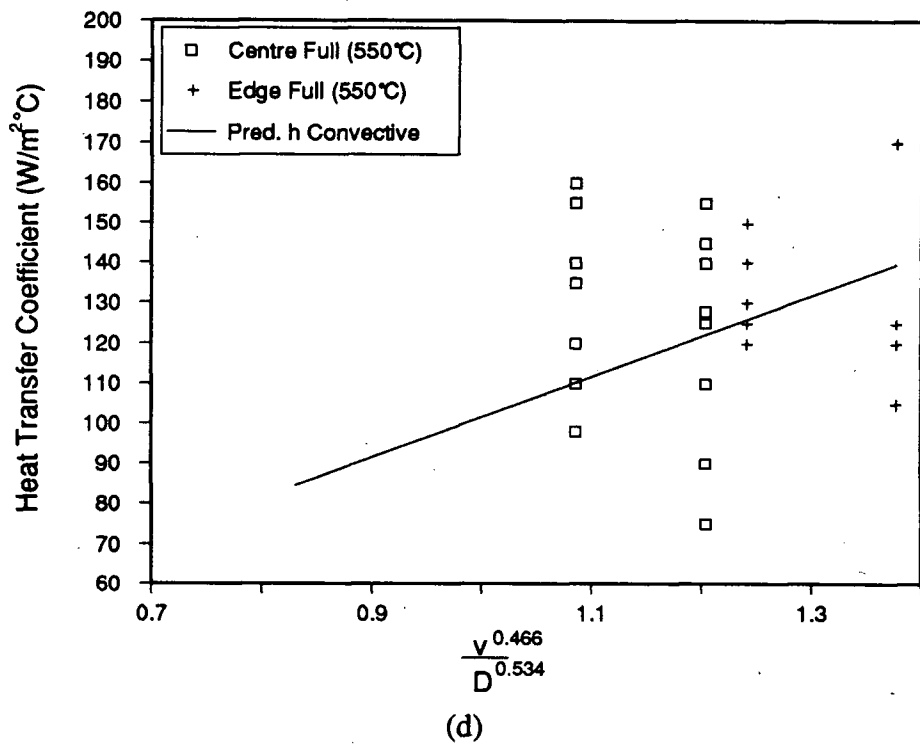
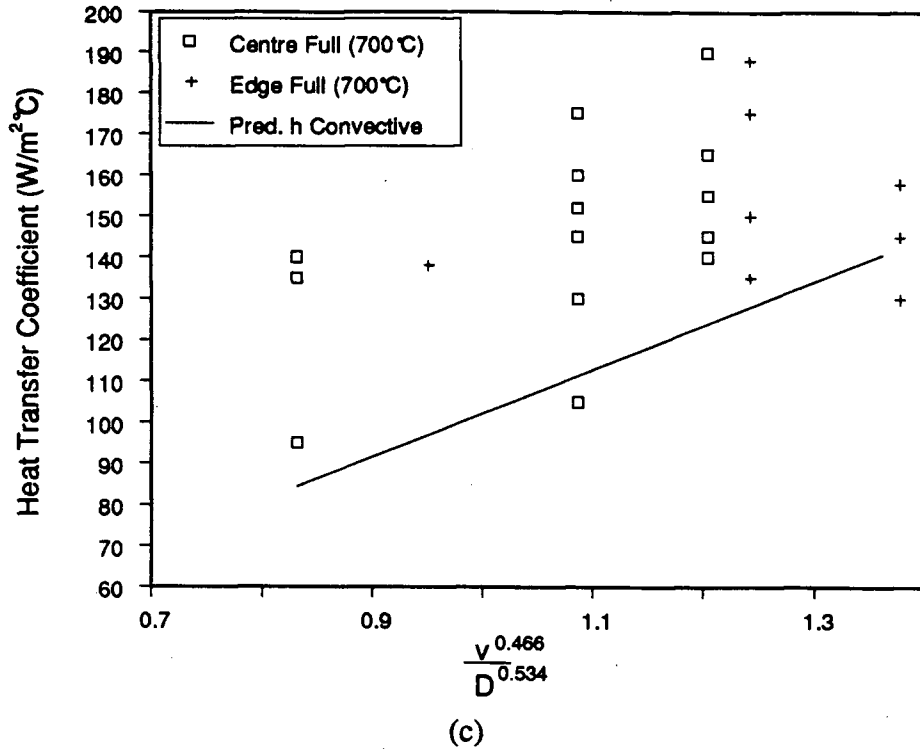


Fig. 7.6 - Measured heat-transfer coefficients for plant full air tests, plotted against (air velocity)^{0.466}/(rod diameter)^{0.534} according to Eq. (6.4). The line included is the predicted value based on convection only. Heat-transfer coefficients measured at (a) 800°C, (b) 750°C, (c) 700°C, (d) 550°C and (e) 450°C.

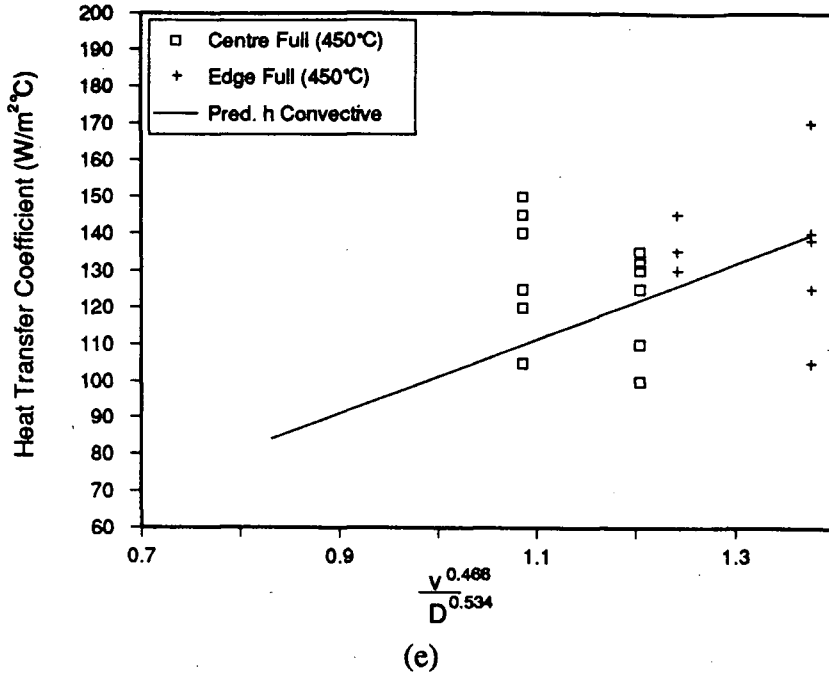


Fig. 7.6 - Measured heat-transfer coefficients for plant full air tests, plotted against (air velocity)^{0.466}/(rod diameter)^{0.534} according to Eq. (6.4). The line included is the predicted value based on convection only. Heat-transfer coefficients measured at (a) 800°C, (b) 750°C, (c) 700°C, (d) 550°C and (e) 450°C.

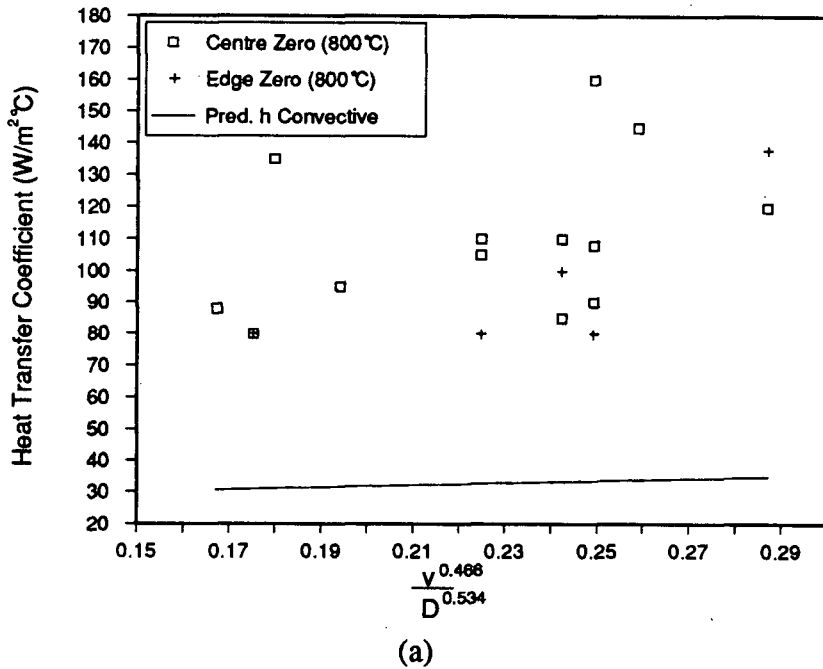


Fig. 7.7 - Measured heat-transfer coefficients for plant zero air tests, plotted against (air velocity)^{0.466}/(rod diameter)^{0.534} according to Eq. (6.4). The line included is the predicted value based on convection only. Heat-transfer coefficients measured at (a) 800°C, (b) 750°C, (c) 700°C and (d) 550°C.

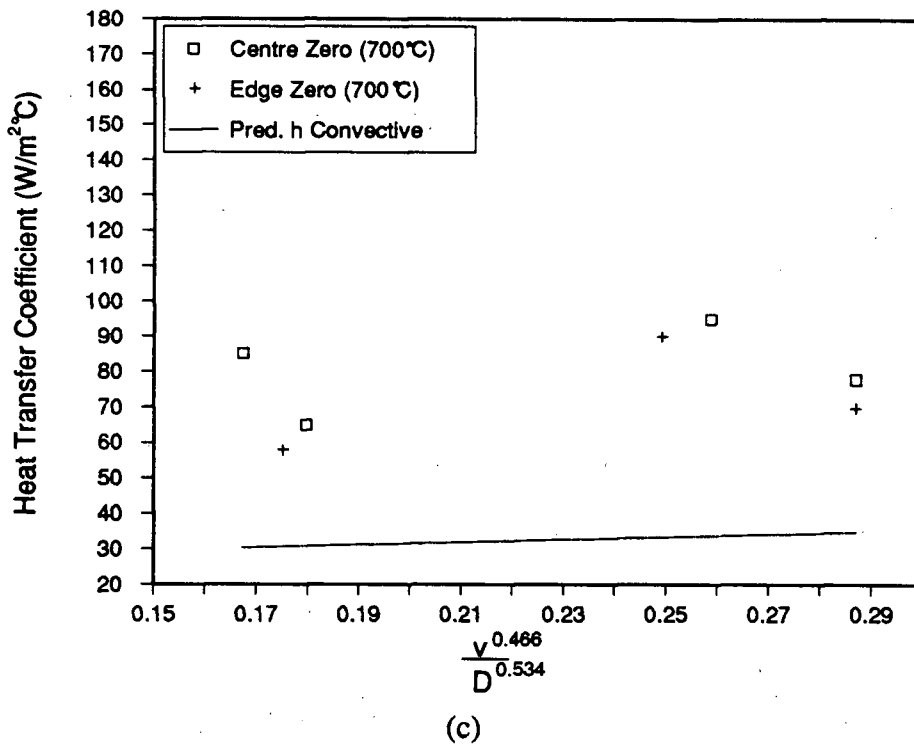
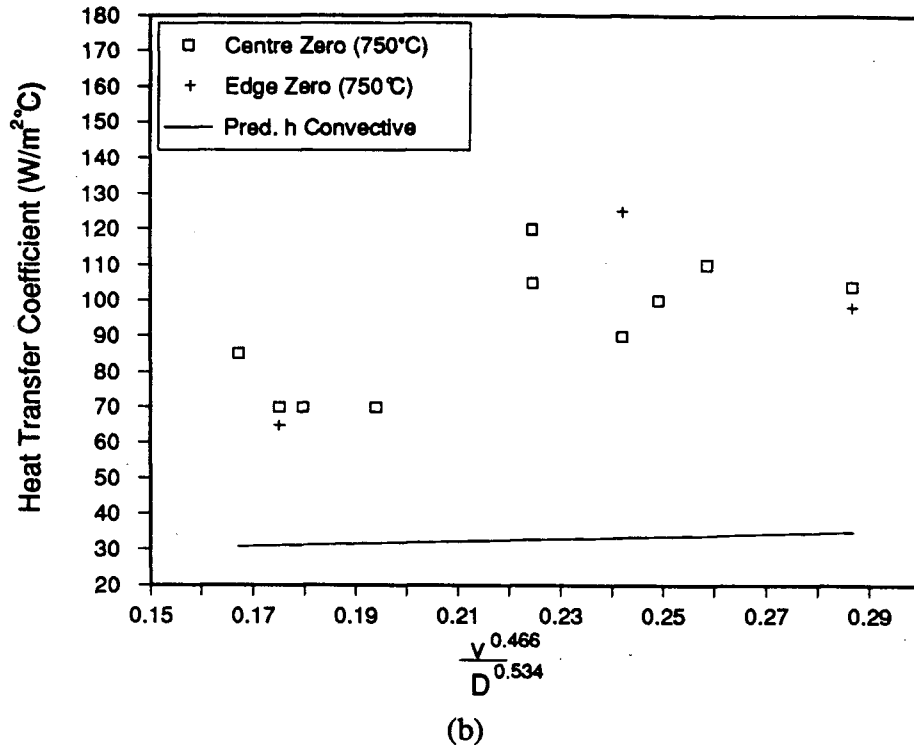


Fig. 7.7 - Measured heat-transfer coefficients for plant zero air tests, plotted against (air velocity)^{0.466}/(rod diameter)^{0.534} according to Eq. (6.4). The line included is the predicted value based on convection only. Heat-transfer coefficients measured at (a) 800°C, (b) 750°C, (c) 700°C and (d) 550°C.

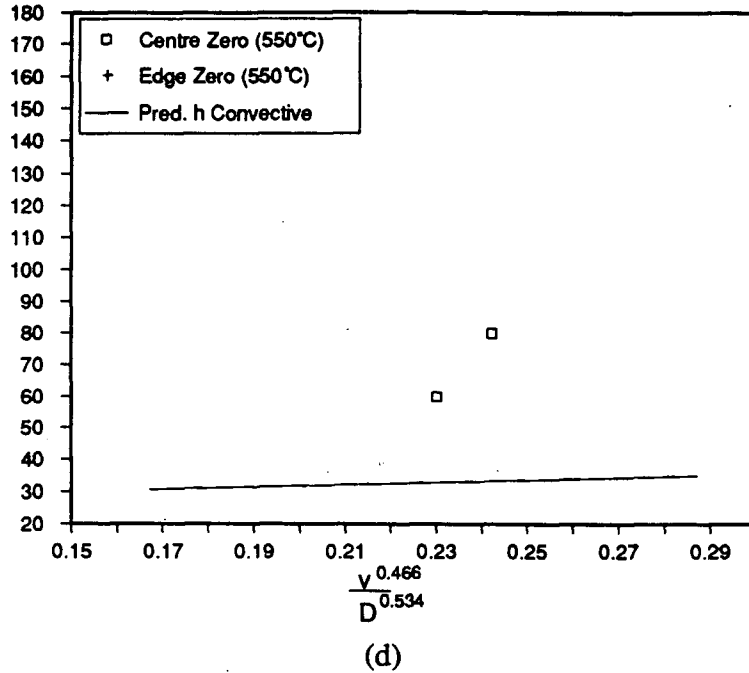


Fig. 7.7 - Measured heat-transfer coefficients for plant zero air tests, plotted against $(\text{air velocity})^{0.466}/(\text{rod diameter})^{0.534}$ according to Eq. (6.4). The line included is the predicted value based on convection only. Heat-transfer coefficients measured at (a) 800°C, (b) 750°C, (c) 700°C and (d) 550°C.

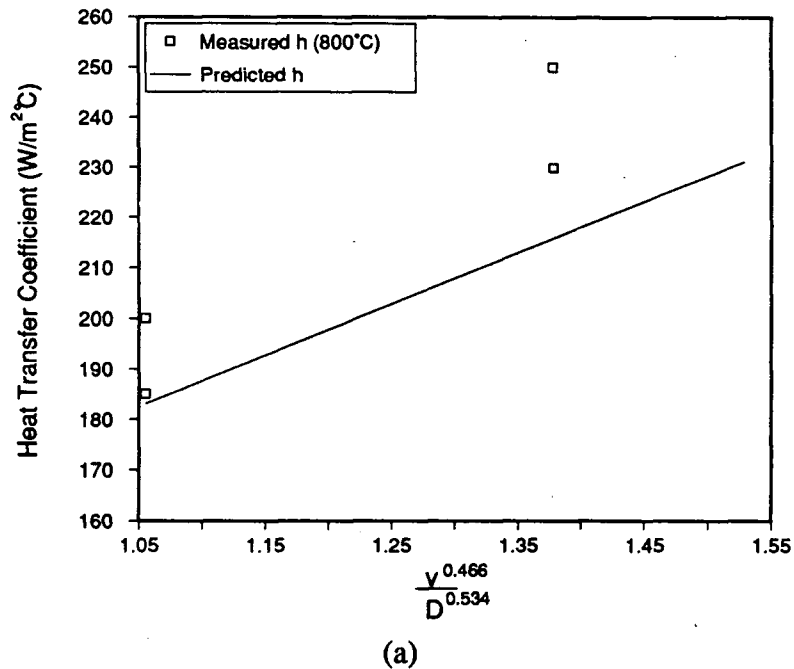


Fig. 7.8 - Measured heat-transfer coefficients for plant trials without production coils on the Stelmor line, plotted against $(\text{air velocity})^{0.466}/(\text{rod diameter})^{0.534}$ according to Eq. (6.4). The line included is the predicted value based on convection and radiation. Heat-transfer coefficients measured at (a) 800°C, (b) 700°C and (c) 450°C.

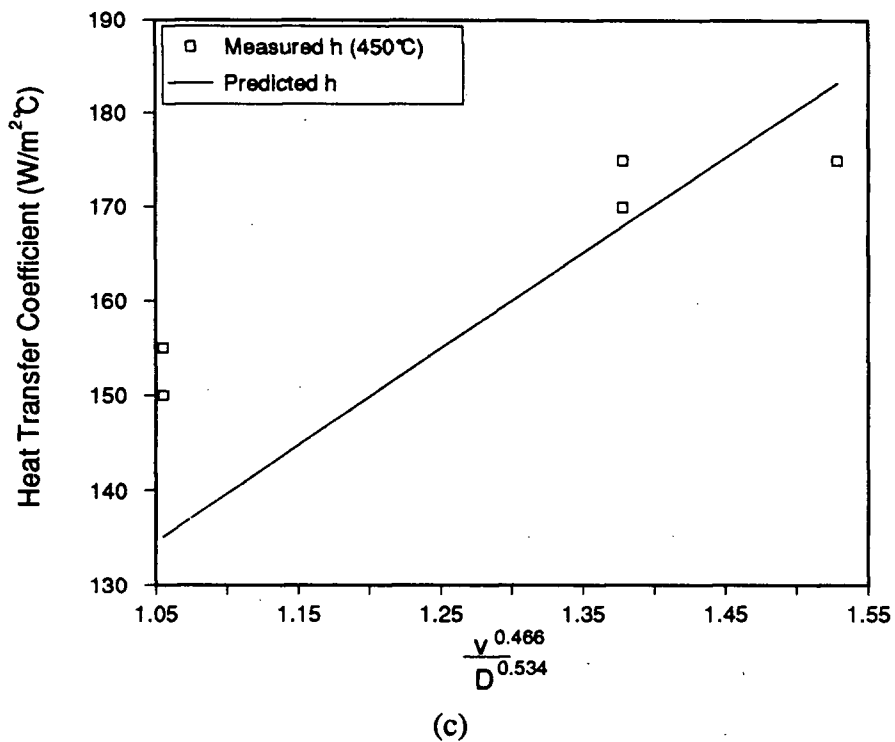
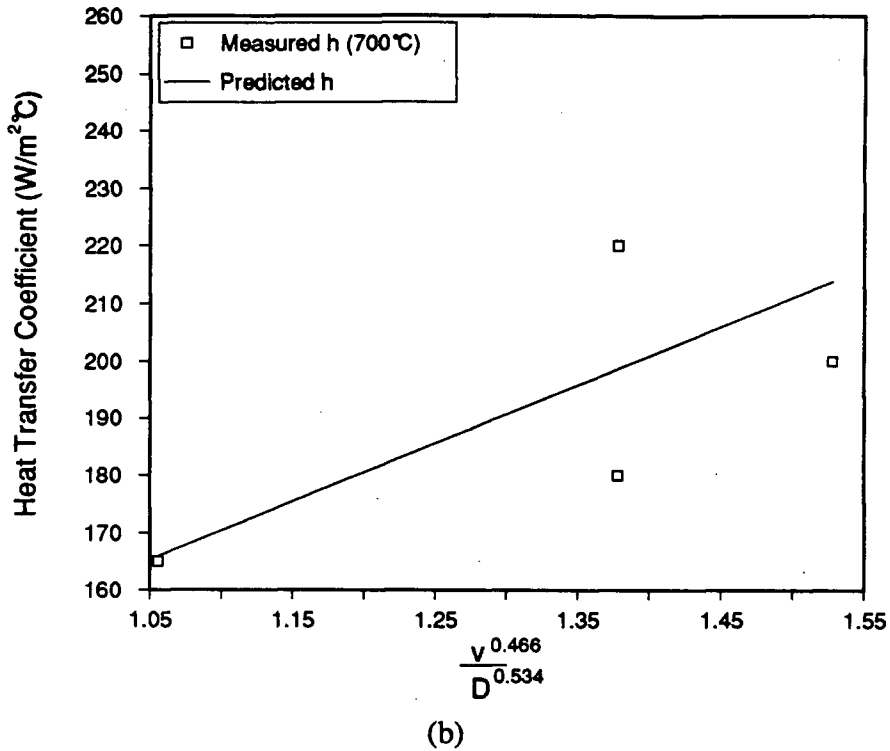


Fig. 7.8 - Measured heat-transfer coefficients for plant trials without production coils on the Stelmor line, plotted against $(\text{air velocity})^{0.466}/(\text{rod diameter})^{0.534}$ according to Eq. (6.4). The line included is the predicted value based on convection and radiation. Heat-transfer coefficients measured at (a) 800°C, (b) 700°C and (c) 450°C.

7.2.2 Regression Equations

The average difference between measured overall and predicted convective heat-transfer coefficients, at five isothermal temperatures, for both edge and centre tests, has been determined employing Figs. 7.6 and 7.7, as a measure of radiative heat transfer. Results are shown in Fig. 7.9, where the predicted radiative heat-transfer coefficients, based on Eq. (3.9), and those calculated from the difference between overall and predicted convective values, are plotted against temperature. As can be seen, the measured values are equal to or lower than the predicted radiative heat-transfer coefficient. It is also evident that the radiative coefficient at the centre of the bed is higher than that at the edge, as expected since the rod packing density at the centre is less than at the edge, and thus reradiation among rods of similar temperature will be smaller at the centre than at the edge. The ratio of measured to predicted radiative heat-transfer coefficients, can be employed to calculate a correction factor for edge and centre conditions. Designated as RCF_E and RCF_C (*radiation correction factor*) for edge and centre of the bed respectively, calculated values for RCF , plotted against temperature, are given in Fig. 7.10. Regression equations for each factor have been determined as:

$$RCF_C = 2.02x^{-0.131}e^{-0.00208x} \quad (7.2a)$$

$$RCF_E = 8.94x^{-0.456}e^{-0.00272x} \quad (7.2b)$$

where x equals $875-T$ in °C. Equation (7.2a) or (7.2b) can then be combined with Eq. (3.9) for the prediction of the radiative heat-transfer coefficient through the following expression:

$$h_r = RCF \sigma \epsilon \frac{(T_s^4 - T_A^4)}{(T_s - T_A)} \quad (7.3)$$

This equation is employed for calculation of h_r , under Stelmor line cooling conditions, in the model.

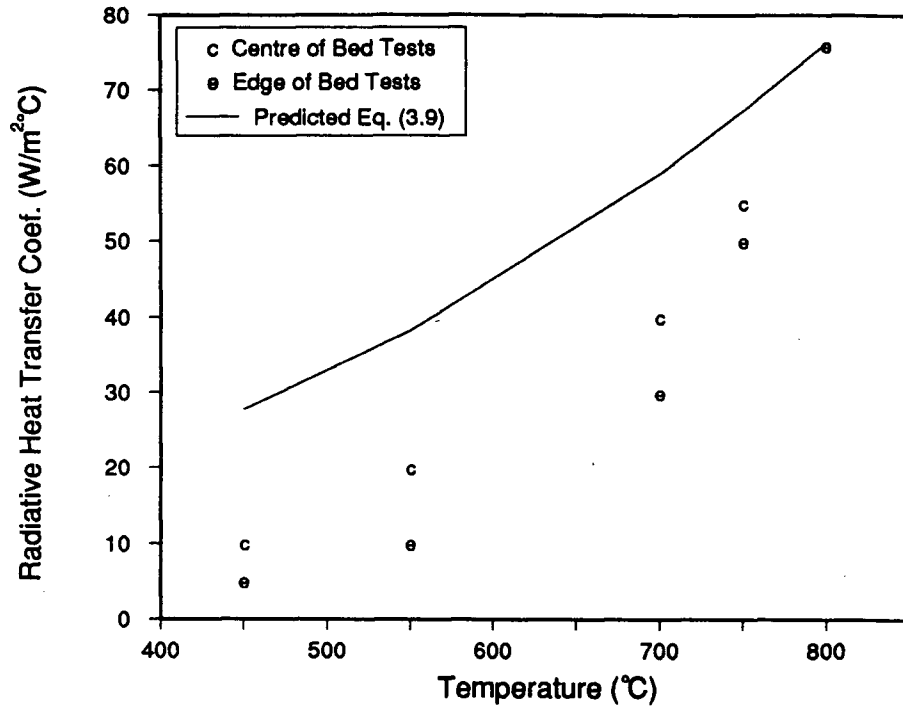


Fig. 7.9 - Calculated values for radiative heat-transfer coefficients from the plant trials, plotted against temperature. Also included is the predicted value from Eq. (3.9).

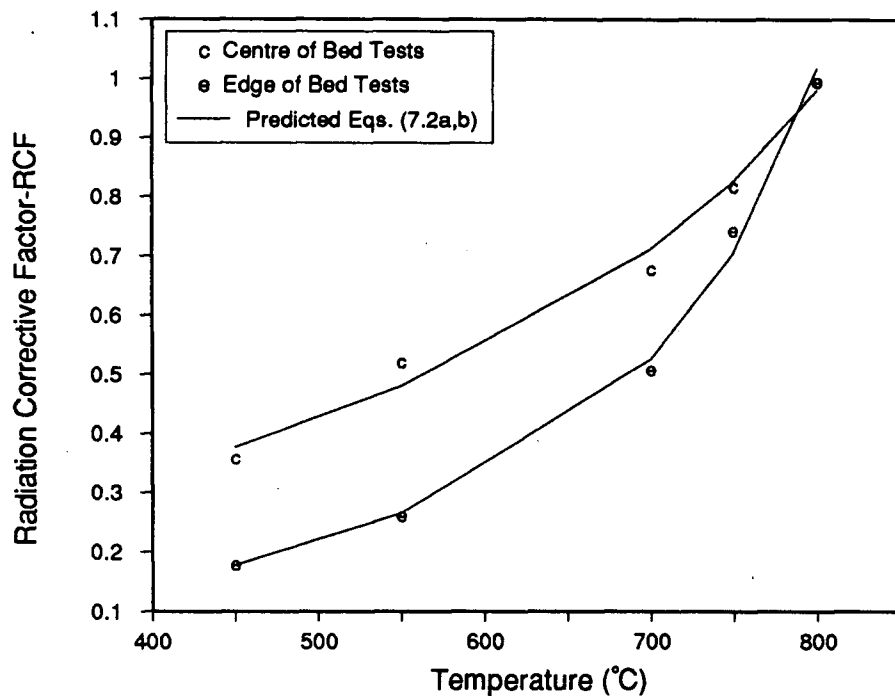


Fig. 7.10 - Radiation Correction Factor "RCF" for centre and edge of bed plotted against temperature. Lines are calculated from the regression equation for both parameters (Eqs. (7.2a) and (7.2b)).

7.3 Microstructures

Microstructures for all rods tested on the Stelmor line, have been characterized in terms of the same three parameters as for the laboratory test rods: ferrite fraction, ferrite grain diameter and pearlite spacing. Results from both image analyzer and SEM studies are presented in the following sections. Also included are the empirical equations developed for each microstructural parameter, based on a combination of laboratory, plant and literature data.

7.3.1 Ferrite Fraction

7.3.1.1 Experimental Results

Ferrite fractions, measured at the centreline of plant trial rods with the image analyzer, are shown in Figs. 7.11 (a), (b) and (c), plotted against the average rod cooling rate, measured at 750°C. The 1080 grade, Steel F, contains a small ferrite fraction, and no relationship between fraction and rod cooling rate is evident, as shown in Fig. 7.11 (a). This observation may be attributed to the difficulty in measuring such small amounts of proeutectoid ferrite, in a predominantly pearlitic microstructure. The error bar plotted on two of the data points in the figure, which represents \pm one standard deviation of the measured value, indicates the large degree of variability in this data. The three 1035-1038 grades, depicted in Fig. 7.11 (b), show a trend towards smaller ferrite fraction with increasing cooling rate. However the major factor influencing ferrite grain diameter is the composition of the steel. Referring to Table 5.1, which contains the chemical analysis for each of the steels plotted in Fig. 7.11 (b), the most hardenable of the three grades is Steel C (1038). It has a carbon concentration of 0.393 wt% and manganese equal to 0.82, whereas the other grades have carbon equal to 0.369 and 0.335, and manganese equal to 0.77 and 0.72, for the G and H steels, respectively. Once again the error bars plotted on three of the points in the graph, indicate \pm one standard deviation of the mean measured value. The % deviation is seen to be smaller for the medium carbon steels in Fig. 7.11 (b) as compared to the eutectoid

grades in Fig. 7.11 (a). Figure 7.11 (c) also displays a decreasing ferrite fraction with increasing cooling rate, for the three 1017-1022 grades. Once again, the composition of the steel seems to be the most important factor, at least for the present range of cooling rates. Referring to Table 5.1, the steel with the smallest fraction of ferrite in Fig. 7.11 (b), Steel J, is seen to possess about the same carbon concentration as Steel E (0.20 and 0.201 wt%), however the manganese concentration is nearly double in Steel J as compared to Steel E (0.95 and 0.50 wt%). The greater hardenability of Steel J results in a lower ferrite fraction. With this in mind, it is somewhat surprising that Steel I doesn't contain a greater fraction of ferrite as its %C and %Mn equal 0.183 and 0.38, respectively. The error bars plotted on three of the data points once again indicate \pm one standard deviation of the mean value.

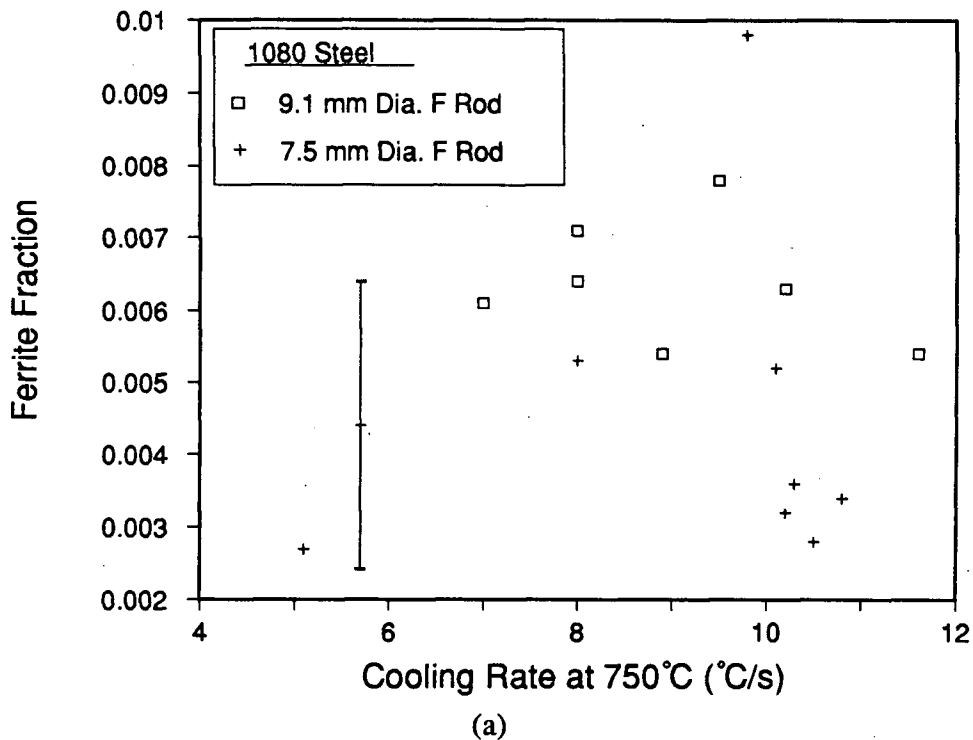


Fig. 7.11 - Measured ferrite fractions for plant trial steels plotted against the average cooling rate at 750°C; (a) Steel F (1080), (b) Steels C (1038), G (1037) and H (1035), and (c) Steels E (1020), I (1017) and J (1022).

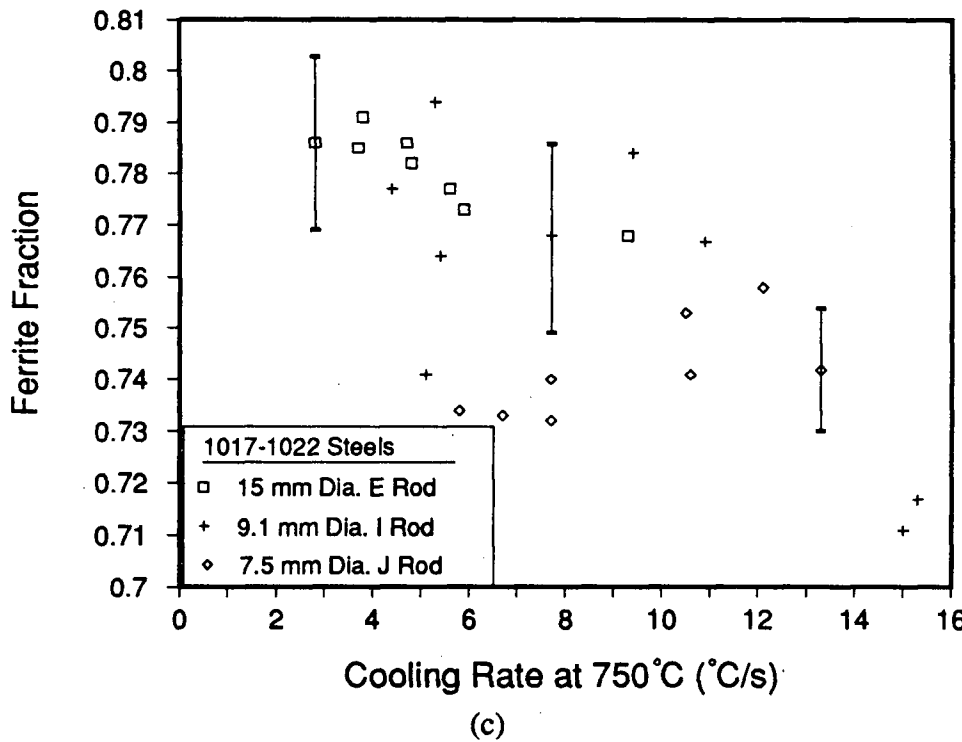
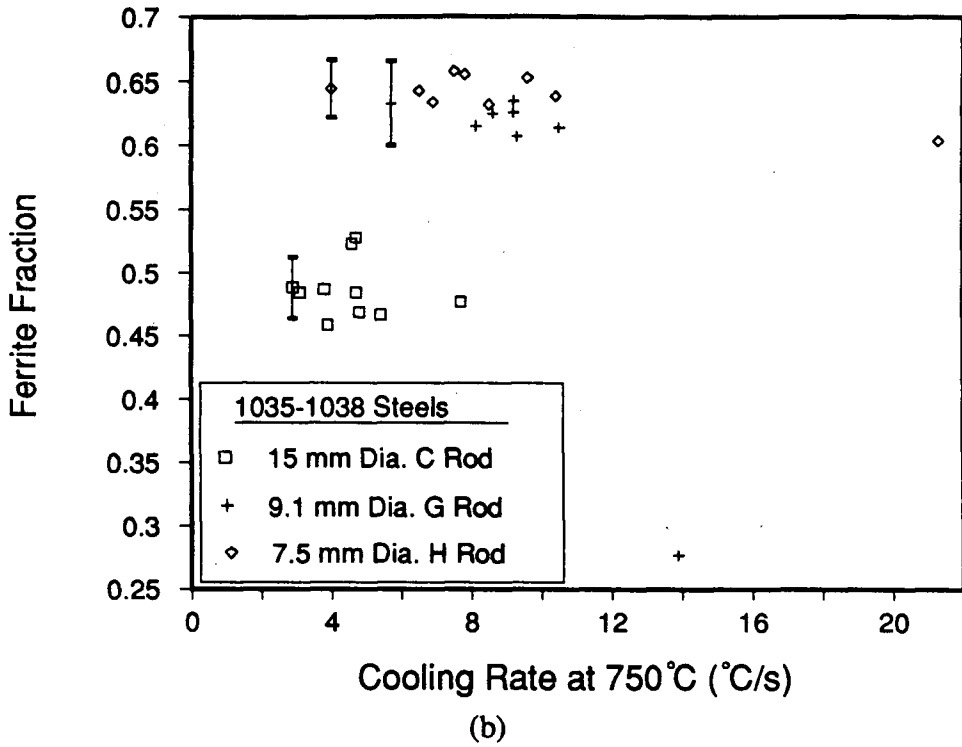
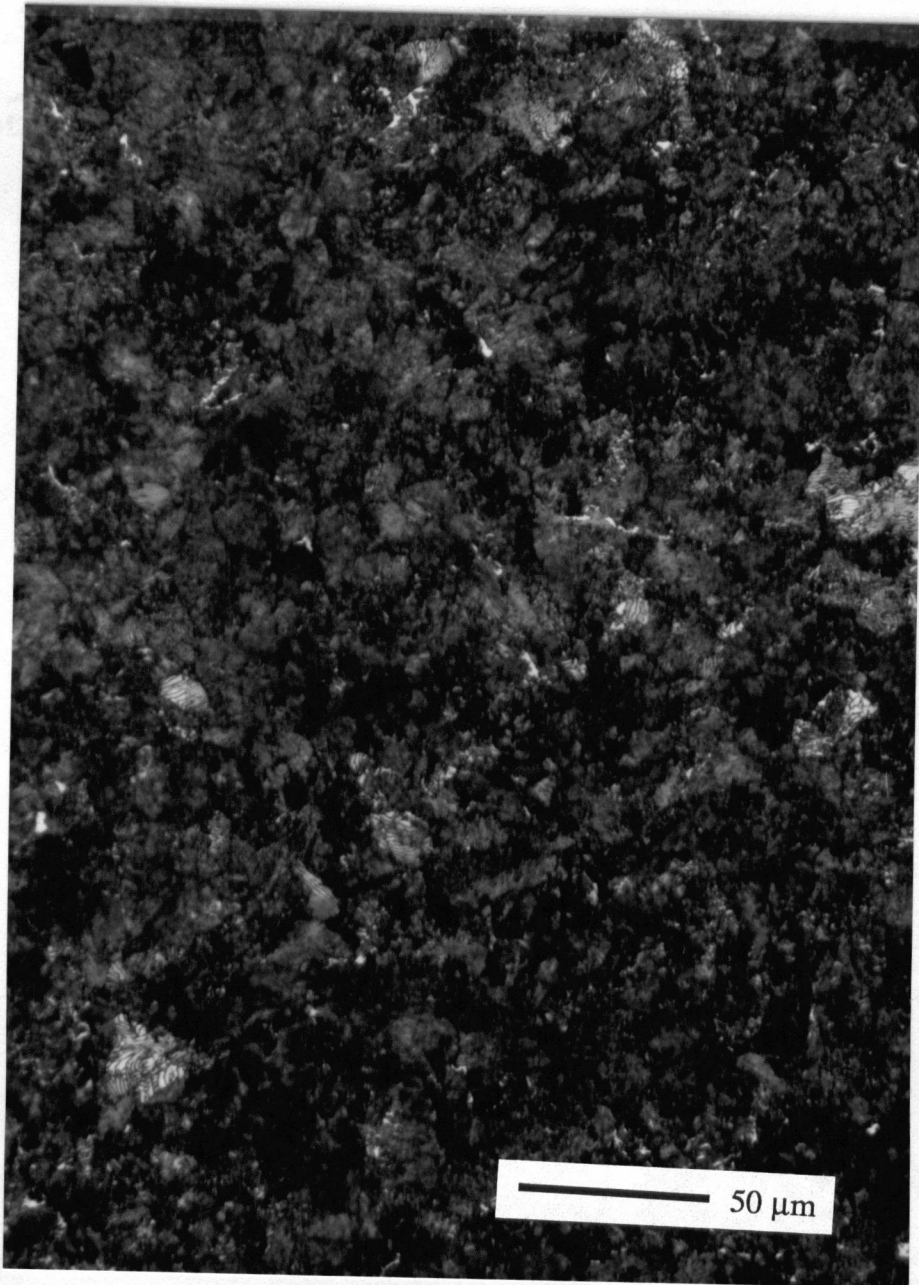
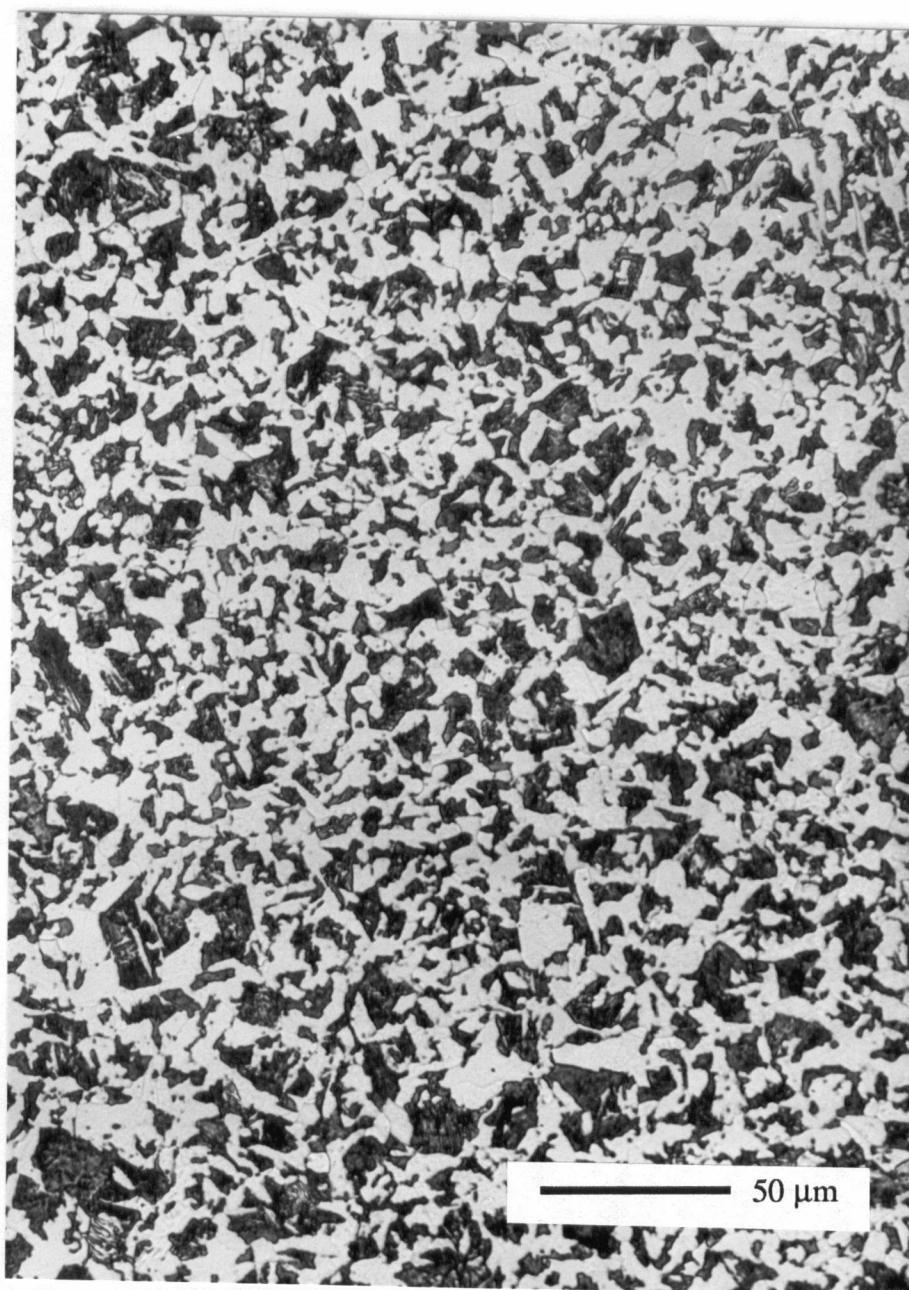


Fig. 7.11 - Measured ferrite fractions for plant trial steels plotted against the average cooling rate at 750°C; (a) Steel F (1080), (b) Steels C (1038), G (1037) and H (1035), and (c) Steels E (1020), I (1017) and J (1022).



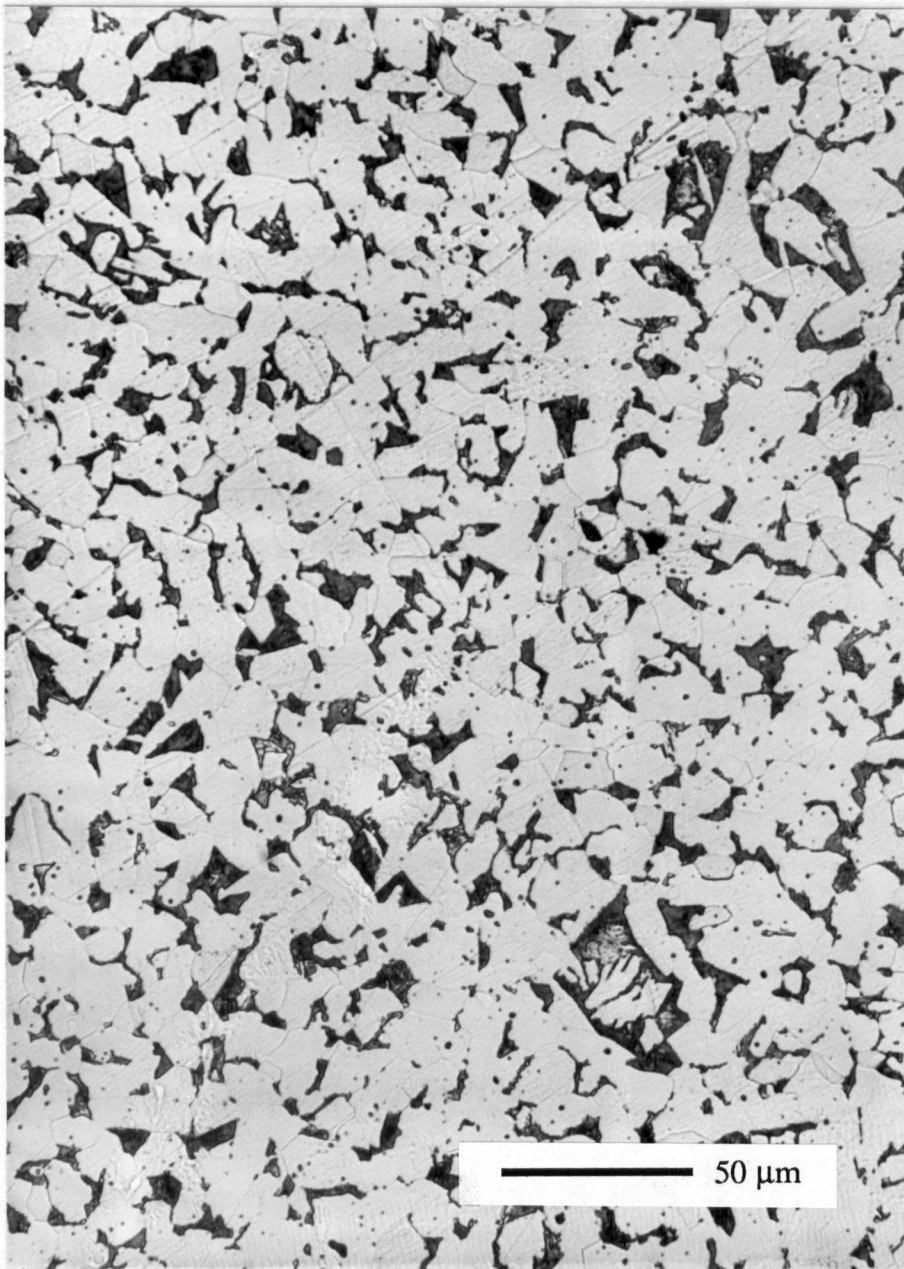
(a)

Fig. 7.12 - Typical photomicrographs taken on the image analyzer; (a) Steel F (1080), (b) Steel G (1037) and (c) Steel J (1022).



(b)

Fig. 7.12 - Typical photomicrographs taken on the image analyzer; (a) Steel F (1080), (b) Steel G (1037) and (c) Steel J (1022).



(c)

Fig. 7.12 - Typical photomicrographs taken on the image analyzer; (a) Steel F (1080), (b) Steel G (1037) and (c) Steel J (1022).

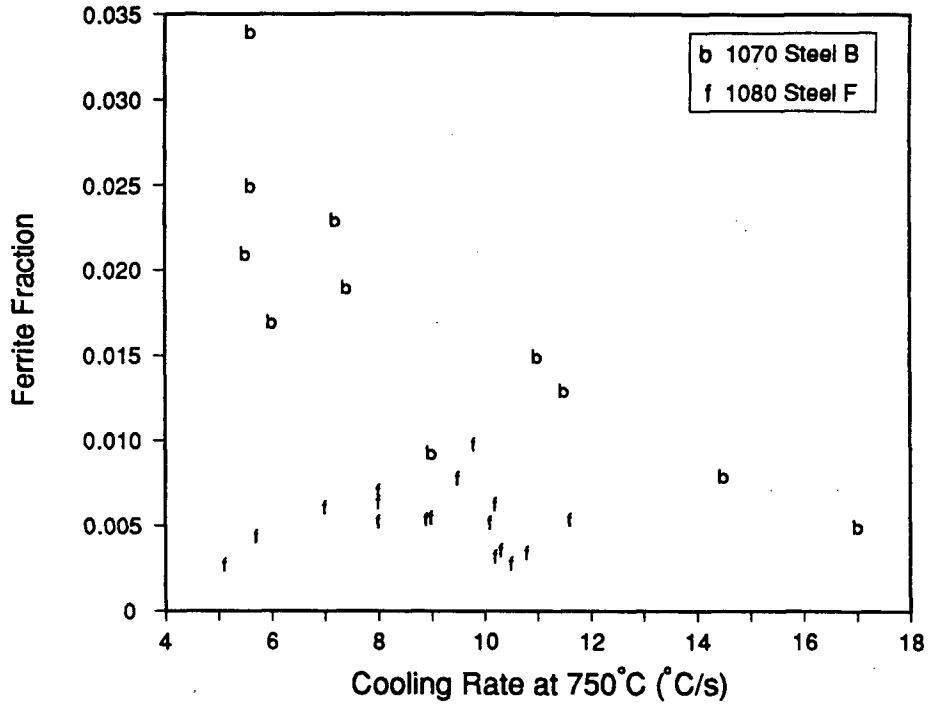
Typical microstructures from the centreline of plant trial rods, are shown in Fig. 7.12 (a), (b) and (c). These micrographs were taken on the image analyzer and are representative of the magnification and etch condition employed for quantifying both ferrite fraction and ferrite grain diameter. The three micrographs display a microstructure consisting of ferrite and pearlite only. As was the case for the laboratory steels all microstructures examined in the plant trial rods, consisted of mixtures of ferrite and pearlite; nonequilibrium phases (i.e. bainite and martensite) were not observed.

7.3.1.2 Regression Equations

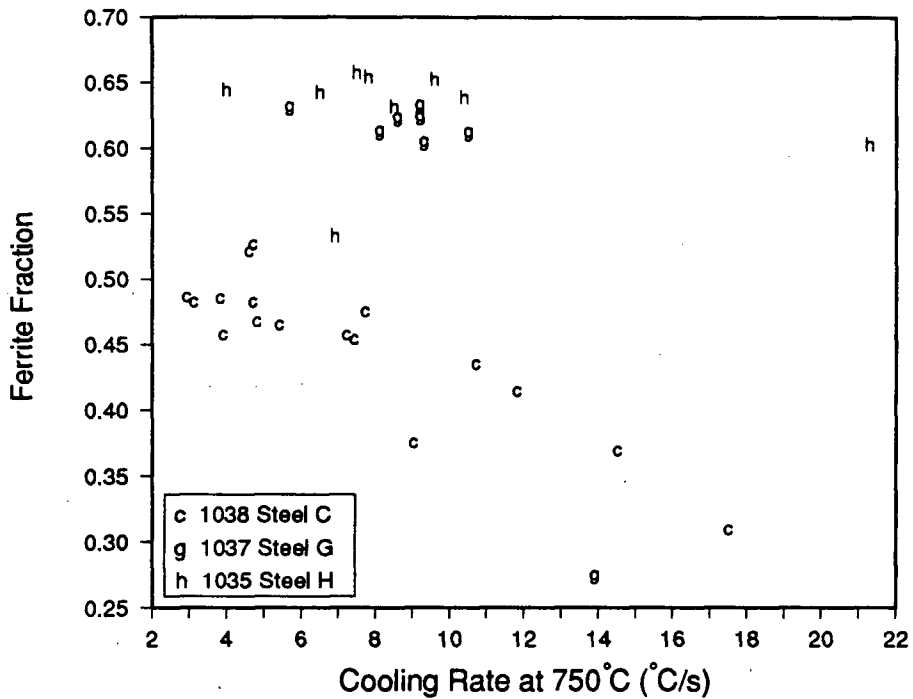
A summary of ferrite fractions measured in laboratory and plant tests is included in Fig. 7.13 (a), (b) and (c), for each range of steel grades. Once again, the fraction is plotted against the average rod cooling rate, measured at 750°C. In each figure, it can be seen that ferrite fraction tends to decrease with increasing cooling rate. Owing to the wider range of cooling rates encountered for the laboratory experiments, in general the lab data seems to show this trend of decreasing ferrite fraction with increasing cooling rate more clearly. Including data for all grades of steel and both sets of experiments, a multiple linear regression technique was applied to determine the best-fit equation for ferrite fraction as a function of cooling rate and steel composition. To obtain a good fit it was necessary to consider individual grades separately; thus, eutectoid or near-eutectoid grades were employed for one equation, and hypoeutectoid grades for another. For the eutectoid data, only two steels could be included, resulting in the following equation:

$$f_{\alpha} = -0.00131(CR) - 0.147(\%C) + 0.131 \quad (7.4)$$

where CR is the average rod cooling rate at 750°C in °C/s, and $\%C$ is the carbon content of the steel. A plot of predicted f_{α} based on Eq. (7.4), versus the measured ferrite fraction, is given in Fig. 7.14 for the two near-eutectoid grades. It can be seen that the variation is small within each grade, and the major factor controlling the ferrite fraction is the carbon content of the steel. In order to increase confidence in an equation of this type, more data for ferrite



(a)



(b)

Fig. 7.13 - Ferrite fraction obtained in all laboratory and plant-trial steels plotted as a function of cooling rate measured at 750°C; (a) near-eutectoid grades, (b) 1035-1038 grades and (c) 1017-1022 grades.

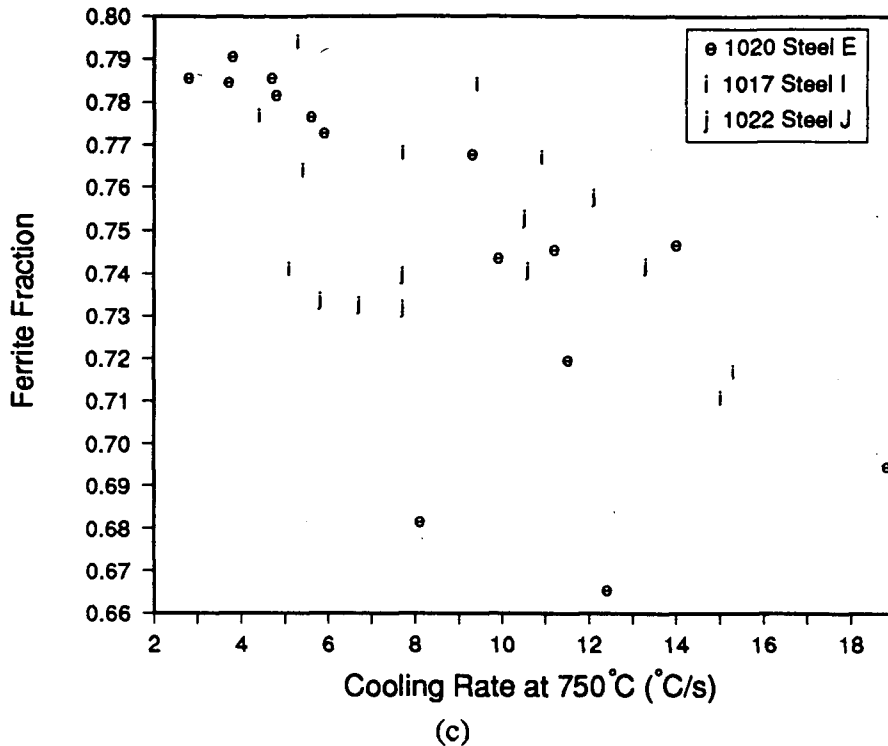


Fig. 7.13 - Ferrite fraction obtained in all laboratory and plant-trial steels plotted as a function of cooling rate measured at 750°C; (a) near-eutectoid grades, (b) 1035-1038 grades and (c) 1017-1022 grades.

fraction in higher carbon steels as a function of cooling rate is required. However, for the present analysis, Eq. (7.4) should supply an adequate prediction of the ferrite fraction in near-eutectoid grades.

For the lower carbon, hypoeutectoid grades, significantly more data are available as witnessed in Figs. 7.13 (b) and (c). A multiple linear regression was also applied to this data, but a different term was inserted to reflect the change in ferrite fraction as a function of steel composition. This term was the equilibrium ferrite fraction and was calculated from the phase diagram for each grade of steel considered. As outlined by Kirkaldy *et al.* [34,35], the phase diagram for plain-carbon steels containing small amounts of alloying elements, can be predicted as a function of the steel composition, based on thermodynamic considerations. Thus, relative positions of the A_3 and A_{cm} lines have been calculated from the steel composition, utilizing the approach of Kirkaldy *et al.*. The intersection of these two lines will occur

at temperature T_{A_1} and at the eutectoid composition. Employing this eutectoid composition, and applying the lever rule, the equilibrium fractions of ferrite ($f_{\alpha EQ}$) and pearlite for the hypoeutectoid grades have been calculated. Including the equilibrium ferrite fraction term in the multiple linear regression for ferrite fraction in hypoeutectoid grades, as well as the rod cooling rate, the following equation has been obtained:

$$f_{\alpha} = -0.00479(CR) + 0.927(f_{\alpha EQ}) + 0.0964 \quad (7.5)$$

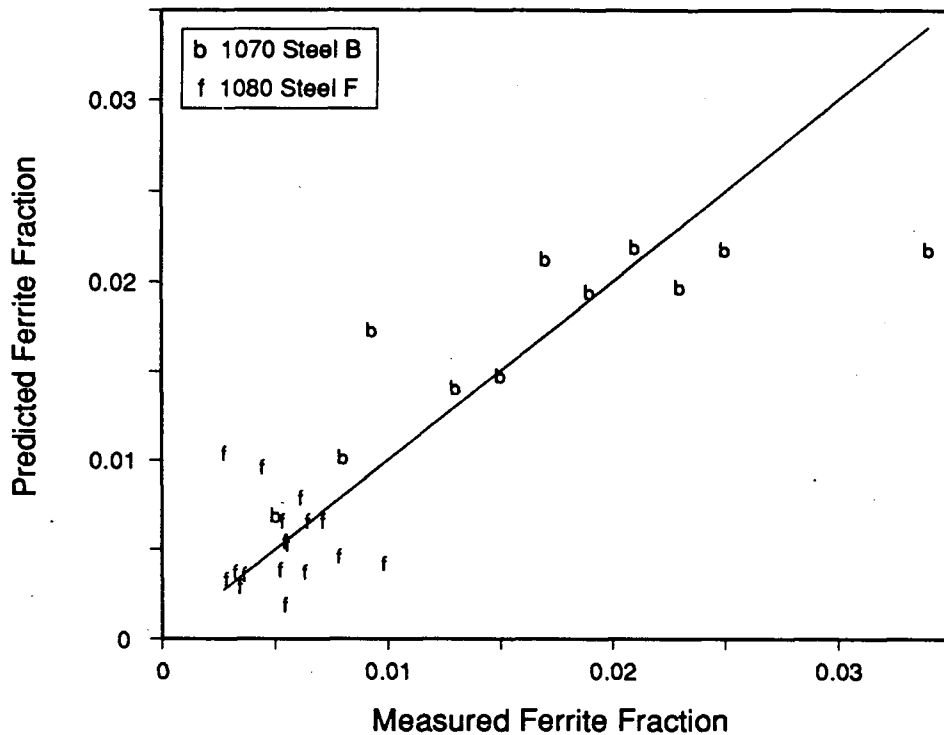


Fig. 7.14 - Predicted versus measured ferrite fraction for near-eutectoid steels. Predicted values are calculated based on Eq. (7.4).

Figure 7.15 displays the predicted (from Eq. (7.5)) against the measured ferrite fraction, and also includes data from the literature. As can be seen, a reasonable fit is obtained over the range of ferrite fractions encountered. However, agreement appears to be worse with increasing carbon content and decreasing ferrite fraction. It would seem that Eq. (7.5) is adequate in estimating the relative fraction of ferrite in plain-carbon steel, but more data is required for higher carbon grades.

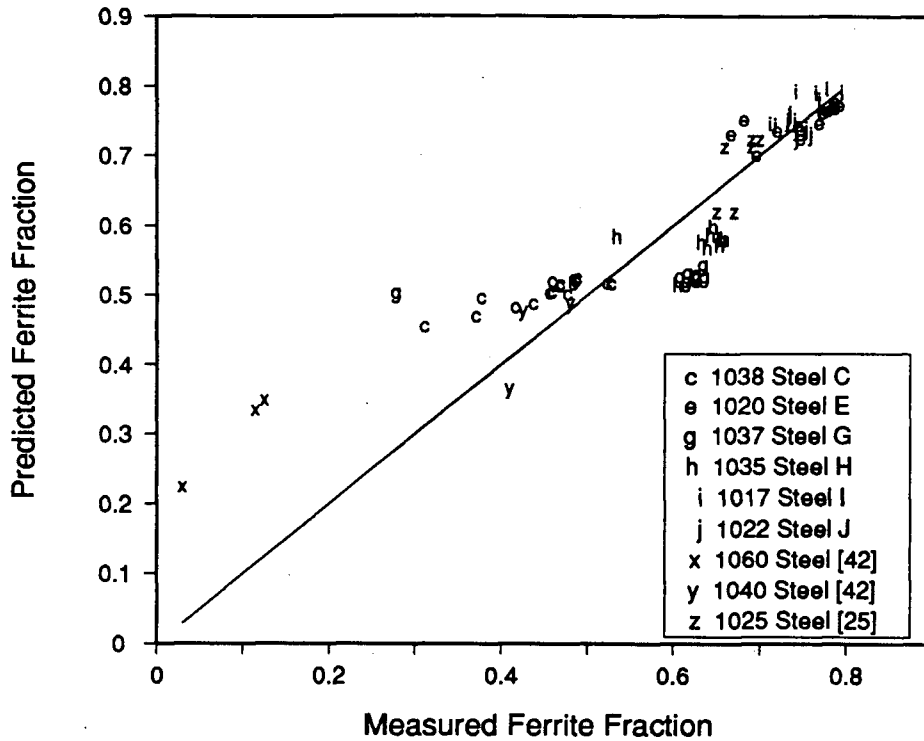


Fig. 7.15 - Predicted versus measured ferrite fraction for hypoeutectoid steels. Predicted values are calculated using Eq. (7.5).

7.3.2 Ferrite Grain Diameter

7.3.2.1 Experimental Results

Ferrite grain diameters measured at the centreline of plant trial rods, are shown in Figs. 7.16 (a), (b) and (c). As was the case for the ferrite fraction, the values are plotted as a function of the average rod cooling rate, measured at 750°C. Similar to the ferrite fractions measured for Steel F (1080), no trend between the measured mean ferrite diameter and average rod cooling rate is apparent in Fig. 7.16 (a). This can be attributed to the small ferrite fractions found in this grade. The error bar plotted in the figure indicates \pm one standard deviation of the measured value, which in the case of Steel F is fairly substantial. Decreasing ferrite grain diameter with increasing cooling rate is exhibited by the data for the 1035-1038 grades, shown in Fig. 7.16 (b), although most of the points are grouped around a cooling rate of 4 to 10°C/s. A similar trend is displayed by the 1017 and 1022 grades in Fig 7.16 (c), however, Steel J (1022), seems to show almost no effect of cooling rate on grain

size. The reason for this behavior is not clear, but it may be related to the much higher manganese content in this grade, 0.95 wt%, as compared to the other grades. As was the case for ferrite fraction, the diameter is also shown to be dependent on the steel composition. As carbon content decreases and ferrite fraction increases, the ferrite grain diameter exhibits a corresponding increase.

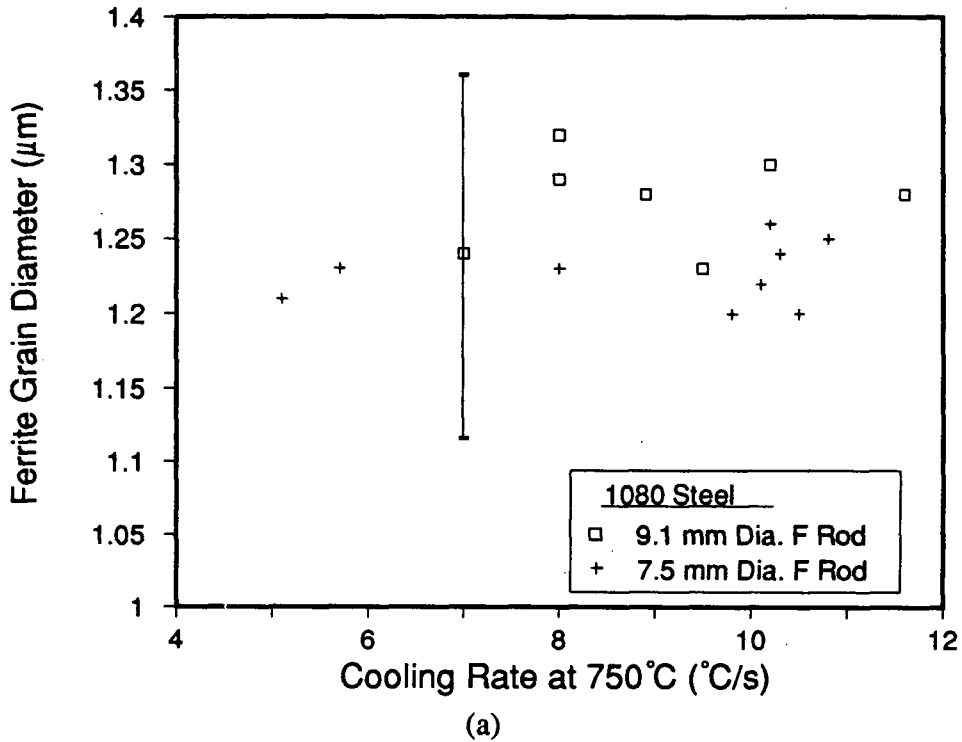


Fig. 7.16 - Measured ferrite grain diameters for plant trial steels plotted against the average cooling rate at 750°C ; (a) Steel F (1080), (b) Steels C (1038), G (1037) and H (1035), and (c) Steels E (1020), I (1017) and J (1022).

7.3.2.2 Regression Equations

A summary of ferrite grain diameters for the combined data from laboratory and plant rod cooling tests, is given in Fig. 7.17. Results are similar to those obtained for ferrite fraction in that a general trend towards smaller ferrite diameters is exhibited with increasing cooling rate. The effect of steel cooling rate, on the grain diameter of ferrite, has been presented in the literature [38,67,85]. Choquet *et al.* have measured ferrite grain diameters in continuously cooled steels after hot torsion testing. Figure 7.18 contains the results for a 0.18 %C, 1.3 %Mn steel. The effect of steel cooling rate on the ferrite grain diameter is apparent in this figure. In addition, the results indicate the degree to which the prior austenite grain size affects the ferrite grain size. The austenite grain sizes quoted in the figure agree well with the range of sizes measured for the laboratory tests presented in Chapter 6. Comparing the results of Choquet *et al.* to the ferrite grain diameters measured in the 1017-1022 steels (Fig. 7.17 (c)), at a cooling rate of 10 °C/s for example, the present data suggests a ferrite grain size of ~6.5 - 9 μm, which is in good agreement with the literature where the grain size is ~6 - 8 μm. The higher Mn content in the literature steel is probably the cause of the slightly lower grain sizes. The good agreement between the measured and literature values is seen to continue as cooling rate is decreased. Results of ferrite grain diameters measured in a 0.15 %C, 0.4 %Mn steel are shown in Fig. 7.18 (b), taken from Tamura [38]. Unlike the previous literature steel, the prior austenite grain size was much larger in the case of Tamura and hence so is the ferrite grain size. However the results once again display the influence of steel cooling rate on the ferrite grain diameter.

Data from the laboratory and plant trials steels has been combined to provide empirical equations for the prediction of ferrite grain diameter based on steel composition and thermal history. The literature [67,68], suggests that ferrite grain diameter is linearly related to the square root of the reciprocal cooling rate during transformation. Considering first the near-eutectoid grades, a multiple linear regression analysis of the results for Steels B (1070) and F

(1080) has been performed. Owing to the lack of data for this range of grades, the only compositional variable included in the regression was carbon. The following equation was obtained for ferrite grain diameter:

$$d_{\alpha} = \frac{0.756}{\sqrt{CR}} - 12.0(\%C) + 10.2 \quad (7.6)$$

where the units for grain diameter are μm and cooling rate is in $^{\circ}\text{C/s}$. The effect of prior austenite grain size on the subsequent grain diameter of ferrite, has been presented in the literature [38,67,85]; however, owing to the small variation measured in d_{α} for the laboratory and plant steels, the effect has not been considered for the present regression analysis.

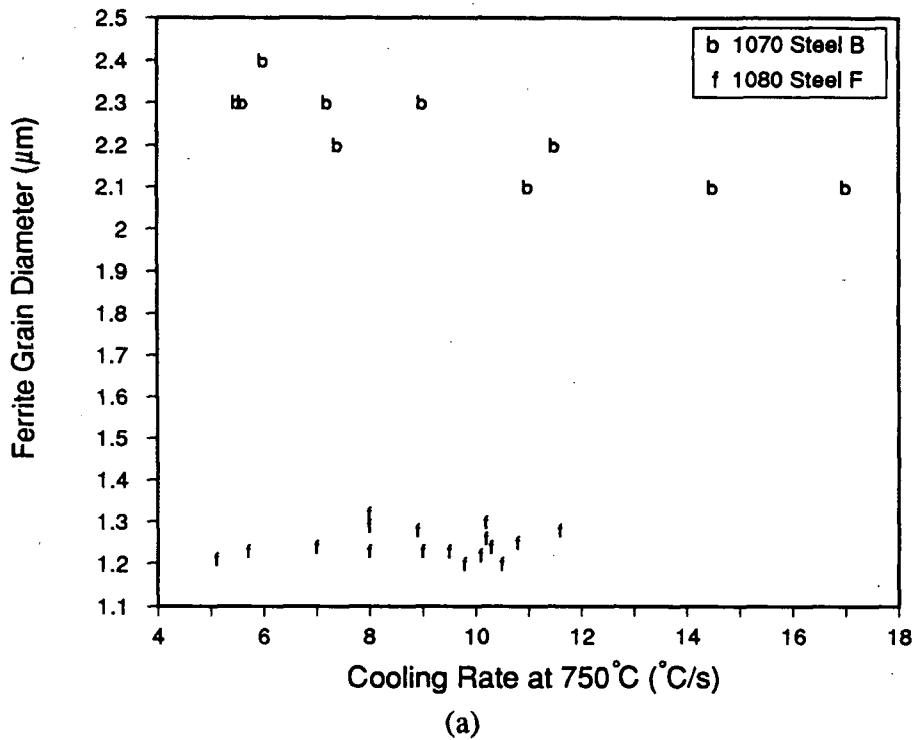
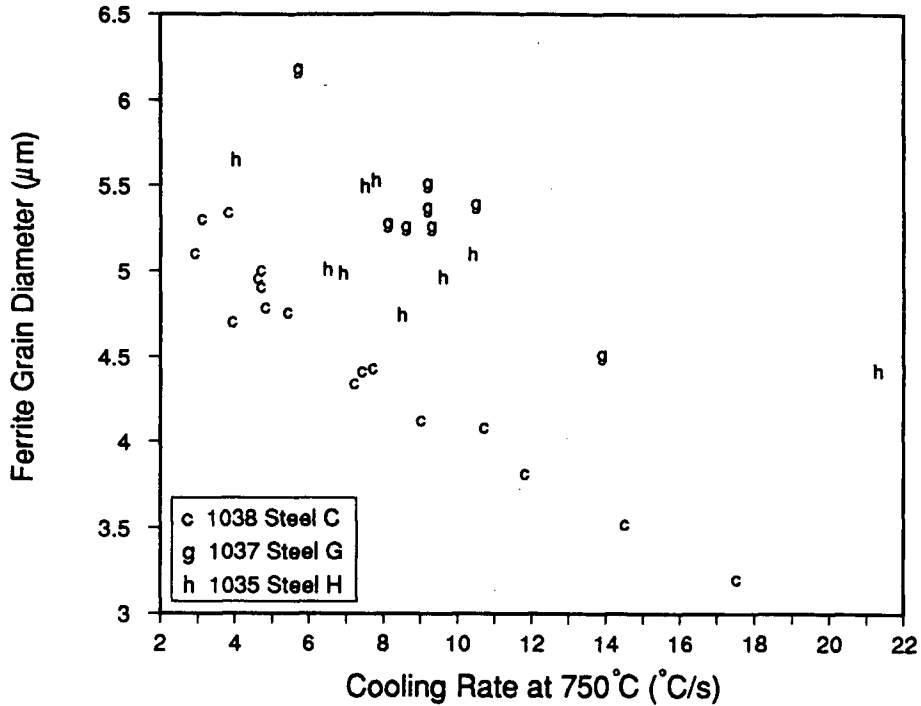
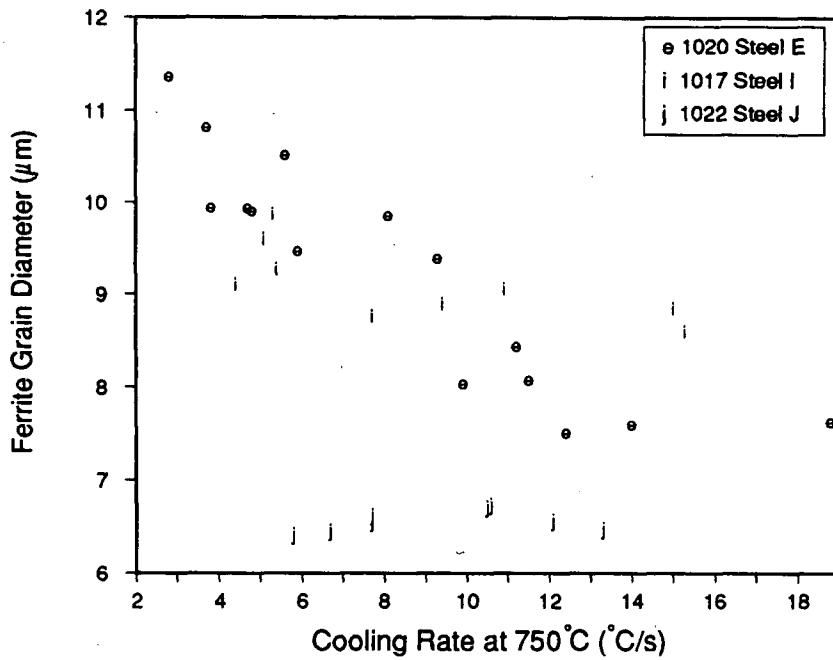


Fig. 7.17 - Ferrite grain diameter in all laboratory and plant-trial steels plotted as a function of cooling rate measured at 750°C ; (a) near-eutectoid grades, (b) 1035-1038 grades and (c) 1017-1022 grades.

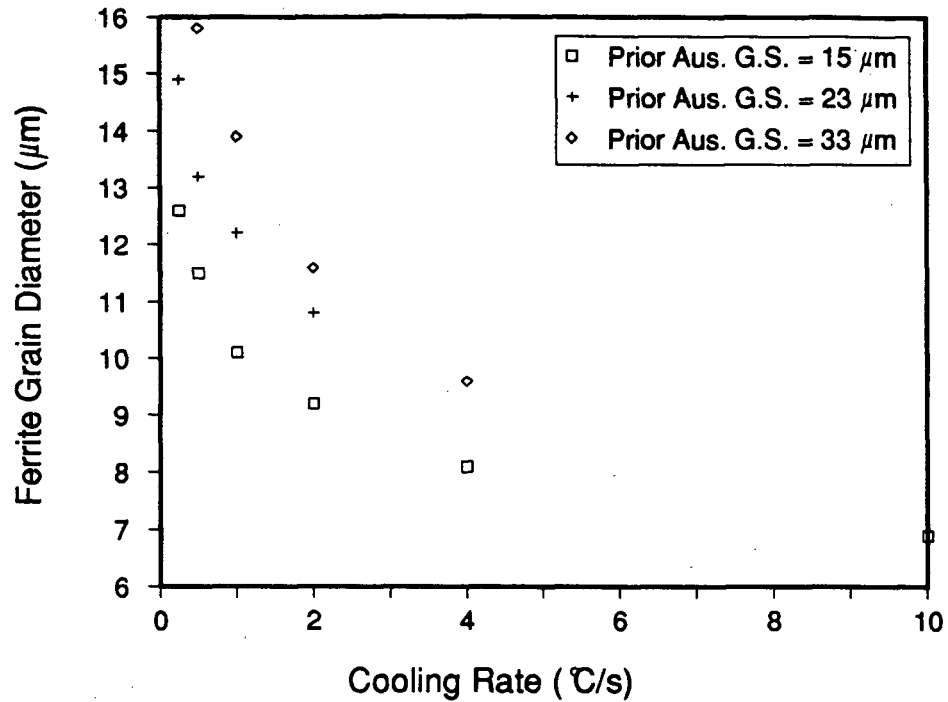


(b)

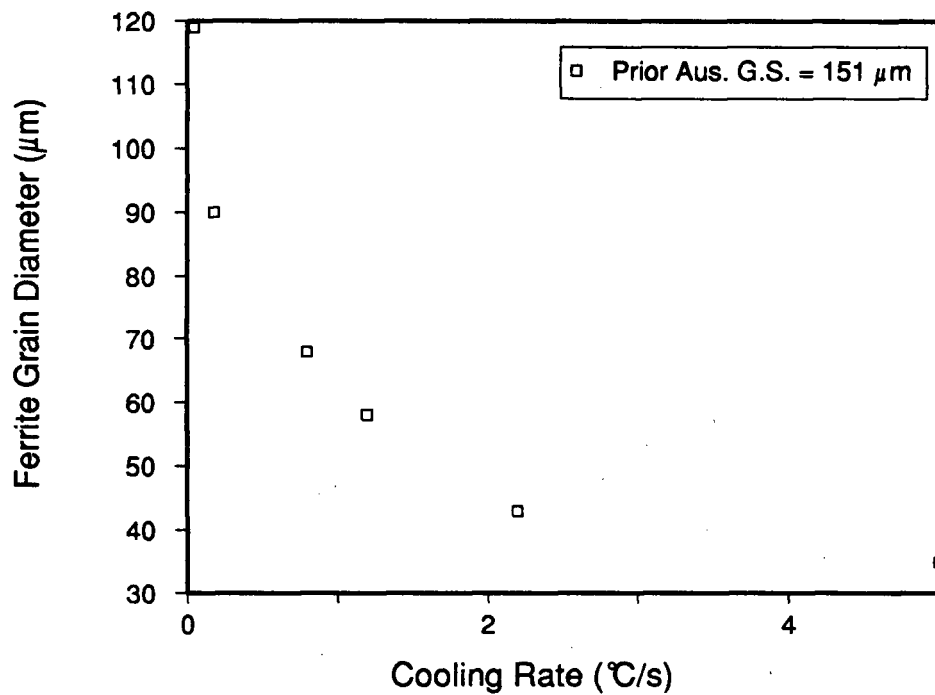


(c)

Fig. 7.17 - Ferrite grain diameter in all laboratory and plant-trial steels plotted as a function of cooling rate measured at 750°C; (a) near-eutectoid grades, (b) 1035-1038 grades and (c) 1017-1022 grades.



(a)



(b)

Fig. 7.18 - Ferrite grain diameter versus cooling rate for steel grades from the literature; (a) 0.18 %C, 1.3 %Mn steel from Choquet *et al.* [85] and (b) 0.15 %C, 0.4 %Mn steel from Tamura [38].

Predicted and measured ferrite grain diameters are compared in Fig. 7.19 for the near-eutectoid grade steels. The agreement is seen to be reasonable; this is expected because of the small range of data. Once again, a greater amount of data would be required to develop a more general relationship between ferrite grain diameter, and steel composition and thermal history.

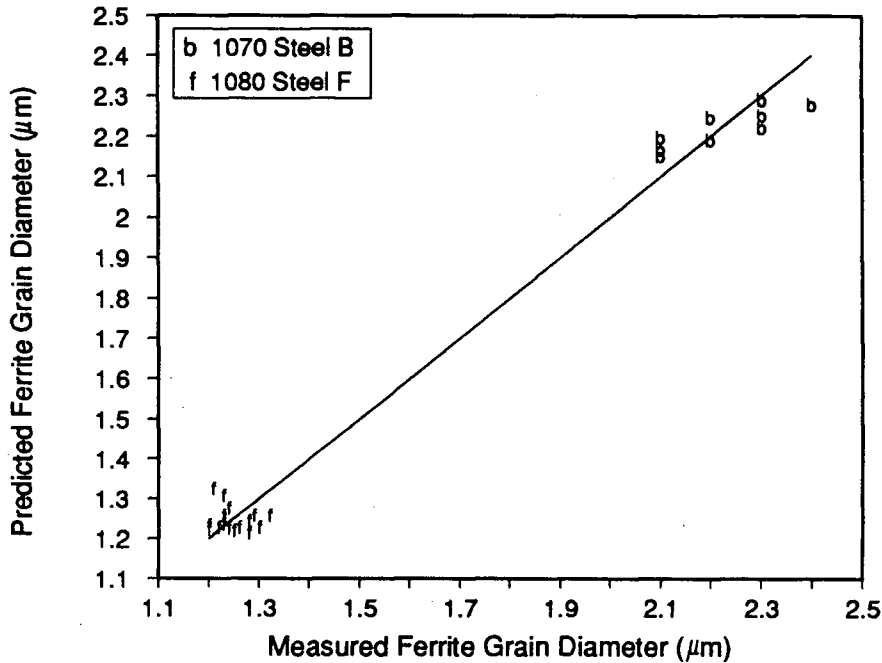


Fig. 7.19 - Predicted versus measured ferrite grain diameters for near-eutectoid steels. Predicted values are calculated using Eq. (7.6).

Regression analysis has also been performed on the data for ferrite grain diameters measured in the hypoeutectoid grade rods. Owing to the larger number of data points available, a term was included for manganese content in the steel. Once again the root of the reciprocal cooling rate was employed, as representative of the relative degree of cooling.

Multiple linear regression yielded the following equation:

$$d_{\alpha} = \frac{6.65}{\sqrt{CR}} - 16.0(\%C) - 4.29(\%Mn) + 11.7 \quad (7.7)$$

The predictive capability of Eq. (7.7) is displayed in Fig. 7.20, where the predicted ferrite grain diameter is plotted against the measured ferrite grain diameter. As can be seen, very good agreement between measured and predicted values has been obtained. Equations (7.6) and (7.7) were employed for prediction of ferrite grain diameter in the mathematical model.

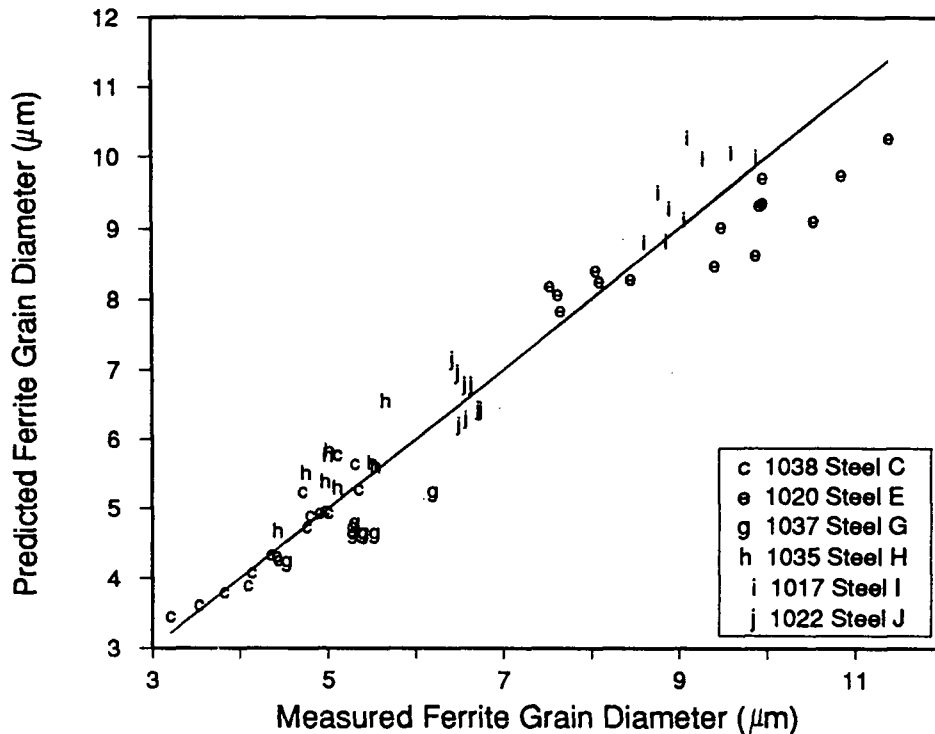
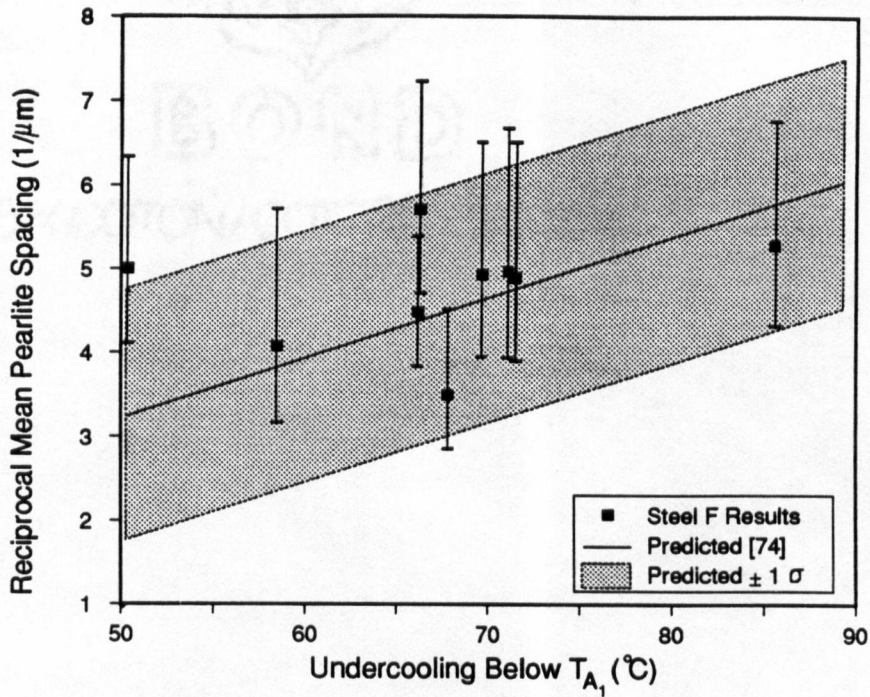


Fig. 7.20 - Predicted versus measured ferrite grain diameters for hypoeutectoid steels. Predicted values are calculated using Eq. (7.7).

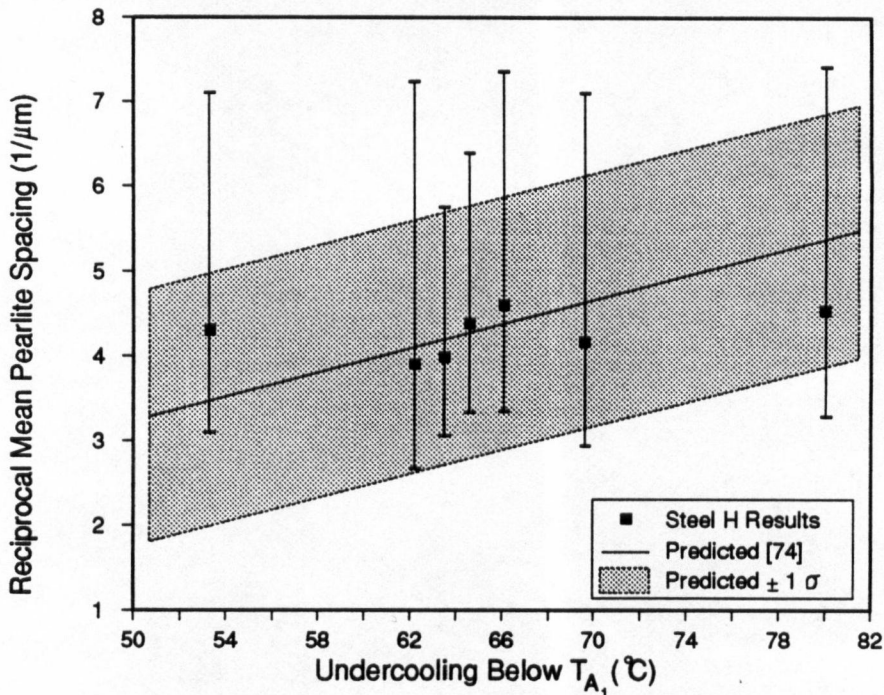
7.3.3 Pearlite Spacing

7.3.3.1 Experimental Results

Two plant trial steel grades were chosen for determination of the apparent interlamellar pearlite spacing, Steel F (1080) and Steel H (1035). Results for the two grades are given in Fig. 7.21, with pearlite spacing plotted against the average undercooling below T_{A1} . The lines provided in the figures are predictions based on the data of Pellisier *et al.* [74]; the shaded area represents plus and minus one standard deviation of the predicted value. The reciprocal pearlite spacings measured in the plant trials rods, agree in magnitude with those reported by



(a)



(b)

Fig. 7.21 - Measured and predicted pearlite spacings for plant trial steels plotted against the average undercooling below T_{A_1} . The line is based on a best-fit from Pellisier *et al.*'s data and the shaded area indicates \pm one standard deviation from the best-fit line. (a) Steel F (1080) and (b) Steel H (1035).

Pellisier *et al.*, although the experimental data seems to be less affected by undercooling than predicted. The undercoolings for the plant trial rods given in the figures were calculated from the measured rod thermal history, and may vary as much as $\pm 15^\circ\text{C}$ due to recalescence caused by the austenite-pearlite transformation. This indicates that there is not one mean pearlite spacing, but a range of spacings, dependent on the range of temperatures over which pearlite was formed. The error bar included with each data point indicates the range of spacings obtained for each sample. A more thorough investigation of the relationship between mean pearlite spacing and undercooling would require isothermal transformations with control over the magnitude of the recalescence and a larger range of undercooling.

Typical SEM micrographs of pearlite formed in the two grades of steel studied, are provided in Fig. 7.22 (a) and (b). Taken with the newer Hitachi SEM, as described in Section 4.6, photographing time was reduced and quality was improved as compared to the results for the laboratory Steel B (Fig. 6.13). The large fraction of ferrite present in Steel H (1035), required a much larger number of micrographs to measure a comparable number of pearlite colonies as obtained in the eutectoid grades.

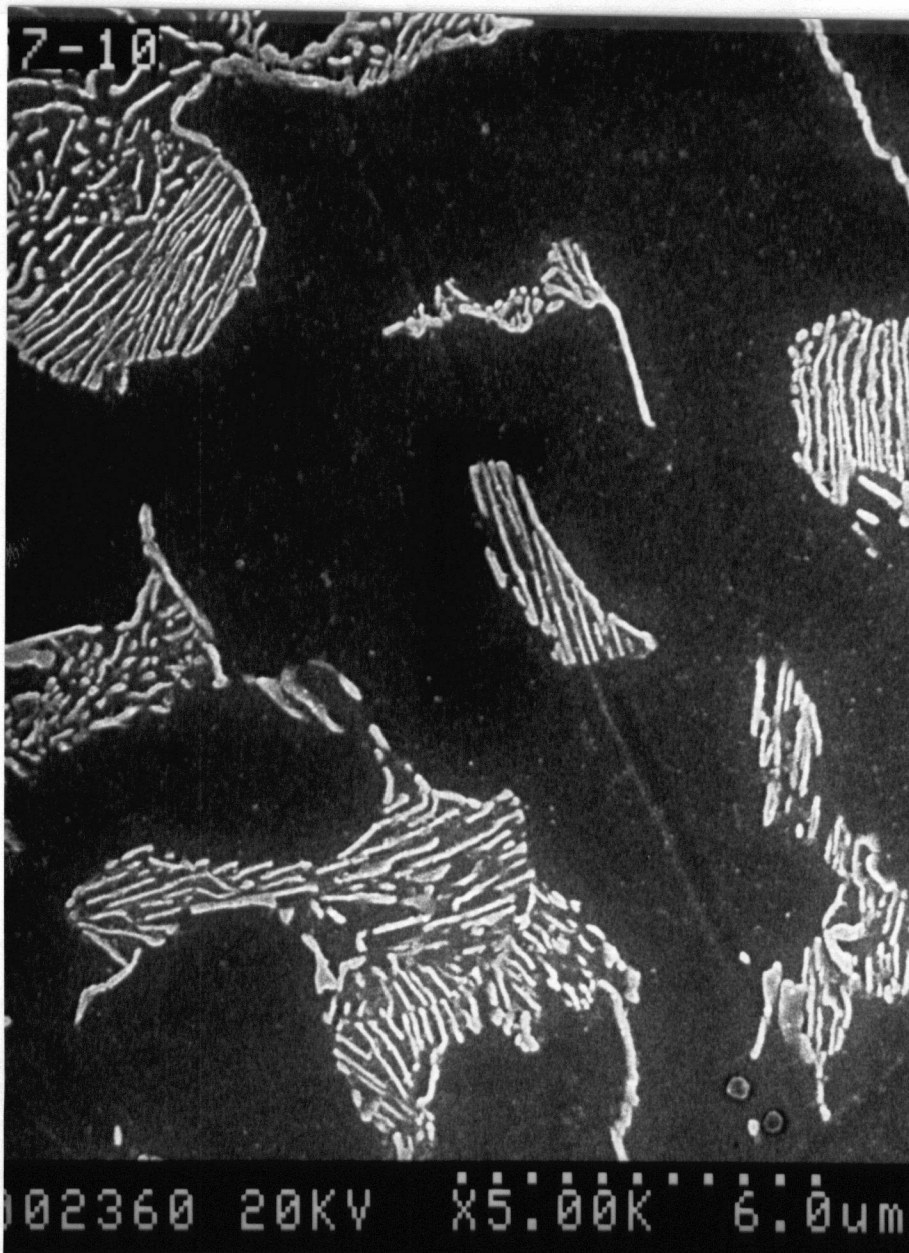
7.3.3.2 Regression Equations

Owing to the narrow range of undercoolings obtained in the laboratory and plant trials tests, two additional experiments were performed on Steel A (1080), employing the dilatometer equipment outlined in Chapter 4. The aim of these tests was to provide samples with pearlite formed under conditions of high and low cooling rates, to achieve maximum and minimum undercoolings below T_{A_1} . The procedure adopted for the tests was identical to that employed for continuous cooling transformation kinetics experiments. The tubular samples were resistively heated to an austenitizing temperature of 850°C , held for 3 min., then cooled at a predetermined rate. To obtain minimum and maximum undercoolings, rates of 0.1 and 43°C/s respectively, were employed. Table 7.1 contains the average undercoolings and apparent pearlite spacings measured in the two samples.



(a)

Fig. 7.22 - Typical micrograph from SEM of steel microstructure displaying pearlite colonies in (a) Steel F (1080) and (b) Steel H (1035).



(b)

Fig. 7.22 - Typical micrograph from SEM of steel microstructure displaying pearlite colonies in (a) Steel F (1080) and (b) Steel H (1035).

Table 7.1 - Measured undercoolings and pearlite spacings in 1080 Steel A.

Test #	Undercooling (°C)	Apparent Spacing (μm)
1	50.6	0.279
2	79.6	0.198

In order to formulate a regression equation for pearlite spacing as a function of undercooling, data from the literature, laboratory and plant trials were combined. Figure 7.23 contains results for all pearlite spacings included in the regression analysis, where the reciprocal spacing is plotted against the average undercooling below T_{A_1} in °C. The three grades from the literature are due to Pellisier *et al.* [74], and include two eutectoid grades and one hypoeutectoid. The best-fit line in Fig. 7.23, based on all data shown, was found to be:

$$\frac{1}{S_p} = 0.0643x + 0.0636 \quad (7.8)$$

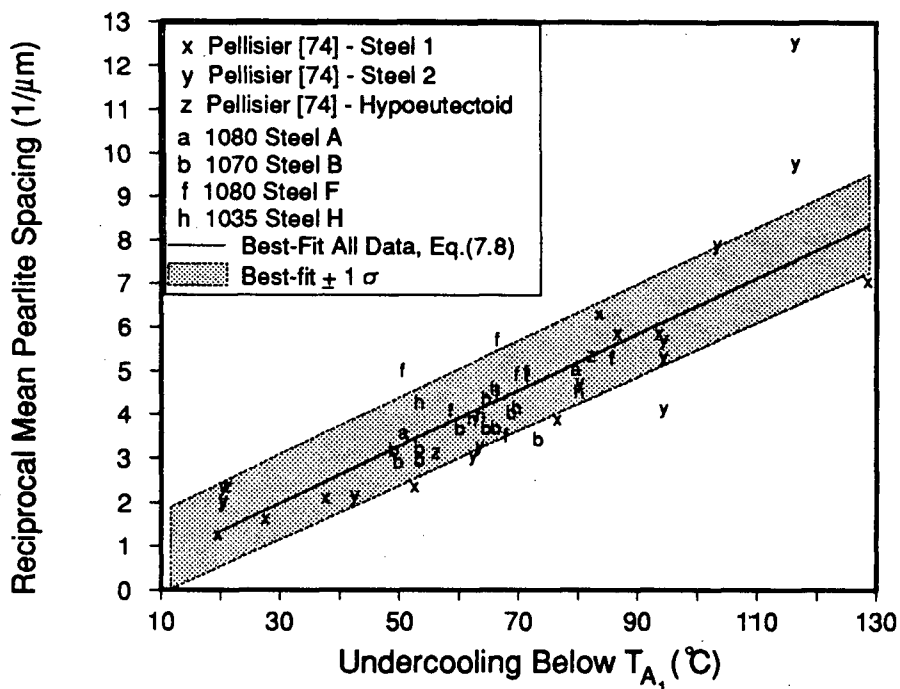


Fig. 7.23 - Reciprocal pearlite spacing plotted against the undercooling below T_{A_1} for experimental and literature steels. The best-fit line is based on Eq. (7.8).

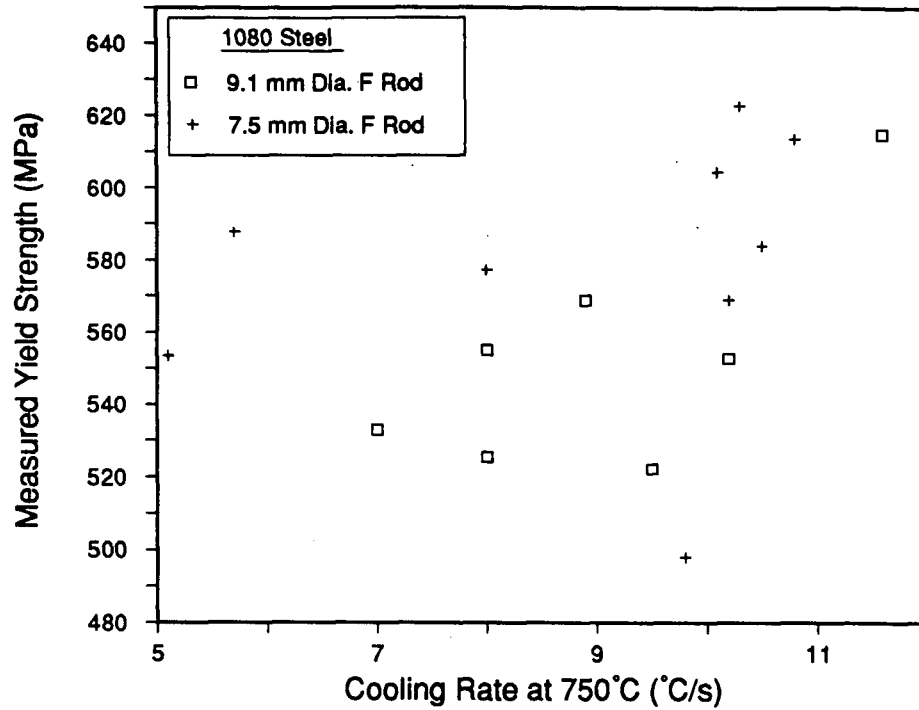
where x is the undercooling below T_{A_1} in °C. As can be seen, despite the scatter, good agreement between predicted and measured mean interlamellar pearlite spacing has been obtained from Eq. (7.8), over the range of undercoolings investigated. The standard deviation of the best-fit line, indicated by the shaded region in the figure, was calculated as $1.13 \mu\text{m}^{-1}$.

Although more data are available from the literature concerning the effect of undercooling on pearlite spacing, in all cases, the steels employed were high purity Fe-C or Fe-C-X alloys or measurements for minimum interlamellar spacing as opposed to mean spacing were reported.

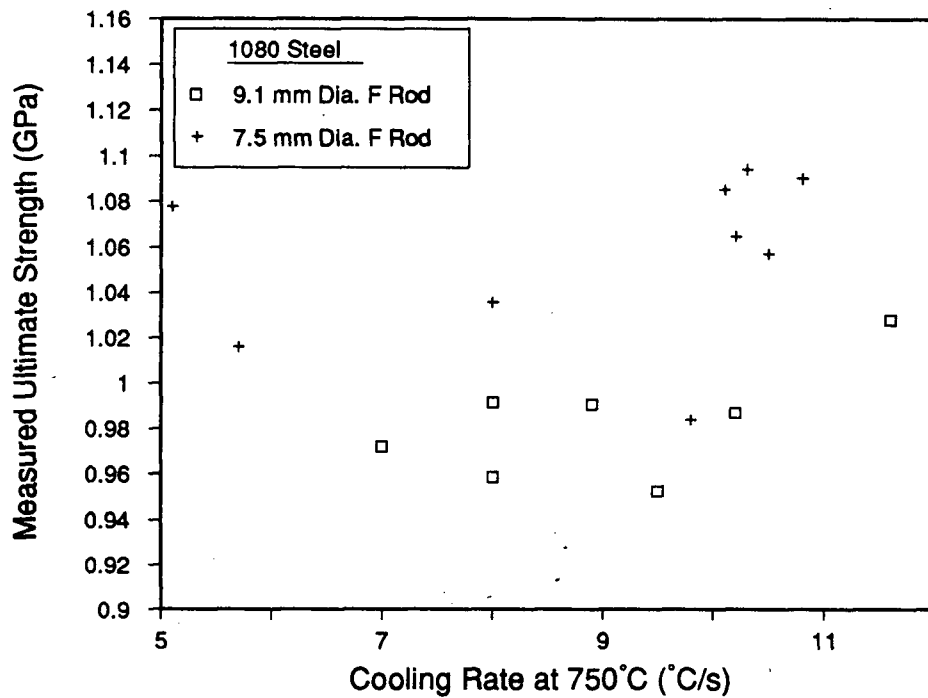
7.4 Mechanical Properties

7.4.1 Experimental Results

Mechanical testing of tensile samples machined from the plant trial rods was accomplished as outlined in Chapter 5. Results included yield strength, ultimate strength and % reduction in area. A complete listing of results obtained from the tests is included in Appendix 3. Figures 7.24 to 7.26 present a summary of measured average yield and ultimate strengths, plotted against the average rod cooling rate, measured at 750°C. The figures are for the 1080, 1035-1038 and 1017-1022 grades, respectively. As was shown for the laboratory tests, the relative strength of the steel is a function of rod cooling rate. In general, as cooling rate increases, a corresponding increase in the rod strength should occur, although this is not exhibited in the data presented in Figs. 7.24 to 7.26. This can be directly related to the change in rod microstructure with varying cooling rate. As was shown in the previous sections, a finer pearlite spacing, decreased ferrite fraction and smaller mean ferrite grain diameter are produced by an increase in steel cooling rate. All of these factors result in an increase in steel strength. However, from the figures, the degree of scatter in the data makes it difficult to distinguish this trend and it can also be seen that the degree to which strength is affected by the cooling rate is related to the composition of the steel.

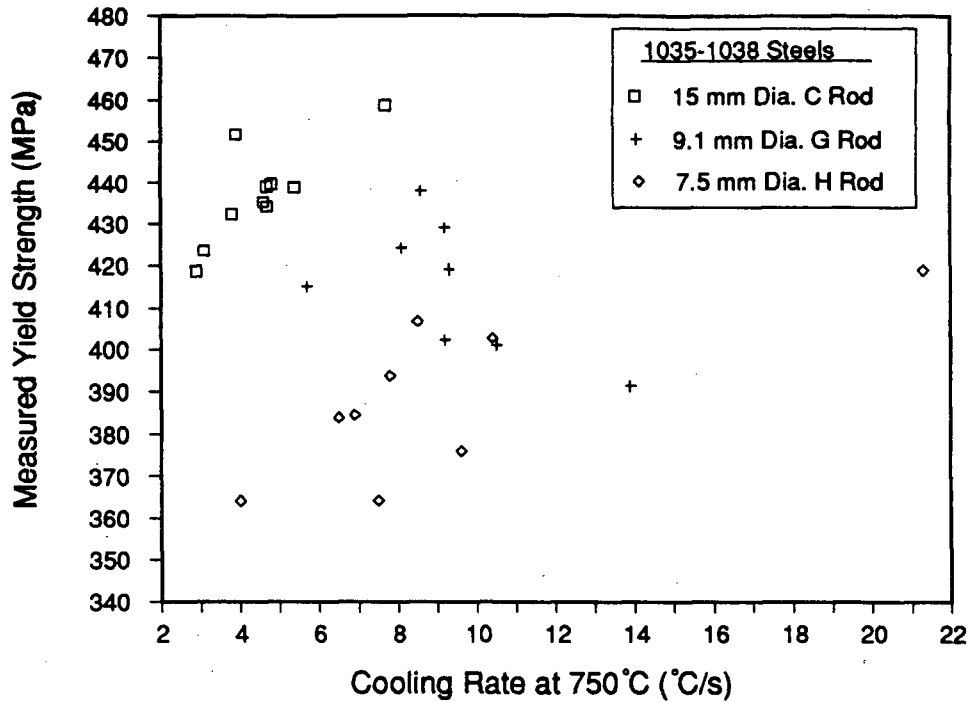


(a)

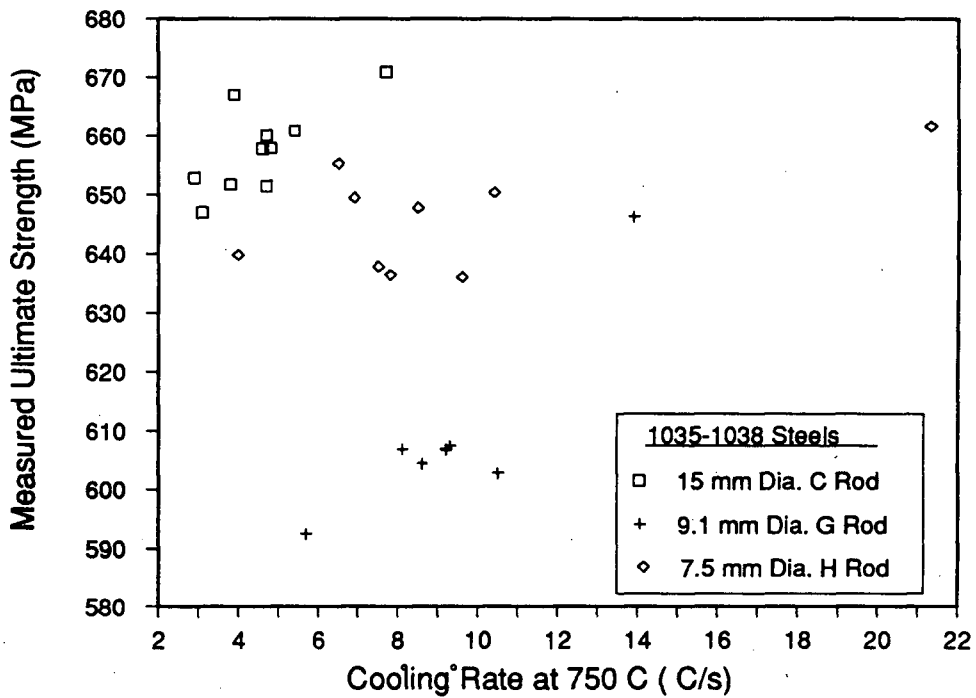


(b)

Fig. 7.24 - Measured strengths of plant trial Steel F (1080) plotted against the average cooling rate at 750°C; (a) yield strength and (b) ultimate strength.



(a)



(b)

Fig. 7.25 - Measured strengths of plant trial Steels C (1038), G (1037) and H (1035) steels plotted against the average cooling rate at 750°C; (a) yield strength and (b) ultimate strength.

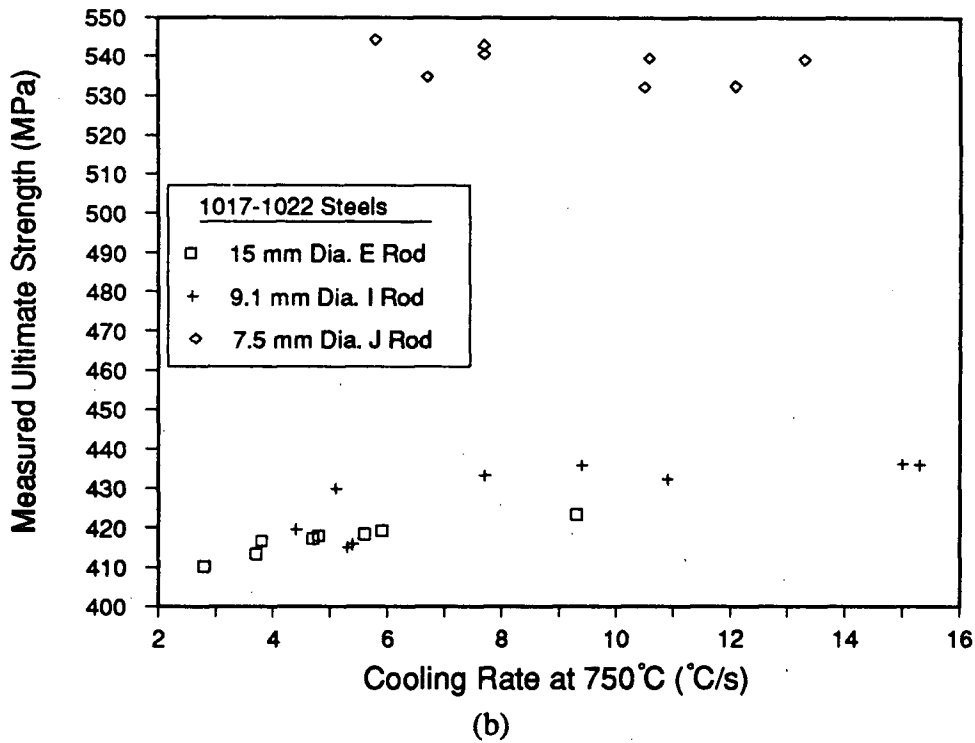
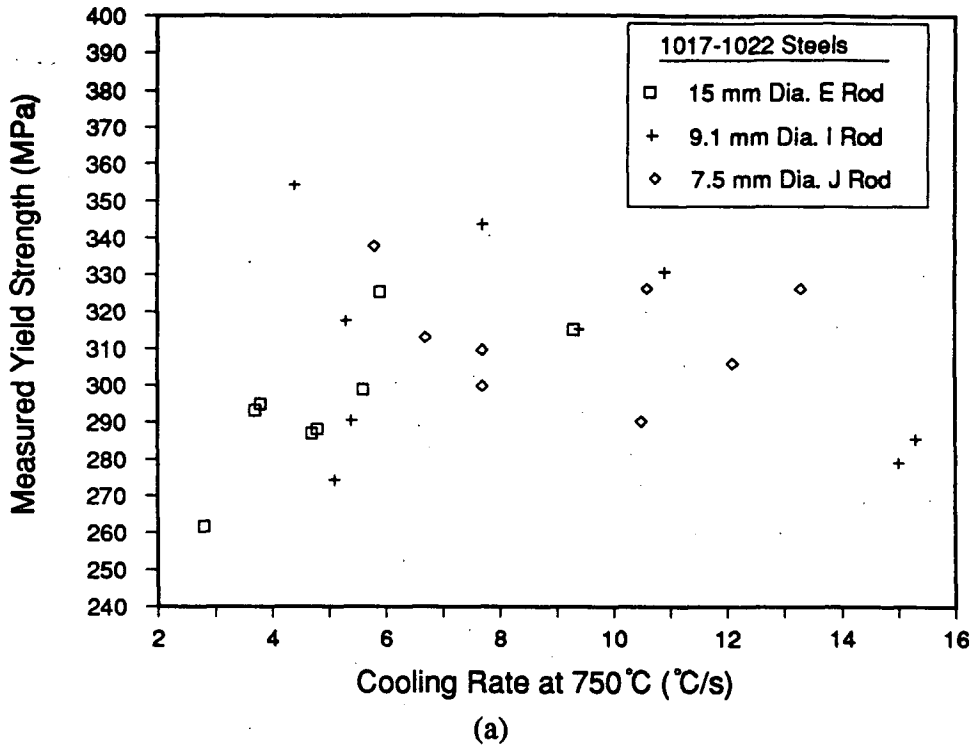


Fig. 7.26 - Measured strengths of plant trial Steels E (1020), I (1017) and J (1022), plotted against the average cooling rate at 750°C; (a) yield strength and (b) ultimate strength.

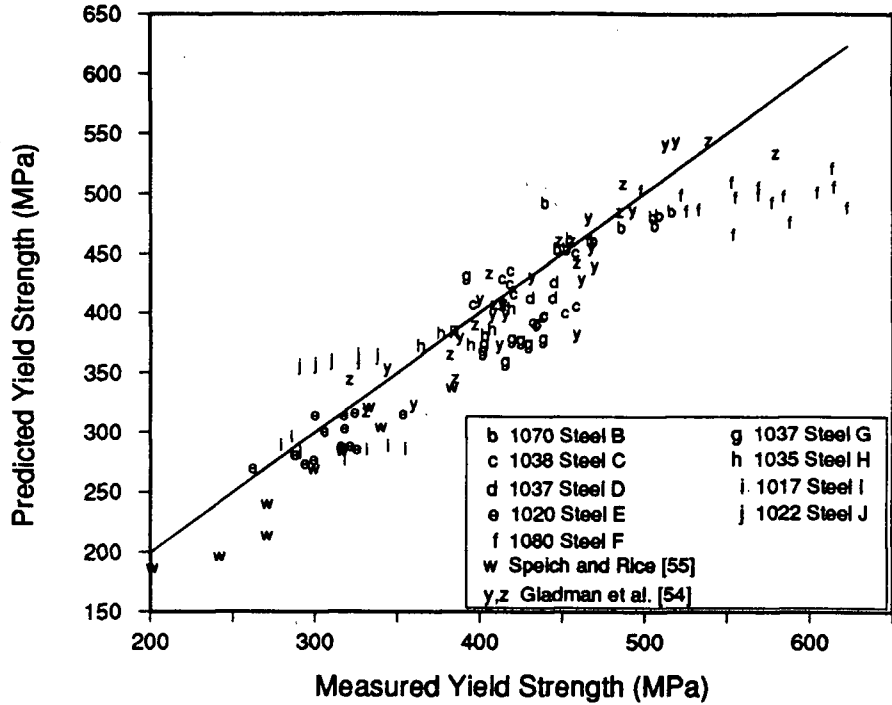
7.4.2 Regression Equations

Prediction of mechanical properties in the laboratory and plant trial steel rods has been attempted applying the equations of Gladman *et al.* [55].

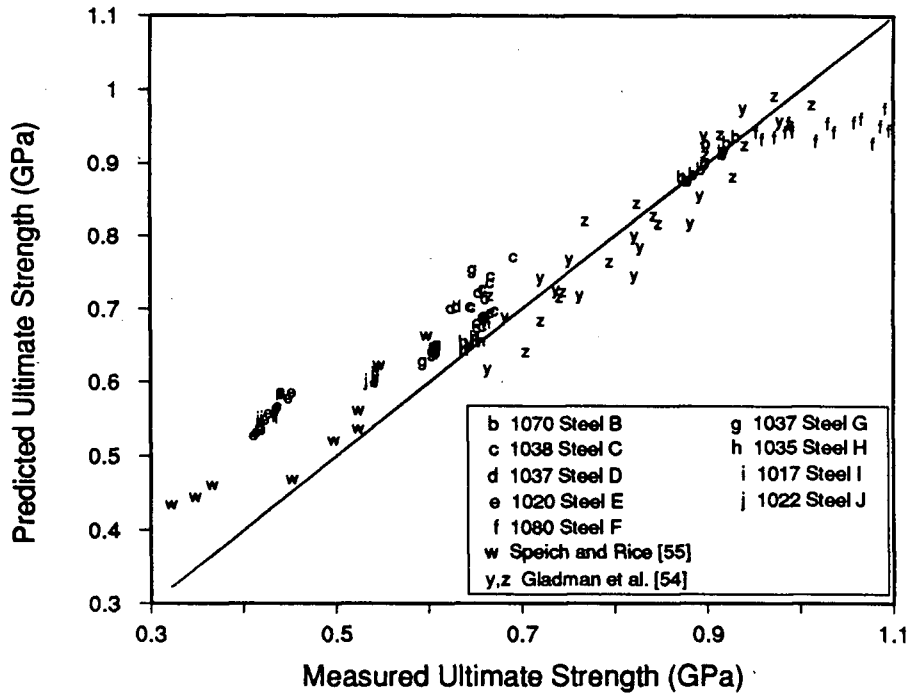
$$YS = f_{\alpha}^{1/3} [35.4 + 58.5\%Mn + 17.4d_{\alpha}^{-1/2}] + (1 - f_{\alpha}^{1/3}) [178.6 + 3.85S_p^{-1/2}] + 63.1\%Si + 425.0\sqrt{\%N} \quad (2.58)$$

$$UTS = f_{\alpha}^{1/3} [246.4 + 1142.7\sqrt{\%N} + 18.17d_{\alpha}^{-1/2}] + (1 - f_{\alpha}^{1/3}) [719.2 + 3.54S_p^{-1/2}] + 97.0\%Si \quad (2.59)$$

These equations were developed employing medium- to high-carbon steels and the nonlinearity of strength with fraction of ferrite is expressed by the f_{α} exponent of 1/3. Utilizing measured microstructural parameters, as determined from the image analyzer and the SEM, and the steel compositions as given in Tables 4.1 and 5.1, predictions of yield strength and ultimate strength in laboratory and plant trial rods have been made. The results are presented in Fig. 7.27 (a) and (b), where predicted yield and ultimate tensile strengths are plotted against the measured values. Pearlite spacings used in the calculations were obtained from the SEM measurements. However, for steels in which the pearlite spacing has not been measured, Eq. (7.8) has been employed to calculate spacing as a function of the relative undercooling below T_{A1} . A large degree of scatter is observed in Fig. 7.27; the fit seems to be poor at low and high carbon contents i.e., small and large ferrite fractions. As an alternative, the equation proposed for yield strength by Kouwenhoven [54] has been considered. However, predominantly low-carbon steels were included in this study and a term for the effect of interlamellar spacing of pearlite on steel strength was not incorporated. Owing to the relatively poor fit obtained with the Gladman equations and the limitations of Kouwenhoven's equation, it seemed that new regression equations, employing laboratory and plant trial data from this study, as well as literature data, should be developed to link strength to steel composition and microstructure.



(a)



(b)

Fig. 7.27 - Predicted-versus-measured strength for laboratory and plant trial rods, as determined from the Gladman equations (Eqs. (2.58) and (2.59)); (a) yield strength and (b) ultimate tensile strength.

The first step was to determine the appropriate form for the equation, recognizing the obvious differences suggested by Gladman *et al.* [55] and Kouwenhoven [54]. For comparison, Kouwenhoven's equation is as follows:

$$YS = 52.9f_{\alpha} + (372.4 + 92.1\%Mn)f_p + 70.6\%Si + 25.5f_{\alpha}d_{\alpha}^{-1/2} \quad (2.57)$$

The Gladman equation for yield strength includes the solid solution strengthening effects of manganese, silicon and nitrogen, whereas Kouwenhoven includes only manganese and silicon. Also, the effect of manganese is attributed to strengthening of the ferrite by Gladman *et al.* whereas it is included in the pearlite term by Kouwenhoven. Due to the observed nonlinear behavior of strength with ferrite fraction in higher carbon steels, the ferrite fraction in the equation of Gladman *et al.* is raised to the 1/3 power. The ferrite exponent is unity in the Kouwenhoven equation. It is not surprising that different equations have been suggested for prediction of yield strength by Gladman *et al.* and Kouwenhoven, when the range of compositions studied by the authors are considered. Most of the grades Kouwenhoven employed, were low-carbon steels with a predominantly ferritic matrix, containing relatively few pearlite colonies. Thus, some strengthening is provided by the pearlite, but it is grain refinement of the ferrite that affects strength the most markedly. However, in the study of Gladman *et al.*, the average carbon content was greater than 0.40% and the pearlite played a much more important role in strengthening of the steel. This resulted in a microstructure in which pearlite formed the matrix, with ferrite being the secondary phase. After comparison of the two equations and identification of the major differences, it was decided that two separate equations could best be utilized to describe strengths in plain-carbon steels; one equation for low-carbon, ferrite-rich microstructures, and the other for high-carbon, pearlite-rich microstructures. Thus, the mechanical properties of steels with less than 50% ferrite were described by adopting the general form of the Gladman *et al.* equations. The mechanical properties of steels with greater than 50% ferrite, were described utilizing a form similar to that of the Kouwenhoven equation.

7.4.2.1 Steels With > 50% Ferrite

For steels containing greater than 50% ferrite, an equation similar to that developed by Kouwenhoven was considered (Eq. (2.57)), employing a ferrite fraction exponent equal to 1. However, a term also was included in the equation to represent the change in strength as a function of pearlite spacing, which was not incorporated in the expression presented by Kouwenhoven. As can be seen in Eq. (2.57), solid solution strengthening due to both manganese and silicon is included. Owing to the small variation of manganese in the laboratory and plant test steels, the regression coefficient calculated by Kouwenhoven has been assumed to be adequate. As a result, a multiple linear regression was performed to determine the coefficients for the effect of microstructural parameters and silicon on the yield strength of steels containing greater than 50% ferrite. The data utilized for the regression analysis included results from laboratory and plant trials, plus yield strengths measured in Stelmor cooled rods by Speich and Rice [56]. Results from Kouwenhoven were not included, because pearlite spacings were not measured in his experiments. The resulting equation is:

$$YS = f_{\alpha} (132 + 11.8d_{\alpha}^{-1/2}) + (1 - f_{\alpha}) (408 + 92.2\%Mn + 0.400S_p^{-1/2}) + 79.7\%Si \quad (7.9)$$

A comparison of regression coefficients between Eqs. (2.57) and (7.9) reveals that the solid solution strengthening effect of silicon in the earlier and the present equations, is essentially the same - 70.6 as opposed to 79.7 MPa/%, respectively. The strengthening coefficient for pearlite friction stress, 372.4 and 407.7 MPa, is comparable in both equations as well. Considering the friction stress associated with ferrite, the value of 131.6 MPa in Eq. (7.9), is in excess of those reported by Eqs. (2.57) and (2.58); 52.9 and 35.4 MPa, respectively. The reason for the difference is not clear but the friction stress is known to be influenced by interstitial and substitutional atoms, precipitates, temperature of testing and strain rate. The contribution of the ferrite grain diameter term is not as significant in the present steels. This may be due to the inclusion of a pearlite spacing term in Eq. (7.9). Figure 7.28 presents a

comparison of calculated yield strength (Eq. (7.9)), versus measured yield strength. Included in the figure are plant and lab test results plus the yield strength of appropriate steel grades from Speich and Rice. The grey region shown in the figure represents \pm one standard deviation of the estimated value; for Eq. (7.9) this was found to be 29 MPa. Good agreement has been obtained between measured and predicted strengths.

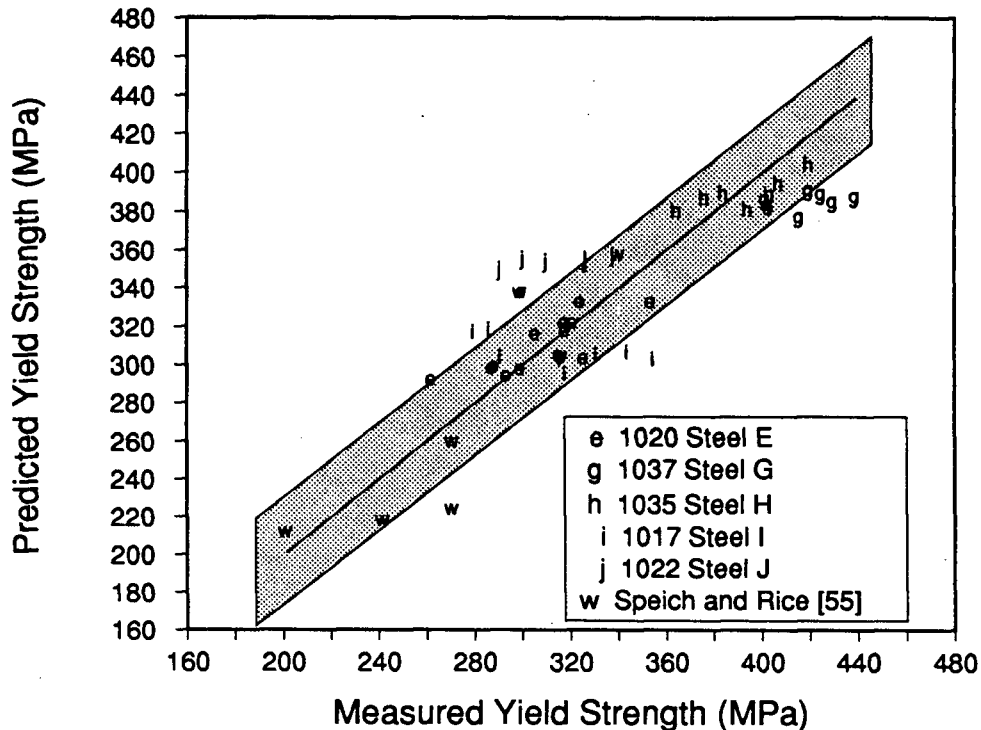


Fig. 7.28 - Predicted-versus-measured yield strength for steels containing greater than 50% ferrite. Predicted values are based on Eq. (7.9).

Although only yield strengths were considered for the development of Eq. (2.57), a similar form has been adopted for the prediction of ultimate strength as a function of steel microstructure and composition. The effect of solid solution strengthening by manganese has not been considered for the UTS, as initial regression analysis attempts resulted in a negative coefficient for the manganese term. In addition, Gladman *et al.* noted that manganese did not contribute significantly to ultimate strength in their study on structure/property relationships. Initial regression equations contained a large coefficient for the solid solution strengthening

effect of silicon; ~ 1000 MPa/%. Compared to coefficients reported in the literature, this value seemed excessively high, and was thus set equal to 500 MPa/%. The regression was completed for the remaining terms. The resulting equation is as follows:

$$UTS = f_{\alpha} (197 + 15.9d_{\alpha}^{-1/2}) + (1 - f_{\omega}) (592 + 0.791S_p^{-1/2}) + 500\%Si \quad (7.10)$$

Considering the constants for ferrite and pearlite strengths, when the ferrite diameter and pearlite spacing go to infinity, indicated by Eq. (7.10), values are comparable to those determined by Gladman *et al.*, Eq. (2.59); 197 and 592 MPa relative to 246.4 and 719.2 MPa respectively. Predictions of UTS based on Eq. (7.10) are displayed in Fig. 7.29. Good agreement is exhibited between the predicted and measured values. Once again the shaded area indicates \pm one standard deviation of the estimated value, which in this case was 18 MPa.

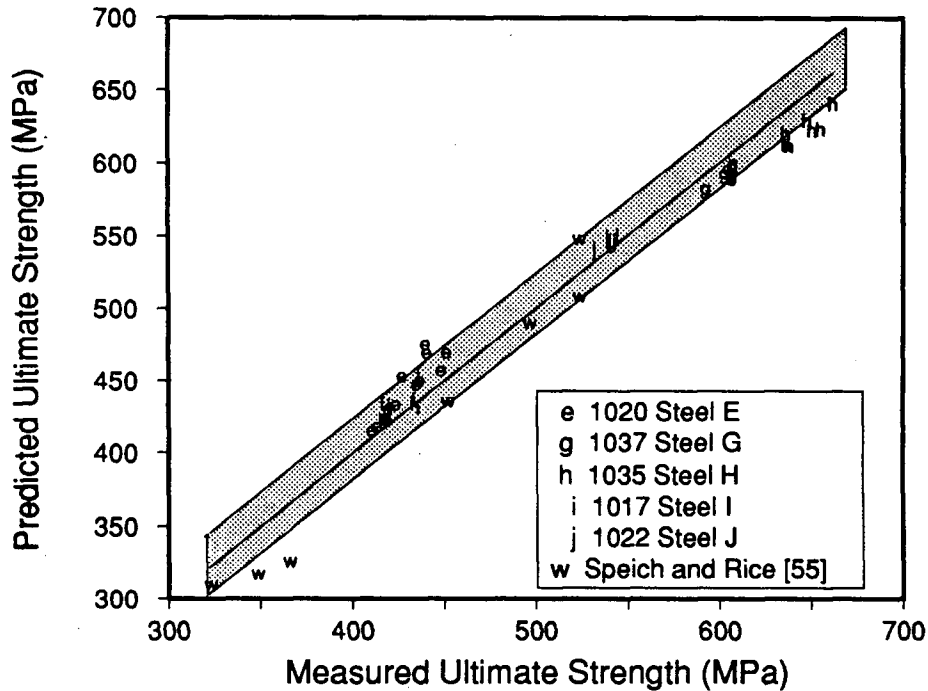


Fig. 7.29 - Predicted-versus-measured ultimate tensile strength for steels containing greater than 50% ferrite. Predicted values are based on Eq. (7.10).

From the good agreement obtained between predicted and measured yield and ultimate tensile strengths in Figs. 7.28 and 7.29, it would seem that Eqs. (7.9) and (7.10) are suitable for estimating steel strength as a function of microstructure and composition, for steels with a grain structure that is predominantly ferrite.

7.4.2.2 Steels With < 50% Ferrite

For steels containing less than 50% ferrite, the form of the Gladman equation, having a ferrite fraction exponent of 1/3, has been assumed. The regression coefficients for silicon and manganese in Eq. (2.58), i.e. yield strength equation, have been assumed to be valid for the present regression analysis. Solid solution strengthening by nitrogen has not been considered in the present analysis, owing to the consistently low nitrogen levels measured in the laboratory and plant trials steels; i.e., 0.004 to 0.006 wt% (Tables 4.1 and 5.1). Employing a multiple linear regression technique, the remaining coefficients in Eq. (2.58) have been evaluated applying data from the laboratory and plant steels as well as those from Speich and Rice [56]. The data of Gladman *et al.* was not included, owing to the much higher levels and greater range of nitrogen, as compared to the laboratory and plant grades. The best-fit regression equation obtained is as follows:

$$YS = f_{\alpha}^{1/3} (136 + 58.5\%Mn + 13.2d_{\alpha}^{-1/2}) + (1 - f_{\alpha}^{1/3})(8.76 + 8.00S_p^{-1/2}) + 63.1\%Si \quad (7.11)$$

A comparison of regression coefficients between Eqs. (7.11) and (2.58), shows similar contributions due to ferrite grain diameter. As well, the friction stress indicated for ferrite is in good agreement with the value determined by Eq. (7.9), 136 MPa as compared to 131.6 MPa. However, both of these values are far greater than those indicated in Eq. (2.58), 35.4 MPa or Eq. (2.57) 52.9 MPa. In addition, the friction stress for pearlite, 8.76 MPa, is less than values given in Eqs. (2.57), (2.58) or (7.9), 372.4, 178.6 and 408 MPa, respectively. This may be due to the large regression coefficient for the effect of pearlite spacing in Eq. 7.11. Different coefficients should be expected due to the omission of the nitrogen term in

the present analysis.

Predicted yield strengths, based on Eq. (7.11), are plotted in Fig. 7.30 as a function of measured yield strengths. Included are predictions for laboratory and plant trials, as well as steels from Speich and Rice. The \pm one standard deviation of the estimated value, as indicated in the figure, is equal to 23 MPa. Agreement between predicted and measured yield strength is seen to be quite good. The most obvious improvement in fit shown in the figure when compared with the predicted yield strength from the Gladman equation (Fig. 7.27 (a)), is the change in predicted strengths for the eutectoid grade (Steel F). Owing to the significantly larger coefficient for pearlite spacing given in Eq. (7.11) as compared to Eq. 2.58, and considering the importance of this term in determining strength in high carbon steels, this may be the most important improvement of the present equation over that due to Gladman *et al.*. To provide a measure of goodness of fit obtained by predicting the yield strength with both of these equations, a simple linear regression analysis has been performed, utilizing the measured strength as the independent variable and the predicted strengths as the dependent variables. Forcing the best-fit line through the origin, the correlation coefficients and slopes have been calculated as 0.66 and 0.92 respectively, for the Gladman equation, and 0.89 and 0.997 respectively for Eq. 7.11. These results display the improved fit obtained with Eq. 7.11.

For correlations between microstructure and ultimate tensile strength, Gladman *et al.* found the effect of manganese to be negligible. The manganese term has thus been dropped for the present analysis of UTS. In addition, the effect of nitrogen has not been included for the reasons outlined previously. Initial regressions equations employing the coefficient for solid solution strengthening of silicon, taken from Eq. (2.59), 97 MPa/%, resulted in poor predictions for several of the steels. Increasing the coefficient to 150 MPa/%, as shown in the following equation, provided a much better fit:

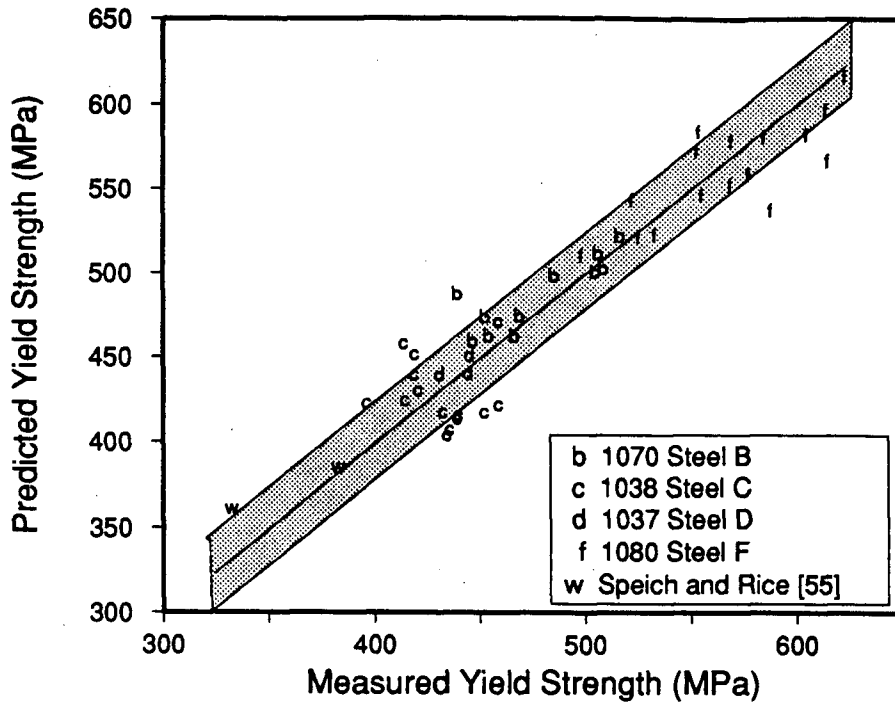


Fig. 7.30 - Predicted-versus-measured yield strength for steels containing less than 50% ferrite. Predicted values are based on Eq. (7.11).

$$\begin{aligned}
 UTS = & f_{\alpha}^{1/3}(197 + 19.7d_{\alpha}^{-1/2}) + (1 - f_{\alpha}^{1/3})(421 + 9.19S_p^{-1/2}) \\
 & + 150\%Si
 \end{aligned} \tag{7.12}$$

The regression coefficients in Eq. (7.12) have been determined by a multiple linear regression technique, employing ultimate tensile strength data from laboratory and plant trials, as well as data from Speich and Rice. Regression coefficients in Eq. (7.12) are comparable to those in Eq. (2.59), except for the strengthening contribution of pearlite.

Predictions based on Eq. (7.12) are included in Fig. 7.31, where predicted ultimate tensile strength is plotted as a function of measured ultimate tensile strength. The figure contains all laboratory and plant data as well as that due to Speich and Rice. Good agreement between predicted and measured UTS is shown for all steels displayed in the plots. The value for standard deviation, included in the plot, was found to be 28 MPa. To compare the better fit obtained with the present equation, over Eq. (2.59) from Gladman *et al.*, a linear regression analysis for the two sets of predicted ultimate tensile strengths as functions of the

measured values, has been performed. The correlation coefficient and slope obtained for Eq. (2.59) were 0.75 and 0.99 respectively, and for the Eq. (7.12) were 0.97 and 1.02 respectively. Once again these results indicate the improvement obtained by the present equation over that of Gladman *et al.*.

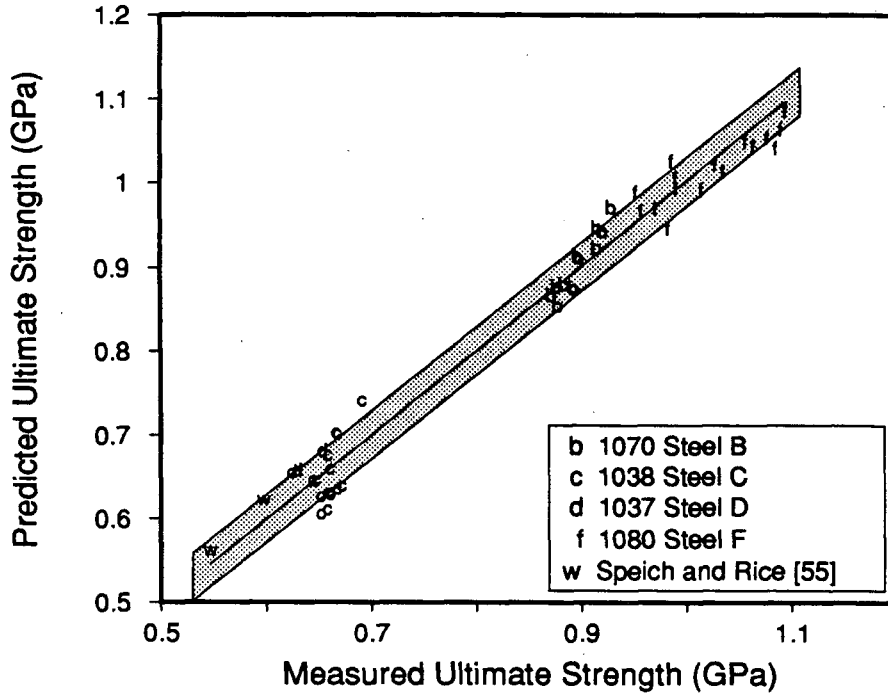


Fig. 7.31 - Predicted-versus-measured ultimate tensile strength for steels containing less than 50% ferrite. Predicted values are based on Eq. (7.12).

7.5 Segregation

Results from segregation checks on the plant and laboratory steels are mostly qualitative in nature. For carbon segregation, visual inspection of the rod cross-section after etching with 2% nital was performed. A low-magnification light microscope aided in the examination, but no appreciable differences in the relative fractions of ferrite and pearlite could be discerned between the central and surface regions in the as received rods. In absolutely no cases was there evidence of centreline segregation. Much the same results were yielded by the sulphur print investigation. For all rods examined, the segregation pattern was

uniform throughout the rod cross-section. The final segregation test performed was the electron probe micro-analysis. Plots of measured Mn% as a function of position in each rod grade are included in Appendix 4. The results show little or no evidence of segregation of manganese in any of the rods tested.

Chapter 8 - MODEL VALIDATION AND PREDICTIONS

8.1 Model Validation

In order to test the internal consistency of the mathematical model, an analytical solution for one-dimensional, radial heat flow from a cylinder has been obtained from the literature. Taken from Kakaç and Yener [86], the solution can be written as:

$$\frac{T(r,t) - T_A}{T_O - T_A} = 2 \sum_{n=1}^{\infty} \frac{1}{\gamma_n} \frac{J_1(\gamma_n) J_o(\gamma_n r/r_s)}{J_o^2(\gamma_n) + J_1^2(\gamma_n)} e^{-\gamma_n^2 Fo} \quad (8.1)$$

where $\gamma_n = \lambda_n r_s$, and $Fo = \alpha t/r_s^2$. Characteristic values for λ_n are the positive roots of the following transcendental equation:

$$\frac{J_1(\lambda r_s)}{J_o(\lambda r_s)} = \frac{Bi}{\lambda r_s} \quad (8.2)$$

where J_1 and J_o are Bessel functions of the first kind, of orders one and zero, respectively. Equation (8.2) can be solved by trial and error, applying the appropriate values for rod diameter and the Biot number. For the present case, the first six roots of Eq. (8.2) were determined.

Solution of Eq. (8.1) has been obtained by setting constant thermophysical properties for steel and assuming values for rod diameter and overall heat-transfer coefficient. The thermophysical properties of steel, as well as initial and ambient air temperatures, were taken as:

$$C_p = 625 \text{ J/kg}^\circ\text{C}$$

$$\rho = 7650 \text{ kg/m}^3$$

$$k = 25 \text{ W/m}^\circ\text{C}$$

$$T_O = 850^\circ\text{C}$$

$$T_A = 20^\circ\text{C}$$

Likewise, the same set of conditions has been applied to the mathematical model, to obtain a numerical solution. Two cooling conditions, representing low and high cooling rates, were considered for comparison between the analytical and model solutions. A rod diameter of 15

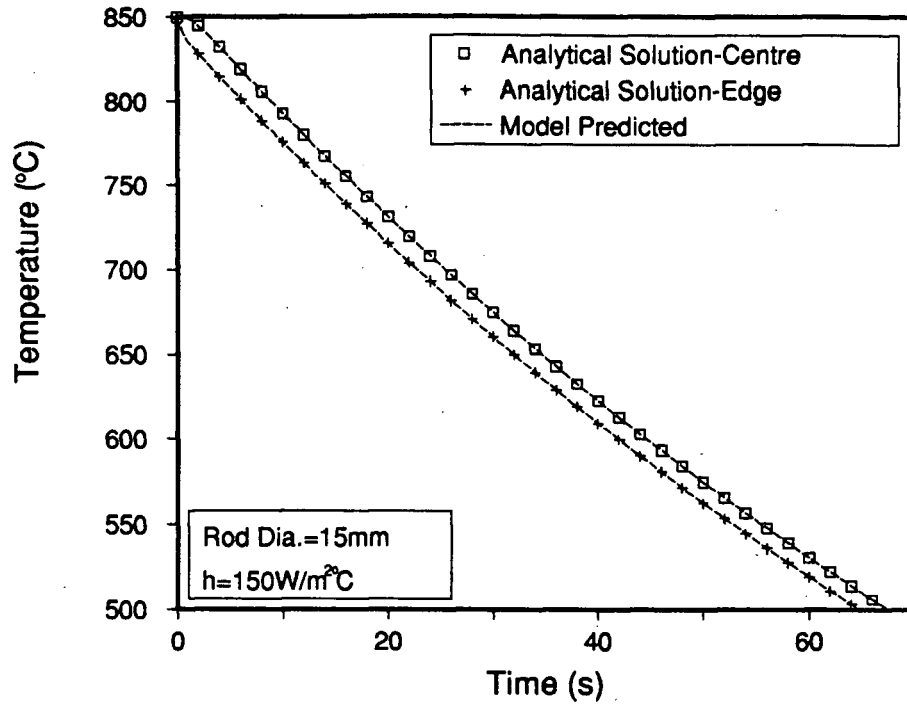
mm and an average heat-transfer coefficient of $150 \text{ W/m}^2\text{C}$, have been utilized for the low cooling rate condition, whereas a 5.5-mm diameter rod and a heat-transfer coefficient of $250 \text{ W/m}^2\text{C}$ represented the high cooling rate. Comparison between the analytical and model solutions is shown in Fig. 8.1 (a) for the 15-mm diameter rod and Fig. 8.1 (b) for the 5.5-mm diameter rod. Plotted in the figures are the predicted cylinder surface and centreline temperatures as a function of time. As can be seen, excellent agreement between the analytical and model solutions has been obtained, thus providing validation of the formulation and numerical technique employed in the model.

8.2 Sensitivity Analysis

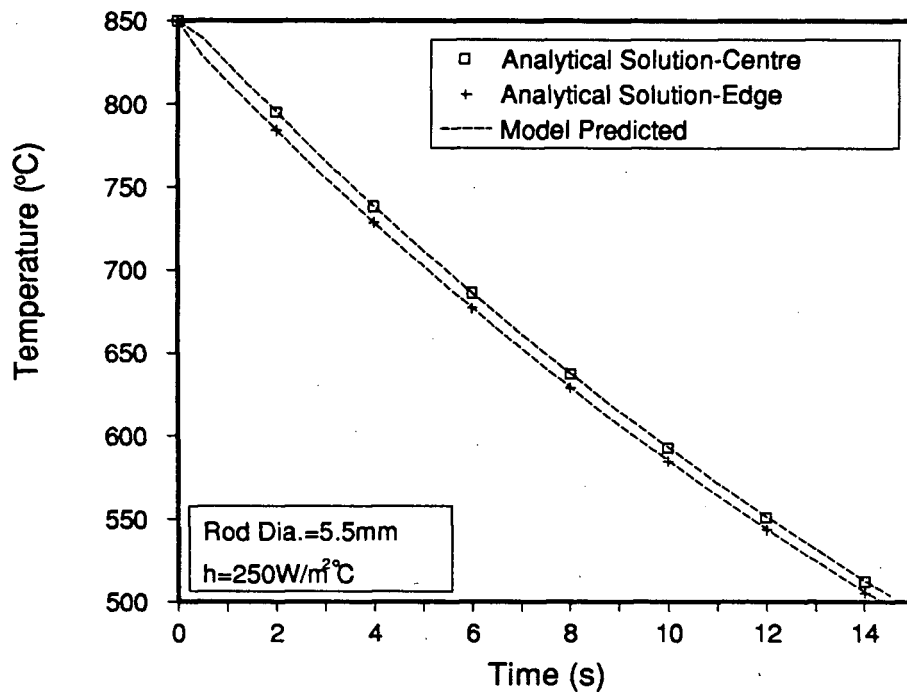
In order to test the influence of some of the variables in the mathematical model on the thermal history, microstructure and mechanical properties of steel rod, a sensitivity analysis has been conducted. Three fictitious steel grades were chosen for the analysis, representing a low-carbon, a medium-carbon and a eutectoid steel. A discussion of results from the sensitivity analysis is included in the following sections. The first section deals with heat-transfer variables, the second with variations in steel composition, and the third with changes that affect the ferrite and pearlite transformation kinetics. A fourth section focuses on the effect of errors involved in the prediction of steel microstructure and their corresponding influence on strength.

8.2.1 Heat Transfer Effects

The most important variables affecting both the thermal history and strength of steel rod are those directly related to heat transfer from the rod. The five parameters included for the sensitivity analysis are the rod diameter, cooling air velocity, heat-transfer coefficient, ambient air temperature and latent heat of the phase transformation. Three general steel grades have been considered for the analysis; 1080 eutectoid, medium-carbon 1040 and low-carbon 1017. The 1080 and 1017 represent the maximum and minimum carbon levels applicable to the model, owing to the compositions of the experimental steels employed in the model development. For comparison, the model-predicted thermal histories for the three



(a)



(b)

Fig. 8.1 - Analytical and model-predicted solution for thermal response at the surface and centreline of a steel rod during cooling. (a) 15-mm diameter rod with $h=150\text{W/m}^2\text{C}$ and (b) 5.5-mm diameter rod with $h=250\text{W/m}^2\text{C}$.

grades are included in Fig. 8.2. As can be seen the 1017 steel has started from a higher initial temperature, which has been necessary because of the higher A_3 temperature for this steel. Evident in this plot is the distinct difference in the cooling behaviour of the three grades corresponding to the austenite decomposition reactions.

Table 8.1 lists the mean values for the parameters included in the analysis. The following paragraphs discuss the results of the sensitivity analysis and the effect of the parameters related to heat transfer.

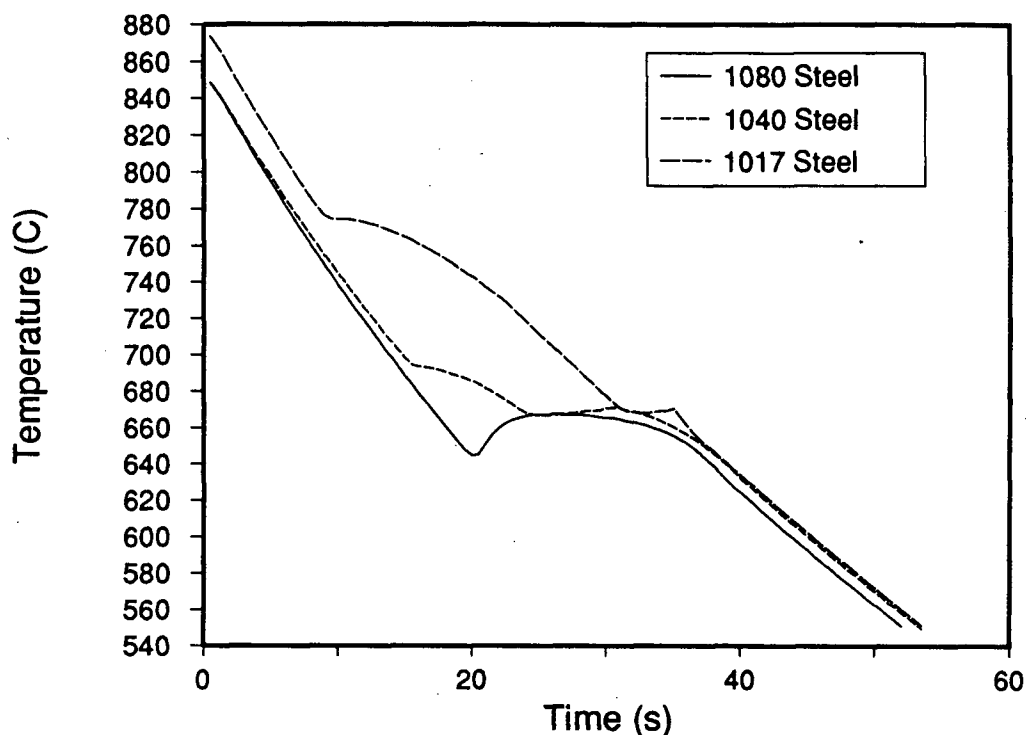


Fig. 8.2 - Model-predicted thermal histories for the 1080, 1040 and 1017 steel grades employed in the sensitivity analysis.

Rod diameter has a strong influence on the cooling rate of the steel as shown in Fig. 8.3 for the maximum and minimum diameters processed on the Stelmor line. The smaller rod diameter produces a lower start temperature for pearlite transformation in the 1080 steel (Fig. 8.3 (a)), which results in an increase in transformation kinetics and a larger relative recalescence for the reaction. These effects are reflected in the microstructure and strength of the

Table 8.1 - Mean values of parameters investigated in the sensitivity analysis of the mathematical model.

Parameter	1080	1040	1017
Rod Diameter (mm)	10	10	10
Air Velocity (m/s)	15	15	15
Heat Trans. Coef. *	n/a	n/a	n/a
Ambient Temp. (°C)	20	20	20
Heat of Transformation *	n/a	n/a	n/a
%C	0.80	0.40	0.17
%Mn	0.75	0.75	0.45
%Si	0.20	0.20	0.20
n_F	n/a	1.16	1.16
n_P	2.2	1.22	0.92
$\ln b_F$ *	n/a	n/a	n/a
$\ln b_P$ *	n/a	n/a	n/a
CCT Ferrite *	n/a	n/a	n/a
CCT Pearlite *	n/a	n/a	n/a
Aust. G.S. (μm)	22	22	22

The (*) symbol in the table indicates parameters investigated in the model which are dependent on steel temperature and cannot be denoted with a mean value. They have been evaluated for the sensitivity analysis by adding or subtracting a predetermined amount from the average predicted value or by correcting the predicted value by a multiplying factor. The values employed for these factors are included in subsequent tables.

1080 material as shown in Table 8.2; as the transformation temperature decreases, a corresponding decrease in pearlite spacing takes place which causes significantly higher strengths. The first line in the table represents the microstructure and strength, as predicted by the model, for the mean steel composition, with mean settings for heat transfer and other parameters as listed in Table 8.1. Thus, the overall effect of varying rod diameter of 10 mm by ± 5 mm, results in up to $\pm 10\%$ variation in the mean predicted yield and ultimate strength. For industrial steel wire rod, a typical, acceptable variation in ultimate tensile strength is ± 70 MPa, which is equivalent to $\pm 7\%$ for a typical eutectoid grade. However, the specification is usually expressed as a minimum desired ultimate tensile strength [87].

Considering the two hypoeutectoid grades, the start temperature for the ferrite transformation has been forced lower with the increase in cooling rate, resulting from a decrease in rod diameter, as shown in Figs. 8.3 (b) and (c). The model predicts a corresponding decrease in ferrite fraction and ferrite grain diameter as given in Tables 8.3 and 8.4. The average pearlite transformation temperature is decreased by the increased cooling rate, which results in a finer pearlite spacing. For the 1040 grade, the strength variation approaches $\pm 10\%$ while for the 1017, it is within $\pm 7\%$ of the predicted mean.

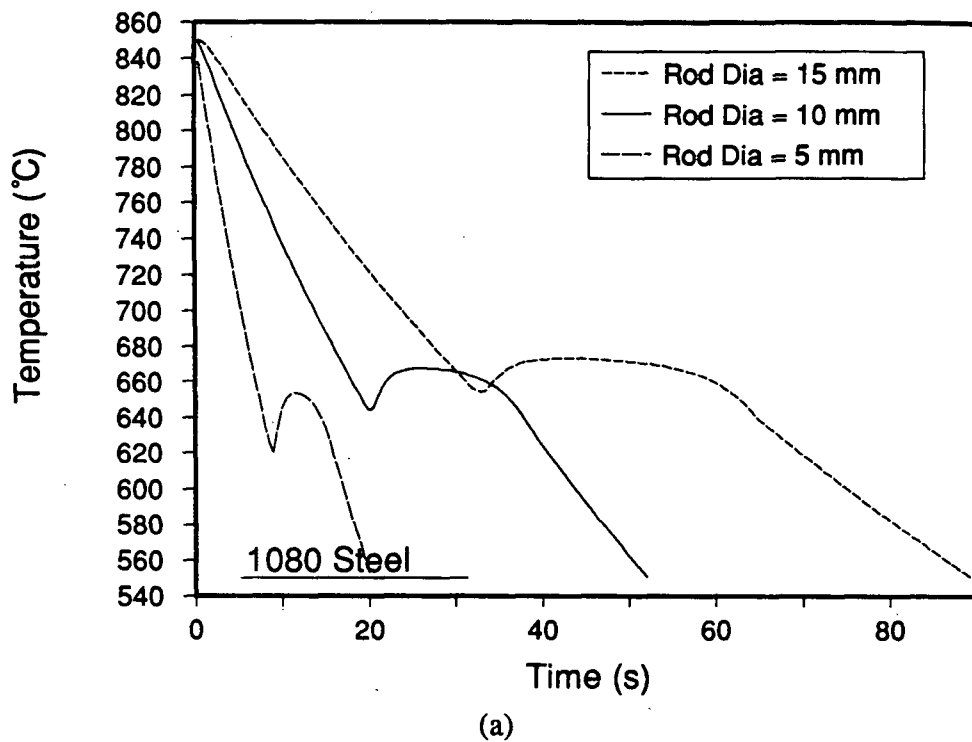


Fig. 8.3 - Effect of variation in rod diameter on the model-predicted thermal history of 10-mm diameter steel rod. (a) 1080 steel, (b) 1040 steel and (c) 1017 steel.

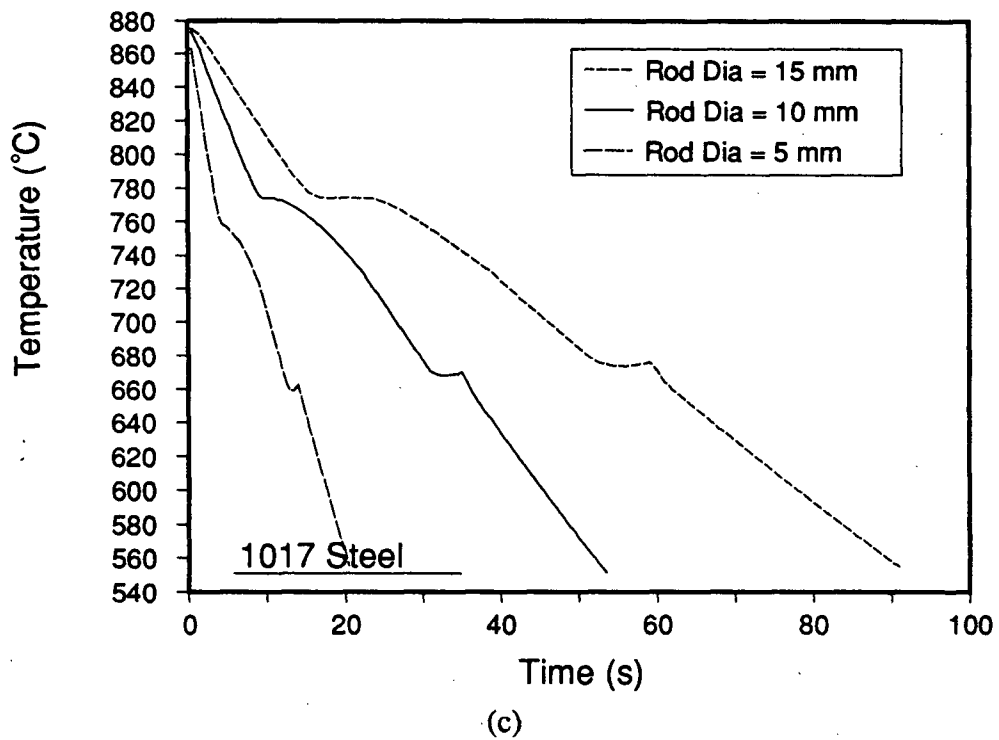
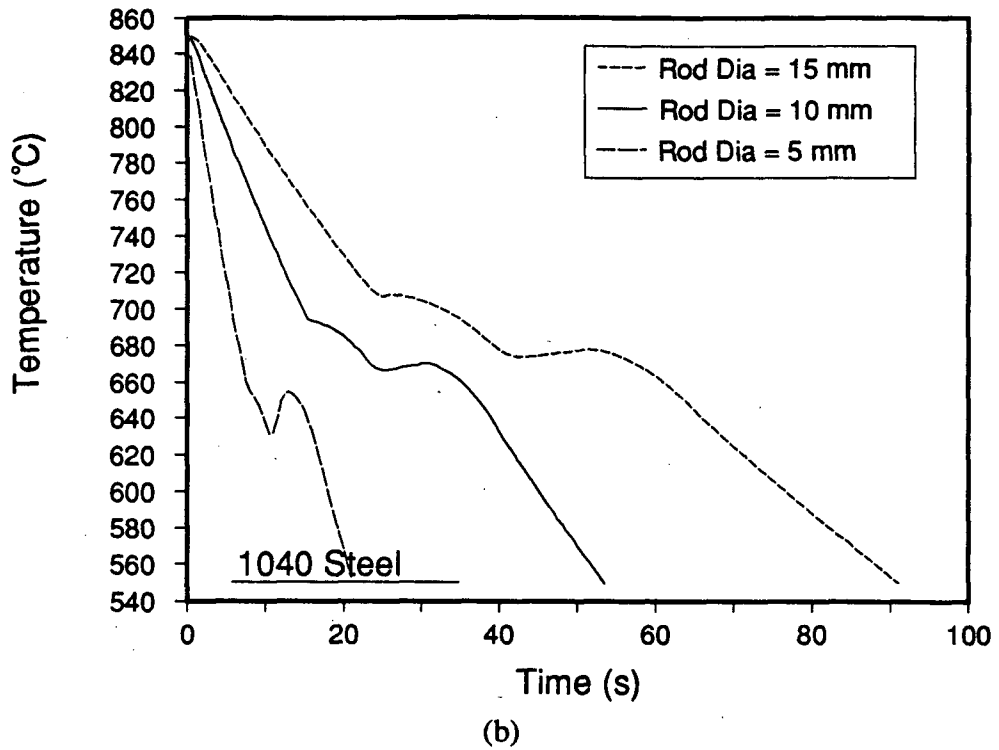


Fig. 8.3 - Effect of variation in rod diameter on the model-predicted thermal history of 10-mm diameter steel rod. (a) 1080 steel, (b) 1040 steel and (c) 1017 steel.

Table 8.2 - Variation in rod microstructure and strength as a function of parameters tested in the sensitivity analysis for 1080 steel.

Parameter	Ferrite Fraction	Ferrite Diameter (μm)	Pearlite Spacing (μm)	Yield Strength (MPa)	UTS (MPa)
Mean Settings	0.000	-	0.239	539.3	1046.3
Rod Dia = 15 mm	0.004	0.95	0.260	533.9	996.7
Rod Dia = 5 mm	0.000	-	0.194	596.2	1111.7
Air Vel = 30 m/s	0.000	-	0.227	552.1	1061.0
Air Vel = 2 m/s	0.003	0.94	0.261	532.4	998.2
h Coef x 1.1	0.000	-	0.235	543.6	1051.3
h Coef x 0.9	0.000	-	0.243	534.4	1040.7
T amb = 40°C	0.000	-	0.240	538.1	1045.0
T amb = 0°C	0.000	-	0.238	539.9	1047.0
Del H x 1.2	0.000	-	0.245	532.7	1038.8
Del H x 0.8	0.000	-	0.231	548.1	1056.4
%C = 0.85	0.000	-	0.237	541.0	1048.3
%C = 0.75	0.005	1.48	0.240	537.4	991.7
%Mn = 0.90	0.000	-	0.238	539.6	1046.7
%Mn = 0.60	0.000	-	0.239	538.5	1045.4
%Si = 0.50	0.000	-	0.239	558.3	1091.4
%Si = 0.02	0.000	-	0.239	527.3	1018.6
CCT P + 2.0 s	0.000	-	0.238	540.5	1047.8
CCT P - 2.0 s	0.000	-	0.240	538.0	1044.8
$n_p + 0.3$	0.000	-	0.254	523.3	1028.0
$n_p - 0.3$	0.000	-	0.223	557.1	1066.8
$\ln b_p + 1.0$	0.000	-	0.255	522.1	1026.6
$\ln b_p - 1.0$	0.000	-	0.222	558.9	1068.9
Aus G.S. = 32 μm	0.000	-	0.226	553.7	1062.9
Aus G.S. = 16 μm	0.000	-	0.249	528.1	1033.5

Table 8.3 - Variation in rod microstructure and strength as a function of parameters tested in the sensitivity analysis for 1040 steel.

Parameter	Ferrite Fraction	Ferrite Diameter (μm)	Pearlite Spacing (μm)	Yield Strength (MPa)	UTS (MPa)
Mean Settings	0.479	4.12	0.246	426.6	644.2
Rod Dia = 15 mm	0.500	4.74	0.275	417.5	633.9
Rod Dia = 5 mm	0.401	3.36	0.201	463.1	707.6
Air Vel = 30 m/s	0.467	3.90	0.225	437.1	660.2
Air Vel = 2 m/s	0.498	4.62	0.281	409.4	617.8
h Coef x 1.1	0.474	4.02	0.234	431.7	651.7
h Coef x 0.9	0.484	4.22	0.252	422.8	638.2
T amb = 40°C	0.480	4.13	0.248	425.7	643.0
T amb = 0°C	0.479	4.10	0.246	427.1	645.0
Del H x 1.2	0.479	4.12	0.244	427.1	644.8
Del H x 0.8	0.479	4.12	0.240	428.0	645.8
%C = 0.43	0.440	3.64	0.240	441.0	671.9
%C = 0.37	0.519	4.59	0.253	415.9	633.0
%Mn = 0.90	0.476	3.47	0.243	448.5	667.2
%Mn = 0.60	0.483	4.76	0.243	409.0	627.3
%Si = 0.50	0.482	4.12	0.241	446.5	689.8
%Si = 0.02	0.478	4.12	0.239	416.9	619.3
CCT F + 3.0 s	0.479	4.12	0.244	427.1	644.9
CCT F - 3.0 s	0.479	4.12	0.244	427.0	644.6
CCT P + 5.0 s	0.479	4.12	0.237	428.7	646.7
CCT P - 5.0 s	0.479	4.12	0.247	426.3	643.9
$n_F + 0.2$	0.479	4.12	0.242	427.4	645.2
$n_F - 0.2$	0.479	4.12	0.243	427.4	645.1
$n_P + 0.3$	0.479	4.12	0.258	424.0	641.2
$n_P - 0.3$	0.479	4.12	0.229	430.7	649.0
$\ln b_F + 0.6$	0.479	4.12	0.246	426.6	644.2
$\ln b_F - 0.6$	0.479	4.12	0.242	427.5	645.3
$\ln b_P + 1.0$	0.479	4.12	0.260	423.5	640.7
$\ln b_P - 1.0$	0.479	4.12	0.224	431.8	650.2
Aus G.S. = 32 μm	0.479	4.12	0.228	430.9	649.1
Aus G.S. = 16 μm	0.479	4.12	0.259	423.7	641.0

Table 8.4 - Variation in rod microstructure and strength as a function of parameters tested in the sensitivity analysis for 1017 steel.

Parameter	Ferrite Fraction	Ferrite Diameter (μm)	Pearlite Spacing (μm)	Yield Strength (MPa)	UTS (MPa)
Mean Settings	0.791	9.27	0.266	315.7	520.6
Rod Dia = 15 mm	0.801	9.60	0.297	311.6	514.0
Rod Dia = 5 mm	0.702	8.31	0.237	340.4	552.4
Air Vel = 30 m/s	0.767	8.83	0.247	323.4	529.9
Air Vel = 2 m/s	0.798	9.51	0.291	312.6	515.6
h Coef x 1.1	0.775	8.94	0.260	321.0	526.8
h Coef x 0.9	0.785	9.14	0.270	317.6	518.1
T amb = 40°C	0.781	9.05	0.275	319.0	520.3
T amb = 0°C	0.779	9.02	0.259	319.7	521.0
Del H x 1.2	0.780	9.03	0.263	319.4	519.6
Del H x 0.8	0.780	9.03	0.269	319.3	521.4
%C = 0.43	0.743	8.58	0.258	329.9	537.7
%C = 0.37	0.805	9.33	0.266	312.3	494.6
%Mn = 0.60	0.779	8.40	0.256	326.3	530.1
%Mn = 0.30	0.781	9.67	0.263	313.0	515.2
%Si = 0.50	0.780	9.02	0.260	343.4	668.5
%Si = 0.02	0.780	9.04	0.273	304.9	434.7
CCT F + 3.0 s	0.781	9.07	0.265	318.8	524.5
CCT F - 3.0 s	0.779	9.01	0.266	319.7	520.6
CCT P + 5.0 s	0.780	9.03	0.248	319.6	521.1
CCT P - 5.0 s	0.780	9.03	0.273	319.3	520.3
$n_F + 0.2$	0.780	9.03	0.266	319.4	522.1
$n_F - 0.2$	0.780	9.03	0.274	319.3	518.2
$n_P + 0.3$	0.780	9.03	0.263	319.4	520.6
$n_P - 0.3$	0.780	9.03	0.271	319.4	520.4
$\ln b_F + 0.6$	0.780	9.03	0.273	319.3	517.1
$\ln b_F - 0.6$	0.780	9.03	0.275	319.3	522.3
$\ln b_F + 1.0$	0.780	9.03	0.281	319.2	520.3
$\ln b_F - 1.0$	0.780	9.03	0.253	319.5	520.9
Aus G.S. = 32 μm	0.780	9.03	0.253	319.5	522.1
Aus G.S. = 16 μm	0.780	9.03	0.275	319.3	519.1

The effect of changing the average air velocity from 15 m/s to 2 m/s and 30 m/s is shown in Fig. 8.4. These values represent maximum and minimum air velocities encountered during the laboratory and plant experiments. The thermal histories exhibit the expected increase in cooling rate with increase in air velocity. As was the case for rod diameter, the overall effect of increasing the cooling rate is to reduce the average transformation temperature, decrease the pearlite spacing, ferrite fraction and ferrite grain diameter, which all produce an increase in rod strength. This effect is seen to be most dramatic for the 1080 steel where a $\pm 5\%$ variation in strength is seen. The strength variation accompanying a change in air velocity is $\pm 4\%$ and $\pm 2\%$ for the 1040 and 1017 grades respectively. The increase in cooling rate and as a result, the increase in steel strength witnessed for an increase in air velocity from 2 to 30 m/s, is not as great as was shown for a decrease in rod diameter from 15 to 5 mm.

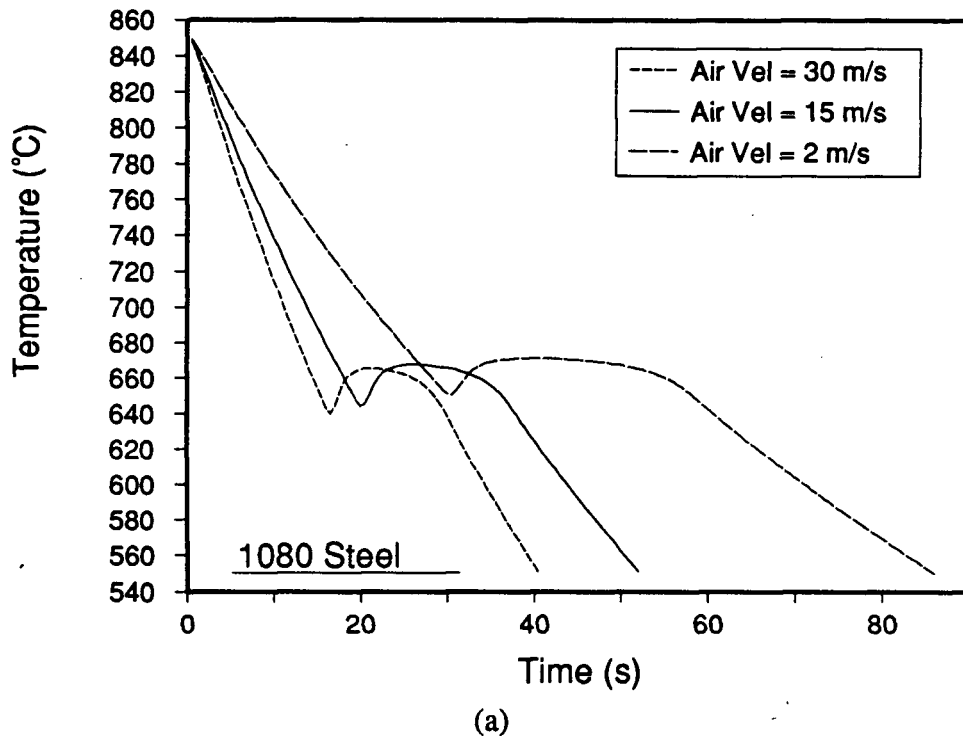
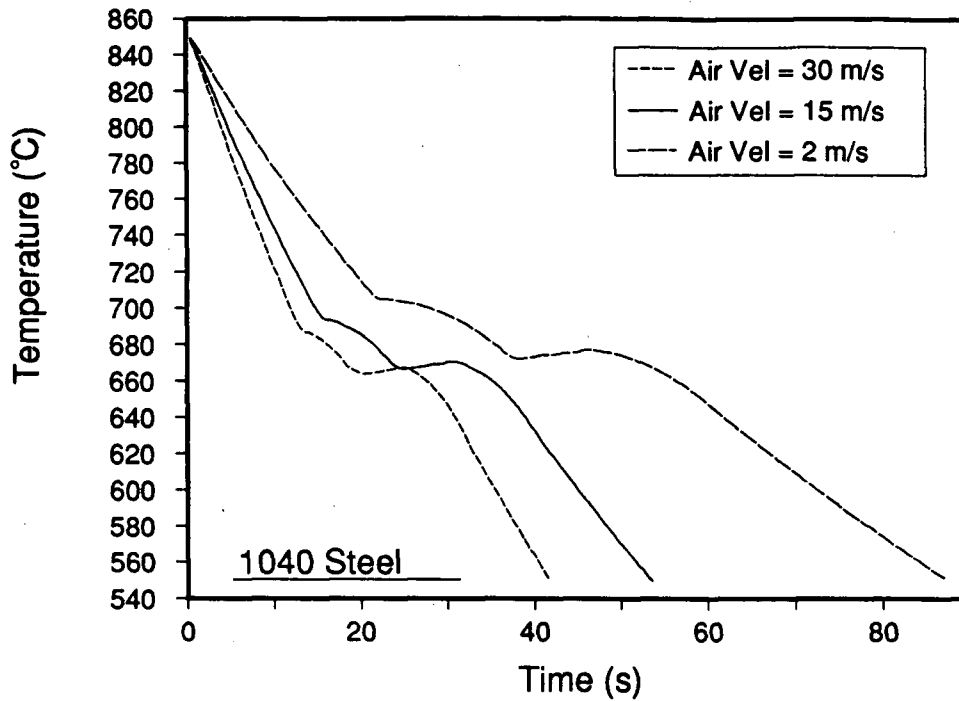
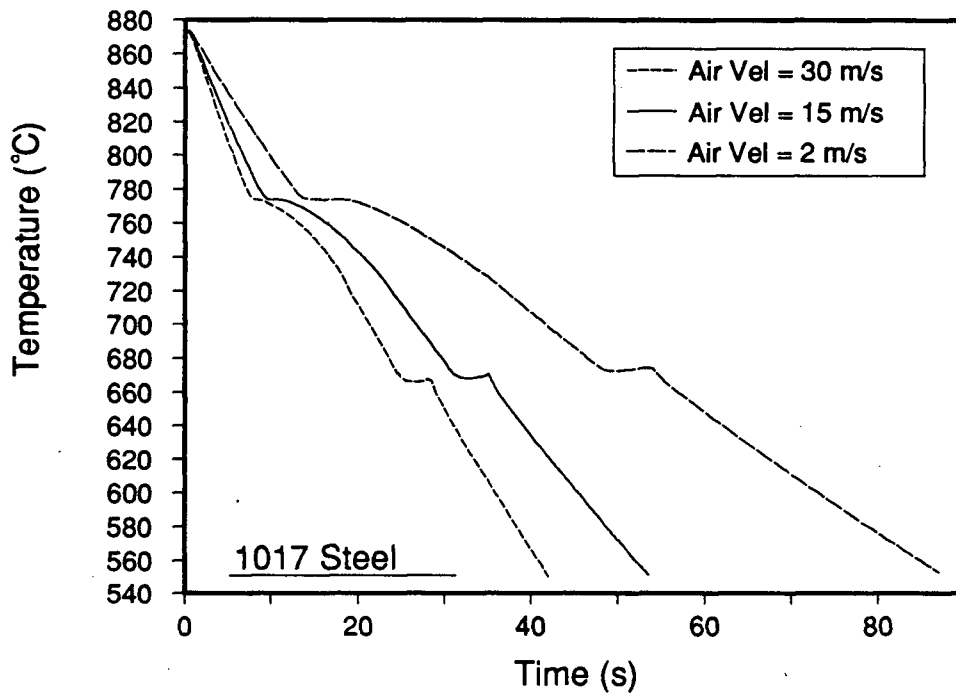


Fig. 8.4 - Effect of variation in cooling air velocity on the model-predicted thermal history of 10-mm diameter steel rod. (a) 1080 steel, (b) 1040 steel and (c) 1017 steel.



(b)



(c)

Fig. 8.4 - Effect of variation in cooling air velocity on the model-predicted thermal history of 10-mm diameter steel rod. (a) 1080 steel, (b) 1040 steel and (c) 1017 steel.

Heat-transfer coefficients in the model are based on the correlations for forced convection and radiation, as outlined in Chapter 3. Owing to the error associated with the use of such correlations for prediction of heat-transfer coefficients, a value of $\pm 10\%$ has been added to the model-predicted overall heat-transfer coefficient to examine its effect on the thermal history and strength of the steel rod. A typical value for the heat-transfer coefficient at the surface of a 10-mm diameter rod in the 500 - 900°C temperature range, is 200 W/m²°C. The predicted thermal histories for these conditions are reported in Fig. 8.5. As can be seen, there is a definite increase in rod cooling rate with increasing heat-transfer coefficient, however, the effect is not as drastic as for the change in rod diameter of 5 to 15 mm or the change in air velocity of 2 to 30 m/s. The change in heat-transfer coefficient results in only a small variation in the predicted microstructure and strength of the steel as seen in Tables 8.2 to 8.4.

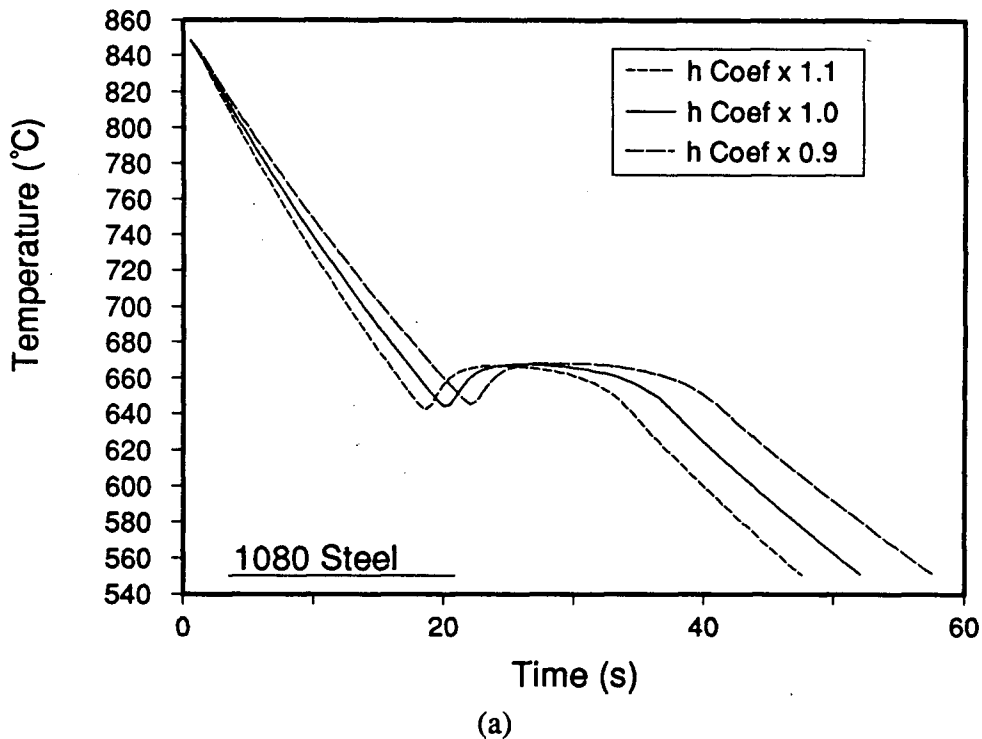
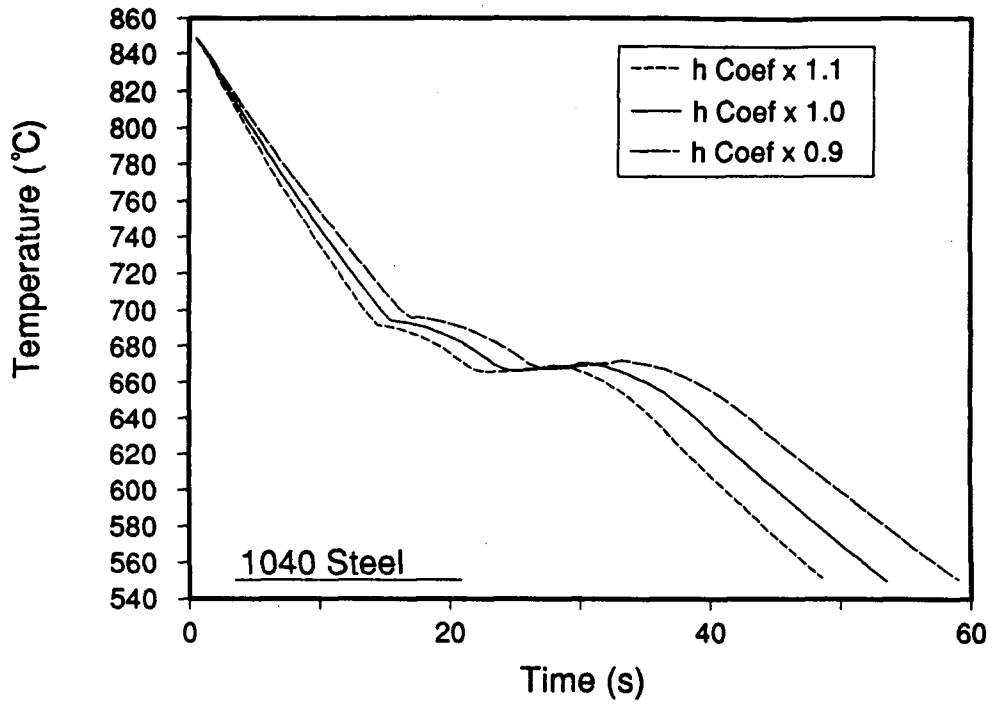
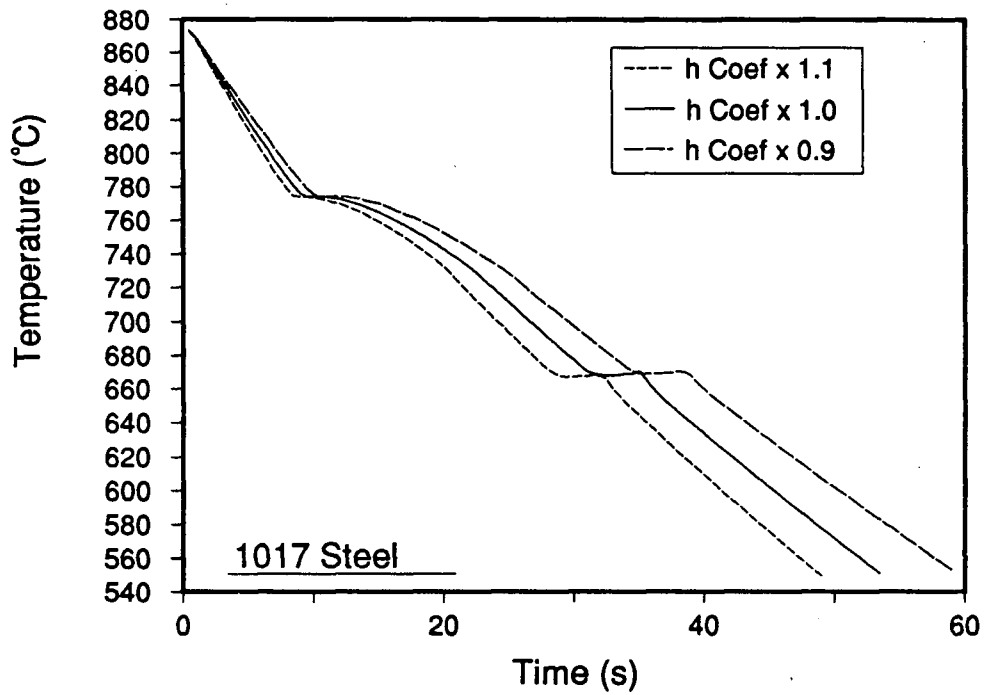


Fig. 8.5 - Effect of variation in heat-transfer coefficient on the model-predicted thermal history of 10-mm diameter steel rod. (a) 1080 steel, (b) 1040 steel and (c) 1017 steel.



(b)



(c)

Fig. 8.5 - Effect of variation in heat-transfer coefficient on the model-predicted thermal history of 10-mm diameter steel rod. (a) 1080 steel, (b) 1040 steel and (c) 1017 steel.

To test the sensitivity of the model to variation in the ambient air temperature, an average temperature of 20°C, with a minimum of 0 and a maximum of 40°C, was chosen. These temperatures represent a realistic variation in the ambient air temperature found during a Canadian winter or summer. Compared with the other variables affecting heat transfer from the rods, the change in air temperature shows little effect on the model-predicted thermal history, Fig. 8.6. As a consequence, there is little change in the microstructure and strength, reported in Tables 8.2 to 8.4. The effect of relative humidity on the heat-transfer coefficient at the surface of the rod was also examined. However, owing to the small amount of water vapor at 100% relative humidity, over the temperature range of interest (~5% volume fraction), it was found that the change in heat-transfer coefficient was negligible. Thus, relative humidity was not included in the sensitivity analysis.

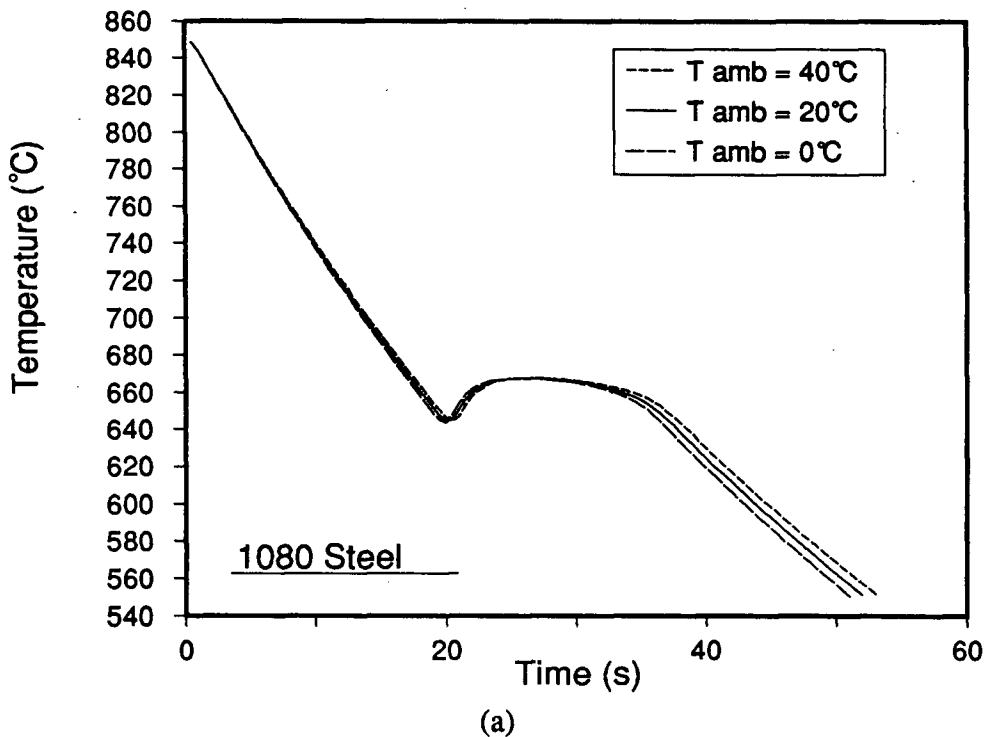
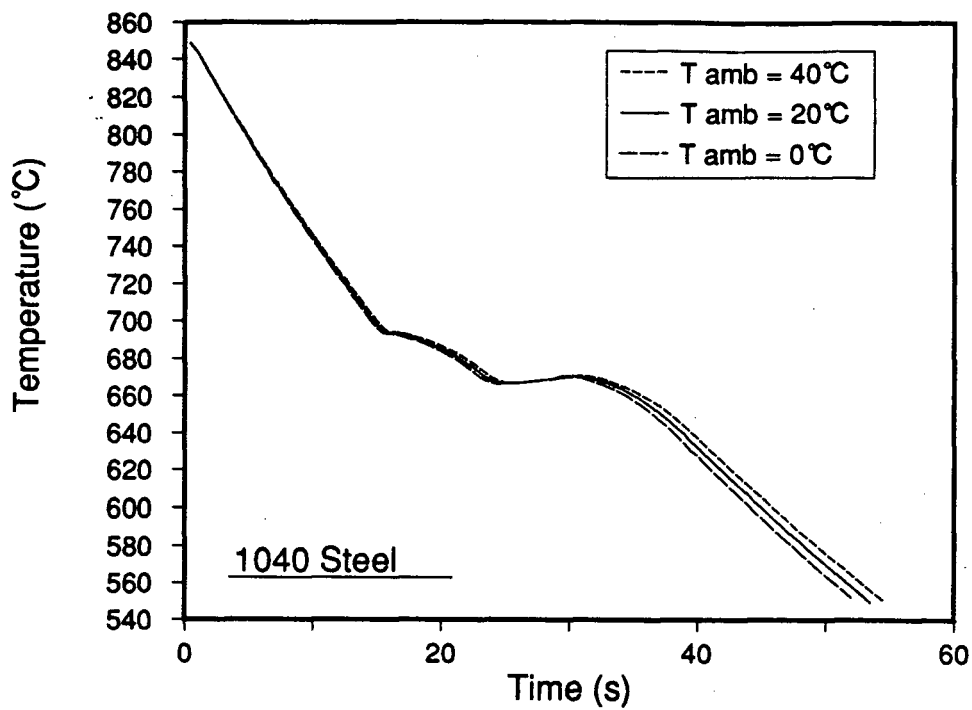
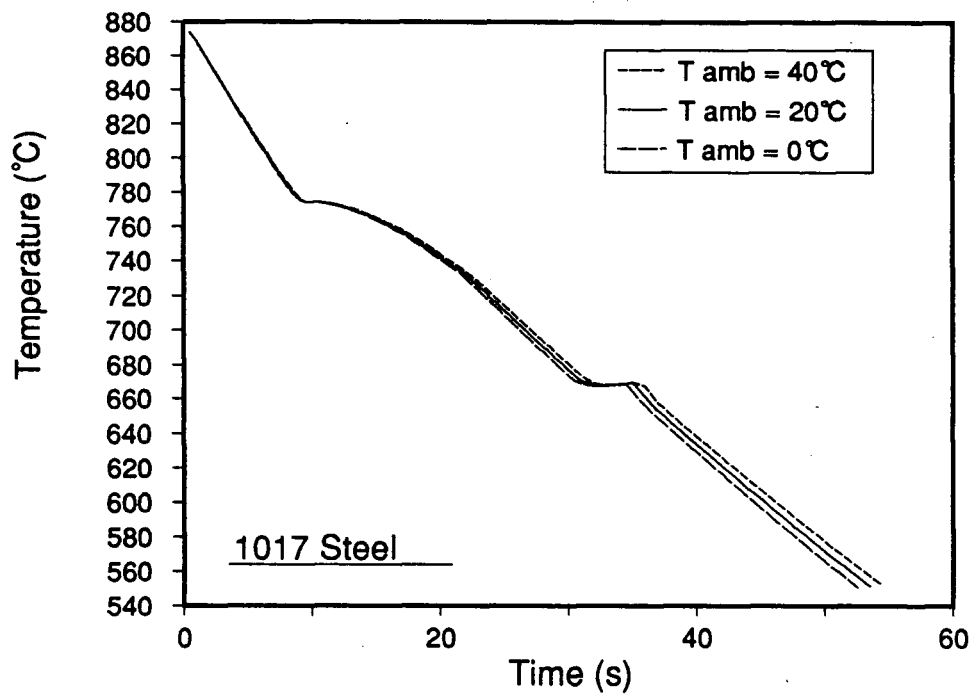


Fig. 8.6 - Effect of variation in ambient air temperature on the model-predicted thermal history of 10-mm diameter steel rod. (a) 1080 steel, (b) 1040 steel and (c) 1017 steel.



(b)



(c)

Fig. 8.6 - Effect of variation in ambient air temperature on the model-predicted thermal history of 10-mm diameter steel rod. (a) 1080 steel, (b) 1040 steel and (c) 1017 steel.

The final parameter to be included in the heat flow sensitivity analysis is the amount of heat released during the phase transformations from austenite to ferrite and pearlite. Literature values for the latent heat of transformation (ΔH) are usually given for pure Fe or Fe-C systems only. It would be expected that the influence of carbon and other alloying elements may change the latent heats of transformation, as indicated by the variation in specific heat of austenite with varying carbon (Fig. 3.2 (a)). Based on this variation and recognizing that the specific heat data used for ferrite has been based on the Fe-C system, a conservative estimate of the error for the prediction of the latent heat of transformation for both reactions has been calculated as $\pm 20\%$. This value was applied to the three steel grades included in the sensitivity analysis, and the results of the predicted thermal histories are reported in Fig. 8.7. The plots show a considerable change in the thermal response of the steel during both the austenite-ferrite and austenite-pearlite phase transformations. The net effect of a decrease in

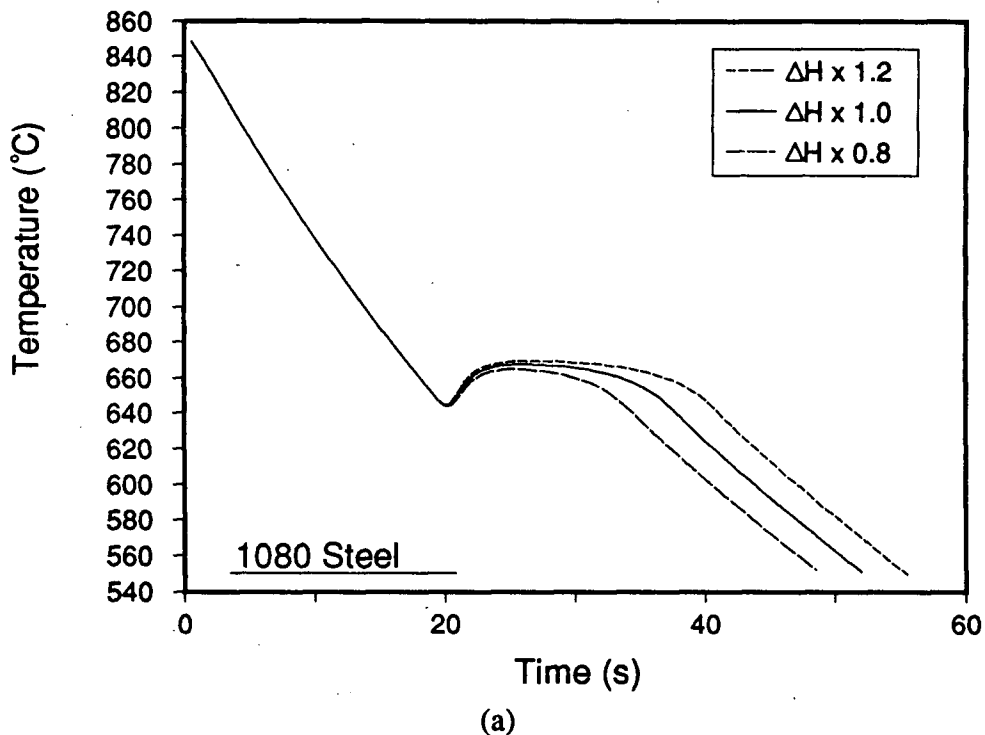
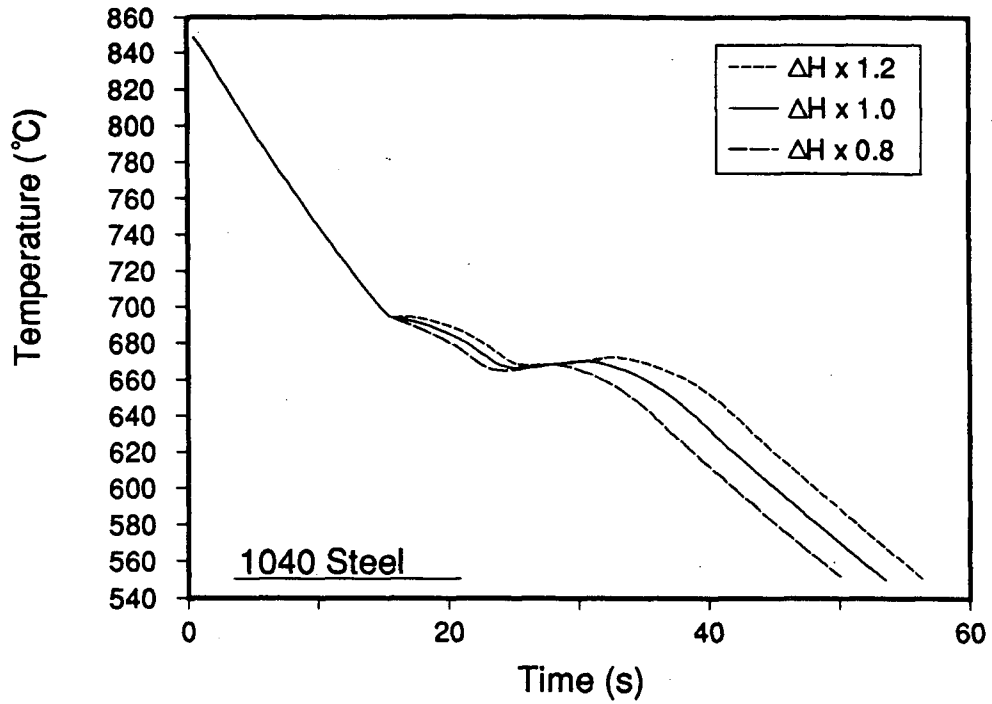
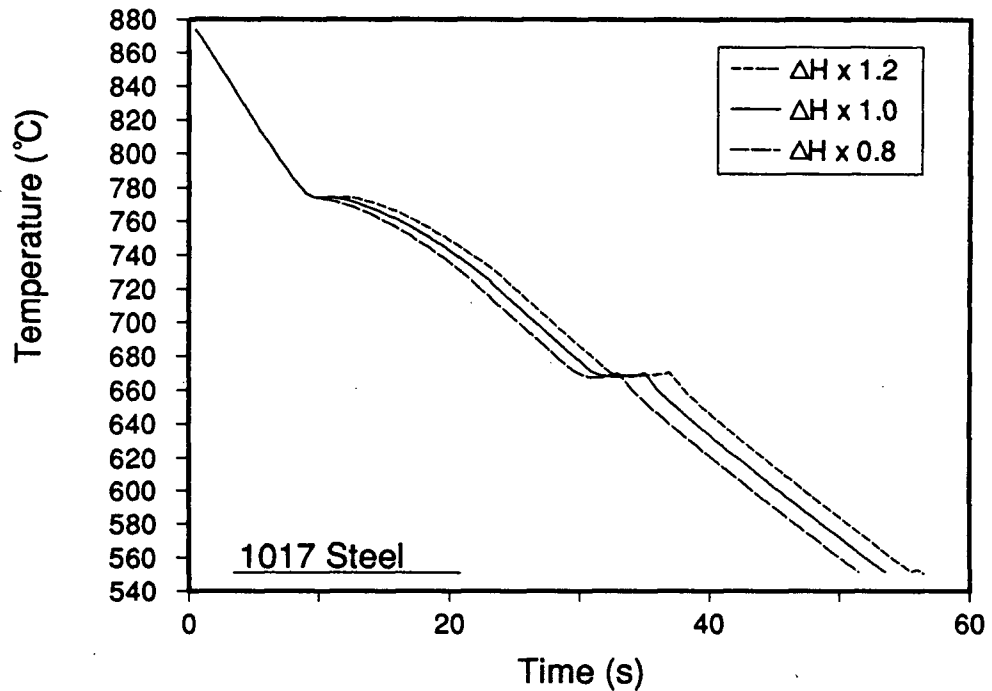


Fig. 8.7 - Effect of variation in latent heat of phase transformation on the model-predicted thermal history of 10-mm diameter steel rod. (a) 1080 steel, (b) 1040 steel and (c) 1017 steel.



(b)



(c)

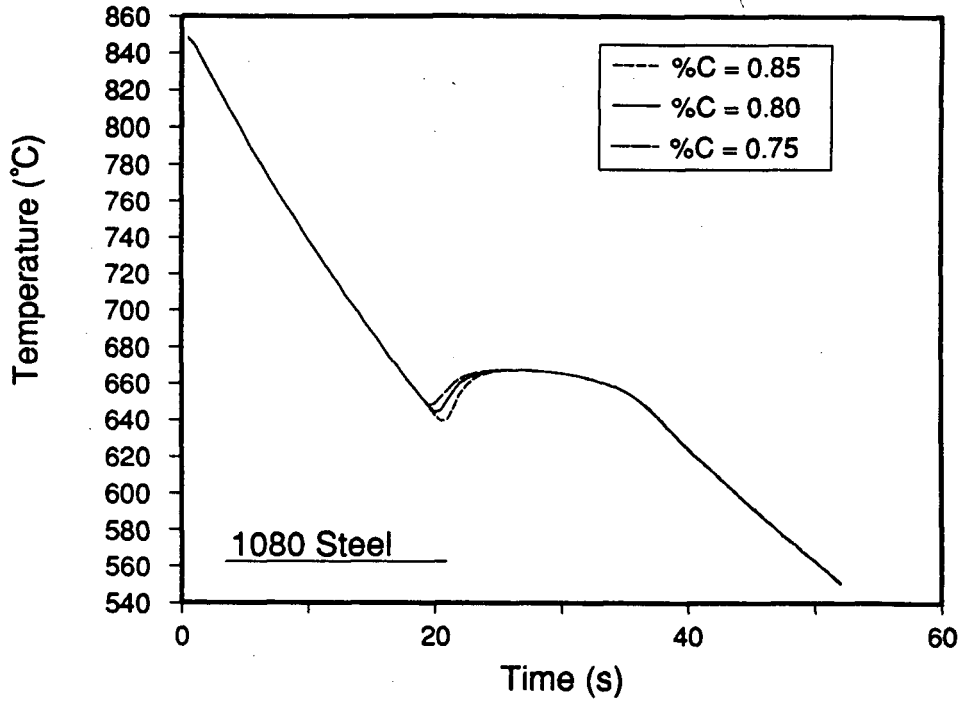
Fig. 8.7 - Effect of variation in latent heat of phase transformation on the model-predicted thermal history of 10-mm diameter steel rod. (a) 1080 steel, (b) 1040 steel and (c) 1017 steel.

the enthalpy of the reaction is to lower the average reaction temperature and to increase the average cooling rate as expected. This change in reaction temperature has resulted in a slight decrease in the pearlite spacing for the 1080 steel, with a corresponding increase in strength, as shown in Table 8.2. However, the effect on the predicted microstructure and strength is not considered to be significant for the two hypoeutectoid grades (Tables 8.3 and 8.4).

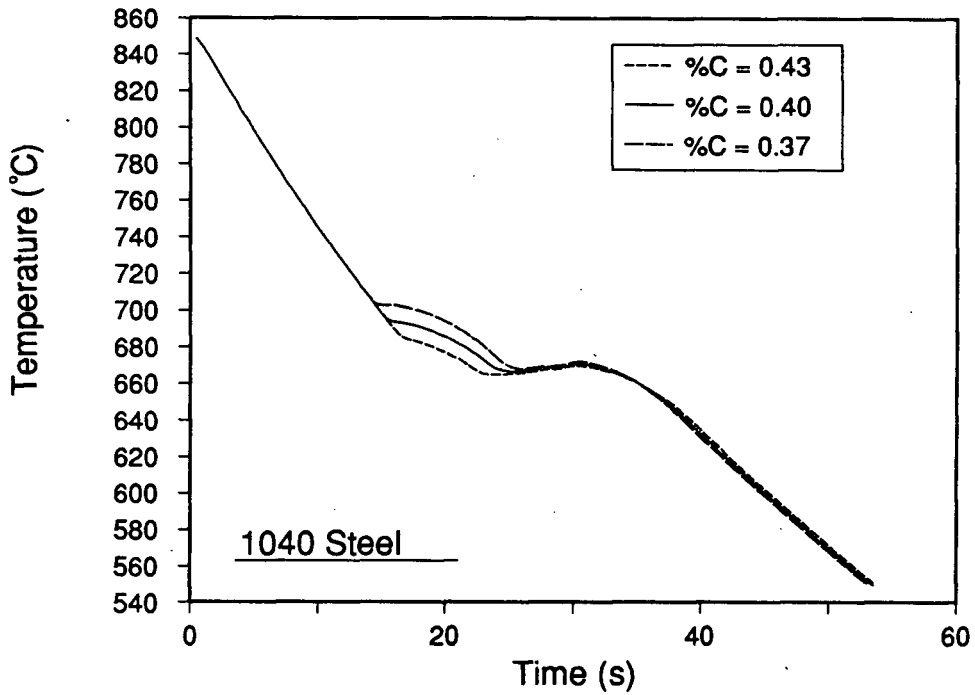
8.2.2 Steel Composition Effects

The major compositional variables in plain-carbon steels are carbon, manganese and silicon. Although many other elements may also be present, by definition they are kept to minor amounts and their effect is considered to be small compared to the primary solutes. The compositions assumed for the steel grades in the analysis are typical of the 10XX steel series [1]. According to the SAE specifications, the concentration of each alloying element has an allowable range. Considering the three steels to be adopted for the sensitivity analysis, the average, maximum and minimum values for these specifications has been applied. As no specification is provided for the concentration of silicon, its values have been determined from typical analyses for plain-carbon steel rod. The mean values for carbon, manganese and silicon concentrations employed in the sensitivity analysis are provided in Table 8.1.

The maximum and minimum carbon levels for each steel grade have been determined from the SAE specifications [1]. They range from 0.15 to 0.20 wt% for the 1017 grade, 0.37 to 0.44 for the 1040 grade and 0.75 to 0.88 for the 1080 grade. For the analysis, the maximum value in the 1040 grade was assumed to be 0.43 and for the 1080, 0.85 %C. It should be noted that although 0.85 %C steel would be expected to form proeutectoid cementite during cooling, for the present case, the microstructure of this grade is assumed to consist of 100% pearlite. Inclusion of this grade is primarily to represent the effect of carbon on the thermal history and properties, of eutectoid plain-carbon steel. Results of thermal history predictions for the variation in carbon concentration are included in Fig. 8.8, while the effect of carbon on the strength of the three grades is given in Tables 8.2, 8.3 and 8.4 for the 1080, 1040 and 1017 steels, respectively. Referring to the thermal history results, the



(a)



(b)

Fig. 8.8 - Effect of variation in carbon content on the model-predicted thermal history of 10-mm diameter steel rod. (a) 1080 steel, (b) 1040 steel and (c) 1017 steel.

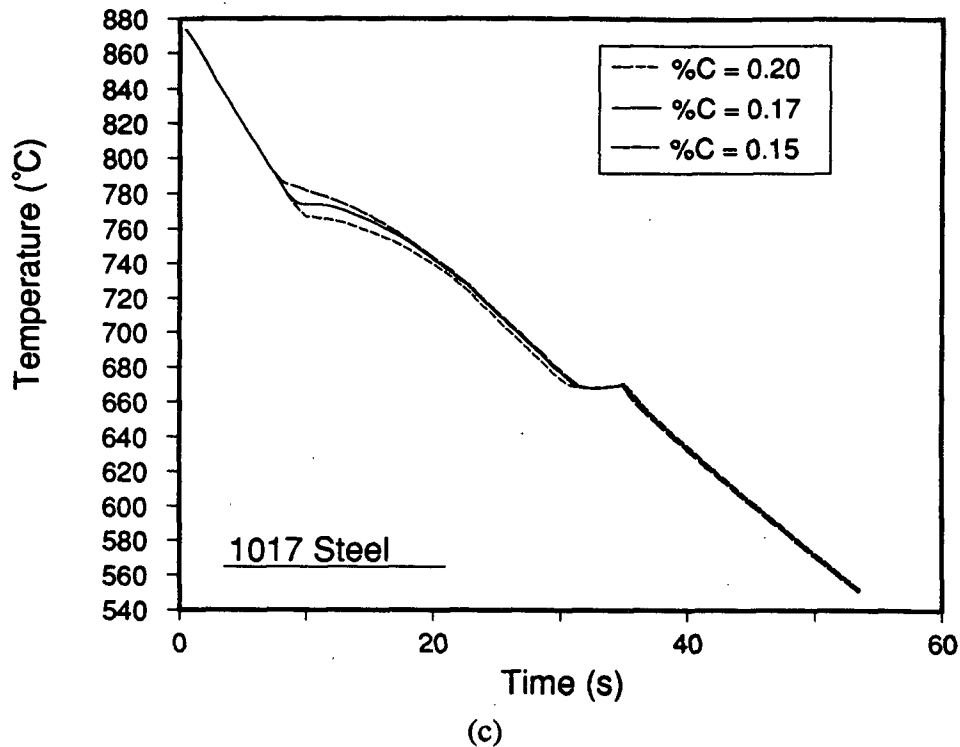


Fig. 8.8 - Effect of variation in carbon content on the model-predicted thermal history of 10-mm diameter steel rod. (a) 1080 steel, (b) 1040 steel and (c) 1017 steel.

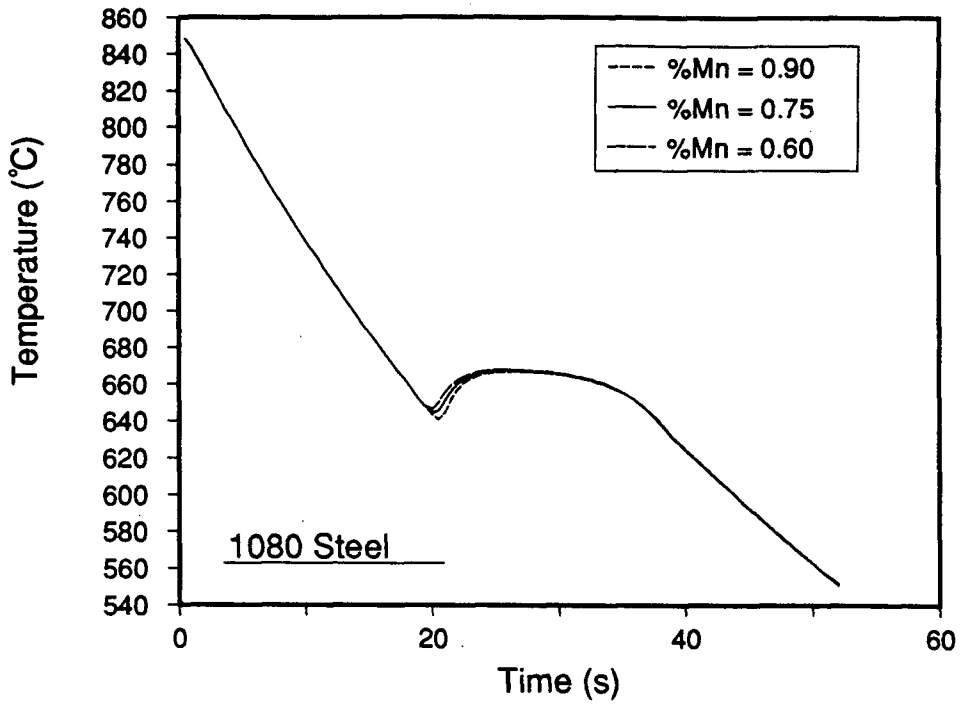
effect of carbon on the start time of the pearlite reaction in eutectoid steel can be seen in Fig 8.8 (a). The increase in carbon makes the steel more hardenable thus decreasing the reaction start temperature. This decrease in reaction temperature is also evidenced by the slight reduction in mean pearlite spacing and increase in strength as reported in Table 8.2. For the 0.75 %C steel, the model has predicted a small fraction of ferrite, 0.005, which has resulted in a significant decrease in the ultimate tensile strength of the material (-5%).

Considering the thermal history results for the 1040 grade, the change in carbon content is seen to have a marked effect on the CCT-start time for the ferrite transformation, as indicated in Eq. (6.12). The ferrite transformation kinetics in the model are also influenced by the carbon content of the steel according to Eq. (6.9), i.e., at a given temperature, an increase in the carbon content of the steel will result in a reduction in the rate of the austenite-ferrite reaction. A change in carbon content also causes variation in steel microstructure and strength, as predicted by the model. As can be seen in Table 8.3, increasing the

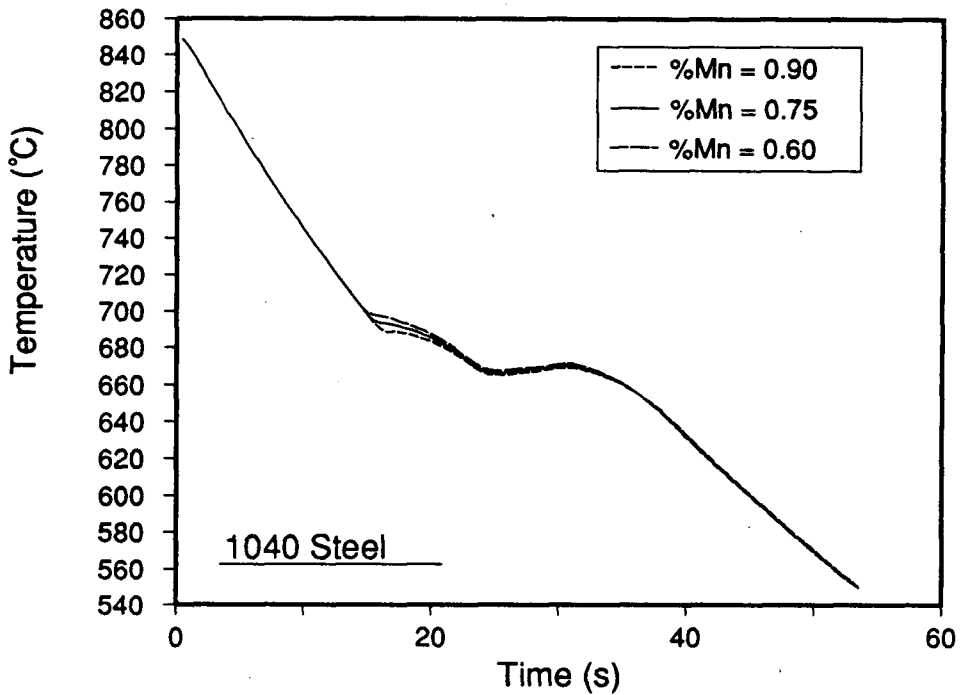
carbon content results in a decrease in the ferrite fraction, ferrite diameter and pearlite spacing, which all combine to increase both yield and ultimate strength. The overall effect is much greater than that seen for the eutectoid grade where the strength increase with increasing carbon content was negligible. For the 1040 grade, the predicted variation in steel strength is ± 2 to 4% of the mean value.

The effect of carbon on the thermal history of 1017 steel is similar to the predictions for 1040, in that there is a significant change in the CCT-start time and the kinetics for the ferrite transformation. In addition, an increase in carbon concentration in the 1017 steel also results in a reduced ferrite fraction, a smaller ferrite grain size and a finer pearlite spacing. The overall effect on variation in strength is of about the same magnitude as that calculated for the 1040 steel.

The effect of variation of manganese on the thermal history for the three steel grades is displayed in Fig. 8.9. The values for %Mn have been determined from the minimum and maximum specified for each grade of steel [1]. For both the 1080 and 1040 grades, the minimum and maximum values are 0.60 and 0.90 wt%, while for the 1017 grade, the specification states 0.30 to 0.60 wt% Mn. Employing these levels in the mathematical model, the effect on thermal history for the three grades is seen to be relatively small. The largest effect observed is a shift in the CCT-start times for the ferrite and pearlite transformations. As was indicated in Eqs. (6.12) to (6.14), the empirical relationships employed for calculating the start times for transformation, include the effect of manganese. In addition, Mn will affect the A_1 and A_3 temperatures, changing the relative undercooling for each reaction. A greater influence is predicted on microstructure and strength of the hypoeutectoid steel grades, as indicated in Tables 8.3 and 8.4. For these grades, manganese is a solid solution strengthening agent and increases hardenability, the latter of which leads to a decrease in ferrite fraction and ferrite grain diameter. The combination of these factors produces an increase in yield and ultimate strength for the hypoeutectoid grades. The effect seems to be greatest for the 1040 grade with strength varying approximately $\pm 3.5\%$ for the Mn levels included. For



(a)



(b)

Fig. 8.9 - Effect of variation in manganese content on the model-predicted thermal history of 10-mm diameter steel rod. (a) 1080 steel, (b) 1040 steel and (c) 1017 steel.

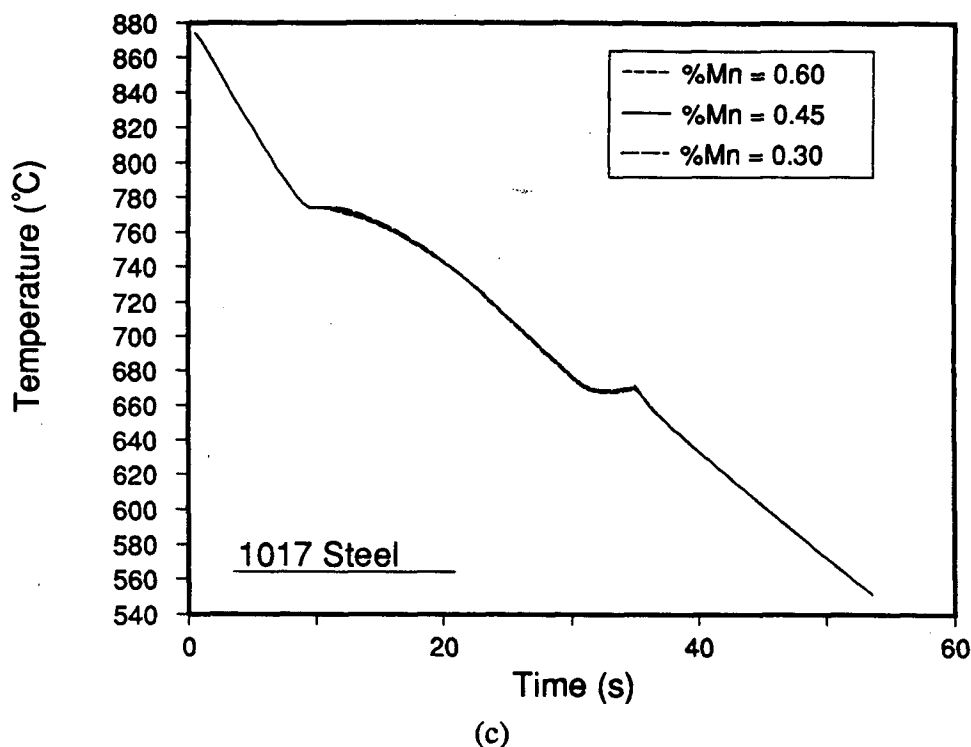


Fig. 8.9 - Effect of variation in manganese content on the model-predicted thermal history of 10-mm diameter steel rod. (a) 1080 steel, (b) 1040 steel and (c) 1017 steel.

the 1080 steel, little or no effect on steel strength is predicted with the change in Mn, since Eq. (7.11) assumes that the solid solution strengthening effect of manganese in predominantly pearlitic steels, takes place only in ferrite. Thus, except for a slight reduction in the pearlite transformation temperature and an associated change in pearlite spacing, the strength and microstructure remain unchanged with a variation in manganese content for the 1080 grade.

The third compositional variable considered in the sensitivity analysis was silicon. Depending on the deoxidizing practice applied in the steelmaking process, silicon levels can vary greatly in steel rod. To reflect this possibility, the minimum and maximum silicon contents have been chosen as 0.02 and 0.50 wt%, respectively. The 0.02 level would be typical of an aluminum-killed steel, while 0.50 would indicate a silicon-killed steel with excess silicon. Referring to Fig. 8.10, silicon is seen to influence the thermal history of the three grades of steel rod only slightly. Owing to the fact that silicon is a ferrite stabilizer and

increases both the A_1 and A_3 temperatures, the ferrite and pearlite CCT-start temperatures are seen to increase with increasing %Si. It should be noted however, that this does not mean that silicon decreases the hardenability of steel; rather, in accordance with the relationships employed for the prediction of CCT reaction start times, silicon affects the relative degree of undercooling. In addition, the transformation kinetics are slightly affected because of their dependence on undercooling below T_{A_1} and T_{A_3} . These changes do not, however, result in a significant change in the predicted steel microstructure. Due to the solid solution strengthening effect of silicon, a considerable increase in strength is predicted with an increase in %Si. This is predicted for all three grades of steel with the greatest effect displayed by the 1017 steel. The increase in strength for the 1017 steel with increasing silicon (+28% for 0.20 to 0.50 wt%) seems excessively high and may be due to the value adopted for the solid solution strengthening coefficient for this element.

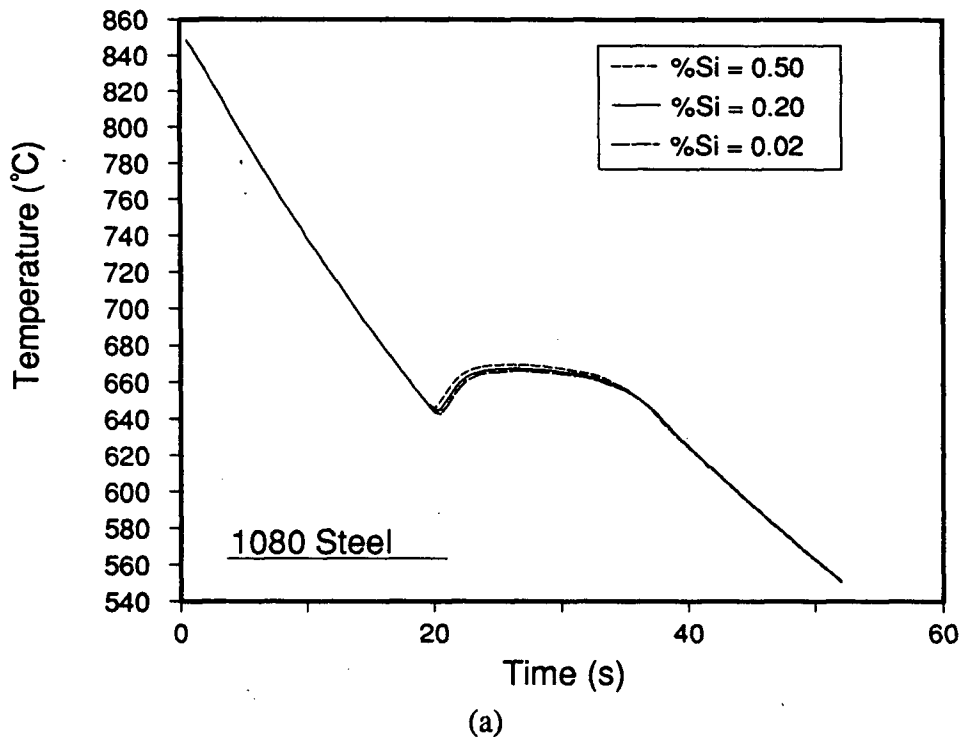
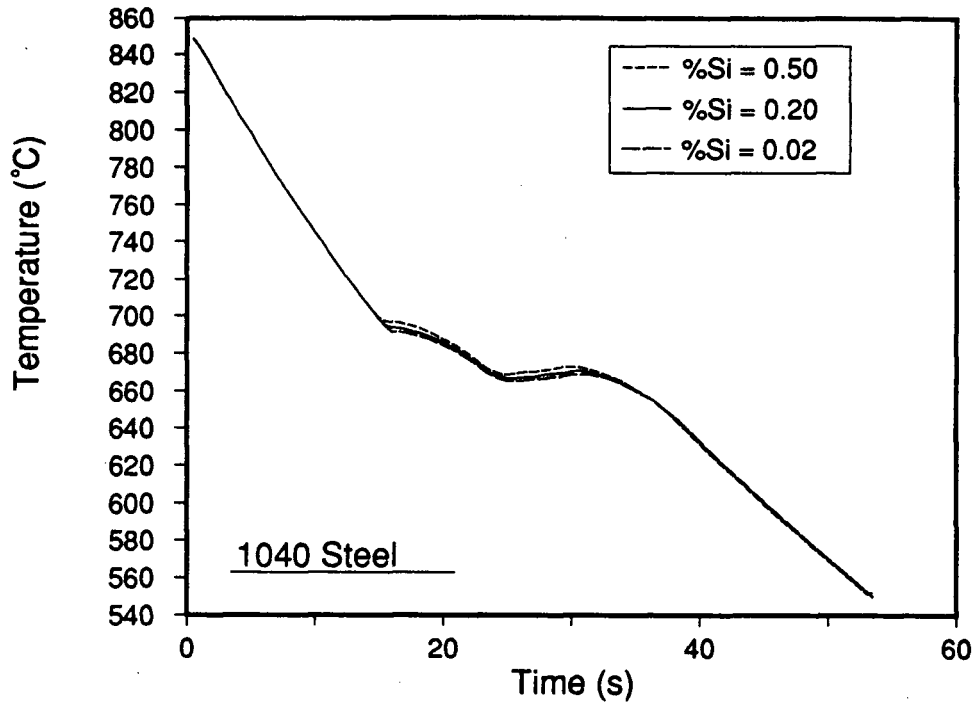
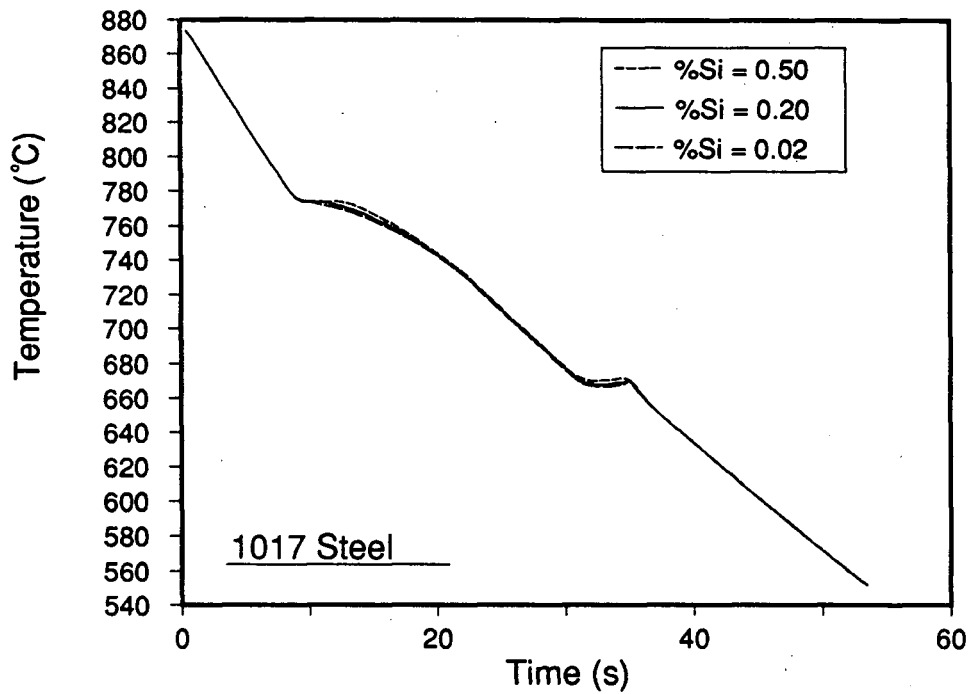


Fig. 8.10 - Effect of variation in silicon content on the model-predicted thermal history of 10-mm diameter steel rod. (a) 1080 steel, (b) 1040 steel and (c) 1017 steel.



(b)



(c)

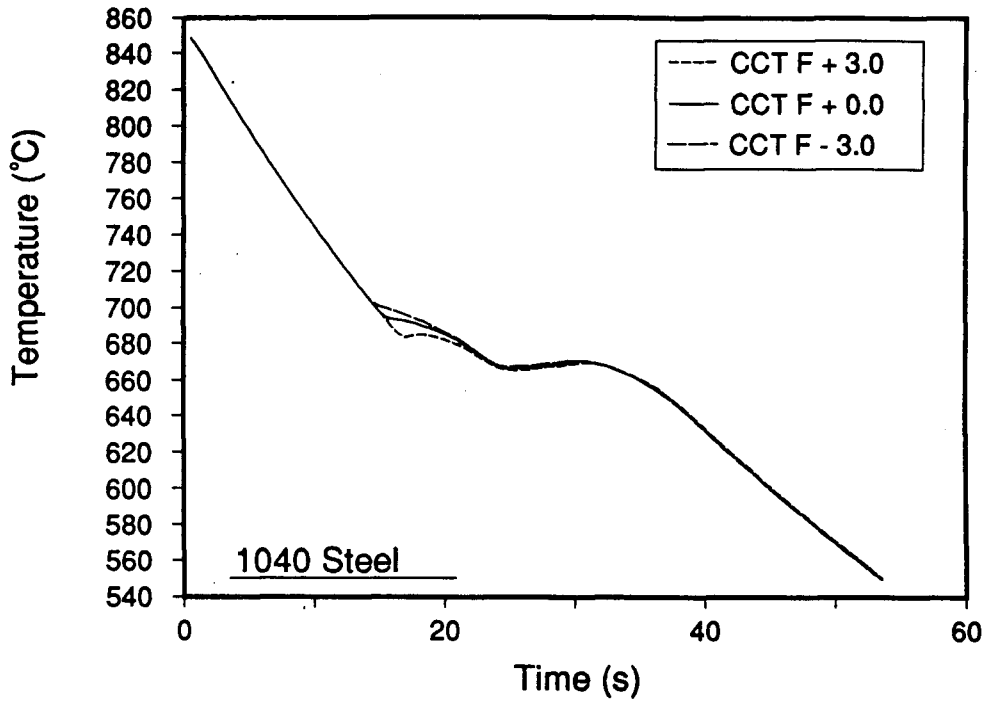
Fig. 8.10 - Effect of variation in silicon content on the model-predicted thermal history of 10-mm diameter steel rod. (a) 1080 steel, (b) 1040 steel and (c) 1017 steel.

8.2.3 Phase Transformation Kinetics Effects

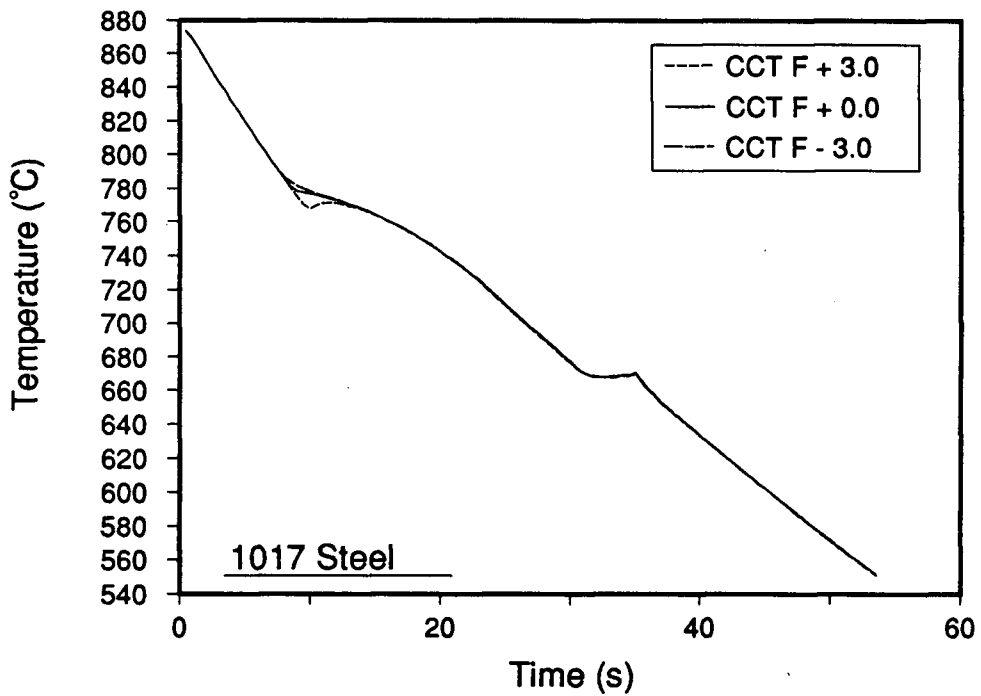
In order to predict phase transformation kinetics in continuously cooled steel rod, it has been necessary to employ empirical equations for the calculation of various parameters including transformation start times and kinetic constants for the Avrami equation. Much of the data utilized for the empirical relationships has been obtained from the dilatometer experiments outlined in Chapter 4. Despite the fact that these measurements were done carefully and under controlled conditions, a certain amount of experimental error remains in the data. The purpose of this section is to assess the effect of changes in the various kinetic parameters used to characterize the phase transformations, on the model predictions of thermal history, steel microstructure and steel strength.

The first parameter analyzed, is the CCT-start time for the ferrite transformation in the two hypoeutectoid grades. From the data for the ferrite CCT-start time and the regression equations developed (Fig. 6.33, Eq. (6.12)), it was estimated that the range of error associated with prediction of the ferrite transformation start time would be ± 3 seconds. As indicated in Tables 8.3 and 8.4, and Fig. 8.11, a reduction in CCT-start time of 3.0 seconds results in an increase in the ferrite start temperature of the reaction. For both grades of steel, the change in ferrite start time does not produce a significant effect on the pearlite transformation and associated recalescence. In addition, the change in ferrite start time does not result in a change of predicted steel microstructure or strength. The fraction of ferrite and ferrite grain diameter remain unchanged because of the method employed for prediction of these parameters in the model, i.e., both are based on cooling rate prior to transformation start.

The CCT-start time for the pearlite transformation has also been examined in the sensitivity analysis. Referring to Fig. 6.35 and Eq. (6.14), the variation in CCT-start time was found to be within ± 2 seconds for pearlite in eutectoid steels. This change results in only a slight variation in the thermal history of the steel as seen in Fig. 8.12 (a) and no change in microstructure and strength of the 1080 steel.



(a)



(b)

Fig. 8.11 - Effect of variation in CCT-start time for ferrite on the model-predicted thermal history of 10-mm diameter steel rod. (a) 1040 steel and (b) 1017 steel.

The data for prediction of pearlite CCT-start time after the ferrite transformation in the 1040 and 1017 grades suggested an error of ± 5 seconds (Fig. 6.34, Eq. (6.13)). As can be seen in Figs. 8.12 (b) and (c), a significant deviation in the predicted temperature response for the pearlite transformation has occurred due to the change in start time. The average temperature for the pearlite transformation is directly related to the pearlite spacing. Thus, steels with later start times and lower transformation temperatures should also possess a finer pearlite spacing. This is found to be true in Tables 8.3 and 8.4. However, as both the 1040 and 1017 steel contain a significant fraction of proeutectoid ferrite, the decrease in pearlite spacing contributes only a slight increase in strength.

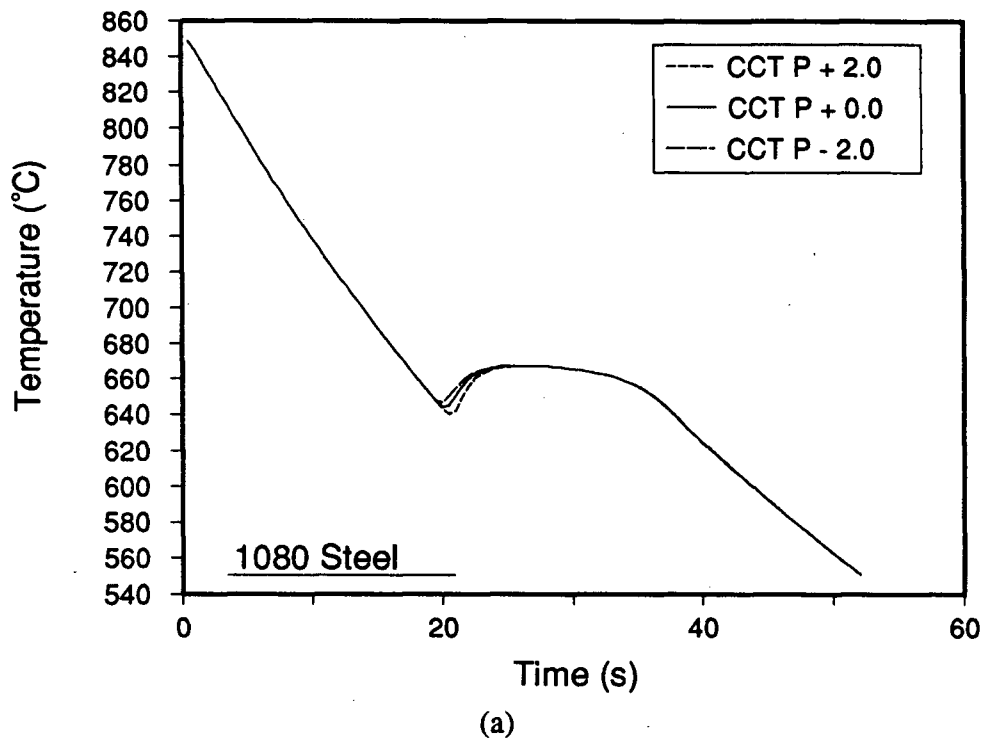
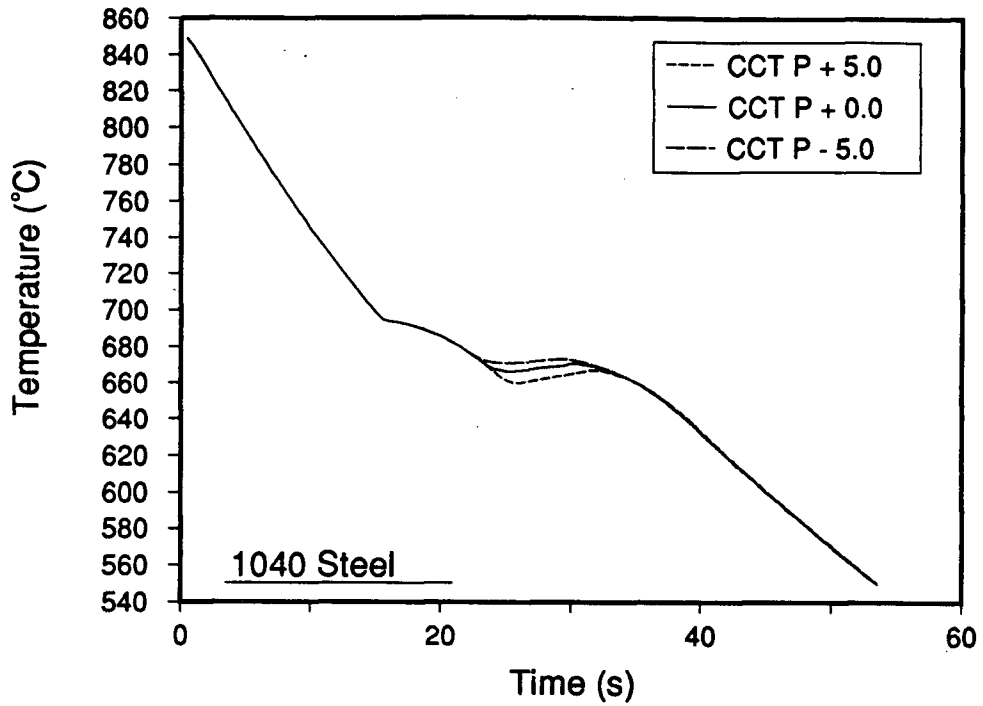
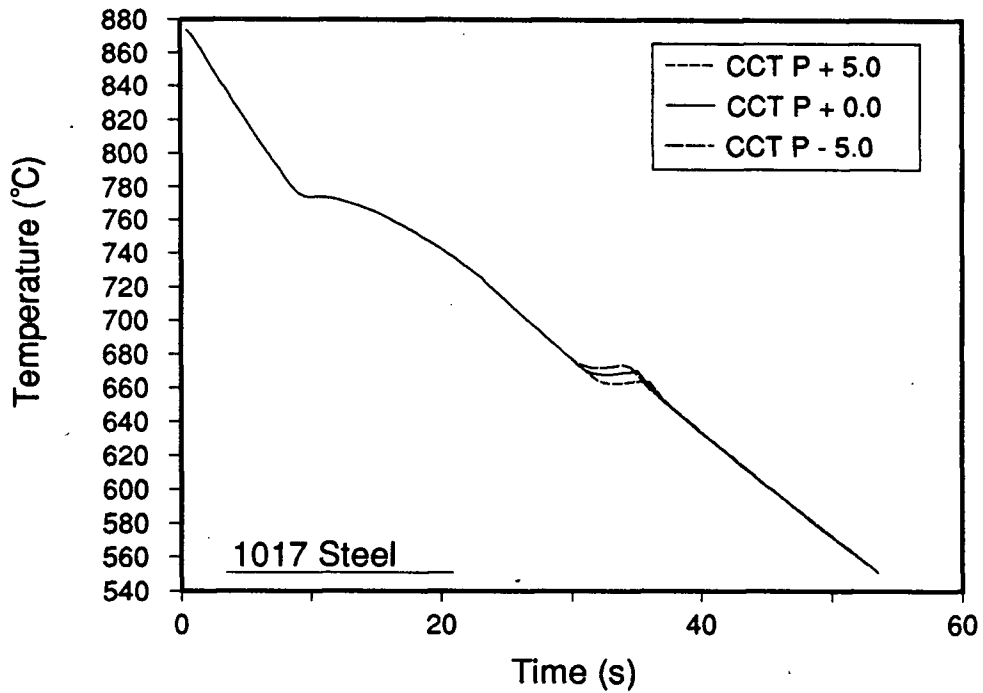


Fig. 8.12 - Effect of variation in CCT-start time for pearlite on the model-predicted thermal history of 10-mm diameter steel rod. (a) 1080 steel, (b) 1040 steel and (c) 1017 steel.

Another important parameter influencing the kinetics of the phase transformations is the n value in the Avrami equation. First, considering the austenite-ferrite transformation, the variation in the value of n_F as determined from the literature and experimental data for steels



(b)

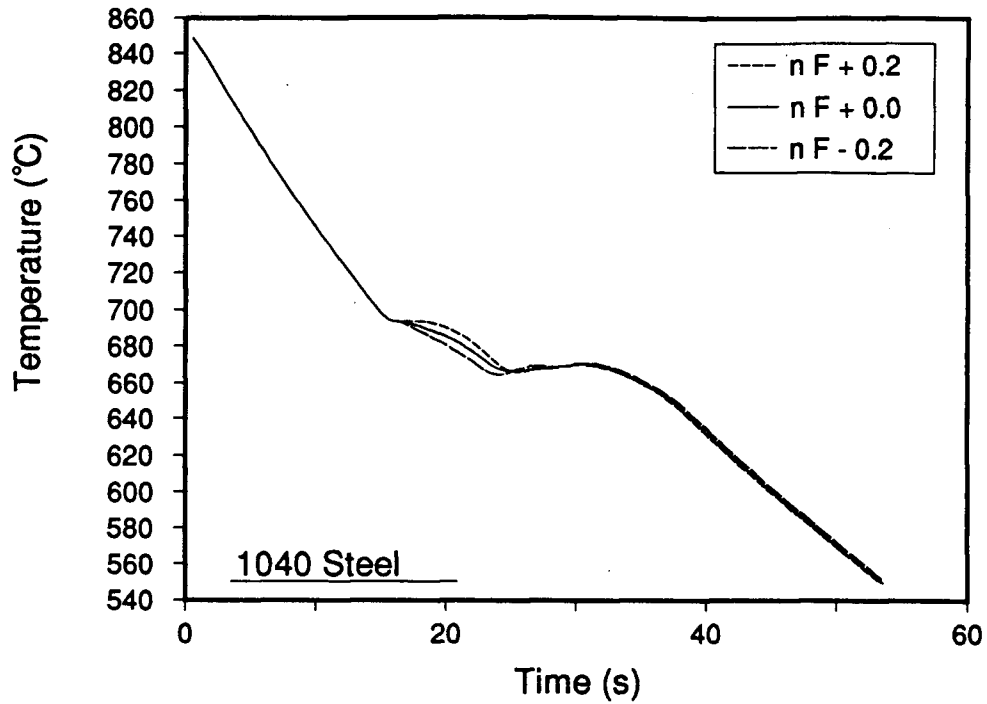


(c)

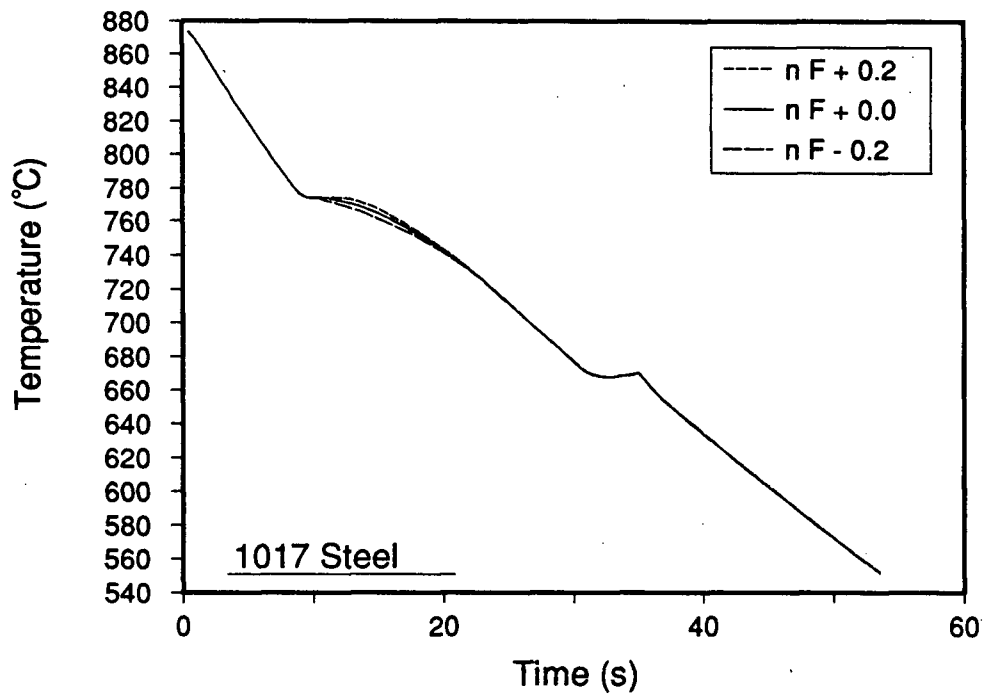
Fig. 8.12 - Effect of variation in CCT-start time for pearlite on the model-predicted thermal history of 10-mm diameter steel rod. (a) 1080 steel, (b) 1040 steel and (c) 1017 steel.

C and E (1038 and 1020), was found to be ± 0.2 (Table 6.2). The effect of this variability on the thermal history of the two hypoeutectoid grades is shown in Fig. 8.13. As the magnitude of n_F increases, the transformation kinetics increase, which results in a more rapid release of the latent heat of transformation. This yields a higher temperature over the time of ferrite transformation. Owing to the fact that the ferrite fraction and grain diameter are determined from the cooling rate prior to transformation start, this higher transformation temperature is not reflected in the microstructure or mechanical properties predicted for the two grades of hypoeutectoid steel (Tables 8.3 and 8.4). In theory however, it would be expected that a higher average temperature for the ferrite reaction should result in a larger ferrite fraction as well as an increased ferrite grain diameter. A more accurate description of the effect of temperature and transformation rate on the fraction and grain diameter of proeutectoid ferrite would have to be applied to resolve this problem.

The effect of varying the magnitude of n for the pearlite transformation was also included in the sensitivity analysis. From both eutectoid and hypoeutectoid grades it was found that the experimental variation in n_p was ± 0.3 , (Fig. 6.29, Eq. (6.8)). The predicted thermal histories for the three steel grades are shown in Fig. 8.14. The results show that an increase in n_p for the eutectoid rod, Fig 8.14 (a), results in quicker transformation kinetics and a more rapid release of the transformation latent heat. As a result, the model predicts a higher average transformation temperature for the steel with the highest n_p . The higher transformation temperature results in a coarser mean pearlite spacing as shown in Table 8.2, and a corresponding decrease in the strength of the rod. The predicted variation in strength is $\pm 2\%$ of the mean predicted value. A similar situation is encountered in the 1040 steel, as the average transformation temperature for pearlite increases with increasing n_p . The effect is not as great as for the 1080 steel, and only a slight increase in pearlite spacing and resulting decreased strength is produced, as shown in Table 8.3. For the 1017 steel, Fig 8.9 (c), the change in n_p results in a negligible variation in thermal history, microstructure and strength. This is attributed to the small pearlite fractions present in this grade.



(a)



(b)

Fig. 8.13 - Effect of variation in n_F on the model-predicted thermal history of 10-mm diameter steel rod. (a) 1040 steel and (b) 1017 steel.

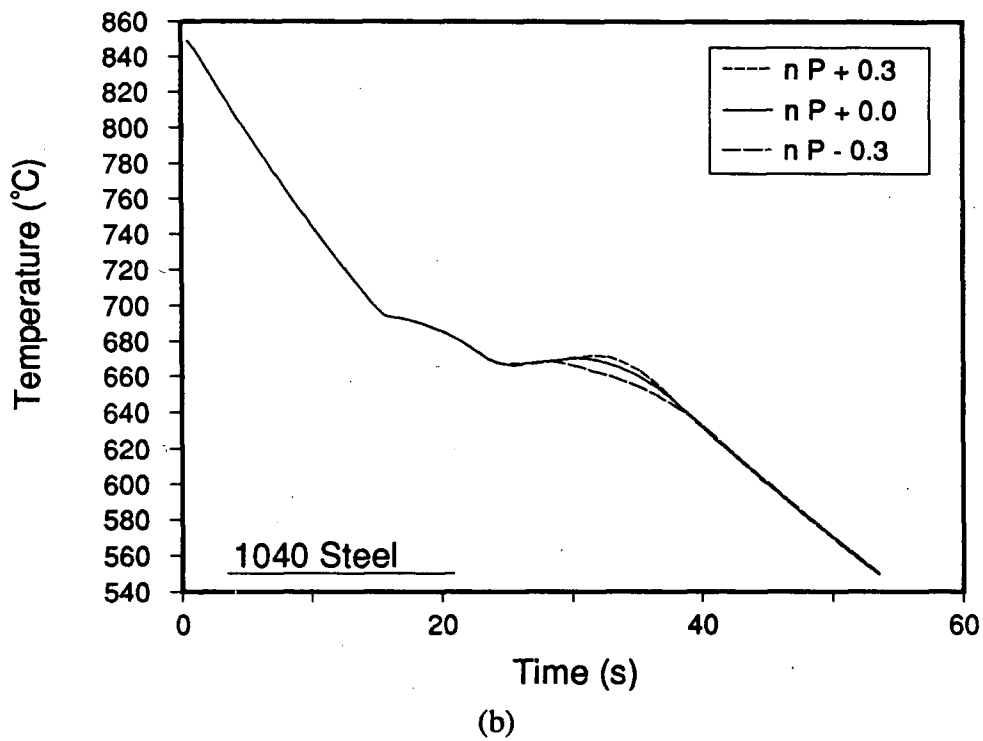
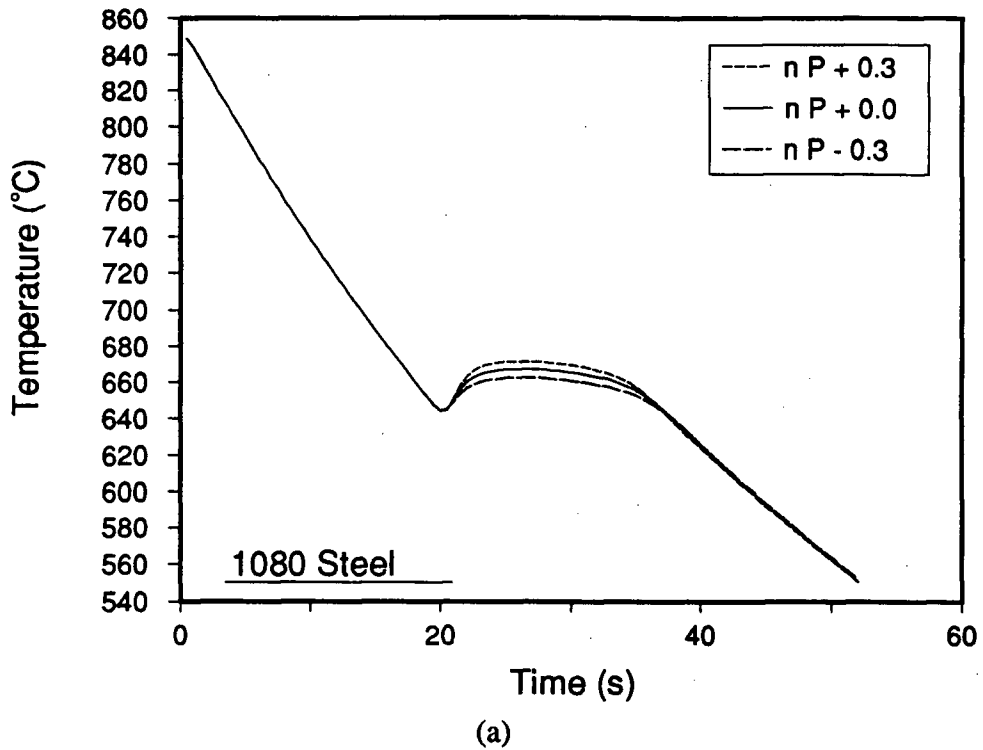


Fig. 8.14 - Effect of variation in n_p on the model-predicted thermal history of 10-mm diameter steel rod. (a) 1080 steel, (b) 1040 steel and (c) 1017 steel.

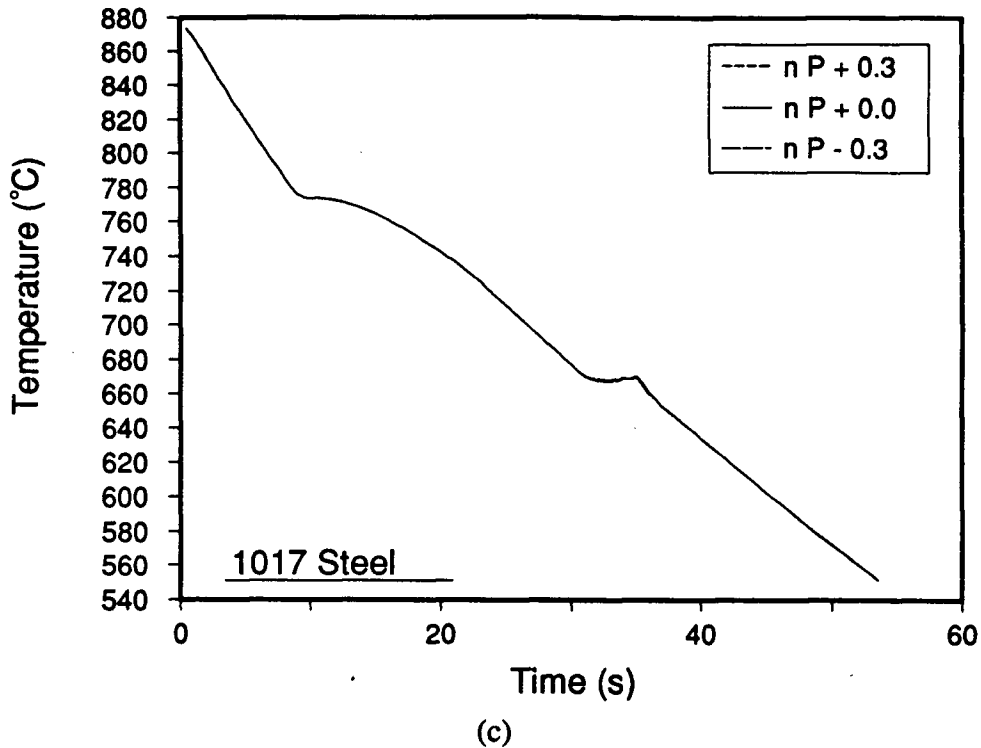
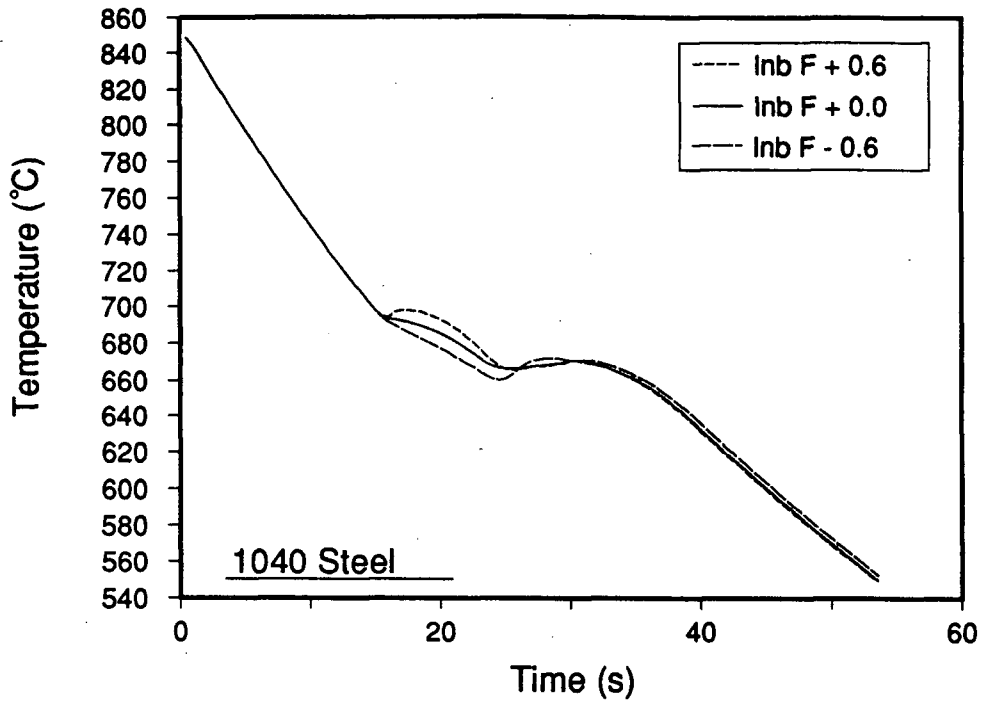
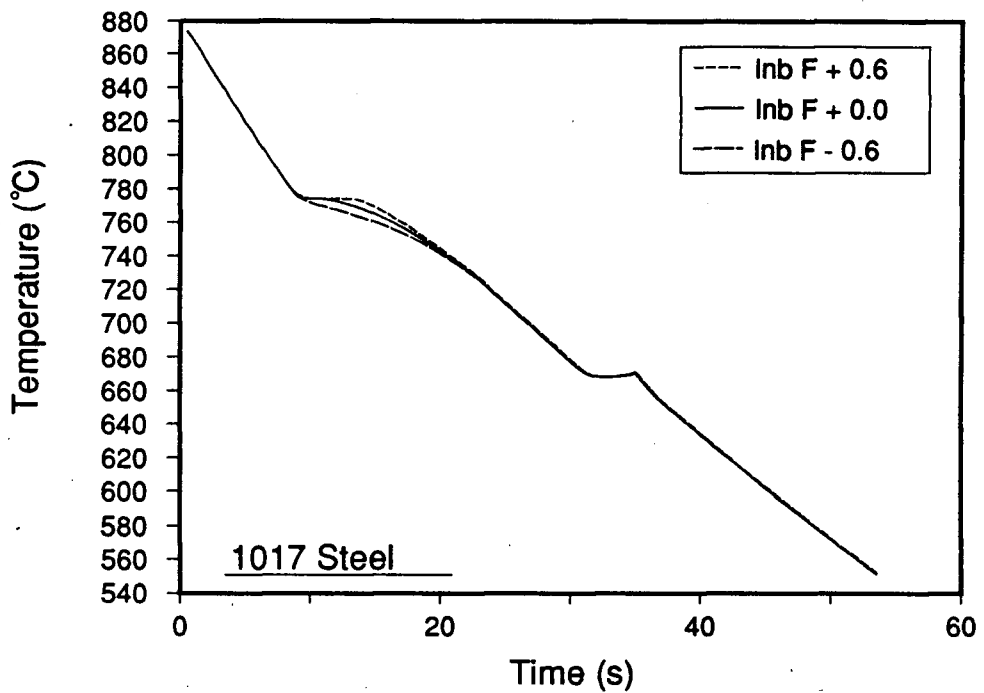


Fig. 8.14 - Effect of variation in n_p on the model-predicted thermal history of 10-mm diameter steel rod. (a) 1080 steel, (b) 1040 steel and (c) 1017 steel.

The second parameter needed to characterize transformation kinetics applying the Avrami equation is b . The value of b in the Avrami equation is directly linked to the reaction kinetics, i.e., as b , or $\ln b$, increases, the reaction kinetics increase. A ± 0.6 variation in the value of $\ln b_F$ has been obtained from the regression equation for the prediction of b_F for the austenite-ferrite transformation (Fig. 6.30, Eq. (6.9)). The effect of a ± 0.6 variation in $\ln b_F$ on the thermal histories as shown in Fig. 8.15, is similar to that obtained from changes to n_p ; decreasing b_F decreases the γ - α kinetics, resulting in a reduced temperature during the ferrite transformation. This is seen to be the case for both grades of hypoeutectoid steel. In the thermal history for the 1040 grade, Fig. 8.15 (a), the slower reaction kinetics for the ferrite reaction actually results in a depression of the start temperature for the pearlite transformation. This reduced temperature causes higher initial pearlite transformation kinetics, and the heat of transformation released results in a larger recalescence than for the other two runs. Variation in the b_F parameter causes no appreciable change in the microstructure or strength



(a)



(b)

Fig. 8.15 - Effect of variation in b_F on the model-predicted thermal history of 10-mm diameter steel rod. (a) 1040 steel and (b) 1017 steel.

of these steels as depicted in Tables 8.3 and 8.4. Once again, this is attributed to the fact that the ferrite fraction and grain diameter are calculated based on the cooling rate prior to transformation start.

The effect of varying the $\ln b_p$ parameter by ± 1.0 for the pearlite transformation has also been included in the sensitivity analysis. The results of the thermal history predictions are included in Fig. 8.16. As is shown in Fig. 8.16 (a), the smallest value for b_p , produces the transformation with the lowest average transformation temperature. This is reflected in the predicted mean pearlite spacings and strengths given in Table 8.2 for the 1080 steel. The change in strength is of the same magnitude as that suggested by a variation in n_p of ± 0.3 . Much the same behaviour is exhibited by the 1040 steel, with the transformation temperature for pearlite being depressed by a decrease in the magnitude of b_p . The effect on pearlite spacing and predicted strength is similar as well, although the strength effect is tempered by the presence of proeutectoid ferrite. The 1017 grade is not affected to the same degree however, and this may be due to its smaller pearlite fraction, as shown in Table 8.4.

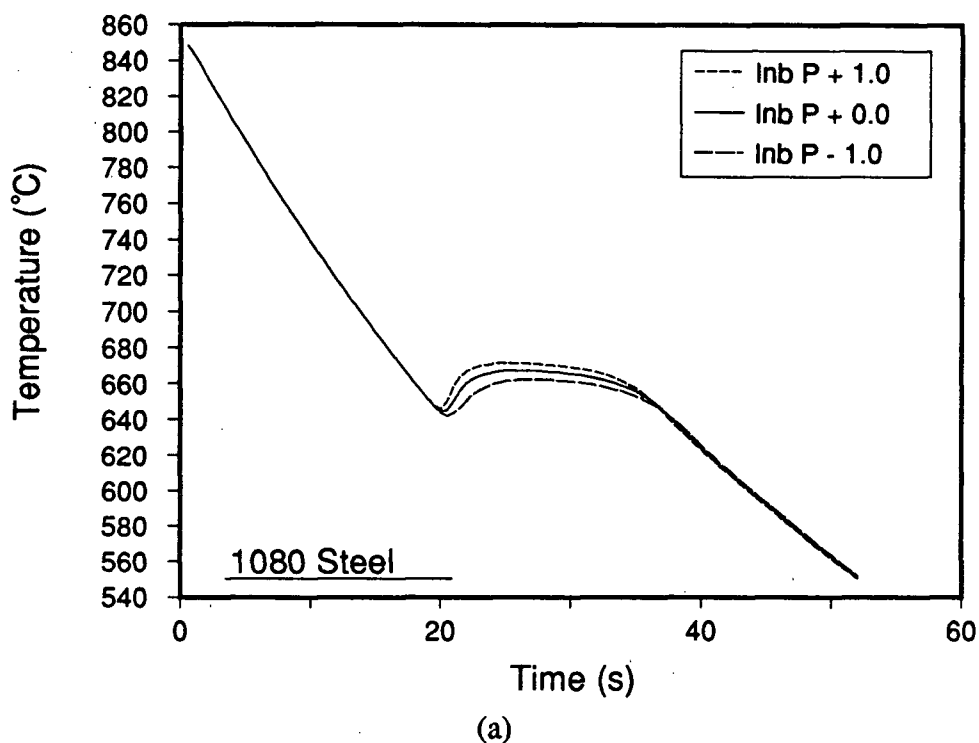
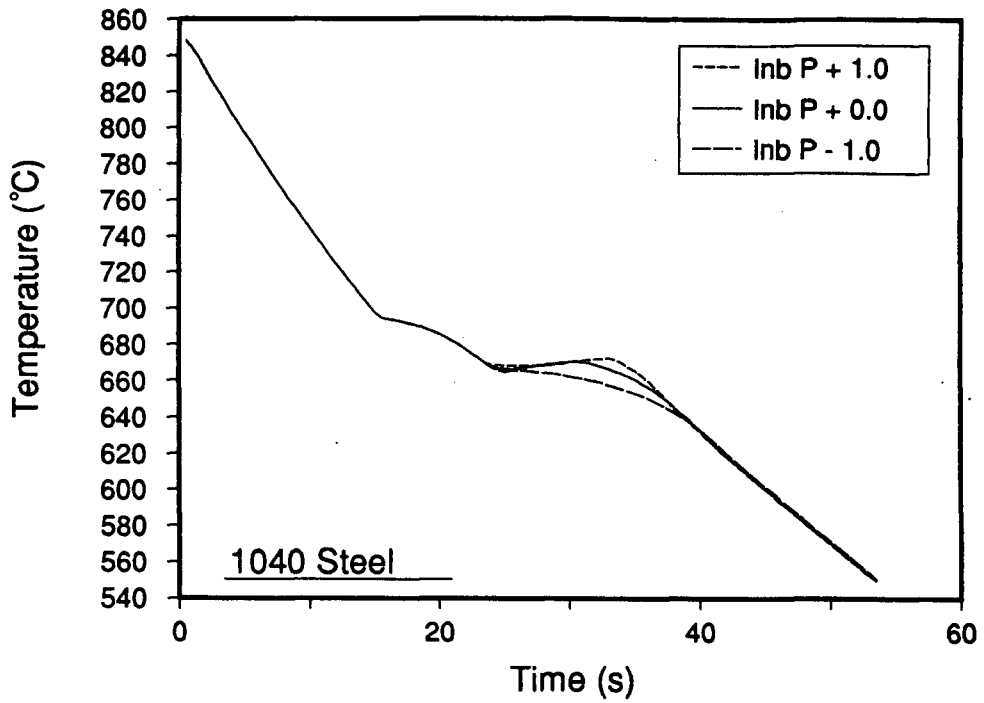
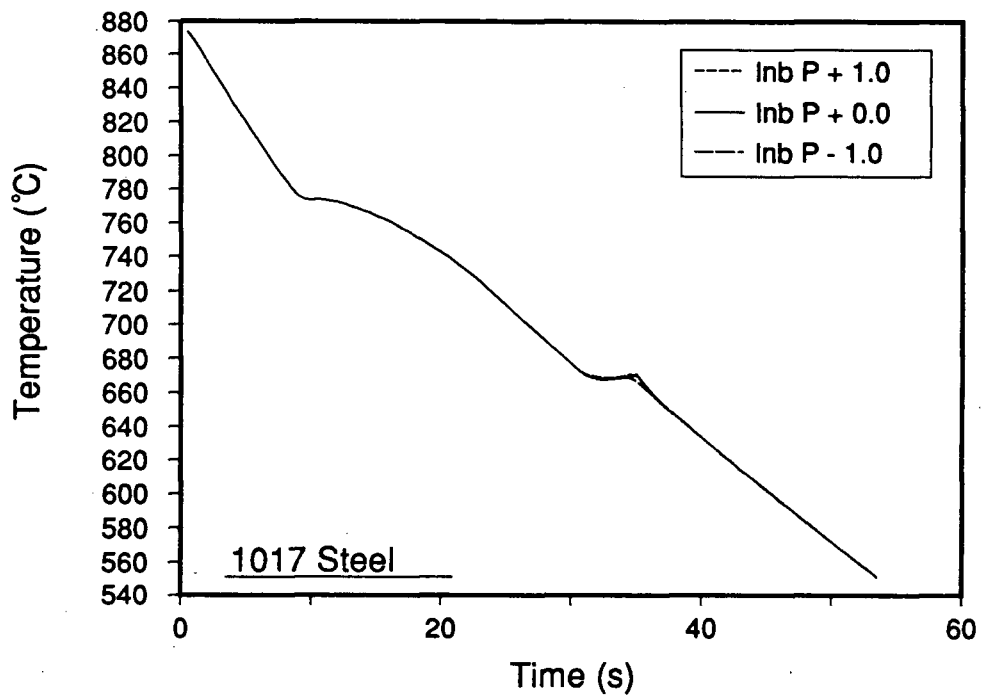


Fig. 8.16 - Effect of variation in b_p on the model-predicted thermal history of 10-mm diameter steel rod. (a) 1080 steel, (b) 1040 steel and (c) 1017 steel.



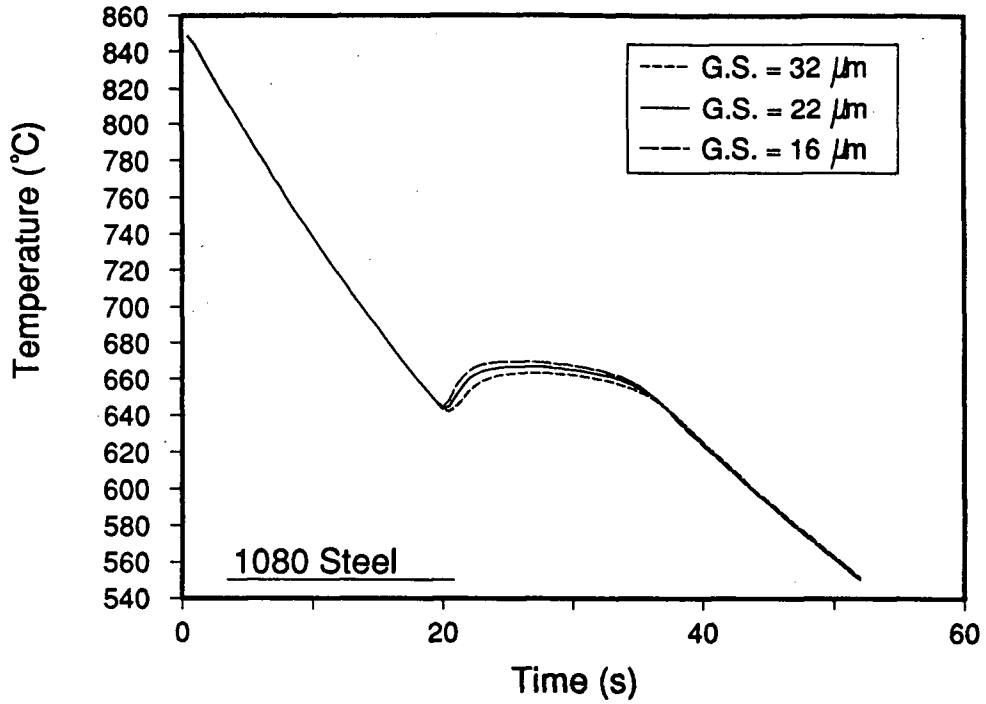
(b)



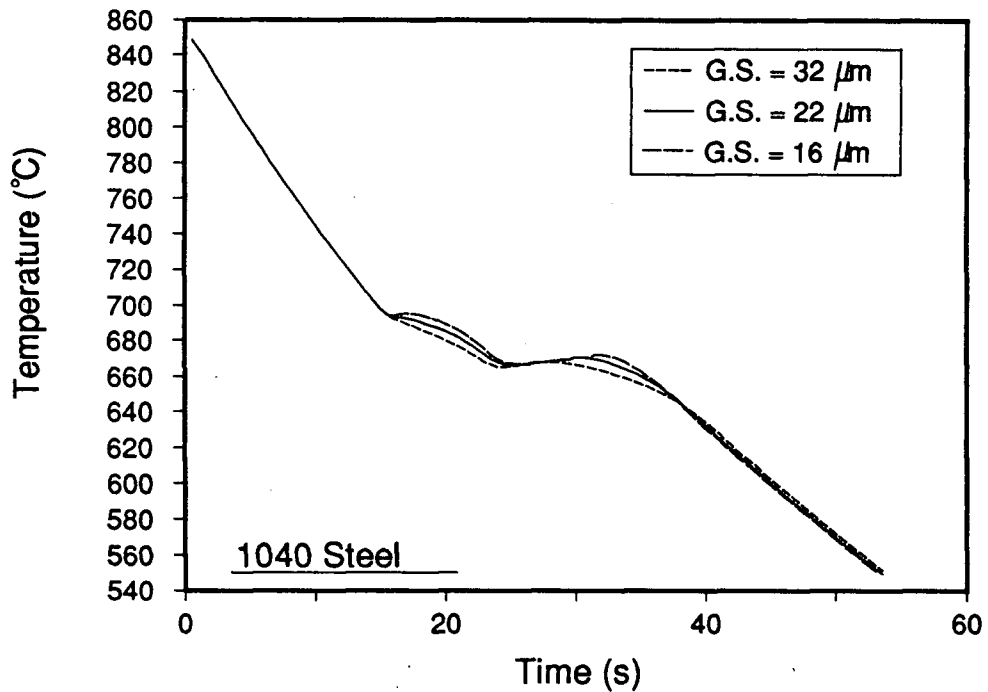
(c)

Fig. 8.16 - Effect of variation in b_p on the model-predicted thermal history of 10-mm diameter steel rod. (a) 1080 steel, (b) 1040 steel and (c) 1017 steel.

The final parameter thought to exert an influence on the ferrite and pearlite transformation kinetics is the prior austenite grain size. As indicated in Chapter 6, prior austenite grain size measurements have been made on both laboratory steel rod as well as an industrial grade. The results showed that the austenite grain size is approximately ASTM 8 ($22\ \mu\text{m}$) with a variation of ± 1 ASTM. Owing to the small variation expected in the austenite grain size after rolling in the rod mill, and to the narrow range of grain sizes measured in the laboratory test rods, the prior austenite grain size has not been included in the regression equations for CCT-start times or ferrite grain diameters. However, the effect of a change in austenite grain diameter on the kinetics of the austenite-ferrite and austenite-pearlite transformations can be gauged by employing Eq. (2.43) (the Avrami equation including a prior austenite grain size parameter). According to Tamura [38], the value for the grain size exponent, m , for the ferrite transformation is equal to approximately 1, while for pearlite it is 2. Employing these values, and the ± 1 ASTM grain size number variation to the mean grain size, the effect on transformation kinetics can be calculated. Results of thermal history predictions for the three steel grades are given in Fig. 8.17. A larger austenite grain diameter provides less grain surface, edges and corners for nucleation and growth of the new phases and will thus result in a decrease in the overall kinetics of the reaction. This is shown to be true for the 1080 and 1040 steels, with a definite decrease in reaction kinetics and lower transformation temperature corresponding to an increase in the average austenite grain size. Once again the effect is not as pronounced for the 1017 grade. In terms of rod microstructure and strength, a finer pearlite spacing will result from the lower transformation temperature in steels with a larger austenite grain size; this will be reflected in an increase in strength, which is greatest in the 1080 steel, as shown in Tables 8.2 to 8.4.



(a)



(b)

Fig. 8.17 - Effect of variation in prior austenite grain size on the model-predicted thermal history of 10-mm diameter steel rod. (a) 1080 steel, (b) 1040 steel and (c) 1017 steel.

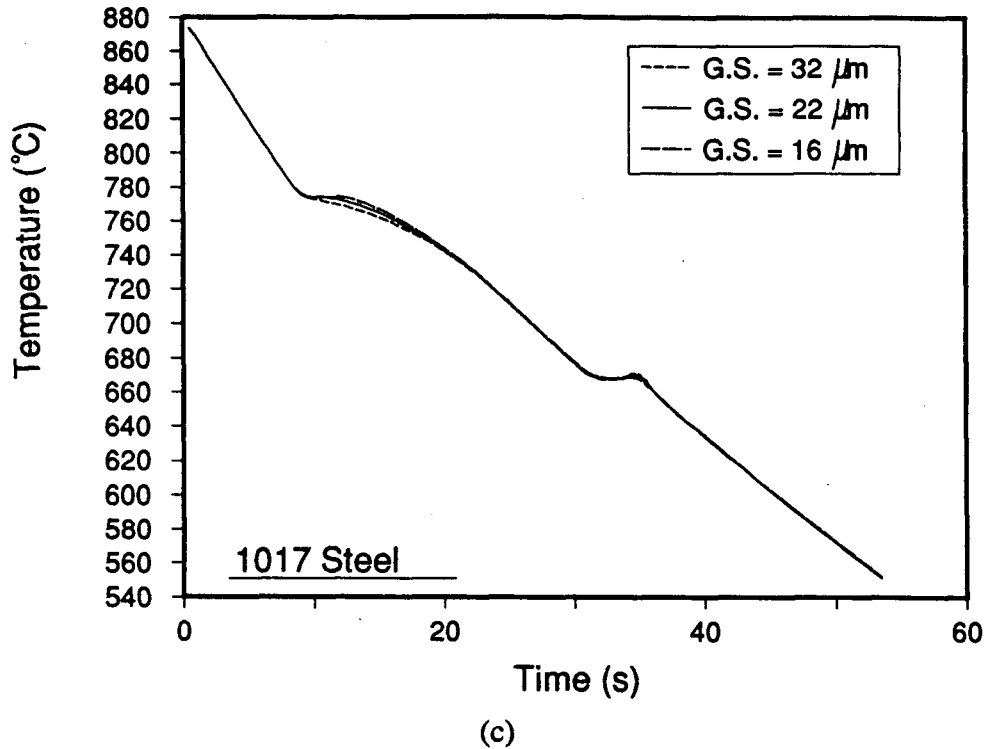


Fig. 8.17 - Effect of variation in prior austenite grain size on the model-predicted thermal history of 10-mm diameter steel rod. (a) 1080 steel, (b) 1040 steel and (c) 1017 steel.

8.2.4 Microstructural Effects

In order to assess the variation in rod strength as a function of individual microstructural parameters, independent of steel thermal history, the mathematical model has been run employing correction factors for the ferrite fraction, ferrite grain diameter and pearlite spacing. The magnitude of the correction factor applied to the ferrite fraction and ferrite grain diameter has been chosen to be \pm one standard deviation of the estimated value obtained from the regression analysis. For the predicted ferrite fraction, as shown in Fig. 7.21, one standard deviation has been calculated to be ± 0.056 . The error associated with one standard deviation of the estimated ferrite grain diameter, from the regression equation, Eq. (7.7), is equal to $\pm 0.6 \mu\text{m}$. From the regression equation developed for pearlite spacings measured in the present study as well as those from the literature, it was found that the error associated with predicting pearlite spacing as a function of the average undercooling below

T_{A1} , is $\pm 20\%$. These estimates of the range of errors for each microstructural parameter have been supplied to the model and the mechanical properties of each grade have been determined employing the mean settings, for all other variables, listed previously in Table 8.1.

Considering first the eutectoid 1080 steel, the results of model-predicted strengths for a $\pm 20\%$ deviation in the pearlite spacing are given in Table 8.5. As this steel does not contain proeutectoid ferrite, pearlite spacing was the lone parameter included in the comparison. As can be seen in the table, a 20% variation in the pearlite spacing results in a substantial change in the predicted yield and ultimate strengths. The predicted yield strength varies from -8 to +11% of the mean value. These strength variations are greater than those attributed to any single parameter variation included for the sensitivity analysis on thermal history, listed in Table 8.2. Similarly, the error associated with $\pm 20\%$ of the mean pearlite spacing for the predicted values of UTS, varies from -5 to +7% of the mean predicted strength. From this analysis, the dramatic effect pearlite spacing has on the strength of eutectoid steel is readily apparent. Thus, the accurate prediction of mechanical properties in plain-carbon eutectoid steels depends critically on valid pearlite interlamellar spacings.

Table 8.5 - Variation in rod strength as a function of changes in pearlite spacing for a 1080 steel.

Parameter	Ferrite Fraction	Ferrite Diameter (μm)	Pearlite Spacing (μm)	Yield Strength (MPa)	UTS (MPa)
Mean Settings	0.000	-	0.239	539.3	1046.3
Mean Spac. x 1.2	0.000	-	0.286	494.1	994.5
Mean Spac. x 0.8	0.000	-	0.191	600.4	1116.5

The model-predicted strengths for the 1040 steel as a function of the microstructural errors are included in Table 8.6. As can be seen, the variation in ferrite fraction accounts for a $\pm 1\%$ change in the yield strength and a $\pm 1.5\%$ change in UTS. This amount is considered to be relatively minor in light of the variations reported for the other parameters, as shown in

Table 8.3. Table 8.6 also shows that the $\pm 0.6 \mu\text{m}$ error in ferrite grain diameter accounts for a change of about $\pm 2.5\%$ of the predicted mean yield and ultimate tensile strengths. Essentially the same level of change is caused by the two pearlite spacings given in the table. Yield strengths vary from ± 2.5 to 3% of the mean value, and UTS from ± 1.5 to 2.5% . The predicted variations in strengths are seen to be reasonable for the type of model being presented.

Table 8.6 - Variation in rod strength as a function of changes in steel microstructure for a 1040 steel.

Parameter	Ferrite Fraction	Ferrite Diameter (μm)	Pearlite Spacing (μm)	Yield Strength (MPa)	UTS (MPa)
Mean Settings	0.479	4.12	0.246	426.6	644.2
Mean Frac. + 0.056	0.535	4.12	0.246	422.7	629.6
Mean Frac. - 0.056	0.423	4.12	0.246	430.9	660.3
Mean Fer. Dia. + $0.6 \mu\text{m}$	0.479	4.72	0.246	416.0	628.5
Mean Fer. Dia. - $0.6 \mu\text{m}$	0.479	3.52	0.246	439.8	664.1
Mean Spac. x 1.2	0.479	4.12	0.295	417.0	633.3
Mean Spac. x 0.8	0.479	4.12	0.197	439.7	659.4

Table 8.7 shows the effect of varying the microstructure on the strength of 1017 steel. As can be seen, the variation in ferrite fraction of ± 0.056 has a considerable effect on the predicted strength. For the yield strength the deviation is about $\pm 4\%$, while for the UTS it is $\pm 3\%$. The effect is somewhat greater than that observed for the 1040 steel, due to the greater fraction of ferrite in the 1017 steel and thus the greater dependence of strength on the ferrite fraction. The effect of varying the ferrite grain diameter displays a much smaller variation in predicted steel strength. For both the yield and ultimate tensile strength, the variation is approximately $\pm 1\%$. This smaller variation, as compared to that observed for the 1040 steel, is due to the fact that the predicted grain diameter is much larger in the lower carbon grade (9.03 and $4.11 \mu\text{m}$) and thus the $\pm 0.6 \mu\text{m}$ change does not have as great an

effect. With regard to pearlite spacing, not surprisingly, the 20% change in the predicted mean value has almost no effect on the predicted rod yield and ultimate strengths. This is due to the small fractions of pearlite contained in the 1017 steel (~ 22%).

Table 8.7 - Variation in rod strength as a function of changes in steel microstructure for a 1017 steel.

Parameter	Ferrite Fraction	Ferrite Diameter (μm)	Pearlite Spacing (μm)	Yield Strength (MPa)	UTS (MPa)
Mean Settings	0.779	9.03	0.265	319.4	525.3
Mean Frac. + 0.056	0.836	9.03	0.265	307.1	509.9
Mean Frac. - 0.056	0.724	9.03	0.265	331.6	540.8
Mean Fer. Dia. + 0.6 μm	0.780	9.63	0.265	316.3	521.2
Mean Fer. Dia. + 0.6 μm	0.780	8.43	0.265	322.8	529.9
Mean Spac. x 1.2	0.780	9.03	0.317	318.9	524.4
Mean Spac. x 0.8	0.780	9.03	0.212	320.0	526.6

8.3 Model Predictions

8.3.1 Laboratory Tests

The mathematical model has been run to predict the thermal history, microstructural evolution and mechanical properties of steel rods cooled under conditions typical for the laboratory tests. Results of the predictions for a variety of experimental conditions, are presented in the following sections.

8.3.1.1 Thermal Histories

To evaluate the ability of the mathematical model for prediction of thermal response at the centreline of continuously cooled steel rod, several laboratory tests have been considered. Firstly, for Steel B (1070), results from the laboratory experiments are included in Figs. 8.18 (a), (b) and (c), together with corresponding predictions of centreline thermal response, as calculated from the model. The heat-transfer coefficient predicted by the model has been adjusted to provide the best agreement with the experimental results by matching the early cooling period of each test prior to transformation; the correction factor is included in each figure. For test B3, shown in Fig 8.18 (a), excellent agreement between measured and

predicted thermal history has been achieved. However, during the pearlite transformation, agreement is not so good, specifically with respect to the magnitude of the recalescence. This can be attributed to a slight under-prediction in the kinetics of the reaction, as the total latent heat released during transformation is correct. With reference to the sensitivity of the model to errors included in Section 8.2.3, due to changes in transformation kinetics parameters (Figs. 8.14 (a) and 8.16 (a)), the under-prediction in transformation rate is considered minor. Similarly, the results for rods B7 and B9, included in Figs. 8.18 (b) and (c), show a good agreement between predicted and measured thermal history. However, it is noted that the predicted start time for transformation seems to be slightly earlier and at a higher temperature than the measured values. Once again referring to the sensitivity analysis, this variation in start time is seen to be well within the error of the predicted CCT for the pearlite reaction (Fig. 8.12 (a)).

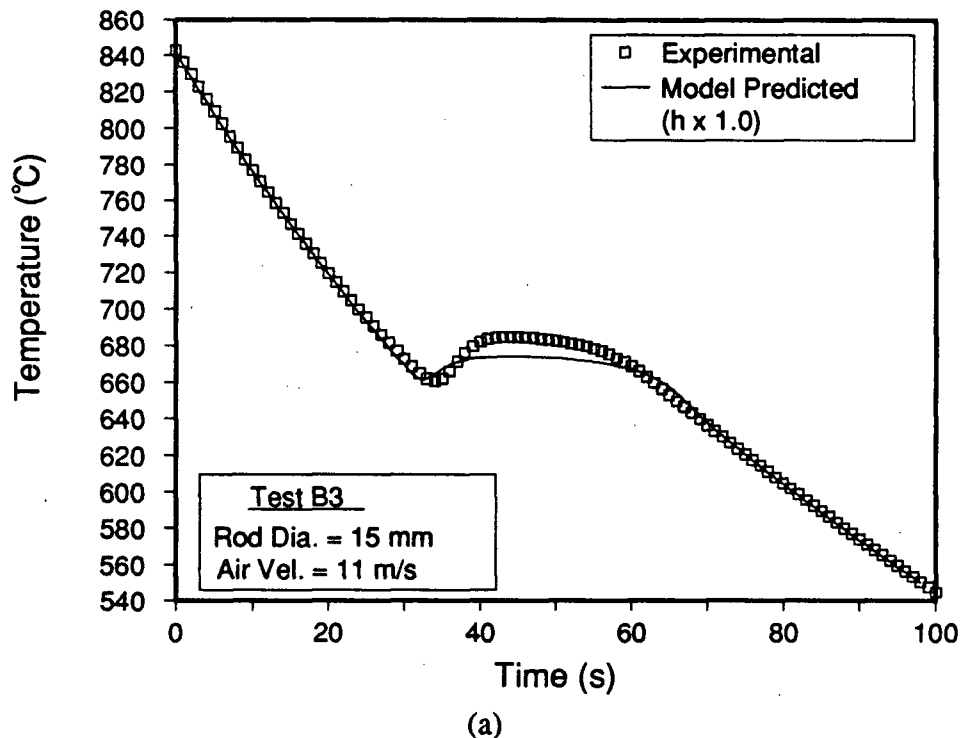
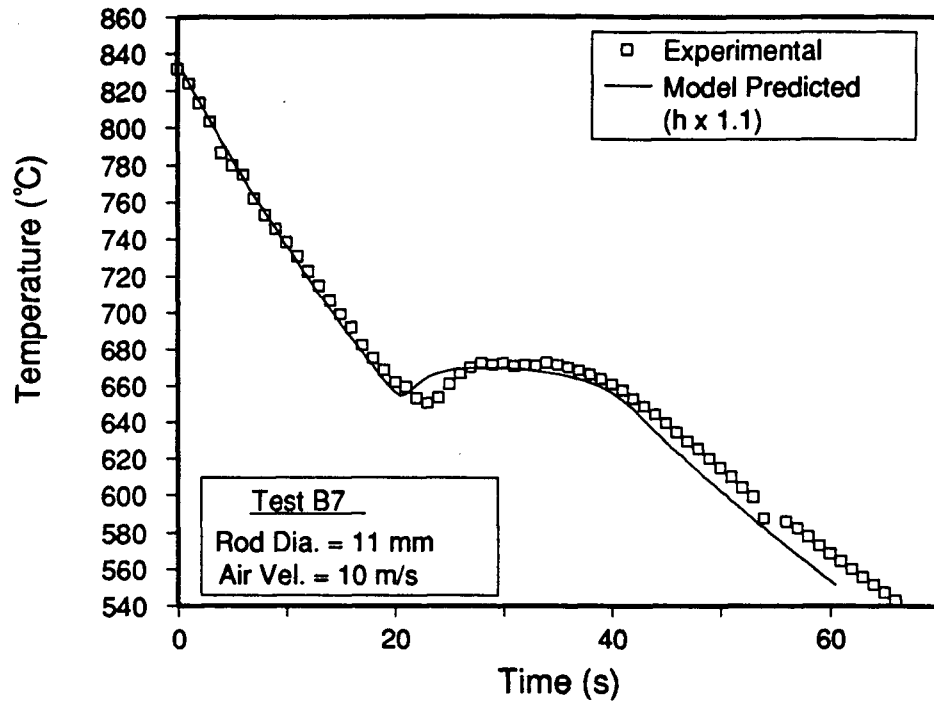
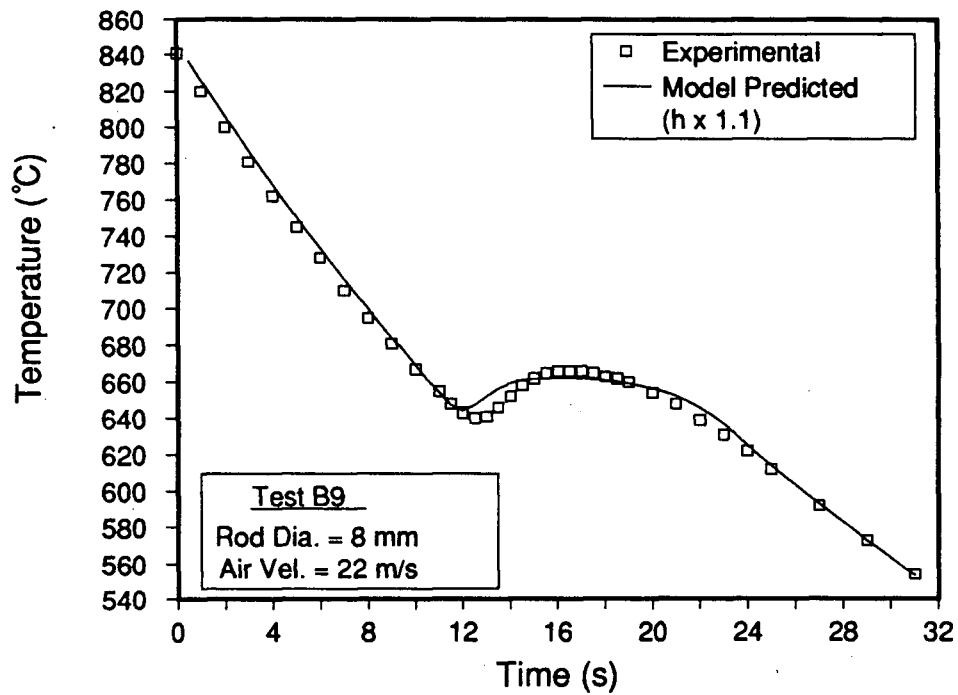


Fig. 8.18 - Measured and model-predicted thermal response at the centreline of a steel rod for Steel B (1070). (a) Test B3, 15-mm diameter, 11 m/s air velocity, (b) Test B7, 11-mm diameter, 10 m/s air velocity and (c) Test B9, 8-mm diameter, 22 m/s air velocity.



(b)



(c)

Fig. 8.18 - Measured and model-predicted thermal response at the centreline of a steel rod for Steel B (1070). (a) Test B3, 15-mm diameter, 11 m/s air velocity, (b) Test B7, 11-mm diameter, 10 m/s air velocity and (c) Test B9, 8-mm diameter, 22 m/s air velocity.

Thermal histories for typical laboratory tests involving Steel C (1038) are included in Figs. 8.19 (a), (b) and (c). As was the case for the 1070 steel, prediction of thermal response in the rods is seen to be excellent, except for the transformation portion of the cooling curve. In general, it seems that the kinetics predicted for the austenite-ferrite transformation in the three tests are too fast. Nevertheless, good agreement between predicted and measured austenite-pearlite transformation kinetics has been achieved. Referring to the factors affecting the austenite-ferrite transformation kinetics in Section 8.2.3, the over prediction in temperature during the transformation can be linked to over-predicted values of either n_F or $\ln b_F$, or both (Figs. 8.13 (a) and 8.15 (a)). Despite the slight error in prediction of ferrite transformation kinetics, the latent heat released during both the ferrite and pearlite reactions is seen to be in agreement with the experimental data, as evidenced by the close agreement between the model-predicted and measured post transformation results.

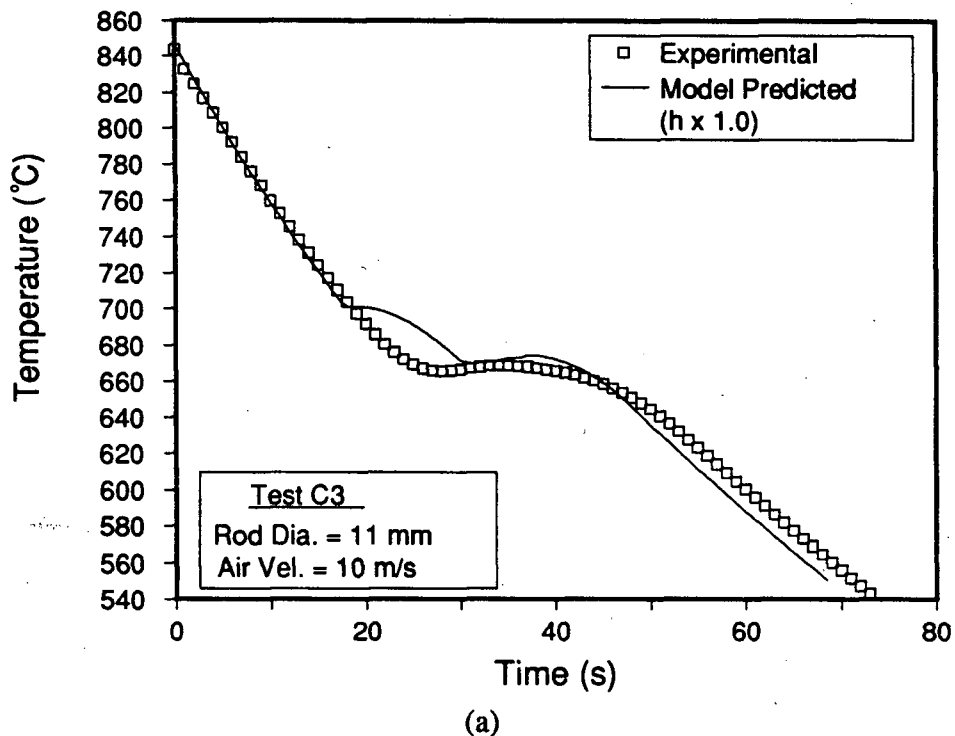
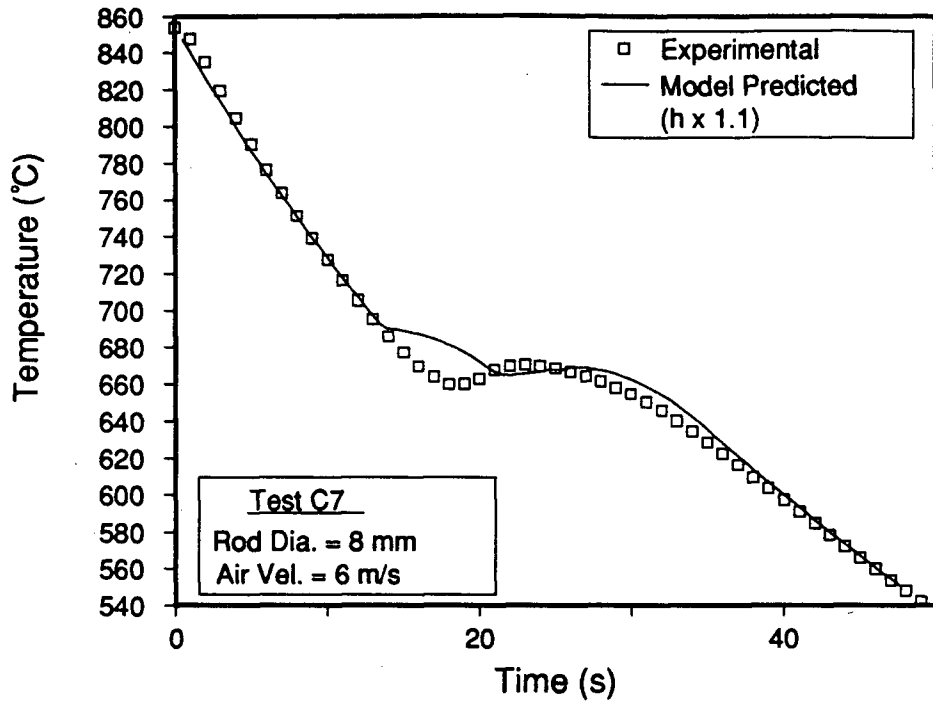
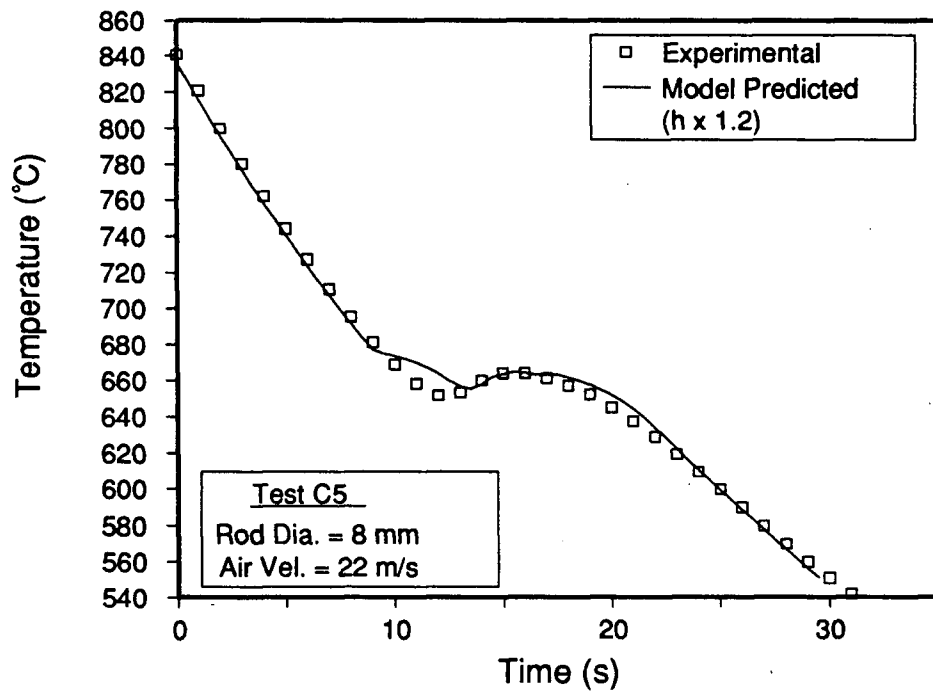


Fig. 8.19 - Measured and model-predicted thermal response at the centreline of a steel rod for Steel C (1038). (a) Test C3, 11-mm diameter, 10 m/s air velocity, (b) Test C7, 8-mm diameter, 6 m/s air velocity and (c) Test C5, 8-mm diameter, 22 m/s air velocity.



(b)



(c)

Fig. 8.19 - Measured and model-predicted thermal response at the centreline of a steel rod for Steel C (1038). (a) Test C3, 11-mm diameter, 10 m/s air velocity, (b) Test C7, 8-mm diameter, 6 m/s air velocity and (c) Test C5, 8-mm diameter, 22 m/s air velocity.

Results of predicted and measured thermal responses for Steel E (1020) are given in Figs. 8.20 (a), (b) and (c). As was the case for Steel C, an excellent agreement between predicted and measured thermal history and latent heat of transformation has been obtained. However, once again, the model-predicted reaction kinetics for the austenite-ferrite transformation, are faster than those measured in the laboratory trials. In addition, the magnitude of the over-prediction seems to increase as cooling rate increases. Reasonable agreement between predicted and experimental thermal history during the pearlite transformation can be seen. The higher model-predicted ferrite transformation kinetics can be attributed to errors in the predicted CCT start times or predicted n_F and $\ln b_F$ values. Variations in prior austenite grain size can also cause changes in the predicted kinetics. Thus referring to Figs. 8.11 (b), 8.13 (b), 8.15 (b) and 8.17 (c) in Section 8.2.3, the difference between the experimental and predicted thermal histories for Steel E can be seen to be within the expected error for the model.

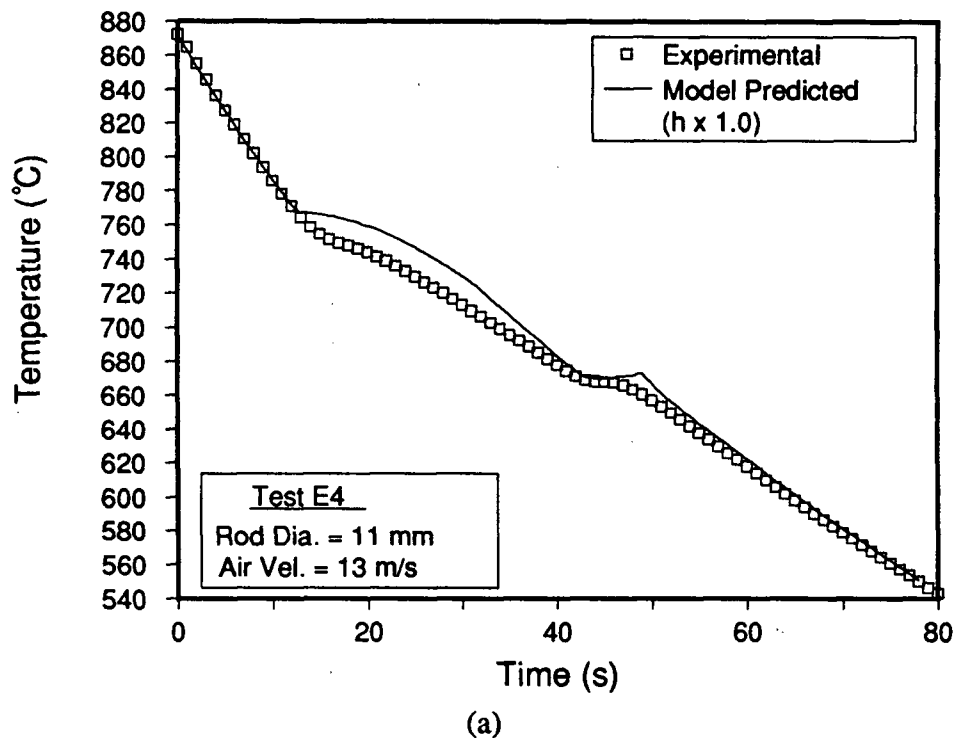
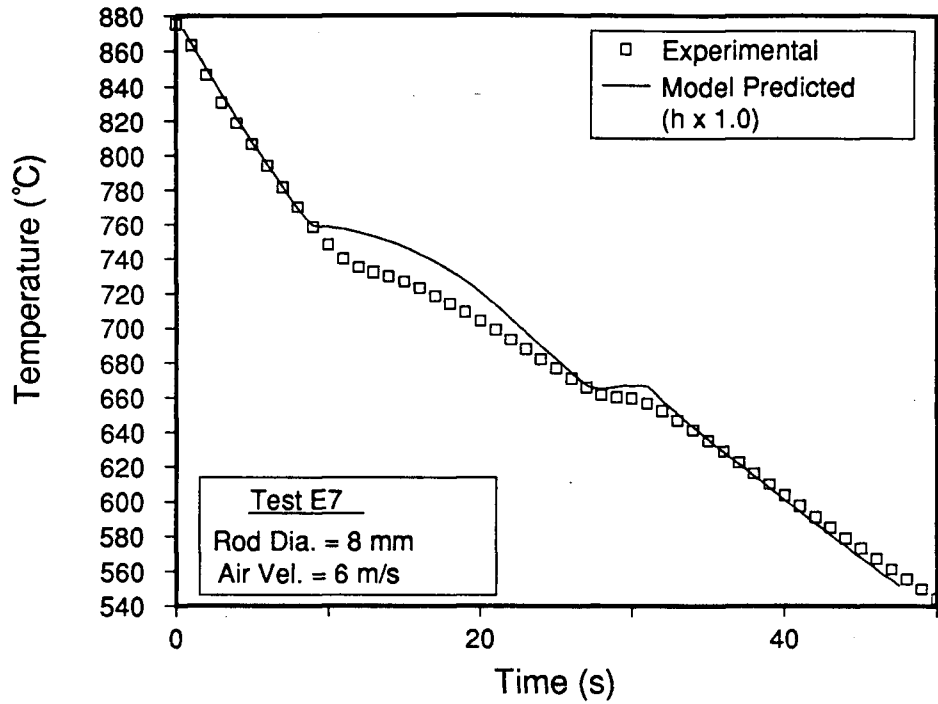
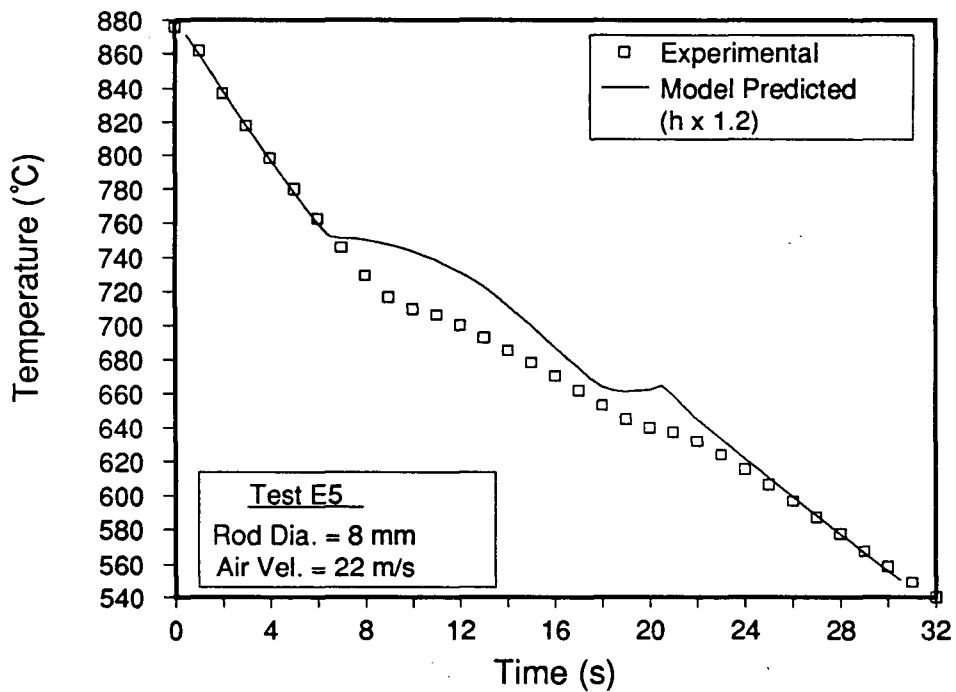


Fig. 8.20 - Measured and model-predicted thermal response at the centreline of a steel rod for Steel E (1020). (a) Test E4, 11-mm diameter, 6 m/s air velocity, (b) Test E7, 8-mm diameter, 6 m/s air velocity (c) Test E5, 8-mm diameter, 22 m/s air velocity.



(b)



(c)

Fig. 8.20 - Measured and model-predicted thermal response at the centreline of a steel rod for Steel E (1020). (a) Test E4, 11-mm diameter, 6 m/s air velocity, (b) Test E7, 8-mm diameter, 6 m/s air velocity (c) Test E5, 8-mm diameter, 22 m/s air velocity.

From the results shown in Figs. 8.18 through 8.20, predicted thermal histories by the mathematical model were seen to be in reasonable agreement with measured laboratory data. To provide increased confidence in the prediction of transformation kinetics, additional dilatometer experiments on the kinetics as a function of temperature, steel composition and prior austenite grain size would have to be performed.

8.3.1.2 Microstructures

Although only a few of the thermal histories obtained during the laboratory tests have been presented in the previous section, model predictions of microstructural parameters have been made for the full complement of lab experiments. Comparisons between predicted and measured ferrite fraction, ferrite grain diameter and pearlite spacing are set out in the following paragraphs.

Predicted-versus-measured ferrite fractions for the laboratory tests are shown in Fig. 8.21. The shaded area in the figure indicates \pm one standard deviation from the regression

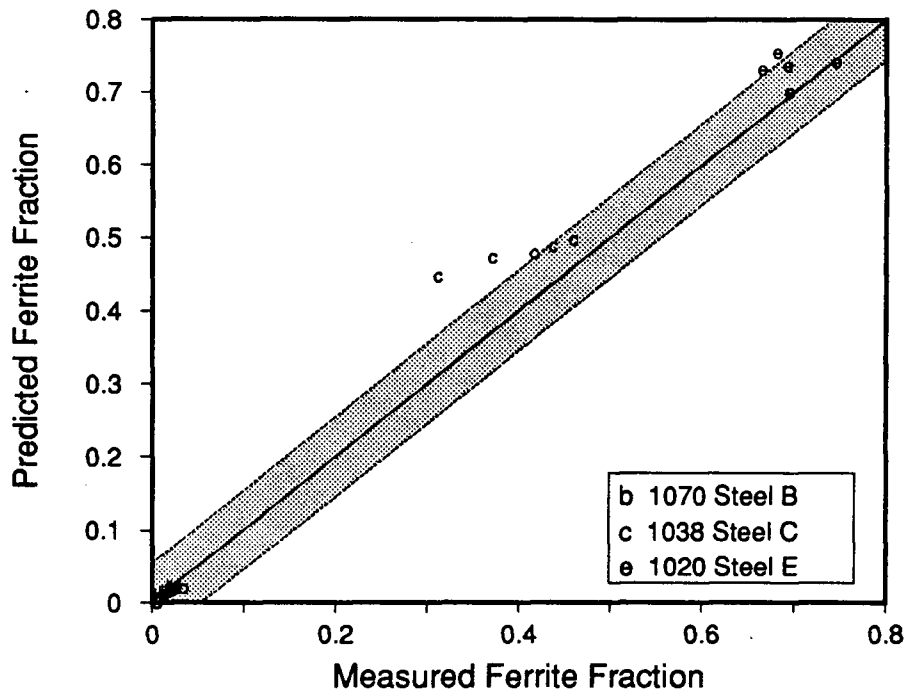


Fig. 8.21 - Model-predicted-versus-measured ferrite fractions for Steels B (1070), C (1038) and E (1020), from the laboratory experiments. The shaded area in the figure indicates \pm one standard deviation of the predicted value.

equation for the prediction of ferrite fraction from composition and cooling rate, Eq. (7.5). Given that measured ferrite fractions for the rods included in the figure have been utilized in developing Eq. (7.5), agreement between measured and model-predicted values is seen to be quite good.

Model-predicted ferrite grain diameters, plotted against the measured values, are presented in Fig. 8.22. Once again the shaded area has been provided to indicate \pm one standard deviation of the predicted value from Eq. (7.6). The ferrite diameter in the prediction is based on the average cooling rate at 750°C and the carbon content of the steel. As can be seen in the plot, excellent agreement between the predicted and measured ferrite diameters has been achieved.

Pearlite interlamellar spacing in the mathematical model is based on the predicted average undercooling below the equilibrium transformation temperature, T_{A1} , employing Eq. (7.8). Results of pearlite spacings predicted from the model for the steels utilized in the

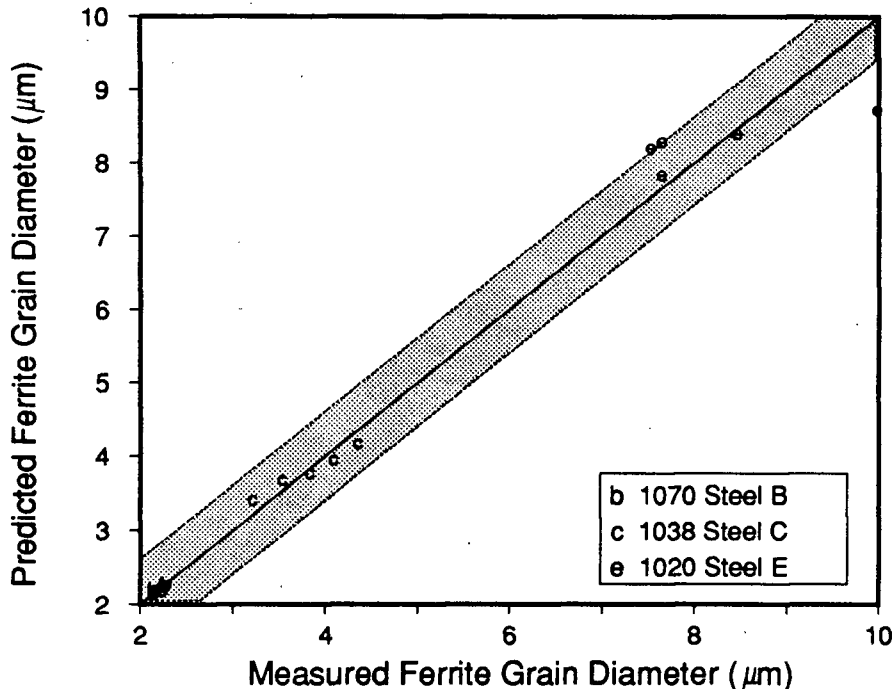


Fig. 8.22 - Model-predicted-versus-measured ferrite grain diameters for Steels B (1070), C (1038) and E (1020), from the laboratory experiments. The shaded area in the figure indicates \pm one standard deviation of the predicted value.

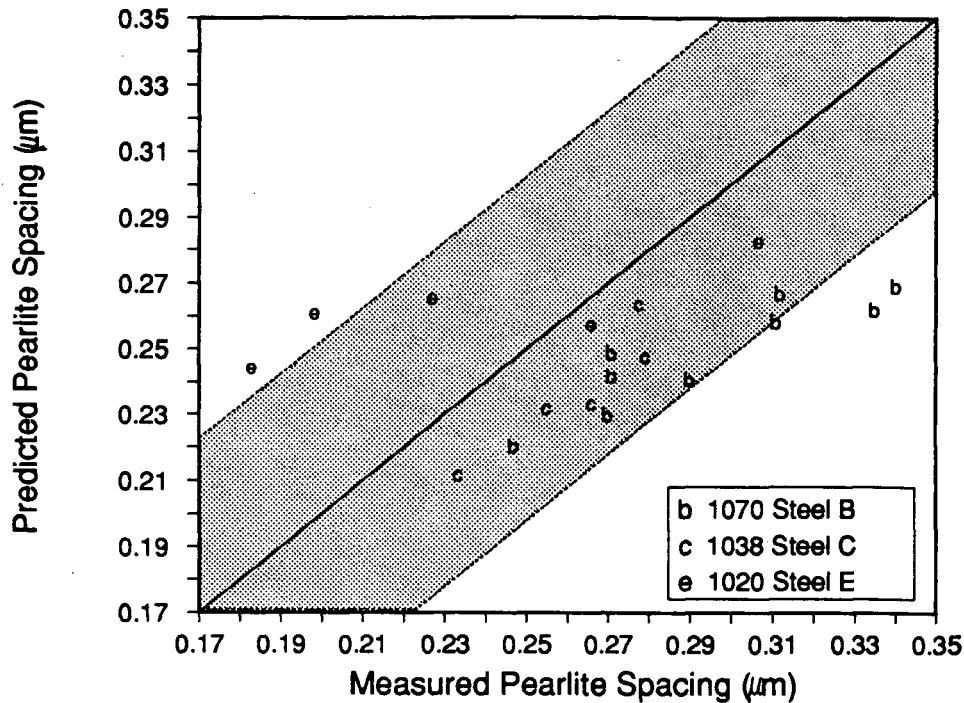


Fig. 8.23 - Model-predicted-versus-measured mean interlamellar pearlite spacings for Steels B (1070), C (1038) and E (1020), from the laboratory experiments. The shaded are represents approximately the \pm one standard deviation in the predicted value.

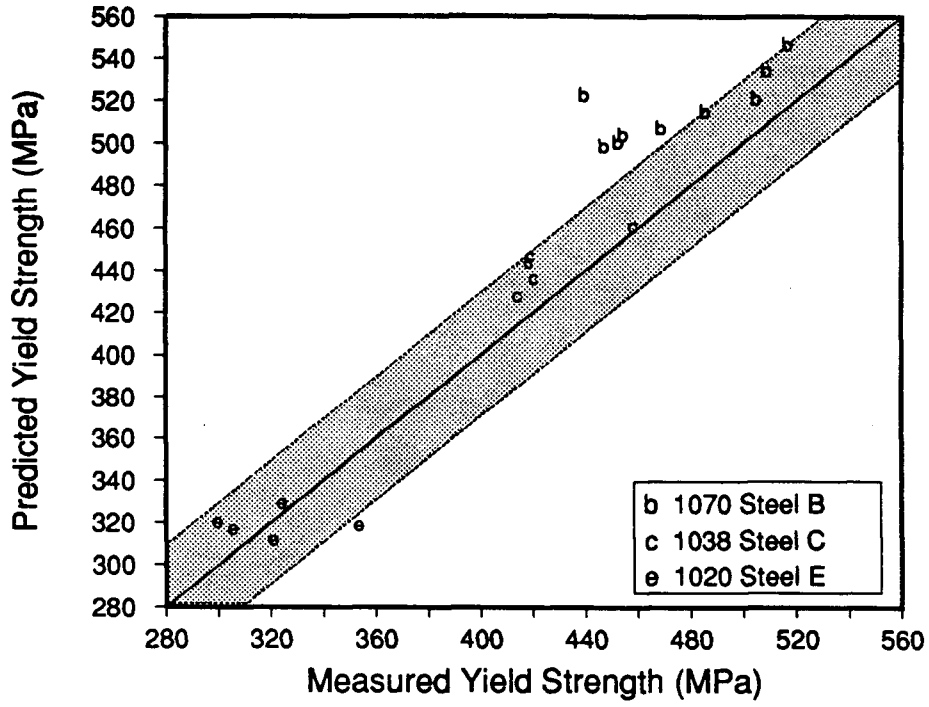
laboratory tests are plotted in Fig. 8.23, against the measured spacings in the case of Steel B and spacings calculated based on measured undercoolings for Steels C and E. As can be seen in the figure, agreement between predicted and calculated values is fair. For Steel B, the predicted pearlite spacings are consistently lower than the measured values. Referring to Fig. 7.23, which displays the experimental measured reciprocal pearlite spacings as a function of undercooling below T_{A1} , predicted spacings for Steel B by Eq. (7.8) are in most cases smaller than the measured values. Thus, it is not surprising that the model also predicts a finer pearlite spacing than measured for this grade of steel. The results for Steel C (1038) show a similar trend; the predicted spacing is less than that measured. For Steel E (1020), the predicted pearlite spacings seem to fall within a narrow range, independent of the magnitude of the measured spacing. This can be attributed to the fact that the predicted pearlite transformation temperatures for Steel E in the model (Figs. 8.20 (a) to (c)), seem to be independent

of steel cooling rate. Thus, in order to improve predictions for pearlite spacings, better correlations for start times would have to be obtained for the pearlite transformation in hypoeutectoid steels.

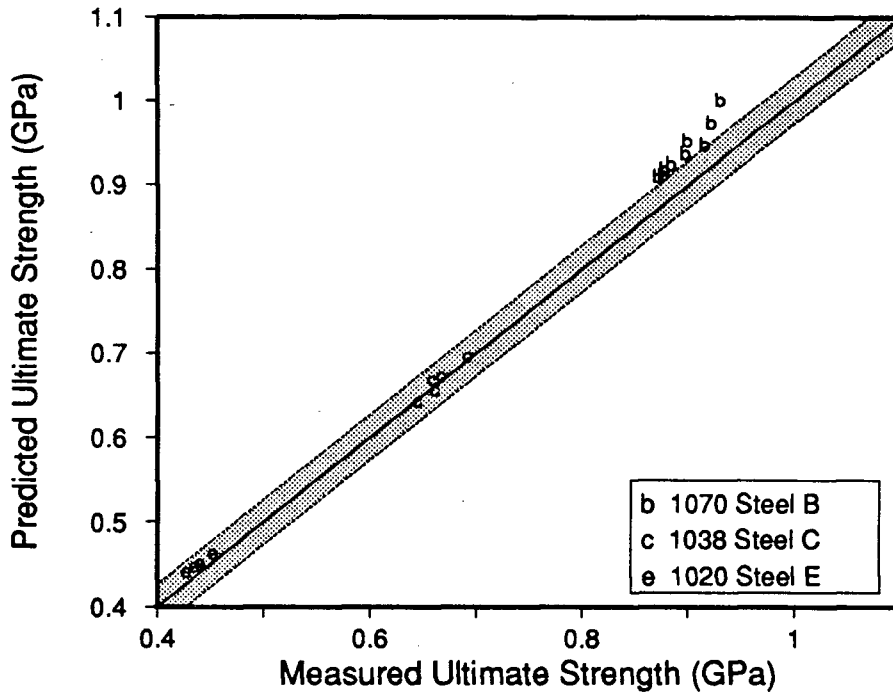
8.3.1.3 Mechanical Properties

Mechanical properties based on steel composition and microstructures predicted in the mathematical model, have been calculated for the laboratory tests. The regression equations employed in the predictions were given in Chapter 7 (Eqs. (7.9) to (7.12)). Model-predicted yield strength plotted against measured yield strength is shown in Fig. 8.24 (a). The shaded area in the figure represents \pm one standard deviation from the regression equations for yield strength. As can be seen, agreement between the measured and predicted values is quite good, although the predicted results for Steel B (1070), seem to be consistently greater than the measured values. The reason for this discrepancy is the under-prediction of pearlite spacing for Steel B, as displayed in Fig. 8.23, and the strong dependency of strength in a high-carbon steel on this variable. Predicted strengths for Steel C (1038) display excellent agreement with the measured. For Steel E (1020), the predicted yield strengths are in good general agreement with the measured strengths. With the exception of one of the predictions for Steel B, the predicted yield strength is within $\pm 10\%$ of the measured values for all laboratory tests shown.

Model-predicted-versus-measured ultimate strengths for the laboratory tests are presented in Fig. 8.24 (b). Once again, the shaded area indicates \pm one standard deviation of the predicted value from the regression equation. Excellent agreement between predicted and measured strengths is shown for the lower carbon grades. However Steel B shows a consistently higher predicted strength. The over-prediction in strength for Steel B has the same origin as the over-prediction of yield strength for this grade. From the plot, it can be seen that the model-predicted UTS is well within $\pm 10\%$ of the measured strength; this is considered as an acceptable strength variation for wire rod [87].



(a)



(b)

Fig. 8.24 - Model-predicted strengths plotted as a function of measured strengths from the laboratory tests; (a) yield strength and (b) ultimate tensile strength.

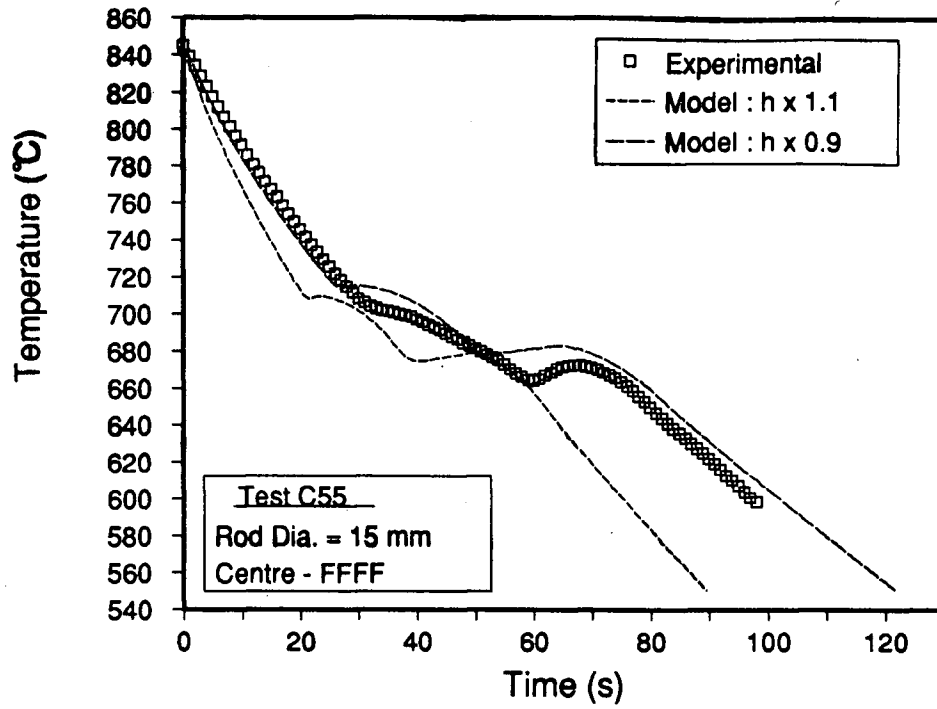
8.3.2 Plant Trials

The mathematical model has been run utilizing steel compositions, rod diameters and line settings identical to a number of plant trial tests. Included in the following sections are model predictions of thermal history, microstructure and mechanical properties for these conditions.

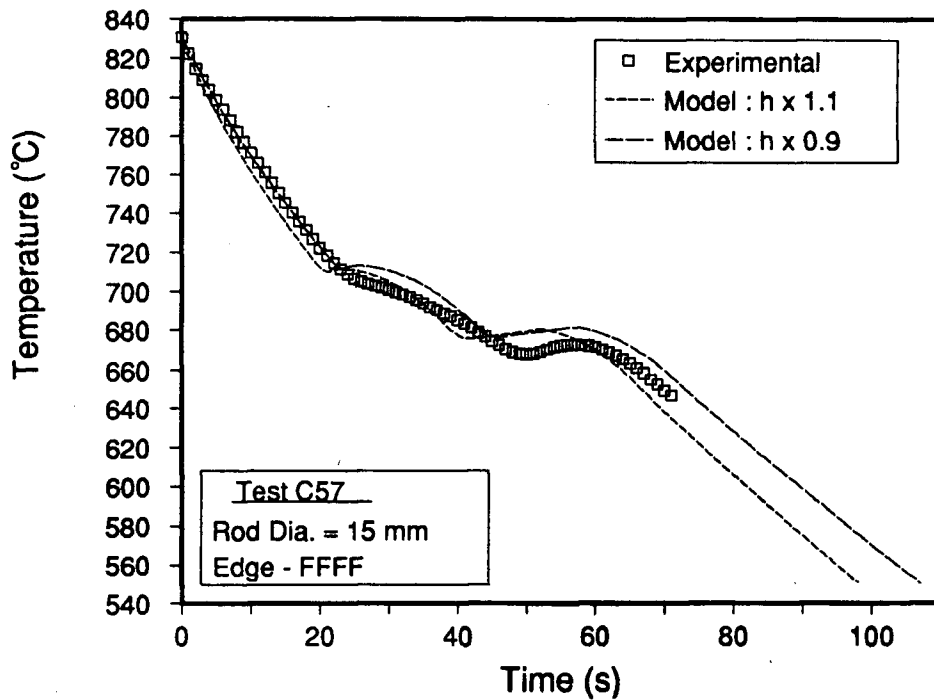
8.3.2.1 Thermal Histories

The model prediction of thermal histories for the plant trials followed a slightly different method, as outlined in Chapter 7. Correction factors have been empirically determined from the plant data, which have enabled the prediction of an effective overall heat-transfer coefficient. However, owing to the scatter exhibited by the measured heat-transfer coefficients and the difficulty in performing the rod cooling experiments on the Stelmor bed, a certain error is expected in the predicted heat-transfer coefficient for the various plant conditions. Thus, predictions of thermal histories in the plant trials have been made employing a $\pm 10\%$ variation in the model-predicted overall heat-transfer coefficient. This variation in heat-transfer coefficient has also been reflected in the microstructure and mechanical properties predictions.

Considering first the 15-mm diameter tests, the measured and model-predicted thermal histories for Steel C (1038) with "air on" are shown in Fig. 8.25 (a) and (b) for the centre and edge of the bed, respectively. As can be seen, the model-predicted cooling conditions show excellent agreement with the measured data. Also displayed is the slightly higher cooling rate suggested for the edge of bed tests. However, as was the case for the laboratory results, phase transformation kinetics predicted for the two tests are faster than the measured values. In light of the variation exhibited in the parameters utilized for the prediction of transformation kinetics and their effect shown in the sensitivity analysis (Section 8.2.3), the agreement between measured and model-predicted thermal histories for the full air tests is considered good. Results of the "air off" tests for Steel C are shown in Fig. 8.25 (c) and (d) for the centre and edge of the bed, respectively; thermocouple contact for the edge test, was

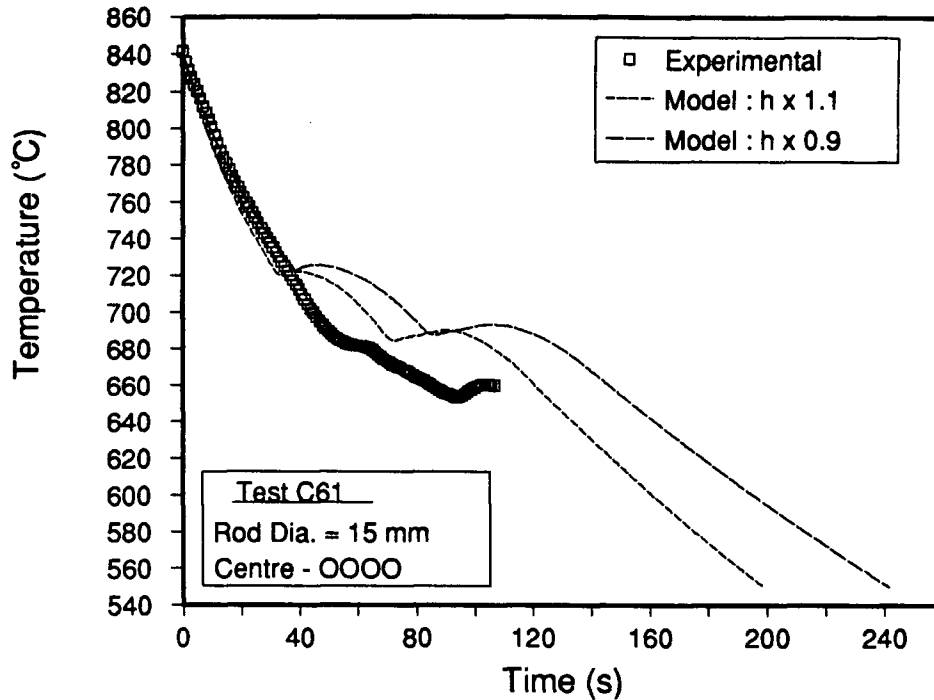


(a)

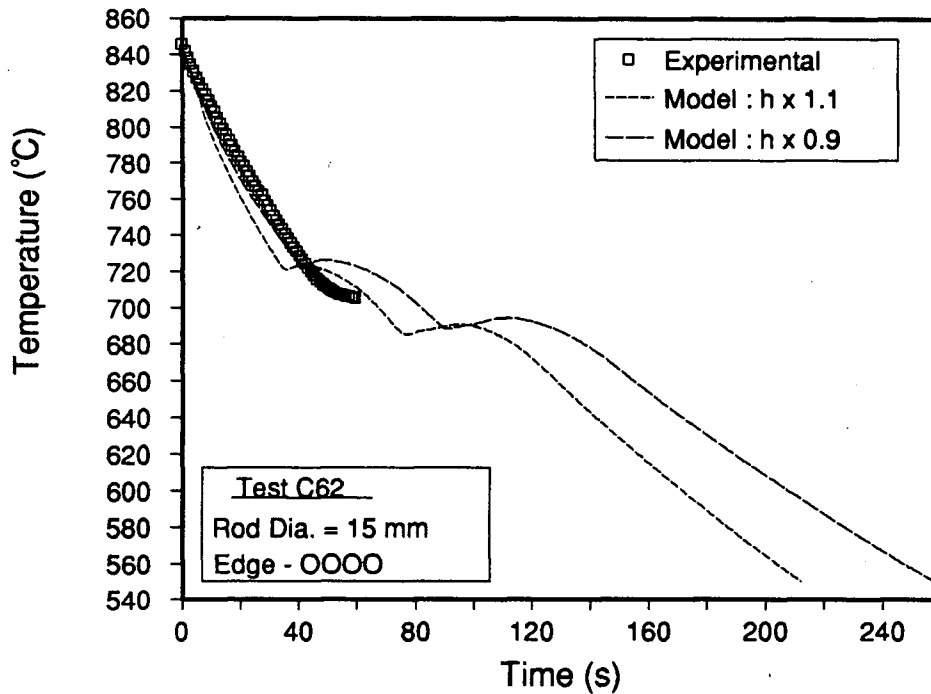


(b)

Fig. 8.25 - Measured and model-predicted thermal history for Steel C (1038), 15-mm diameter rods cooled plant tests. (a) Test C55, centre - "air on", (b) Test C57, edge - "air on", (c) Test C61, centre - "air off" and (d) Test 62, edge - "air off".



(c)



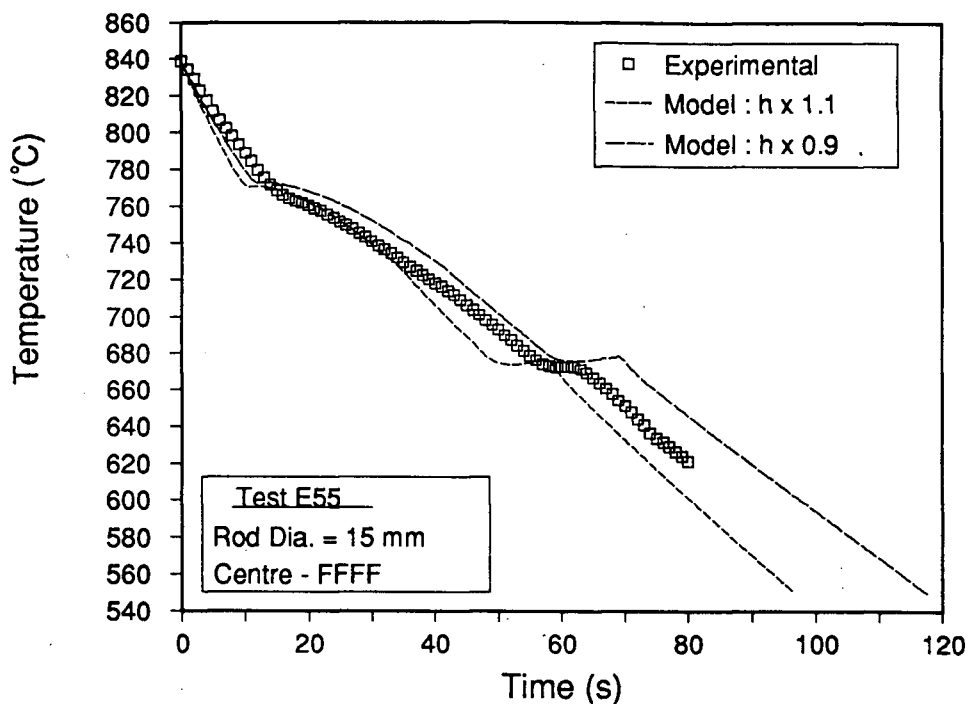
(d)

Fig. 8.25 - Measured and model-predicted thermal history for Steel C (1038), 15-mm diameter rods cooled in plant tests. (a) Test C55, centre - "air on", (b) Test C57, edge - "air on", (c) Test C61, centre - "air off" and (d) Test C62, edge - "air off".

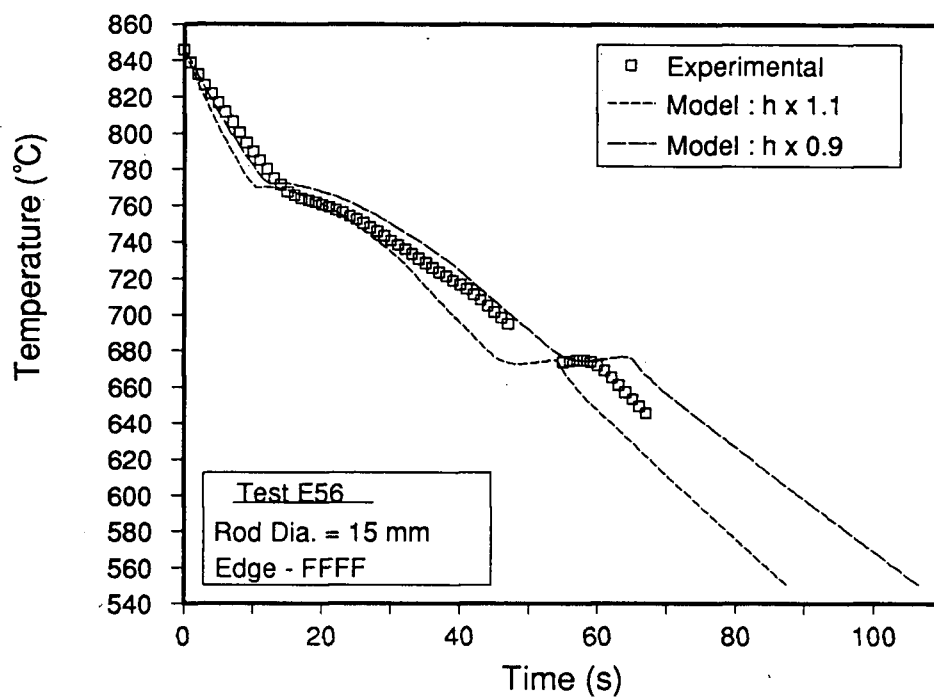
lost between 50 and 60 s. The initial part of the thermal history for both tests is in good agreement with the model-predicted results. Comparison between the "air on" and "air off" tests for Steel C, shows that the average cooling rate is approximately doubled with the "air on", as displayed by the time required to cool to 550°C. For the centre test, Fig. 8.25 (c), the start time for the ferrite transformation predicted by the model is much earlier than that indicated by the measured data. Referring to Chapter 7, Fig. 7.2 (a), thermal histories for all Steel C plant tests are compared. As can be seen, the results for the centre "air off" condition, Test C61, display a much lower transformation start temperature than any of the other tests, including those with a much higher cooling rate. It would thus seem that the transformation portion of this curve is in error, considering the excellent agreement displayed for the remainder of the results for Steel C in Fig. 7.2 (a).

The results of the four Steel C tests (Figs. 8.25 (a) to (d)), show the ability of the mathematical model to accurately predict cooling conditions on the Stelmor line prior to the onset of transformation. However, predictions for phase transformation kinetics were not as good; considering the variations in the parameters required for predicting kinetics, the results are considered only reasonable and in one case poor. In general, it would seem that the ferrite transformation kinetics are over-predicted by the model, which results in an early pearlite start time. A decrease in ferrite kinetics would provide a much better predicted thermal history, compared to the measured data.

The second 15-mm diameter grade included in the plant trials, was Steel E (1020); the results for this grade are displayed in Fig. 8.26. The "air on" test results are shown in Fig. 8.26 (a) and (b) for the centre and edge of bed tests, respectively. In both cases, the model-predicted results show excellent agreement with the measured data, including the phase transformation portions of the curves. Particularly good agreement is displayed for the pearlite transformation start time and apparent kinetics. A good agreement between measured and model-predicted thermal history is also displayed in Fig. 8.26 (c), for the centre "air off" test. The measured data seems to show a lower rate of latent heat release for the ferrite



(a)



(b)

Fig. 8.26 - Measured and model-predicted thermal history for Steel E (1020), 15-mm diameter rods cooled in plant tests. (a) Test E55, centre - "air on", (b) Test E56, edge - "air on" and (c) Test E51, centre - "air off".

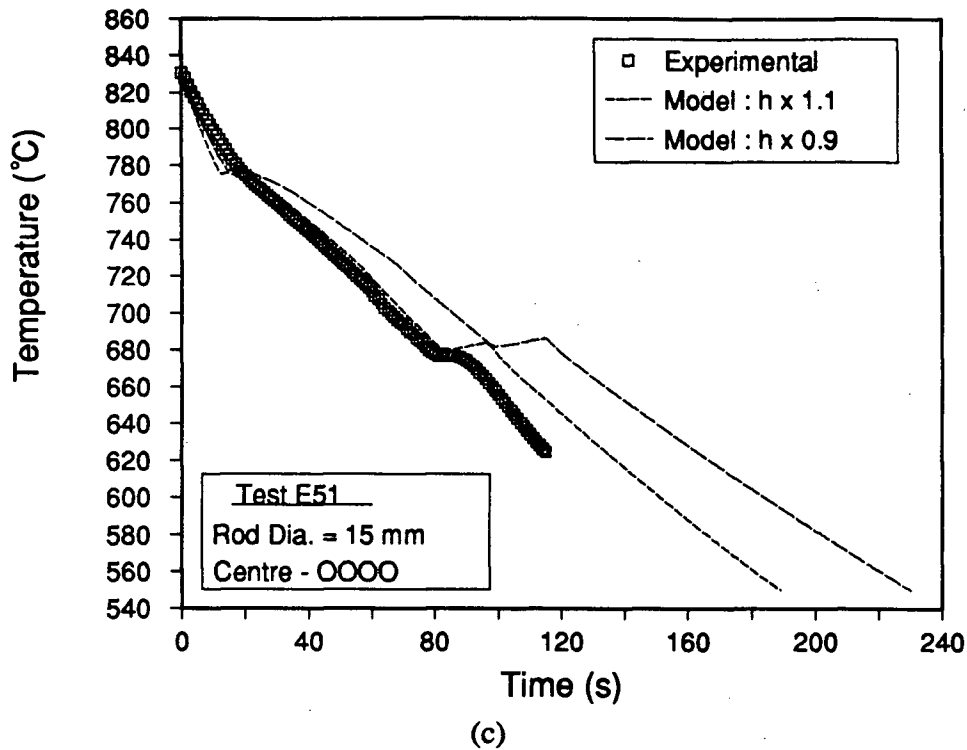
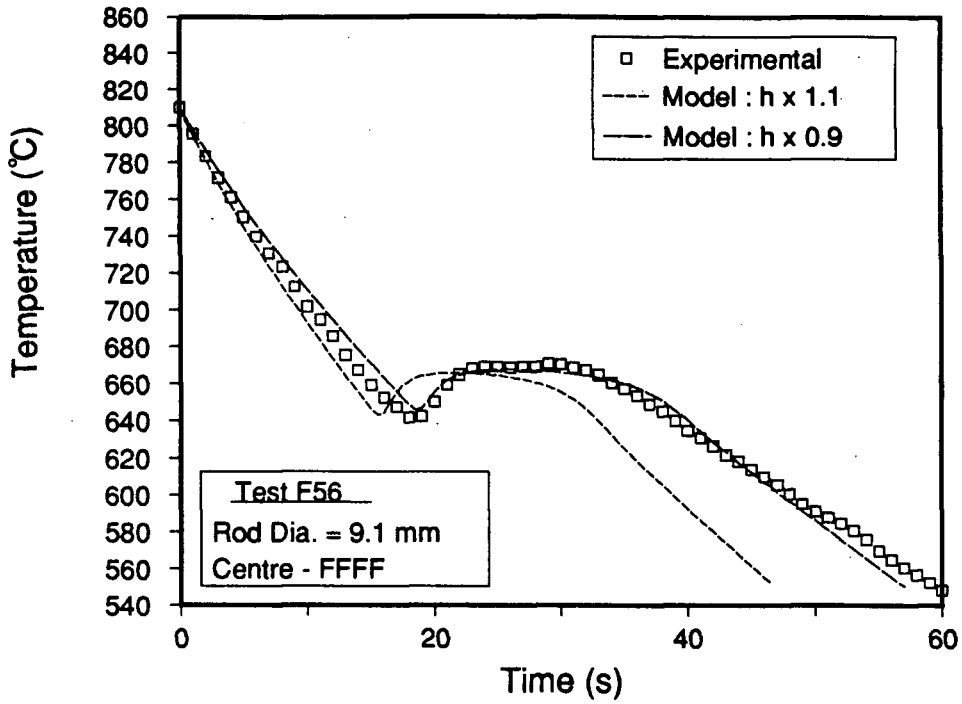


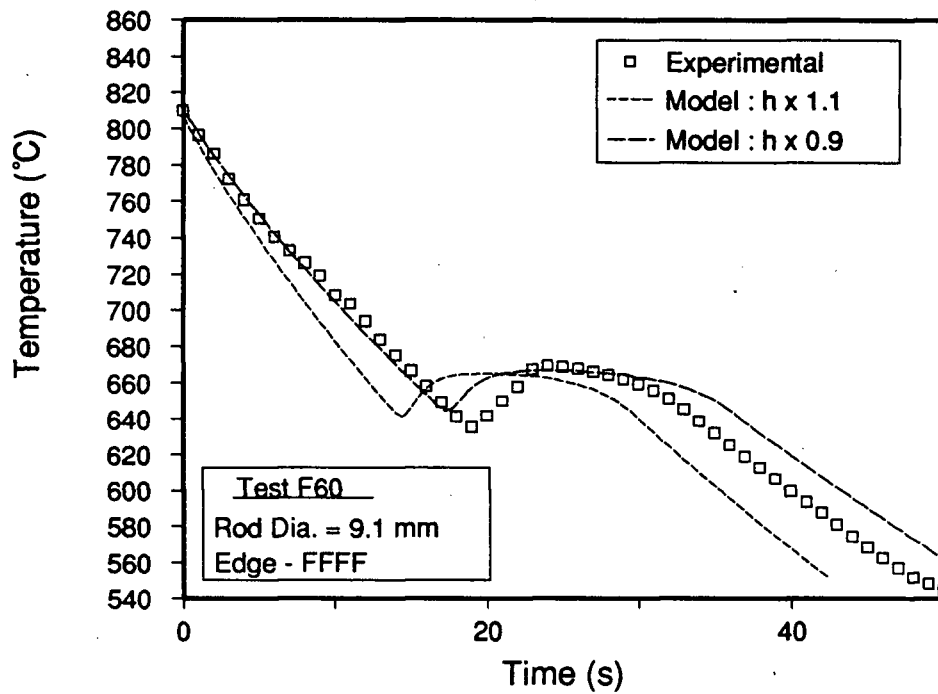
Fig. 8.26 - Measured and model-predicted thermal history for Steel E (1020), 15-mm diameter rods cooled in plant tests. (a) Test E55, centre - "air on", (b) Test E56, edge - "air on" and (c) Test E51, centre - "air off".

transformation which results in a slight under-prediction in rod temperature during later stages of cooling. The reason for this behaviour is not known; previous laboratory and plant cooling comparisons for Steel E have displayed excellent prediction of latent heat release during transformation. Once again, predicted pearlite start time and kinetics show good agreement with the measured data.

Only two plant trial conditions were found to be suitable for comparison with model predictions, among the tests on Steel F (1080), 9.1-mm diameter rod. High-carbon grades processed on the Stelmor line are generally cooled as fast as possible to achieve a fine pearlite spacing. Owing to the fact that the test rods were matched with industrial coils of similar grade during the plant trials, "air on" conditions usually were employed. The results of the model-predicted and measured thermal histories are shown in Fig 8.27 (a) and (b) for a typical centre and edge of the bed test, respectively. Excellent agreement between predicted



(a)



(b)

Fig. 8.27 - Measured and model-predicted thermal history for Steel F (1080), 9.1-mm diameter rods cooled in plant tests. (a) Test F56, centre - "air on" and (b) Test F60, edge - "air on".

and measured thermal histories for the two tests is displayed, with the exception of the pearlite transformation portion for the edge test, Fig 8.27 (b). This is considered to be relatively minor when compared to the results of other "air on" tests for this grade, shown in Fig. 7.3 (a). As can be seen in that figure, the start temperature for the five "air on" tests varies by about 10°C.

The second 9.1-mm diameter grade employed for the plant trials was Steel G (1037). Model-predicted and measured thermal histories for this grade are shown for three plant conditions in Fig. 8.28. The "air on" tests, shown in Fig. 8.28 (a) and (b) for the centre and edge of bed, respectively, display good agreement between predicted and measured results. Once again, however, the predicted ferrite transformation initiates earlier than suggested by the measured data. As before, this results in an early model-predicted start time for the pearlite transformation. Nevertheless, latent heat released for each transformation, predicted by

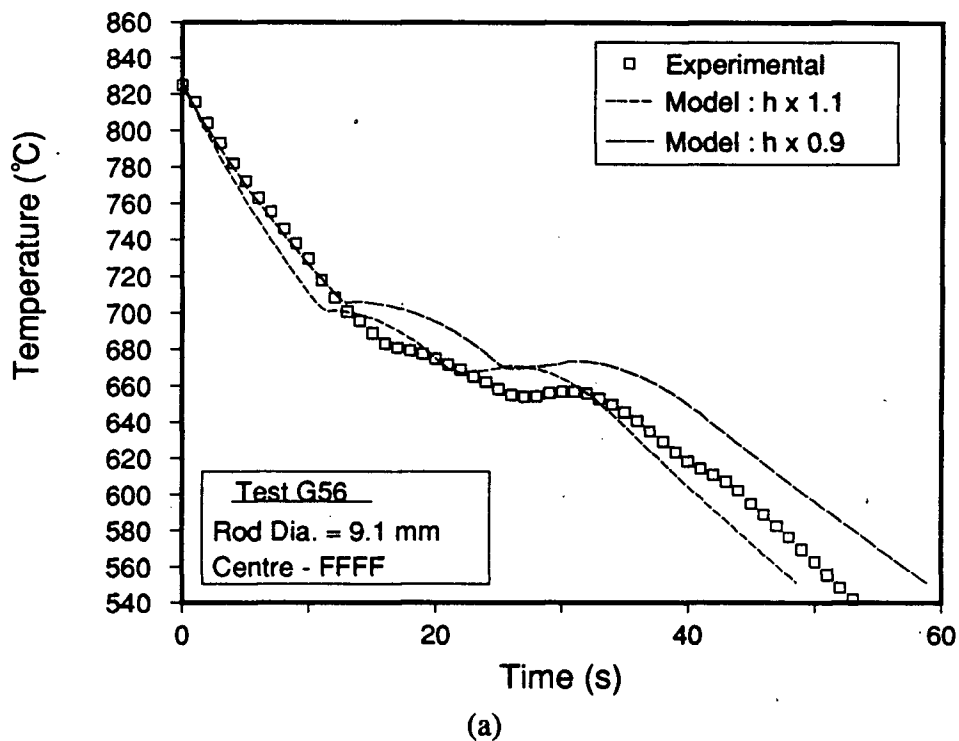
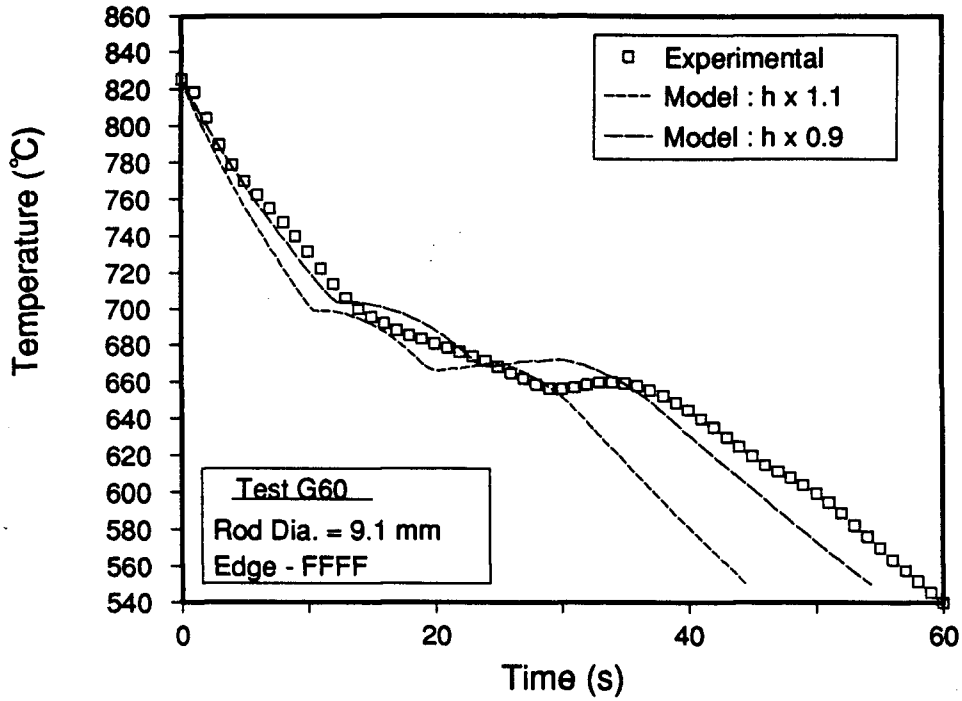
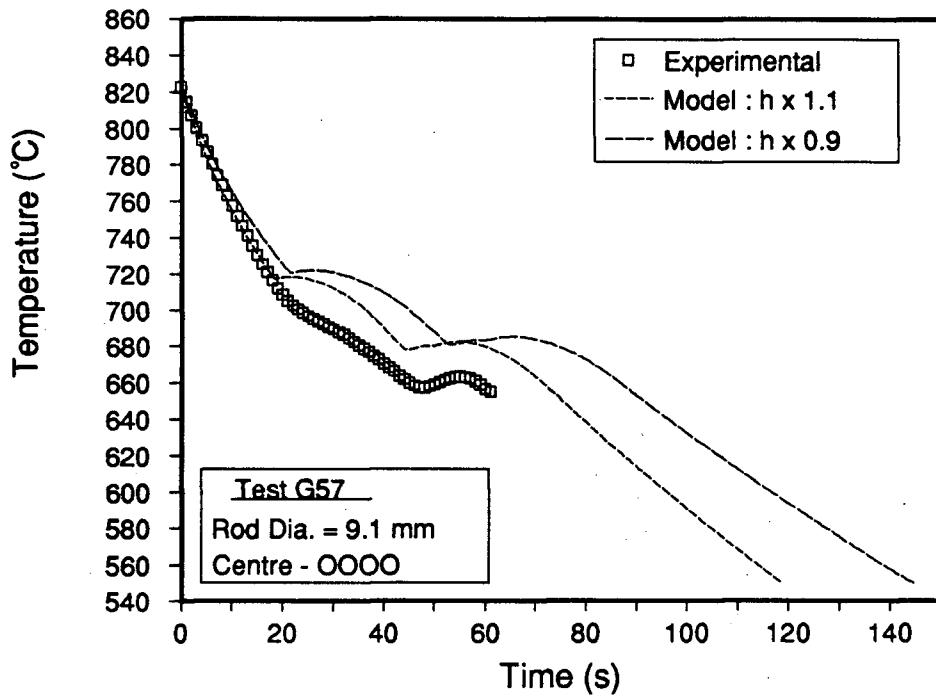


Fig. 8.28 - Measured and model-predicted thermal history for Steel G (1037), 9.1-mm diameter rods cooled in plant tests. (a) Test G56, centre - "air on", (b) Test G60, edge - "air on" and (c) Test G57, centre - "air off".



(b)

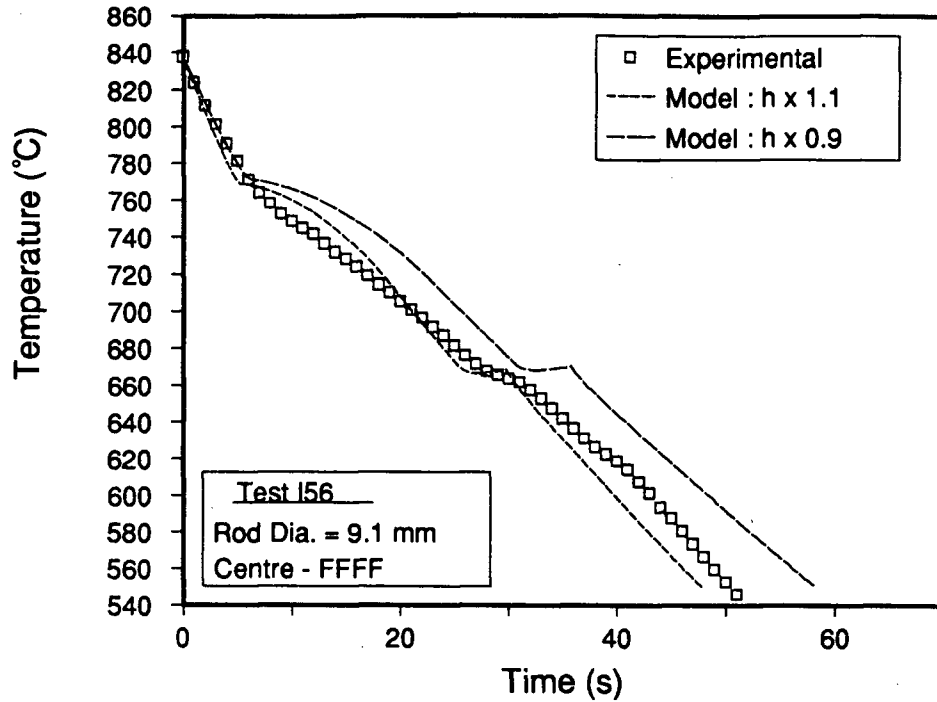


(c)

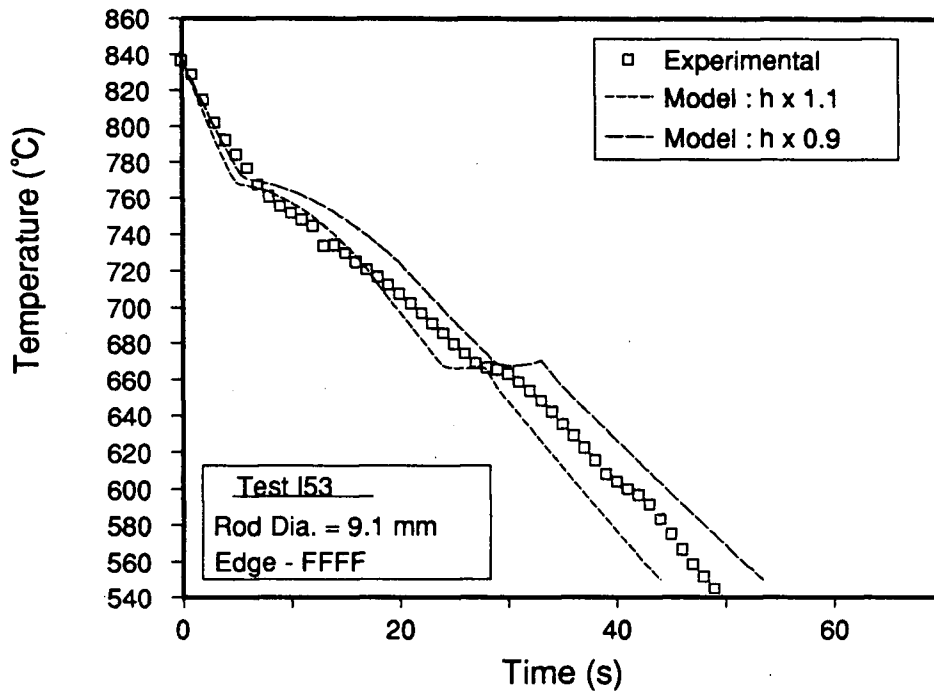
Fig. 8.28 - Measured and model-predicted thermal history for Steel G (1037), 9.1-mm diameter rods cooled in plant tests. (a) Test G56, centre - "air on", (b) Test G60, edge - "air on" and (c) Test G57, centre - "air off".

the model, shows excellent agreement with the measured values. The third test considered for Steel G is shown in Fig. 8.28 (c), and is for centre "air off" conditions. As can be seen the austenite-pearlite transformation was not completed before the measured data became interrupted, however good agreement for the initial cooling period was achieved with the model predictions. The model-predicted ferrite transformation start time and kinetics seem to be more rapid than the measured values, as witnessed in the previous comparisons for medium-carbon grades.

Model-predicted and measured thermal histories for plant trials on Steel I (1017), 9.1-mm diameter rod are presented in Fig. 8.29. Considering the "air on" tests, shown in Figs. 8.29 (a) and (b) for the centre and edge of the bed, respectively, excellent agreement is evident between the predicted and measured results. For both figures, the transformation start times predicted for ferrite and pearlite, agree well with the measured values. The predicted ferrite kinetics seem to be slightly faster than that suggested from the measured data, but this is considered minor in light of the variations witnessed in the sensitivity analysis. In the other two tests reported for Steel I, the air for the first cooling zone of the Stelmor line was turned off but the remaining three zones were on. The thermal histories for these tests are shown in Figs. 8.29 (c) and (d). As can be seen, the exact point at which the test rod crossed from the first to second zone is difficult to determine. The start of the ferrite transformation is also hard to detect from the results, especially for Test I60. In spite of these problems, the model-predicted thermal histories show reasonable agreement with the measured data. Ideally, the time and temperature at which the cross-over between zones takes place should be determined and the model synchronized to yield a comparable result.

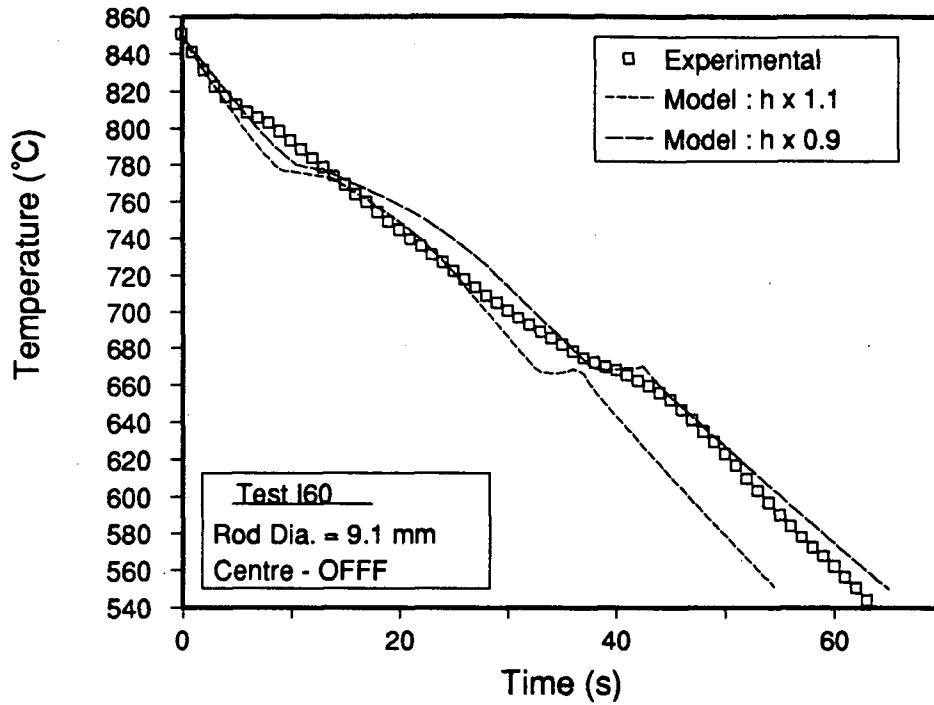


(a)

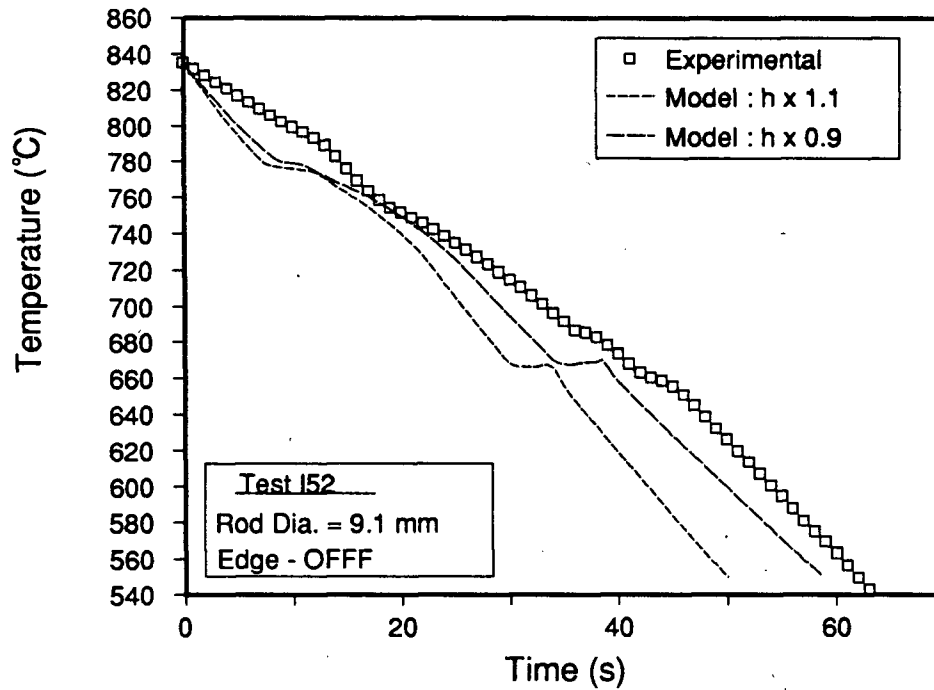


(b)

Fig. 8.29 - Measured and model-predicted thermal history for Steel I (1017), 9.1-mm diameter rods cooled in plant tests. (a) Test I56, centre - "air on", (b) Test I53, edge - "air on", (c) Test I60, centre - "air off" zone 1, "air on" remaining zones and (d) Test I52, edge - "air off" zone 1, "air on" remaining zones.



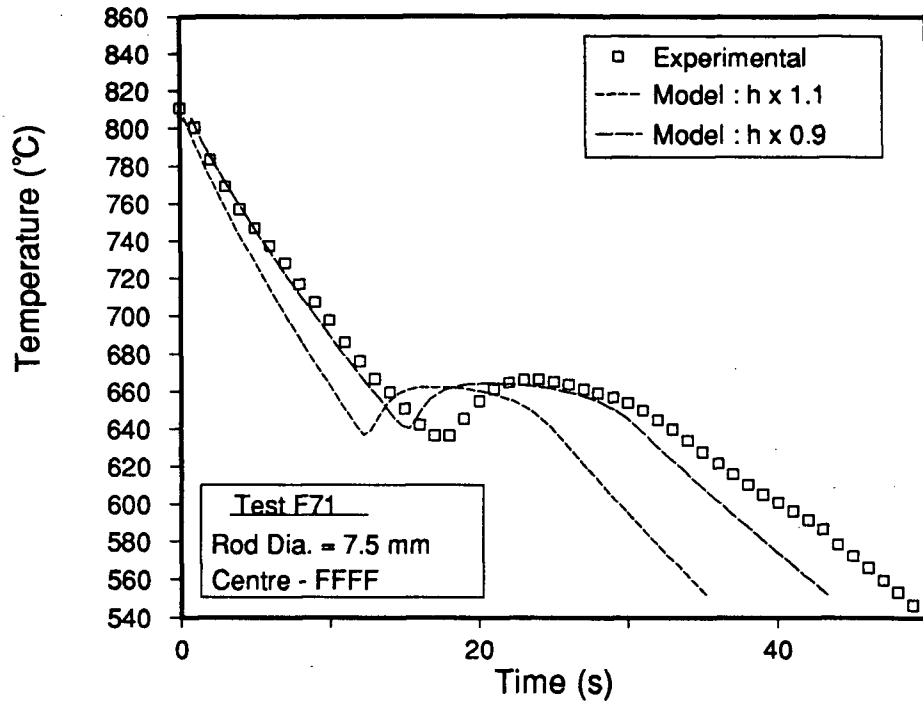
(c)



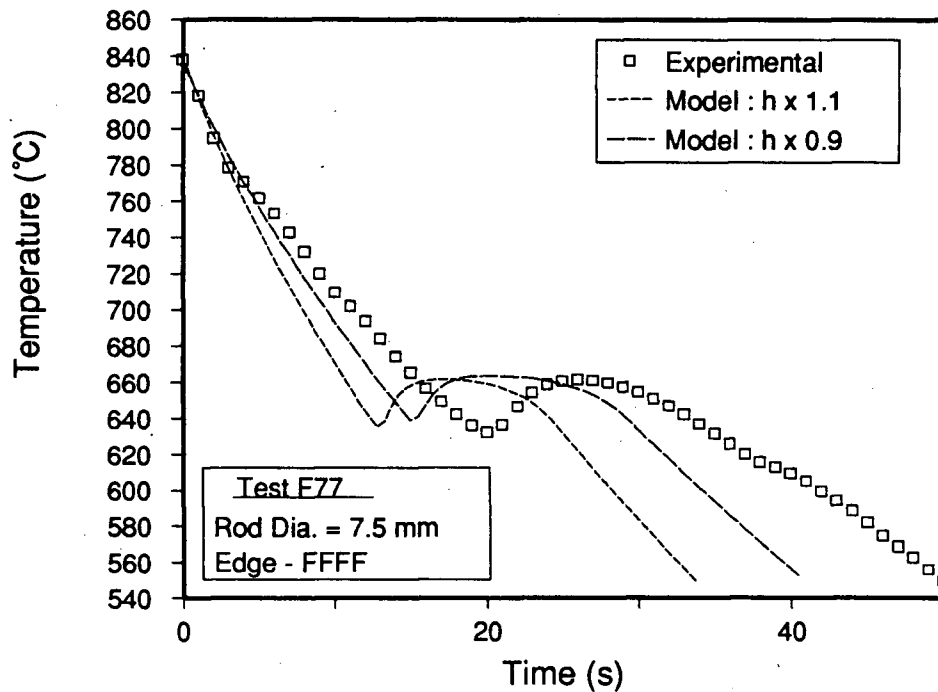
(d)

Fig. 8.29 - Measured and model-predicted thermal history for Steel I (1017), 9.1-mm diameter rods cooled in plant tests. (a) Test I56, centre - "air on", (b) Test I53, edge - "air on", (c) Test I60, centre - "air off" zone 1, "air on" remaining zones and (d) Test I52, edge - "air off" zone 1, "air on" remaining zones.

Considering once again Steel F (1080), the results of the model-predicted and measured thermal histories for the 7.5-mm diameter tests are included in Fig. 8.30. Firstly, "air on" tests for the centre and edge positions, respectively, are presented in Figs. 8.30 (a) and (b). Both tests reveal an over-prediction in the heat-transfer coefficient by the model, but good agreement with the measured data in terms of pearlite transformation temperature and kinetics. A reason for the over-prediction in heat transfer coefficient is not known, however, as shown in Figs. 7.6 (a) to (e), the variation in the calculated heat-transfer coefficient for similar plant tests seems to be greatest for the 7.5-mm diameter rod. This is not surprising, when the thermal mass of the rods is considered; the smallest 7.5-mm diameter rod would be expected to be most sensitive to changes in heat-transfer conditions. In addition, referring to Fig. 7.4 (a), where thermal histories for the complete complement of plant tests on 7.5-mm diameter rods of Steel F rod are shown, a considerable variation in pearlite transformation start time and temperature is seen, for similar cooling conditions. Also observed, is a significant difference in average rod cooling time over the course of the test; Test F75 and Test F74, which are both edge "air on" tests, take 50 and 65 s respectively, to reach 500°C. Considering these variations, the model-predicted thermal histories plotted in Figs. 8.30 (a) and (b), show reasonable agreement. The mathematical model has also been employed to predict thermal histories in plant tests for which the air flow through the Stelmor line was off. A comparison of the model-predicted and measured results for this condition is depicted in Figs. 8.30 (c) and (d). As can be seen, reasonable agreement between the predicted and measured data has been achieved. The predicted pearlite transformation kinetics seem to be slightly slower than the measured values, as the recalescence is greater and the transformation time shorter in the plant data. Referring to the effect of variations in kinetic parameters on the pearlite transformation kinetics shown in Section 8.2.3 of the sensitivity analysis, the differences between the reaction kinetics displayed in Figs. 8.30 (a) and (b), are not considered significant.

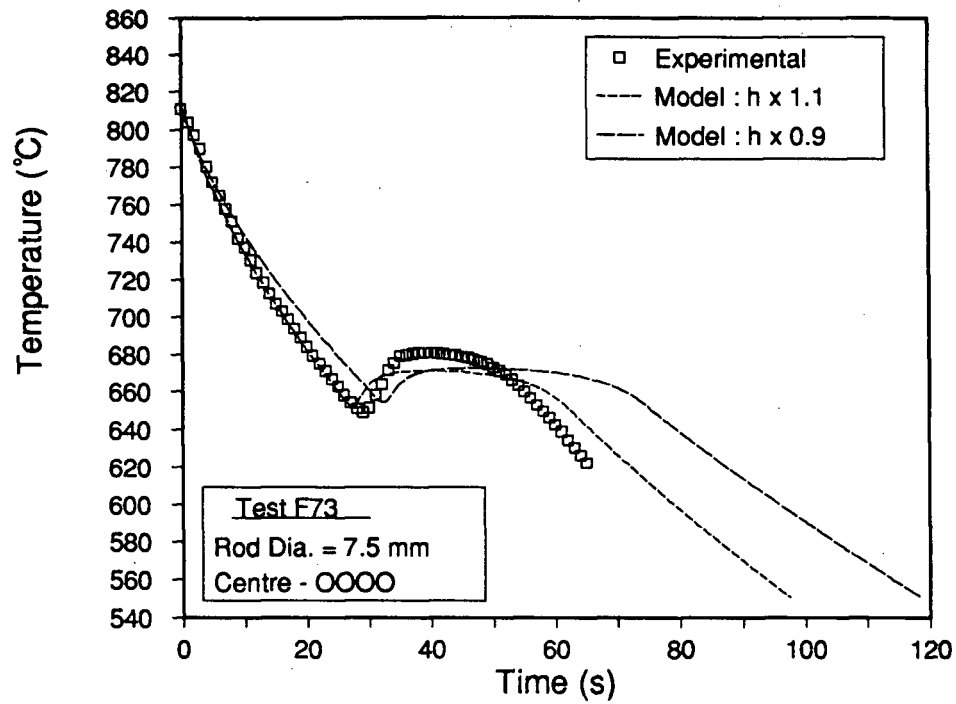


(a)

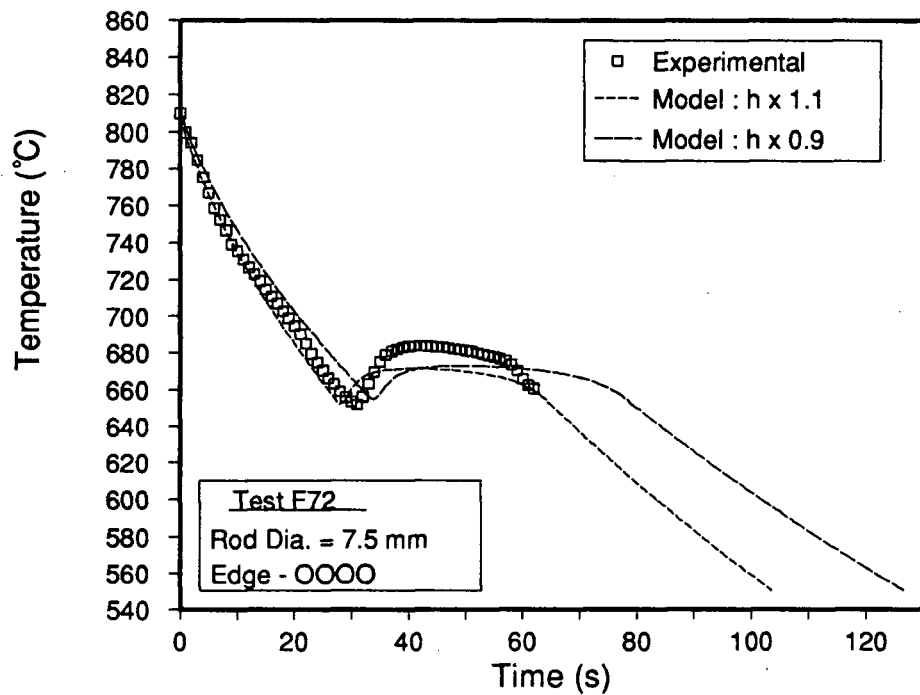


(b)

Fig. 8.30 - Measured and model-predicted thermal history for Steel F (1080), 7.5-mm diameter rods cooled in plant tests. (a) Test F71, centre - "air on", (b) Test F77, edge - "air on", (c) Test F73, centre - "air off" and (d) Test F72, edge - "air off".



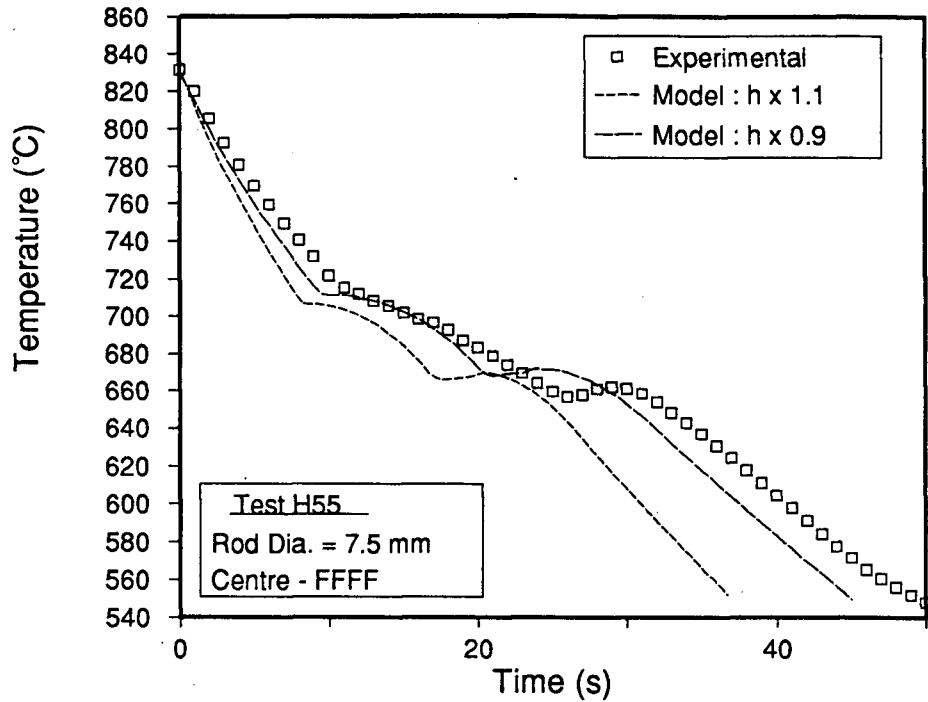
(c)



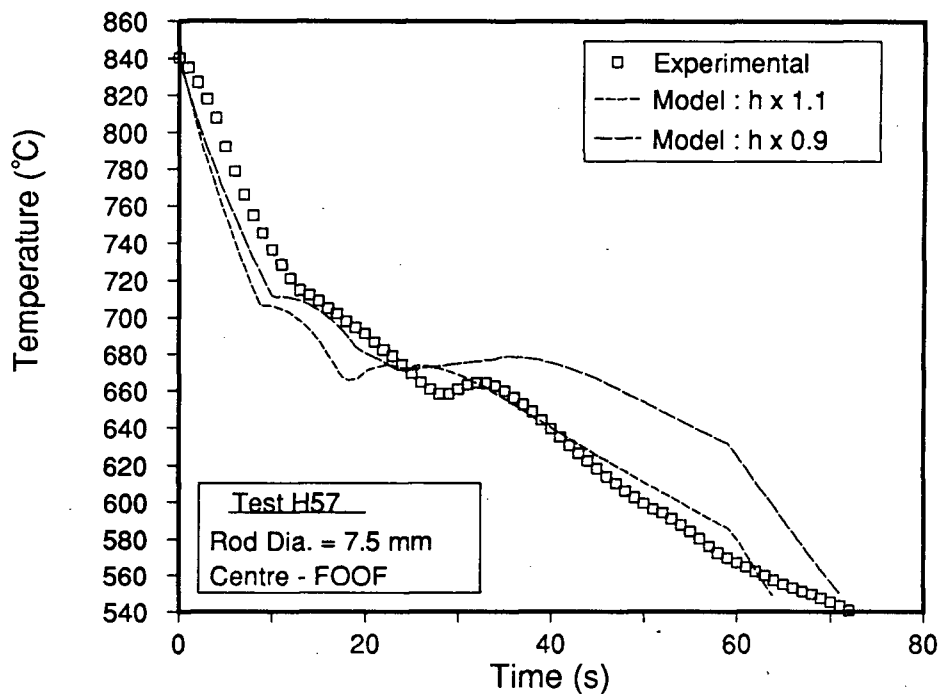
(d)

Fig. 8.30 - Measured and model-predicted thermal history for Steel F (1080), 7.5-mm diameter rods cooled in plant tests. (a) Test F71, centre - "air on", (b) Test F77, edge - "air on", (c) Test F73, centre - "air off" and (d) Test F72, edge - "air off".

Model-predicted and measured thermal histories for plant tests on 7.5-mm diameter rod of Steel H (1035), are presented in Fig. 8.31. Results of the comparison for "air on" tests are shown in Fig. 8.31 (a) for the centre of the bed. Unfortunately, a consistent, measured thermal history was not obtained for these conditions at the edge of the Stelmor bed. Figure 8.31 (a) reveals good agreement between the model and measured data, especially for the ferrite transformation portion of the cooling curve. There does however seem to be a high model-predicted pearlite start temperature, and a slight over-prediction of the heat-transfer coefficient suggested by the data. As was pointed out for the 7.5-mm diameter tests on Steel F, this error is reasonable when the variation in calculated heat-transfer coefficient for these tests is considered. Referring to Fig. 8.31 (b), predicted and measured thermal histories for a centre of the bed test are shown, in which the air settings for zones one through four were on-off-off-on, respectively. As pointed out before, synchronization of the model to the changes in air settings occurring on the line was difficult, owing to the lack of indication of changes displayed in the measured thermal history. Nevertheless, comparison between the predicted and measured thermal histories has been made and, for the most part, agreement is good. During the later stages of cooling, the cooling rate corresponding to the resumption of air flow in the model increases, whereas the cooling rate suggested by the plant data distinctly decreases. The reason for this is that the test rod was most likely taken off of the Stelmor deck thereby reducing the heat-transfer conditions. The predicted ferrite transformation start time is in reasonable agreement with the measured data, however, the predicted kinetics seem to be slightly higher. In addition, the pearlite start time predicted by the model is in advance of the start time suggested by the plant data. Similarly, Fig. 8.31 (c) displays the results of a cooling test on Steel H, for which the air flow was turned off for the first zone and on for the remaining zones. The figure reveals excellent agreement between the model-predicted and measured thermal histories, during the initial stages of cooling. Good agreement has been achieved for the ferrite transformation as well. However, the pearlite transformation exhibits an early predicted start time as compared to the measured data.



(a)



(b)

Fig. 8.31 - Measured and model-predicted thermal history for Steel H (1035), 7.5-mm diameter rods cooled in plant tests. (a) Test H55, centre - "air on", (b) Test H57, centre - "air on" zone 1, "air off" zones 2 and 3, "air on" zone 4 and (c) Test H60, centre - "air off" zone 1, "air on" zones 2 to 4.

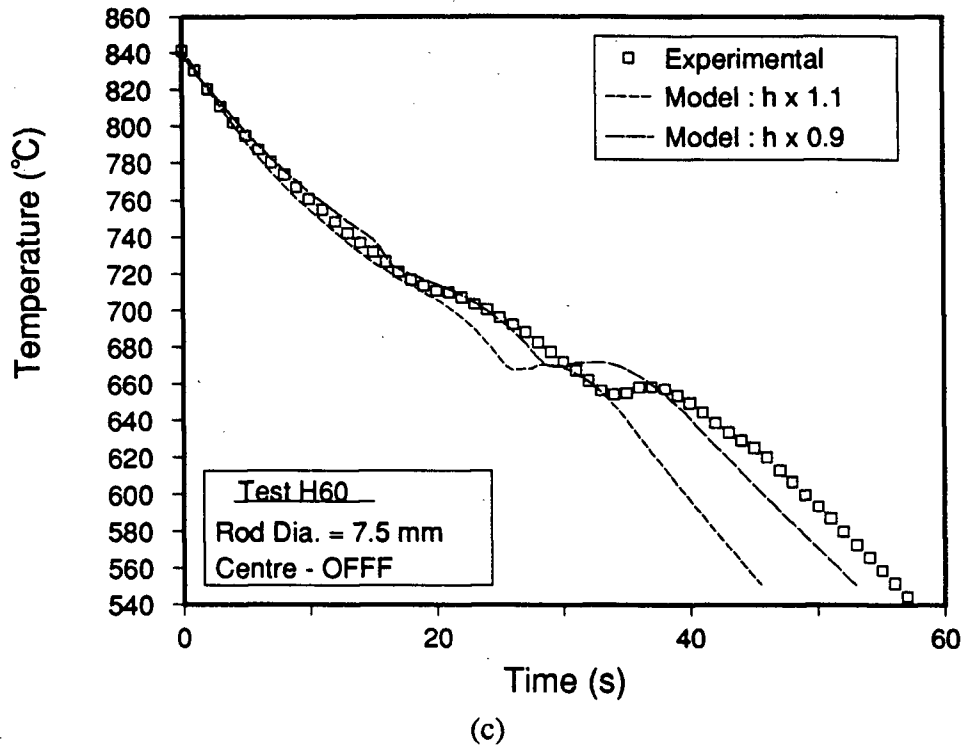
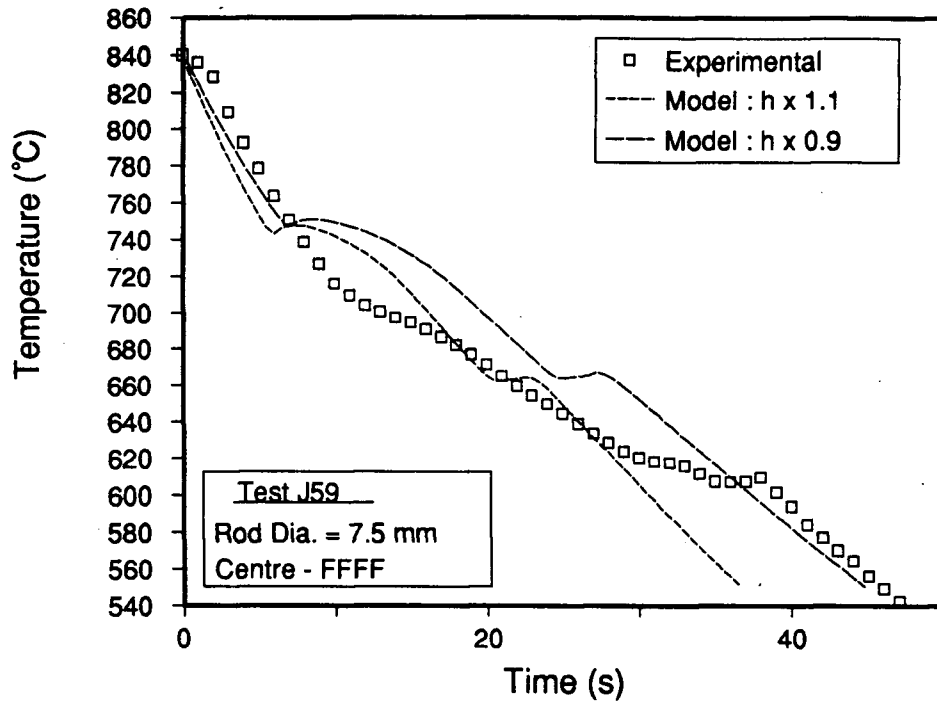


Fig. 8.31 - Measured and model-predicted thermal history for Steel H (1035), 7.5-mm diameter rods cooled in plant tests. (a) Test H55, centre - "air on", (b) Test H57, centre - "air on" zone 1, "air off" zones 2 and 3, "air on" zone 4 and (c) Test H60, centre - "air off" zone 1, "air on" zones 2 to 4.

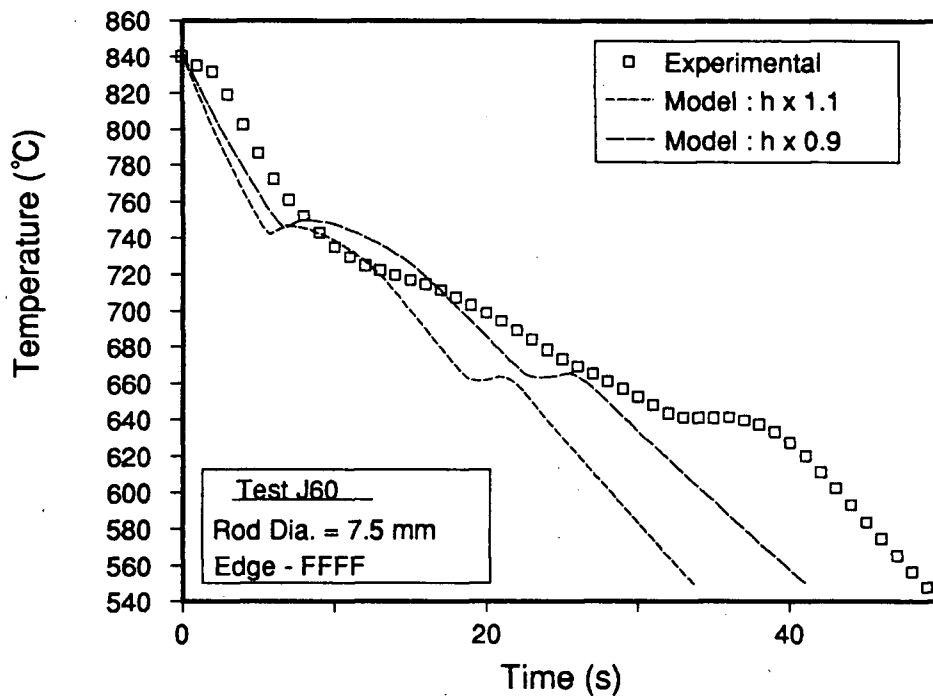
The final grade of steel included in the plant trails, Steel J (1022), also had a 7.5-mm diameter. Model-predicted and measured thermal histories for "air on" tests are included in Fig. 8.32 (a) and (b) for centre and edge tests, respectively. Although the cooling conditions are similar for the two tests, the transformation start temperatures for both ferrite and pearlite, can be seen to be markedly different. Additional thermal histories for this grade, given in Fig. 7.4 (c), show significant variation in transformation temperatures between Test J59 and J60. Once again, the inconsistency shown in the thermal histories plotted in Fig. 7.4 (c), display the effect of changes in cooling conditions on the temperature of 7.5 mm-diameter rod. The other point to note about Figs. 8.32 (a) and (b), is the kinetics displayed for the ferrite transformation. For both plant tests, the ferrite transformation seems to be taking place over a wide temperature range, and at a slow rate compared to the predicted results. The reason for this is thought to be related to the fact that Steel J contains a high concentration of

manganese, i.e., 0.95 wt% which is the highest found in any of the grades employed for the laboratory or plant trials, and is significantly higher than the Mn concentrations in the other low-carbon grades. Owing to the fact that the regression equation for $\ln b_F$ does not include a term for the effect of manganese, the over-prediction for reaction kinetics is to be expected. The presence of 0.95% Mn in a 1022 steel would be expected to significantly increase hardenability as compared to 0.50% Mn. In order to provide better predictions of thermal histories for higher manganese steels, additional phase transformation kinetics experiments would have to be performed to determine the effect of Mn on n and b , for the ferrite and pearlite transformations. Figure 8.32 (c) contains the results of model-predicted and measured thermal histories for a centre test in which the Stelmor air settings for zones one to four were on-off-off-on, respectively. As can be seen in the figure, the ferrite transformation kinetics predicted by the model are much faster than those measured, similar to the previous tests. In addition, the pearlite transformation start temperature is higher. The increased Mn in this steel grade seems to be forcing the pearlite transformation to lower temperatures as well. The effect of changing from "air off" to "air on" can be seen in both predicted and measured results, in the form of an abrupt increase in cooling rate at approximately 50 and 70 s respectively. The model-predicted and measured thermal histories for a centre test with off-on-on-on Stelmor air settings, are shown in Fig. 8.32 (d). Similar to the previous tests, the predicted ferrite and pearlite transformation kinetics seem earlier than those suggested by the measured data. In general however, the predicted thermal history for the test is reasonable.

From the model-predicted and measured thermal histories for the various steel grades and plant cooling conditions presented in the preceding paragraphs, the mathematical model was shown to be capable of predicting reasonable rod centreline thermal histories, during Stelmor line cooling. In order to increase the accuracy of the model, additional measurements of phase transformation kinetics, on a wider range of steel grades, are required. For the present investigation, the model-predicted thermal histories are considered adequate for the prediction of steel microstructure.

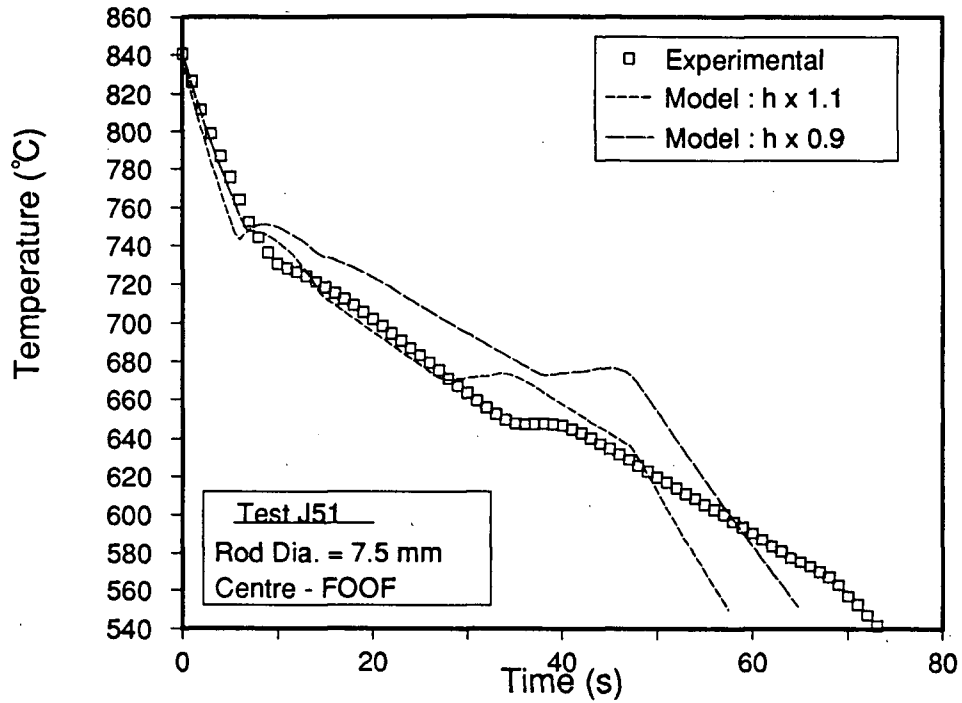


(a)

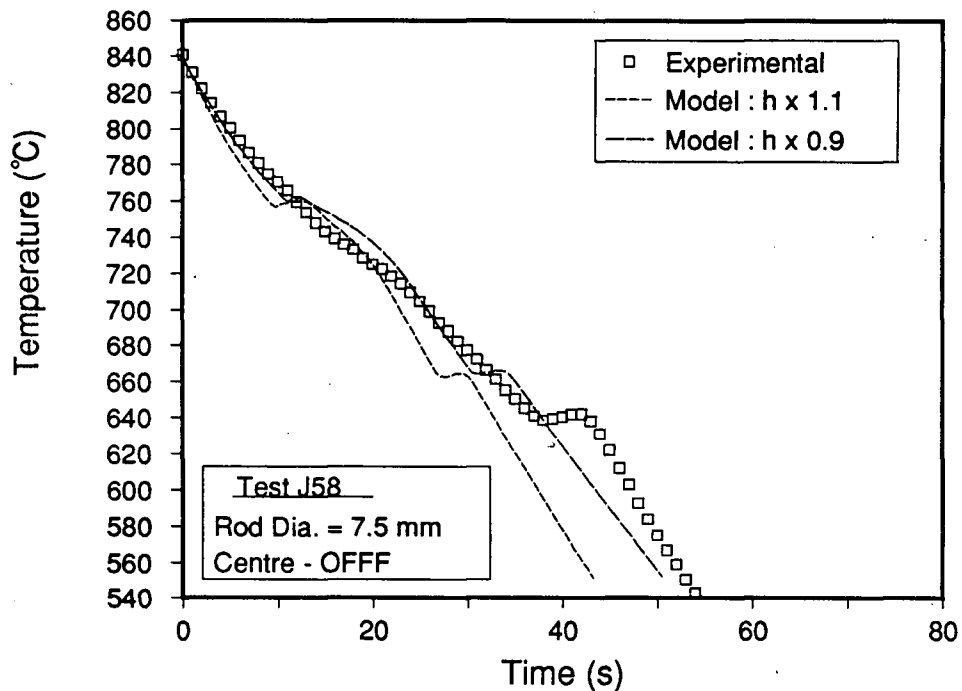


(b)

Fig. 8.32 - Measured and model-predicted thermal history for Steel J (1022), 7.5-mm diameter rods cooled in plant tests. (a) Test J59, centre - "air on", (b) Test J60, edge - "air on", (c) Test J51, centre - "air on" zone 1, "air off" zones 2 and 3, "air on" zone 4 and (d) Test J58, centre - "air off" zone 1, "air on" zones 2 to 4.



(c)



(d)

Fig. 8.32 - Measured and model-predicted thermal history for Steel J (1022), 7.5-mm diameter rods cooled in plant tests. (a) Test J59, centre - "air on", (b) Test J60, edge - "air on", (c) Test J51, centre - "air on" zone 1, "air off" zones 2 and 3, "air on" zone 4 and (d) Test J58, centre - "air off" zone 1, "air on" zones 2 to 4.

8.3.2.2 Microstructures

The mathematical model has been employed to predict the microstructure evolved during rod cooling under plant conditions, for the complete range of rod grades and diameters included in the study. The following paragraphs present the results for predicted ferrite fraction, ferrite grain diameter and pearlite interlamellar spacing.

Model-predicted-versus-measured ferrite fractions for the plant trial steels are plotted in Fig. 8.33. The points shown in the plot are somewhat blurred by the fact that each measured value includes two predicted fractions, based on $\pm 10\%$ of the mean heat-transfer coefficient. The shaded area in the figure represents \pm one standard deviation of the estimated value, as determined from the regression equation for ferrite fraction as a function of composition and cooling rate. The results show excellent agreement for Steels C, I and J, with slight under-predictions for Steels G and H. Steel F, although included in the plot, has such a small ferrite fraction that comparison is not realistic on the scale depicted in the figure. Referring back to Fig. 7.15, which contains the results of the predicted ferrite fraction, plotted against the measured ferrite fraction, based on Eq. (7.5) and the measured fraction, a similar behaviour for Steels G and H is seen; the regression equation under-estimates the fraction. Thus, it is not surprising that the model also yields a similar result. Also of note in Fig. 8.33, is the insensitivity of the ferrite fraction to changes in predicted cooling rate. The fractions corresponding to $\pm 10\%$ of the mean heat-transfer coefficient are barely distinguishable. Overall, the model predicted ferrite fractions are seen to agree well with the measured values.

Ferrite grain diameters predicted by the mathematical model are plotted in Fig 8.34, against the measured grain diameter for rods from the plant trials. Two points have been utilized to represent the predicted value, corresponding to the $\pm 10\%$ of the mean h , cooling conditions. Comparing the ferrite grain diameter with the results for ferrite fraction, a variation in steel cooling rate seems to exert a larger influence on the former than on the latter. The results in Fig. 8.34 show reasonable agreement between model-predicted and measured grain diameters, although Steel E shows a consistently low predicted value. Referring to Fig.

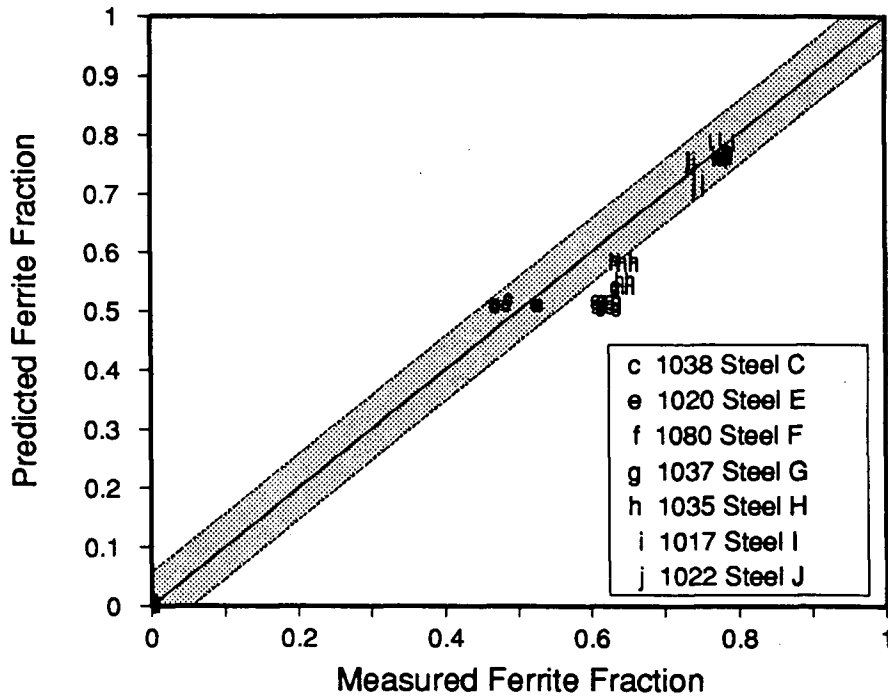


Fig. 8.33 - Model-predicted-versus-measured ferrite fractions for Steels C (1038), E (1020), F (1070), G (1037), H (1035), I (1017) and J (1022) from the plant trials. The shaded area in the figure indicates \pm one standard deviation of the predicted value.

7.20, a similar trend is shown for the ferrite grain diameter in Steel E, based on the regression equation, Eq. (7.7). Thus, an under-prediction in ferrite grain diameter for this grade would be expected from the model.

Owing to the method employed for prediction of ferrite fraction and ferrite grain diameter in the model, as long as a good prediction is made for the average steel cooling rate prior to the start of the ferrite transformation, reasonable estimations of the relative fractions and grain sizes will be made. A major flaw in this method is encountered when these parameters are to be predicted for cooling tests in which the cooling rate changes during the ferrite transformation. Although an increased cooling rate would be expected to result in a decrease in the ferrite fraction and corresponding grain diameter, and vice versa for a decrease in cooling rate, the model, as presently written, would predict the same relative fraction. Fortunately, most settings employed for Stelmor line cooling result in uniform cooling conditions

interlamellar pearlite spacing was actually measured. The variation in the average under-cooling predicted during the course of the pearlite transformation, as a function of a change in the heat-transfer coefficient can be seen in the figure. For the lower carbon grades the effect is quite small, however for the medium- to high-carbon grades, the variation in spacing is as high as 10%. These results indicate the need for an accurate thermal history prediction in order to predict interlamellar pearlite spacing.

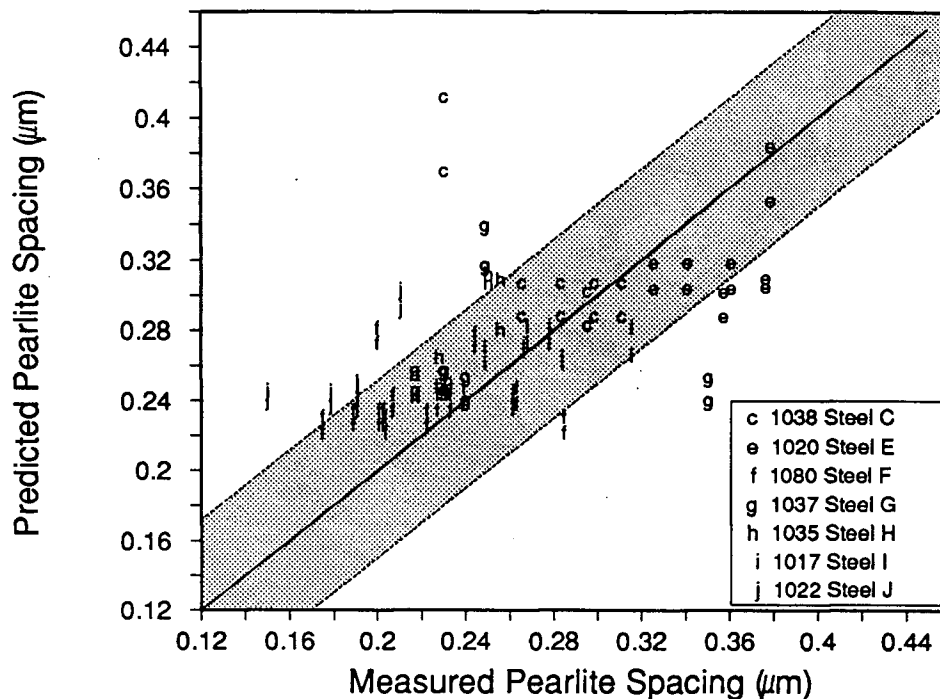


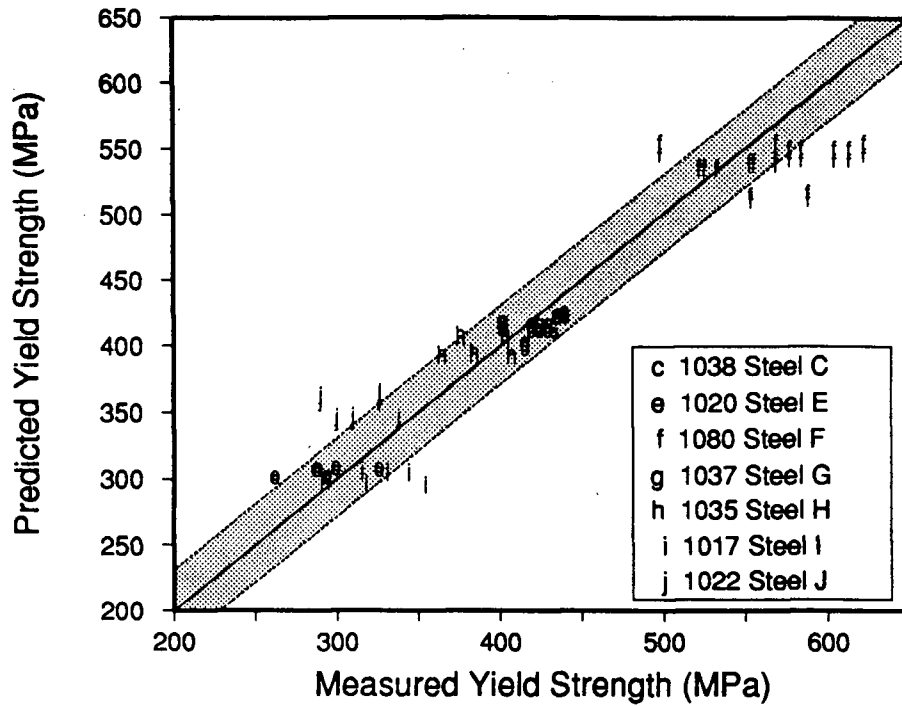
Fig. 8.35 - Model-predicted-versus-measured pearlite spacing for Steels C (1038), E (1020), F (1070), G (1037), H (1035), I (1017) and J (1022) from the plant trials. The shaded area in the figure indicates \pm one standard deviation of the predicted value.

8.3.2.3 Mechanical Properties

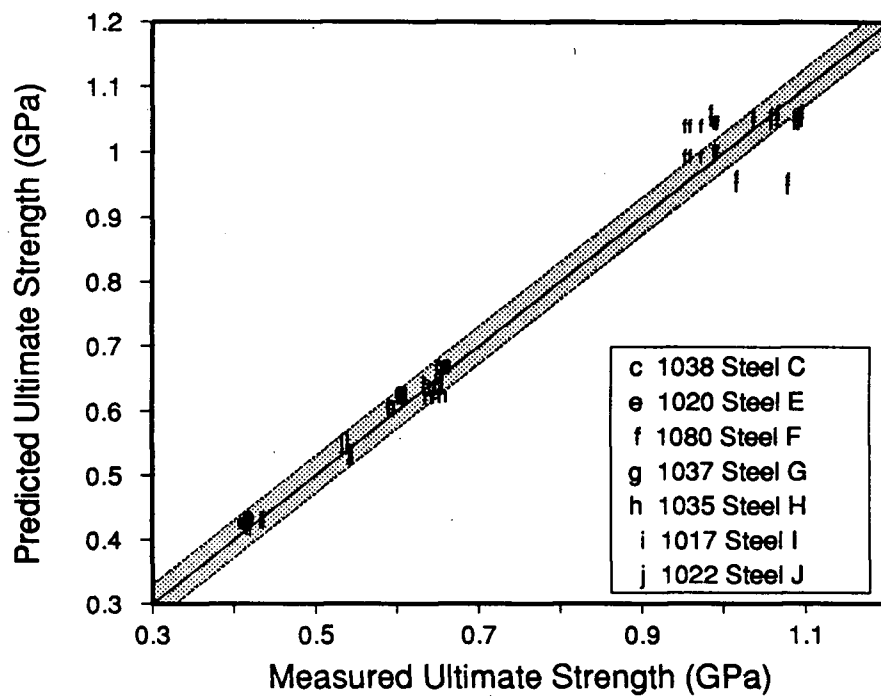
The final test for the model is its ability to predict the mechanical properties of steel cooled on the Stelmor line. Figure 8.36 (a) presents model-predicted-versus-measured yield strengths for the plant trial steels. The figure also includes \pm one standard deviation of the predicted value, depicted by the shaded area. For the most part, the predicted yield strengths are within the \pm one standard deviation area with two exceptions. Firstly, Steel J (1022)

reveals a consistently high predicted yield strength. The reason for this can be related back to the model-predicted results for ferrite fraction and grain diameter for this grade, Figs. 8.33 and 8.34. In these figures, the model under-predicted both ferrite fraction and grain diameter. Thus, recognizing that a decrease in either of these parameters results in an increase in steel strength, the over-prediction in steel strength is expected. For the worst case shown, the predicted yield strength is ~20% higher than the measured strength. The second grade which shows a relatively poor prediction of yield strength is Steel F (1080), which exhibits low predicted strength as compared to measured values. As was mentioned in the discussion of predicted strengths for laboratory steels, the strength of eutectoid steels depends to a large extent on the interlamellar spacing of pearlite. Referring to Fig. 8.35, it would thus seem that the over-prediction in pearlite spacing for several of the Steel F tests, has resulted in a low prediction of yield strength. The maximum difference between the predicted and measured strength shown in Fig. 8.36 (a) is ~12%. Results of the predicted-versus-measured yield strength, also indicate the effect of a change in cooling rate on the relative yield strength of plain carbon steels. As can be seen, each prediction in the figure includes two points, corresponding to $\pm 10\%$ of the predicted mean heat-transfer coefficient. The variation in yield strength with this change in heat transfer coefficient is seen to be relatively minor, within $\pm 2\%$ for the medium- and low-carbon grades, and $\pm 2.5\%$ for the higher carbon grades.

Model-predicted-versus-measured ultimate tensile strengths for the plant trial rods are shown in Fig. 8.36 (b). As can be seen in the figure, excellent agreement between the predicted and measured strengths has been achieved for the medium- and low-carbon steel grades; however, Steel F once again displays a wider range of predicted strengths than the other grades. The large variation in UTS for several of the Steel F rods is due to the presence of ferrite, formed only for the low heat-transfer coefficient condition. In general, the model predictions for ferrite fraction in the + 10% h tests, indicated a 100% pearlite microstructure. However, for the -10% h tests, small ferrite fractions were predicted. The



(a)



(b)

Fig. 8.36 - Model-predicted strengths plotted as a function of measured strengths from the plant trials; (a) yield strength and (b) ultimate tensile strength.

presence of ferrite results in a significantly lower UTS prediction, compared to a totally pearlitic steel. For the worst case shown in Fig. 8.36 (b) for Steel F, the predicted UTS is 11% lower than the measured.

8.3.3 Rods from Normal Plant Production

In order to provide an independent validation of the predictive capability of the mathematical model, the ultimate tensile strength for several industrial steel rod grades was measured during the plant trials. The method employed for retrieving and testing the tensile samples was identical to that utilized for routine inspection of Stelmor-cooled rod. Loops of the desired grades were cut from the coils as they passed over the final Stelmor cooling zone. Tensile testing was performed by plant personnel, employing a Tinius-Olsen machine, situated in the No. 2 Rod Mill laboratory. Test samples were approximately 450-mm long, and testing of the material was completed without prior straightening. Yield strengths are not usually determined from these tests. Table 8.8 contains a summary of the grades and conditions obtained for these tests. As can be seen they cover the range of grades utilized for the plant and laboratory rod cooling tests.

Table 8.8 - Summary of Stelmor-line cooled, industrial rod grades and diameters employed for comparison with model UTS predictions.

Grade	Rod Diameter (mm)	%C	%Mn	%Si	Air Settings
1065	7.1	0.63	0.78	0.23	FFFF
1022	7.5	0.21	0.98	0.017	OFFF
1022	7.5	0.22	0.91	0.29	OFFF
1070	7.5	0.70	0.77	0.23	FFFF
Torque Rod	9.1	0.58	0.95	0.25	FFFF
1060	9.1	0.61	0.75	0.24	FFFF
1015	9.1	0.16	0.54	0.02	OFFF
1038	12.7	0.38	0.77	0.27	OOOO
Spring	12.7	0.66	0.96	0.25	FFFF

Utilizing the steel compositions and line settings for these grades, as well as $\pm 10\%$ of the mean heat-transfer coefficient, the mathematical model has been run to predict the rod UTS. Model-predicted-versus-measured ultimate tensile strengths for the industrial grades are

shown in Fig. 8.37. The shaded area in the figure represents \pm one standard deviation from the regression equation for UTS. Agreement between the predicted and measured strengths is seen to be good, with the exception of one grade (~ 920 MPa measured UTS). The reason for

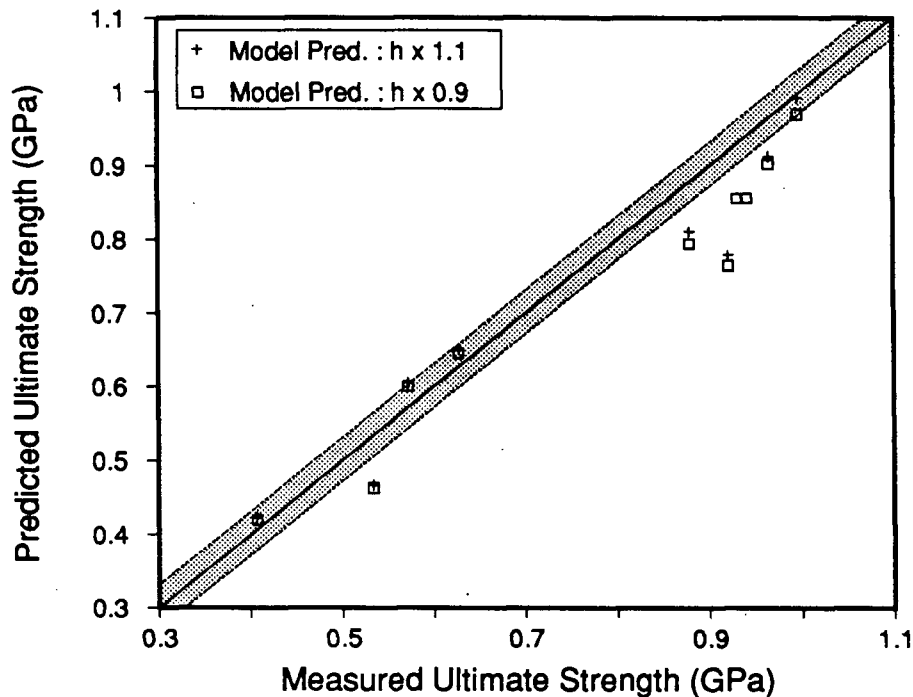


Fig. 8.37 - Model-predicted-versus-measured ultimate tensile strength of industrial Stelmor-cooled rod. The shaded area in the figure indicates \pm one standard deviation of the predicted value.

this is related to the fact that the development of the mathematical model has been based on three grades of steel, 1070, 1038 and 1020, although literature data has been employed to augment experimental data in some cases. Correlations for the various phase transformation kinetics parameters, calculated by the model for eutectoid steel grades, have been based on results from Steel B (1070), with some literature data. For hypoeutectoid grades, a majority of the data employed for the transformation kinetics has come from Steel C (1038) and E (1020). Obviously, owing to the wide gaps between grades, the model would not be expected to perform well for steel grades in the 1050 to 1065 range, or below 1015, with respect to the carbon concentration. However, the model should be capable of a good prediction of microstructural evolution and mechanical properties for steels in the range 1017 to 1045 and

1070 to 1080. This ability is clearly displayed in Fig. 8.37. The 1070 grade listed in Table 8.8 shows excellent agreement between predicted and measured UTS (highest strength in figure). The same can be seen for the four grades of steel in the low- to medium-carbon range, at the lower strength range in the figure. As mentioned, the worst prediction would be expected for the higher carbon hypoeutectoid grades, which is also readily depicted by Fig. 8.37.

Chapter 9 - SUMMARY AND CONCLUSIONS

9.1 Summary

A mathematical model has been developed, based on the concept of microstructural engineering, for the prediction of mechanical properties in steel rod subjected to Stelmor cooling. The solution for temperature in the model assumes one-dimensional heat flow, utilizing a finite-difference technique in cylindrical coordinates. The kinetics of the austenite-ferrite and austenite-pearlite phase transformations, have been calculated adopting the Avrami equation; and the latent heat of transformation for both reactions has been included in the heat balance. The required kinetic parameters for the Avrami equation have been determined experimentally.

In order to verify empirical correlations for the prediction of the convective heat-transfer coefficient at the surface of a cooling rod, a series of rod cooling experiments were performed in the laboratory. The experiments were designed to simulate the Stelmor process, i.e., cooling was provided by a cross-flow of air, employing a specially designed duct, and temperature at the rod centreline was sensed by a chromel-alumel thermocouple. In addition, the test rods were employed for determination of microstructure and mechanical properties. The microstructure was quantified through the use of a SEM and a computer-controlled image analyzer, to characterize the ferrite fraction, ferrite grain diameter and pearlite interlamellar spacing. Tensile testing was performed to obtain the yield strength and ultimate tensile strength for each rod sample. A variety of rod diameters, cooling air velocities and rod grades allowed the effect of steel thermal history and composition on the microstructure and mechanical properties of the rod, to be determined.

A similar set of experiments was conducted on an operating Stelmor line at the Stelco No. 2 Rod Mill. Steel rods heated adjacent to the line and instrumented with a centreline mounted thermocouple were cooled with production coils on the Stelmor deck. Heat-transfer

coefficients at the surface of the cooling test rods were calculated from the measured thermal histories and utilized to estimate the relative magnitude of the convective and radiative components of the overall heat-transfer coefficient. This data made possible the prediction of an accurate heat-transfer coefficient, as a function of operating variables on the Stelmor cooling line. Test rods were also employed to determine the microstructural parameters quantitatively and for mechanical testing.

Owing to a lack of data in the literature concerning the quantitative prediction of microstructure and strength of continuously-cooled plain-carbon steel, results from both the laboratory and plant experiments have been combined to develop empirical equations for the prediction of ferrite fraction, ferrite grain diameter and pearlite spacing as a function of steel composition and thermal history, and yield strength and UTS as a function of composition and microstructure. These equations have been employed in the mathematical model for the prediction of microstructure and strength in steel rod.

9.2 Conclusions

Based on the results and predictions of thermal history, microstructure and mechanical properties made by the model, the following conclusions can be drawn:

- (1) The mathematical model has demonstrated the ability to predict accurately the thermal history of steel rod cooled in the lab and under plant conditions on the Stelmor line.
- (2) Predictions of phase transformation kinetics for the austenite-pearlite reaction during continuous cooling showed excellent agreement with measured values in eutectoid steels. Agreement between measured and predicted austenite-ferrite kinetics was reasonable, however a consistently early prediction for reaction start time and rate was predicted by the model for ferrite.

- (3) Regression equations developed in the study revealed good agreement between measured and predicted ferrite fraction and ferrite grain diameter. The predicted values for pearlite spacing were reasonable but did not show a strong relationship to steel thermal history.
- (4) Strengths calculated for both the laboratory and plant test rods showed excellent agreement with measured values. The results indicated the importance of the pearlite spacing on the strength of eutectoid steel and the relative insensitivity of strength to steel cooling rate for all grades.
- (5) The agreement shown between the predicted and measured UTS for the independent group of rods taken from the Stelmor line, clearly demonstrate the utility of the model for prediction of mechanical properties and microstructures of continuously-cooled plain-carbon steel rod.

9.3 Future Work

Although the mathematical model has displayed the capability of predicting mechanical properties in Stelmor-cooled steel rod, additional work in certain areas would provide increased accuracy and theoretical consistency in the model. The primary weakness of the predictions was the over-estimation of the transformation kinetics for a majority of the austenite-ferrite reactions in both the laboratory and plant trial hypoeutectoid grades. The reason for this is not clear, but it may be due to decarburization and/or temperature gradients in the dilatometer sample or differences in the state of stress in the dilatometer sample as compared to the solid rod sample. The discrepancy suggests the need for additional work on the transformation kinetics of ferrite in hypoeutectoid steels, under both isothermal and continuous cooling conditions.

Owing to the fact that the steels employed for the rod cooling tests, both in the lab and in the plant, were obtained from industrial grades, no control over the composition of the material could be achieved. As a result, there is a lack of data for steel grades between 0.40 and 0.70 %C, causing a range of grades for which the model is not applicable. This was

demonstrated for the prediction of strength in the industrial rods, Fig. 8.37. Phase transformation kinetics, microstructural analysis and mechanical properties measurement for this range of grades should thus be performed.

An additional problem resulting from the fact that experimental steels were obtained from industrial grades, was the lack of control over variation of manganese concentration. The levels of Mn contained in the experimental grades, although typical for the steels considered, did not allow a clear determination of the role manganese played in such events as phase transformation start times, b values or ferrite grain diameters. Additional tests with a systematic variation in the %Mn in the steel rod should be conducted to reveal its effect.

Finally, the next step in the project should involve the prediction of mechanical properties in low-alloy steel grades produced on the Stelmor line. The same modelling technique can be applied to these grades, however, additional experimental work on the phase transformation kinetics, microstructural evolution and structure/property relationships in these steels would have to be performed.

References

1. The Making, Shaping and Treating of Steel, W.T. Lankford, Jr., N.L. Samways, R.F. Craven and H.E McGannon Eds., AISE, Herbick and Held, Pittsburgh, PA, 1984.
2. Jalil A.A., "Retarded Cooling Stelmor - Operating Experience and Results", Iron and Steel Engineer, (59), 1982, pp 46-48.
3. Tendler A., "Controlled Cooling of Rods", Wire Journal, (14), 1981, pp 84-91.
4. The Stelmor Process, The Morgan Construction Company, Worcester, MA.
5. J.W. Christian, The Theory of Transformations in Metals and Alloys, Pergamon Press, Oxford, U.K., 1975, pp 1-20.
6. J.N. Hobstetter, "Theory of Nucleation in Solid-Solid Transformations", in Decomposition of Austenite by Diffusional Processes, V.F. Zackay and H.I. Aaronson, eds., Interscience Publishers, New York, N.Y., 1962, pp 1-38.
7. W.A. Johnson and R.F. Mehl, "Reaction Kinetics in Processes of Nucleation and Growth", Trans. AIME, (135), 1939, pp 416-442.
8. M. Avrami, "Kinetics of Phase Change I" J. of Chem. Physics, (7), 1939, pp 1103-1112.
9. M. Avrami, "Kinetics of Phase Change II", J. of Chem. Physics, (8), 1940, pp 212-224.
10. M. Avrami, "Kinetics of Phase Change III", J. of Chem. Physics, (9), 1941, pp 177-183.
11. C. Zener, "Kinetics of the Decomposition of Austenite", Trans. AIME, (167), 1946, pp 550-583.
12. H.I. Aaronson, "The Proeutectoid Ferrite and Proeutectoid Cementite Reactions", in Decomposition of Austenite by Diffusional Processes, V.F. Zackay and H.I. Aaronson eds., Interscience Publishers, New York N.Y., 1962, pp 386-548.
13. W.T. Reynolds, Jr., M. Enomoto and H.I. Aaronson, "The Proeutectoid Ferrite Reaction", in Phase Transformations in Ferrous Alloys, A.R. Marder and J.I. Goldstein eds., TMS-AIME, Warrendale, PA, 1984, pp 155-200.
14. G.R. Speich, L.J. Cuddy, C.R. Gordon and A.J. DeArdo, "Formation of Ferrite from Controlled-Rolled Austenite", in Phase Transformations in Ferrous Alloys, A.R. Marder and J.I. Goldstein eds., TMS-AIME, Warrendale, PA, 1984, pp 341-389.
15. J.W. Cahn, "The Kinetics of Grain Boundary Nucleated Reactions", Acta. Met., (4), 1956, pp 449-459.
16. M. Hillert, "The Role of Interfacial Energy during Solid State Phase Transformations", Jernkont. Ann., (141), 1957, pp 757-789.
17. M. Hillert, "The Formation of Pearlite", in Decomposition of Austenite by Diffusional Processes, Interscience Publishers, New York, N.Y., 1962, pp 197-247.
18. N. Ridley, "The Pearlite Transformation", in Phase Transformations in Ferrous Alloys, A.R. Marder and J.I. Goldstein eds., TMS-AIME, Warrendale, PA, 1984, pp 201-236.

19. E. Scheil, "The Incubation Time Austenite Transformation", Archiv. Eisenhüttenwesen, (8), 1938, pp 565-567.
20. J.W. Cahn, "Transformation Kinetics During Continuous Cooling", Acta. Met., (4), 1956, pp 572-575.
21. J.W. Cahn, "On the Kinetics of the Pearlite Reaction", Trans. AIME, Jan. 1957, pp 140-144.
22. M.B. Kuban, "Kinetics of Nucleation and Growth in a Eutectoid Plain Carbon Steel", M.A.Sc. Thesis, University of British Columbia, 1983.
23. P.K. Agarwal and J.K. Brimacombe, "Mathematical Model of Heat Flow and Austenite-Pearlite Transformation in Eutectoid Steel Rod for Wire", Met. Trans. B, (12B), 1981, pp 121-133.
24. E.B. Hawbolt, B. Chau and J.K. Brimacombe, "Kinetics of Austenite-Pearlite Transformation in Eutectoid Carbon Steel", Met. Trans. A, (14A), 1983, pp 1803-1815.
25. E.B. Hawbolt, B. Chau and J.K. Brimacombe, "Kinetics of Austenite-Ferrite and Austenite-Pearlite Transformations in a 1025 Carbon Steel" Met. Trans. A, (16A), 1985, pp 565-578.
26. R. Kamat, B. Chau, E.B. Hawbolt and J.K. Brimacombe, "The Application of Isothermal Phase Transformation Kinetics to Predict Continuous Cooling Behaviour", Presented at Phase Transformations '87, University of Cambridge, The Institute of Metals, London, 1987.
27. M. Umemoto, N. Komatsubara and I. Tamura, "Prediction of Hardenability Effects from Isothermal Transformation Kinetics", J. Heat Treat., (1), 1980, pp 57-64.
28. R. Kamat, Unpublished Ph.D. Research, 1988.
29. J.S. Kirkaldy and R.C. Sharma, "A New Phenomenology for Steel IT and CCT Curves", Scripta Met., (16), 1982, pp 1193-1198.
30. J.S. Kirkaldy, "Prediction of Alloy Hardenability from Thermodynamic and Kinetic Data", Met. Trans., (4), 1973, pp 2327-2333.
31. K.C. Russell, "Grain Boundary Nucleation Kinetics", Acta. Met., (17), 1969, pp 1123-1131.
32. R.A. Grange and J.M. Keifer, "Transformation of Austenite on Continuous Cooling and Its Relation to Transformation at Constant Temperature", Trans. ASM, (29), 1941, pp 85-116.
33. J.S. Kirkaldy, G.O. Pazonis and S.E. Feldman, "An Accurate Predictor for the Jominy Hardenability of Low-alloy Hypoeutectoid Steels", Proceedings of the 16th International Heat Treatment Conference, Heat Treatment '76, 1976, pp 169-175.
34. J.S. Kirkaldy, B.A. Thomson and E.A. Baganis, Prediction of Multicomponent Equilibrium and Transformation Diagrams for Low Alloy Steels", in Hardenability Concepts with Application to Steels, D.V. Doane and J.S. Kirkaldy eds., AIME, Warrendale, PA, 1978, pp 82-125.

35. J.S. Kirkaldy and E.A. Baganis, "Thermodynamic Prediction of the A_{e_3} Temperature of Steels with Additions of Mn, Si, Ni, Cr, Mo, Cu", Met. Trans. A, (9A), 1977, pp 495-501.
36. J.S. Kirkaldy and D. Venugopalan, "Prediction of Microstructure and Hardenability in Low Alloy Steels", in Phase Transformations in Ferrous Alloys, A.R. Marder and J.I. Goldstein eds., TMS-AIME, Warrendale, PA, 1984, pp 125-148.
37. N. Shimizu and I. Tamura, "Effect of Discontinuous Change in Cooling Rate during Continuous Cooling on Pearlite Transformation Behavior in Steel", Trans. ISIJ, (17), 1977, pp 470-476.
38. I. Tamura, "Some Fundamental Steps in the Thermomechanical Processing of Steels", Trans. ISIJ, (27), 1987, pp 763-779.
39. M. Umemoto, N. Nishioka and I. Tamura, "Prediction of Hardenability from Isothermal Transformation Diagrams", J. Heat Treat., (2), 1981, pp 130-138.
40. M. Umemoto, K. Horiuchi and I. Tamura, "Pearlite Transformation during Continuous Cooling and its Relation to Isothermal Transformation", Trans. ISIJ, (23), 1983, pp 690-695.
41. M. Umemoto, N. Nishioka and I. Tamura, "Kinetics of Proeutectoid Ferrite Reaction during Isothermal Holding and Continuous Cooling in Plain Carbon Steels", in Proceedings of the Third International Congress on Heat Treatment of Materials, Shanghai, China, published by The Metals Society, London, 1983, pp 35-43.
42. E.B. Hawbolt, B. Chau and J.K. Brimacombe, Unpublished Research, University of British Columbia, 1983.
43. R. Blondeau, Ph. Maynier, J. Dollet and B. Vieillard-Baron, "Mathematical Model for the Calculation of Mechanical Properties of Low-Alloy Steel Metallurgical Products: a Few Examples of its Applications", Proceedings of the 16th International Heat Treatment Conference, Heat Treatment '76, 1976, pp 189-200.
44. Y. Sakomoto, M. Saeki, M. Nishida and T. Tanaka, "Mathematical Model Simulating Phase Transformation in Low Alloy Hot-Rolled Sheet Steel", Internal Communication, Kawasaki Steel Corporation, Mizushima Research Department, 1981.
45. T. Reti, G. Bobok and M. Gergely, "Computing Method for Non-isothermal Heat Treatments", in Proceedings of the International Congress on Metals Engineering, Heat Treatment '81, The Metals Society, London, 1981, pp 91-96.
46. M. Gergely, T. Reti, P. Tardy and G. Buza "Prediction of Transformation Characteristics and Microstructure of Case Hardened Engineering Components", in Heat Treatment '84, The Metals Society London, 1984, pp 20.1-20.6.
47. T. Reti, M. Gergely and P. Tardy "Mathematical Treatments of Non-isothermal Transformations", Mater. Sci. Technol., (3), 1987, pp 365-371.
48. M. Suehiro, K. Sato, Y. Tsukano, H. Yada, T. Senuma and Y. Matsumura, "Computer Modeling of Microstructural Change and Strength of Low Carbon Steel in Hot Strip Rolling", Trans. ISIJ, (27), 1986, pp 439-445.

49. H. Yada, "Prediction of Microstructural Changes and Mechanical Properties in Hot Strip Rolling", in Proceedings of International Symposium on Accelerated Cooling of Rolled Steel, G.E. Ruddle and A.F. Crawley eds., Pergamon Press, Oxford, U.K., 1988, pp 105-119.
50. Y. Tomota and I. Tamura, "Mechanical Behavior of Steels Consisting of Two Ductile Phases", Trans. ISIJ, (22), 1982, pp 665-677.
51. Z. Hashin, "Analysis of Composite Materials - A Survey", Journal of Applied Mechanics, (50), 1983, pp 481-505.
52. A.R. Marder, "Structure-Property Relationships in Ferrous Transformation Products", in Phase Transformations in Ferrous Alloys, A.R. Marder and J.I. Goldstein eds., TMS-AIME, Warrendale, PA, 1984, pp 11-41.
53. E. Orowan, Internal Stresses in Metals and Alloys, Institute of Metals, London, 1948.
54. H.J. Kouwenhoven, "The Influence of Ferrite Grain Size and Volume Fraction of Pearlite on the Lower Yield Stress and Luders Strain of Carbon Steel", Trans. ASM, (62), 1969, pp 437-446.
55. T. Gladman, I.D. McIvor and F.B. Pickering, "Some Aspects of the Structure-Property Relationships in High-Carbon Ferrite-Pearlite Steels", IISI, (208), 1972, pp 916-930.
56. G.R. Speich, and L.C. Rice, "Controlled Slow-Cooling of Low- and Medium-Carbon Steel Rods", Iron and Steelmaker, (11), 1984, pp 36-43.
57. F. Kreith and W.Z. Black, Basic Heat Transfer, Harper and Row, New York, N.Y., 1980.
58. B. Carnahan, H.A. Luther and W.O. Wilkes, Applied Numerical Methods, Wiley, New York, N.Y., 1979, pp 466.
59. British Iron and Steel Research Association, Physical Constants of Some Commercial Steels at Elevated Temperatures, Butterworths Scientific Publications, London, 1953.
60. L.S. Darken and R.W. Gurry, Physical Chemistry of Metals, McGraw-Hill, New York, 1953.
61. I. Barin, O. Knacke and O. Kubaschewski, Thermochemical Properties of Inorganic Substances: Supplement, Springer-Verlag, Berlin, 1977.
62. The Thermal Research Laboratory, Dow Chemical Company, JANAF Thermochemical Tables, 1960.
63. R.E. Smallman, Modern Physical Metallurgy, Butterworths, London, 1985.
64. S. Taniguchi, T. Murakami, A. Watanabe and A. Kikuchi, "Phase Transformation and Heat Transfer during Cooling of Steel", Tetsu-to-Hagane, (74), 1988, pp 318-325.
65. J.J. Kramer, G.M. Pound and R.F. Mehl, "The Free Energy of Formation and the Interfacial Enthalpy in Pearlite", Acta Met., (6), 1958, pp 763-771.
66. J.R. Iyer, "Mathematical Modelling of Phase Transformation in a Plain Carbon Steel", M.A.Sc. Thesis, University of British Columbia, 1983.

67. C.M. Sellars, "Physical Metallurgy of Hot Working", Proceedings of Hot Working and Forming Processes, Metals Society, London, 1980.
68. W. Roberts, A. Sandberg, T. Siweki and T. Werlefors, "Prediction of Microstructure Development During Recrystallization Hot Rolling of Ti-V Steels", Conference Proceedings for HSLA Steels Technology and Applications, ASM, Metals Park, OH, 1984, pp 67-84.
69. N. Ridley, "A Review of the Data on the Interlamellar Spacing of Pearlite", Met. Trans. A, (15A), 1984, pp 1019-1036.
70. G.F. Bolling and R.F. Richman, "Forced Velocity Pearlite", Met. Trans., (1), 1970, 1037-1045.
71. D. Brown and N. Ridley, "Rates of Nucleation and Growth and Interlamellar Spacing in a Low-Alloy Eutectoid Steel", J. Iron and Steel Inst., (204), 1966, pp 811-816.
72. D. Cheetham and N. Ridley, "Isovelocity and Isothermal Pearlite Growth in a Eutectoid Steel", J. Iron and Steel Inst., (211), 1973, pp 648-652.
73. D.D. Pearson and J.D. Verhoeven' "Forced Velocity Pearlite in High Purity Fe-C Alloys: Part 1 Experimental", Met. Trans. A, (15A), 1984, pp 1037-1045.
74. G.E. Pellisier, M.F. Hawkes, W.A. Johnson and R.F. Mehl, "The Interlamellar Spacing of Pearlite", Trans. ASM, (30), 1942, pp 1049-1081.
75. J. Williams and S.G. Glover, Personal communication to D. Cheetham and N. Ridley in "Isovelocity and Isothermal Pearlite Growth in a Eutectoid Steel", J. Iron and Steel Inst., (211), 1973, pp 648-652.
76. E.E. Underwood, Quantitative Stereology, Addison Wesley, Reading, MA, 1970.
77. J.C. Russ, Practical Stereology, The University of North Carolina, Raleigh, N.C., 1985.
78. American Society for Testing of Materials, Annual Book of ASTM Standards, Test A370 - 86a, "Standard Test Methods and Definitions for Mechanical Testing of Steel Products", vol. 01.03, 1987.
79. American Society for Testing of Materials, Annual Book of ASTM Standards, Test E112 - 85, "Standard Methods for Determining the Average Grain Size", vol. 03.01, 1987.
80. A.G. Stacey, "The Influence of Segregation on the Drawability of High-Carbon Steel Rod", Wire Journal, (13), 1980, pp 92-97.
81. C.J.C.J. Van Vuuren "Operating and Quality Control Aspects of the Production of Critical Low- and High-Carbon Products From Continuously Cast Blooms", Open Hearth Steelmaking Conference Proceedings, AIME, Warrendale, PA, 1978, pp 306-334.
82. T. Sawatani, T. Ikuta, T. Ooka and N. Urushiyama, "Microsegregation in Continuously Cast Carbon Steel Wire Rods", Proceedings of an International Conference on X-Ray Optics and Microanalysis, 1972.

83. Y. Hanada, K. Ueno, A. Noda, H. Kondoh, T Sakamoto and K Mine, "New Type Stelmor Equipment of Wire Rod and Bar Mill", Kawasaki Steel Technical Report, (15), 1986, pp 50-57.
84. L. Kaufman, S. V. Radcliffe and M. Cohen, "Thermodynamics of the Bainite Reaction", in Decomposition of Austenite by Diffusional Processes, V.F. Zackay and H.I. Aaronson, eds., Interscience Publishers, New York, N.Y., 1962, pp 313-352.
85. P. Choquet, A. LeBon and Ch. Perdix, "Mathematical Model for Prediction of Austenite and Ferrite Microstructures in Hot Rolling Processes", International Conference on the Strength of Metals and Alloys, J.-P. Bailon, J.I. Dickson, J.J. Jonas and M.G. Akben, eds., Pergamon Press, Oxford, 1986.
86. S. Kakaç and Y. Yener, Heat Conduction, Hemisphere Publishing, Washington, DC, 1985.
87. M. Wells, Private Communication, Stelco Inc., 1988.

Appendix 1 - Development of Nodal Equations

The purpose of this appendix is to provide derivations for the system of nodal equations obtained for the finite-difference model. For the geometry under consideration, assuming one-dimensional radial heat flow, three distinct node types can be distinguished:

- (1) central,
- (2) general internal,
- (3) surface.

(1) Central Node

Referring to the diagram given in Fig. A1.1, the central node as the name implies, considers the region at and surrounding the centreline of the cylinder. The notation used for development of the equations is also given in the figure with subscript i and n representing node number and time step, respectively. Performing a heat balance on node i , the wedge shaped volume element, shown in Fig. A1.1, is assumed to have a thickness of Δx . To facilitate formulation of the equations, the thermophysical properties of steel have been assumed to be independent of temperature. It should be noted however, that in the model these properties are evaluated as a function of the appropriate nodal temperature. Thus, heat flow from node i to node $i+1$ across AB will take place by conduction and can be expressed as:

$$q_{i,i+1} = -k \frac{\Delta r \Delta \phi \Delta x}{2} \frac{(T_{i+1,n} - T_{i,n})}{\Delta r} \quad (\text{A1.1})$$

where k is the thermal conductivity, Δr is the node thickness in the radial direction as shown in Fig. A1.1, $\Delta \phi$ is the small nodal angle as shown in Fig. A1.1, and $T_{i+1,n}$ and $T_{i,n}$ are the temperatures at node $i+1$ and i , during time step n , respectively.

Heat accumulated in the central node is determined by comparing the temperature at the present time step with that from the previous time step. Thus,

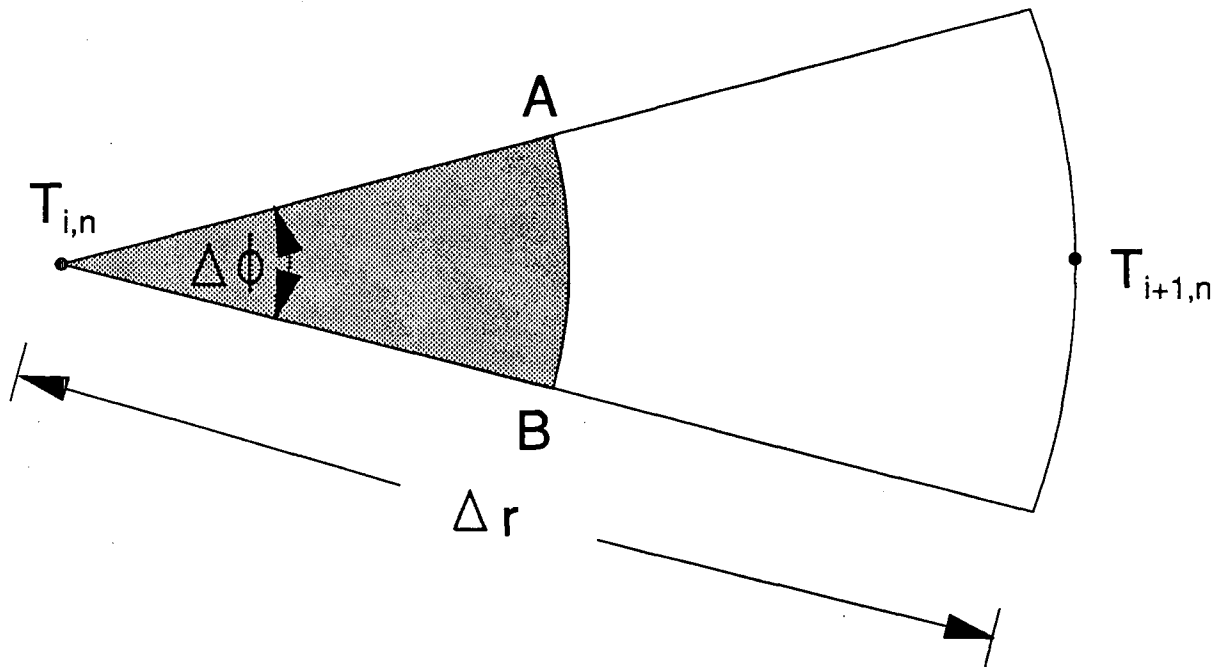


Fig. A1.1 - Diagram depicting the central node used for development of the finite difference equations.

$$q_{ACC} = \frac{\rho C_p \Delta \phi \Delta x}{2} \left(\frac{\Delta r}{2} \right)^2 \frac{(T_{i,n} - T_{i,n-1})}{\Delta t} \quad (A1.2)$$

where ρ is the density and C_p is the specific heat of the steel. Owing to the possibility of an austenite decomposition reaction, the heat of transformation also must be considered and is equal to:

$$q_{TR} = \frac{H \rho \Delta \phi \Delta x}{2} \frac{\Delta X}{\Delta t} \left(\frac{\Delta r}{2} \right)^2 \quad (A1.3)$$

where H is the latent heat of transformation and ΔX is the fraction of austenite transformed over the time step Δt .

According to the heat balance, the heat accumulated in the node must be equal to the heat flow in from node $i+1$ plus the heat released by the phase transformation. Thus, combining terms and simplifying,

$$T_{i,n} \left(1 + \frac{\rho C_p \Delta r^2}{4k \Delta t} \right) - T_{i+1,n} = T_{i,n-1} \left(\frac{\rho C_p \Delta r^2}{4k \Delta t} \right) + \frac{H \rho \Delta X \Delta r^2}{4k \Delta t} \quad (\text{A1.4})$$

(2) General Internal Node

Unlike the central node, a heat balance about the general internal node must consider heat flow to two neighboring nodes. Figure A1.2 shows the notation used for the formulation of nodal equations for internal nodes. Performing a heat balance on the node, heat flow by conduction takes place from node i to both node $i-1$ and node $i+1$. Thus the heat flow from node $i-1$ to i is given by:

$$q_{i-1,i} = k \Delta \phi \left(r_i - \frac{\Delta r}{2} \right) \frac{(T_{i-1,n} - T_{i,n})}{\Delta r} \quad (\text{A1.5})$$

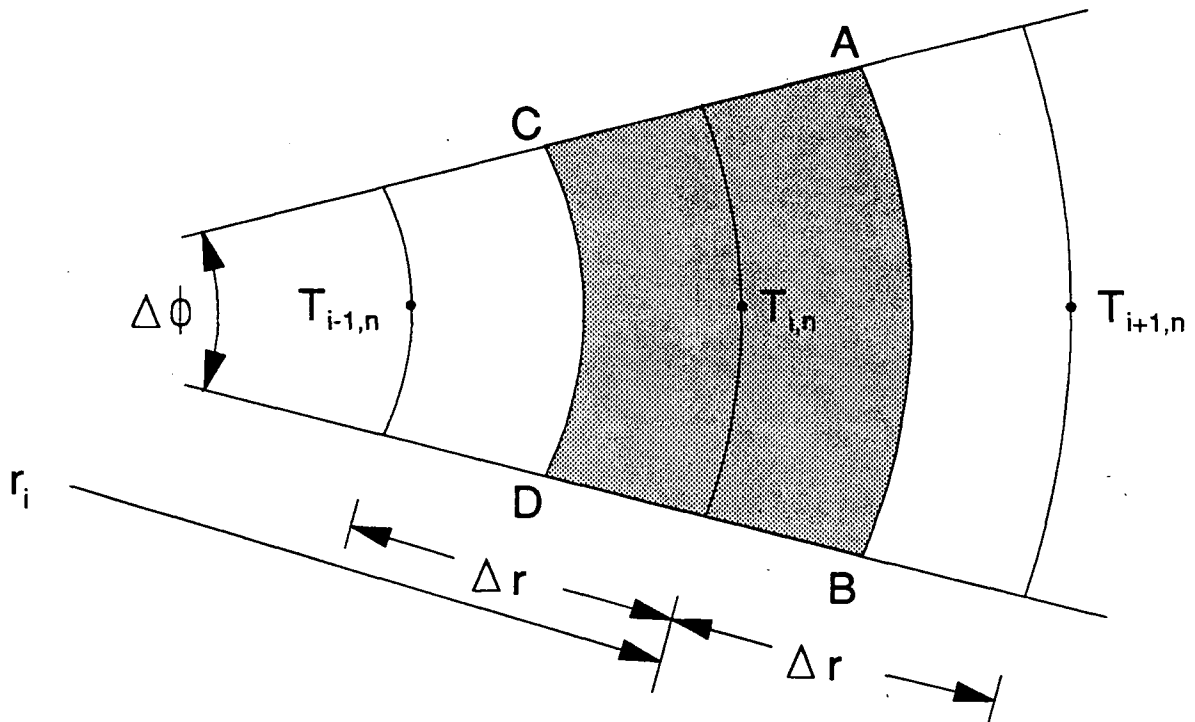


Fig. A1.2 - Diagram depicting the general internal node used for development of the finite difference equations.

and the heat flow from node i to $i+1$ is

$$q_{i,i+1} = k\Delta\phi\left(r_i + \frac{\Delta r}{2}\right)\frac{(T_{i,n} - T_{i+1,n})}{\Delta r} \quad (\text{A1.6})$$

where r_i is the radius at node i .

Heat accumulated in node i between the present and previous time steps is equal to:

$$q_{ACC} = \rho C_p \Delta\phi r_i \Delta r \frac{(T_{i,n} - T_{i,n-1})}{\Delta t} \quad (\text{A1.7})$$

Once again the heat generated by the phase transformation must be considered and can be shown as:

$$q_{TR} = \rho H r_i \Delta r \Delta\phi \frac{\Delta X}{\Delta t} \quad (\text{A1.8})$$

From the previous equations, a heat balance around the node can be performed. The difference between heat flow into the node and heat flow out, combined with the heat released during transformation must be equal to heat accumulated. Thus, combining equations and simplifying,

$$\begin{aligned} -T_{i-1,n} k \left(r_i - \frac{\Delta r}{2}\right) + T_{i,n} \left[k \left(r_i - \frac{\Delta r}{2}\right) + k \left(r_i + \frac{\Delta r}{2}\right) + \frac{\rho C_p r_i \Delta r^2}{\Delta t} \right] \\ - T_{i+1,n} k \left(r_i + \frac{\Delta r}{2}\right) = T_{i,n-1} \left(\frac{\rho C_p r_i \Delta r^2}{\Delta t} \right) + \frac{\rho H \Delta X r_i \Delta r^2}{\Delta t} \end{aligned} \quad (\text{A1.9})$$

(3) Surface Node

The heat balance for the volume element around the surface node, can be performed similarly to the previous two cases. However, convection from the surface must be included as well as heat transfer by conduction. Referring to Fig. A1.3, it can be seen that the heat flow from node $i-1$ to i can be written as:

$$q_{i-1,i} = -k\Delta\phi\Delta x \left(r_s - \frac{\Delta r}{2}\right)\frac{(T_{i-1,n} - T_{i,n})}{\Delta r} \quad (\text{A1.10})$$

Considering convective heat transfer from the surface, heat flow out of node i can be written as:

$$q_{i,AMB} = hr_s \Delta\phi \Delta x (T_{i,n} - T_A) \quad (A1.11)$$

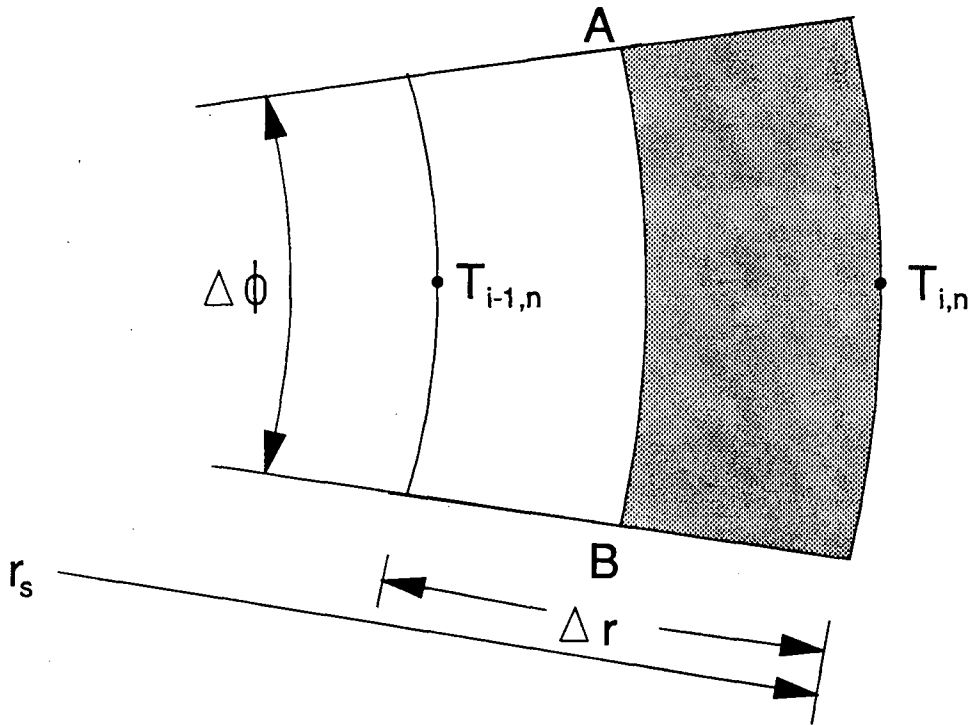


Fig. A1.3 - Diagram depicting the surface node used for development of the finite difference equations.

As before the heat accumulated in the node is

$$q_{ACC} = \frac{\rho C_p \Delta\phi \Delta x \Delta r}{2} \left(r_s - \frac{\Delta r}{4} \right) \frac{(T_{i,n} - T_{i,n-1})}{\Delta t} \quad (A1.12)$$

The heat released by the phase transformation must also be considered and is given by:

$$q_{TR} = \frac{\rho H \Delta\phi \Delta x \Delta r}{2} \left(r_s - \frac{\Delta r}{4} \right) \frac{\Delta X}{\Delta t} \quad (A1.13)$$

Rearranging and recognizing that the heat flow into the surface node less the heat lost to the surroundings plus the heat released by the transformation must equal the heat accumulated, the overall equation for the node is:

$$\begin{aligned}
 & T_{i-1,n} k \left(\frac{\Delta r - 2r_s}{2} \right) + T_{i,n} \left[k \left(\frac{2r_s - \Delta r}{2} \right) + hr_s + \frac{\rho C_p \Delta r (4r_s - \Delta r)}{8\Delta t} \right] \\
 & = T_{i,n-1} \left(\frac{\rho C_p \Delta r (4r_s - \Delta r)}{8\Delta t} \right) + hr_s T_A + \frac{\rho H \Delta r (4r_s - \Delta r) \Delta X}{8\Delta t} \quad (A1.14)
 \end{aligned}$$

Equations (A1.4), (A1.9) and (A1.14) can be arranged into a tridiagonal form for the solution of temperature at any time step, employing Thomas' algorithm [57].

Appendix 2 - Mechanical Properties of Laboratory Steels

The following series of tables contains the results for mechanical testing of laboratory test rods. Included are the yield strength, the ultimate tensile strength and the % reduction in area.

Table A2.1 - Results of mechanical tests on laboratory Steel C (1038).

Test Rod #	Sample #	Diameter (mm)	Y.S. (MPa)	U.T.S. (MPa)	%R.A.
C1	1	6.20	424.7	662.1	62.4
	2	6.22	416.1	658.9	63.9
C2	1	6.30	418.9	661.6	62.5
	2	6.25	408.4	670.2	63.0
C3	1	6.83	419.8	641.8	61.9
	2	6.25	418.9	645.5	62.2
C4	1	6.15	401.0	643.1	61.4
	2	6.10	390.9	649.3	62.0
C5	1	3.86	457.9	689.6	65.7
	2	3.86	459.8	689.6	66.3
	3	3.86	444.6	689.6	65.7
	4	3.89	470.6	695.7	66.2
C6	1	3.76	418.8	671.3	64.5
	2	3.78	425.1	668.3	65.6
	3	3.89	410.6	660.0	65.6
	4	3.78	427.1	668.3	65.6
C7	1	3.86	423.7	659.2	62.0
	2	3.84	419.7	658.4	64.0
	3	3.89	408.8	654.4	62.5
	4	3.89	421.9	660.0	65.0

Table A2.2 - Results of mechanical tests on laboratory Steel B (1070).

Test Rod #	Sample #	Diameter (mm)	Y.S. (MPa)	U.T.S. (MPa)	%R.A.
B1	1	8.81	466.6	893.1	45.9
	2	8.41	-	-	40.6
B2	1	8.71	451.4	870.8	46.4
	2	8.86	457.0	885.1	45.9
B3	1	8.76	447.3	870.7	45.3
	2	8.76	457.3	884.0	45.3
B4	1	8.79	441.4	865.3	44.3
	2	8.79	452.1	878.5	45.3
B5	1	6.25	501.2	910.3	50.0
	2	6.25	508.5	921.2	49.5
B6	1	6.25	507.7	917.5	49.1
	2	6.30	504.6	914.2	49.4
B7	1	6.30	477.4	887.8	49.9
	2	6.27	493.6	906.5	46.4
B8	1	6.25	466.5	884.8	46.8
	2	6.10	470.9	884.0	49.3
B9	1	3.91	525.6	927.3	55.1
	2	3.84	546.7	939.4	54.1
	3	3.89	480.0	915.0	55.9
	4	3.76	513.0	937.8	53.6
B10	1	3.73	518.0	920.2	50.0
	2	3.78	529.9	925.3	52.8
	3	3.81	476.0	916.9	52.7
	4	3.84	510.1	922.1	54.0
B11	1	4.09	421.6	880.5	53.8
	2	4.11	448.2	899.8	53.0
	3	4.11	456.6	901.5	53.7
	4	4.06	430.4	912.2	53.2

Table A2.3 - Results of mechanical tests on laboratory Steel D (1037).

Test Rod #	Sample #	Diameter (mm)	Y.S. (MPa)	U.T.S. (MPa)	%R.A.
D1	1	6.27	443.2	628.8	64.1
	2	6.25	446.8	675.3	63.4
D2	1	6.17	449.0	628.1	64.5
	2	6.12	439.1	631.0	54.3
D3	1	6.17	430.4	622.2	63.3
	2	6.25	-	626.0	64.6

Table A2.4 - Results of mechanical tests on laboratory Steel E (1020).

Test Rod #	Sample #	Diameter (mm)	Y.S. (MPa)	U.T.S. (MPa)	%R.A.
E1	1	6.25	404.7	441.0	71.8
	2	6.15	302.0	439.2	72.9
E2	1	6.17	309.2	434.9	72.4
	2	6.12	301.7	434.5	72.7
E3	1	6.17	320.4	435.6	72.4
	2	6.07	315.1	437.2	71.9
E4	1	6.12	330.3	427.0	72.0
	2	6.12	311.4	426.2	72.3
E5	1	3.89	328.1	453.8	74.0
	2	3.86	342.0	452.2	73.7
	3	3.96	292.2	447.3	75.5
	4	3.89	333.8	451.9	73.5
E6	1	3.89	-	466.9	72.4
	2	3.78	322.3	448.8	72.6
	3	3.81	329.7	448.7	72.4
	4	3.99	299.2	447.0	73.8
E7	1	3.89	271.9	442.5	73.0
	2	3.89	307.5	438.8	74.0
	3	3.89	318.8	438.8	73.5
	4	3.89	-	438.8	74.0

Appendix 3 - Mechanical Properties of Plant Trial Steels

The following series of tables contains the results for mechanical testing of plant trials rods. Included are the yield strength, the ultimate tensile strength and the % reduction in area.

Table A3.1 - Results of mechanical tests on plant trials Steel C (1038).

Test Rod #	Sample #	Diameter (mm)	Y.S. (MPa)	U.T.S. (MPa)	%R.A.
C51	1	8.84	432.1	657.5	61.0
	2	8.84	438.6	658.3	61.0
C52	1	8.84	428.1	652.1	61.8
	2	8.87	440.4	650.9	60.1
C53	1	8.84	440.8	659.7	61.3
	2	8.81	437.5	660.6	60.8
C54	1	8.81	458.6	670.8	60.5
	2	8.81	458.6	671.1	61.6
C55	1	8.81	432.4	659.1	59.1
	2	8.81	446.9	656.9	59.9
C56	1	8.81	434.5	656.9	59.1
	2	8.81	403.2	648.9	60.2
C57	1	8.81	444.7	658.4	59.3
	2	8.81	433.1	663.5	59.9
C58	1	8.84	434.3	631.4	61.8
	2	8.84	456.0	665.2	61.0
C59	1	8.84	435.0	653.2	59.6
	2	8.84	435.3	652.8	59.6
C60	1	8.84	458.9	667.0	60.7
	2	8.84	444.4	667.0	60.1
C61	1	8.84	431.4	651.9	59.9
	2	8.84	433.5	651.9	59.3
C62	1	8.84	423.4	645.2	59.6
	2	8.81	424.0	648.9	59.1

Table A3.2 - Results of mechanical tests on plant trials Steel E (1020).

Test Rod #	Sample #	Diameter (mm)	Y.S. (MPa)	U.T.S. (MPa)	%R.A.
E51	1	8.79	250.8	407.0	69.2
	2	8.81	272.7	413.4	69.8
E52	1	8.81	266.8	403.9	69.3
	2	8.81	269.8	403.9	68.8
E53	1	8.79	293.7	416.6	69.4
	2	8.84	296.5	416.9	70.0
E54	1	8.84	283.5	416.1	70.8
	2	8.81	293.1	420.0	71.3
E55	1	8.81	274.9	414.9	69.3
	2	8.84	299.4	419.8	71.0
E56	1	8.84	297.2	417.8	71.5
	2	8.81	300.8	419.2	71.1
E57	1	8.81	289.5	414.1	69.3
	2	8.84	297.2	413.2	70.0
E59	1	8.81	296.7	418.5	70.8
	2	8.76	354.1	420.1	71.0
E60	1	8.79	319.0	423.2	72.4
	2	8.74	311.6	423.6	71.6

Table A3.3 - Results of mechanical tests on plant trials Steel F (1080).

Test Rod #	Sample #	Diameter (mm)	Y.S. (MPa)	U.T.S. (MPa)	%R.A.
F52	1	4.70	613.1	1027.3	46.4
	2	4.57	620.1	1029.5	47.3
F53	1	4.60	546.7	984.8	44.7
	2	4.62	559.1	989.7	47.6
F54	1	4.67	561.4	993.2	44.6
	2	4.70	548.9	990.1	43.2
F55	1	4.70	540.0	979.9	45.8
	2	4.70	525.9	964.5	46.4
F56	1	4.60	519.9	946.0	47.2
	2	4.62	524.7	952.7	49.1
F58	1	4.67	549.7	986.7	46.5
	2	4.62	543.2	985.8	47.8
F59	1	4.67	531.6	964.6	45.8
	2	4.62	519.4	953.2	45.9
F60	1	4.65	576.8	996.3	46.5
	2	4.65	561.0	985.8	46.5
F71	1	3.91	564.4	1065.9	48.0
	2	3.89	603.7	1063.0	46.6
F72	1	3.89	558.7	1087.3	42.8
	2	3.84	548.6	1068.3	42.8
F73	1	3.91	564.4	1015.9	42.7
	2	3.76	611.3	1016.2	42.1
F74	1	3.89	502.4	986.1	45.1
	2	3.86	493.9	982.0	45.9
F75	1	3.91	621.8	1088.1	47.3
	2	3.84	623.7	1101.1	44.4
F76	1	3.89	568.0	1083.6	43.5
	2	3.84	641.0	1087.6	45.2
F77	1	3.91	570.0	1064.1	42.7
	2	3.96	568.3	1066.2	46.6
F78	1	3.91	627.3	1082.6	45.0
	2	3.89	599.9	1098.6	45.1
F79	1	3.89	588.7	1036.7	50.3
	2	3.86	566.0	1035.2	48.9

Table A3.4 - Results of mechanical tests on plant trials Steel G (1037).

Test Rod #	Sample #	Diameter (mm)	Y.S. (MPa)	U.T.S. (MPa)	%R.A.
G52	1	4.65	398.5	600.4	63.7
	2	4.70	404.0	605.4	62.4
G54	1	4.67	394.2	643.1	62.0
	2	4.67	389.0	649.6	63.1
G55	1	4.62	418.7	609.5	64.9
	2	4.65	430.0	604.3	64.7
G56	1	4.67	422.7	608.1	65.1
	2	4.65	415.5	606.9	64.8
G57	1	4.65	423.4	592.5	62.1
	2	4.67	407.1	592.5	62.6
G58	1	4.70	406.6	605.4	65.0
	2	4.72	451.7	608.3	64.9
G60	1	4.60	399.3	607.0	64.5
	2	4.62	405.4	606.8	63.8
G61	1	4.75	471.9	611.2	63.7
	2	4.67	404.5	597.7	63.6

Table A3.5 - Results of mechanical tests on plant trials Steel H (1035).

Test Rod #	Sample #	Diameter (mm)	Y.S. (MPa)	U.T.S. (MPa)	%R.A.
H51	1	3.86	-	666.7	67.5
	2	3.73	384.0	644.0	67.1
H52	1	3.86	399.0	653.4	67.5
	2	3.96	414.9	642.2	66.3
H53	1	3.89	359.9	635.5	66.2
	2	3.86	368.5	640.1	66.9
H54	1	3.91	366.4	638.4	64.8
	2	3.89	361.8	641.1	66.2
H55	1	3.71	395.4	654.9	66.1
	2	3.73	410.4	646.0	67.8
H56	1	3.91	421.9	662.5	67.2
	2	3.71	416.0	661.1	67.9
H57	1	3.71	383.1	636.4	67.3
	2	3.94	369.1	635.8	67.6
H58	1	3.76	370.8	633.4	66.4
	2	3.76	416.9	639.4	63.9
H59	1	3.84	354.2	583.3	69.4
	2	3.84	292.6	581.3	70.0
H60	1	3.91	401.6	649.5	67.2
	2	3.79	367.7	-	-

Table A3.6 - Results of mechanical tests on plant trials Steel I (1017).

Test Rod #	Sample #	Diameter (mm)	Y.S. (MPa)	U.T.S. (MPa)	%R.A.
I51	1	4.67	380.3	436.7	68.6
	2	4.62	322.8	421.4	70.3
I52	1	4.57	356.4	420.7	70.6
	2	4.60	352.2	418.6	69.0
I53	1	4.65	313.4	436.5	70.6
	2	4.72	317.2	435.2	70.6
I55	1	4.62	309.5	432.0	71.7
	2	4.60	377.6	434.6	69.0
I56	1	4.62	346.1	433.9	71.2
	2	4.65	315.3	430.6	70.1
I57	1	4.62	274.3	433.3	69.8
	2	4.62	274.3	434.6	70.8
I58	1	4.57	276.6	433.9	70.1
	2	4.65	281.8	438.4	71.1
I59	1	4.67	343.4	412.9	70.0
	2	4.65	291.7	417.5	68.7
I60	1	4.57	258.7	414.5	70.1
	2	4.57	322.4	417.2	69.6
I61	1	4.62	291.5	434.6	71.7
	2	4.62	279.6	437.2	70.8

Table A3.7 - Results of mechanical tests on plant trials Steel J (1022).

Test Rod #	Sample #	Diameter (mm)	Y.S. (MPa)	U.T.S. (MPa)	%R.A.
J51	1	3.89	304.3	532.4	76.6
	2	3.86	275.4	531.9	75.3
J52	1	3.76	304.7	533.2	75.5
	2	3.86	307.7	531.9	76.3
J53	1	3.89	301.8	536.2	78.1
	2	3.86	315.3	539.5	77.8
J54	1	3.89	307.4	545.5	77.1
	2	3.89	292.4	539.9	76.6
J55	1	3.86	341.9	547.1	77.3
	2	3.71	337.4	541.6	78.0
J56	1	3.84	315.7	539.0	76.5
	2	3.89	303.7	541.8	76.6
J57	1	3.79	316.3	537.7	77.9
	2	3.86	315.3	543.3	75.8
J58	1	3.73	310.8	530.2	77.3
	2	3.86	315.3	539.5	76.8
J59	1	3.76	336.7	541.2	75.0
	2	3.84	315.7	537.1	78.5
J60	1	3.94	306.9	539.0	77.2
	2	3.86	345.7	539.5	77.3

Appendix 4 - Results of Electron Probe Micro-Analysis for Manganese Segregation

Results of the electron probe micro-analysis investigation into segregation of manganese in the laboratory and plant trials steels are included in Figs. A4.1 to A4.8. The Mn concentrations, measured by EPMA, are plotted as a function of position in the cross-section of the rod. Also supplied in each figure is the Mn concentration as supplied by Stelco Inc., which was determined by spectrographic analysis. Excellent agreement between the two methods for determining manganese is seen in the plots. Also evident is that Mn shows no signs of segregation in any of the steel grades investigated.

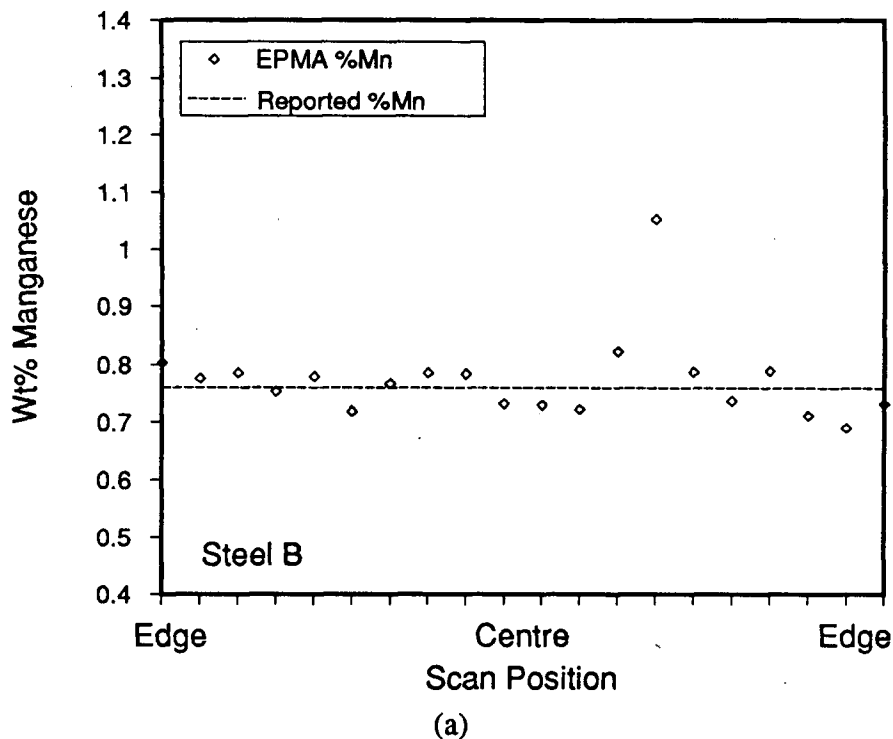


Fig. A4.1 - Manganese concentrations measured by EPMA, as a function of position in the rod. The dashed line represents the results of the spectrographic analysis. (a) Steel B (1070).

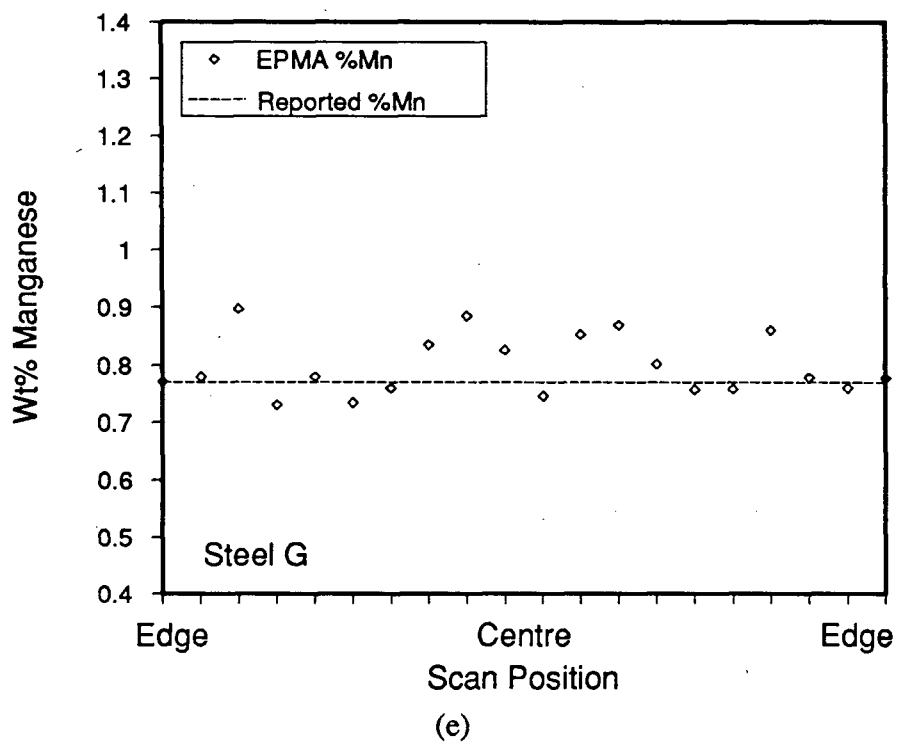
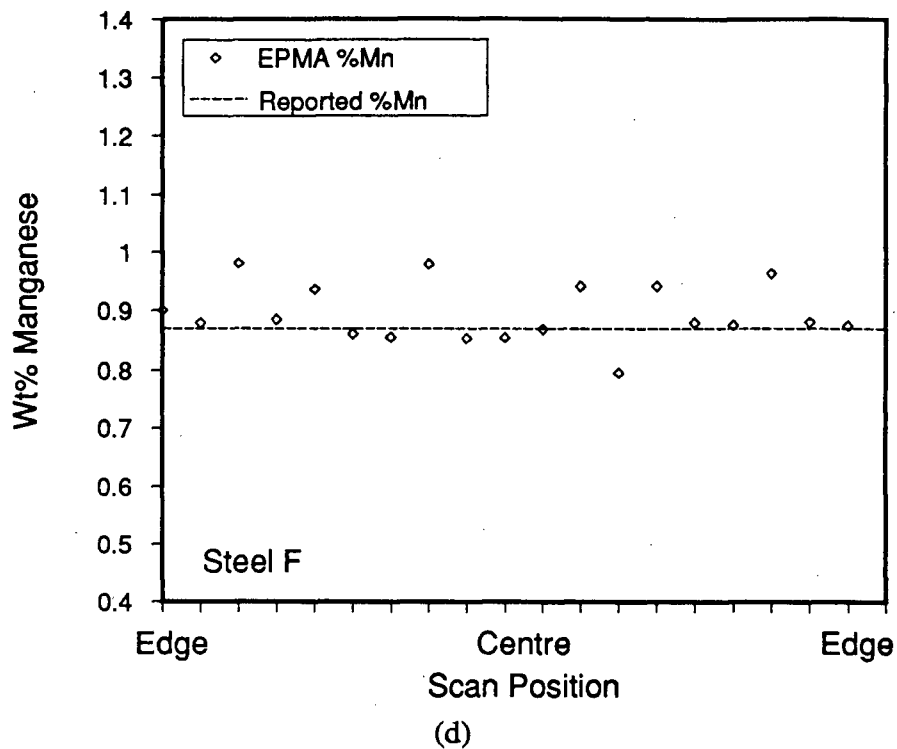
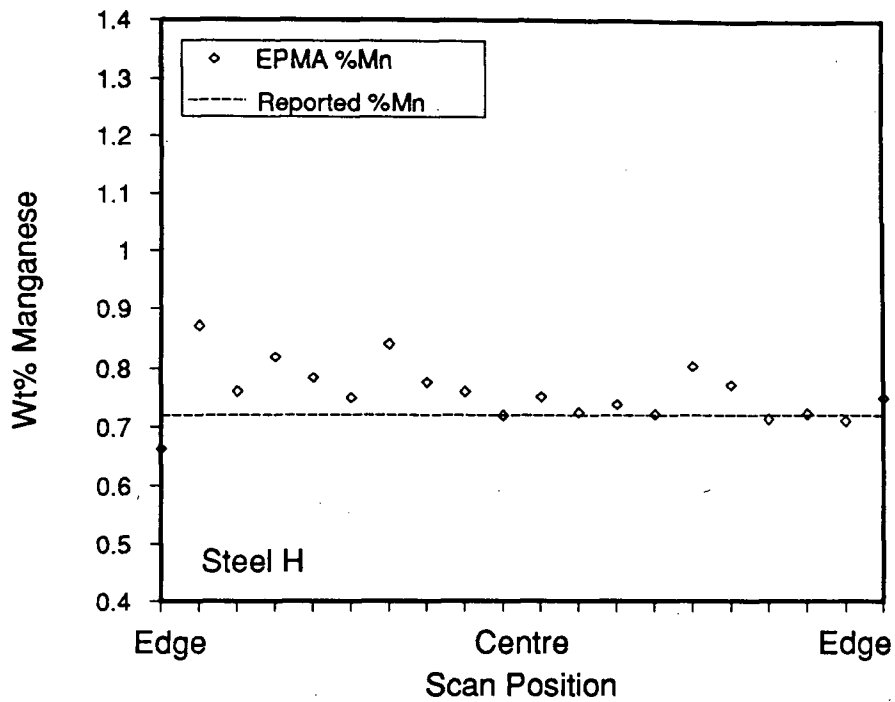
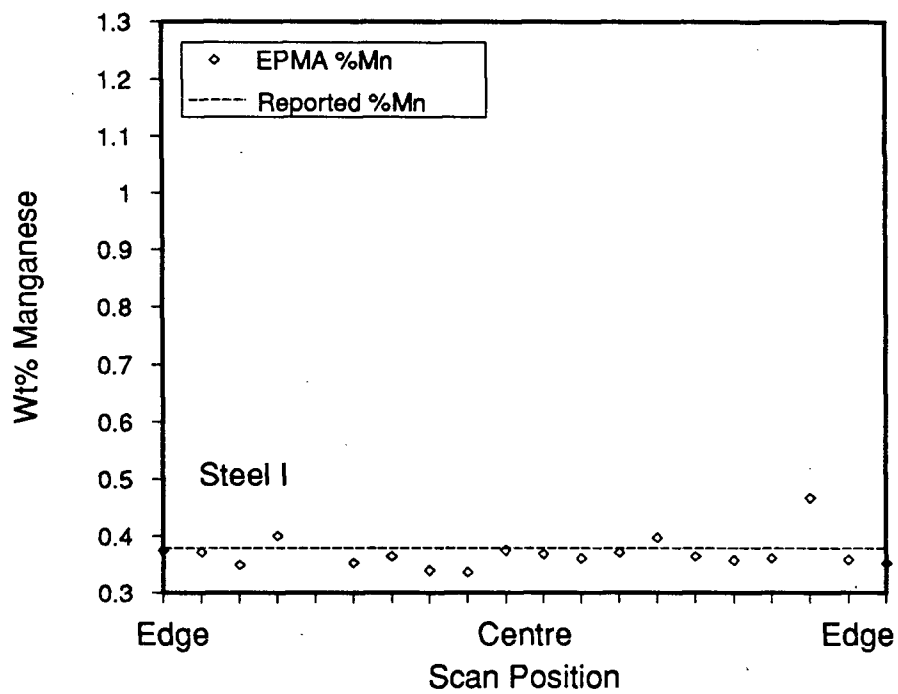


Fig. A4.1 - Manganese concentrations measured by EPMA, as a function of position in the rod. The dashed line represents the results of the spectrographic analysis. (d) Steel F (1080), (e) Steel G (1037).



(f)



(g)

Fig. A4.1 - Manganese concentrations measured by EPMA, as a function of position in the rod. The dashed line represents the results of the spectrographic analysis. (f) Steel H (1035), (g) Steel I (1017).

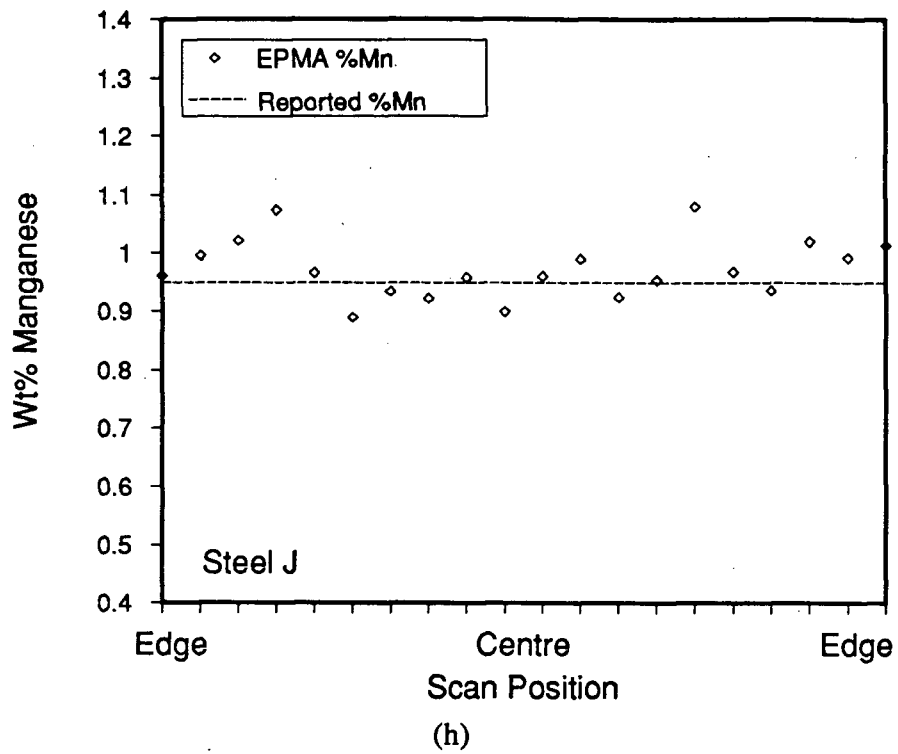


Fig. A4.1 - Manganese concentrations measured by EPMA, as a function of position in the rod. The dashed line represents the results of the spectrographic analysis. (h) Steel J (1022).